PROCEEDINGS OF THE CEReS INTERNATIONAL SYMPOSIUM ON REMOTE SENSING

"MONITORING OF ENVIRONMENTAL CHANGE IN ASIA"

December 16-17, 2003
Center for Environmental Remote Sensing,
Chiba University, Japan

CEReS
Center for Environmental Remote Sensing,
Chiba University

Published by the Center for Environmental Remote Sensing,
Chiba University,
1-33 Yayoi-cho, Inage, Chiba, 263-8522 Japan

Cover image ; SeaWiFS Project, NASA/Goddard Space Flight Center, and ORBIMAGE
Collage designed by T. Ishiyama

当シンポジウムの開催資金の一部は
「財団法人ちば国際コンベンションビューロー」
の援助によりました

Proceedings of The CEReS International Symposium on Remote Sensing

"Monitoring of Environmental Change in Asia"

December 16-17, 2003
Center for Environmental Remote Sensing,
Chiba University, Japan

(Editors)
T. Ishiyama, C. Hongo and R. Tateishi

Proceedings of The CEReS International Symposium on Remote Sensing "Monitoring of Environmental Change in Asia"

Contents

Keynote

Land Cover Change

Terrestrial Ecosystem Dynamics

Water and Carbon in Biosphere

Ocean Primary Productivity

Sea Ice and Snow Cover

Earth Radiation Budget

Atmospheric Gases

Observation and Data Archive System for RS

Keynote

Supporting Multi-national Environmental Conventions and Terrestrial Carbon Cycle Science by Remote Sensing

A. Rosenqvist, M. Shimada, T. Igarashi, M. Watanabe, T. Tadono and H. Yamamoto
Japan Aerospace Exploration Agency, Earth Observation Research & Applications Center
Harumi Triton Square X-23F, Harumi 1-8-10, Chuo-ku, Tokyo 104-6023, Japan
E-mail: ake.rosenqvist@jaxa.jp

Abstract

Climate change and environmental degradation are issues of major concern amongst the general public in most parts of the world, as our current actions affect us now and for generations to come, at any level from local to national, to regional and global. In efforts to curb and reverse the current destructive trends, a number of environmental conventions and declarations have been discussed and, in some cases, ratified. To adequately follow-up implementation however, requires the availability of systems for monitoring and surveillance of the environment and its changes over time, and given the spatially extensive, cross-border nature of the human-induced and natural phenomena concerned – e.g. fire, land cover change, drought - Earth Observation techniques have a natural potential to substantially support this cause, if properly integrated with field measurements and ancillary data.

This paper describes the Kyoto & Carbon Initiative, which is an international collaborative project initialised in 2000 by NASDA (since Oct. 2003 known as JAXA), that is set out to support data- and information needs raised by certain multi-national environmental conventions and by global carbon cycle science, through provision of data products and high level information derived from ALOS, JERS-1 and ADEOS-II data [1]. The conventions primarily in focus are the UNFCCC Kyoto Protocol and the Ramsar Convention on Wetlands, to which fine-resolution, multi-scale information about the status and changes in forests and wetlands will be derived. There is apparent synergy with terrestrial carbon cycle science information needs, where improved spatial information about carbon pools, sources and sinks at local, regional to global scales are of high priority. The Kyoto & Carbon Initiative is also set out to support the UN Millennium Development goal on water access, as well as to the UN Convention to Combat Desertification.

Recognising the limited usefulness of the fragmented and local-focus data observation schemes characteristic for most fine resolution Earth Observation missions to date, dedicated Data Acquisition Strategies are being implemented for ALOS (launch 2005) and ADEOS-II (Dec. 2002 – Oct. 2003), with particular emphasis on ALOS' polarimetric L-band Synthetic Aperture Radar (PALSAR) and the 250 metre resolution Global Imager (GLI) sensor on ADEOS-II.

1. Background

1.1 The UNFCCC and the Kyoto Protocol

Climate change, caused by the rapid and uncontrolled increase of greenhouse gases in the Earth's atmosphere during the past 150 years, is a major public, political and scientific concern worldwide. Public concern resulted in the 1992 United Nations Framework Convention on Climate Change (UNFCCC) and subsequently the Kyoto Protocol (1997), which demonstrate an official acknowledgement of the climate change phenomenon as such, as well as a recognition by most national policy makers that immediate cross-border actions are required to halt and reverse the current destructive trend. If ratified, the Kyoto Protocol will provide legally binding national emission reduction commitments and a timetable for implementation. Although politically controversial, the Protocol not only constitutes a landmark agreement for the global environment, but also for the international scientific community in that it puts political pressure for quantitative measurements of carbon sources and sinks with high, verifiable accuracy.

1.2 Global carbon cycle science

Viewing the climate change issue in a broader context than the Kyoto Protocol, the central role of the global carbon cycle has long been recognised by the international science community. The major concern here is incomplete understanding of the processes that govern the global carbon cycle, and the large uncertainties that are associated with current models and measurements. These uncertainties are partly results of lack of appropriate data or inadequacy of existing data sets. This deficiency is being addressed by the Integrated Global Observing Strategy Partnership (IGOS-P), which calls for a united multi-disciplinary scientific effort to resolve the present uncertainties, through the establishment of a dedicated global carbon cycle observation strategy. This strategy involves characterisation of the terrestrial, atmospheric and oceanic components of the carbon cycle by synergetic utilisation of *in situ*, modelling and other measurement techniques, including remote sensing.

Although carbon cycle science thematically is more exhaustive than the Kyoto Protocol, we note that both relate to the same basic information needs—that for accurate measurements of carbon sources and sinks—and research and support to one topic will thus inevitably also benefit the other.

1.3 The Ramsar Convention on Wetlands

The Ramsar Convention, signed 1971 in Ramsar, Iran, is an intergovernmental treaty, which provides the framework for national action and international co-operation for wetlands and their resources. The mission of the convention is the conservation and wise use of all wetlands through local, regional and national actions and international co-operation, as a contribution towards achieving sustainable development throughout the world (Ramsar COP8, 2002). The Ramsar Convention relies on voluntary actions by the signatory parties—thereby making it less controversial than the Kyoto Protocol—and it aims to halt and reverse the global trends of wetland degradation and destruction through the dissemination of information, involvement of local communities and establishment of sustainable management plans.

Wetlands International is an official International Organisation Partner of the Convention and acts as a specialist adviser and provider of data on wetland inventory as well as managing, under contract, the Convention's Ramsar Sites Database. The importance of remote sensing technology in this context is evident as adequate access to up-to-date spatial and temporal information about the wetlands and their catchment basins is a fundamental component in the development of wetland management plans for conservation and sustainable utilisation.

While not explicitly addressed by the Ramsar Convention, it is furthermore well known that both natural and anthropogenic wetlands (e.g. rice paddies) constitute significant sources of atmospheric methane, CH_4, thereby linking also the wetlands issue to carbon science. As the emissions from wetlands are poorly quantified over regional to global scales, improved understanding of wetland inundation dynamics is of high priority in the climate change context.

1.4 WSSD & UNCCD

Adequate access to freshwater for all people in the world is a critical need, which has been raised during several international meetings and fora during the past few years, most notably during the World Summit on Sustainable Development (WSSD) in Johannesburg in 2002. The WSSD Implementation Plan states the over-reaching goal to "halve, by the year 2015, the proportion of people who are unable to reach or afford safe drinking water as outlined in the UN Millennium Declaration...". The situation is most acute in arid and semi-arid areas, with particular emphasis on the African continent and central Asia, which also are the regions most severely affected by land degradation and desertification, as addressed by the 1994 UN Convention to Combat Desertification (UNCCD).

Remote sensing data can contribute as a tool for water prospecting, as well as for monitoring and mapping of land vulnerability in support to action plans aiming to halt and reverse degradation.

2. The Kyoto & Carbon Initiative

2.1 Outline

The Kyoto & Carbon Initiative is based on the conviction that remote sensing technology can play a significant role in supporting some of the information needs posed by both certain environmental treaties and by carbon cycle science. In a report by the Terrestrial Carbon Theme Team of IGOS-P, the need for such support was voiced: *"The challenges [to a terrestrial carbon observation strategy] are to ensure that important existing observations continue and key new observations are initiated [and] to identify activities and agencies willing to contribute to establishing global carbon observations..."* [2].

The Kyoto & Carbon Initiative should be seen as a response by JAXA to this call.

Led by the Earth Observation Research and Applications Center (EORC) of JAXA, the Initiative is being established as an international collaborative project, building on the existing network established within the JERS-1 Global Forest Mapping project [3]. A decentralised organisation is being implemented, set up around four main themes, each supported by the K&C systematic data observation strategies:

(i) Forest and Land Cover Change
Focused to support the Kyoto Protocol and the part of the carbon research community concerned with CO_2 fluxes from terrestrial sinks and sources.

(ii) Wetlands & CH_4
Serving Ramsar information needs and the significance of wetlands from a CH_4 perspective.

(iii) Desert & Water
Addressing issues relevant to water supply and land degradation in arid areas.

(iv) Mosaic Products
Generation of satellite image mosaics, primarily to be utilised as intermediate products by the K&C science team, the mosaics will also be made available in the public domain.

2.2 Systematic Data Observation Strategies

2.2.1. Fragmented data archives

Climate change and environmental degradation are cross-border multi-scale phenomena, which require the availability of systematic and consistent data sets at local, regional and global scales. This fundamental need for coherent multi-scale data applies both to environmental convention support as well as in the carbon cycle context, and it is highlighted in Article 10(d) of the Kyoto Protocol which states that countries shall *"co-operate in scientific and technical research and promote the maintenance and the development of systematic observation systems and development of data archives to reduce uncertainties related to the climate system, [and] the adverse impacts of climate change..."*.

Provision of systematic observations and establishment of data archives for long-term studies is clearly one of the *potential* strengths of Earth Observation from space. However, fine resolution remote sensing data are generally not acquired homogeneously over large areas, but instead most often collected with local focus over sites that have been specifically requested by commercial or scientific users. This results in inconsistent and fragmented data archives that are inadequate for any application that require extrapolation of locally developed methods and results to a regional or global scale context.

The need for improved data observations is acknowledged by IGOS-P, who states that *"it is evident that further progress in our understanding of the global carbon cycle and its likely future evolution depends on improved observations of the terrestrial carbon processes"*[2]. Hence, if we are indeed serious in our objectives to support climate change research and convention support on anything but local scales, it is imperative that data acquisitions are planned in a systematic manner, with regional-continental scale coverage, fixed sensor characteristics, and adequate temporal repetition frequency (Figure 1).

JAXA has acknowledged the critical need for consistent data and by setting aside a significant share of the ALOS PALSAR and ADEOS-II GLI acquisition capacities for this purpose, allowed the establishment of an unprecedented, global Data Observation Strategy in support to climate change research and environmental conventions, as outlined within the Kyoto & Carbon Initiative.

Figure 1. Mainland Southeast Asia. Example of systematic data observations over regional scales: 35 JERS-1 SAR passes acquired consecutively during a 35-day period in Jan.-Feb.1997. © NASDA/METI

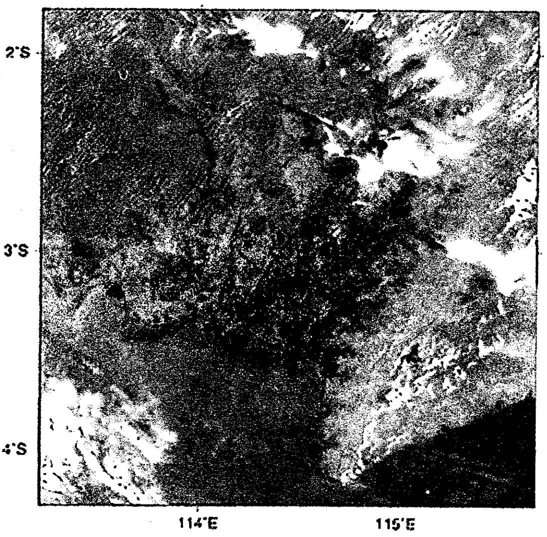

Figure 2. Extract from a wide swath (1600 km), medium resolution (250 m) coverage by ADEOS-II Global Imager (GLI) over southern Kalimantan, Indonesia, 21 February, 2003. © NASDA

2.2.2 The PALSAR Observation Strategy

The Advanced Land Observing Satellite (ALOS) is scheduled for launch in 2005 and it will operate with 46-day repeat orbit and 70 km swath. The Synthetic Aperture Radar (PALSAR) on ALOS is an active microwave instrument, which thus can acquire data regardless of sunlight and cloud cover. And like its predecessor on JERS-1, the radar instrument operates with a wavelength (L-band; 23.5 cm) that is particularly sensitive to vegetation structure and inundation state, hence making it particularly suitable for environmental monitoring.

In the design of the PALSAR systematic data observation strategy, focused on the collection of data for geo- and biophysical parameter retrieval over regional scales, the following basic acquisition concepts - outlined in [4] - have been taken into account:

1. Spatial and temporal consistency over regional scales (i.e. continental-scale coverage within short time windows);
2. Adequate revisit frequency (i.e. acquisition repetition adapted to the individual forest-, wetlands- and desert thematic needs);
3. Accurate timing (targeting acquisitions to the most suitable season);
4. Consistent sensor configuration (limiting the number of sensor modes used, to increase intercomparability and regional homogeneity, and to minimise internal acquisition conflicts);
5. Long-term continuity (annual repetition of the strategy to the end of mission).

The draft K&C observation strategy for PALSAR comprises full global acquisitions at fine resolution (20 metres) twice per year during the mission lifetime. Observations are timed to be performed once during summer season (or dry season in the tropical zone) and once during the winter season (tropical rainy season). The intention is to establish an extensive global archive of PALSAR data, in which consistent time-series of fine resolution data is to be available for any arbitrary point on the Earth. This part of the acquisition plan is primarily designed to fulfil the data requirements pertaining to the Forest and Land Cover Change, and the Desert & Water themes, and it comprises the annual acquisition of more than 235,000 PALSAR scenes at fine resolution.

In support to the Wetlands & CH4 objectives, in which more frequent acquisitions than semi-annual are required to capture the rapid seasonal changes in wetland inundation or paddy growth that occur (see 2.4 below), every 46-day coverage during one full year using the 100 metre resolution (ScanSAR) mode are planned. These cover a selection of significant wetland and paddy areas on the globe, amounting to some 13,000 ScanSAR scenes to be acquired annually.

2.2.3 The GLI Observation Strategy

ADEOS-II (Advanced Earth Observation Satellite II) was in launched in December 2002, but was in operation only until October 2003, due to a technical failure. Amongst the six remote sensing instruments on-board, the payload included the Global Imager (GLI) - a 36-channel multi-spectral scanner. Six of the GLI bands were dedicated for terrestrial use, resembling MODIS and ETM+ in their spectral definitions, but all operating with a spatial nadir ground resolution of 250 metres. The image swath was 1600 km and the revisit cycle 4 days (Figure 2).

The Observation Strategy for GLI was designed for 4-day repeat coverage over the Asian region, over which direct downlink via Data Relay Satellite (DRTS) could be performed. Over regions out of reach for DRTS, coverage will be less frequent due to limitations in the on-board storage. The GLI-250 acquisition strategy is described in [5].

2.2.4 An archive for the future

It should be emphasised that not all data outlined within the Observation Strategies are foresee, or even intended, to be processed immediately. Rather, one of the basic objectives is to provide policymakers and science community with comprehensive data archives from which consistent PALSAR and GLI time series can be found for an arbitrary location of interest. It is believed that this type of data archive will prove useful also for applications far beyond those of convention support and carbon cycle science, for a long time to come.

2.3 The Forest and Land Cover Change Theme

2.3.1 Kyoto information requirements

While it even may be considered an obligation by the space agencies (of the ratifying countries) to actively support the UNFCCC Kyoto Protocol, it is not entirely clear what the Protocol information requirements are, and how - and if - they can be supported by remote sensing technology. In a review performed by the ISPRS in 1999 to investigate this particular issue [6], revised in 2003 [7], five main areas of potential support were identified:

1. Provision of systematic observations of relevant land cover (Art. 5, 10d);
2. Support to the establishment of a 1990 carbon stock baseline (Art. 3.1);
3. Detection and spatial quantification of change in land cover (Art. 3.3, 3.4, 12);
4. Quantification of above-ground vegetation biomass stocks and associated changes therein (Art. 3.3, 3.4, 12);
5. Mapping and monitoring of sources of anthropogenic CH_4 (Art. 3, 5, 10).

While topic #2 is out of scope for the Kyoto & Carbon Initiative, the remaining four points are very relevant. The requirement for systematic observations (#1) has been adequately addressed in the Systematic Observation Strategies for PALSAR and GLI described above and will not be dealt with further here. The last point on anthropogenic CH_4 sources (#5) will be discussed under the Wetlands Theme below (§2.4). Topics 3 and 4 however, relating to detection and quantification of changes in forest- and land cover, constitute the main focus within this theme.

2.3.2 Kyoto definitions

Central in this context is Article 3.3 in the Protocol and the key concepts of forest and afforestation, reforestation and deforestation (ARD). *Forest* was defined at the UNFCCC COP7 meeting in Marrakesh as *"a minimum area of land of 0.05-1.0 hectares with tree crown cover, or equivalent stocking level, of more than 10-30 % and containing trees with the potential to reach a minimum height of 2-5 m at maturity"* [8]. The definition to be adopted by a country is optional within the intervals given for minimum area and crown cover.

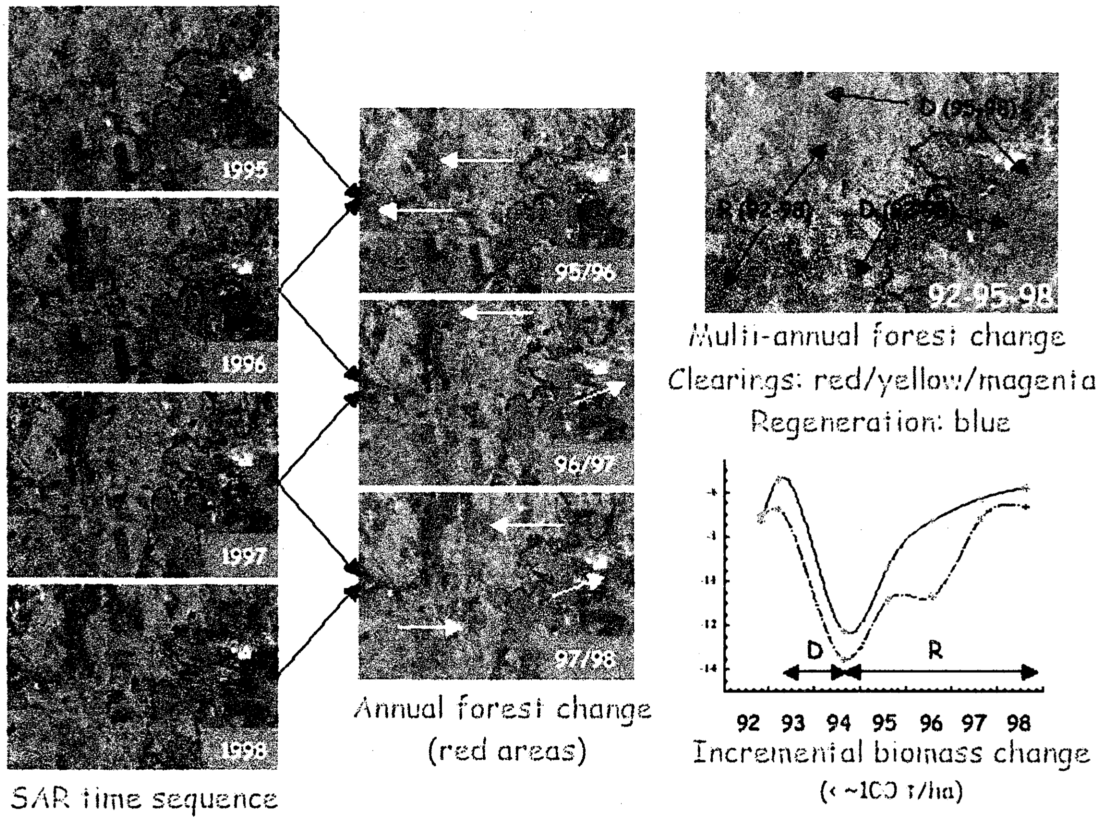

Figure 3. Simple approach for detection and spatial quantification of change in land cover ("ARD monitoring"), by using a consistent time-series of SAR data (far left), acquired systematically during the same season every year. Annual change images (centre) indicate clearfellings performed between two consecutive years, which appear in red colour. A multi-year image composite (right, top) also reveals regeneration (blue colour, indicated by "R"). The diagram (right, bottom) illustrates changes in radar backscatter over time, flowing deforestation (D) and subsequent, regeneration. © NASDA/METI

Afforestation is defined as direct human-induced (DHI) conversion of land that has not been forested for a period of at least 50 years, while *reforestation* implies DHI conversion of previously forested land that did not contain forest on Dec. 31, 1989. *Deforestation* is simply defined as the DHI conversion of "forest" to "non-forest" [8].

Important to note is that forest and ARD activities within Kyoto are defined on the basis of change in *land use*, rather than of land cover as is observed by remote sensing. This implies that distinction of land belonging to either "forest", or the inverse "non-forest" category, and in turn recognition of A, R or D as changes between these categories, cannot be performed directly or solely in remote sensing data, without use of *in situ* or other land-use based information sources.

2.3.3 Carbon science requirements

In the context of terrestrial carbon cycle science, the basic information requirement is raised by IGOS-P: *"Estimates of above- and below- ground biomass provide fundamental information on the size and changes of the terrestrial carbon pool as land use and associated land management practices change"* [2].

Synergy with Kyoto information requirements is apparent, although the focus is on *land cover*, comprising both human-induced and natural activities. With improved understanding of the carbon budget a scientific goal, accuracy requirements are less stringent than what can expected for Kyoto Protocol implementation and verification (not yet defined), where CO_2 equivalent emissions will be associated with a financial value.

2.3.4 Forest stocks and changes

With consistent annual time series of fine resolution PALSAR data available (§2.2.2), plain identification and subsequent spatial quantification of changes in forest cover is a rather straightforward task, which to a large extent can be performed in an operational manner. The 0.05-1.0 ha minimum area requirement within Kyoto [8] implies an effective ground resolution of 20-100 metres, which is within the range of the PALSAR capacity. Figure 3 illustrates the appearance of such land cover changes in a 4-year time series of JERS-1 L-band SAR data. Although not quantified in terms of carbon changes, spatial knowledge about *where* and *when* changes have occurred, and *how large* areas that are affected, is important information to be utilised in the accounting process in combination with other data.

Retrieval of above-ground biomass stocks is a Holy Grail for carbon budget research, and while it is not an explicit Kyoto requirement, quantification of biomass loss following for instance a deforestation event, does require an estimate of the biomass levels prior to clearfelling. While biomass stock inventories in mature forest stands above the L-band sensitivity range must be ruled out, retrieval of biomass-related biophysical parameters in sparse and regenerating areas may be foreseen. It is included in the Initiative as an R/D topic, with focus on the boreal zone with biomass levels within the L-band SAR sensitivity range.

Biomass retrieval algorithms can be improved with *a priori* information about species distributions and land cover available. Archived ADEOS-II GLI data will be utilised to generate regional-scale land cover classifications at 250 m resolution over the Asian continent to complement the 1 km classifications presently available.

2.4 The Wetlands & CH4 Theme

2.4.1 Wetlands and CH4

Irrigated rice is a significant anthropogenic source of CH_4 which is not currently included within the Kyoto Protocol, but may have to be accounted for in the future. Rice paddy is easily distinguishable in time series of SAR data, from which cultivated area, timing and number of crop cycles can be obtained (Figure 4).

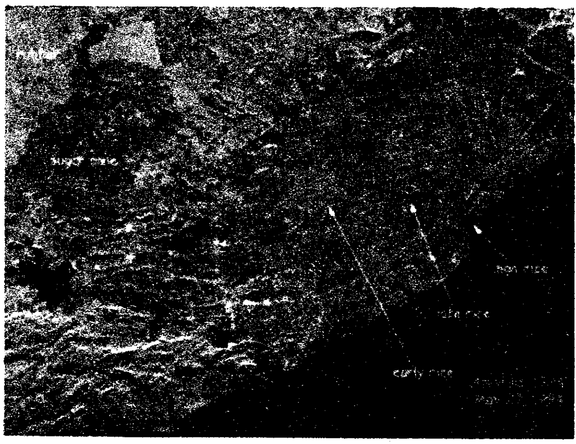

Figure 4. Irrigated rice (Perlis, Malaysia). Multi-temporal JERS-1 SAR. Rice paddy can be distinguished from other land use/land cover classes through its characteristic temporal signature. Local variations in the crop cycle are visible as green and blue. © NASDA/METI

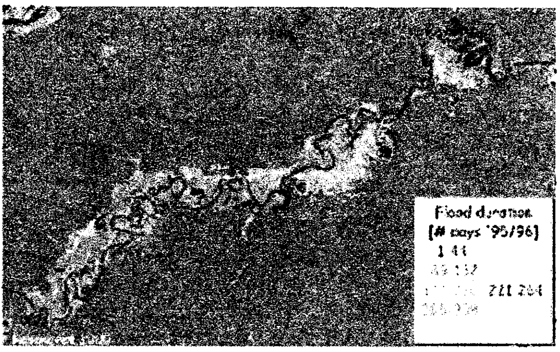

Figure 5. Flood duration map (Jaú river, Amazonas, Brazil) derived from a time-sequence of 9 consecutive JERS-1 SAR scenes, acquired during one seasonal flood cycle (Oct. 1995 - Oct. 1996). © NASDA/METI

Amongst non-anthropogenic CH_4 contributors, floodplains and wetlands areas are sources of major importance, and IGOS-P remark that *"satellite observation techniques and modelling tools should be developed to estimate methane fluxes from wetlands"*[2]. While CH_4 fluxes *per se* cannot be measured by remote sensing, key input parameters to emission models in forms of the spatial extents of flooding and its variations over time can be obtained, as demonstrated by JERS-1 SAR (Figure 5). The uniqueness and importance of L-band SAR for mapping of inundated vegetation cannot be overly emphasised, as it is the only space-borne sensor configuration with the capacity of deriving such information.

2.4.2 Wetlands and conservation

The Ramsar Convention Bureau has officially endorsed the Kyoto & Carbon Initiative, and has together with JAXA and Wetland International identified three areas where the Initiative can collaborate with, and support the convention [9]:

1. Inundation mapping;
2. Disturbance monitoring:
3. Support to a global wetlands inventory:

Inundation mapping:

Mapping of spatio-temporal characteristics of inundation phenomena in global wetlands is not only an issue for CH_4 modelling, but also from an environmental aspect as seasonal flooding is a key ecological driver. Spatio-temporal information about hydrological dynamics is at present generally not available and would be highly valued to support the development of sustainable wetland management plans. Scales of interest range from semi-continental (e.g. Amazon, Congo basins), regional (e.g. Pantanal wetlands) to local (individual Ramsar-designated sites).

PALSAR data acquired in 100 m resolution ScanSAR mode, with 46-days' repetition during a period of one full year, as outlined in the PALSAR Observation Strategy (§2.2.2) will be required to characterise the variations associated with forest inundation and rice cultivation.

Disturbance monitoring:

Identification and monitoring of human-induced and natural disturbances in both Ramsar-designated and other wetlands is another important remote sensing application. The PALSAR Observation Strategy plan for repetitive annual global fine resolution observations at 20 metres resolution will be utilised for identification and spatial assessment of changes, complemented with 250 metre GLI observations at weekly-monthly repetition.

Support to a global wetlands inventory:

As the locations and extents of wetlands in the world are not all recorded, identification and delineation of global wetland areas in support to the Ramsar Data Base, maintained by Wetlands International, is a third important contribution area where PALSAR and GLI data will be utilised. As the attributes, which characterise wetlands, differ widely, the usefulness of PALSAR and GLI data has to be evaluated on a case-by-case basis. Also the 100 metre JERS-1 SAR continental-scale mosaics generated within the Global Forest Mapping project [3] will be used to support the inventory.

2.5 The Desert & Water Theme

By incorporating the on-going SAHARASAR project [10] into the Kyoto & Carbon Initiative, we aim to support WSSD and the UN Millennium Declaration goal for access to safe drinking water. As microwave signal can penetrate dry sand layers, subsurface geomorphological and hydrological features can be revealed (Figure 6). To this end, JERS-1 SAR mosaics over Eastern Sahara have been generated in 2002. The area will be expanded to cover the entire Sahara desert and the Arabian Peninsula with dual-polarimetric ALOS PALSAR data.

2.6 International framework and scientific support

Links with national and international bodies involved in convention implementation and synergy and alignment with other international carbon- and forest related efforts—notably the CEOS Global Observations of Forest Cover (GOFC) project and the GTOS Terrestrial Carbon Observation (TCO) theme—is imperative for the Initiative, and to this end, an international Scientific Advisory Panel was established in 2001 to oversee and review the definition of the project. The 25-member panel consists of well-renowned scientists active in the fields of carbon modelling and biophysical parameter retrieval, SAR experts, representatives from Wetlands International, GTOS/TCO, FAO, GOFC, space agencies, universities and public research institutions.

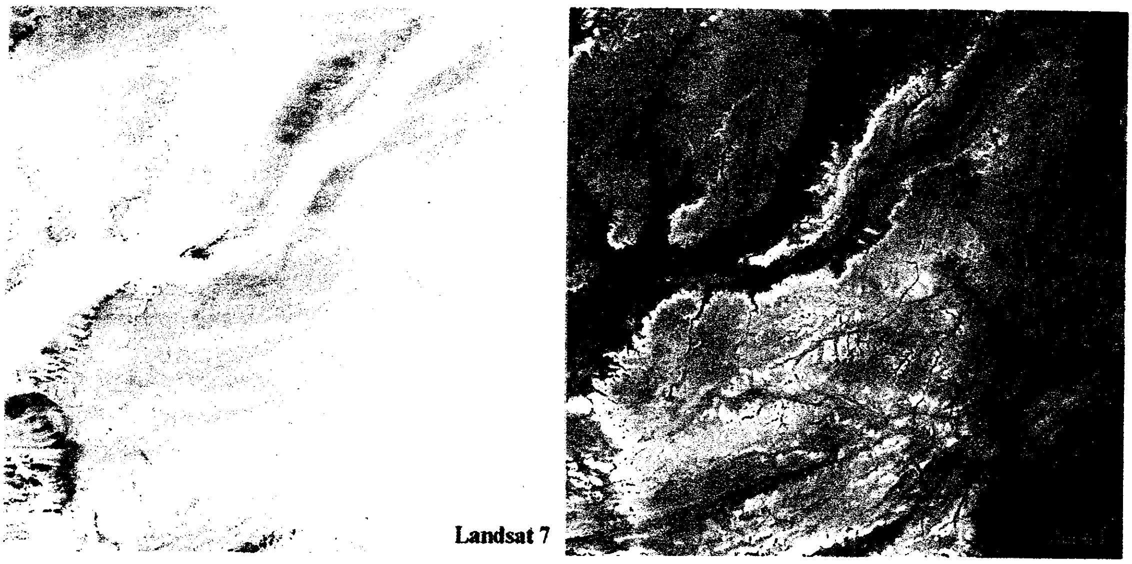

Figure 6. East Sahara as viewed by optical (left - LANDSAT ETM+ quick-look mosaic) and microwave (right - JERS-1 SAR) sensors. Devoid of soil moisture, microwave signals penetrate the dry sand layers to reveal paleo-hydrological structures and other sub-surface geomorphological structures. © NASA, © NASDA/METI

3. Acknowledgement

The present paper is a modified and up-dated version of [1].

4. References

[1] A. Rosenqvist, M. Shimada, T. Igarashi, M. Watanabe, T. Tadono and H. Yamamoto, *Support to Multi-national Environmental Conventions and Terrestrial Carbon Cycle Science by ALOS and ADEOS-II – the Kyoto & Carbon Initiative.* Proc. IGARSS'03, Toulouse, France. July 21-25, 2003.

[2] Cihlar J., *et al.* (Eds.), 2001. *IGOS-P Carbon Cycle Observation Theme: Terrestrial and atmospheric components.* A report to IGOS-P by the Terrestrial Carbon Theme Team.

[3] Rosenqvist A., Shimada M., Chapman B., Freeman A., De Grandi G.F., Saatchi S. and Rauste Y. *The Global Rain Forest Mapping Project - a review.* Int'l Journal of Rem. Sensing, 2000, Vol. 21, No. 6&7, pp 1375-1387.

[4] Rosenqvist, A., Milne T. and Zimmermann, R., 2003. *Systematic Data Acquisition—A Pre-requisite for Meaningful Biophysical Parameter Retrieval?* IEEE Trans. on Geoscience and Rem. Sensing, Communication, Vol. 41, No. 7, pp.1709-1711.

[5] A. Rosenqvist, N. Matsuura, T. Igarashi, H. Yamamoto and Y. Nakajima. *Terrestrial 250 m observations with ADEOS-II Global Imager (GLI).* Proceedings of SPIE Vol. 5234, Sensors, Systems and Next generation Satellites. Barcelona, Spain, Sept. 8-10, 2003.

[6] ISPRS, 1999. (Eds. Rosenqvist, A., Imhoff, M., Milne T. and Dobson C.). *Remote Sensing and the Kyoto Protocol: A Review of Available and Future Technology for Monitoring Treaty Compliance.* Workshop Report (159 pp.). Ann Arbor, MI, USA, Oct. 20-22, 1999. (http://www.eecs.umich.edu/kyoto)

[7] Rosenqvist, A., Milne T. Lucas R., Imhoff, M. and Dobson C., 2003. *A review of remote sensing technology in support of the Kyoto Protocol.* Environmental Science & Policy, (October 2003) Vol. 6, No. 5, pp 441-455.

[8] UNFCCC, 2001. *The Marrakesh Accords & the Marrakesh Declaration,* Seventh Conference of the Parties (COP 7), Marrakesh, Morocco, Oct.29-Nov.9, 2001. FCCC/CP/2001/13/Add.1 (Annex, sect. A).

[9] Ramsar Bureau and Wetlands International. Personal communication. October 9-10, 2002.

[10] Paillou P. and Rosenqvist, A., 2003. *The SAHARASAR Project: Potential support to water prospecting in arid Africa by SAR.*. Proc. IGARSS'03, Toulouse, France. July 21-25, 2003.

Kyoto & Carbon Initiative Home page: http://www.eorc.jaxa.jp/ALOS/kyoto/kyoto_index.htm

Land Cover Change

Global Land Cover Mapping and Change Monitoring

Ryutaro Tateishi
Center for Environmental Remote Sensing, Chiba University
E-mail: tateishi@faculty.chiba-u.jp

Abstract

This paper describes existing global land cover data, and on-going global land cover mapping projects; these projects are initiated by US Geological Survey, European Commission/Joint Research Centre, Boston University, Global Mapping project, and Japan Aerospace Exploration Agency (JAXA). Also, the present trend of global land cover mapping are explained. Furthermore, a study to extract/analyze land cover changed/unchanged areas using global AVHRR NDVI data from 1981 to 2000 is shown.

1. Introduction

Land cover is one of key environmental parameters for global environmental sciences/policies and it is also necessary for land use planning and agricultural area planning. Before the production of global AVHRR data (1992-1993), existing thematic maps were the main information sources for global land cover mapping. However these global land cover map without the use of satellite images had poor quality. After the use of global AVHRR data, global land cover mapping has developed rapidly. In this paper, presently available global land cover data and on-going projects are introduced and their characteristics and trends are explained. Land cover data shows usually land cover information of a specific time (year). Another necessary land cover information is that of changed/unchanged area. These changed/unchanged information can be extracted by time series satellite data. At the last section of this paper, a study to extract changed/unchanged areas using global time series AVHRR NDVI data is explained.

2. Existing global land cover data

The following four global land cover data derived from satellite data are available.

(1) IGBP-DISCover

The first 1-km global land cover data was developed by a U.S. Geological Survey (USGS) and other organizations. Working under the auspices of the IGBP, Loveland et al. (1999, 2000) developed and applied a global land cover characterization methodology using 1992-1993 1-km AVHRR NDVI data. The methodology is based on unsupervised classification with extensive post-classification refinement. The IGBP DISCover classification provides a general picture of global land cover based on a 17-class land cover legend. The accuracy of the IGBP DISCover land cover data was established through an independent IGBP accuracy assessment. Scepan (1999) determined that the DISCover overall accuracy was 59-71 percent depending on the specific validation procedures used.

(2) University of Maryland

A group of John Townshend and Ruth DeFries used the same satellite data as IGBP-DISCover to make a global land cover map with the different land cover legend from IGBP-DISCover land cover data. This group focuses now not on categorical classification but on the estimate of area percentage representation of basic land cover types in a pixel.

(3) Boston University

A group of Mark Friedl uses MODIS data for the global 1-km land cover classification with the same legend of 17 classes as the IGBP-DISCover. This group tries to make a global map every six months to detect land cover changes.

(4) GLC2000

The Joint Research Centre of European Commission coordinated the GLOBAL LAND COVER 2000 Project (GLC 2000) in collaboration with a network of partners around the world. The general objective of GLC2000 is to provide for the year 2000 a harmonized land cover database over the whole globe. The year Two Thousand is considered as a reference year for environmental assessment in relation to various activities, in particular the United Nation's Ecosystem-related International Conventions. To achieve this objective GLC 2000 makes use of a dataset of 14 months of pre-processed daily global data acquired by the VEGETATION instrument on board the SPOT 4 satellite. The legend of GLC2000 is defined by FAO's Land Cover Classification System (LCCS).

3. On-going global land cover mapping projects

The following four global land cover mapping projects are going on.

(1) USGS intiative
A new global land cover mapping project using MODIS 500 m data has started. The mapping will be completed within a few years.
(2) EC/JRC initiative
A new global land cover mapping project called "GLOBECOVER" using ENVISAT/MERIS 300 m data has started. The mapping will be completed within a few years.
(3) JAXA intiative
The initially planned global land cover mapping project using GLI 250 m data will not be achieved by the failure of ADEOS II satellite. However a project of land cover mapping for the whole Asia using GLI 250 m data from April to October 2003 continues.
(4) Global Mapping project
As Global Map version 2, a new global land cover map with the resolution of 1 km will be produced by the cooperation with other projects by 2007.

4. Trend of global land cover mapping

The present global land cover mapping projects have the following features and trends.
(1) global mapping of individual land cover classes
Some key land cover classes important for environmental studies such as wetland, paddy, mangrove, and lake are planned to be mapped individually in different projects.
(2) categorial data ＋ percent area cover of basic land cover types
In addition to the categorical classified land cover map, percent area cover of basic land cover types in a pixel is considered to give actual information of the ground surface. Tree, grass, cropland, urban, and bare ground are examples of basic land cover types.
(3) harmonization of land cover legend
Different land cover legends are used in different projects and in different regions. In order to covert one legend to another one, we a tool to define land cover classes by a common system. The ideal tool for this is Land Cover Classification System (LCCS) developed by FAO.
(4) improvement of resolution
1 km resolution of AVHRR data was improved to 500 m of MODIS, 300 m of MERIS, and 250 m of GLI.
(5) optical sensor ＋ SAR ＋ lidar
In addition to optical sensor data, global SAR data or lidar data may be used for global land cover mapping. SAR data have a potential to derive information of wetland and forest, and lidar data have a potential to derive vegetation height.
(6) development of global land cover ground truth data
Quality of land cover map is mainly dependent of training sample data (ground truth data) used for the classification. However ground truth data are not exchanged and accumulated. Development of global land cover ground truth data by the cooperation of different projects and for the common use will improve the quality of a land cover map.

5. Global land cover change monitoring

Using time-series AVHRR NDVI data, extraction of land cover changed areas was tried in global area and problems of this method were identified.

5.1 Data used

Normalized Difference Vegetation Index (NDVI) of NOAA NASA Pathfinder Land Data Set (PAL data) from 1982 to 2000 were used in this study. In order to remove cloud effects, Temporal Window Operation (TWO) method (Park and Tateishi 1999) was applied to NDVI data. The TWO method is an algorithm to make a seasonally smooth change pattern for temporal variables at least longer than one year. The TWO-processed data were resampled to 4′ (approximately 8 km at the equator) grid raster data in the geographic (latitude/longitude) coordinate system.

5.2 Methodology

(1) The averages of 10-day NDVI from 1982 to 1984 were calculated, and similarly from 1998 to 2000 too.
(2) The difference from the averaged NDVI 1982-84 to the averaged NDVI 1998-2000 were calculated for the corresponding 10-day time period.
(3) The sum of the above difference was calculated for thirty-six 10-day (or one year).
(4) The positive value of the above sum is considered as areas of increasing vegetation activity, and negative value is considered as areas of decreasing vegetation activity.
(5) In order to investigate the trend of time series NDVI values, time-series NDVI curves of unchanged areas of different land cover types such as desert, snow, and forest were analyzed.

5.3 Result

By using large positive and negative threshold values, potential of land cover changed areas were extracted.

However, the following noises and distortions cause wrong results as land cover changed areas.

- high or low NDVI noises remaining after preprocessing
- misregistration along seashore lines
- difference of NDVI levels in different NOAA satellites

Examples of time-series NDVI curves of extracted real land cover changed areas are shown in Fig. 1 and Fig. 2.

6. Conclusions

- Four global land cover data are available
- several global land cover mapping projects are going on
- Trends of global land cover mapping were identified
- Time series NDVI data are effective for global land cover change detection. Noises and trend of NDVI must be eliminated.

References

Chandra Giri, Zhiliang Zhu, Thomas Loveland, 2003, Global and regional land cover characterization and mapping, Proceedings of the CEReS International Symposium on Remote Sensing, paper No.1-1, 16-17 December 2003, Chiba, Japan

GLC2000
http://www.gvm.sai.jrc.it/glc2000/defaultGLC2000.htm
accessed on 29 October 2003

Global Land Cover Ground Truth (GLCGT) Database Version 1.2
http://www.cr.chiba-u.jp/database.html

Global Mapping project
http://www1.gsi.go.jp/geowww/globalmap-gsi/globalmap-gsi.html

LCCS
http://www.fao.org/SD/2001/EN0101a_en.htm
accessed on 29 October 2003

Loveland, T.R., Zhu, Zhiliang, Ohlen, D.O., Brown, J.F., Reed, B.C., and Yang, Limin, 1999, An analysis of the IGBP global land-cover characterization process: Photogrammetric Engineering and Remote Sensing, v. 65, no. 9, p. 1,021-1,032.

Loveland, T.R., Reed, B.C., Brown, J.F., Ohlen, D.O., Zhu, Z., Yang, L., Merchant, J.W., 2000. Development of a global land cover characteristics database and IGBP DISCover from 1 km AVHRR data. International Journal of Remote Sensing 21(6/7): 1303-1330.

Park, J.G. and Tateishi, R., 1999, A proposal of the Temporal Window Operation (TWO) method to remove high-frequency noises in AVHRR NDVI time series data, Journal of the Japan Society of Photogrammetry and Remote Sensing, 38(5), 36-47.

Rosenqvist,A., M.Shimada, T.Igarashi, M.Watanabe, T.Tadano and H.Yamamoto, 2003, Support to multi-national environmental conventions and terrestrial carbon cycle sciences by ALOS and ADEOS-II – the Kyoto & Carbon Initiative, Proc. of the Int. Geoscience and Remote Sensing Symposium (IGARSS'03), Toulouse, France, July 21-25, 2003

Scepan, J., 1999. Thematic Validation of High-Resolution Global Land-Cover Data Sets. Photogrammetric Engineering and Remote Sensing 65(9): 1051-1060.

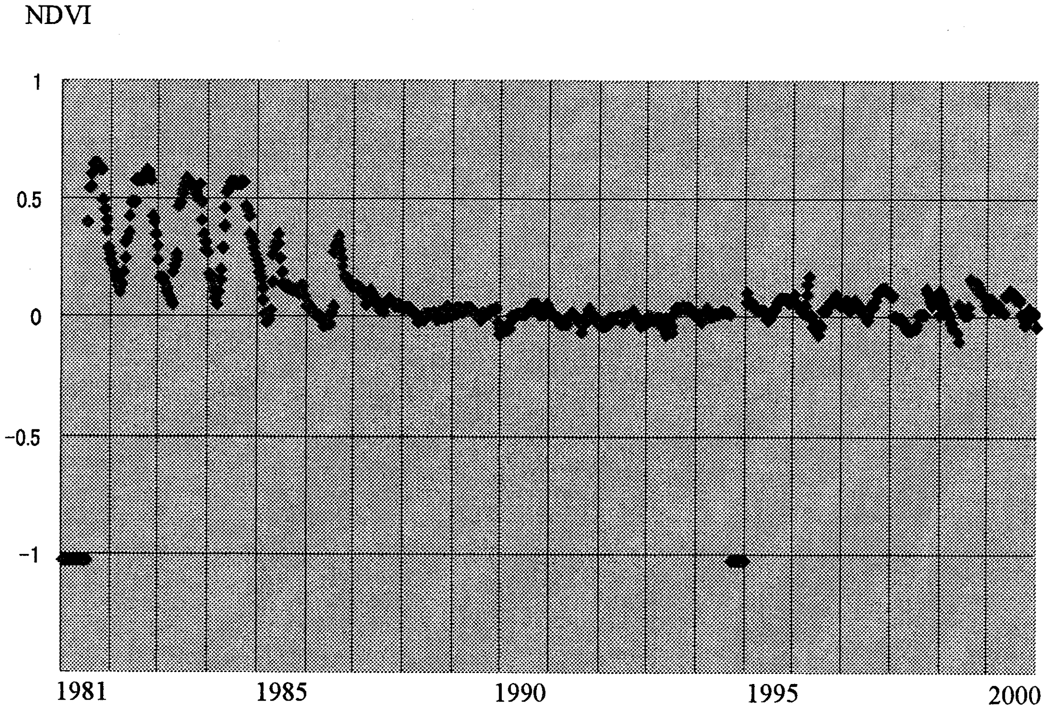

Figure 1 Time-series NDVI curve 1981-2000
Eastern Iran 31° 28'N, 61° 40'E Decease of vegetation

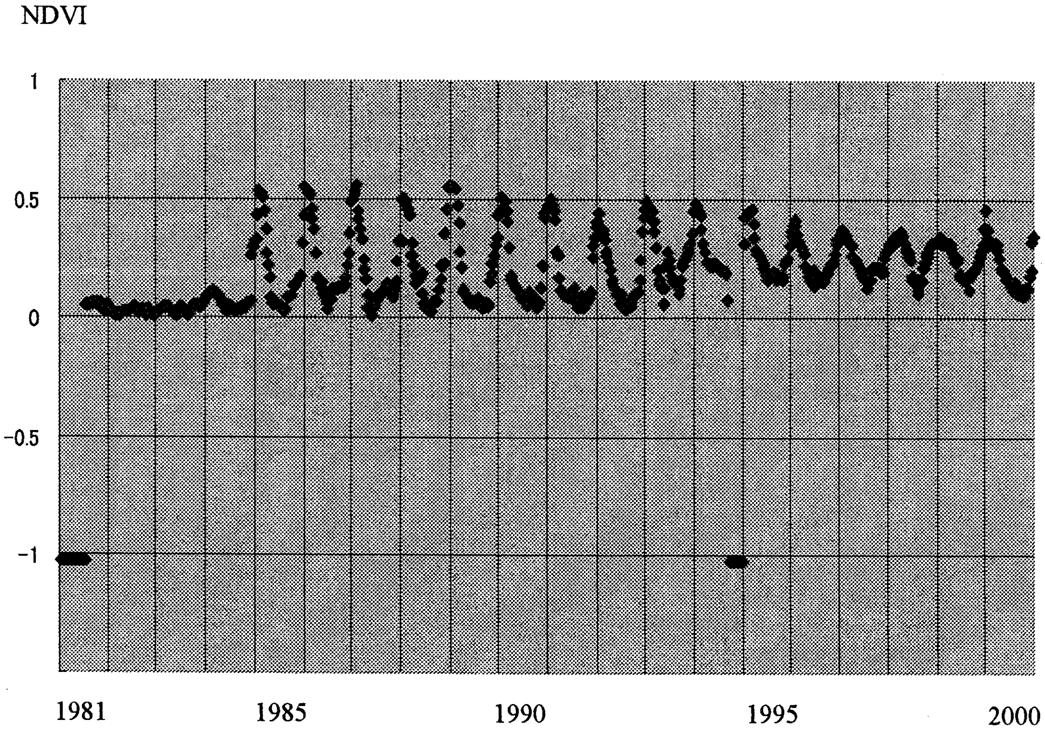

Figure 2 Time-series NDVI curve 1981-2000
Saudi Arabia 19° 52'N, 44° 48'E Irrigation

Land cover classification in Asia using near and short wave infrared bands of SPOT/VGT data

H. P. SATO [1†], R. TATEISHI [2], L. LAI [1]

[1] Geography and Crustal Dynamics Research Center, Geographical Survey Institute,
Tsukuba 305-0811, Japan
† hsato@gsi.go.jp
[2] Center for Environmental Remote Sensing (CEReS), Chiba University,
Chiba 263-8522, Japan

Abstract

A land cover classification map is necessary for modeling interactions between the land surface and the atmosphere, monitoring the environment and estimating food production. In order to classify land cover in Asia in 2000, the possibility of using reflectance of near infrared (NIR) and short wave infrared (SWIR) bands was examined. In this study, Systeme pour l'Observation de la Terra (SPOT) / VEGETATION data were used. The number of months when the reflectance of the SWIR band is higher than that of the NIR band was counted (SWIR > NIR month-count condition) in each pixel, and it was found that pixels with counts of 10 was correspondent to "Sparse Herbaceous / Shrub" and of 11 or 12 was to "Bare Areas", respectively. By way of trial, SWIR > NIR month-count condition was applied to land cover mapping with NDVI monthly change data

1. Introduction

For global land cover mapping, the normalized difference vegetation index (NDVI) calculated from the reflectance of the red and near infrared (NIR) bands of NOAA / AVHRR data has been used in many previous studies. As a result, global land cover dataset was obtained as the International Geosphere-Biosphere Programme, Data and Information System (IGBP-DIS) data classified into 17 items (Loveland et al., 2000).

In comparison with the NOAA / AVHRR sensors, the Systeme pour l'Observation de la Terra (SPOT) / VEGETATION (VGT) sensor was designed with a number of improvements for studying the vegetation and land surface (Xiao et al., 2002). SPOT / VGT has four spectral bands, blue (430–470 nm), red (610–680 nm), NIR (780–890 nm) and SWIR (1,580–1,750 nm), at the resolution of approximately 1 km (1°: 112 pixels). There are few studies on the use of NIR and SWIR bands time series data for land cover mapping. The objective is to explore the potential of multi-temporal NIR and SWIR bands SPOT / VGT data for land cover mapping in Southeast Asia in 2000. In this study the number of months when the reflectance of the SWIR band is higher than that of the NIR band was counted (SWIR > NIR month-count condition) in each pixel. And the count more than 9 was used for mapping of poor vegetated areas. In this paper this method is explained in detail.

2. Method

2.1 Remote sensing data

In this study, 10-day synthesis of SPOT / VGT data (VGT-S10 products) of 2000 were downloaded from the web site of http://free.vito.vgt.be. Downloaded data contain the NDVI and reflectance of these bands in 8-bit and 16-bit Digital Number (DN) values at the resolution of about 1 km, respectively. To reduce the possibilities of cloud contamination as well as to ease the problems of handling large volumes of data, the VGT-S10 product were recomposed into monthly images based on the maximum NDVI value in the month.

2.2 Relation between NIR, SWIR and water contained in leaves

In the vegetative area, the reflectance of the NIR band is the highest. The reflectance decreases in the order of TM3 (red), 4 (NIR) and 5 (SWIR) (Ishiyama et al., 1996). The SWIR band is absorbed by water contained in leaves but the NIR band is not (Tucker, 1980). When leaves are dry, the reflectance of the SWIR band increases and that of the TM5 becomes approximately equal to that of the TM4 (Knipling, 1970; Fig. 1).

On the basis of this relationship between the reflectance of SWIR (S) and NIR (I) bands and water contained in leaves, it is assumed that $S < I$ is always satisfied in vegetative areas but $S > I$ is not considered. In this study, $S > I$ was examined using SPOT / VGT data. It was assumed that if $S > I$ is satisfied in some parts of the area, the land cover in that area is non- or sparsely vegetative. The number of months when $S > I$ is satisfied (SWIR > NIR month-count condition) was counted in each pixel and the spatial distribution of this number was examined.

3. Method

Fig.2 shows the spatial distribution of the SWIR > NIR month-count condition. In the Fig.2, for a pixel not satisfying the condition, the pixel value is indicated as 0 throughout all 12 months, and when it satisfies the condition throughout all 12 months, the value is 12. In the Fig.2, close agreement was obtained between the spatial distribution of the value 12 and the areas of the deserts, and the value of 0 and vegetation-rich areas.

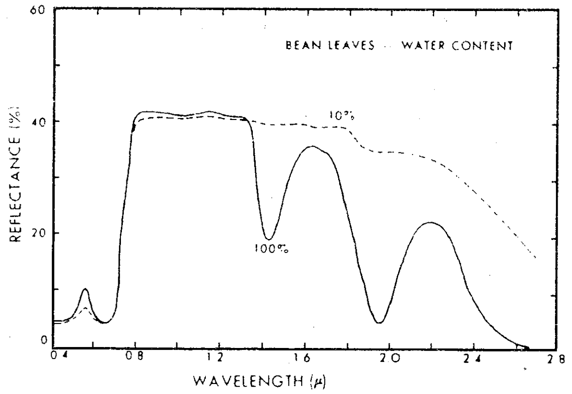

Fig.1. Reflectance and leaf water content (Knipling, 1970)

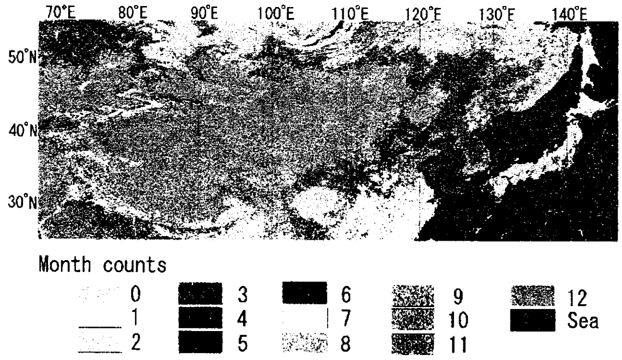

Fig.2. Distribution of SWIR > NIR month-count condition

4. Discussion

Ground truth (GT) sites were collected and the relationship between pixel values in Fig.2 on the GT sites was examined. In advance, the 17 items of the GT sites are shown in table 1.

Ground truth (GT) sites were collected and the relationship between pixel values in Fig.2 on the GT sites was examined. In advance, the 17 items of the GT sites are shown in table 1.

4.1. Land cover items

Recently, Food and Agricultural Organization (FAO) created Land Cover Classification System (LCCS) for mapping exercises independent of map scale and map use (FAO, 2000). Land cover items in table 1 are according to the Sato and Tateishi Land Cover Guideline (ST-LCG) legend (Sato and Tateishi, 2002), created by the LCCS. The LCCS only provides framework to identify the land cover, and when legend is required, it is necessary to create it by the LCCS. It is difficult to add new items to the conventional legends such as the SiB and IGBP-DIS legends because of lack of criteria for the addition. In this sense, The LCCS is useful to make the land cover legend that is easily correspondent to the other legends created by the LCCS. Comparative tables in detail between ST-LCG legend and IGBP-DIS legend, refer to Sato and Tateishi (2002).

4.2. Ground truth collection

GT sites were gathered for China, Japan, Mongolia, and around Lake Baikal in Russia by three methods: field surveys, reference to a world atlas and domestic maps, and consultation with people familiar with the on-site current situation. The methods were used either separately or together to gather the GT sites. GT sites were plotted on the 60-class unsupervised classification result performed on 12-month VGT-S10 NDVI data. Next, GT sites were manually or automatically delineated. In the automatic delineation, three by three pixel squares of GT sites were automatically generated. As a result, the area of each GT site was at least 9 pixels (approx. 3 km by 3 km).

Each GT site has a monthly NDVI curve for 2000. When the GT site is classified as Bare Areas or

Broadleaf Evergreen Forest, the curve maintains low or high values through the year, respectively. The curve for each GT site was examined, and GT sites that have appropriate NDVI curve for their own classification were finally selected. In table 1, the number of GT sites and total pixel counts are shown.

Table 1. Land cover items in this study and GT. A: The number of GT sites; B: Pixel counts.

Code and land cover item	Ground truth		IGBP-DIS code
	A	B	
1. Broadleaf Evergreen Forest	4	105	2
2. Broadleaf Deciduous Forest	5	228	4
3. Needleleaf Evergreen Forest	6	126	1
4. Needleleaf Deciduous Forest	2	527	3
5. Mixed Forest	4	65	5
8.Herbaceous, single layer	14	2,906	10
9.Herbaceous Vegetation with Sparse Tree / Shrub	2	25	10
10.Sparse Herbaceous / Shrub	2	24	16
11. Cropland	6	113	12
14. Wetland	2	35	11
16. Bare Areas	2	18	16
17. Urban	1	154	13
104. Coconut	1	22	1
120. Rice, paddy	3	102	12
201. Pasture	1	382	10
202. Mixed fields of corn & bean	1	22	11
203. Mixed fields of rice & corn	1	16	11

4.3. Ground truth and SWIR > NIR month-counts

In the Fig.3, average month counts and standard deviation on the GT sites are shown. The land cover classification code on the abscissa in Fig.3 corresponds to the code in the left column of table 1.

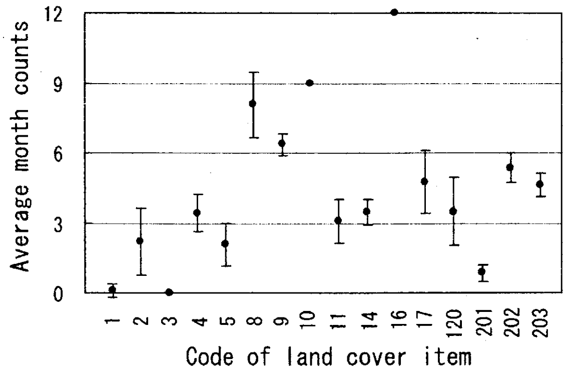

Fig.3. Month counts and land cover item

In the Fig.3, average month counts for code 10 (Sparse Herbaceous / Shrub) and code 16 (Bare Areas) are larger than those of any other codes. It is easy to separate codes 10 and 16 from other codes, but code 10 has the possibility to be confused with code 8 (Herbaceous, single layer). According to FAO's LCCS, land is bisected into primary vegetated and primary non vegetated classes. When vegetative cover is at least 4 % for at least two months of the year, the land is classified into the former, and when vegetative cover is less than 4 % for more than 10 months of the year, the land is classified into the latter (FAO, 2000). Here, it is assumed that when the month count is 10, the pixel is classified as Sparse Herbaceous / Shrub, and when it is 11 or 12, the pixel is classified as Bare Areas.

As shown in Fig. 3, land covers correspond to denser vegetative cover than codes 10 and 16 seem to be adequate to use NDVI for land cover mapping, because NDVI is a sensitive index for vegetation. To classify land cover, it is thought that when the land is non- or sparsely vegetative such as codes 10 and 16, the SWIR > NIR month-count condition is applied, and when the land is vegetative such as the other items, monthly NDVI data is applied. Land cover in Fig.4 was classified as follows. First, supervised classification with the GT sites was performed on monthly NDVI changes data, based on the maximum likelihood method. Next, when SWIR > NIR month-count condition is 10, the pixel was rewrote as Sparse Herbaceous / Shrub, and when it is 11 or 12, the pixel is rewrote as Bare Areas. Confusion matrix of the Fig.4 is shown in the table 2. Comparing the table

2 with the confusion matrix in case of only using monthly NDVI data, the result was not necessary better. Details will be reported in Sato and Tateishi (in press).

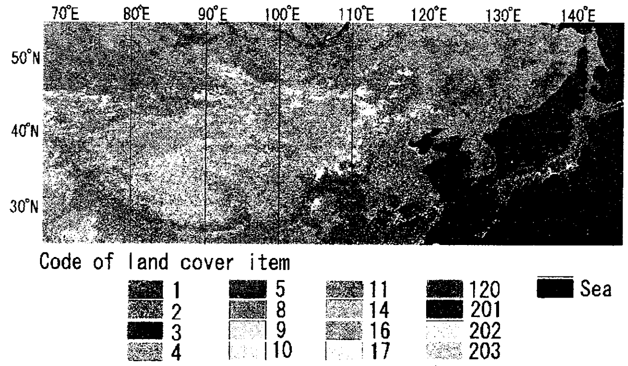

Fig.4. Land cover map using NDVI and SWIR > NIR month-count conditions

Table 2. Confusion matrix of the Fig.4.

Code		Result																Grid counts	Correct ratio %
		1	2	3	4	5	8	9	10	11	14	16	17	120	201	202	203		
GT	1	105	0	0	0	0	0	0	0	0	0	0	0	0	0	0	0	105	100.0
	2	0	226	0	0	2	0	0	0	0	0	0	0	0	0	0	0	228	99.1
	3	0	0	126	0	0	0	0	0	0	0	0	0	0	0	0	0	126	100.0
	4	0	0	3	524	0	0	0	0	0	0	0	0	0	0	0	0	527	99.4
	5	0	7	0	0	58	0	0	0	0	0	0	0	0	0	0	0	65	89.2
	8	0	0	0	14	0	2798	0	56	0	0	38	0	0	0	0	0	2906	96.3
	9	0	0	0	0	0	0	25	0	0	0	0	0	0	0	0	0	25	100.0
	10	0	0	0	0	0	0	0	24	0	0	0	0	0	0	0	0	24	100.0
	11	0	0	0	0	0	4	0	0	109	0	0	0	0	0	0	0	113	96.5
	14	0	0	0	0	0	0	0	0	0	35	0	0	0	0	0	0	35	100.0
	16	0	0	0	0	0	0	0	0	0	0	18	0	0	0	0	0	18	100.0
	17	0	0	0	0	0	0	0	0	0	0	0	154	0	0	0	0	154	100.0
	120	0	0	0	0	0	0	0	0	0	0	0	0	102	0	0	0	102	100.0
	201	0	0	0	0	0	0	0	0	0	0	0	0	0	382	0	0	382	100.0
	202	0	0	0	0	0	0	0	0	0	0	0	0	0	0	22	0	22	100.0
	203	0	0	0	0	0	0	0	0	0	0	0	0	0	0	0	16	16	100.0

5. Conclusion

In this study example of land cover mapping using NDVI and reflectance of SWIR and NIR bands was shown. It is the subject how SWIR>NIR month-count condition should be used with monthly NDVI change data. In this study, distribution of SWIR > NIR condition in each month is not considered. There is left to study this distribution for the land cover mapping.

References

FAO, 2000. *Land Cover Classification System (LCCS) classification concepts and user manual.* 179p.

Ishiyama, T., Nakajima, Y., and Kajiwara, K., 1996. Vegetation index algorithm for vegetation monitoring in arid and semi arid land. *Journal of Arid Land Studies*, 6 (1), pp.35-47.

Knipling, E.B., 1970. Physical and physiological basis for the reflectance of visible and near-infrared radiation. *Remote Sensing of Environment*, 1, pp.155-159.

Loveland, T.R., Reed, B.C., Brown, J.F., Ohlen, D.O., Zhu, Z., Yang, L., and Merchant, J.W., 2000. Development of a global land cover characteristics database and IGBP DISCover from 1-km AVHRR data. *International Journal of Remote Sensing*, 21, pp.1303-1330.

Sato, H.P., and Tateishi, R., 2002. Proposal for global land cover guideline legend based on FAO's LCCS. *Asian Journal of Geoinfomatics*, 3 (2), pp.35-45.

Sato, H.P., and Tateishi, R., in press. Land cover classification in Southeast Asia using near and short wave infrared bands. *International Journal of Remote Sensing*.

Tucker, C.J., 1980. Remote sensing of leaf water content in the near infrared. *Remote Sensing of Environment*, 10, pp.23-32.

Xiao, X., Boles, S., Frolking, S., Salas, W., B. Moore III, C., Li, C., He, L., and Zhao, R., 2002. Landscape-scale characterization of cropland in China using Vegetation and Landsat TM images. *International Journal of Remote Sensing*, 23, 3579-3594.

Ground surface conditions of oases surrounding the Taklimakan Desert

Takashi Ishiyama[1], Shinji Hujikawa[2], Kazumichi Ohkawa[2] and Soichiro Tanaka[2]

[1] Center for Environmental Remote Sensing, Chiba University
E-Mail: ishiyama@ceres.cr.chiba-u.ac.jp

[2] GEOTECHNOS Co.Ltd
E-Mail: soichiro-tanaka@geotechnos.co.jp

Abstract

The analysis of images taken around the Taklimakan desert Desert with a camera onboard CORONA during the 1960's and with multispectral sensors, ASTER and, MODIS onboard TERRA in 2000 indicated a number of features. Specifically, oases on the southern edge of the desert have more potential as farmland than those on the northern edge based on the ratio of both NDVI and high-density NDVI (HD NDVI) derived from MODIS data. Furthermore, the total vegetation area around the boundaries of large oases has increased, indicating increases in farmlands and forest areas during the last 40 years. An in situ survey revealed that a great efforts have has been continued made since the end of 1950 to increase forests to protect against the invasion of desert sand and also to increase farmlands. Irrigation canals and reservoirs for supplying farmlands with the water were also built during this period.

Introduction

The most fundamental and important approach to investigating the mechanism of recent desertification is to extract the time-series variation of the ground state, find the relationship between the variation of the ground state and the various factors likely to be related to desertification, such as climate and human activities. Until now, however, very little data concerning the ground state in arid and semi-arid lands has been available because of the difficulty of collecting data from vast areas under severe weathers conditions.

The remote sensing data collected from the satellite contain much useful information on ground states. Furthermore, remote sensing techniques can collect the data from vast areas instantaneously and repeatedly. In addition to these excellent capabilities, previously gathered data has been accumulated.

For example, the camera onboard CORONA collected data over the Taklimakan desert in China during the 1960s was collected. In addition to this older data, data acquired by new satellite sensors such as the multispectral sensors, ASTER and, MODIS onboard TERRA are now available. Accordingly, it is now possible to compare the old satellite data with the new data in order to extract time-series variations of the ground state over a vast area.

We investigated the land use around oases along the southern and northern edges of the Taklimakan desert. In this paper, we report on the present ground state of the oases using the data of the MODIS onboard TERRA. We then investigate the variation of ground states in the oases of Pishn and Hotan located on the southern edge of the Taklimakan desert based on the data acquired from CORONA in the 1960's and ASTER in 2001.

Results and Discussion

Present Ground State of Oases Surrounding the Taklimakan Desert

By calculating the ratio of both NDVI(0.4-0.9) and HD NDVI(0.6-0.9) derived from MODIS data is shown Fig. 1, it is possible to estimate the potential and scales of irrigation farmland. Figure. 2 illustrates the relationship between

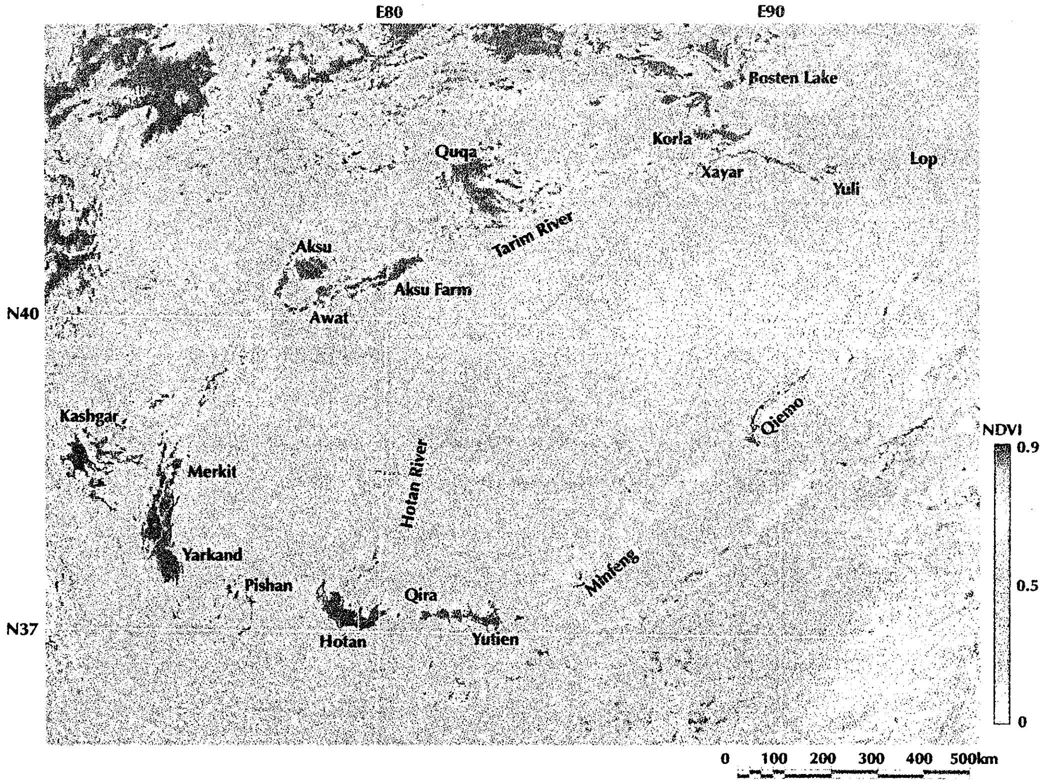

Fig. 1. Distribution of vegetation index around Tarim basin derived from geo-coded MODIS data on July 29th 2000.

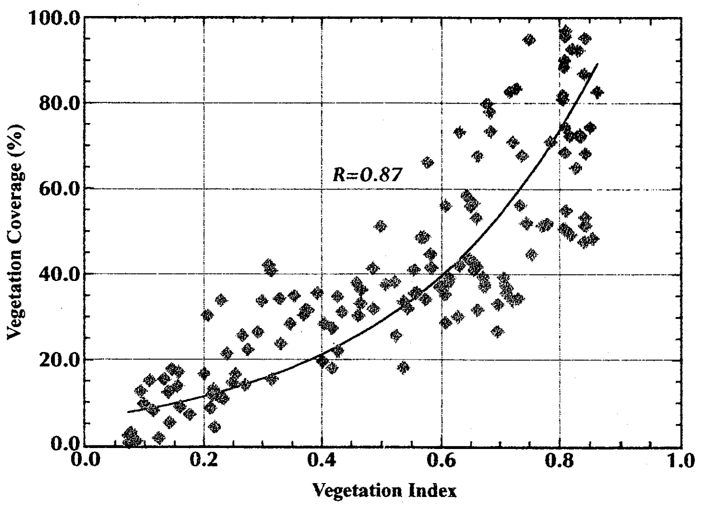

Fig. 2. MODIS NDVI as shown in Figure 1 vs vegetation coverage.

MODIS NDVI shown in Fig. 1 and vegetation coverage derived from in situ measurement. Fig. 3 depicts the in situ measurement of the vegetation cover based on the method of a 100m cross a length of vegetation laid out in two 100m orthogonal lines. The results suggest a greater potential as farmland for the oases on the southern edge of the Taklimakan desert than on the northern edge.

There are many extensive oases over 1500 square kilometers in area on the northern edge of the Taklimakan desert, and the ratio of NDVI to HD NDVI exceeds 0.3 as shown in Table 1. This means that the utilization as irrigated farmland is high, and these oases are dependent on the quantity of water of the large tributaries flowing into the Tarim River. The Tarim River originates in glacier and snow fields in the mountains and was formed by three tributaries, the Hotan River (supplies 22% of the water), the Yarkand River (supplies 6%), and the Aksu River (supplies 72%) is shown in Fig. 4. Therefore, the volume of river water from the Tianshan mountain range enables the existence of formation of larger oases on the northern edge of the Taklimakan desert than on the southern edge. (1). Generally, small oases are more abundant on the southern edge, and the ratio of NDVI to HD NDVI is 0.15, so there are large areas of unutilizable grounds around the oases. The utilization factor as farmland obviously depends on the quantity of the irrigation water.

Fig. 3 In situ measurement of the vegetation cover based on the method of 100m cross (length of the vegetation in orthogonal 100m lines).

Therefore, on the northern edge, the quantity of river water of from the Tianshan mountain range enables the formation of large oases. On the southern edge, there is only a small amount of meltwater from the mountain range, and the river channel is long and segmented. This quantity of water is the main reason and that the oases are small, and have a low land utilization factor. The vegetation area around the Taklimakan desert is about 23,000 square kilometers (derived from MODIS NDVI), which is about ten times the area of Metropolitan Tokyo, Japan.

This area presently faces the threat of desertification. The areas of the Taklimakan desert as derived from MODIS data, is 303,834 square kilometers. The literatures gives an area of 270,000 square kilometers (New Encyclopedia Britannica) and 320,000 square kilometers. The total area of the oases is less than the area of the Taklimakan desert. As a result, the vegetation area in the oases does not seem to contribute to controlling dust storms.

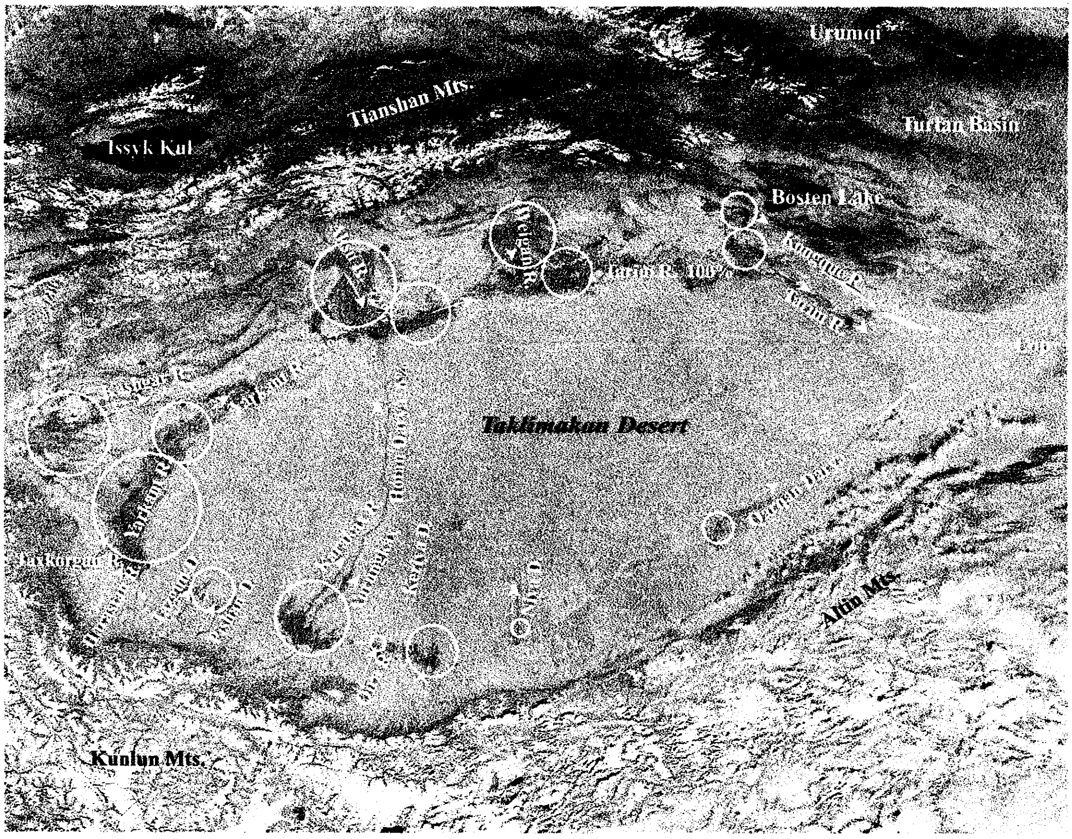

Fig. 4. MODIS true-color image around the Tarim basin. The circles indicate various area oases surrounding the Taklimakan Desert. The blue shows the lakes and reservoirs. The arrows show the drainage patterns (October 7, 2001).

Extraction of Desertification Areas

The change of surface conditions around the southern edge is complicated (2,3,4). The land cover change of Pishan and Hotan oases can be estimated from the CORONA data acquired from early 1960 and data acquired by ASTER from2000. Prior to comparing the 1960 CORONA images with the 2001 ASTER images, geometrical correction (affine transformation) is necessary. CORONA imagery from 1960 was co-registered with ASTER data from 2001 by comparing the positions of the same point in two images. Figure 5 shows the color image composed of a reverse image of the panchromatic CORONA image in red and reverse images of ASTER band 1 in both green and blue prepared to extract land cover changes, particularly vegetation features during this period in Pishan. The result shows that reservoir and irrigation canals were constructed recently in these oases which develop in the alluvial fan, and that there is an expansion of the farmland around oases. At the same time, however, here is declining vegetation in the downstream area due to water shortages. Though irrigation for Pishan oasis depends on small rivers and ground water, the extension of farmland is difficult, since the quantity of water is very small. There is a small reservoir, but the irrigation water is not distributed sufficiently in the downstream area, and the extending farmland is difficult. During the last 40 years the desert areas obviously extended towards the inner oasis. In particular, the land degradation crisis progresses because of the invasion of the desert sand in the circumference in the oases. In addition, the Hotan oasis was formed from two large rivers, and the oasis also forms some large reservoirs, and contributes to the extension of farmland. Table 2 indicates the land cover change in Pishan and Hotan oases from 1960 to 2000 as derived from CORONA and ASTER data. In this region, the water control system does not function, and water is not being fairly allocated at present. This further contributes to the suppression of agriculture in the lower current area and land degradation downstream. Appropriate water resource management will thus be significant in the success or failure of efforts to prevent desertification of forestland around the oases.

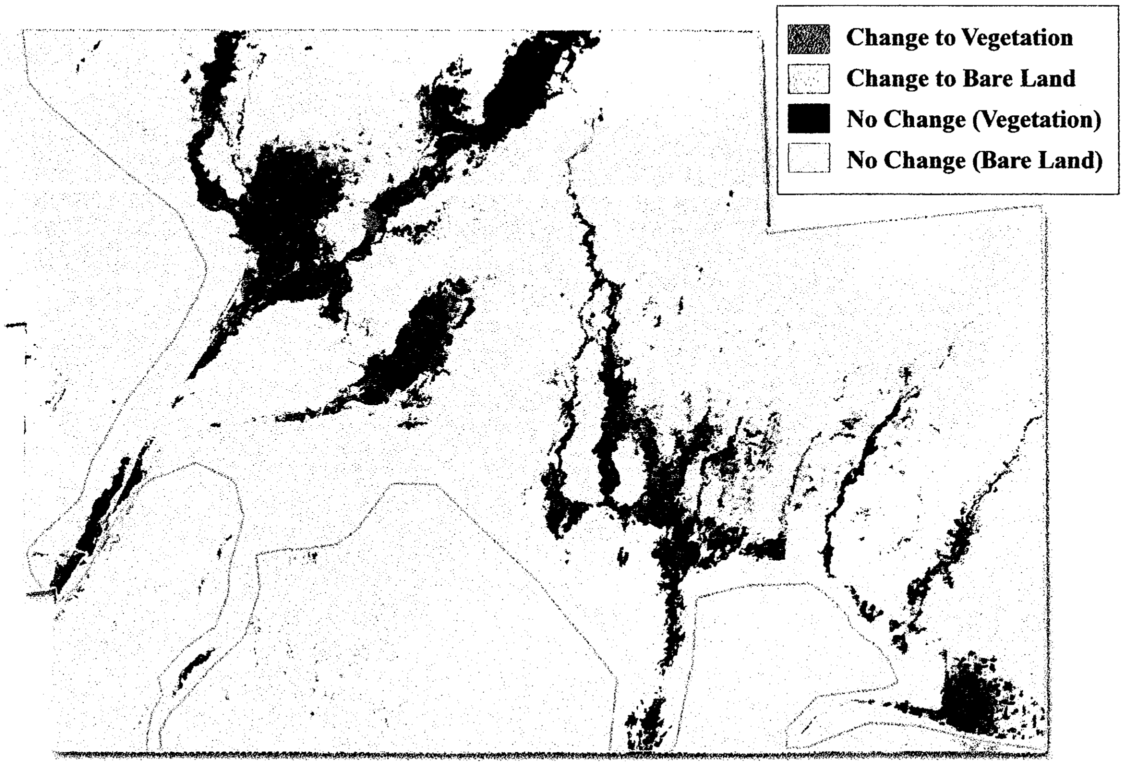

Fig. 5. Land cover change in the Pishan area between 1960 and 2000, derived from CORONA and ASTER images.

Thus, the comparison between the imagery obtained in the 1960's and 2001 suggests that large scale desertification has continued for 40 yeas but has been increased as a results of irrigation and forestation. Accordingly, a possible decrease in the vegetation in the desert areas located downstream may be detected by comparing data from CORONA with data from new satellite sensors such as ASTER and, Landsat ETM. The images of the downstream area should be compared to further investigate the effect of water consumption due to irrigation in the upstream area upon the vegetation in the down stream area.

Table 1. The areas of the oases around the Tarim Basin derived from MODIS NDVI and its ratio.

Oasis	NDVI (0.4-0.9)	HD NDVI (0.6-0.9)	Ratio of NDVI (0.6-0.9)/(0.4-0.9)
(Northern Edge)			
Aksu	1,406.9	438.4	0.31
Aksu Farm	1,423.4	549.0	0.39
Awat	709.9	48.2	0.07
Quqa	1,934.7	267.9	0.14
Xayar	2,178.7	109.6	0.05
Yuli	1,539.9	260.1	0.17
Korla	843.3	340.6	0.40
(Western Part)			
Yarkand	3,290.7	1,277.4	0.40
Merkit	1,242.9	108.0	0.09
Kashgar	3,017.8	670.9	0.22
(Southern Edge)			
Qiemo	846.5	97.6	0.12
Minfeng	193.4	3.0	0.02
Yutien	1,060.2	125.5	0.12
Qira	421.4	68.7	0.16
Hotan	2,464.9	365.9	0.15
Pishan	296.9	41.9	0.14
Total	22,871.2 km^2	5,082.8 km^2	

Table 2. Land cover change in Pishan and Hotan oases during 1960 and 2000, derived from CORONA and ASTER data.

	Pishan	Hotan
Change to Vegetation from Bare Land	75.0	441.8
Change to Bare Land from Vegetation	106.9	195.0
No Change (Vegetation)	161.5	157.3
No Change (Bare Land)	1680.3	1814.1

(km^2)

References

1) T. Ishiyama : Estimation of surface conditions around oases in alluvial fan of Tarim Basin based on satellite data, Proceedings of the third symposium on Xinjian Uyghur, China, 15-18, CEReS, Chiba University, November, 2003.

2) S. Sugihara, T. Ishiyama and M. Naya : Desertification monitoring based on the satellite data., RIKEN Review, No. 5, April, 1994.

3) T. Ishiyama, Y. Nakajima, Koji Kajiwara : Vegetation Index Algorithm for Vegetation Monitoring in Arid Arid and Semi Arid Land, J. of Arid Land Studies 6-1, 19(9), 35-47, 1996.

4) T. Ishiyama, S. Tanaka, K. Uchida, S. Fujikawa, Y. Yamashita and M. Kato : Relationship among vegetation variables and vegetation features of arid lands derived from satellite data, Advanced in Space Research, 28, 183-188, Elsevier, 2001.

Influence of land use and land cover change due to urbanization on hydrological environments: a case study of Shijiazhuang, China

Yanjun Shen[1], Jieying Xiao[1], Akihiko Kondoh[2], Ryutaro Tateishi[2]

[1] Graduate School of Science and Technology, Chiba University
Email: sheny@graduate.chiba-u.jp and xiaojy@graduate.chiba-u.jp
[2] Center for Environmental Remote Sensing, Chiba University
Email: kondoh@faculty.chiba-u.jp and tateishi@ceres.cr.chiba-u.ac.jp

Abstract

This study demonstrates some preliminary results of the analyzing on influence of land use and land cover change due to urbanization on hydrological environment. Two Landsat TM and ETM+ images are used for detection of the land cover changes from 1987 to 2001 through maximum likelihood classifier. Then, an analysis on the change of thermal environment and water balance is conducted to assess the impact of urbanization.

1 Introduction

Urbanization is an important aspect of human activities in influencing the climate system. During the process of urbanization, the reflectivity of land surface is violently changed when large amount of natural or agricultural lands are converted to built-up surfaces. These changes strongly affect the atmosphere/land surface energy exchange (Grimmond and Oke, 1995; Quattrochi and Ridd, 1994) and local weather and climate regimes (Changnon, 1992; Oke, 1987; Roth et al., 1989). As for the hydrological cycle, most of the processes between land and atmosphere, surface and subsurface (Grimmond and Oke, 1991; Hammer, 1972) are completely influenced by urbanization.

In recent 2 decades, China experienced a rapid development. Accompanied with the outstanding growth in economy, an evident change in land cover is due to urbanization. In North China Plain, where water shortage is becoming the biggest environmental problem, the change aggregated the vulnerable hydrological environment. Therefore, it is necessary for urban planning and hydrological modelling to study how the urbanization affect environment.

In this case study, the authors attempt to evaluate the influence of urbanization on local hydrological environment through analyzing the main changes in hydrological processes from a perspective of remote sensing.

2 Study area and method

2.1 Study area

The study area is located in the east part of China between the range of 114°23′-114°42′E and 37°58′-38°60′N with an area of around 341.63 km^2, which covers the whole city of Shijiazhuang and its near suburban fringe. Shijiazhuang lies on the alluvial fan of Hutuo River with a slight slope of about 1.5‰ declining from northwest to southeast. The semiarid monsoon climate determines its precipitation is only about 500 mm/year with around 2/3 of which is occurred in July and August. Hutuo River runs through the north side of Shijiazhuang, and has become a seasonal river today mainly due to the mass utilization of water resources and climate change since the late 1970's.

Shijiazhuang is the largest city of Hebei province as its important position in administration, culture, economy and transportation. The population is around 1.6 million now. In the last 20 years of economic reform, urban sprawl happened in Shijiazhuang is very significant. According to the economic annals, its population and built-up area are 1.6 million and 165.5 km^2 in 2001.

The water source of this city is almost from groundwater because the river near it has become dry in 1990s. A little part of the water is introduced from a reservoir to west in the latest years.

2.2 Data and processing

The satellite remote sensing data used in this study are two subscenes of Landsat Thematic Mapper images on June 29, 1987 and May 10, 2001, respectively. After geometrically corrected to UTM map projection, the two images were separately classified by using a supervised classifier. And then, the statistical characteristics were calculated for different land classes. The changes in built-up area are detected. And finally, the impacts of the changes on hydrological cycle are evaluated with link to some ground statistic data.

2.3 Normalized Difference Temperature Index, *NDTI*

A consequent environmental phenomenon occurring with urban expansion is the growth of urban heat island. Even though heat island is a meteorological term related to the increase of air temperature above urban area, the satellite observed land surface temperature usually is used to evaluate heat island. In this study, we use the normalized difference temperature index (*NDTI*) to evaluate the thermal environmental change regarding to urban expansion.

$$NDTI = \frac{T - T_{\min}}{Ts_{\max} - T_{\min}} \tag{1}$$

where T is surface temperature, T_{min} and T_{max} are the minimum and maximum temperature on the image.

2.4 Impervious surface cover

An indicator to describe the fractional cover of urban or built-up area is impervious surface cover (ISA) (Ridd, 1995; Carlson and Arthur, 2000). ISA constitutes the fractional cover of a pixel for which the surface can neither evaporate water nor permit rainwater to penetrate. A reasonable definition of ISA can be addressed by satellite is (Carlson and Arthur, 2000),

$$ISA = (1 - f_v)_{dev} \tag{2}$$

where the subscript, dev, indicates that the quantity is defined only for regions classified as developed or built-up; f_v is fractional vegetation cover, calculating by

$$f_v = \frac{NDVI - NDVI_{\min}}{NDVI_{\max} - NDVI_{\min}} \tag{3}$$

where, $NDVI_{max}$ and $NDVI_{min}$ are the vegetation indices for dense vegetation and bare soil, respectively. In this study, we use 0.8 and 0.05 for these parameters.

2.5 Water balance evaluation

In order to evaluate the impact of urbanization on hydrological cycle, we calculate the water balance before and after these changes. Because almost all of the agricultural lands in this region are irrigative, the runoff in the agricultural lands can be considered as nearly zero since the slope of this region is only around 1.5‰.

Because of the deep groundwater in this region, the exchange between soil and groundwater can be ignored. The water balance for a single rainfall event can be expressed as

$$P = Int + E + Inf + R \tag{4}$$

where P is total precipitation of a rainfall event; Int is the interception by vegetation; E is evaporation during the rainfall event; Inf is the infiltration into soil; and R is runoff. On an annual base, the water balance components can be expressed as

$$R = P \cdot ISA \tag{5}$$

$$ET = P \cdot (1 - ISA) \tag{6}$$

3 Results

3.1 Land cover change detection

Figure 1 illustrates the land cover maps of the study area in 1987 and 2001, respectively. In these two maps, the land cover is classified as 9 classes: urban, residential, trees, orchards, vegetable fields, crop fields, grassland, water surface, and sandy soil (Xiao et al., 2003). The urban and residential areas are treated as built-up area in the analysis of urbanization.

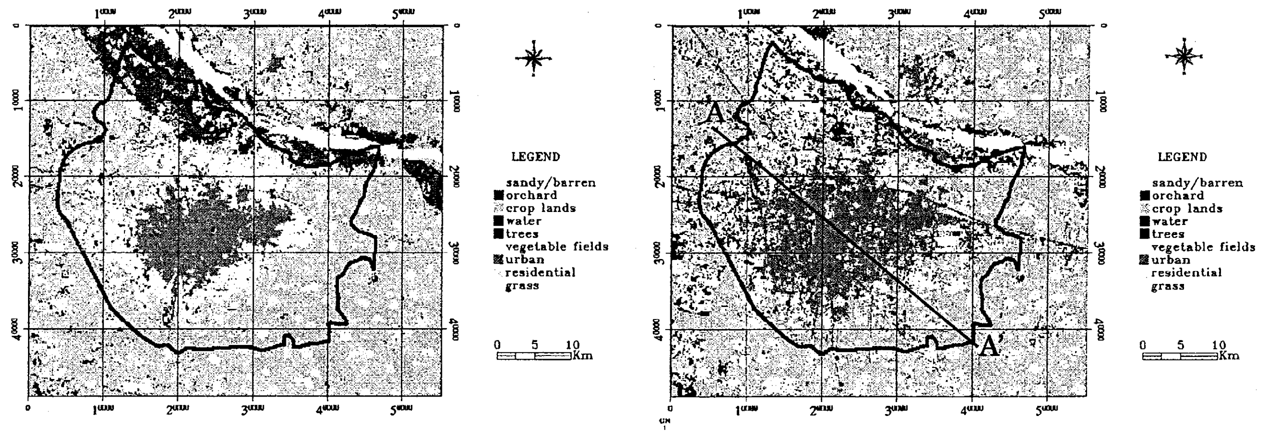

Figure 1 The land use and land cover maps of Shijiazhuang in 1987 (left) and 2001 (right). (The line AA' is a cross section for analyzing the change in thermal environment)

An obvious change according to the two class maps is the evident enlargement of built-up area and the decrease of trees (including orchards) and cropland. Table 1 shows the statistics of the changes between the two years.

Table 1 The conversion matrix of land use types during 1987 to 2001 (unit: hectare)

1987 \ 2001	Built-up	Fields	Trees	Others	Total
Built-up	12 327.91	13 16.66	46.79	203.52	13 894.88
Fields	4 744.57	10 927.57	588.15	321.17	16 581.46
Trees	537.84	1 826.24	811.55	199.93	3 375.56
Others	88.07	163.48	41.17	18.18	310.90
Total	17 698.39	14 233.95	1 487.66	742.80	34 162.80
Change rate (%)	27.37	-14.16	-55.93	138.92	----

$$* \ \mathit{Change} \quad \mathit{rate}\,(\%) = \frac{\sum A_{2001} - \sum A_{1987}}{\sum A_{1987}} \times 100$$

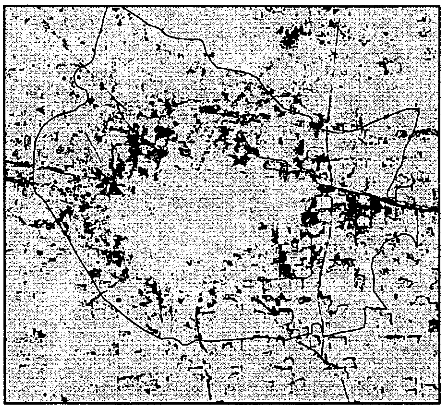

Figure 2 The distribution of sprawled built-up area during 1987~2001.

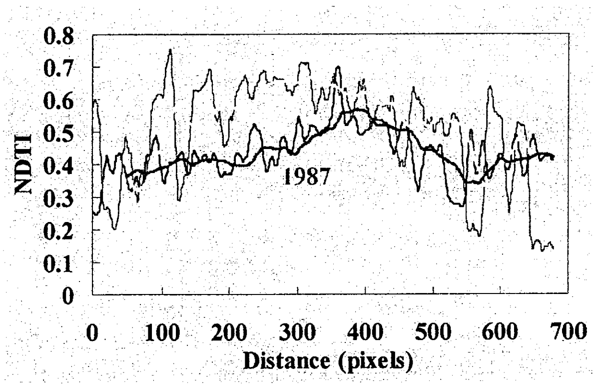

Figure 3 Enlargement of urban heat island due to urbanization

Figure 2 shows the sprawled built-up area during the 14 years. Totally, the increased area is around 3800 ha, and the increasing rate is 27.4%.

3.2 The influence of urbanization on thermal environment

An obvious effect of urbanization on environment is the thermal environment will be significantly changed because the urbanized surface prevent water being vaporized into atmosphere, therein, the net radiation in such surface will only be converted into ground and sensible heat according to the surface heat balance law. This is the most reason to the phenomenon of so-called urban heat island enlargement. Here, we use the indictor of NDTI to analyze the change thermal environment. The NDTI profiles along the cross section of AA' shows an evident increase in 2001 than in 1987 (Figure 3).

3.3 The influence of urbanization on water balance

Another important impact of urbanization on environment is the process of urbanization strongly affects the surface water balance and then affects other hydrological and meteorological factors.

Here, we use the Equation 5 and Equation 6 to evaluate the water balance of the study area in the 2 years. Table 2 shows the water balance in 1987 and 2001. Even though the annual precipitation of 2001 is slightly less than that of 1987, the runoff of 2001 is increased around 18% than 1987 because of the urbanization. This implies that the urbanization make the risk of urban flood increasing in extreme rainfall event.

Table 2 Change in water balance due to urbanization

	P (mm)	R (mm)	ET (mm)
1987	312.9	127.3	185.6
2001	289.8	150.1	139.7
Change (%)	-7.4	17.9	-24.7

4 Discussions

In this study, we evaluate the influence of urbanization on hydrological environment. Actually, assessing the influence is a very complicated work. Here, we only give the preliminary results on the analysis of thermal environment and water balance. Large amount of meteorological data is in processing now. On the other hand, in this present paper we only treated the physical aspects of the impacts and not give any assessment of the impacts on chemical aspect of the environment, i.e. pollution, which is one of the most important aspects as well.

References:

Carlson, T.N. and Traci Arthur, S., 2000. The impact of land use-land cover changes due to urbanization on surface microclimate and hydrology: a satellite perspective. *Global and Planetary Change*, 25, 49-65.

Changnon, S.A., 1992. Inadvertent weather modification in urban areas: Lessons for global climate change. *Bull. Ame. Meteorol. Soc.*, 73, 619-627.

Grimond, C.S.B. and Oke, T.R., 1991. An evapotranspiration-interception model for urban areas. *Water Resour. Res.*, 27,1739-1755.

Grimond, C.S.B. and Oke, T.R., 1995. Comparison of heat fluxes from summertime observations in the suburbs of four North American cities. *J. Appl. Meteorol.*, 34, 873-889.

Hammer, T.R., 1972. Stream channel enlargement due to urbanization. Water Resour. Res., 8, 1530-1540.

Oke. T.R., 1987. *Boundary layer climates.* NY: Methuen Press. pp435.

Quattrochi, D.A. and Ridd, M.K., 1994. Measurement and analysis of thermal energy responses from discrete urban surfaces using remote sensing data. *Int. J. Remote Sens.*, 15, 1991-2022.

Ridd, M.K., 1995. Exploring a V-I-S (vegetation-impervious surface-soil) model for urban ecosystem analysis through remote sensing: comparative anatomy for cities. *Int. J. Remote Sens.*, 16, 2165-2185.

Roth, M., Oke, T.R., Emery, W.J., 1989. Satellite derived urban heat islands from three coastal cities and the urbanization of such data in urban climatology. *Int. J. Remote Sens.*, 10, 1699-1720.

Xiao, J., Tateishi, R., Shen, Y., Ge, J., Liang, Y., Chang, C., 2003. Analysis on urban sprawl and land cover change using TM, ETM+, and GIS. In: Proceedings of the 24th Asian Conference on Remote Sensing & 2003 International Symposium on Remote Sensing, pp314-316. Busan, Korea, Nov. 3-7, 2003.

Terrestrial Ecosystem Dynamics

Crop production monitoring by a photosynthesis-based index using meteorological data and NDVI

Daijiro Kaneko[1]

1 Department of Civil Engineering, Matsue National College of Technology
E-mail address: kand@ce.matsue-ct.ac.jp

Abstract

This paper first explain the necessity for monitoring crop production in China and India in the present age of increasing water-resource restrictions. Conventional early watching based on the growth index GDD deriving from the effective air temperature gave inaccurate estimates, as shown by data for the Crop Situation index in three specific years. It is necessary to construct and time-integrate a photosynthesis-based crop production index incorporating the effect of solar radiation in order to express the mechanism of photosynthesis. The monitoring system should include a surveillance model that takes into consideration the daily weather conditions. The author proposes a photosynthesis-based crop production index (CPI) that accounts for solar radiation, air temperature, vegetation biomass, and stomatal opening, and uses satellite and world weather data. Special emphasis should placed on rice production because of the demand for abundant irrigation in paddy fields and the fact that most rice is grown for local use, so that falls in production have greater consequences in purchasing countries.

***Key Words**: monitoring, crop production index, Remote Sensing, photosynthesis, World Weather Data, water stress*

---

1. Introduction

Given the atmospheric phenomenon of global warming, shortage of fresh water resources is now an capacity to support life. Unusual reductions in the discharge in the lower reaches of irrigation rivers are being observed, and a continuing fall in the groundwater level as a result of water usage. Such well-known organizations as the World Bank, the Worldwatch Institute (Sandra Postel, 1999) and World Water Council (2003) have warned about the present unsustainable use of water resources for irrigation in China, India, and the U.S., which have significant influence on the total quantity of grain production. These problems originate from the rapid increase in global population, currently 6 billion, which underlies many of the present global environment issues. Water shortages due to increasing demand by cities restricts grain production, and makes predictive crop surveillance important in order to estimate future supply and demand in Asia.

This work aims to develop a predictive method of monitoring the grain quantity in production that would be useful in the present era of increasing world population that needs both food and water. Knowledge of an impending bad harvest in China or India would assist in the planning of both Japanese internal affairs and foreign policy, reducing the economic and social strains caused by the consequent leap in grain prices and improving the security of the food supply; Japan produces only about 40% of its own grain. The author believes that a specific organization should be established to monitor grain production in the context of the social circumstances and security of the food supply in areas of Asia.

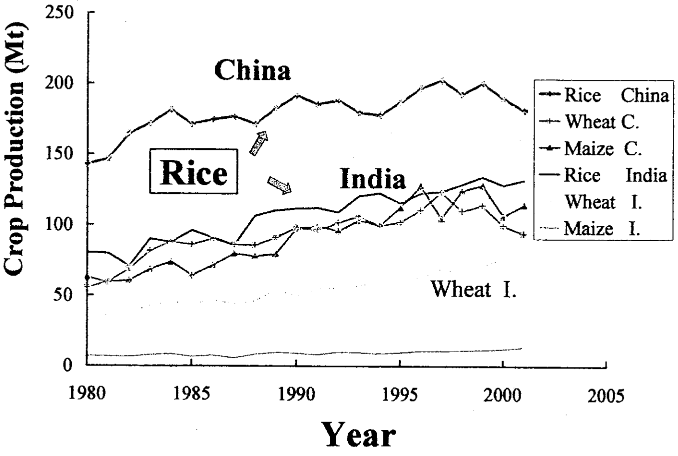

Fig. 1. Comparison of annual trend of crop production of rice and wheat in China and India, emphasizing the amounts of rice.

2. Relevance and background of the proposal for crop monitoring in view of limitations on water resources

2.1. Present status and issues in world trade and crop production in China and India

Fig. 1 shows the amount of grain production in China and India. Trends in the grain yield of these countries have wide significance because of their huge population and consumption. Chinese rice production should be 189.8 million tons in 2000 (FAO, 2003); rice is the staple that supports the gigantic Chinese population, providing twice the quantity of food as wheat or corn. Rice in India has twice the production of wheat, and its rice harvest is increasing rapidly, from 80.3 million tons in 1980 to 131.9 Mt in 2001 as a result of population increase. Rice production in China increased gradually from 142.8 Mt in 1980 to 202.7 Mt in 1998, but has since fallen a little with the loss of paddy areas to industrialization (Otsubo, 1999). Clearly rice is an excellent grain food, which supports the population in China and India. In view of the need for urgent imports to countries that would suffer a poor harvest, the present authors pay close attention to supply capability and the trade price of rice. Fig. 2 shows exports of rice from Thailand, which is the largest rice exporting country in the world, along with the amount of wheat and corn exported from the U.S., which is the largest crop exporting country in the world market. The amount of rice exported from Thailand in 2000, 6.14 Mt, is small compared with the corn export of 47.97 Mt and the wheat export of 27.83 Mt in the same year. It is well known that people who cultivate paddy areas aim to support themselves and their nation, in contrast to wheat and corn, much of which is grown for export. Problems with the rice crop could therefore have a catastrophic effect on countries that import rice and other crops.

Figs. 1 and 2 show this fact, that although there is a large production of paddy rice, most is grown for self-support. Only 5% or less of the total world rice production is exported/imported, compared to 25% for wheat. A poor harvest of paddy rice therefore causes a major disturbance in the world grain market. Moreover, although the yield of paddy rice per unit area is higher than that of wheat, and it is able to support large populations, rice demands about 3-4 times as much water per unit weight as wheat. To maintain security of their grain supply, it is therefore important for countries to be aware of the grain situation in their neighbors. This involves the development of methods for finding in advance whether a neighboring harvest will be inadequate, and the provision of policies ahead of any resulting crisis so as to minimize its impact.

2.3. Water Resources and issues of crisis management

1) Population increase and water demands

Increasing restrictions on freshwater resources is causing concern over supply and demand of grain with the rapid increase of world population; irrigation in Asian agriculture involves the greatest use of water-resources. The writer focuses on paddy rice rather than other staples such as wheat, corn and beans because paddy rice demands so much water and so many people are dependent on rice as their staple food.

2) Recent trends in climate change

A fall in annual precipitation in Japan has become clear in recent years, with a reduction of about 80mm in the 100 years to 2000. Global warming makes both heavy rain and drought more likely, increasing fluctuations in the pattern of precipitation.

A few early warning systems exist that are promoted by the Food and Agriculture Organization (FAO, 2003) of the United Nations, and an early watch system by DEWA of Earthwatch , and by USGS. However, these are not based on quantitative monitoring and modeling as described in this paper, but are forecasts based on agricultural weather conditions, involving mainly the seasonal temperature and precipitation.

2.5. Annual climate change and the Japanese situation in grain supply and demand

1) Bad harvest and the mechanism of annual climate change

Annual climate changes which cause a poor harvest may involve fluctuations in the latitude of the monsoon rain band, or in the date at which the rainy season begins. Crop production has a statistical character due to annual meteorological variation, and a notably poor harvest used to occur roughly every ten years. More recently, grain production tends to give good harvests worldwide, so that the price has fallen continuously for several years. The present market in crops is based on continuing good meteorological conditions.

2) Issues in crop supply and demand in Japan

In the 2002 fiscal year, Japan produced 28% of the grain it needed based on weight, 40% based on calories, and 60% based on weight of staple food. This is the lowest value among the advanced nations and raises concerns about the security of the food supply in Japan.

3. Method for monitoring crop production

3.1. Conventional methods for monitoring crop production

Much work on the monitoring of grain production has been published by the crop fraternity in the Agronomy Journal, or in the fields of equipment metrology for agricultural measurement (Idso 1979, Aase 1981, Jackson et al. 1981). However, most of this work is from the U.S., which produces the largest

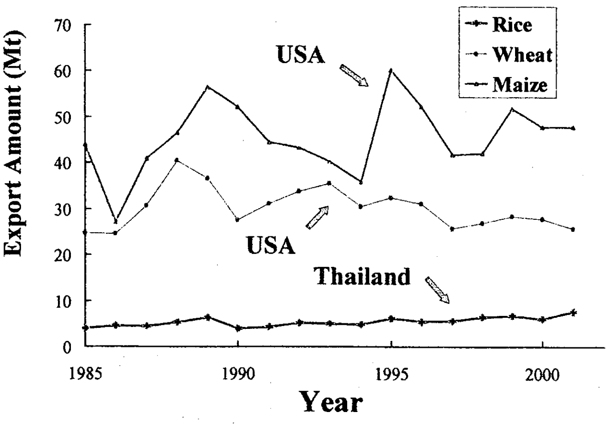

Fig. 2. Small export amounts of rice compared to wheat and maize in main exporting countries.

export crop in the world, and concerns wheat and corn rather than rice (Idso 1979, Diaz 1983). Papers on the monitoring of crop production in China or India over nationwide areas come only from the Chinese study group of Gao et al. (1998). Moreover, crop surveillance in India uses the presumptive methods of correlating crop production and satellite data (Murthy 1996, Manjunath 2002).

Many conventional crop studies have correlated the grain quantity in production with the growth index of Growing Degree Day GDD, or with water stress indices such as stress degree day (Idso 1979, Bollero 1996).

$$GDD = \frac{T_{\max} - T_{\min}}{2} - T_b \qquad (1)$$

where, T_{max} is the maximum daily air temperature, T_{min} is the minimum daily air temperature, and T_b is a threshold temperature for the crop, below which physical activity is inhibited and equal to 10 ℃.

In conventional research using remote sensing, the vegetation index NDVI (Aase 1981, Groten 1992, Quarmby 1993, Hayes 1996), concerning the vegetation biomass, is related to the crop production or modeled functions of the vegetation index NDVI and the photosynthetically active radiation PAR to estimate the grain quantity that will be produced (Rasmussen, 1992).

In these parameters, global solar radiation and stomatal opening are variables which change every day and are hard to account for in the amount of vegetation biomass represented by the NDVI. In crop studies to date, air temperature has been used instead of global solar radiation, and another water stress factor – transpiration control – is often also taken into consideration. In grain production forecasting using the latest remote sensing, daily values of the photosynthetically active radiation PAR and the vegetation biomass (NDVI) are taken into the model. Rasmussen (1992) defined the integrated NDVI (iNDVI) and related it to the grain quantity in production.

$$Yield = a \cdot \int_{t1}^{t2} NDVI(t)dt + b \qquad (4)$$

where, a and b are regression coefficients, and t1 and t2 are the day number of seeding and harvesting. Furthermore, Rasmussen (1998) gave the net primary production NPP using satellite data according to the following formula:

$$NPP = \varepsilon \int_0^t (aNDVI + b) \cdot PAR \cdot dt \qquad (5)$$

where ε is the efficiency coefficient,, t is the time, and PAR is the photosynthetically active radiation.

This NPP is a photosynthesis- type model. However, this formula does not allow for such important factors as temperature influences on photosynthesis, temperature sterility and stomatal opening of crops. The present research improves modeling based on the photosynthesis type of crop production index so as to incorporate the effects of global solar radiation, temperature, stomatal opening, and vegetation biomass. Although the areas of crop study and remote sensing have generated much research, especially on the production of wheat and corn, it is all restricted to consideration of the water stress or formulas based on vegetation indices. To give a more accurate value of the grain quantity in production, the crop production index should take the form of the photosynthesis velocity so as to express the growth of crop vegetation and filling of grain, both of which relate directly to the quantity produced.

3.2. New photosynthesis type of crop production index

1)Concept of modeling

The final purpose of this work is to carry out early surveillance of the crop quantity in production in China and India in the present era of water-resource restriction by using the photosynthesis type of crop production index mentioned above. Apart from insect damage, the following factors are the main causes of reduced crop production: insufficient solar radiation, water stress due to rain shortage (including reduced irrigation); and insufficient fertilizer. Observation of solar radiation is not easy, and reduced solar radiation lowers the air temperature, so that many researchers have used the air temperature instead of solar radiation (Idso 1979, Williams 1989, Bollero 1996). In another words,

Distribution of Observation Sites for World Weather

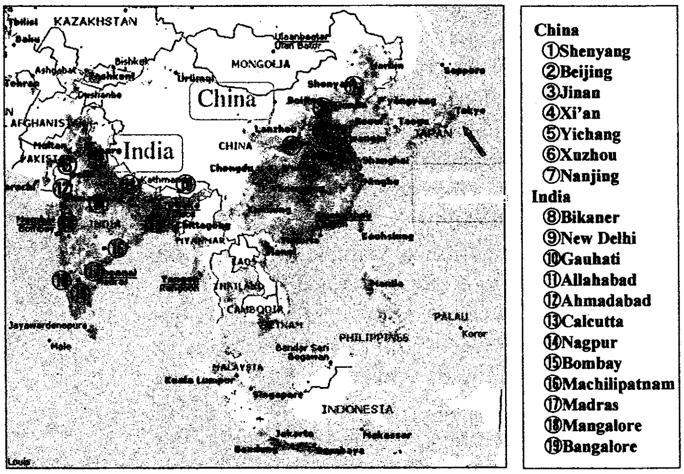

Fig. 3. Distribution of monitoring sites in China and India at World Weather points, including test sites for modeling and validation of crop production indices.

it is necessary to account for the effects of transpiration from stomata as well as solar radiation. The author believes that the crop quantity in production depends fundamentally on the integrated value of the photosynthesis rate, which depends on stomatal opening as well as solar radiation and vegetation biomass. In addition, there are the plant-physiological factors of low temperature sterility and high temperature injury during flowering and filling out of crops, which must be taken into account as well as the photosynthesis rate in the grain production index.

In view of global warming, many researches have reported the effect of the CO_2 concentration on grain production through the photosynthesis rate, from field and laboratory experiments (Moya 1998, Seneweera et al. 2002). However, since the density of CO_2 in the atmosphere is stable enough to guarantee the carbon supply for crop production, the effect of the CO_2 concentration is not taken into consideration in the grain production index. Moreover, the effect of fertilizer can be reflected in the vegetation index NDVI showing the crop vegetation biomass. Similarly, damages by blight and harmful insects are disregarded since they appear in the NDVI. The present model therefore expresses the photosynthesis rate using the solar radiation, temperature dependence on photosynthesis, water stress, vegetation biomass, and low-temperature sterility and high temperature injury effects on flowering and filling.

2) Monitoring method using photosynthesis type of crop production index

The photosynthesis rate depends on the factors considered above including solar radiation, stomatal opening, and vegetation biomass. Therefore, while modeling of crop production expresses plant growth by the vegetation index that indicates the density of crop vegetation, it is also necessary to model stomatal opening according to soil moisture and weather conditions, as in the SiB (Sellers, 1989) model in meteorology. Although soil moisture has been closely studied for many years, accurate estimates are difficult because the earth surface is confused by vegetation.

Water stress in crop studies focuses on the amount of precipitation; quantitatively, a crop water stress index can be defined by $CWSI=1-E_{ac}/E_p$. Several researchers examined the relation between water stress and the grain quantity in production using this method (Jackson et al. 1981, Diaz et al. 1983, Abdul-Jabbar 1985). However, it is not easy to model the actual evapotranspiration in defining water stress on the regional scale. The present research seeks to develop a photosynthesis-type of monitoring method by measuring the water stress so as to improve the formula (5) presented by Rasmussen. The final form of the photosynthesis rate is defined in formula (6), which takes into consideration the solar radiation, air temperature, stomatal opening, and vegetation biomass (Kaneko 2003).

$$PSN = \frac{a \cdot APAR}{b + APAR} \cdot f_{ster}(T_c) \cdot \beta_s \cdot eLAI \tag{6}$$

where, PSN is the photosynthesis velocity, APAR is the absorbed photosynthetically active radiation, β_s is the stomatal opening, a and b are Michaelis -Menten reaction constants, T_c is the canopy temperature, eLAI is the effective leaf area index, and f_{ster} is the sterility response function of air temperature.

The integrated photosynthesis type of crop production index CPI is defined by the following formula concerning the period from seeding ts to harvest th.

$$CPI = \int_{t_s}^{t_h} PSN \cdot dt \tag{7}$$

Many researchers have presented crop simulation models that involve growth of crops and incorporate remote sensing data from previous years (Wiegand et al. 1986, Maas 1988, Williams et al. 1989, Perez et al. 2002). However, it is desirable to express the mechanism of growth and filling more simply than in these models, which are complex and contain many empirical constants (Monteith 1996, Sinclair and Seligman 1996). By measuring growth of crop vegetation using remote sensing instead of simulation, the present paper estimates the photosynthesis rate by treating the growth of crop as a known variable. Estimation of the total quantity of crop produced is then easy, and the result is accurate since it is based on the actual observed value of the vegetation biomass deduced from satellite data even for foreign areas where data is not available. Above, modeling has proceeded as far as the incorporating factors into the crop production index CPI such as solar radiation, air temperature, and vegetation biomass. The proposed method improves the accuracy of estimates of crop yield over methods based on the

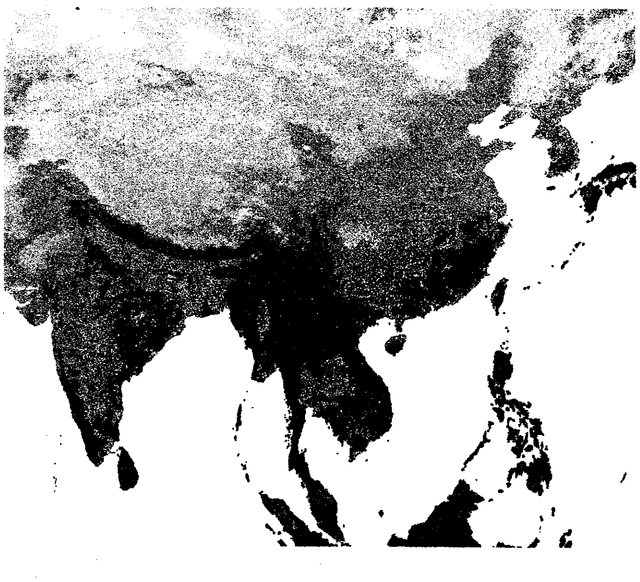

Fig.4. Distribution of the normalized difference vegetation index NDVI in Asia for use in crop production indices such as integrated NDVI and the CPI as defined in the present paper.

cumulative effective temperature GDD, and the integrated NDVI. This is because the writer estimates the photosynthesis rate from meteorological factors, and then integrate it.

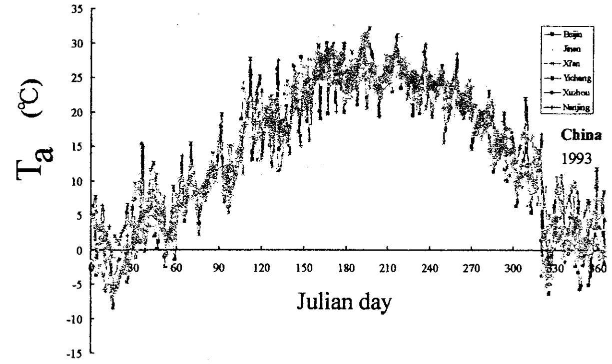

Fig. 5. Seasonal variations of air temperature at 7 monitoring points of world weather sites in China for modeling the effects of temperature in the crop production index CPI.

4. Data used in the modeling

4.1. World Weather data and its characteristics

Fig. 6 depicts the distribution of observation points of world weather data, showing the population density distribution in China and India, which is important for grain transportation and consumption. Names surrounded by frames are the monitoring sites where weather data are applied to consider the grain production index CPI in this research. World weather data for the crop production index is selected for the following reason. Estimation of the photosynthesis rate needs daily data of solar radiation and air temperature, so that the meteorological data must be routine daily weather data as taken throughout the world. The world weather data is most suitable for the index CPI because daily regular data are currently observed as weather reports in real time. As study target points the author takes 7 points in China and 13 points in India. The CPI index requires cloud coverage to give the solar radiation at these points, and also the cloud coverage and solar radiation to verify the estimated solar radiation from the cloud amount (Kaneko 2002).

4.2. NDVI derived from satellite

Fig. 7 shows the distribution of the vegetation index NDVI in Asia using a data set derived from NOAA AVHRR by Tateishi (2001). The crop production index CPI requires the vegetation index NDVI at the positions of the world weather sites for which data are available as daily weather reports. The monitoring sites for CPI are 8 observation sites in China and 12 in India, along with validation points at meteorological observatories or AMeDAS sites in Japan. The vegetation index NDVI is extracted at pixel numbers calculated from the longitude and latitude of the weather observatories.

4.3. Crop statistics

The background analysis of the grain quantity of production in China and India was based on data from the Food and Agriculture Organization FAO of the United Nations. Japanese domestic data for the grain trade and the total grain tonnage produced are based on the agricultural statistics information database of the Ministry of Agriculture, Forestry, and Fisheries. Crop statistics from the FAO were used in constructing the figures for annual changes in grain tonnage in Fig.1, and the amount of grain trade in the major countries in Fig. 2.

5. Results by growing index and Crop production index

The crop production index CPI and several indices are scrutinized with the Crop Situation index for paddy rice at the large complex of paddy fields around Kuki in the mid-region of the Tone river in Kanto plain, Japan. The main results so far are as follows.

5.1. Growing index GDD

Fig.9 shows variations in the cumulative effective air temperature at monitoring sites in China. These curves are applied to practical use via the well known index of growth index GDD at seven paddy rice and spring wheat sites in China. The cumulative effective temperature as a growth index GDD is required in the form of a photosynthesis type of crop production index for the modeling of growth. Fig. 8 shows seasonal changes of the

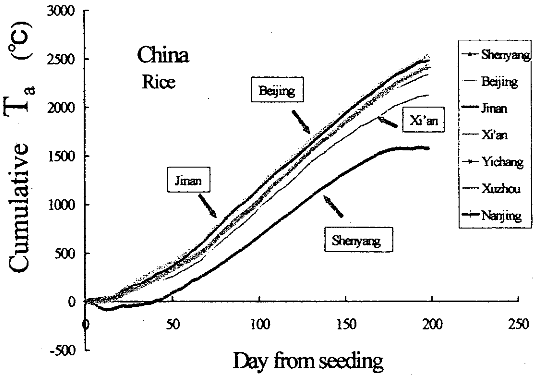

Fig.6. Variation of cumulative effective air temperature at monitoring sites in China. These curves are applied to practical use

effective temperature accumulated during each period of planting as the growing degree days index GDD for paddy rice and spring wheat at the monitoring points of the world weather points shown in Fig. 6. To examine the value of the growing index GDD as a grain production index, Fig. 10 shows the relation between the GDD and the Crop Situation index for paddy rice at Kuki, which is a verification site in Japan. The growth index GDD was able to represent the poor harvest, having low Crop Situation index 74 of paddy rice, following damage by exceptionally cold weather in 1993, but GDD could not represent the bad harvest of Crop Situation index 98 in 1998 that was due to insufficient solar radiation even though the temperature was adequate. Moreover, the GDD must distinguish between the small good harvest of Crop Situation index 102 in 1997 and the Crop Situation index 98 in 1998. Although the GDD is a growth index, it is not a direct index of grain production. In the field of agriculture, there is also a method of predicting the total grain tonnage using the shape of the growth curve of the seasonal NDVI. However, the growth curve of NDVI is not a grain production index, but a growth index, as is the integrated vegetation index iNDVI.

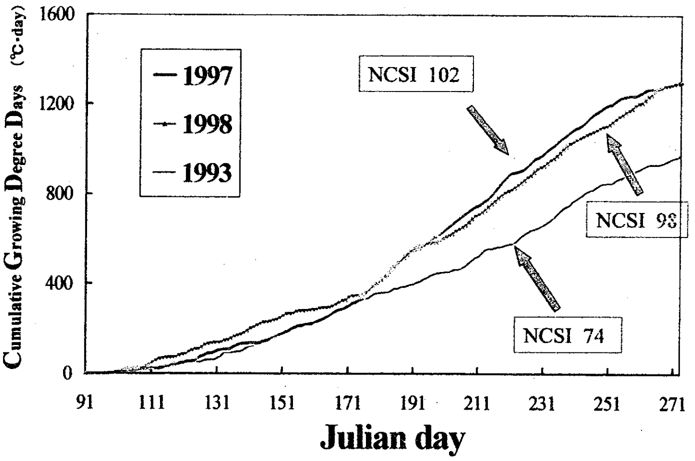

Fig.7. Seasonal curves of cumulative GDD and relation to the crop situation index NCSI of rice at Kuki site in Japan.

5.2. Integrated NDVI (iNDVI)

Satellite data is effective in foreign areas where it is difficult to obtain weather data. Fig. 11 shows the integrated NDVI mentioned above around the monitoring points in China. If there is neither water stress nor low temperature sterility around the time of flowering, the crop quantity of production should be high in crop areas where the integrated vegetation index iNDVI is large. Therefore the large values of the integrated vegetation index at Jinan or Yichan in Fig. 11 suggest a good harvest in those areas. This iNDVI is the integrated value of the vegetation biomass, which is incorporated also in the photosynthesis type of crop production index CPI. The iNDVI is a vegetation growing index, which measures the crop plant density. It was designed as a monitoring tool for the total grain tonnage. However, the iNDVI is really a growth index; it cannot, for example, express the effect of a lack of sunshine, or effects of low-temperature sterility during flowering and filling. Even if stomata close and photosynthesis is limited by shortage of soil moisture, leaves remain vivid green so that the reduced photosynthesis is not captured by the vegetation indexes NDVI and iNDVI. This is why Rasmussen (1992, 1998) proposed the improvement in formula (5) to take into account photosynthetically active radiation. However, the model still does not allow for low temperature sterility or water stress.

5.3. Photosynthesis type of crop production index CPI

Fig. 12 shows the photosynthesis-based crop production index CPI taking into consideration the vegetation index NDVI as vegetation biomass as well as solar radiation and effective air temperature GDD. The values of the Crop Situation index at Kuki site in Saitama prefecture are included in the figure. The CPI index clearly shows the poor harvest due to low temperatures in 1993, and that due to lack of sunshine in 1998,and captures also the quantitative difference between the good harvest in 1997 and these poor harvests. The discernment ability is much greater than the growing indices GDD and iNDVI. The photosynthesis-based crop production index CPI turns out to be a good index for monitoring.

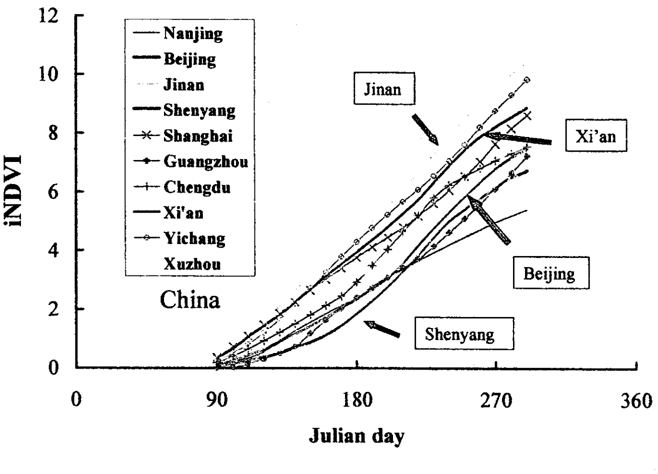

Fig. 8. Integrated NDVI (iNDVI) of paddy fields in China as a growth index for crop production.

One of the authors (Kaneko, 2003b) is also proposing a CPI that accounts for sterility below air temperatures of 18.5 centigrade and injury above 40 degrees (Matsui et al. 1997, 1997b).

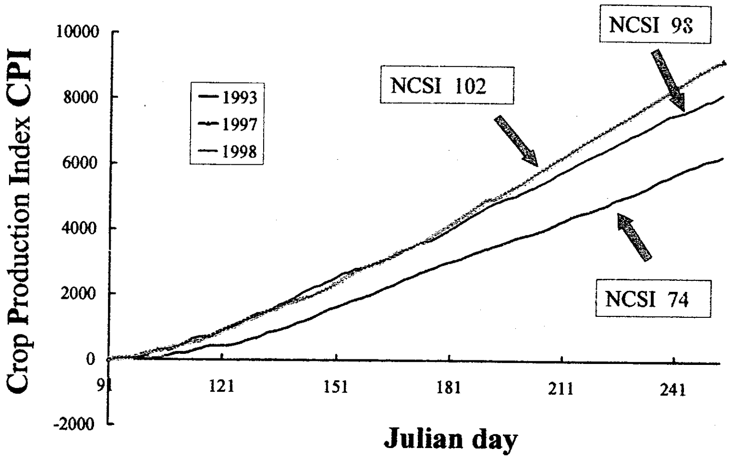

Fig. 9. Daily variation of crop production index CPI at the Kuki site in Japan with values of the crop situation index.

6. Conclusions

This paper have proposed a daily surveillance system for monitoring crop production in China and India that uses an improved photosynthesis-based crop production index, necessary to take into account water stress of crops. Monitoring of the crop quantity in production in these countries has the social background of the increasing Asian population, and the purpose is to give advance warning of poor crop production in the present era of water-resource restrictions. The proposed method for surveillance of the grain quantity in production in both countries has the following features.

It is important to monitor crop production in China and India in the present and coming era of water-resource restrictions. The background to the proposal involves social issues in Japan and its neighbors. The monitoring system includes the surveillance model, which takes into consideration daily changes in weather conditions. The model proposes to use world weather data in the monitoring model, specifically daily weather data for China and India. Without simulating the growth of crops, remotely sensed data can give the vegetation biomass of the crops in both countries using satellite data. Conventional predictive monitoring based on the growing index GDD derived from the effective air temperature was inaccurate, as shown by the Crop Situation Index in 3 years. It is necessary to construct a photosynthesis-based crop production index incorporating the effect of solar radiation so as in to express the mechanism of photosynthesis. The vegetation index NDVI from satellite should be taken into the crop production index CPI for the vegetation biomass, as proposed by Rasmussen. The author proposes a photosynthesis-based crop production index CPI taking into consideration such factors as solar radiation, air temperature, vegetation biomass, and stomatal opening using satellite data and world weather data. The present CPI index proved more accurate than the conventional cumulative GDD and the integrated NDVI as a crop production index for early monitoring of paddy rice.

Acknowledgment

This study is funded by Grants-in-Aid for Scientific Research and University of Chiba, for which I thank Center for Environmental Remote Sensing (CEReS) and also the Japan Society for the Promotion of Science, which is part of the Ministry of Education, Culture, Sports, Science and Technology.

Refferences

Aase, J. K., and Siddoway, F. H., 1981. Spring wheat yield estimates from spectral reflectance measurements, IEEE Transactions on Geoscience and Remote Sensing, GE-19(2), 78-84.

Abdul-Jabbar, A. S., Lugg, D. G, Sammis, T. W., and Gay, L. W., 1985. Relationships between crop water stress index and alfalfa yield and evapo- transpiration, Transactions of the American Society of Agricultural Engineers, 28[2], 454-461.

Bollero, G. A., Bullock, D. G, and Hollinger, S. E., 1996. Soil temperature and planting date effects on corn yield, leaf area, and plant development, Agronomy Journal, 88, 385-390.

Diaz, R. A., Matthias, A. D., and Hanks, R. J., 1983. Evapotranspiration and yield estimation of spring wheat from canopy temperature, Agronomy Journal 75(9-10), 805-810.

Food and Agriculture Organization of the United Nations, 2003. FAO FAOSTAT Database: http:// apps.fao.org/ cgi-bin/ nph-db.pl?subset= agriculture.

Gao, Y., Jin, G, and Chen, H., 1998. Simulating the optimal growing season of rice in the Yangtze River Valley and its adjacent area, China, Agricultural and Forest Meteorology, 91,251-262.

Groten, S. M. E., 1992. NDVI-crop monitoring and early yield assessment of Burkina Faso, International Journal of Remote Sensing, 14(8), 1495-1515.

Hayes, M. J., and Decker, W. L., 1996. Using NOAA AVHRR data to estimate maize production in the United States Corn Belt, International Journal of Remote Sensing, 17(16), 3189-3200.

Idso, S. B., Pinter, Jr. P.J., Hatfield, J. L., Jackson, R. D., and Reginato, R. J., 1979. A remote sensing model for the prediction of wheat yields prior to harvest, Journal of Theoretical Biology, 77, 1979, 217-228, 1979.

Jackson, R. D., Idso, S. B., Reginato, R. J., and Pinter Jr, P. J., 1981. Canopy temperature as a crop water stress indicator, Water

Resources Research, 17(4), 1133- 1138.

Kaneko, D., 2002. Estimation of global solar radiation using world weather data for early monitoring of crop production by satellites, Proceedings of 6th symposium on water resources, Tokyo, 677-682. (In Japanese with English abstract).

Kaneko, D., Onishi, M., and Ishiyama T., 2003. Proposal of early monitoring method for crop production in China and India in the recent era of water resources restriction Environmental Systems Research, Japan Society of Civil Engineering, 31, 235-244. (In Japanese with English abstract).

Kaneko, D., Onishi, M., 2003b. Modeling on indices for monitoring crop production using meteorological data and Vegetation Index NDVI, Japanese Journal of Crop Science, 72(Extra issue 2), 92-93. (In Japanese)

Maas, S. J., 1988. Using satellite data to improve model estimates of crop yield, Agronomy Journal, 80, 655-662.

Manjunath, K. R. and Purohit, N. L., 2002. Large area operational wheat yield model development and validation based on spectral and meteorological data, International Journal of Remote Sensing, 23(15), 3023-3038.

Matsui, T., Namuco, O. S., Ziska, L. H. and Horie, T., 1997, Effects of high temperature and CO_2 concentration on spikelet sterility in indica rice, Field Crops Research, 51, 213-219.

Matsui, T., Omasa, K., and Horie, T., 1997b, High temperature -induced spikelet sterility of Japonica rice at flowering in relation to air temperature, humidity and wind velocity conditions, Japanese Journal of Crop Science , 66(3), 449-455.

Monteith, J. L., 1996. The quest for balance in crop modeling, Agronomy Journal, 88, 695-697.

Moya, T. B., Ziska, L. H., Weldon, C., Quilang, J. E. P., Jones, P., 1997. Microclimate in open-top chambers: implications for predicting climate change effects on rice production, Transactions of the American Society of Agricultural Engineers, 40(3), 739-748.

Murthy, C. S., Thiruvengadachari, S., Raju, P. V., and Jonna, S., 1996. Improved ground sampling and crop yield estimation using satellite data, International Journal of Remote Sensing, 17(5), 945-956.

Otsubo, K., 1999. Regional differences in future food supply in China – viewed from the land-use grid data –, Proceedings of 1999 NIES Workshop on Information Bases and Modeling for Land-use and Land-cover Changes Studies in East Asia, Center for Global Environmental Research, ISSN 1341-4356, 172-177.

Perez, P., Ardlie, N., Kuneepong, P. Dietrich, C., and Merritt, W. S., 2002. CATCHCROP: modeling crop yield and water demand for integrated catchment assessment in northern Thailand, Environmental Modeling & Software, 17, 251-259.

Quarmby, N. A., Milnes, M., Hindle, T. L., and Silleos, N., 1993. The use of multi- temporal NDVI measurements from AVHRR data for crop yield estimation and prediction, International Journal of Remote Sensing, 14(2), 199-210.

Rasmussen, M. S., 1992. Assessment of millet yields and production in northern Burkina Faso using integrated NDVI from the AVHRR, International Journal of Remote Sensing, 13(18), 3431-3442.

Rasmussen, M. S., 1998. Developing simple, operational,
consistent NDVI-vegetation models by applying environmental and climatic information: Part II. Crop yield assessment, International Journal of Remote Sensing, 19(1), 119-137.

Sandra Postel, 1999. Pillar of sand – Can the irrigation miracle last? -, W. W. Norton & Company, Inc., New York, U.S.A. with the Worldwatch Institute, Washington, D.C.,U.S.A .

Sellers, P. J., Shuttleworth, W. J., and Dorman, J. L., 1989. Calibrating the simple biosphere model for Amazonian tropical forest using field and remote sensing data. Part I : Average calibration with field data, Journal of Applied Meteorology, 28, 727-759.

Sinclair, T. R. and Seligman N. G., 1996. Crop modeling: from infancy to maturity, Agronomy Journal, 88, 698-704.

Seneweera, S. P, Conroy, J. P., Ishimaru, K., Ghannoum, O. Okada, M., Lieffering, M., Kim, H. Y., and Kobayashi, K., 2002. Changes in sourceA-sink relations during development influence photosynthetic acclimation of rice to free air CO_2 enrichment (FACE) , Functional Plant Biology, 29(8), 947-954.

Tateishi R.: Twenty-year global 4-minute AVHRR NDVI dataset, CEReS, Chiba University, 2001.

Wiegand, C. L. Richardson, A. J., Richardson, A. J., Jackson, R. D., Pinter, Jr. P. J., Aase J. K., Smika, D., Lautenschlager, L. F., and McMurtrey, Ⅲ J.E., 1986. Development of Agrometeorological crop model inputs from Remotely sensed information, IEEE Transactions on Geoscience and Remote Sensing, GE-24(1), 90-98, 1986.

Williams, J. R., Jones, C. A., Kiniry, J. R. and Spanel, D. A., 1989. The EPIC crop growth model, Transactions of the ASAE, 32(2), 497-511.

World Water Council, 2003. The 3rd World water forum, Summary forum statement, Thematic/Regional statements Ministerial declaration, 105pp.

Livestock mapping in Mongolia using satellite and statistical data

R.Tsolmon, R.Tateishi and Ts .Enkhzaya
Center for Environmental Remote Sensing, Chiba University

Abstract: Livestock production makes an important contribution to most economies. The contribution of livestock data to the calculation of poverty indicators or in identifying livelihood strategies, which is primary in remote areas of developing countries, such as Mongolia is significant.

Assessing livestock production and its requirements in relation to other possibly competing natural resource sectors (wildlife, forestry) is becoming necessary.

This study carried out an investigation to determine the relationship between number of livestock and vegetation derived NOAA satellite data. The research tries to identify what data are needed for livestock mapping in grassland area. Output livestock mapping can be used to contribute to sustainable management of grasslands in Mongolia and improve animal production and feeding with locally available feed resources.

Key words: *pasture land, livestock, vegetation index, and socio-economic data*

1. Introduction

Grasslands are one of the main natural resources used for livestock. The extended grasslands of Mongolia have been used for five kinds of animals: camels, horses, cattle, sheep and goats. Mongolian livestock breeding have been based on the use of natural pasture throughout the year, as 80% of the total territory is used for pastures(Figure 1).

Environmental degradation and desertification from human pressure and land use has become a major problem. Changes in the spatial distribution and size of the livestock population effects on the other sectors of agriculture.

The state of the resource base of the Mongolian rural area should be examined in relation to population pressure by integrating vegetation growth. It is essential to understand nomadic animal husbandry with the information related to environmental and socio-economic variables.

The objective of this paper is to examine the relationship between number of livestock and vegetation growth derived from NOAA satellite data of four different natural zones.

2. Study area and data

The study area is Mongolia, is located in the central part of Asia continent:

N40°35′-52°09′ and E87°44′-119°56′Total area: 1.56 million square km. Climate: short-dry summer and long-cold winter season. Growing season: from May to September.

In general, Mongolia can be divided into main 4 natural zones: high mountain, forest, steppe, and desert-steppe. This research will examine the following 4 provinces from each natural zone: Bayan-Ulgii, Dornod, Tuv and Dundgovi. NOAA AHVRR NDVI data 8 km, 1995-2000 and statistical data from years 1995-2001 were carried for this research (Figure 2).

3. Methodology and analyses

Livestock populations are not static. Livestock distributions change with the seasons, droughts

$$\Delta L = F(V + \Delta V, S, P, M) - L(V, S, P, M)$$

and with vegetation growth In this study the relationship between numbers of livestock and NDVI was analysed using DUMMY VARIEBLIES method. Partial increments of vegetation and change where L is numbers and densities of livestock ,V is vegetation index, S seasonal change, P is productivity parameters and intensification levels and M is movement of livestock husbandry.

We examined the relationships between livestock number and vegetation growth over 1995-2001 (Figure 3).

4. Conclusions

According to the monthly NDVI composite images, we can determine the temporal and spatial changes of vegetation growth. We calculated normal values using monthly composite NDVI of July for each region and all natural zones have different NDVI value, especially in growing season. We can describe that there have other factors, such as economic interest from the statistical data and need to examine and integrate other social-economic data.

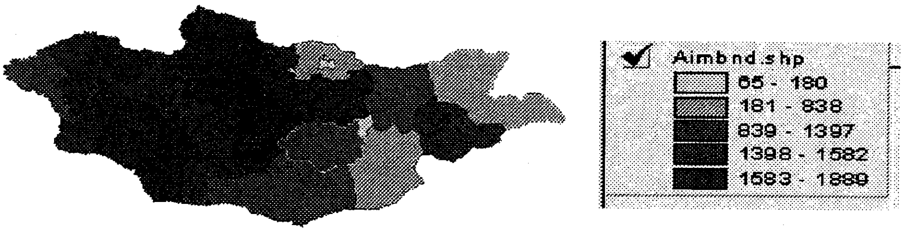

Figure 1. Livestock in the study area by 2001 year

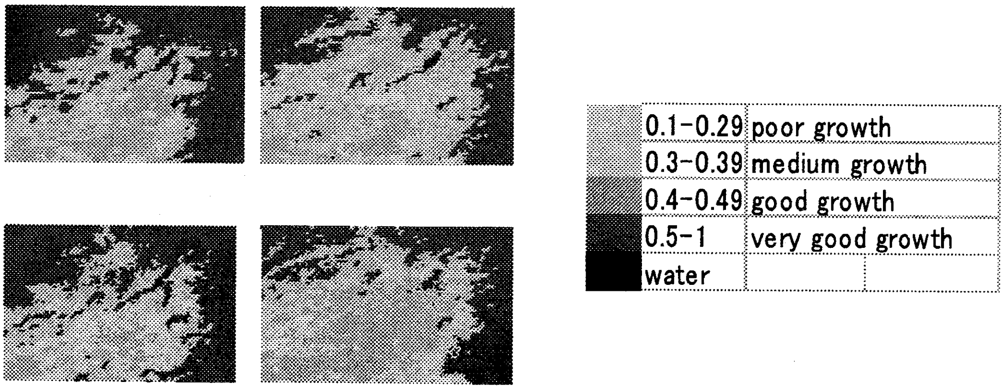

Figure 2 . Vegetation growth in selected 4 areas of Mongolia in 1995-2001

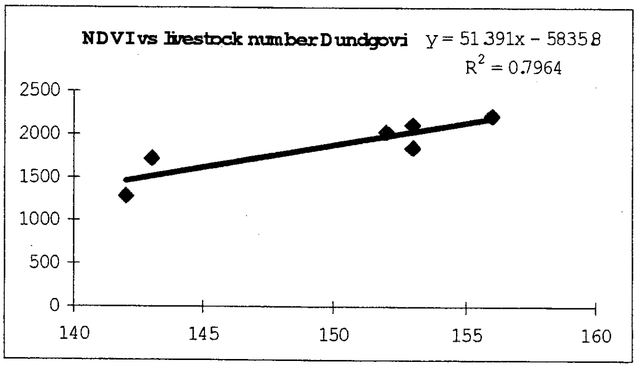

Figure 3. Relationship between NDVI and livestock in 1995-2001

References

Tateishi, R., Hastings, Global Environmental Databases, Vol.2, 2002.

Tsolmon, R., Methodology to estimate coverage and biomass of boreal forests using satellite data, Doctoral dissertation, (Chiba university) 2003.

Erdenetuya, M., Khudulmur, S., Land cover and pasture estimation of Mongolia from space. Website: http://www.GISdevelopment.net/application/environment/conservation/envc0002

Mongolia Environmental Monitor, 2003. Land resources and their management

Synergetic use of SPOT/Landsat and IKONOS data for terrace rice fields monitoring.

Nobuyuki MINO
Himeji Institute of Technology
/ Awaji Landscape Planning and Horticulture Academy
E-mail: minonobu@awaji.ac.jp

Abstract

Although satellite remote sensing provide large-scale coverage of traditional agricultural region, most "high-resolution" instruments, such as Landsat ETM+, SPOT HRVIR, provide limited descriptive resolution of the such landscape. With the launch of the IKONOS satellite in 1999, imagery with a 4 m spatial resolution in multispectral mode can now be combined with other satellite data archives for change detection. We demonstrate this potential by combining SPOT/Landsat and IKONOS image to detect change in the traditional terrace rice fields for Awaji Island, Hyogo, Japan. According to our analysis using data in 1990 and 2001, losses in rice paddy fields over this period are faster at the hilly mountainous region and slower in flat agricultural region. Synergetic use of IKONOS and SPOT/Landsat appears to be a relevant source of information to show change and fragmentation in traditional terrace rice fields.

1. Introduction

Traditional terrace rice fields provide a variety of ecosystem services including the provision of shelter from storms, a wealth of biodiversity, and cultural fundamentals. However, many processes including rising imported agricultural products pressure and aging of farmers communities are forecast to threaten such traditional agricultural landscape over the coming decades. As terrace rice fields in Japan experience increasing stress from global processes, scientists and resource managers must look to large-scale methods of ecosystem assessment.

Although satellite remote sensing provide large-scale coverage of traditional agricultural landscape, most "high-resolution" instruments, such as Landsat ETM+, SPOT HRVIR, provide limited descriptive resolution of the ecosystem. Since 1999, however, the successful launch of IKONOS has largely overcome the spatial constrain to satellite remote sensing. IKONOS acquires both 4 m spatial resolution multispectral and 1 m spatial resolution panchromatic data. The multispectral data consist of four bands, three in visible (red, green, blue) and one in the near-infrared; the wavelength range of these bands is comparable to the first four bands of Landsat TM and ETM+ sensors. In this study, we assess the potential of IKONOS imagery combined with SPOT/ Landsat to detect changes in traditional terrace rice fields, using Awaji Island in Japan as a case study.

2. 2. Material and Methods

2.1. Approarch

Paddy fields are flooded during the rice-planting season and only a single crop is cultivated in them yearly. Due to small difference in the stages of growth, paddy fields are easily identified from the satellite data acquired in the rice-planting season. Especially, satellite data equipped with a middle-infrared band, such as Landsat TM, ETM+, SPOT HRVIR, can discriminate paddy fields distribution in the landscape clearly (Okamoto et al. 1996, 1998). In this study, overlay analysis applied to the Landsat TM data acquired in June 19, 1990 and SPOT HRVIR for June 16, 2001, changed area from paddy fields to the other land covers were identified (figure 1). Discrimination of paddy fields in each satellite data was performed using the Near-Infrared / Red – Middle-Infrared / Red coordinates. Middle-infrared / Red clearly reflects the flooded conditions, and the Near-Infrared / Red, that is vegetation index, is sensitive to the vegetation cover. In such coordinate, only paddy fields are plotted in the areas which have low Near-Infrared/Red and Middle-infrared/Red values. For fine scale mapping (4m resolution), high Near-Infrared / Red values distribution map from IKONOS data acquired in June 12, 2001 overlaid to the SPOT/Landsat-based analysis result.

2.2. Descriptions of study site

Awaji Island is located in the eastern part of Setouchi Sea, and covers 595.64 km squares. The northern part of this area is characterized by hilly and steep slope landscape and result in many terrace rice paddy fields dominant agricultural region. In contrast, central part of this area has almost flat topography and become rich large-scaled agricultural region. Most of losses in rice paddy fields have occurred in the northern part of Island.

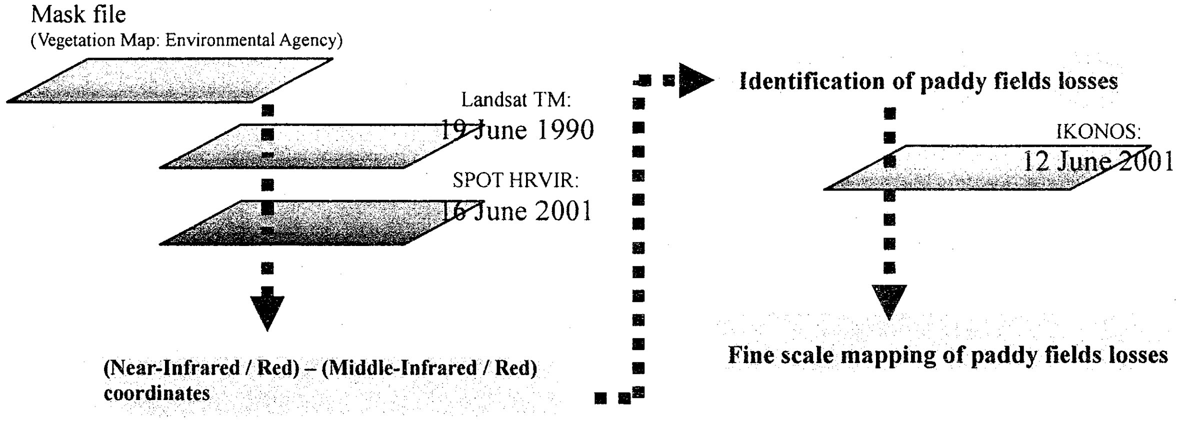

Figure 1. Flow of analysis on identification of paddy fields losses

3. Results

Paddy fields losses in Awaji Island can be detailed spatially as follows. Most of paddy fields losses concentrated in hilly mountainous region, especially at the border of forest cover. On the other hand, a few paddy fields losses we observed in the flat agricultural region. Soil fertility and labor cost are considered to be significant factors for those differences on paddy fields losses. Those results of this preliminary study were almost consistent with statistical data in annual agricultural reports. Fine scale map derived from SPOT/ Landsat and IKONOS satellite can be considered to be excellent indicator of the current change process on traditional agricultural landscape.

4. Conclusion

The trend of traditional rice fields decrease can be examined by the combination of IKONOS and SPOT/Landsat data. According to our analysis using data in 1990 and 2001, losses in rice paddy fields over this period are faster at the hilly mountainous region and slower in flat agricultural region. That tendency was almost consistent with the statistical reports on rice paddy field acreage. Therefore, synergetic use of IKONOS and SPOT/Landsat appears to be a relevant source of information to show change and fragmentation in traditional agricultural landscape. The degree of generalization of this approach must be cautiously stated due to high diversity of rice field configurations.

References

OGAWA, S., INOUE, Y., MINO, N., and TOMITA, A., 1999, Monitoring of rice field using SAR data and optical data. *Proceedings of the Second International workshop on retrieval of bio- and geo-physical parameters.* p.151-159.

OKAMOTO, K., and FUKUHARA, M., 1996, Estimation of paddy field area using the area ratio of categories in each mixel of Landsat TM. *International Journal of Remote Sensing*, 17(9), 1735-1750.

OKAMOTO, K., YAMAKAWA, S., and KAWASHIMA, H., 1998, Estimation of flood damage to rice production in North Korea in 1995. *International Journal of Remote Sensing*, 19(2), 365-371.

OKAMOTO, K., and KAWASHIMA, H., 1999, Estimation of rice-planted area in the tropical zone using a combination of optical and microwave satellite sensor data. *International Journal of Remote Sensing*, 20(5), 1045-1048.

Development of Forest Cover Density Mapping Methodology

Atsushi Rikimaru and Ryutaro Tateishi
Nagaoka University of Technology
E-mail; rikimaru@nagaokaut.ac.jp
Center for Environmental Remote Sensing, Chiba University
E-mail;tateishi@faculty.chiba-u.jp

Abstract

Forest cover density is one of the most useful parameters to consider in the planning and implementation of rehabilitation program. This study is development of bio-physical analysis model for obtaining of Forest Canopy Density (FCD) using LANDSAT TM data image analysis. The four key components of FCD model are viz. vegetation, bare soil, thermal and shadow. The initial and medium stages of this study was implemented under the research project of International Tropical Timber Organization (ITTO).

1. Introduction

As generally applied in forestry, conventional RS methodology is based on qualitative analysis of information derived from training areas (i.e. ground-truthing). This has certain disadvantages in terms of the time and cost required for training area establishment, and the accuracy of results obtained. In this new methodology, forest status is assessed on the basis of canopy density. The methodology is presently identified as the Forest Canopy Density Mapping Model, or for short the FCD Model. Unlike the conventional qualitative method, the FCD Model indicates the growth phenomena of forests which are quantitative analysis. (Shown in Fig. 1) The degree of forest density is expressed in percentages: i.e. 10% FCD; 20%; 30%; 40% and so on. FCD data indicates the intensity of rehabilitation treatment that may be required. The method also makes it possible to monitor transformation of forest conditions over time including degradation. Additionally, it can assess the progress of reforestation activities.

The Forest Canopy Density (FCD) Mapping and monitoring Model utilizes forest canopy density as an essential parameter for characterization of forest conditions. FCD data indicates the degree of degradation, thereby also indicating the intensity of rehabilitation treatment that may be required.

The source remote sensing data for FCD model is LANDSAT TM data. The FCD model comprises bio-physical phenomenon modeling and analysis utilizing data derived from four (4) indices: Advanced Vegetation Index (AVI), Bare Soil Index (BI), Shadow Index or Scaled Shadow Index (SI, SSI) and Thermal Index (TI). It determines FCD by modeling operation and obtaining from these indices.

The canopy density is calculated in parentage for each pixel. The FCD model requires less information of ground truth. Just for accuracy check and so on.

FCD model is based on the growth phenomenon of forests. Consequently, it also becomes possible to monitor transformation of forest conditions over time such as the progress of forestry activities. The application tests were implemented in this area. The evergreen forests are in the islands of Luzon (Philippines) and Sumatra (Indonesia); and for monsoon (subtropical deciduous) forests in Ching-Mai (Thailand) and Terai (Nepal).

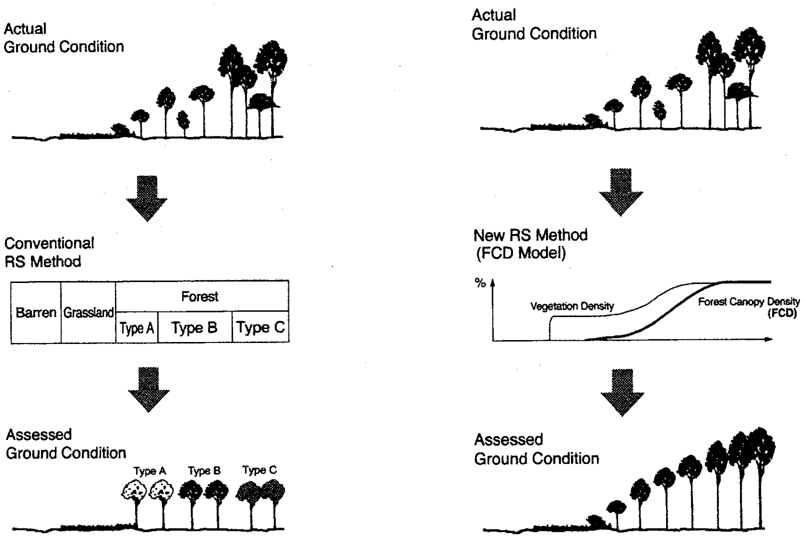

Fig. 1 Analysis by conventional (left) and FCD (right) methods

2. Characteristics of Four Prime Indices

The indices have some characteristics as below. The Forest Canopy Density Model combines data from the four (4) indices. Fig.1.2.3 illustrates the relationship between forest conditions and the four indices (VI, BI, SI and TI). Vegetation index responses to all of the vegetation cover such as the forest, bushes, scrubs and grassland. Advanced vegetation index (AVI) reacts sensitively for the vegetation quantity compared with NDVI. Shadow and thermal index increases as the forest density and vegetation quantity increases respectively. Black colored soil area shows a high temperature. Bare soil index increases as the bare soil exposure degrees of ground increase. These index values are calculated for every pixel. Fig.2 shows the characteristics of four indices compared with forest condition.

Note that as the FCD value increases there is a corresponding increase in the SI value. In other words where there is more tree vegetation there is more shadow. Concurrently, if there is less bare soil (i.e. a lower BI value) there will be a corresponding decrease in the TI value. It should be noted that VI is “saturated” earlier than SI. This simply means that the maximum VI values that can be recorded appear earlier in the analysis. This happens because the VI captures data from the total bio-mass, regardless of the density of the trees or forest. On the other hand, the SI values are primarily dependent on the amount of tall vegetation such as trees which cast a significant shadow. Table.1 shows combination characteristics between four indices.

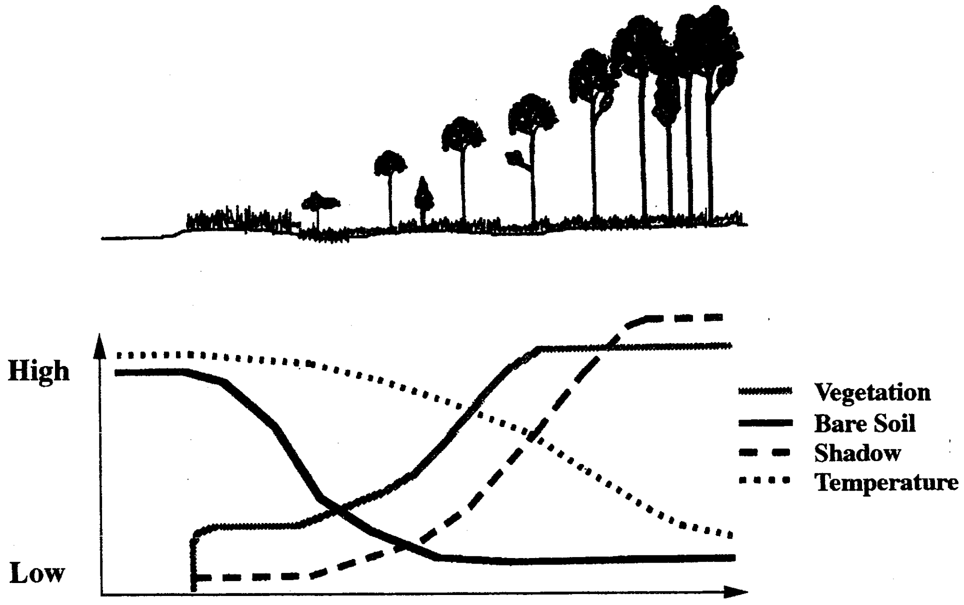

Fig. 2 The characteristics of four prime indices of the forest condition

Table.1 Characteristics combination between major four indices

Indices	Hi- FCD	Low-FCD	Grass Land	Bare Land
AVI	Hi	Mid	Hi	Low
BI	Low	Low	Low	Hi
SI	Hi	Mid	Low	Low
TI	Low	Mid	Mid	Hi

3. Calculation of Four (4) Indices

3.1 Advanced Vegetation index (AVI)

When assessing the vegetation status of forests, the new methods first examine the characteristics of chlorophyll-a using a new Advanced Vegetation Index (AVI) that is calculated with the following formulae.

B1-B7: TM Band 1-7 data

B43=B4-B3 after normalization of the data range.

CASE-a $B\,43 < 0$ $AVI = 0$

CASE-b $B\,43 > 0$ $AVI = ((B\,4 + 1) \times (256 - B3) \times B\,43)^{1/3}$

3.2 Bare Soil Index (BI)

The *value* of the vegetation index is not so reliable in situations where the vegetation covers less than half of the area. For more reliable estimation of the vegetation status, the new methods include a bare soil index (BI) which is formulated with medium infrared information. The underlying logic of this approach is based on the high reciprocity between bare soil status and vegetation status. By combining both vegetation and bare soil indices in the analysis, one may assess the status of forest lands on a continuum ranging from hi vegetation conditions to exposed soil conditions.

$$\mathbf{BI = [(B5+B3)-(B4+B1)] / [(B5+B3) + (B4+B1)] \times 100 + 100;} \quad 0 < BI < 200$$

The range of BI is converted within 8 bits range

3.3 Shadow index (SI)

One unique characteristic of a forest is its three dimensional structure To extract information on the forest structure from RS data, the new methods examine the characteristics of shadow by utilizing (a) spectral information on the forest shadow itself and (b) thermal information on the forest influenced by shadow. The shadow index is formulated through extraction of the low radiance of visible bands.

$$\mathbf{SI = [(256-B1) \times (256-B2) \times (256-B3)]^{1/3}}$$

3.4 Thermal Index (TI)

Two factors account for the relatively cool temperature inside a forest. One is the shielding effect of the forest canopy which blocks and absorbs energy from the sun. The other is evaporation from the leaf surface which mitigates warming. Formulation of the thermal index is based on these phenomenons. The source of thermal information is the thermal infrared band of TM data.

4. The Procedure of FCD Model

The flowchart of the procedures for FCD mapping model are illustrated in Fig.1.2.4. Image processed results corresponding to the flow chart shows in Fig.3.

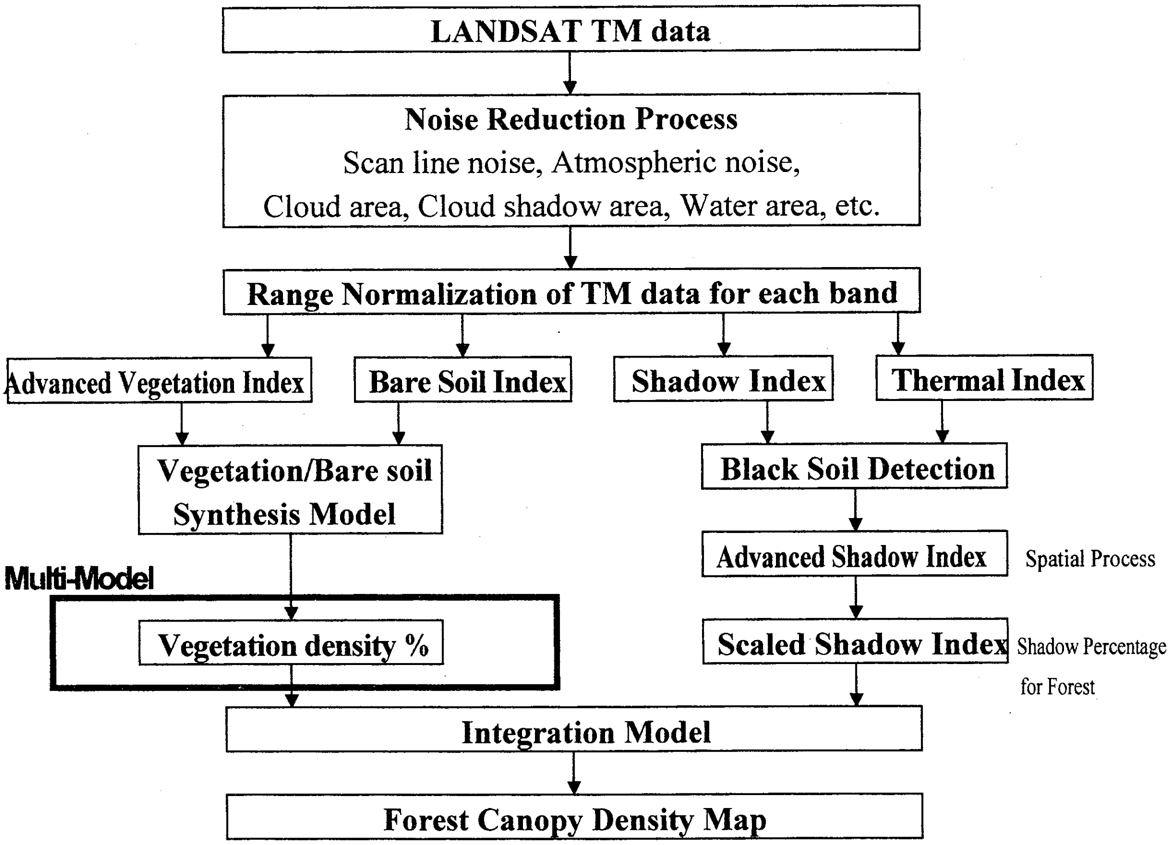

Fig. 3 Flow Chart of FCD Mapping Model

4.1 Noise Reduction; Clouds, cloud shadow and water area

Clouds have a higher irradiance value than ground data. Moreover, the amount of irradiance varies depending on whether the clouds are white, gray, black or combinations of different shades. These factors adversely influence statistical treatment and analysis of imagery data. Furthermore, cloud shadow can be confused with shadow cast by adjacent mountains. These problems can be minimized by creating a cloud shadow mask, using a histogram based on data derived from TM band 1, 2, and 3. Thereafter, a shadow mask of the mountain shadow area is formed at the ground level. This is done through parallel transformation of the mask of the cloud area. Water bodies create similar problems. Since water absorbs near infrared, water bodies should (and can) also be masked using a histogram of TM Band4.

4.2 Vegetation Density and Multi Vegetation Density Model; VD

It is the procedure to synthesize VI and BI by using principal component analysis. Since, VI and BI have high negative correlation. Then it is scaled between zero to hundred percent. Details in (Rikimaru, 1996)

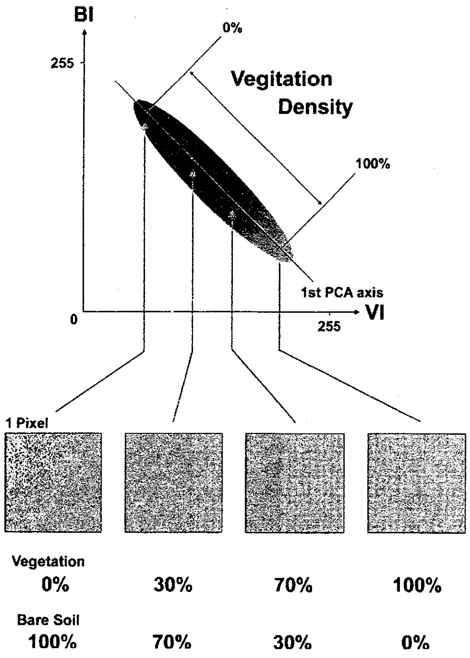

Fig.4 Concept of VD
(Vegetation Density)

Consideration of the seasonal effects of forest conditions represented by leaf-shedding in the deciduous forest as the factors to affect the FCD analysis, study for upgrading of the FCD Model was carried out.

In the previous study of FCD model, the vegetation area was treated as a single component to compute the FCD-Single Model. In this study, the vegetation item is classified several groups , taking into forest considerations.

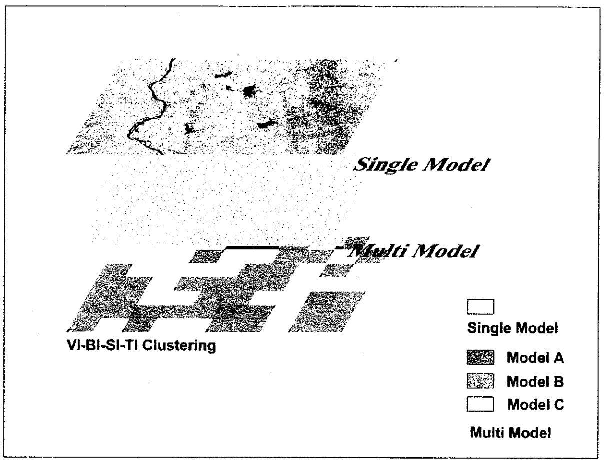

Fig.5 Concept of Model Area (Single Model, Multi Model)

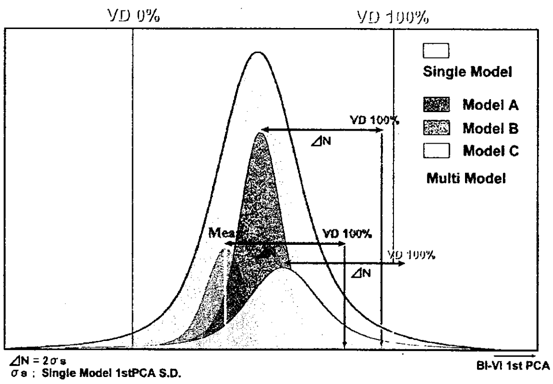

Fig.6 VD Upper Level Threshold in Each

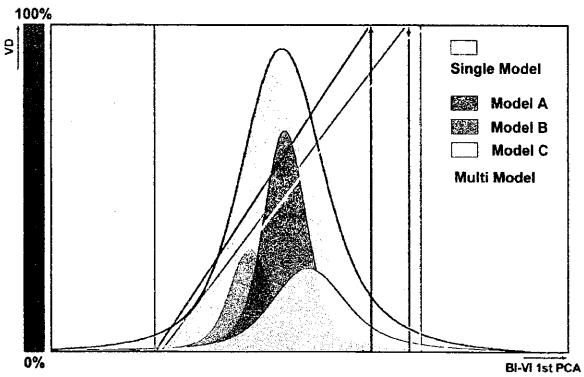

Fig.7 Transformation of VD in Each Model

4.3 Black Soil Detection

SI data is extracted from the low irradiance area of each visible band. Where the soil is black or appears to be black due to recent slash-and-burn, low irradiance data may confuse shadow phenomenon with black soil conditions. This is because black soil usually has high temperature due to its high absorption rate of sun energy. But shadows lead to a decrease in soil temperature. By overlaying TI data and SI data this confusion can be avoided. Overlays are also useful when evaluating the relative irradiance of different parcels of land characterized by various shades of black soil.

4.4 Advanced Shadow Index; ASI

When the forest canopy is very dense, satellite data is not always be able to indicate the relative intensity of the shadow. Consequently, crown density might be underestimated. To deal with this problem, the new methods include those described below for determining the spatial distribution of shadow information. Details in (Rikimaru,1996)

4.5 Scaled Shadow Index; SSI

The shadow index (SI) is a relative value. Its normalized value can be utilized for calculation with other parameters. The SSI was developed in order to integrate VI values and SI values. In areas where the SSI value is zero, this corresponds with forests that have the lowest shadow value (i.e.0%). In areas were the SSI value is 100, this corresponds with forests that have the highest possible shadow value (i.e. 100%). SSI is obtained by linear transformation of SI.

With development of the SSI one can now clearly differentiate between vegetation in the canopy and vegetation on the ground. This constitutes one of the major advantages of the new methods. It significantly improves the capability to provide more accurate results from data analysis than was possible in the past.

4.6 Integration process to achieve FCD model

Integration of VD and SSI means transformation for forest canopy density value. Both parameter has no dimension and has percentage scale unit of density. It is possible to synthesize both indices safely by means of corresponding scale and units of each.

FCD = (VD x SSI+1)1/2 -1

Fig.8 shows the procedure for forest canopy density (FCD) mapping model

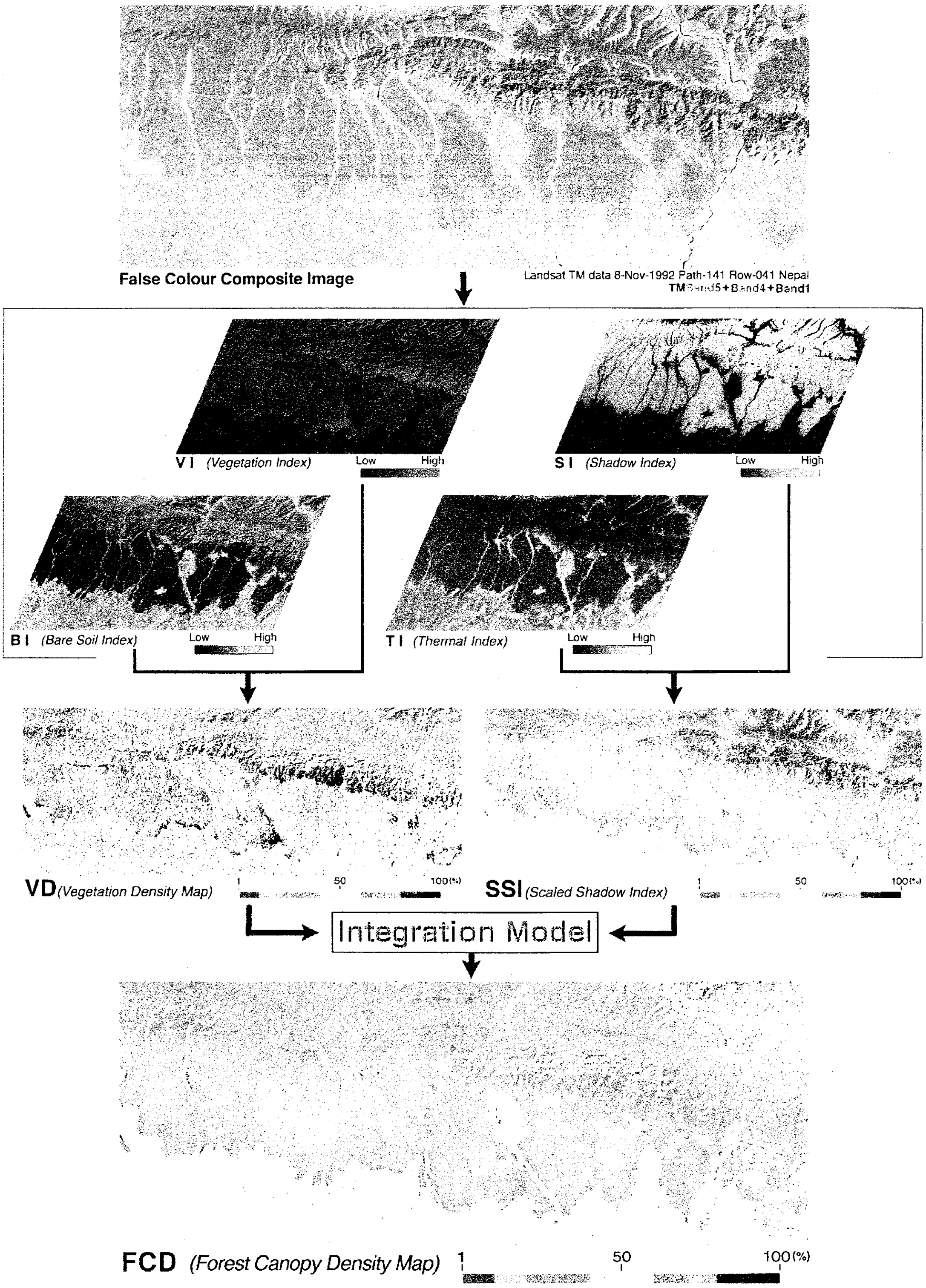

Fig. 8 Procedure for Forest Canopy Density (FCD) mapping model

5.Conclusion

Forest Canopy Density model is one of the most useful parameters for forest monitoring. Conventional remote sensing methodology is based on qualitative analysis of information derived from study area i.e. ground truth information. This has certain disadvantages in terms of time and cost required for ground reference information collecting. FCD model is one the solution of it. But in the present status, for the optimize of model or verification of model results, it is still necessary the calibration test site. One of small test information site is under setting up at the Niigata prefecture , near by Nagaoka university of technology camps.

References

JOFCA.1991.Classification system on logged-over forests. A workshop for the ITTO project PD 2/87(F) Sub- project II. Rehabilitation of logged-over forests in Asia/Pacific region. Manila, Philippines, December 1991

JOFCA.1993.Rehabilitation of logged-over forests in Asia/Pacific region, final report of Sub-project II. Prepared for ITTO. March 1993. Part II pp.1-41

JOFCA.1995.Proceedings of the workshop on utilization of remote sensing in site assessment and planning for rehabilitation of logged-over forests. Cisarua, Bogor, Indonesia, September 25-28, 1995.

JOFCA.1996.Proceedings of the workshop on utilization of remote sensing in site assessment and planning for rehabilitation of logged-over forests. Bangkok, Thailand, July 30- August 1, 1996.

A.Rikimaru.1996.LANDSAT TM Data Processing Guide for Forest Canopy Density Mapping and Monitoring Model , ITTO workshop on utilization of remote sensing in site assessment and planning for rehabilitation of logged-over forests. Bangkok, Thailand, July 30- August 1, 1996. pp.1-8

JOFCA.1997.Utilization of remote sensing in site assessment and planing for rehabilitation of logged-over forests. Project report on PD32/93 Rev.2(F) Rehabilitation of logged-over forests in Asia/Pacific region, Sub-project III. Prepared for ITTO. January 1997.

Spectral Observations for Estimating the Yield and quality of Rice, and studies on optimal amount of fertilizer at ear forming stage of rice.

Takeshi Kanemoto

Hiroshima prefecture agricultural research center

Abstract

We already cleared that it is possible to estimate yield of rice from NDVI at heading time. NDVI is expected to be important factor for manuring practice (*i.e.* topdressing at ear forming stage). In this study, the spectral technique using a handheld Multispectral Radiometer was examined to estimate yield and quality of rice. We found that it was possible to estimate the yield of rice from NDVI at a ear forming stage, the amount of topdressing at ear forming stage, daily mean temperature and daily amount of precipitation from a ear forming stage to a harvest time. We also observed that it was possible to assume the nitrogen concentration of brown rice by estimating the amount of nitrogen absorbed to unhulled rice by the technique as in yield. For the future, it will become possible to determine the optimal amount of topdressing at ear forming stage by further research of weather factors.

Materials and Method

Location : Hiroshima prefecture agricultural research center (field)

Crop : Paddy rice (cultivar: Hinohikari)

Table1 Fertilizing treatments(amount of nitrogen application(kg/10a)

year	basal		supplement		topdressing at ear forming
2000～	0		0		0
2001	(0,4)	x	2	x	(0,1,2,3)
2002	(2,4,6)	x	2	x	(0,2,4)

basal application : end of May

supplement application : beginning of June

topdressing at ear forming stage : end of July

Management

transplanting : end of May

ear forming stage : end of July

heading stage : middle of August

harvest : end of September

Spectral properties measurement

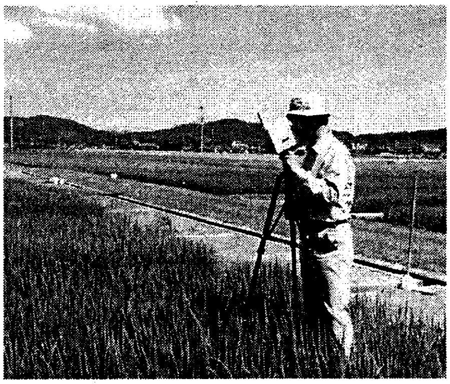

- ·Wavelength of Reflectance factors : 450, 550, 625, 650, 675, 700,8 50 and 950nm (whiteboard as standard (100%))
- ·Sensor height : 170cm
- ·Field of view : 10 deg
- ·Sensor angle : -30 deg (depression angle) in the direction of transplanting row
- ·Time &Day: 10:00～15:00 at ear forming stage

Result

Table2 Correlation coefficient between yeild an
NDVI at ear forming stage

year	Corelation coeffincient	*n*
2000	0.614^{**}	20
2001	0.734^{**}	20
2002	0.433^{**}	36
2000～2002	-0.075	96

Though NDVI calculated from R850(reflectance factor of paddy rice at 850nm) and R675 [(R850-R675)/(R850+675)] at ear forming stage was correlated significantly with yield in each year, there was no significant relationship between NDVI and yield in three years(2000～2002)(table 2).

So we tried multiple linear regression using NDVI at ear forming stage, amount of topdressing at ear forming stage and weather factors from ear forming stage to harvest time as independent variable, yield as dependent variable.

Table3 Multiple linear regression analisis for yeild using NDVI,amount of topdressing, and
weather factors from ear forming to harvest time

	regression coefficient			standard	correlation	
variable	partial	standard	judgement	error	partial	simple
NDVI	263	0.620	**	37.8	0.636	0.225
topdressing	3.68	0.698	**	0.32	0.808	0.736
daily mean temperature	12.2	0.875	**	1.52	0.689	0.181
daily amount of precipitation	9.06	0.662	**	1.20	0.668	-0.060
constant	-508		**	47.9		
multiple correlation	0.879^{**}					

We can get high multiple correlation coefficient with NDVI, topdressing, daily mean temperature, daily amount of precipitation and constant as variable for the estimation of yield (table 3).

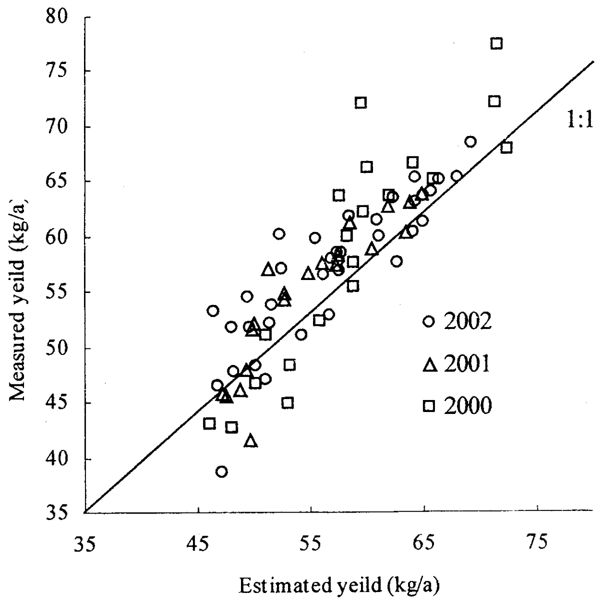

Fig.1 Relationship between measured yeild and estimated yeild

It is also necessary to estimate the quality of rice. Nitrogen content of brown rice is most important factor of quality of rice taste. Unfortunately we don't have enough data of nitrogen content of brown rice, therefore we used unhulled rice data to estimate rice quality.

Multiple linear regression analysis was examined using NDVI at ear forming stage, amount of topdressing at ear forming stage and weather factors from ear forming stage to harvest time as independent variable, amount of nitrogen absorbed to unhulled rice as dependent variable.

Table4 Multiple linear regression analisis for nitrogen absorbed to unhulled rice using NDVI, amount of topdressing, and weather factors from ear forming to harvest time

	regression coefficient			standard	correlation	
variable	partial	standard	judgement	error	partial	simple
NDVI	3.27	0.598	**	0.49	0.624	0.293
topdressing	0.05	0.729	**	0.00	0.821	0.760
daily mean temperature	0.13	0.738	**	0.02	0.627	0.084
daily amount of precipitation	0.11	0.621	**	0.02	0.646	-0.026
constant	-5.92		**	0.65		
multiple correlation	0.880**					

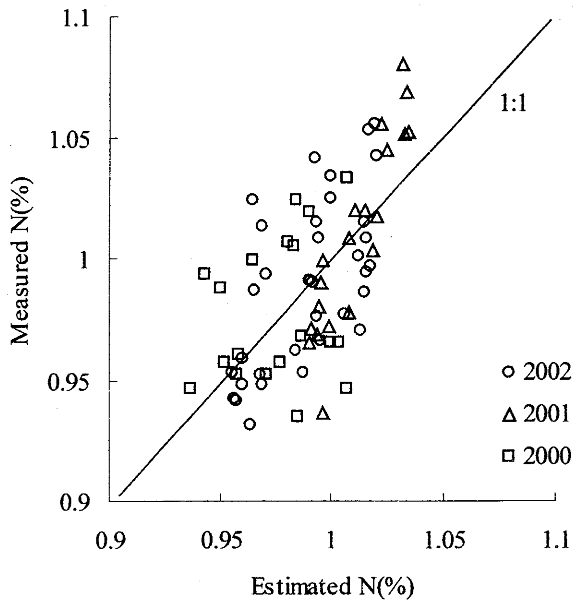

Fig.2 Relationship between measured N% of and estimated N% of unhulled rice

There is significant relation between nitrogen content of unhulled rice and brown rice (correlation coefficient $r=0.757^{**}$).By estimating amount of nitrogen absorbed to unhulled rice, it is possible to estimate nitrogen content of brown rice.

Development of New Method for Field Survey of Stand Parameters on Mangrove Forest
— A Kind of Remote Sensing in the Forest —

Sato Kazuhiro[1] and Tateishi Ryutaro[2]
1: Faculty of Agriculture, University of the Ryukyus
E-mail: sato4408@agr.u-ryukyu.ac.jp
2: Center for Environmental Remote Sensing, Chiba University
E-mail: tateishi@ceres.cr.chiba-u.ac.jp

Abstract

It is difficult to measure tree height, trunk volume and so on for many trees in mangrove forest. But it is necessary for calculation of stand parameters such as the average of them. We have calculated trunk volume of a tree by conventional ways that are to measure diameter at each height with intervals of some meter by climbing up or cutting down a tree. If it is not allowed to cut down trees, we measure diameter at each height by climbing. But the measurement is hard, riskful and not expected with accuracy.

We tried to develop a new method with combination a pole composed of drawtubes and a digital camera operated by remote control. Six laser pointers were parallelized in a box fixed bellow the camera, and the unit composed the box and camera was fixed at the top of drawtubes, could be panned horizontally. Red points on a trunk with laser pointers functioned as scales. It was useful against many trees at different distance, and it became possible to know a diameter at any height on a taken imagery zoomed in. This method is a kind of remote sensing in the forest.

With main two improvements introduced in the first prototype for three years, this method has been almost completed. And it became safe and easier to collect data for stand parameters of mangrove forest combined to the satellite data.

1. Introduction

The information on stand parameters of mangrove forest was almost unknown approximately twenty years ago, because mangrove forest had been classified as the other forest except primal forests. Recently, the importance of mangrove forest has been recognized in the global environment and the coastal ecosystem.

In forestry we are mainly concerned to know the volume of trunks and we measure diameter at breast height (DBH) and tree height to estimate the volume. After measurement of DBH or tree height, we must make clear correlation between them and trunk volume, and obtain regression equations among them. Although it is difficult to measure parameters on the form of trees than the crop, the tables and equations have been improved for estimation of trunk volume by DBH and tree height for primal forests. Collection and integration of the information on the mangrove forests intend to be started, but it is more difficult than the ordinary land forest because of deep muddy sedimentation and complex prop roots, knee roots and erect roots.

We have calculated trunk volume of a tree by conventional ways that were to measure diameter at each height with intervals of some meter by climbing up or cutting down a tree. If it is not allowed to cut down trees, we measure diameter at each height by climbing. But the measurement is hard, riskful and not expected with accuracy. As it is necessary to measure the distance between a trunk and an instrument for measurement of a vertical angle to the tip of tree, the measurement of tree height of mangrove also is hard because of the site condition. Furthermore it is not easy to find a point where the tip of tree can be penetrated many leaves and branches.

The purpose of these serial studies was to develop an efficient method without hardness and riskiness introducing the point of view of remote sensing into the field survey in mangrove forest. The data of stand parameters are needed for the analysis on the relationships between satellite data and stand parameters of mangrove forest. Such analysis should be useful to grasp update and broad circumstances on mangrove forest as fundamental information for sustainable management and control of it.

2. Methodology and prototypes

We had read remote sensing works for meanings of actions in the conventional ways mentioned above. They were to measure diameter of trunk at a height, and to estimate the distance from the highest position can be climbed to the tip of trunk by eyeballing with a guide rod. The former was read for taking photograph of trunk at a height and the latter for measuring the height of camera where the tip of trunk can be seen in the center of view

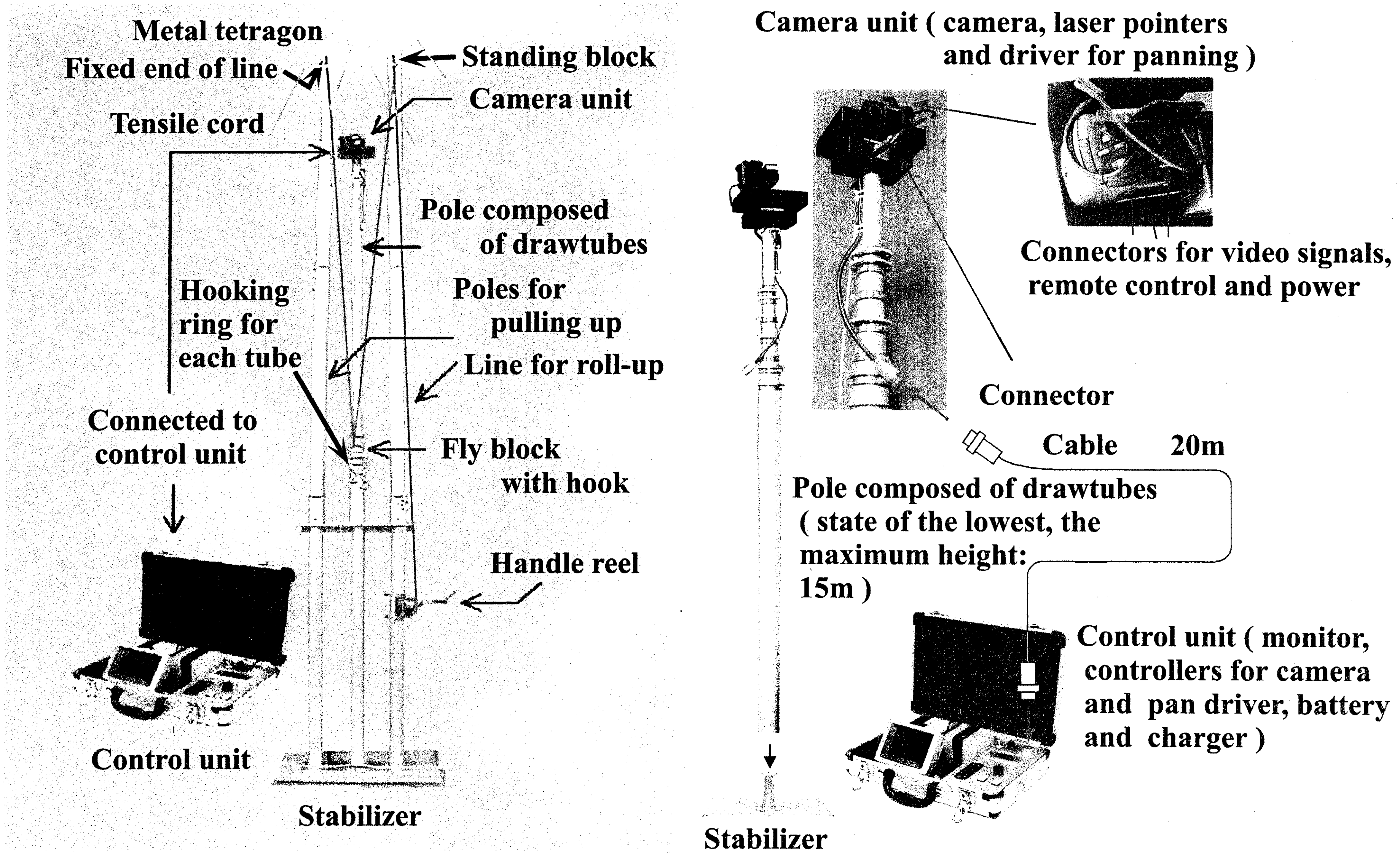

Fig. 1 The first prototype of this method (right:ACRS'01) and improved prototype (left:ACRS'02)

Fig.2 Conventional way (left above) and circumstances of measurement by the first and second prototype

finder, with a fine surveyor's tape fixed zero to the side of camera. The volume of a trunk can be calculated from the sectional measurement of volume that sum up volumes of several frustums and a tip cone.

In these serial studies, a digital camera was adopted. The main reason was that it was difficult to develop films and print pictures in the field. Certainly it is possible to calculate using developed and printed pictures later, but it becomes difficult to keep correspondence between measurement and the panel in films. Using a digital camera, it is easy to assemble and process imageries in a day. The assurance and mobility with a digital camera is higher than an ordinary film camera. If the process on the measurement of trunk diameter is systematized and programmed, it becomes possible to calculate trunk volume in the field.

For calculation of trunk diameter on an imagery or picture by a digital or a film camera, it is necessary to know the focal length of a camera and the distance from the camera to an objective trunk. But measurement of the distance by walk is hard as mentioned above. As a solution for this problem, we applied several laser pointers. Six laser pointers were parallelized and fixed in a box and laser beams were irradiated through six apertures of the box. As red points on a trunk by laser irradiation work as several length scales, the diameter at a height of camera supported by the pole can be calculated with these scales regardless of the distance from the camera or zoom ratio. So it becomes no need to measure the distance between a trunk and the pole against some target trees.

Our prototype was composed with a pole, camera unit and control unit. The composition and connection of this system were shown Fig. 1.

The first prototype was reported at ACRS'01[1)] and improved it reported at ACRS'02[2)]. The main improvements introduced in the first prototype were two points. First point was a handle reel and two poles combined at the top for pulling drawtubes up[2)]. Second point was the devise for self-leveling of the camera unit at the top of drawtubes. This point was reported in this paper. The self-leveling of the camera unit was shown in Fig. 3.

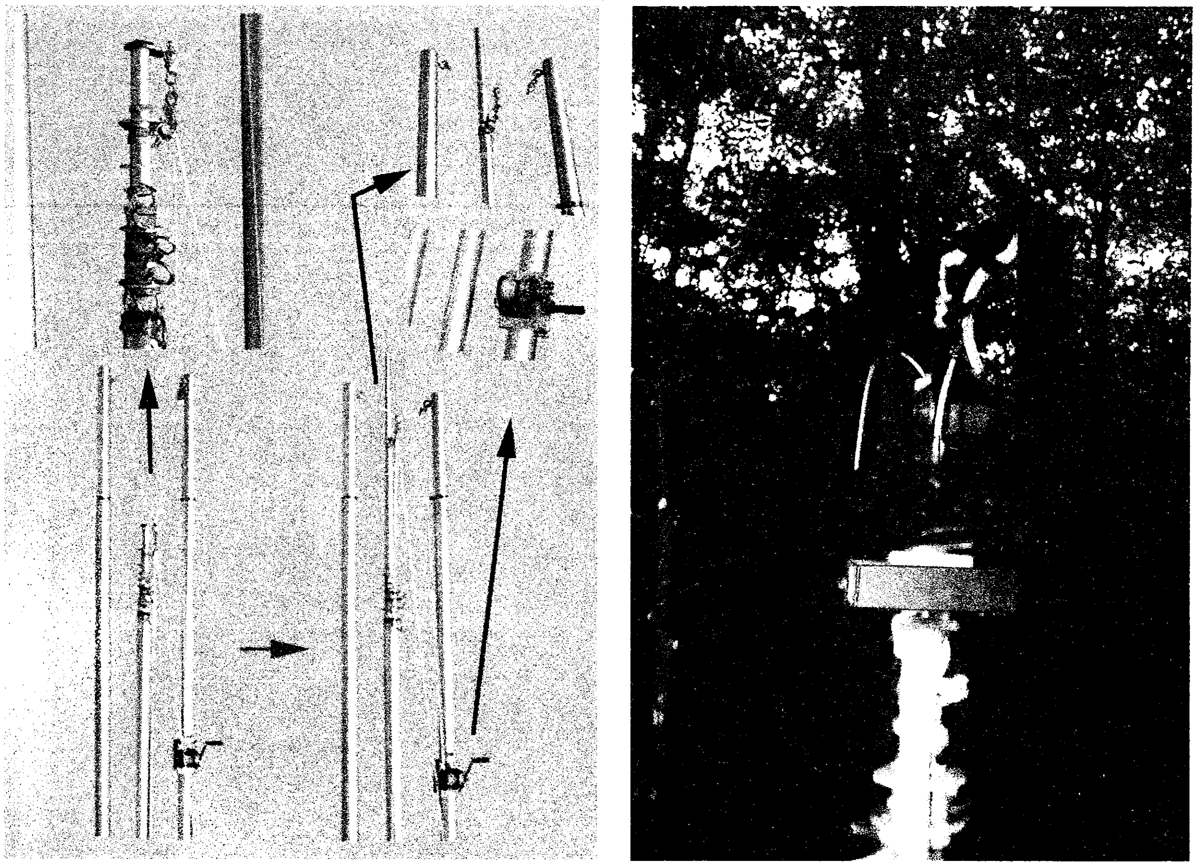

Fig.3 Operation of hook, string and handle reel for pulling drawtubes up (left) and the final improvement of self-leveling of camera unit (right)

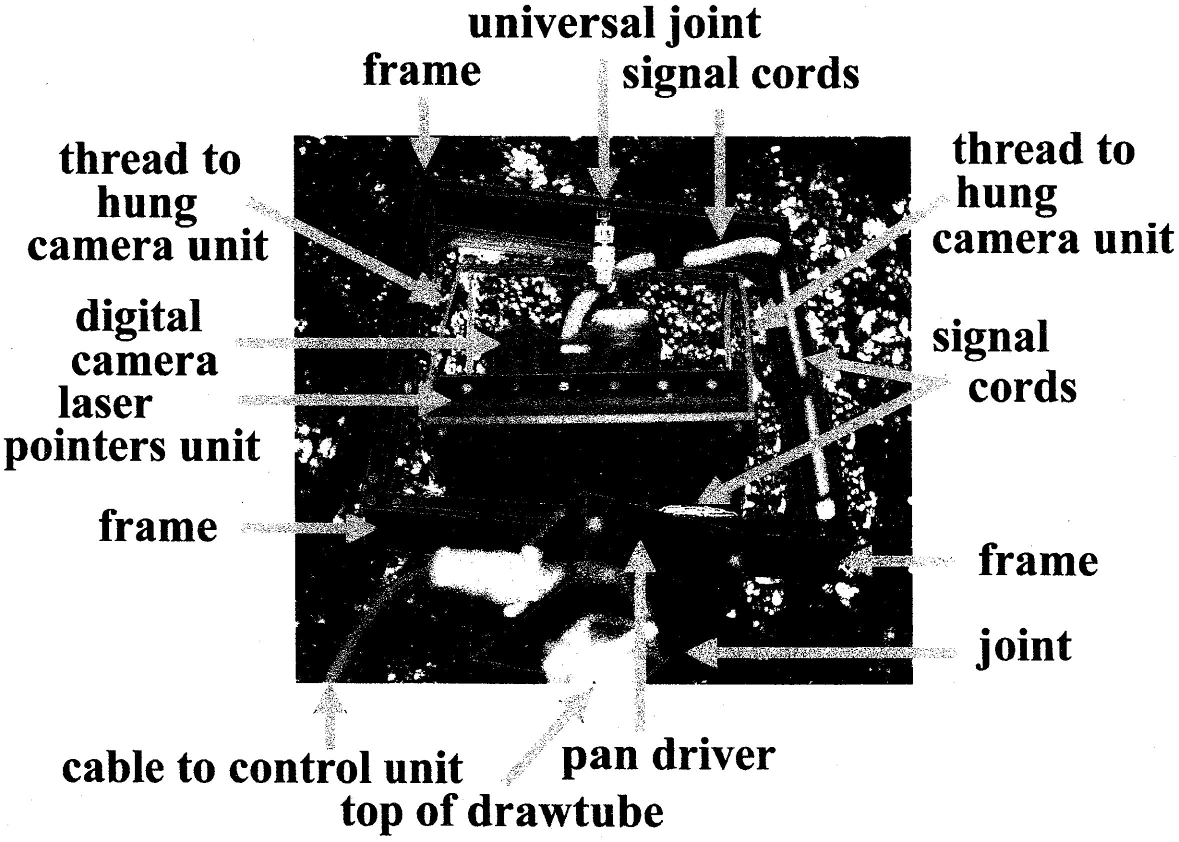

Fig.4 Details of self-leveling of camera unit

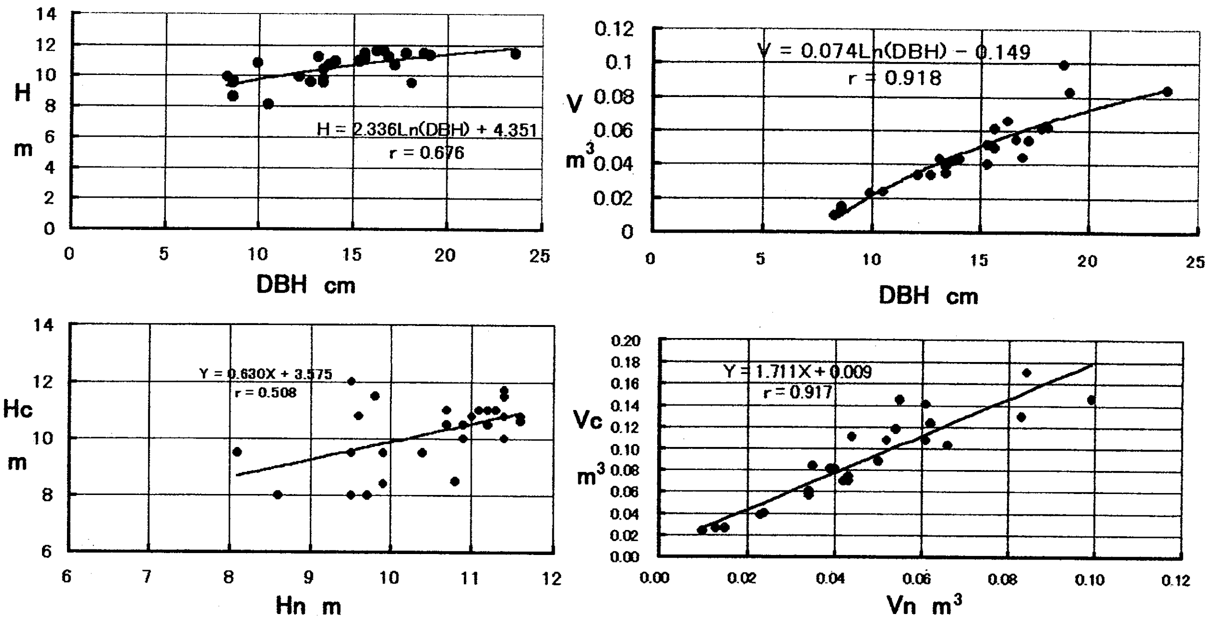

Fig.5 Two relationships between DBH ant tree height (H), trunk volume (V) of measurements and calculated values by the final improved system (above), and comparison of tree height and trunk volume by the system (Hn,Vn) and conventional way (Hc,Vc)(below)[2)]

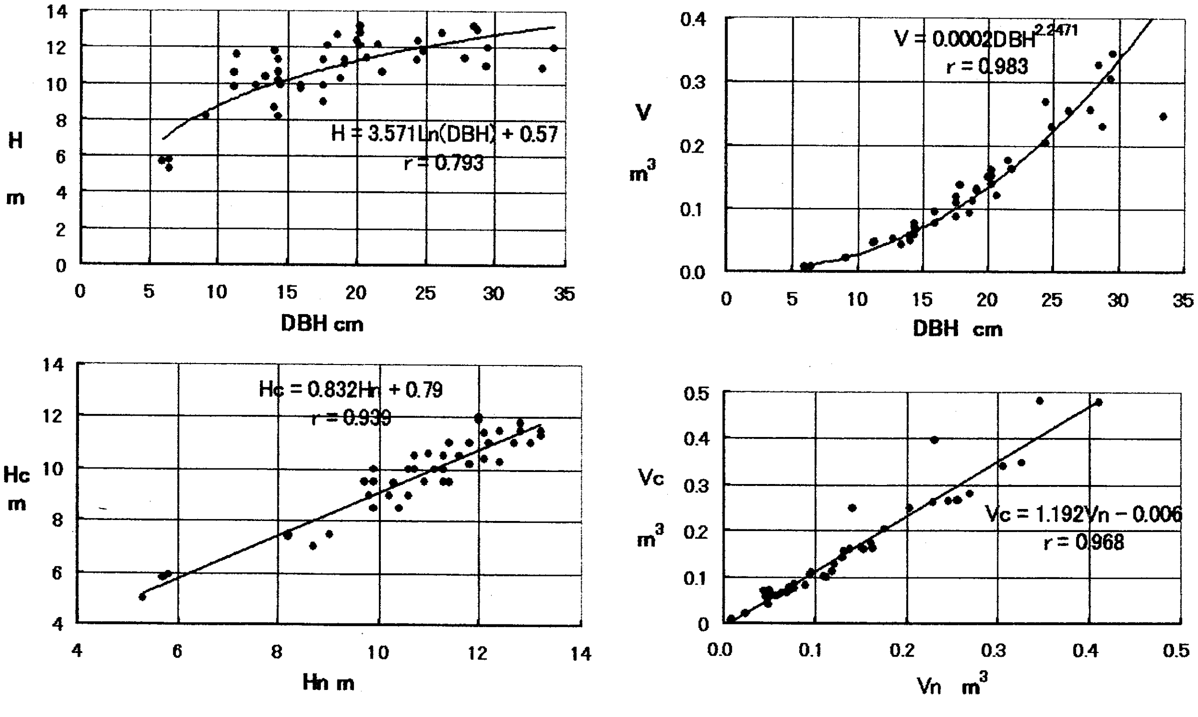

Fig.6 Two relationships between DBH ant tree height (H), trunk volume (V) of measurements and calculated values by the final improved system (above), and comparison of tree height and trunk volume by the system (Hn,Vn) and conventional way (Hc,Vc)(below)

3. Application test

Application tests of these developed and improved systems were done comparatively with the conventional ways at some plots in several stands of the mangrove forest in the river mouth of Fukido-gawa River in Ishigaki Island, the most southern part of Japan.

For conventional ways, a retractable ladder of 6 m length was prepared to climb a trunk. Diameter at each height with intervals of 1 or 2 m was measured by climbing a trunk and the distance from the highest position can be climbed to the tip of trunk was estimated by eyeballing with guide rod. Time was recorded separately as the time for moving and setting up the ladder and measuring time from start of climbing till completely getting off the ladder.

For this method, the poles were stood on the stabilizer and fixed with bolts in the shorten posture of all drawtubes, camera unit was fixed to the top of the thinnest drawtube, after that all connectors were connected. Each drawtube was pulled up stepwise and made a junction with next drawtube. We could read the scale of the fine surveyor's tape fixed zero to the side of camera as the height of camera. At a height, pan driver was adjusted to irradiate symmetrically laser red points to a target trunk and imagery was taken. If trunk and red points were too small in the monitor, the function of zoom up could be used properly. After taking all imageries of target trunks at same height, tube was pulled up to next height and same works were repeated. At the last phase, tree height was measured with the tape adjusting the height of camera to capture the tip trunk in the center of monitor. Time was recorded separately as the time for setting up this system, taking all imageries needed, measuring the height of target trees and setting off this system.

Diameter of a trunk at a height could be calculated from proportional relation between width of the trunk and distance of red laser points in the imagery. The volume of each trunk was calculated as total volume of all divided frustums and the tip cone.

4. Results and discussion

Time required for measurement per a tree was 4 minutes 38 seconds with conventional way and 4 minutes 26 seconds with this method. It was considered that the former was almost the limit but the latter could be reduced by experience$^{2)}$. In case of application test in this year, average time of the latter was slightly longer than the former. It is considered that the difference of time required for measurement results from stand conditions such as tree size, tree density and so on, and proficiency of the measurement crew. The improvement of safety and accuracy is more important than the shortening in time required.

The results of measurements by the first improved system were shown in Fig. 5$^{2)}$. And the results by the final improved system were shown in Fig. 6. Correlation coefficients of four relationships in Fig. 6 were clearly higher than them in Fig. 5.

In Fig. 5, measurements of tree height had scattered in wide range. And calculated values of trunk volume by conventional way were too much comparing with those values by this method. The reasons were probably eyeballing length of tip cone and tying a tape diagonally against trunk for measurement of the perimeter with insecure attitude on a ladder or trunk, and the works was an unaccustomed works for the crew of students. For the relationships between DBH and trunk volume (V) in Fig. 5 and 6, different regression equation were applied because of the difference between the ranges to be collected data. It could be evaluated that the accuracy of measurement was improved by this method.

By these improvements, operational safety and stability were advanced remarkably. And the accuracy of measurement also was raised because of the advancement in preserving the pole to support the camera upright. Although this method has a demerit that the number and weight of equipments increase, it is realized that cutting down trees and climbing up trunks are avoided. The matters are the most important merits from the points of view of the safety and minimizing the hardness of field works. It can be suggested that this method explains the possibilities to develop small scale remote sensing in the forest.

5. Device and improvement

In the field survey the weight of equipment becomes the most severe problem. Especially in mangrove forest the transportation of poles is hard, but the weight of about 50 kg must be accepted in consideration for its place, strength and shorten length during transportation. We divided it into two and brought them in the field.

Although the main improvement was completed in these serial studies, problems of making the system sturdier and higher are remained.

References

1) Sato K. & Tateishi R.: Development of New Method for Field Survey of Stand Parameters on Mangrove Forest – A Prototype and Application Test –, Proceedings of the 22nd Asian Conference on Remote Sensing, 1344–1349, 2001

2) Sato K., Tateishi R., Tateda Y. & Sugiti S.: Field Works in Mangrove Forest on Stand Parameters and Carbon Amount as Fixed Carbon Dioxide for Combining to Remote Sensing Data, CD-ROM Proceedings of the 23rd Asian Conference on Remote Sensing, Paper No. 161, 2002

Water and Carbon in Biosphere

Role of Soil Water of the Subsurface Water Resources in the Semi-arid Region - Some results in Mongolia -

KAIHOTSU Ichirow[1], YAMANAKA Tsutomu[2], HIRATA Masahiro [3], MURAMATSU Kanako[4], OISHI Kazato[5], YAN Xiong[6], KONDOH Akihiko[7] and KOIKE Toshio[8]

[1] Department of Natural Environmental Sciences, Sogokagaku-bu, Hiroshima University, Higashi-hiroshima, 739-8521, Japan, E-mail: kaihotu@hiroshima-u.ac.jp
[2] Terrestrial Environment Research Center, University of Tsukuba, Tsukuba, 305-8577, Japan, E-mail: tyam@suiri.tsukuba.ac.jp
[3] Division of Applied Bioscience, Faculty of Agriculture, Kyoto University, Kyoto, 606-8502, Japan, E-mail: masahiro@kais.kyoto-u.ac.jp
[4] KYOUSEI Science Center for Life and Nature, Nara Women's University, Nara, 630-8506, Japan, E-mail: muramatu@ics.nara-wu.ac.jp
[5] Graduate School of Agriculture, Kyoto University, Kyoto, 606-8502, E-mail: kazato@kais.kyoto-u.ac.jp
[6] Graduate School of Human Culture, Nara Women's University, Nara, 630-8506, Japan, E-mail: yuu@ics.nara-wu.ac.jp
[7] CEReS, Chiba University, Chiba, 263-8522, Japan, E-mail: kondoh@faculty.chiba-u.jp
[8] Department of Civil Engineering, University of Tokyo, Tokyo, 113-8656, Japan, E-mail: tkoike@hydra.t.u-tokyo.ac.jp

Abstract

To understand soil water behaviors and to establish the estimation method of water resources and soil moisture in the large area of the semi-arid land, the study area was set up in the Mongolian plateau. Hydrological and meteorological ground-based monitoring with a few intensive observations was carried out in the study area. The water balance calculation showed that slight precipitation contributed to the soil water storage. However, intensive groundwater recharge in late spring and early-mid summer when plants grow highly can be considered to contribute mostly the annual soil water storage for the plant development in spite of slight amount. We succeeded in the validation of AMSR-E (Advanced Microwave Scanning Radiometer - EOS) algorithm for soil moisture measurement using the monitoring data and suggested the high capability of the large area soil moisture measurement by AMSR-E.

1. Introduction

Soil water plays an important role in the water cycle and water resources in the semi-arid and arid lands. The atmospheric and subsurface water cycles are actually controlled by the soil water behaviors. Many scientists (e.g., Beljaaras et al: 1996, Kanae et al.,: 1998) pointed out the importance of the soil water behavior study in the water cycle. Soil water behaviors have remarkably an influence to plant growth and small animal lives in the semi-arid and arid lands where precipitation roughly and frequently fluctuates in small amount. In order to grasp the spatial distribution of soil water and plant, the satellite observation can be considered to be effective. We should try to measure precisely and spatially soil water content in such a region.

This study aimed to the following things:

1) To understand the real state of water cycle in the semi-arid.
2) To evaluate soil water storage in the large area.
3) To discuss usefulness of satellite soil moisture measurement by AMSR-E of AQUA

In order to achieve the purposes, we carried out various observations in the Mongolian plateau.

2. Observation in Mongolia

2.1 Study area

The study area where is located in 250 km southwest of Ulaanbaatar and is also for the ground truth study of ADEOSII and AQUA sensor validation of the AMPEX project (Kaihotsu et al., 2002). The soil surface is almost covered with grass and small shrubs. The annual precipitation of the study area is between 100 mm and 200 mm (National Statistical Office of Mongolia, 2001) and the range of altitude is approximately from 1300s m to 1500s m. The study area is in the inner drainage basin (Batima and Dagvadorj, 2000).

2.2 Observation methods

We conducted meteorological and hydrological monitoring by AWS (Automatic Weather Station) and soil hydrological monitoring by ASSH(Automatic Station of Soil Hydrology), floral investigation including the plant water measurement by the sampling and oven method in the study area. Satellite observation by AQUA-AMSR-E and ADEOS II–AMSR was done as an algorithm validation of the soil water and plant water contents. The data of Mongol routine meteorological observation were also employed for this study.

Five AWSs and twelve ASSHs have been monitoring since summer in 2000 and June in 2001, respectively. The five AWSs were installed in Mandalgobi site (MGS), Delgetsogt site (DGS), Deren site (DRS), Tsagaandelger site (TDS) and Bayantsaagan site (BTS) and ASSHs were perfectly set in the soil at measurement points with the density of the 20 km-30km intervals. Measurement elements of AWS and ASSH are shown in the web site [http://home.Hiroshima-u.ac.jp/ampex/hm].

2.3 AMSR-E algorithm for soil water measurement

Brightness temperature measured by AMSR/AMSR-E was expressed as follows:

$$T_b = \exp(-\tau_c) \cdot E_s \cdot T_s + [1 - \omega_c][1 - \exp(-\tau_c)]T_c \qquad (1)$$

Where T_b is brightness temperature, T_c canopy physical temperature, ω_c single scattering albedo, τ_c optical depth, T_s soil physical temperature, and E_s soil emissivity. Soil moisture index (ISW) and polarization index (PI) (Koike et al., 2000) were derived from Eq. (1). ISW and PI were shown respectively as follows:

$$ISW = [T_{bi} - T_{bj}]/[(T_{bi} + T_{bj})/2] \qquad (2)$$

$$PI = [T_{bV} - T_{bH}]/[(T_{bV} + T_{bH})/2] \qquad (3)$$

Where i is high frequency, j low frequency, H H polarization, and V V polarization. ISW and PI depend on the soil water content change and the plant water content of the plant layer on the soil surface, respectively. We can estimate the soil water and plant water contents from a lookup table that is made by ISW and PI calculated from the AMSR/AMSR-E data.

3. Results and Discussion

3.1 Water cycle in the study area

Many monitoring data from 2001 summer to 2002 summer by AWS were obtained. Figure 1 presents a part of the AWS monitoring results at MGS from Sep. 2001 to Aug. 2002 as an example. Similar seasonally changes in the monitoring results were seen at the other sites.

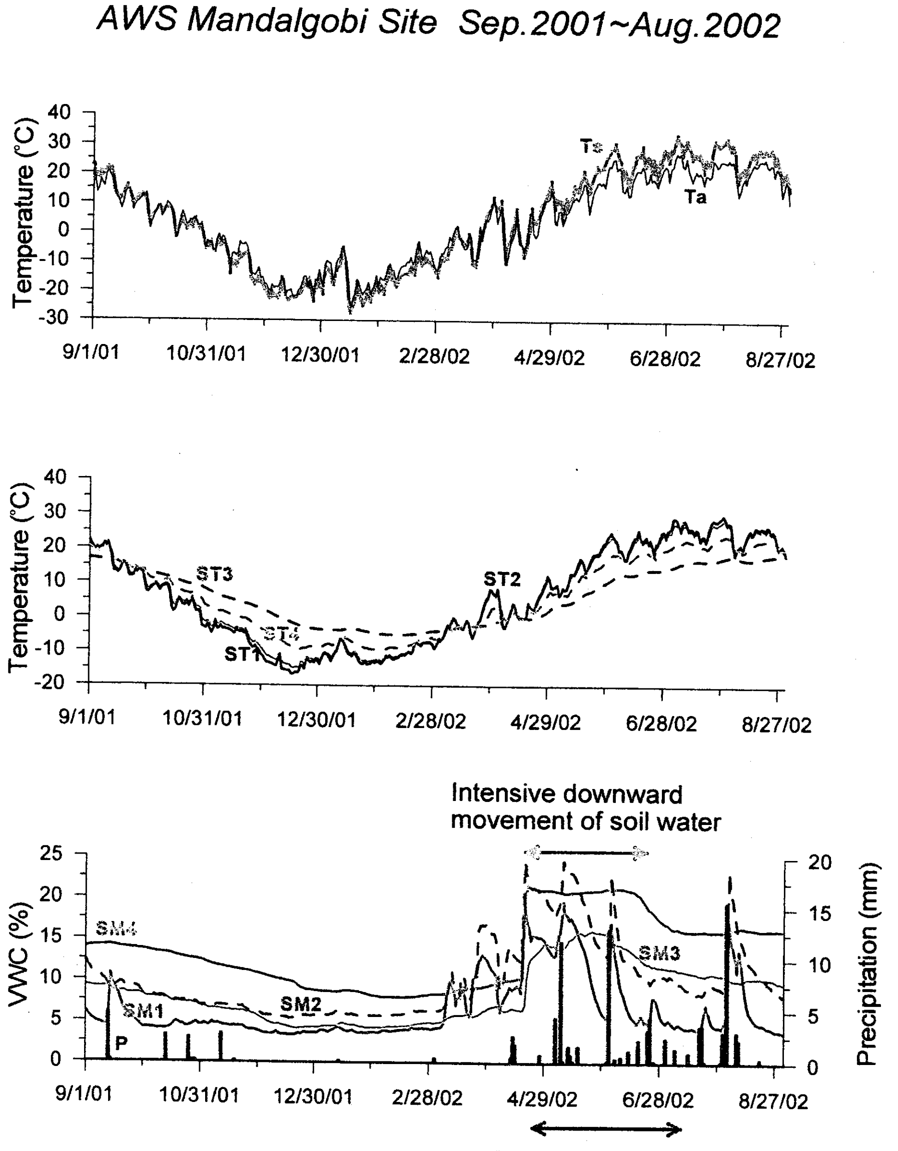

Fig. 1 Monitoring results at MGS (Mandalgobi site)[Ts: surface soil temperature, Ta: air temperature, ST: soil temperature, P: precipitation, SM: soil moisture in volumetric water content (VWC), 1: 3 cm depth, 2: 10 cm depth, 3: 40 cm depth, 4: 100 cm depth]

Soil water change was clearly shown in Fig.1. The frequently fluctuated soil water content with some big rainfall events from April to June results in the water contents increase in deeper soils. This means the intensive downward of soil water with rainfalls. As plants grow highly during this period, this downward movement of soil water can be considered to contribute almost to the plant growth.

ASSH monitoring results of three stations were represented in Fig. 2. There are long distances more than 100 km between ASSH 5 and ASSH 9, about 60km between ASSH 7 and ASSH 9, and about 70km between ASSH 5 and ASSH 7. The rapidly increased change (spike) of soil water content at the 3 cm depth means the rainfall event. If so, comparing each other with the three ASSH monitoring results at the 3cm depth, we can see some spikes with the deviated occurrence timing. However, as shown in the three figures, two spikes in mid–August (Aug. 17) and early September came in the equal time and these rainfall events were seen in other all ASSH data. This fact implies that there were two kinds of he atmospheric water cycles that were regional water cycle over the study area and local one within the study area.

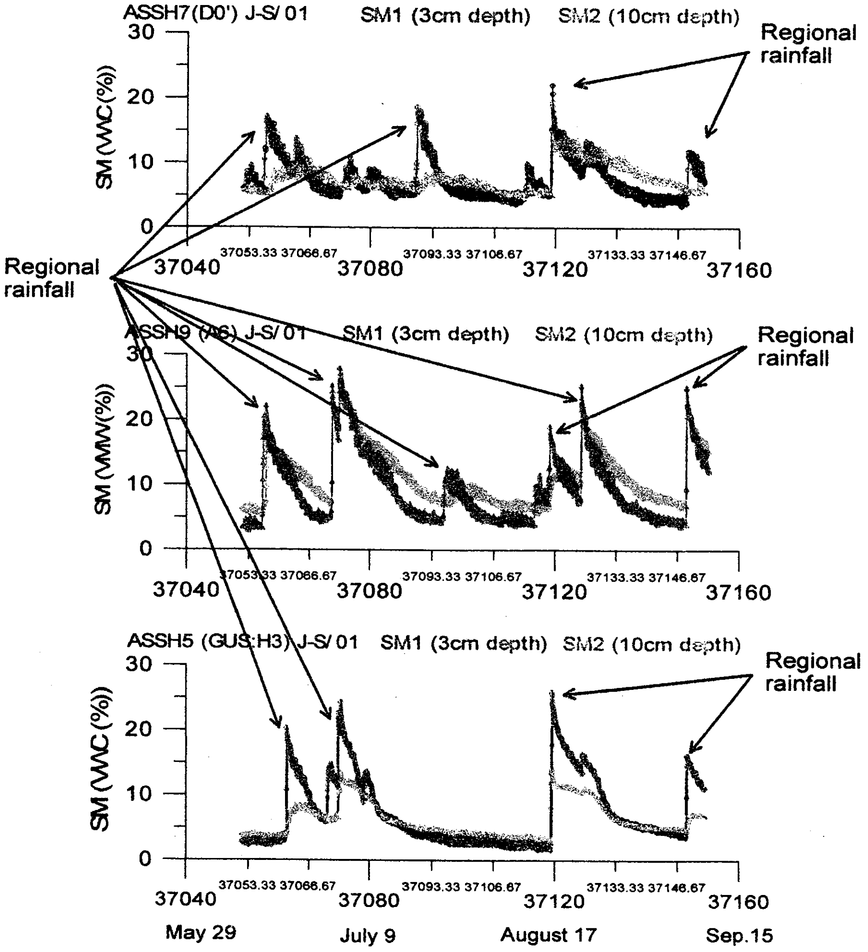

Fig. 2 ASSH monitoring results [SM: volumetric water content of soil]

3.2 Estimation of the annual soil water storage

We calculated the annual soil water storage ΔS from September 2001 to August 2002 by the following water balance method:

$$\Delta S = P - E - GR \tag{4}$$

Where P is precipitation, E evapotranspiration by the Takahashi method (Takahashi, 1979), GR groundwater recharge by the Richards equation (Brooks and Corey, 1964). As a result, the soil water storages were 8 mm at MGS, 8.2 mm at DRS and 6mm at BTS. The soil water storage was about 8 % of the precipitation at most.

3.3 Soil water content estimation by the AMSR-E measurement

Comparison with the ASSH monitoring data and the calculated results by the AMSR-E algorithm in summer of 2002 led to the good validation. Figure 3 shows the soil water content estimated in Mongolia by this algorithm. The distribution pattern in Fig.3 was shown to be reasonable comparing also with the soil and similar to that of precipitation (Batima and Dagvadorj, 2000).

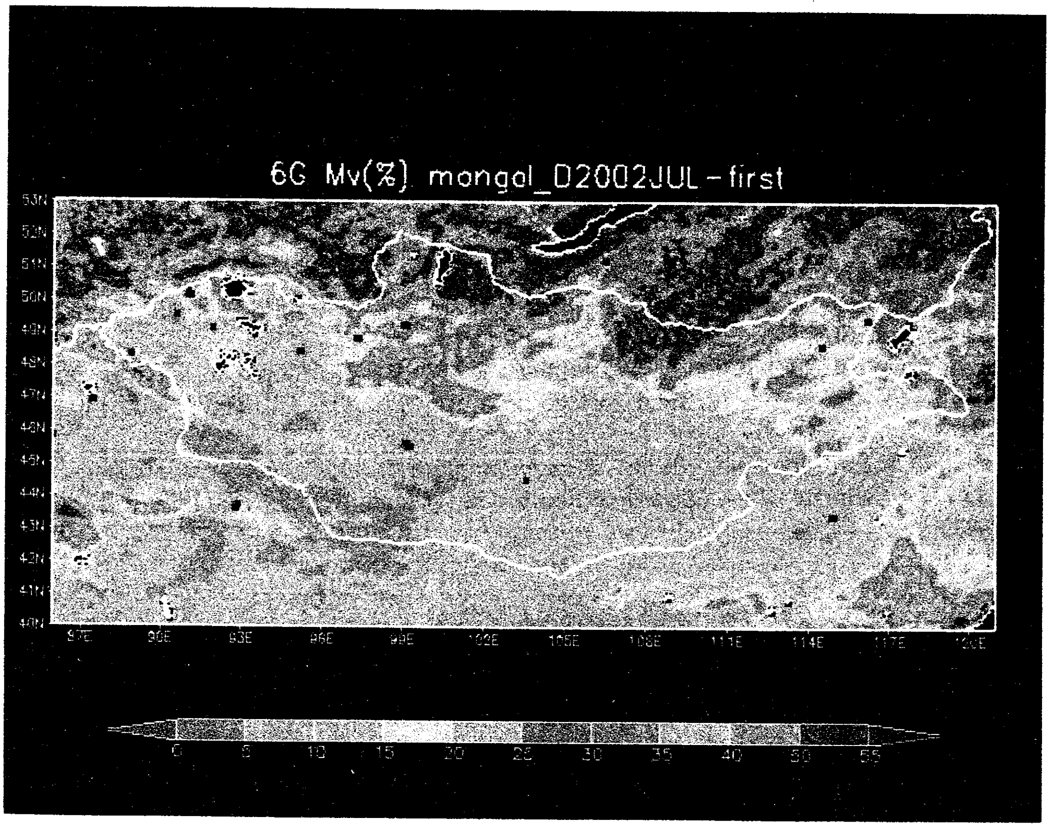

Fig. 3 Soil water content distribution in the first ten day of July in 2002 by the AMSR-E measurement

4. Conclusions

Water balance calculation showed that precipitation almost contributed to evapotranspiration and soil water storage was less than 8 % of precipitation. However, intensive downward of soil water in late spring and early-mid summer can be considered to contribute almost to the plant growth.

There is a high possibility for the spatial soil water measurement by AMSR-E. However, the ground-based observation should be actively and widely done to obtain ground truth data fro the long time.

Acknowledgments

This study was supported by JAXA (former NASDA) and Heiwa Nakajima Foundation as a part of the AMPEX (ADEOS II Mongolian Plateau Experiment) project. We appreciate the contribution of the Institute of Meteorology and Hydrology of National Agency of Meteorology, Hydrology and Environment Monitoring of Mongolia, Dr. Azzaya, D., Dr. Davaa, G. and Mr. Oyunbaatar, D.

References

Batima, P and Dagvadorj, D.(2000): *Climate changes and its impacts in Mongolia.* JEMR Pub., 227p., 2000.

Beljaars,A.C.M., P. Viterbo, M.J. Miller and A.K. Betts(1996): The anomalous rainfall over the United States during July, 1983: Sensitivity to land surface parameterization and soil moisture anomalies, Mon. Wea. Rev., **124**, 362-383.

Brooks, R.H. and Corey, A.T. (1964): *Hydraulic properties of porous media.* Hydrology Papers No3, Colorado State Univ., Ft. Collins, 27p.

Kaihotsu, I., Yamanak, T., Oyunbaatar, D., Hirata, M., Oishi, K., Muramatsu, K., Miyazaki, S., Kondoh, A., and Koike, Toshio (2002): Preliminary ground-based observation for the soil moisture measurement validation of ADEOS II-AMSR/AMSR-E. Proceedings of the 3rd Workshop on Remote Sensing of Hydrological Processes and Applications, 1-6.

Kanae, S., Oki, T. and Mushiake, K.(1998): The impact of soil moisture on precipitation in a regional climate model. J. Japan Soc. Hydrol. and Water Resour., 11(5), 482-491.

Koike, T., Shimo, C., Ohata, T., Fujii, H., and Shibata, A. (2000): Development and validation of a microwave radiometer algorithm for land surface hydrology. Annual J. of Hydraulic Eng., JSCE, 247-252.

National Statistical Office of Mongolia (2001): *Mongolian Statistical Yearbook.* Ulaaanbaatar, 301p.

Takahashi, K. (1979): Estimate of evapotranspiration based on monthly temperature and precipitation. Tenki, **26**, 29-32.

Key words : soil water, semi-arid region, AMSR/AMSR-E, AQUA

A Study of Water Cycle and Water Resources Security Using Isotopic and Remote Sensing Technologies in North China Plain

Xianfang Song, Jun Xia and Jingjie Yu

Key Lab. of Water Cycle & Related Land Surface Processes,
Institute of Geographic Sciences & Natural Resources Research,
Chinese Academy of Sciences (CAS), 100101, Beijing, China

Introduction

Since 1980's, dramatic increases in water and unplanned groundwater development along with rapid growth in urban population have caused some critical water and eco-environmental problems such as both the water resource and runoff in the mountain areas have substantially decreased, drying-up of river system, large water level depression by over pumping, subsequent increase in potentials of land subsidence, lake & wetland degradation, and water pollution in plain area etc. It was shown in the case of Haihe River Basin that among the total rivers of 10,000 km, the rivers of 4,000 km have been turned to be seasonal rivers. Comparing with the beginning of 1950s, the wetland area within the Basin decreased from 10,000 km^2 to 1,000 km^2 at present. Over-extraction of groundwater, this area covers nearly 90,000 km^2, 70% of the plain areas. Comparing with that of the end of 1950s, the accumulated over-extracted groundwater is 90 billion m^3. Water and soil loss area in mountainous region□110,000 km2, rating two thirds of the mountainous area. The sandstorms induced by desertification endangering Beijing and other cities. Thus, the problems of water shortage and related eco-environmental issues in North China have become the most significant issue to impact sustainable development in this very important region that are political, cultural and economic center of China.

To study these urgent issue in North China, Chinese Academy of Science (CAS) has supported a Key Project, namely Water Cycle and Water Resources Scurety in North China, with total budget of 110 million USD from 2002-2005, leading by Prof. Xia Jun, Director General, Key Laborotoary of Water Cycle & Related Surface Processes, CAS.

Objectives

By cooperation of the key project founding by Chinese Academy of Science and the facilities from Key Laborotoary of Water Cycle & Related Surface Processes, CAS, and other international cooperation preojects, we try to focus on Integrating Watershed and Aquifer Dynamics to understand interaction between groundwater and surfacewater, and provide recover ways for urgent groundwater degredation due to over exploiation.

Methods

Two research lines are selected: one is the most important area, where is the capital area of China, from Yanshan Mountain to Bohai Sea; another one is farm area, where is most important food area, from Taihang Mountain to Bohai Sea. A scheme of research is following (Fig.). The first step is hydrological field investigation by using environmental tracers, remote sensing and GIS. The environmental iostopes are defined as those isotope, which are either naturally present or artificially produced and released, and become distribued in the environment by natrual processes and are thansported with water through the hydrological cycle. Environmental isotopes, and water quality either natural or pullted could be used, according to field experience in different topogaraphies in Japan, Indonesia and Sri Lanka, as effective trcers for groudwater flow investigation.

Environmental tracers

Radioactive isotopes

Tritium and Carbon-14 are very usful tracers. Tritium is a radioactive isotopic specics of hydrogen with half life of 12.43 yr. Th natural source of tritium is in the stratosphere and the tritium is supplied from the stratosphere to the troposphere through the tropopause in the higher latitude zone. Therefore the natural level of tritium concentration in precipitation is high in the polar zone and low in the tropics,. The same is stratosphere in the northern hemisphere. The high tritium concentration in precipitation hasbeen used as a tracer for water cycle mostly in the middle and high latitude zones in the northern hemisphere. Carbon-14 is a radioactive isotopic specics with half life of 5730 yr, it is exyebsively applied in hydrogeology and date groundwater. Natrural production in upper atmosphere is balanced by decey and burial to maintain a steady-state atmosperic $^{14}CO_2$ activity of about 13.56 disibtegrations per minute (dpm) per gram of C or about 1 ^{14}C atom per 1012 stable C atoms. However, the high neutron fluxes associated with the explosion of nuclear devices also produced large quantities of radiocarbon so that by 1964 the atmosphere concentrations in the northern hemisphere had almost doulbed. This readiocarbon has now been almost "washed out"but can be found both in plant materials and the oceans□

Stable isotpoes

The deuterium and oxygen-18 are most commonly used environemntal istopoes in hydrology□ The stable isotope species will show circulation pattern closely related those of the bulk water in the hydrological cycle□ HDO and $H_2{}^{18}O$ will show systematic devation from the circulation patern of $H_2{}^{16}O$ because evaporation and condensation cause slight fraction of the isotopic species□These deviation would be predictable if one knew in detail the pattern of water circulation in nature□ Stable isotpoe techniques have mostly been appled in hydrology to trace a single arc of the hydrological cycle such as the vapor tranport in the atmosphere or groundwaetr comtribution to runoff□ The principle processes which cause to fractionate stable isotpoic composition of water in nature are evaporation and condensation□ Resulatant fraction effects are recognized as temperature effect□ altitude effect□ inland effect□ and amount effect□The present research aimed at more detailed process study□ that includes whole water cycle starting from sea water to atmospheric vapor□ precipitation□ soil awter retourn to atmosphereic vapor from soil water□ lake water□ groudwater□ spring water□ river water□ and return to atmospheric vapor from irrigation water□ We tried to elucidate vatious hydrological processes occuring in Norch China Plain□ through the changes in isotopic composition in waters sampled in field□

Remote Sensing and GIS

There is a national key laborotry of remote sensing and GIS in our institute□The NOAA□MODIS and TM data□and GIS data are usful□

The second step is predication (Diagnosis) by using model, which is distributed model including surface water and subsurface water, water quantity and water quality.

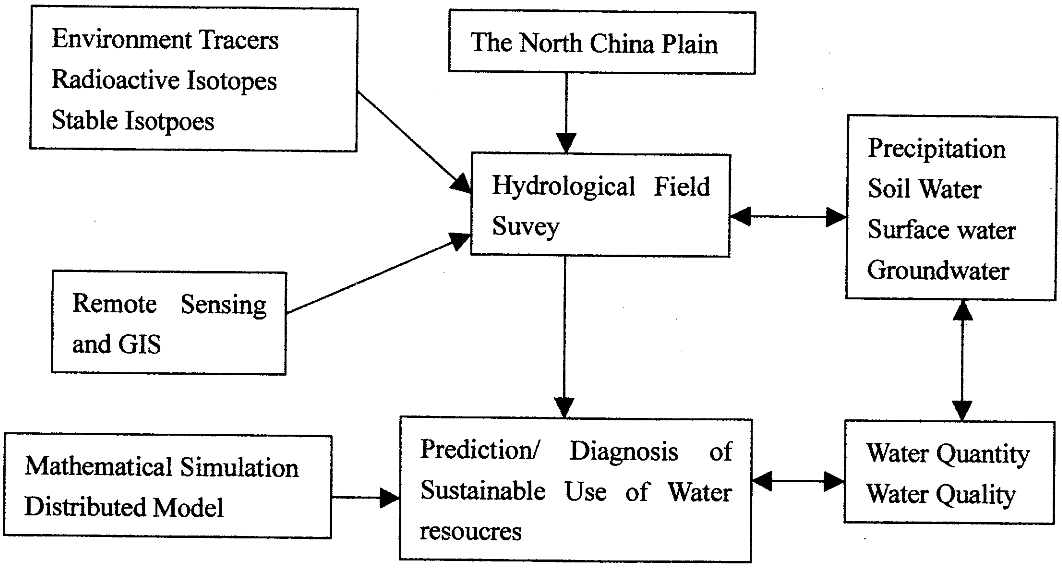

Fig. 1 Methods of Scientific understanding of hydrological cycle

Acknowledgements

This research was supported by the following research grants: the knowledge Innovation Key Project (KZCX-SW-317/CX10G-E01-08), Chinese Academy of Sciences and the director's grant of Institute of Geographical Sciences & Natural Resources Research, Chinese Academy of Sciences.

REFERENCES

Chen, J. Q. & Xia, J. (1999) Facing the challenge: barriers to sustainable water resources development in China. Hydrol. Sci. J. 44(4), 507–516.

Huang, G.H., and J.Xia (2001), Barriers to sustainable water quality management, J. of Environmental

Management, 61(1), 1-23.

International Atomic Energy Agency(1981): Stable isotope hydrology. Deuterium and oxygen--18 in the water cycle, Technical Reports Series No.210, IAEA, Vienna, 273p.

Kayane, I. (1992): Water cycle and water use in Bali island. Institute of Geoscience, University of Tsukuba. 320p.

Liu Changming and Yu Jingjie (2001), Groundwater Exploitation and Its Impact on the Environment in the North China Plain, Water International, 26(2),pp.265-272;

Plate, E. J. (1993) Sustainable development of water resources: A challenge to science and engineering. Water International, 18(2), 84-93.

Song, X. Kayane, I. Tanaka, T. & Shimada, J.(1999)□ A study of groundwater cycle using stable isotope in Sri Lanka. Hydrological Processes. Vol. 13(10), 1479-1496.

WMO & UNESCO (1988) Water resources assessment. Handbook for review of national capabilities, WMO, Geneva.

Xia Jun, & David Chen, (2001), Water problems and opportunities in hydrological Sciences in China, Hydrological Science Journal , 46(6), 907-922 .

An algorithm for estimating regional evaporation and transpiration using remote sensing data

Yanjun Shen[1], Akihiko Kondoh[2], Changyuan Tang[1], Yongqiang Zhang[3], Mohammed Aslam M.A[1]

[1] Graduate School of Science and Technology, Chiba University
Email: sheny@graduate.chiba-u.jp and cytang@faculty.chiba-u.jp
[2] Center for Environmental Remote Sensing, Chiba University
Email: kondoh@faculty.chiba-u.jp
[3] Institute of Geographical Sciences and Natural Resources Research, Chinese Academy of Sciences
Email: zhangyq@igsnrr.ac.cn

Abstract

Accurate estimation of evapotranspiration in a regional scale is very important for agricultural water management, drought monitoring, and fire risk assessment. However, separately estimating regional soil evaporation and vegetation transpiration using remote sensing is also important on the research of hydrological process and the land surface atmosphere interactions. The authors proposed a remote sensing algorithm using satellite data to estimate evaporation and transpiration separately in a regional scale in this study. Based on the concept of soil water deficit and a 'dual-source' conceptual evapotranspiration model relation to soil moisture dynamics, this algorithm is composed of two sub models of calculating soil water deficit index, and potential evaporation and transpiration.

Application to North China Plain shows the algorithm plays a good performance in the case of low vegetation cover, however, when vegetation cover is high, this algorithm seems make an underestimate of evapotranspiration.

1 Introduction

Nowadays, we can fairly well understand the major hydrological processes at a plot scale, however, knowledge of these processes, e.g. evapotranspiration or infiltration, at a catchment or larger spatial scale is indispensable for prediction of floods or assessing the impact of droughts (Choudhury, 1994). In an agricultural region, it is more important for efficient water management to obtain the spatial information, such as evapotranspiration and soil water status, instantly and accurately as well.

Remote sensing has the potential for providing synoptic spatial information on surface radiative property, surface temperature, and vegetation at regional scale. This information is relevant to energy balance modeling over regions containing significant spatial variation in vegetation and soil moisture (Price, 1990). In the past two decades, remote sensing has been widely used in estimating evapotranspiration and heat balance in a large scale. Brown et al. (1973) proposed a crop resistance-evapotranspiration model based on energy balance and crops resistance theory. Subsequently, Sequin (1983) developed a statistical model for daily ET based on differentiation between the temperatures of the canopy and the air. These temperatures were derived from thermal-infrared satellite sensor data. Fox (2000) introduced a new method for the determination of evapotranspiration rates using direct measurements of changes in soil moisture content derived from SAR data. Many other modified ET models have been presented to fit the features of certain study areas (e.g. Chen 1988, Price 1990, Carlson et al. 1995). Yet, remote sensing cannot provide important atmospheric variables such as wind speed, air temperature, and vapor pressure. Assuming non-advective conditions, the remotely sensed information along with a few ancillary meteorological data can be used for estimating regional energy and water fluxes.

Here, an improved VITT method for determining the soil water status in irrigated agricultural region under semiarid climate is proposed and applied to estimating the energy and water fluxes from land surface. At the same time, the dual-source conceptual evapotranspiration model developed in the former chapter will applied to estimate the potential and then actual evapotranspiration as a theoretical base. At last, the remotely estimated energy and water fluxes are compared with the ground surface measurements for validation.

2 Algorithm

In this research, we assume that no significant advective heat flow occurred near land surface and use a pixel-based energy balance algorithm for estimating the surface evapotranspiration in a regional scale. The schematic flow of the algorithm is illustrated in Figure 1. Besides remote sensing data, some ancillary data such as air temperature (Ta), Vapour Pressure (e_a), and wind speed (U) are used in the algorithm.

First of all, the geographical and atmospheric rectified satellite image is processed with multi-spectral analysis to obtain the initial maps, e.g. NDVI, surface temperature (Ts), albedo, and net radiation (Rn). Second, using the information for vegetation cover and soil thermal properties from NDVI, Ts, and albedo calculate the ground heat flux (G). Then, assimilating some ground meteorologically ancillary data such as air temperature, vapour pressure, and wind speed, with the precedent maps of Rn, G, NDVI, and Ts, using Penman-Monteith method to calculate potential latent heat (LEp). The soil water stress status map is obtained through analyzing VI-Ts scattergram. Finally, to computing actual evapotranspiration using the pixel-based potential ET and soil water deficit index (WDI).

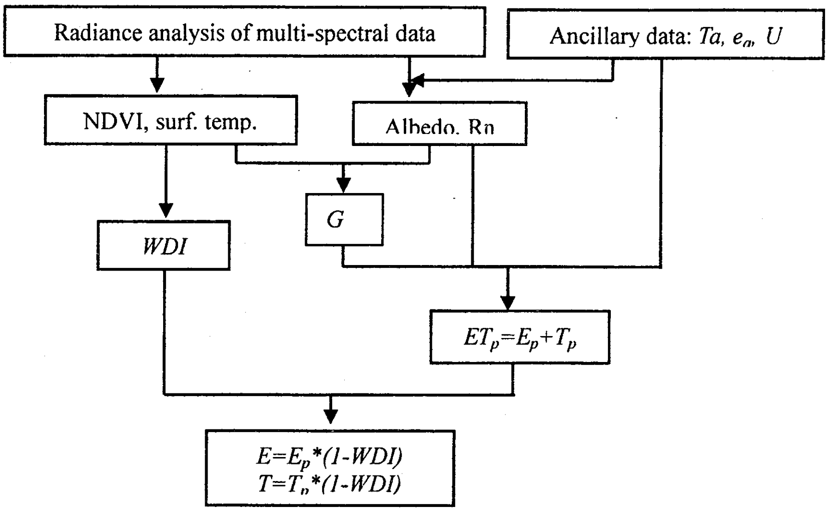

Figure 1 Schematic flowchart of the land surface evaporation and transpiration estimating algorithm

2.1 Simplified method for determining soil water deficit index, WDI

In order to determine crop water stress index, we adopted the so-called VITT model (Vegetation Index-surface Temperature Trapezoidal Model) proposed by Moran et al. (1994) but with some significant simplification in determination of the "wet" and "warm" edges, and improving its applicability to semiarid irrigative agriculture region, i.e. North China Plain.

The new version method we proposed here to determine WDI is based on three important assumptions:

- The first assumption is that at least one "water saturated" point/pixel and, simultaneously, one "completely water stressed" point/pixel, exist in the whole research region/image.
- The second assumption is that, under a given soil water condition, the surface temperature is linearly decreasing with the increase of vegetation coverage;
- The third assumption is that, under a given vegetation condition (coverage), the surface temperature is linearly increase with the increase of WDI.

For the first assumption, we assume that there are at least two points, where the WDI of soil moisture are equal to 0 and 1 respectively, to be occurred in the research area simultaneously. This situation is rather possible occurring at semiarid irrigative agriculture region. Therefore, only to analyze the scattergram of VI-Ts relationship can determinate the wet and warm edges. This overcomes the difficulty in determining the four characteristic vertices in Moran's VITT model, which uses the surface-air temperature difference (Ts-Ta) and vegetation index to determine the vertices. At many cases, the wet and warm edges determined through the four points cannot cover all pixels and produce significant error in calculating WDI. Moreover, the difficulties in estimating air temperature spatially limit the accuracy as well.

For the second and third assumptions, we simplified the definition of water deficit index (WDI), which is firstly proposed by Jackson et al. (1981) with the direct proportion of drought extent (WDI) to the surface and air temperature difference (Ts-Ta). Consideration of the difficulty in accurate estimation of air temperature (Ta) of each pixel from remote sensing images, the determination of WDI can be calculated using an approximate equation only by surface temperature as the following style.

$$WDI(x,y) \approx \frac{Ts_{\min}(x,y) - Ts(x,y)}{Ts_{\min}(x,y) - Ts_{\max}(x,y)} \qquad (1)$$

where, Ts_{min} and Ts_{max} are the theoretical minimum and maximum surface temperature, at which the evapotranspiration of land surface are equal to potential ET and 0 respectively, under a given vegetation cover. (x, y) denotes the values at different pixels with a spatial variation. Because of the interactive mechanism between land surface and boundary layer atmosphere, the near surface air temperature is strongly affected by surface temperature through the coupling between vegetation and air. Therefore, this simplification cannot produce significant error in WDI calculation. Thus, we prefer the surface temperature- vegetation cover (f_v) relation to *(Ts-Ta)-SAVI* in determine the *WDI* in consideration of the flexibility and simplicity in regional *ET* estimation (Nishida et al., 2003).

In the operation of the proposed method, firstly, the pixels of water body are to be excluded through a boundary condition of vegetation cover, $f_v < 0$. f_v is fractional vegetation cover, calculated by

$$f_v(x,y) = \frac{NDVI(x,y) - NDVI_{\min}}{NDVI_{\max} - NDVI_{\min}} \tag{2}$$

where, $NDVI_{min}$ and $NDVI_{max}$ are the values of *NDVI* for bare soil and full covered vegetation, which are set to 0.05 and 0.8 respectively, according to the annual *NDVI* histogram analysis.

After excluding water surface, the maximum (Ts_x, f_v_x) and minimum temperature pixels (Ts_m, f_v_m) of non-water surface are found from the Ts_f_v scattergram (see Figure 2).

Based on the second assumption, for the "wet edge", we assume the theoretical minimum temperature is decreasing when the vegetation coverage increases; and the same assumption is applied to "warm edge". Therefore, pick out the minimal surface temperature pixels (black dots in Figure 2) at the wet edge, where f_v falls into the range of $0 \sim f_v\_m$; while, at the warm edge pick out the maximal surface temperature pixels (white dots in Figure 2), where f_v falls into the range of $f_v\_x \sim f_v\_max$.

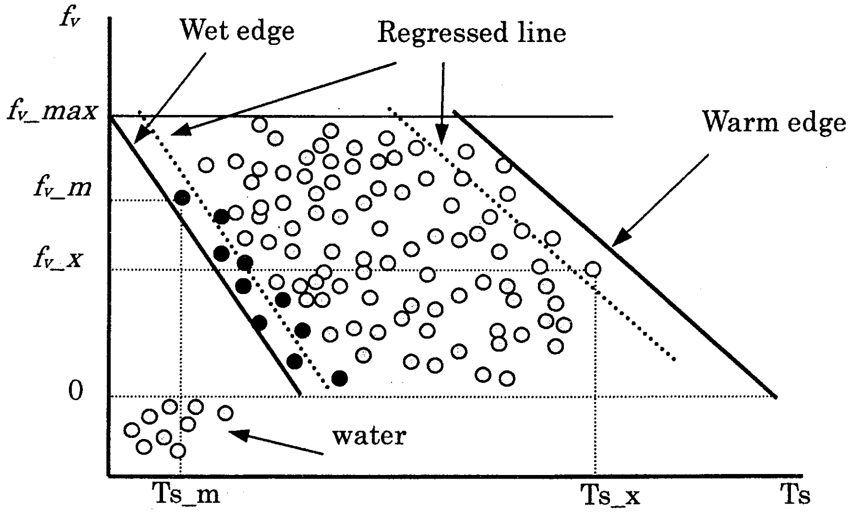

Figure 2 Ts-f_v scattergram and the concept of determining theoretical minimum and maximum Ts. Black dots and white dots denote for wet and warm pixels respectively.

Finally, use of linear regression applied for estimating the "approximate" regressed wet and warm edges, respectively. And then, parallel move of the regressed lines to their tangent positions to the pixels at WDI of 0 and 1, respectively (the thick lines in Figure 2), as the following equations.

$$Ts_{\min}(x,y) = a_1 + b_1 \cdot f_v(x,y) \tag{3}$$

$$Ts_{\max}(x,y) = a_2 + b_2 \cdot f_v(x,y) \tag{4}$$

Now, the theoretical minimum and maximum temperature of Ts_{min} and Ts_{max} under any vegetation coverage can be calculated from the above two equations. And then, calculate the WDI at any pixel.

2.2 Estimation of net radiation, R_n

The energy received from the sun is the main source that governs the heat exchange processes in the soil–plant–atmosphere system. The net radiation, $R_n(x,y)$, is the principal energy source that drives the land surface heat fluxes. It is the algebraic sum of all incoming and outgoing radiation integrated over all wavelengths, and can be calculated as:

$$R_n(x,y) = R_s \cdot (1 - r_o(x,y)) + L_\downarrow - L_\uparrow(x,y) \tag{5}$$

where, R_s is the global radiation; r_o is the surface albedo. $L_\downarrow$ and $L_\uparrow$ are the downwelling and upwelling long wave radiation, respectively; The notation of *(x,y)* means a specific parameter varies in the horizontal space domain with a resolution of one pixel. The parameter without *(x,y)* notation is considered as constant spatially. R_s is from the surface observation. The surface albedo, r_o, is estimated from multi-spectral information obtained by satellite. Brest and Goward (1987) had developed an empirical equation for estimating surface albedo from the narrow band reflectance of band 2 and band 4 of TM as

$$r_0(x,y) = 0.526 \cdot B2(x,y) + 0.362 \cdot B4(x,y) + 0.056 \cdot B4(x,y) \quad \text{for vegetated surface} \tag{6}$$

$$r_0(x,y) = 0.526 \cdot B2(x,y) + 0.474 \cdot B4(x,y) \qquad \text{for bare soil} \tag{7}$$

Wang *et al.* (2000) integrated the former researchers methods (Irons and Ranson, 1988; Ranson *et al.*, 1991; and, Dubayah, 1992) and gave the following method,

$$r_0(x,y) = 0.221 \cdot B1(x,y) + 0.162 \cdot B2(x,y) + 0.102 \cdot B3(x,y)$$
$$+ 0.354 \cdot B4(x,y) + 0.068 \cdot B4(x,y) + 0.059 \cdot B5(x,y) + 0.0195 \cdot B7(x,y) \tag{8}$$

where, B1 to B7 are the surface reflectance at nadir calculated from TM/ETM+ band 1 to band 7 data. In the present study, we employ the equation (6-5) to calculate land surface albedo.

The surface efflux of longwave radiation, $L_\uparrow$, is a function of surface temperature, $T_s(x,y)$, and the average surface emissivity, $\varepsilon(x,y)$. According to Stefan-Boltzmann law, the surface longwave eradiation can be calculated as

$$L_\uparrow(x,y) = \varepsilon(x,y) \cdot \sigma \cdot T_s^4(x,y) \tag{9}$$

where, σ is the Stefan-Boltzmann constant.

The downward atmospheric longwave radiation, $L_\downarrow$, is determined predominantly by the humidity and temperature profiles through the atmosphere. Here, we use a simply empirical method proposed by Brutsaert (1975) and modified by Culf and Gash (1993) to determine the atmospheric downward radiation.

$$L_\downarrow = 1.31 \cdot \sigma \cdot T_a^4 \left(\frac{e}{T_a}\right)^{1/7} \tag{10}$$

where, e is the vapour pressure , and T_a is the near surface air temperature.

2.3 Determination of surface emissivity, $\varepsilon(x,y)$

The surface emissivity of a partial vegetated pixel is described as a linear combination of surface emissivity of vegetation cover and bare soil (Valor and Caselles, 1996).

$$\varepsilon(x,y) = f_v \cdot \varepsilon_{veg} + (1 - f_v) \cdot \varepsilon_{soil} + 4 \cdot d\varepsilon \cdot f_v \cdot (1 - f_v) \tag{11}$$

where, ε_{veg} and ε_{soil} are the emissivities of full vegetation covered and bare soil surface; $d\varepsilon$ is vegetation structure parameter. The values of $\varepsilon_{veg,}$ $\varepsilon_{soil,}$ and $d\varepsilon$ are set to 0.99, 0.91 and 0.02, respectively, as suggested by Valor and Caselles (1996) and Roerink et al. (1999).

2.4 Estimation of soil heat flux, *G*

The soil heat flux (*G*) is the energy used for warming or cooling the subsurface soil volume. The previous investigations have shown that mid-day *G* fraction is reasonably predictable from remote sensing determinants of vegetation characteristics, and can be expressed as (Daughtry *et al.* 1990):

$$G = C \cdot R_n \tag{12}$$

where C is the soil heat flux/net radiation fraction (G/R_n). However, the attenuation of radiative and conductive heat transfer in canopy and soil, respectively, changes significantly with soil cover. From the literature in study of soil heat flux/net radiation fraction (Clothier et al., 1986; Choudhury, 1989; Kustas and Daughtry, 1990; van Oevelen, 1993), it is found that the fraction of G/Rn shows a non-linear relation with NDVI.

In this study, we adopt the method suggested by Bastiaanssen et al. (1998), which integrated the effects of surface temperature, albedo, and NDVI, and expressed as

$$\frac{G(x,y)}{R_n(x,y)} = \frac{T_s(x,y)}{r_o(x,y)} \cdot (0.0032 r_o(x,y) + 0.0062 r_o^2(x,y)) \cdot (1 - 0.978 \cdot NDVI(x,y)^4) \tag{13}$$

For bare soil, the Equation 12 is used for calculating soil heat flux.

$$G = 0.23 * Rn \tag{14}$$

2.5 Estimation of leaf area index, *LAI*

Kanemasu et al. (1977) established a simple relationship between the fractional vegetation cover and leaf area index for various agricultural plants:

$$LAI(x,y) = a + b \cdot \ln(1 - f_v(x,y)) \tag{15}$$

where, a and b are empirical coefficients. In this research, we analyzed the ground observation results of *LAI* and f_v from space remote sensing and specified a and b as –0.08 and –2.41 for wheat, –0.80 and –4.94 for maize, respectively.

2.6 Calculation of potential latent heat flux, *LEp*

It is of importance to calculate correctly potential evapotranspiration of the land surface for estimating the actual evapotranspiration and then therein energy fluxes accurately. Here, we use Penman-Monteith method to calculate potential evapotranspiration. So, the potential latent heat flux (LE_p) can be written as

$$LE_p = \frac{\Delta \cdot (Rn - G) + \rho \cdot Cp \cdot D / r_a}{\Delta + \gamma \cdot (1 + r_{cp} / r_a)} \tag{16}$$

where, r_{cp} is canopy resistance at the situation of potential evapotranspiration; r_a is aerodynamic resistance; D is vapour pressure deficit; Δ and γ are the slope of saturated vapour pressure-air temperature curve and the psychrometric constant.

The resistance of plant canopy under potential evapotranspiration, r_{cp}, is calculated from the following equation (Allen et al.,1989).

$$r_{cp} = \frac{r_{sm}}{a \cdot LAI} \tag{17}$$

r_{sm} is minimum stomatal resistance. It is suggested that 0.5 is an appropriate value of a for grass (Allen et al., 1989). However, since the resistance of woody or herbaceous natural vegetation is approximately double that of agricultural crops (Radersma and Rider, 1996), we use the value of 0.25 after Rey (1999). The minimum stomatal resistance is estimated according our field measurements as described in Shen et al. (2002). The values of minimum stomatal resistance for different growing seasons are listed in Table 1.

Table 1 The minimum stomatal resistance used in this study (Unit: s/m)

Growth stages	~ Jointing	Heading	Blooming	Milking	Maturing
Winter wheat	50	25	12.5	25	50
Maize	80	---	50	50	---

2.7 Calculation of aerodynamic resistance, r_a

An essential parameter in estimating surface heat or vapour flux is aerodynamic resistance. The term of "resistance" is a concept introduced from physics since the water transfer in soil-plant-atmospheric system is considered as a continuous and steady flow and abides by Ohm law (Monteith and Unsworth, 1990). Therefore, the resistance to evapotranspiration can be divided as surface resistance (r_c), the resistance to vapour transferring from soil or leaf stomata to near surface air, and aerodynamic resistance (r_a), the resistance to vapour transferring from near surface air to boundary layer atmosphere.

In neural conditions, the aerodynamic resistance, r_a, is usually estimated as

$$r_a = (\ln\frac{z-d}{z_{0m}})^2/(k^2\cdot u_z) \tag{18}$$

where, z_{0m} and d are roughness length for momentum transfer and zero displacement height, respectively; z is reference height; k is Von Karman's Constant; u_z is wind speed at the reference height.

Mathematically, for calculating the sensible heat flux using remotely sensed data, a single-source model is often used as

$$H = \rho\cdot Cp\frac{Ts-Ta}{r_{ah}} \tag{19}$$

where, Ts and Ta are surface and air temperature respectively; r_{ah} is the aerodynamic resistance to sensible heat transfer from surface to reference height. r_{ah} is computed as follows:

$$r_{ah} = \frac{1}{k\cdot u^*}\cdot\left[\ln(\frac{z-d}{z_{oh}})-\psi_h\right] \tag{20}$$

with

$$u^* = k\cdot u\cdot\left[\ln(\frac{z-d}{z_{om}})-\psi_m\right]^{-1} \tag{21}$$

where, u^* is the friction velocity; z_{0m} and z_{0h} are the roughness lengths governing momentum and heat transfer from the surface to the reference height; Ψ_m and Ψ_h are the stability corrections for momentum and heat, respectively. z_{om} and d are calculated from

$$z_{0m} = 0.13\cdot h \tag{22}$$

$$d = 0.67\cdot h \tag{23}$$

where h is height of vegetation. In this study, h is calculated from remotely estimated LAI using the following equations according to our field measuring results.

$$h = 0.0154\cdot LAI^3 - 0.1221\cdot LAI^2 + 0.3317\cdot LAI \qquad \text{(wheat season)} \tag{24}$$

$$h = 0.0582\cdot LAI^3 - 0.4495\cdot LAI^2 + 1.3722\cdot LAI \qquad \text{(maize season)} \tag{25}$$

The roughness length of heat, z_{0h}, can be calculated from the following relation (e.g. Zhan et al., 1996)

$$z_{om}/z_{oh} = \exp(kB^{-1}) \tag{26}$$

where, kB^{-1} is a parameter accounting for difference in momentum and heat exchanges at the surface (Brutsaert, 1982), and is estimated using an empirical formula introduced by Kustas et al. (1989) as,

$$kB^{-1} = s_{kB}u(T_{rad}-Ta) \tag{27}$$

where T_{rad} is radiometric surface temperature, s_{kB} is an empirical coefficient to be observed varying between

0.05 and 0.25 with some studies suggesting that s_{kB} should be related to the magnitude of H (Troufleau et al., 1997; Lhomme et al., 1997; Kustas et al., 1995).

For estimating stability corrections, a number of formulations are available. Kustas *et al.* (1989) used the formulation of Garratt (1978), Matthias *et al.* (1990) and Bastiaanssen (1995) used the Fiedler and Panofsky (1972) approach for determining the aerodynamic resistance. In the present study, Fiedler and Panofsky's approach is used for estimating stability corrections with combining with the kB^{-1} method reported by Kustas et al. (1989) and thus the distributed aerodynamic resistance of the heat transport.

The stability correction factor of Ψ_m is dependent on the surface characteristics and the bulk Richardson number (*Ri*) between the canopy surface and the reference height (Monteith and Unsworth, 1990). The bulk Richardson number is expressed as a ratio of the production of energy by buoyancy forces to dissipation of energy by mechanical turbulence.

$$Ri = \frac{g \cdot (z-d) \cdot (Ts - Ta)}{u^2 \cdot (Ta + Ts)/2} \tag{28}$$

where *g* is the acceleration of gravity.

In unstable conditions, the stability factors for momentum and heat transfer can be computed as (Dyer and Hicks, 1970; Monteith and Unsworth, 1990),

$$\left.\begin{aligned} \psi_m &= (1 - 16 \cdot Ri)^{-0.25} \\ \psi_h &= (1 - 16 \cdot Ri)^{-0.5} \end{aligned}\right\} \qquad Ri < -0.1 \tag{29}$$

From measurements in stable and slightly unstable conditions, the stability correction factors can be computed as (Webb, 1970; Monteith and Unsworth, 1990),

$$\psi_m = \psi_h = (1 - 5 \cdot Ri)^{-1} \qquad -0.1 \le Ri \le 1 \tag{30}$$

Then, the aerodynamic resistance can be deduced by

$$r_a = r_{ah} + r_x \tag{31}$$

where, r_x is termed as "excess resistance" to r_{ah}, and calculated as

$$r_x = \frac{kB^{-1}}{ku*} \tag{32}$$

3 Application to North China Plain

3.1 Data and processing

Totally, 13 sub-scenes of Landsat TM and ETM+ images are used in this study. Each image covers around a region of 1000 km^2 near our ground experimental site, Luancheng Experimental Station for Agro-ecosystem Research (LESA), the Chinese Academy of Sciences. These images are selected from 3 years; basically, they can well demonstrate the major growth stages of winter wheat and maize through a whole crop-year. Table 2 shows the agricultural specifications of these images with some basic hydrological information of precedent precipitation or irrigation.

Before calculate the energy and evapotranspiration fluxes, all images were pre-processed for geometric rectification (or geographical encoding) and atmospheric radiance rectification.

3.2 Remotely estimated evaporation and transpiration

Figure 3 shows the maps of evaporation and transpiration in two periods, when the wheat is in the growth stages of emerging (LAI is almost 0) and blooming (the maximum LAI period), respectively.

The maps of the two periods illustrate the extreme situations of evaporation and transpiration. During emerging period, the land surface almost bare soil except for the villages where there are some trees and the transpiration from villages is larger. However, as for the blooming stage, the land surface of fields almost full covered by crop canopy and the transpiration from field is very significant, while the evaporation is minor.

Table 2 Agricultural specifications of the selected Landsat images

DOY	Image date	Sensor	Main crop	Growth stage	DAP/DAI*	P/I (mm)
288	2000/10/14	ETM+	Wheat	Emerging	4	39.9
90	2001/03/31	TM		Pre-revival	3	60
96	2000/04/05	ETM+		Revival	14	0.8
101	2002/04/11	ETM+		Jointing	6	19.6
106	2001/04/16	TM		Jointing	6	11.3
117	2002/04/27	ETM+		Heading	5	3.0
130	2001/05/10	ETM+		Blooming	11	69.6
146	2001/05/26	ETM+		Milking-Maturing	7	60
170	2001/06/19	TM	Maize	Post-harvest/sowing	2	40.1
194	2001/07/13	ETM+		Jointing	3	60
234	2001/08/22	TM		Blooming	3	42.6
256	2000/09/12	ETM+		Milking-Maturing	7	94.7
274	2001/10/1	ETM+		Pre- sowing	1	1.4

*: DAP/DAI means the days after precipitation or days after irrigation.

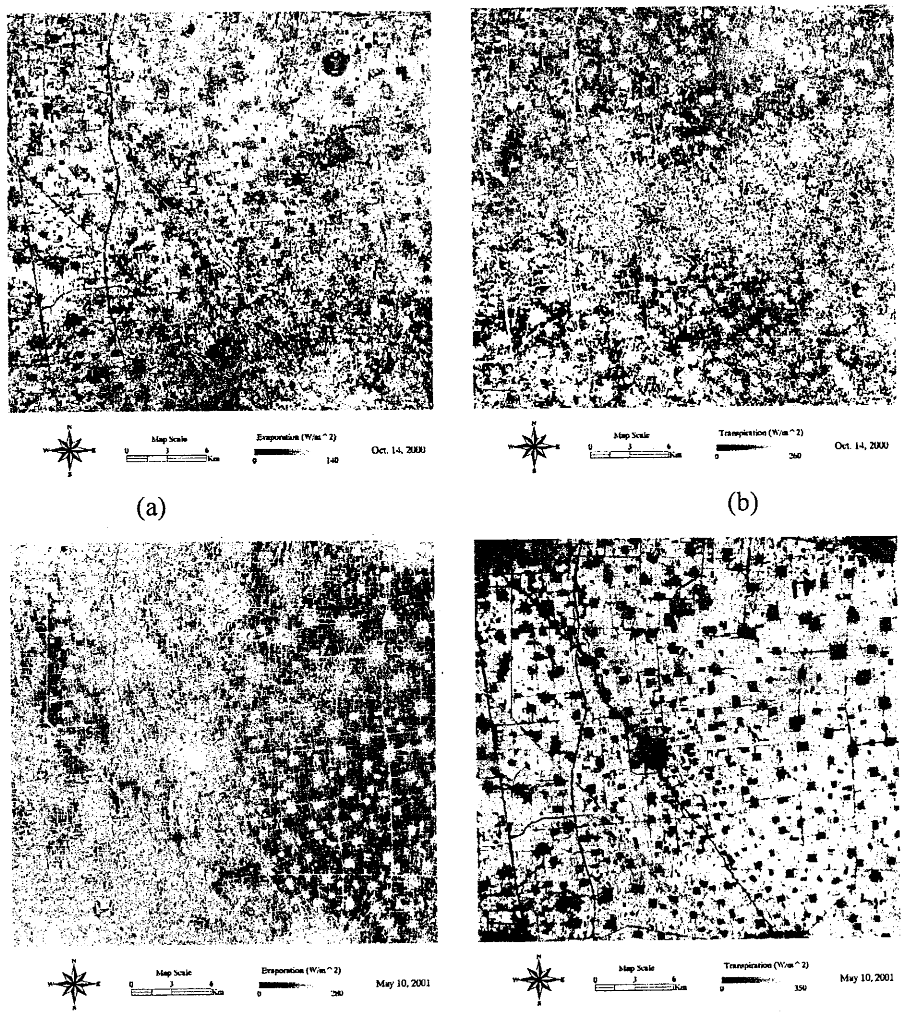

(a) (b)

(c) (d)

Figure 3 The output maps of evaporation and transpiration during the wheat emerging and blooming periods. (a) and (b) are the situations for emerging period; (c) and (d) are the situations for blooming period.

Figure 4 shows the results of remotely estimated evaporation (E) and transpiration (T) at our experimental site, Luancheng Experimental Station for Agro-ecosystem Research (LESA), Chinese Academy of Sciences. The results of Apr. 5, 2000, Sep. 12, 2000, Apr. 11, 2002, and Apr 27, 2002 are also plotted in the figure. The results show very smooth seasonal changes. The change of LE shows 2 peaks at April and August respectively.

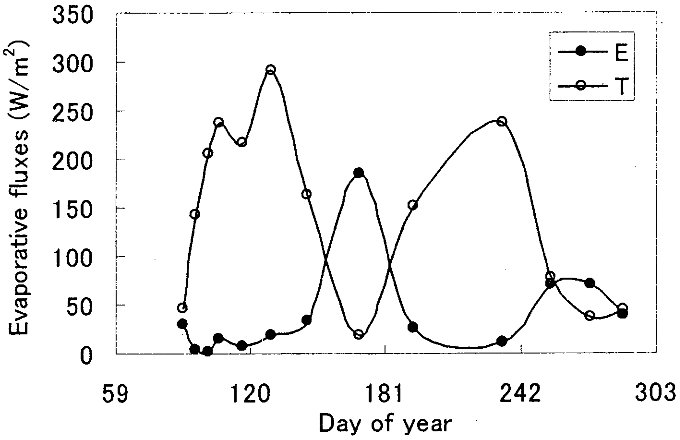

Figure 4 The estimated results of evaporation (E) and transpiration (T) at LESA

3.3 Validation

Accuracy of the proposed algorithm is highly dependent on the accuracy in estimating soil water status, *WDI*, and the potential evapotranspiration, *LEp*. Because we lack ground separate measurements of evaporation and transpiration, in order to assess the accuracy of the remote sensing algorithm, we only compared the remotely estimated value of evapotranspiration flux and soil water deficit index with ground measurements at LESA.

3.3.1 Soil water deficit index, *WDI*

In order to assess the accuracy of *WDI* estimation, we use measured extractable soil water (*ESW*) as a standard to conduct the validation. In strict definition, *WDI* is a concept based on water stress and can be quantitatively defined as the following equation (Shen, 2003),

$$WDI = \left[\begin{array}{cc} 0 & \theta > \theta^* \\ \dfrac{\theta - \theta^*}{\theta_w - \theta^*} & \theta_w \le \theta \le \theta^* \\ 1 & \theta < \theta_w \end{array} \right. \tag{33}$$

where, θ and θ_w are actual soil moisture and wilting point, respectively; θ^* is called incipient stress point of soil moisture.

On the other hand, *ESW* means the fractional content of plant available moisture. Therefore, the relationship between WDI and ESW can be described as follows,

$$(1 - WDI) = \frac{\theta - \theta_w}{\theta^* - \theta_w} \quad > \quad ESW = \frac{\theta - \theta_w}{\theta_f - \theta_w} \tag{34}$$

The above inequality is reasonable because the threshold point of sol moisture at incipient water stress, θ^*, must be less than field capacity. Here, (1-WDI) can be considered as an 'undeficit' index.

Figure 5 compares the soil water deficit status with ground measurements of extractable soil water at 0-40 cm layer. It is shown that most of the data lies on the up side of the 1:1 line meaning the unequal relation in Equation 34. This fact implies that the simplified method for determine WDI plays a good performance.

For a given soil type, the field capacity and wilting point can be considered as constants, but the incipient stress threshold point (θ^*) should be various in different phase of vegetation growth, therefore, at this point, it is linked with the phenological aspect of vegetation.

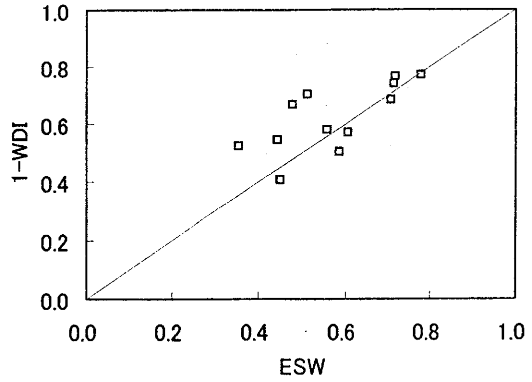

Figure 5 Comparison of remotely estimated WDI and measured ESW of 0-40cm layers.

3.3.2 Evapotranspiration flux, *ET*

The remotely estimated latent heat flux (ET_RS) at LESA is compared with the ground measurement by Bowen ratio system (ET_BW) in Figure 6. Figure 6a shows an annual course by arranging the 13 sub-scenes in a series of DOY. It is shown a good consistence of estimated ET with the measurements during low vegetation cover stages.

Figure 6b illustrates the correlation between estimated and measured ET at LESA. The Pearson's coefficient is 1.07, and regression coefficient is around 0.887 for the low vegetation cover situation. However, for the high vegetation cover, the dual-source model underestimates the total evapotranspiration. The facts imply that the proposed algorithm can estimate the evapotranspiration well when the vegetation cover is low.

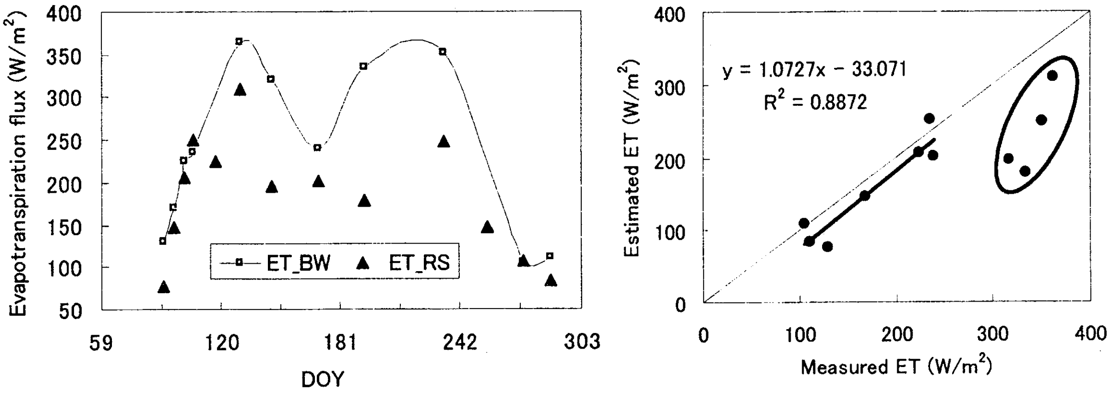

Figure 6 Comparison of remotely estimated and ground measured latent heat flux.

4 Conclusions

In this research, we proposed an algorithm for estimating regional evaporation and transpiration of land surface using remote sensing data. The application in irrigated agricultural region, i.e. NCP, shows a good performance when the vegetation cover is low. However, during the high vegetation cover period, it seems that the algorithm need to be improved. At least two important conclusions can be highlighted as follows:

References

Allen RG, Jensen ME, Wright JL, Burman DR. 1989. Operational estimates of reference evapotranspiration. *Agon. J.* 81: 650-662.

Bastiaanssen WGM, Menenti M, Feddes RA, Holtslag AAM. 1998. A remote sensing surface energy balance algorithm for land (SEBAL): 1. Formulation. *J. Hydrol.* 212-213: 198-212.

Bastiaanssen WGM, Pelgrum H, Wang J, MaY, Moreno JF, Roerink GJ, van der Wal T. 1998. A remote sensing surface energy balance algorithm for land (SEBAL): 2. Validation. *J. Hydrol.* 212-213: 213-229.

Bastiaanssen WGM. 1995. *Regionalization of surface flux densities and moisture indicators in composite terrain.* Ph. D. thesis. Agricultural University, Wageningen, the Netherlands. pp. 288.

Bastiaanssen WGM. 2000. SEBAL-based sensible and latent heat fluxes in the irrigated Gediz Basin, Turkey. *J. Hydrol.* 229: 87-100.

Brest CL and Goward SN. 1987. Deriving surface albedo measurements from narrow band satellite data. *International Journal of Remote Sensing*, **8**: 351-367.

Brown KW and Rosonberg HT. 1973. A resistance model to predict evapotranspiration and its application to a sugar beet field. *Agronomy J.* 65: 341-347.

Brutsaert W. 1975. On a derivable formula for long-wave radiation from clear skies. *Water Resources Research*, **11**: 742-744.

Brutsaert W. 1982. *Evaporation into Atmosphere.* Reidel, Dordrecht. pp. 299.

Carlson TN, Caphert WJ, Gillier RR. 1995. A new look at the simplified method for remote sensing of daily evapotranspiration. *Remote Sens. Environ.* 54: 161-167.

Chen JM. 1988. The main problem with modern remote sensing evapotranspiration model and

Choudhury BJ. 1989. Estimating evaporation and carbon assimilation using infrared temperature data. In: Asrar G. (Eds.). *Vistas in modeling, in Theory and Applications of Optical Remote Sensing.* Wiley, New York. pp. 628-690.

Choudhury BJ. 1994. Synergism of multispectral satellite observations for estimating regional land surface evaporation. *Remote Sens. Environ.* 49: 264-274.

Clothier BE, Clawson KL, Pinter PJ Jr., Moran MS, Reginato RJ, Jackson RD. 1986. Estimation of soil heat flux from net radiation during the growth of alfalfa. *Agric. For. Meteorol.* 37: 319-329.

Culf AD and Gash JH. 1993. Longwave radiation from clear skies in Niger: A comparison of observations with simple formulas. *Journal of Applied Meteorology*, **32**: 539-547.

Daughtry CST, Kustas WP, Moran MS, Pinter PJ Jr., Jachson RD, Brown PW, Nichols WD, Gay LW. 1990. Spectral estimates of net radiation and soil heat flux. *Remote Sens. Environ.* 32: 111-124.

Dyer AJ and Hicks BB. 1970. Flux-gradient relationships in the constant flux layer. *Q. J. Roy. Meteorol. Soc.* 96: 715–721.

Fox NI, Saich P, Collier CG. 2000. Estimaing the surface water and radiation balance in an upland area from space. *Int. J. Remote Sens.* 21: 2985-3002.

Garratt JR. 1978. Flux-profile relations above tall vegetation. *Q. J. Roy. Meteorol. Soc.* 104: 199–211.

Irons JR and Ranson KJ. 1988. Estimating big bluestem albedo from directional reflectance measurements. *Remote Sensing of Environments*, **25**: 185-199.

Jackson RD, Idso SB, Reginato RJ, Pinter PJ Jr. 1981. Canopy temperature as a crop water stress indicator. *Water Resour. Res.* 17: 1133-1138.

Kanemasu T, Rosenthal UD, Raney PJ, Stone ThP. 1977. Evaluation of an evapotranspiration model for corn. *Agron. J.* 69: 461-464.

Kustas WP and Daughtry CST. 1990. Estimation of soil heat flux/net radiation ratio from spectral data. *Agric. For. Meteorol.* 49: 205-223.

Kustas WP, Choudhury BJ, Moran MS, Reginato RJ, Jackson RD, Gay LW, Weaver HL. 1989. Determination of sensible heat flux over sparse canopy using thermal infrared data. *Agric. For. Meteorol.* 44: 197-216.

Kustas WP, Humes KS, Norman JM, Moran MS. 1995. Single and dual-source modeling of surface energy fluxes with radiometric temperature. *J. Appl. Meteorol.* 35: 110-121.

Lhomme JP, Troufleau D, Monteny B, Chehbouni A, Bauduin S. 1997. Sensible heat flux and radiometric surface temperature over sparse Sahelian vegetation II. A model for the kB^{-1} parameter. *J. Hydrol.* 188-189: 839-854.

Monteith JL and Unsworth MH. 1990. *Principles of Environmental Physics (2^{nd} edn).* Arnold Press (London). pp22.

Moran MS, Clarke TR, Inoue Y, Vidal A. 1994. Estimating crop water deficit using the relation between surface-air temperature and spectral vegetation index. *Remote Sens. Environ.* 49: 246-263.

Nishida K, Nemani RR, Running SW, Glassy JM. 2003. An operational remote sensing algorithm of land surface evaporation. *J. Geophys. Res.* 108 (D9):4270. doi: 10. 1029/2002JD002062.

Price JC. 1990. Using spatial context in satellite data to infer regional scale evapotranspiration. *IEEE Trans Geosci. Remote Sens.* 28: 940-948.

Radersma S and Ridder N. 1996. Computed evapotranspiration of annual and perennial crops at different temporal and spatial scales using published parameter values. *Agric. Water Manag.* 31: 17-34.

Ranson KJ, Irons JR, Daughtry CST. 1991. Surface albedo from bi-directional reflectance. *Remote Sensing of Environment*, **35**: 201- 211.

Rey JM. 1999. Modelling potential evapotranspiration of potential vegetation. *Ecol. Modelling.* 13: 141-159.

Roerink GJ, Su Z, Menenti M. 1999. S-SEBI: a simple remote sensing algorithm to estimate the surface energy balance. *Physics and Chemistry of the Earth,* 25: 147-157.

Sequin B and Itier B. 1983. Using midday surface temperature to estimate daily evapotranspiration from satellite thermal-IR data. *Int. J. Remote Sens.* 4: 371-384.

Shen Y, Kondoh A, Tang C, Zhang Y, Chen J, Li W, Sakura Y, Liu C, Tanaka T, Shimada J. 2002. Measurement and analysis of evapotranspiration and surface conductance of a wheat canopy, *Hydrological Processes,* 16: 2173-2187.

Shen Y. 2003. *Study on Hydrological Processes of Land and Atmospheric System in Semiarid Agricultural Region.* Doctoral thesis, Chiba University, Japan. pp69-81.

Troufleau D, Lhomme JP, Monteny B, Vidal A. 1997. Sensible heat flux and radiometric temperature over sparse Sahelian vegetation: 1. An experimental analysis of the kB^{-1} parameter. *J. Hydrol.* 188-189: 815-838.

Valor E and Caselles V. 1996. Mapping land surface emissivity from NDVI: application to European, African, and South American areas. *Remote sensing of Environment,* 57: 167-184.

van Oevelen PJ. 1993. *Determination of the available energy for evapotranspiration with remote sensing.* M.Sc. Thesis, Agricultural University of Wageningen. p.68.

Wang J, White K, Robinson GJ. 2000. Estimating surface net solar radiation by use of Landsat-5 TM and digital elevation models. *Int. J. Remote Sens.* 21: 31-43.

Webb EK. 1970. Profile relationships: the log-linear range, and extension to strong stability. *Q. J. Roy. Meteorol. Soc.* 96: 67-90.

Zhan X, Kustas WP, Humes KS. 1996. An intercomparison study on models of sensible heat flux over partial canopy surfaces with remotely sensed surface temperature. *Remote Sens. Environ.* 58: 242-256.

Seasonal variations in surface moisture status over east China by AVHRR

Atsushi Higuchi[1] and Akihiko Kondoh[2]
1 Hydrospheric Atmospheric Research Center (HyARC), Nagoya University, Japan
E-mail: higu@hyarc.nagoya-u.ac.jp
2 Center for Environmental Remote Sensing (CEReS), Chiba University, Japan
E-mail: kondoh@faculty.chiba-u.ac.jp

Abstract

To identify the boarder of "wet" and "dry" in the surface moisture status (SMS), we applied the relationship Normalized Difference Vegetation Index (NDVI) and surface temperature (Ts), so-called VI/Ts method or TVX over the east China by AVHRR dataset. AVHRR dataset received by CEReS we used. After procedure about AVHRR imageries (wide-swath cut, solar angle correction and cloud screening), we adopted simple VI/Ts method (only estimation of the regression line within a window matrix of 10pixels by 10 lines). Preliminary results could be summarized as follows. Slope performed well for represent the SMS even though the simple estimation (only estimate regression line). Inter-annual variability also seems to be detectable in this methodology (wet and dry boarder was steeper in 1998 in September). However, internal phenomenon was not deeply understood, so overall analysis would be required (analysis of reanalysis dataset, and so on).

1. Introduction

For better understanding of land surface processes over a regional scale, fully utilization of satellite remote sensing dataset is essential. Particularly, surface moisture status (wet or dry; SMS) directly affected on the partitioning available energy at land surface into the sensible (heat) and the latent (water) heat fluxes into the atmosphere. Algorithms or methodologies for estimation of surface moisture by satellite data have been developed using optical and/or microwave imagers. In this article, we focus on the methodology based on the relationship between Normalized Difference Vegetation Index (NDVI) and surface temperature (Ts: so-called VI/Ts method or TVX, hereafter VI/Ts method). Nemani and Running (1989) was demonstrated firstly this relationship, after that many articles or reports have been represented the variability and/or utilizations of VI/Ts method (e.g., Nemani *et al.*, 1993; Kondoh *et al.*, 1998, Nishida *et al.*, 2002; Higuchi *et al.*, 2004). We applied VI/Ts method over east China and try to understand;

a. Is this possible to apply VI/Ts method into relatively wet region? In the drying period, Kondoh *et al.*, already applied and proofed the variability of VI/Ts method. However whole of a year, especially "Meiyu (rainy season in China)" is not yet.
b. Interannual variability is detectable or not using this methodology? In 1998, over the Yangi River had damaged by big floods, other hands in 1999 was not. Shinoda and Uyeda (2002) mentioned that paddy field (wet land) played important role on the developing deep convection due to supplying water vapor into the atmosphere by high spatial resolution's two dimensional model. So the boarder of "wet" and "dry" is important information not only hydrologists or hydrometeorologists but also meso-scale meteorologists.

2. Data processing

We used CEReS received AVHRR dataset (hereafter CEReS AVHRR) during 1998-2000. We procedure all dataset preparations and cloud screening as follows:

2.1. AVHRR preparations

CEReS AVHRR is consists of ten channels (original five AVHRR channels [already converted physical data: i.e., AVHRR Aledo for ch.1 & 2; brightness temperature for ch.3 to 5], NDVI, solar azimuth angle, scan angle, sea surface temperature [SST] and solar zenith angle). We processed the dataset especially ch.1 & 2 as follows:

a). Cut a part of image whose more than 40 degrees data in scan angle (due to the wide-swath of AVHRR)
b). Solar zenith angle correction: simply divided as cosine of solar zenith angle.

Atmospheric correction and sensor degradation correction were conducted in this analysis.

2.2. Cloud screening

Cloud screening is important process to detect "real" land surface status from optical sensors. Many cloud-screening schemes are available for AVHRR, we adopted the cloud screening thresholds noticed in White *et al.* (2002) as follows: 1. Ch.1 reflectance (AVHRR Aledo) above 35% and ch.4 less than 288 K (15 °C). We used stricter threshold in ch.1 as above 20%. 2. Simple ratio (ch.2 / ch.1) less than 1.2. 3. Difference between ch.4 and ch.5 less than –1.5K and greater than 4.5K and 4. difference between ch.3

and ch.4 greater than 15 K. **Figure 1** shows an example of original ch.2 image and after the procedure of cloud screening by above thresholds. Cloud screening look like works well. After cloud screening, we estimated NDVI obtained from ch.1 and ch.2, and surface temperature derived from split-window technique by McMillin and Crossby (1984) using ch.3, ch.4 and ch.5.

2.3. Estimate "slope" within a window (TVX matrix)

After the procedure of cloud screening, we estimated the "slope" within a scatter diagram of NDVI with Ts (window). Previous studies used some algorithms for the screening of low-NDVI data or the estimation of "always negative" value in slope (e.g., Nemani *et al.*, 1993; Kondoh *et al.*, 1998). This analysis, our target is to detect the boarder of wet and dry, so spatial information would be required. A window we selected is 10pixels by 10lines (i.e., spatial resolution is approximately 10km both in latitude and longitude). Due to the shortness (in maximum 100 pixels-data available) for the determination of slope (regression line), we simply estimated the regression line without some screening automatically. Thus, both negative (most of VI/Ts studies focus on) and positive value (Higuchi et al., 2004, mentioned about the reasons why estimate positive values in the whole of monsoon Asia) could be obtained.

3. Results and discussion

Figures 2 to **4** represent the spatial distribution of slope in "Meiyu (June, **Figure 2**)", after Meiyu (July, **Figure 3**) and dry period (September, **Figure 4**) in 1998 (flood in Yangi River) and 1999 (normal year). As general features in both 1998 and 1999, slope seems to be detectable the SMS, and performed well about seasonal march of wetness (northward migration of wet part due to the activities of Meiyu fronts by comparisons of **Figures 2** and **3**; expansion of "dry part" due to strong sunshine; compare **Figures 3** with **Figure 4**). The boarder of "wet" and "dry", around –20 in slope, were found in Figures. Inter-annual variability also can see in **Figure 4**. Latitudinal gradient was steep in 1998 (steep positive value from Yangi River to near of Heihe River) but in 1999, not confirm such definite gradient. Steep "positive" slope means that "surface temperature increase with NDVI", in a sense of energy budget over the vegetated cover, this phenomenon cannot explain. The mean NDVI around this steep positive slope area, was very small (ranged with 0.2 to 0.3, Figure not shown), this small values in NDVI maybe lead the estimation instability of slope, however similar mean NDVI also confirmed in normal negative slope region near of Peking (38N 117E). We expected that this positive slope represented the damaged region by flood, as an evidence, Ts value around this positive slope value region was less than 300K (most of this image reached more than 305K, also Figure not shown).

4. Concluding remarks

We have to see carefully each processed images for identify that "what happen over this area". Additionally to deepen our knowledge, especially interaction between land and the atmosphere have to be focused. Fortunately GAME reanalysis dataset provide fine both in spatial and time resolution in 1998, as a future study, one-by-one relationship detection between reanalysis data and satellite datasets.

References

Higuchi, A., Hiyama, T., Fukuta, Y. and Fukushima, Y. (2004): A behavior of surface temperature/vegetation index (TVX) matrix derived from 10 days AVHRR composite imageries over monsoon Asia. *Hydrological Processes*, (submitted).

Kondoh, A., Higuchi, A., Kishi, S., Fukuzono, T. and Li, J. (1998): The use of multi-temporal NOAA/AVHRR data to monitor surface moisture status in the Huaihe River Basin, China. *Advances in Space Research*, **22**, 645-654.

McMillin, L.M. and Crossby, D.S. (1984): Theory and validation of the multiple window sea surface temperature technique. *Journal of Geophysical Research*, **89**(C3), 3655-3661.

Nemani, R.R. and Running, S.W. (1989): Estimation of regional surface resistance to evapotranspiration from NDVI and thermal-IR AVHRR data. *Journal of the Applied Meteorology*, **28**, 276-284.

Nemani, R.R., Pierce, L., Running, S.W. and Goward, S. (1993): Developing satellite-based estimates of surface moisture status. *Journal of the Applied Meteorology*, **32**, 548-557.

Nishida, K., Nemani, R.R., Running, S.W. and Glassy, J.M. (2003): An operational remote sensing algorithm of land surface evaporation. *Journal of Geophysical Research*, **108**(D9), 4270, doi:10.1029/2002JD002062.

Shinoda, T. and Uyeda, H. (2002): Effective factors in the development of deep convective clouds over the wet region of Eastern China during the summer Monsoon season. *Journal of Meteorological Society of Japan*, **80**, 1395-1414.

White, M.A., Nemani, R.R., Thornton, P.E. and Running, S.W. (2002): Satellite evidence of phonological differences between urbanized and rural areas of the Eastern United States deciduous broadleaf forest. *Ecosystem*, **5**, 260-277.

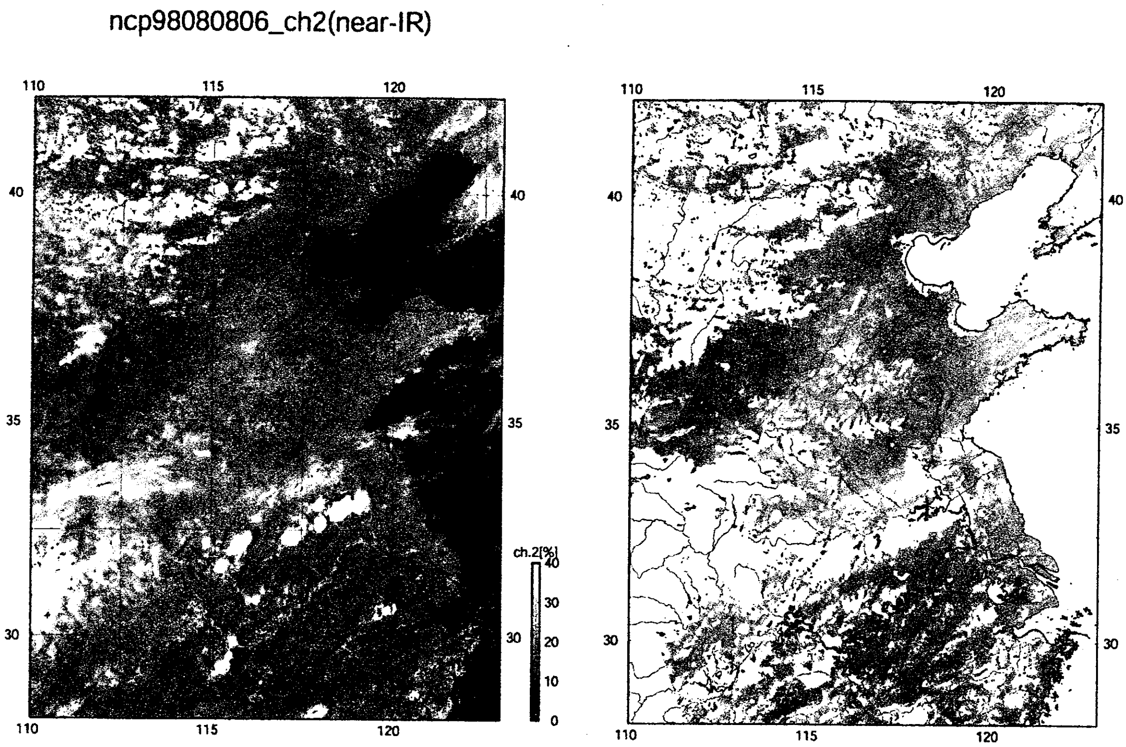

Figure 1: Original ch.2 CEReS AVHRR (left) and after cloud screening (right).

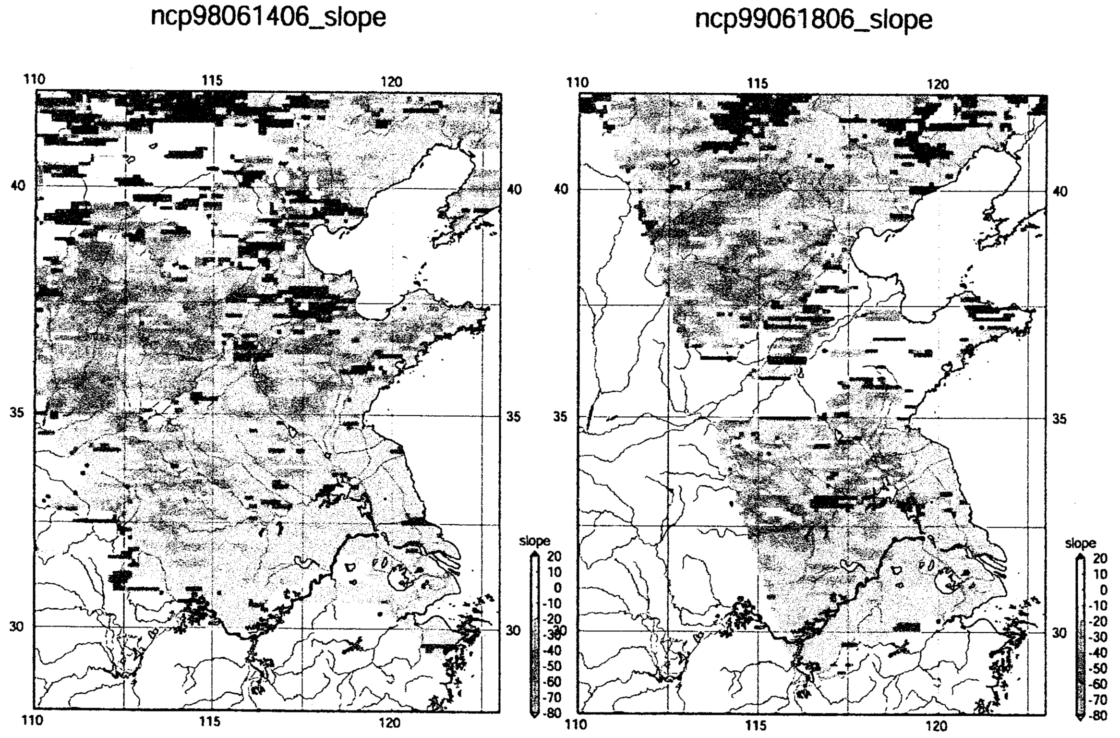

Figure 2: Estimated "slope" during "Meiyu" season (middle June), in 1998 (left: June 14, 1998), and in 1999 (right: June 18, 1999).

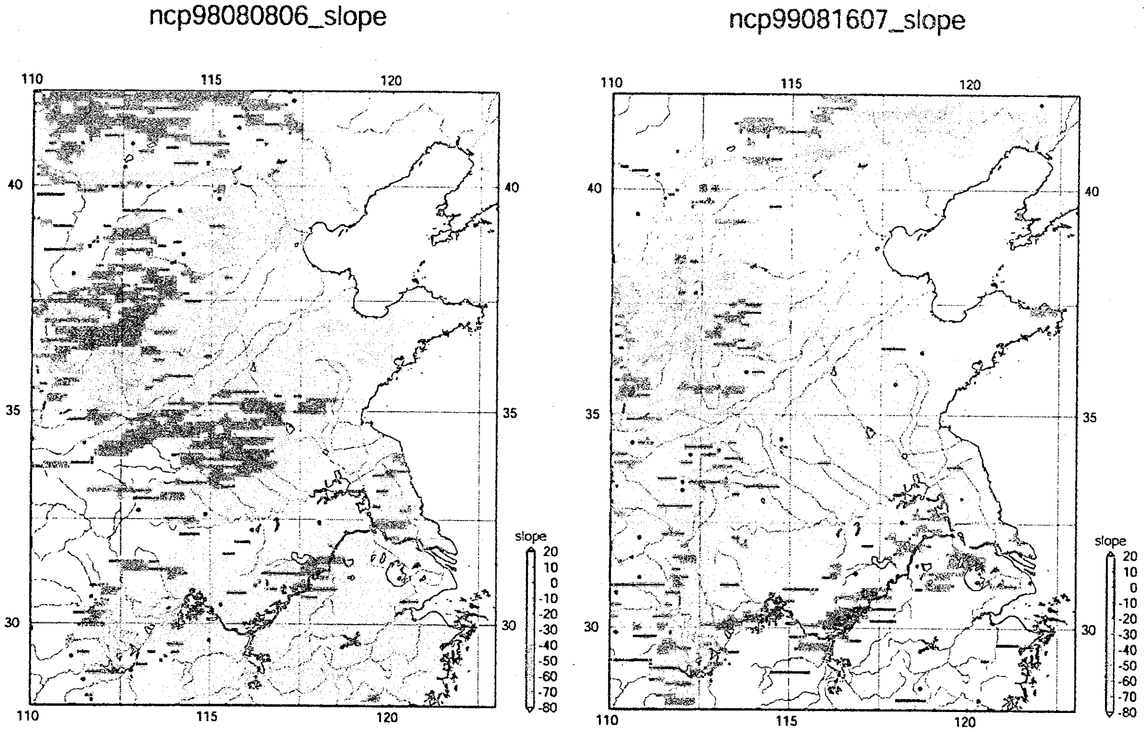
ncp98080806_slope

ncp99081607_slope

Figure 3: Estimated slope after Meiyu season (August), in 1998 (left: August 08, 1998), and in 1999 (right: August 16, 1999).

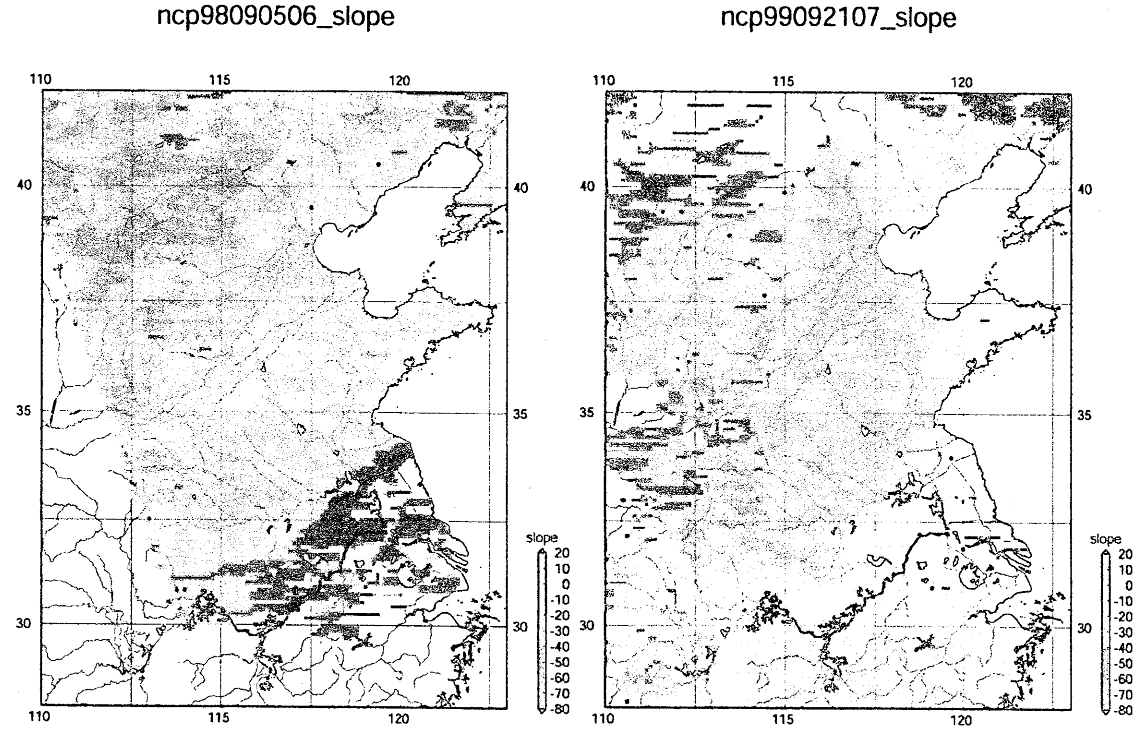
ncp98090506_slope

ncp99092107_slope

Figure 4: Estimated slope during dry period (September), in 1998 (left: September 05, 1998), and in 1999 (right: September 21, 1999).

Distribution, Biodiversity and Long-term Changes of Seagrass Beds in Okinawa Island: Effects of Terrestrial Ecosystems

Chika Ishibashi[1], Akihiko Kondoh[2] and Masahiro Nakaoka[3*]
1 Faculty of Science, Chiba University
2 Center for Environmental Remote Sensing, Chiba University
3 Graduate School of Science and Technology, Chiba University
*Corresponding Author: E-mail: nakaoka@faculty.chiba-u.jp

Abstract

We investigated large-scale distribution and biodiversity of seagrass beds and their temporal changes along eastern coast of Okinawa Island by an integrated approach using RS, GIS and field monitoring. Nine seagrass beds of various sizes are recognized by maps and aerial photographs along the middle part of the eastern coast. Patterns of temporal changes in distribution between 1977 and 1993 varied among different seagrass beds, with some seagrass beds extending its area, whereas others remaining stable. Regional and local species diversity of seagrasses also varied among beds. Species diversity was low in beds with larger watershed areas behind coastline, and high in beds with smaller watershed, suggesting possible impacts of terrestrial ecosystems on seagrass beds through river discharge.

1. Introduction

Seagrass bed is one of the most conspicuous components of coastal ecosystems around the world (Short & Green 2003). It is known as the most productive habitats in the world with its annual productivity equivalent to that of tropical rain forest (Hemminga & Duarte 2000). It also provides habitats for a variety of plant and animals species, producing "hot spot" of biodiversity in marine ecosystems (Williams & Heck 2001).

Over the past centuary, seagrass beds have been decreasing due to a variety of human-induced disturbance worldwide (Shorts & Wyllie-Echeverria 1996), and especially in tropical regions (Fortes 1988, 1995). For example, deforestation causes massive sediment discharge from terrestrial to coastal areas, resulting in increase in turbidity and light attenuation. Urbanization along the river areas and development of farmland and aquaculture hatcheries cause heavy nutrient loads, leading to serious eutrophication in coastal waters. Seagrass beds are considered to be most susceptible to alteration of terrestrial ecosystems because they generally locate soft bottoms near river mouth.

To promote conservation of seagrass beds, we first need to know their exact distribution and its temporal changes over large spatial scales. For such purposes, macroscale analyses using RS and GIS have been shown to be effective and adopted widely for terrestrial and open ocean ecosystems, but to less extent for coastal ecosystems.

The aims of the present study are (1) to determine large-scale distribution of seagrass beds along eastern Okinawa Island, (2) to examine spatial and temporal changes in seagrass beds by integrating existing data on past distribution by GIS, and (3) to examine effects of terrestrial ecosystems on distribution, abundance and biodiversity of seagrass beds. We analyzed spatial and temporal changes in large-scale distribution of seagrass beds using existing maps and aerial photographs in addition to field census on seagrass distribution and species diversity. We also analyzed spatial and temporal changes in terrestrial ecosystems corresponding to watershed areas behind each seagrass bed using maps of land use and satellites images.

2. Materials & Methods

2.1 Study site

This research was carried out at eastern coast of Okinawa Island where seagrass beds are known as major components of shallow water ecosystems (Fig. 1). Based on existing information on literature (Toma 1999, Yoshida et al. in press), we selected our study areas along the coastline between Cape Teniyazaki (26°34' N; 128°9' E) and Cape Kinn (26°26' N; 127°57' E). Nine subtidal seagrass beds are chosen as main study sites; East Kayo, West Kayo, Abu, Henoko, Toyohara, Matsuda, Ginoza, Kanna, and Kinn.

In this region, eight seagrass species have been known to occur. They are *Zostera japonica*, *Halophila ovalis*, *Thalassia hemprichii*, *Syringodium isoetifolium*, *Cymodocea serrulata*, *Cymodocea rotundata*, *Halodule uninervis* and *Halodule pinifolia* (Toma 1999). All the species except *Z. japonica* occur at subtidal zone of these seagrass beds.

For the investigation of the influence of terrestrial ecosystems, we collected data for the whole watershed area of coastline where nine seagrass beds exist, which corresponded to ca. 70 km^2 area in middle part of Okinawa Island, covering districts of Nago City, Ginoza Town and Kinn Town.

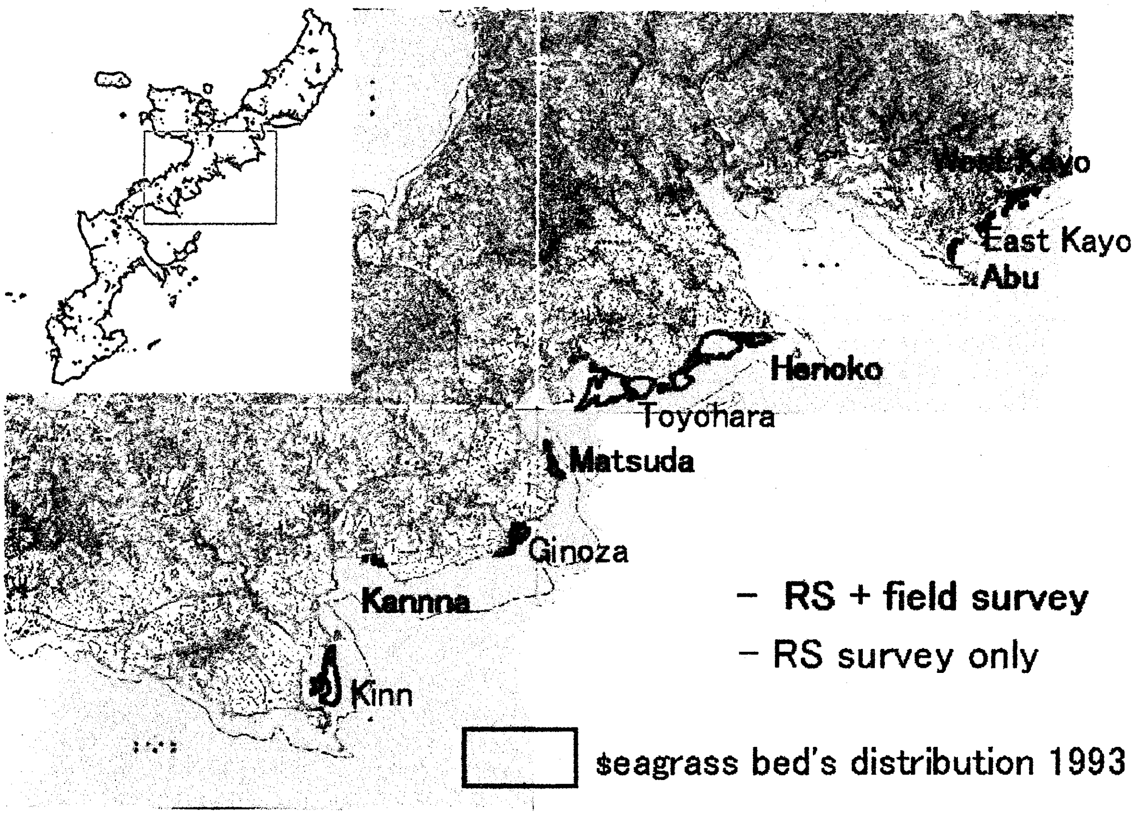

Fig.1. Study site along eastern coast of Okinawa Island. Nine seagrass beds are analyzed using RS among which field survey was carried out at five seagrass beds (East Kayo, Abu, Henoko, Matsuda and Kanna).

2.2 Analyses of seagrass bed distribution

Large-scale spatial distribution of seagrass beds and its temporal change were analyzed using map data and aerial photographs as follows. (1) Color aerial photographs of 1/10,000 magnification taken in 1977, (2) those taken in 1993, (3) Wildlife and Plant Distribution Map of Okinawa Prefecture that was made based on the 2^{nd} National Survey on the Natural Environment (Environment Agency of Japan 1981) in which seagrass distribution was surveyed between 1978 and 1979, and (4) Environmental Sensitivity Index Map issued in 2000 (Ministry of the Environment of Japan 2000). Data on seagrass distribution of the latter two maps were used after digitalization with a scanner. Aerial photographs were first digitalized, and the area of seagrass beds were then discerned and plotted by eye. These data were superimposed on to the same map using GIS. Area of seagrass beds in each dataset was then calculated directly on the map.

2.3 Field survey

Field survey of seagrass beds was carried out in July and September 2003 at five sites: East Kayo (July 2003), Abu, Henoko, Matsuda and Kannna (September 2003). At each site except for Henoko, we established a census plot of 15,000 m^2 in area. Three to five parallel transects were first set perpendicular to shoreline at the interval of 50 m. Along each transect, three to five census points were set at the interval of 50 m. As the result, a grid consisting of 15-25 census points were established at each station (three to five points parallel to the shoreline, times three to five points along the depth gradient). For Henoko, census was undertaken for overall seagrass distribution by setting a grid at the interval of 200 m (See Yoshida et al. in press).

At each point, we randomly placed three to five 0.5 x 0.5 m quadrates haphazardly. Species composition of seagrasses and coverage by each seagrass species were recorded for each quadrat by one observer. Later, biases in coverage estimates among observers were calibrated using the methods in Yoshida et al. (in press). Data on coverage of each seagrass species per quadrat were averaged for each census point.

Diversity of seagrasses in each seagrass bed was represented by two parameters: species richness and Simpson diversity index (See Miyashita & Noda 2003 for detailed information and methods of calculation of these two indices). They were calculated at the two different spatial scales: local diversity (per each census point within a site, based on seagrass occurrence and coverage per 1.25 m^2) and regional diversity (per each seagrass beds by using data of all the census points). For Simpson index, the subtraction from the latter estimates

(D_γ) by the former (D_α) equals turnover diversity (D_β) representing differences in species composition and abundance among census points at each site (Miyashita & Noda 2003).

2.4 Analyses of terrestrial ecosystems

For each of nine watersheds behind each seagrass bed, we collected data on land use and satellite images. For the land use map, we analyzed the fine grid data for 1976, 1987, 1991. Five different satellite images taken at the different periods were collected for the whole watershed areas; i.e., Landsat-1 MSS 1976, Landsat-5 TM 1985, JERS-1 VNIR SWIR 1993, ADEOS Mu Pa 1998, and Landsat-7 ETM 2002. The maps and satellite images are digitalized and analyzed using GIS.

3. Results and Discussion

Nine seagrass beds along the eastern coastline of Okinawa Island varied greatly in size. According to the data from aerial photographs in 1993, the largest bed extend continuously between Henoko and Toyohara, followed by Kinn, Ginoza, Matsuda, West Kayo, East Kayo, Abu and Kanna. Estimated area of each seagrass bed varied greatly among four different sources. Analysis of temporal changes in seagrass distribution cannot be made using data in 1981 and 2000 because of different survey methods in these studies. We thus used two aerial photograph data for examining temporal changes in seagrass bed. Comparison of seagrass bed distribution in 1977 and 1993 revealed different patterns of temporal changes in different seagrass beds. For example, the seagrass bed extended largely toward shoreward in Henoko during 1977 and 1993, whereas the distribution was relatively stable in Kayo.

Seven seagrass species were found in all of the five seagrass beds where the field survey was conducted, except for *C. serrulata* in Abu (Table 1). Thus, regional diversity over entire seagrass bed scale measured by species richness did not differ largely among seagrass beds. However, greater among-site variation in regional diversity was found in Simpson diversity index (D_γ). It was highest at East Kayo, followed by Kanna, Abu, Henoko and Matsuda. For local species diversity at smaller spatial scale (within each census point), average species richness per 1.25 m^2 area was higher in the two northern seagrass beds (East Kayo and Abu) than the three southern seagrass beds (Henoko, Matsuda and Kanna). Local diversity measured by Simpson diversity index (D_α) showed a similar pattern of spatial variation. Turnover diversity (D_β), representing spatial heterogeneity in species composition, was greatest at Kanna and lowest in Abu.

Table 1. List of species and species diversity of seagrasses at five seagrass beds surveyed in summer 2003.

Seagrass bed	Occurrence of each seagrass species							Species richness	Mean species richness per station	Simpson's diversity		
	Ho	*Th*	*Cr*	*Cs*	*Hu*	*Hp*	*Si*		(1.25m^{-2})	D_α	D_β	D_γ
East Kayo	○	○	○	○	○	○	○	7	4.8	0.59	0.20	0.79
Abu	○	○	○	×	○	○	○	6	3.4	0.60	0.02	0.62
Henoko	○	○	○	○	○	○	○	7	2.0	0.36	0.18	0.53
Matsuda	○	○	○	○	○	○	○	7	2.7	0.13	0.36	0.49
Kannna	○	○	○	○	○	○	○	7	2.7	0.23	0.49	0.72

Ho: Halophila ovalis; Th: Thalassia hemprichii; Cr: Cymodocea rotundata; Cs: Cymodocea serrulata
Hu: Halodule uninervis; Hp: Halodule pinifolia; Si: Syringodium isoetifolium

Watershed of three northern seagrass beds (East Kayo, West Kayo and Abu) is smaller in area than that of five southern seagrass beds (Fig. 2). The latter five contain larger areas of forest, agricultural and urban areas than the former three.

Present study revealed that combinational analyses of RS, GIS and ground survey of seagrass beds are effective for understanding large-scale distribution of seagrass beds and its long-term dynamics. Spatial variation in distribution, abundance and species diversity of seagrass beds was found to be large in east coast of Okinawa Island. Most notably, species diversity in northern seagrass beds with smaller watershed area was greater than that in southern beds with larger watershed, suggesting different impact of terrestrial ecosystems. In reality, environmental deterioration due to run-off of massive red soil from rivers has been known to be intense in the southern seagrass beds such as Henoko and Matsuda, which are likely to affect distribution and species composition of seagrasses.

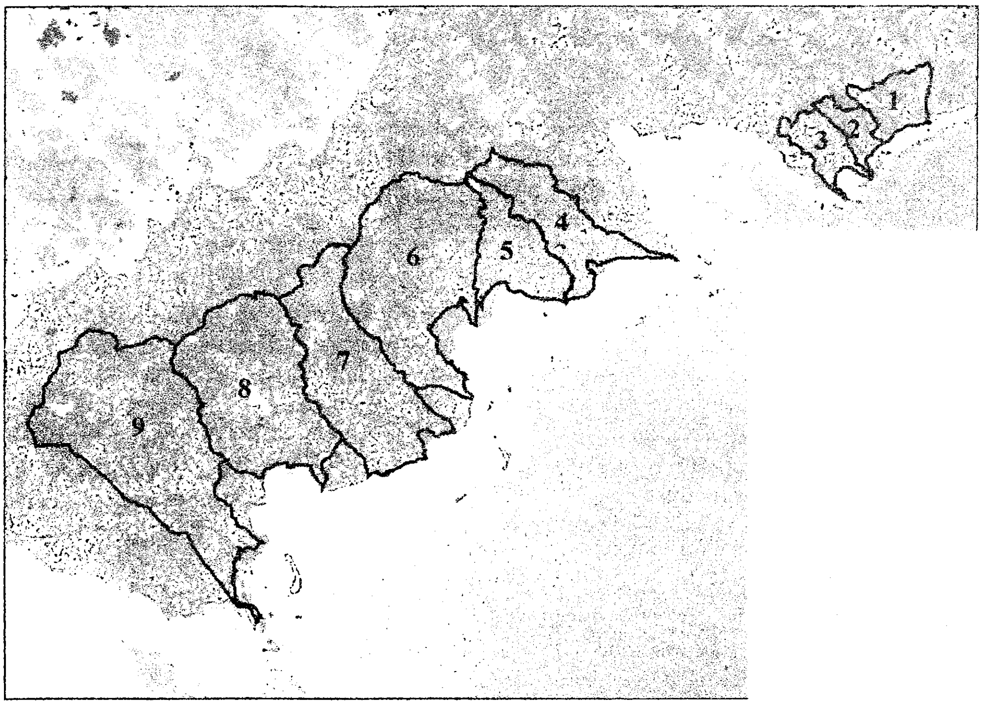

Fig.2. A map showing watershed areas behind nine seagrass beds in the present study. 1: East Kayo, 2: West Kayo, 3: Abu, 4: Henoko, 5: Toyohara, 6: Matsuda, 7: Ginoza, 8: Kanna, 9: Kanna.

In future studies, incorporation of information on coastal environmental processes such as hydrodynamics and water quality changes is necessary for further understanding of the processes and mechanisms how alteration of terrestrial ecosystems affects large-scale and long-term dynamics of seagrass beds locating along the coastal areas of Okinawa Island.

Acknowledgements

We are grateful to NACS-J for kindly permitting us to use their data on seagrass census. We wish to thank M. Yoshida, N. Kouchi for their help in data analyses on seagrass distribution and biodiversity, N. Kouchi, E. Sakamaki and participants of 5th and 6th Jangusa Watch for their help in the field survey, and F. L. Tjandra and other members of Kondoh Lab for instructions on the use of GIS.

References

Environment Agency of Japan (1981) Wildlife and Plant Distribution Map of Okinawa Prefecture. The 2nd National Survey on the Natural Environment. Environment Agency of Japan, Tokyo

Fortes MD (1995) Seagrasses of East Asia: Environmental and Management Perspectives. RGU/EAS Technical Report Series No. 6. United Nations Environmental Programme, Bangkok

Fortes MD (1988) Mangrove and seagrass beds of East Asia: habitats under stress. Ambio 17: 207-213

Hemminga MA and Duarte CM (2000) Seagrass Ecology, Cambridge University Press, Cambridge

Ministry of the Environment of Japan 2000 Environmental Sensitivity Index Map. http://www.env.go.jp/earth/esi/esi_title.html

Miyashita T and Noda T (2003) Community Ecology. Univ. Tokyo Press, Tokyo

Shorts FT and Wyllie-Echeverria S (1996) Natural and human-induced disturbance in seagrass. Environ. Conserv. 23: 17-27

Toma T (1999) Seagrasses from the Ryukyu Islands. I. Species and Distribution. Biol. Mag. Okinawa 37: 75-92

Williams SL and Heck Jr. KL (2001) Seagrass Community Ecology. In: Bertness MD, Gaines SD and Hay ME (eds), Marine Community Ecology, Sinauer, Sunderlandm MA, pp.317-337

Yoshida, M Kouchi, N and Nakaoka M (in press) Citizens' Involvement for Seagrass Watch Survey in Okinawa Island. Japanese Journal of Conservation Ecology

Ocean Primary Productivity

PAR dependent time and depth resolved primary productivity model

Ichio Asanuma
JAMSTEC
Frontier Research Promotion Department, JAMSTEC
3173-25, Showa, Kanazawa, Yokohama 236-0001, JAPAN
asanumai@jamstec.go.jp

ABSTRACT:

A water column distribution of photosynthetically available radiation (PAR) was modeled based on the chlorophyll-a concentration in the surface layer with an empirical equation to support a depth and time resolved primary productivity model. A vertical distribution of PAR exhibited a variation for certain chlorophyll-a concentration, where a variation of diffused attenuation coefficient is expected. An empirical equation was proposed to model an optimum vertical distribution of PAR with chlorophyll-a concentration in the surface layer. This optically optimized PAR dependent depth and time resolved primary productivity model was validated with the in-situ measurements on the Equatorial Pacific, the East China Sea, and the Northwestern Pacific. The result indicated a good correlation between the model estimated primary productivity and the in-situ measurements, where the model showed a significant improvement from the previous one.

1. INTRODUCTION

A contribution of biota to a global warming in a long time scale is a strong interest of human beings as a storage of carbon dioxide. Also, it is expected that biota exhibits its variation of standing stock relative to a climate change. Bengtsson et al. (1999) studied perceived inconsistencies between global temperature observations over the last two decades and results from climate simulations with some hypothesis for the slower global warming. The biosphere may have a certain contribution to the global warming. The terrestrial biosphere has been essentially in balance with implying compensating growth of the biosphere (Houghton et al. (1997)). But oceanic biota has not been studied well. Langenfelds et al.(1999) pointed a variation of oceanic biota to the carbon flux with the atmosphere shows a temporal variability. Christian et al. (1997) estimated the net flux of carbon across particular depth and pointed the biological pump being a sink for atmospheric CO2 in the North Pacific Subtropical Gyre.

Now, we have a continuous observation of ocean color sensors since 1996. A discontinuity of ocean color measurements between the Ocean Color Temperature Scanner (OCTS) (Shimada et al. 1999) and the Sea-Viewing Wide Field-of-View Sensor (SeaWiFS) (McClain et al. 1992) was only two months. Although there are some overlaps of satellite programs, it has a possibility of data sets to study a contribution of phytoplankton to a climatological change for these 10 years. The OCTS and the SeaWiFS provide a similar specification with bands, FWHM, maximum radiance and SNR, which are based on the experience from the Coastal Zone Color Scanner (CZCS). In contrast, the Moderate Resolution Imaging Spectrometer (MODIS) and the Global Imager (GLI) have a narrow band width with 36 bands, to establish multi-purpose missions on ocean, land, atmosphere, and cryosphere.

Primary productivity of the glove estimated from the ocean color measurement by satellite is an approach to discuss a contribution of the oceanic biota to the global warming in a positive or negative contribution. Behrenfeld et al. (1997) and Falkowskie et al. (1998) proposed a light-dependent, depth-resolved model for carbon fixation based on the satellite data. Arrigo et al. (1998) implied a possibility of the primary production model in Southern Ocean waters.

In partly, those models worked in some extent. But less consistency on a primary productivity of the globe was observed. We proposed a photosynthetically available radiation (PAR) dependent time and depth resolved primary productivity model (Asanuma et al. (2000)). A vertical distribution of PAR is defined as an empirical equation of the chlorophyll *a* concentration in the surface, which is observed by an ocean color sensor. A carbon fixation rate is defined as a function of PAR and temperature. Primary productivity over the globe was computed and studied. Through the validation process of our primary productivity model, we realized that our model exhibited over estimates relative to in-situ measurements on the case II and similar waters.

2. PRIMARY PRODUCTIVITY MODEL

2.1 Depth and time resolved primary productivity model

We proposed a time and depth resolved primary productivity model to estimate a primary productivity from a satellite measurement (Asanuma et al. (2001a); Asanuma et al. (2001b)). This model provides vertical estimates of photosynthetically available radiation, chlorophyll *a* concentration, and primary productivity, which were not resolved by single layer models. A concept of our model is given as follows;

$$PPeu=\int_t\int_z C(z)Pb\{z,PAR(z,day),T\}PAR(0,t)/PAR(0,day)\,dz\,dt \quad .....(1)$$

,where $PPeu$ is the primary productivity (mgC.m^{-2}. day^{-1}), Pb is the carbon fixation rate (mgC.mgChl-a^{-1}. m^{-3}.day^{-1}), $PAR(0,t)$ is the photosynthetically available radiation for each hour (Ein.m^{-2}. hour^{-1}), $PAR(z,day)$ is the photosynthetically available radiation for a day (Ein.m^{-2}. day^{-1}) , C is chlorophyll *a* concentration (mg.m^{-3}), T is the water temperature (deg-C), z is the depth in m and t is the time from 0 to 24 hours. We proposed the carbon fixation rate, Pb, as a function of PAR, temperature and depth from the in-situ measurement along the Equator and the middle latitude in the Pacific. The carbon fixation rate is given as follows;

$$Pb(z,PAR(z,day),T)=24\ [1-\exp\{-0.006\ a\ PAR\%(z)\}]\ \exp\{-0.005\ b\ PAR\%(z)\} \quad .....(2)$$

,and

$$a=0.1\ s\ PAR(0,\ day)+i$$

$$s=-0.00012T^3+0.0039T^2-0.0007T+0.2557$$

$$i=0.00023T^3-0.0108T^2+0.0868T-0.1042$$

$$b=0.00048T^3-0.0196T^2+0.1134T+3.1214$$

We empirically defined a vertical distribution of photosynthetically available radiation along the depth in percentage, $PAR\%(z,C_0)$, as a function of chlorophyll *a* concentration in the surface as follows;

$$Log(PAR\%(z,C_0))=(aC_0+b)Z+2 \quad ...(3)$$

,where C_0 is chlorophyll *a* concentration in the surface, which could be replaced by a satellite observation, Z is the depth, and a (-0.025) and b (-0.017) is empirical constants.

A vertical distribution of chlorophyll *a* concentration is proposed by the following function as a function of a vertical distribution of PAR and chlorophyll *a* concentration in the surface.

$$C(z)=[0.1-a\ C_0\ \exp\{-b\ PAR\%(z,C_0)\}]\exp\{-b\ PAR\%(z,C_0)\}+C_0 \quad .....(4)$$

,where a (0.7) and b (0.8) are empirical constants. In contrast, some empirical equations to estimate the vertical distribution of chlorophyll *a* were proposed using the Gausian function. In this study, chlorophyll *a* distribution is expressed empirically based on the vertical distribution of PAR, which determines the light field in the water and phytoplankton accommodates in the light field.

2-2. Photosynthetically available radiation

A determination of the PAR on the surface is another key issue to estimate the primary productivity. Frouin (2000) proposed a research product for the PAR from SeaWiFS measurement. The PAR at the surface for the day is computed with a remote sensing reflectance from SeaWiFS measurement. This method needs raw data of the globe for daily basis and it is difficult to conduct computation at the end user. In this study, a simple code is proposed to compute PAR with combining a model result and a probability function of cloud from satellite observation. ***PAR(t)*** at the sea surface is computed by MODTRAN-4.3 for the ideal atmospheric condition as a function of the time, ***t***, on the day of the year and the latitude. In this computation, the aerosol model is selected to the maritime extinction with 23 km visibility under the model for the mid-latitude summer atmosphere. Then, a probability function of cloud distribution is estimated from the SeaWiFS chlorophyll *a* distribution data set, where missing data is considered as the presence of cloud. Weekly composite data is selected to estimate a cloud probability function. Although there remains a possibility of the sun glint region in the missing data as discussed by Frouin (2000), an assumption was made that a weekly composite may have smaller possibility of the sun glint region than a daily composite. The averaged ***PAR(t)*** for the hour and for one month was computed by MODTRAN-4.3. Then, the PAR is given empirically with a probability function of cloud as follows:

$$PAR(t) = (0.9 - 0.05\, \Sigma Cloud)\, PAR(t) \quad .....(5)$$

,where ***Cloud*** is defined as 1.0 for the missing chlorophyll *a* data from a weekly composite chlorophyll *a* data. This research and GSFC showed a different PAR in higher latitude. Frouin (2000) estimated the PAR on the surface from the PAR on the top of the atmosphere with a transmission through the atmosphere. The maximum difference between two PARs is around 25 % at the higher latitude and the negligible difference in the lower latitude. The probability function of clouds from missing data has a possibility of the difference between two algorithms. Unfortunately, we are missing in-situ measurements of PAR over the higher latitude and it will be an important issue for the in-situ measurements in future.

2-3. Validation of primary productivity model

We computed a monthly primary productivity over the globe based on chlorophyll *a* distribution from the OCTS and the SeaWiFS, and the sea surface temperature distribution from the MCSST data sets generated by JPL from NOAA/AVHRR observation. The results of the primary productivity are verified with the in-situ measurements along the equatorial Pacific, the northwestern Pacific, and the East China Sea. In-situ measurements of the primary productivity were obtained by the in-situ and the on-deck simulated in-situ incubation using ^{13}C solvent as the tracer. The incubation hours were set to 12 hours or 24 hours for the measurements. Figure 1 shows a scatter diagram between the primary productivity estimated by our model and in-situ measurements. Data along the equatorial Pacific and the Northwestern Pacific indicated a good agreement. Some data on the East China Sea indicated over estimates for in-situ measurements over 500 $mgC.m^{-2}.day^{-1}$. This over estimate suggests (i) a possibility of measurements over the different water mass between the model and in-situ data, where satellite data is spatially and temporally averaged for 9 km and one month each, (ii) a possibility of over estimates of primary productivity depending on the PAR vertical distribution, and (iii) a possibility of over estimates of carbon fixation rate depending on the PAR at the depth.

3. OPTICALLY OPTIMIZED PAR

3-1. Diffused attenuation coefficient and PAR

Fig.1 suggested the over estimate on the turbid waters or on the case II waters. Our estimate of vertical distribution of PAR is based on chlorophyll *a* concentration in the surface by the equation (3). In contrast, a general light attenuation through the water column is expressed by the following equation;

$$PAR(z) = PAR(0) \exp(-Kd\, z) \quad .....(6)$$

,where ***Kd*** is the down-welling diffused attenuation coefficient (m^{-1}), which depends on the wavelength, and 490 nm is used practically to indicate the property of the water.

Figure 2 shows vertical distributions of PAR estimated by our current model using the equation (3) and estimated by the equation (6). Vertical distributions of PAR for three typical sets of chlorophyll *a* concentration are plotted for the equation (3), including 0.05 (◆), 0.5 (▲) and 5.0 (■) $mg.m^{-3}$ with three block lines. For these three sets of chlorophyll *a* concentration, two sets of diffused attenuation coefficient for 490 nm are selected for each chlorophyll *a* concentration from the SeaWiFS monthly product over the East China Sea and the western Pacific Ocean in July of 2001. ***Kd***(490)s for chlorophyll *a* concentration of 0.05 $mg.m^{-3}$ are 0.028 and 0.033 (◇) m^{-1}, 0.5 $mg.m^{-3}$ are 0.065 and 0.085 (△) m^{-1}, and 5.0 $mg.m^{-3}$ are 0.2 and 0.35 (□) m^{-1}. The vertical distributions of PAR for these ***Kd***(490) are plotted by dotted lines. The vertical distribution of PAR for chlorophyll *a* concentration of 0.05 $mg.m^{-3}$ is between the vertical distributions of PAR for ***Kd***(490) of 0.028 and 0.033 m^{-1}. The vertical distribution of PAR for chlorophyll *a* concentration of 0.5 $mg.m^{-3}$ is deeper than that of PAR for ***Kd***(490) of 0.065 and 0.085 m^{-1}. The vertical distribution of PAR for chlorophyll *a* concentration of 5 $mg.m^{-3}$ is shallower than that of PAR for ***Kd***(490) of 0.2 and 0.35 m^{-1}. The difference of the vertical distribution of PAR for chlorophyll *a* (5 $mg.m^{-3}$) and ***Kd*** (0.2 and 0.35 m^{-1}) indicates that our model estimates the light field doesn't penetrate the water column, where more photosynthesis is expected in the deep layer of the surface water. The difference of PAR for chlorophyll *a* (0.5 $mg.m^{-3}$) and ***Kd*** (0.065 and 0.085 m^{-1}) indicates that our model estimates the light field penetrates more than expected by ***Kd***(490), where less photosynthesis is expected along the water column.

Currently, chlorophyll *a* concentration and diffuse attenuation coefficient are studied independently, and the empirical equations from two parameters are proposed independently. O'Reilly et al. (2000) proposed 4 bands ratio for three range of chlorophyll *a* concentration and applied to SeaWiFS products, where ratio of 510 to 555 nm, 490 to 555 nm, and 443 to 555 nm are used from low to high chlorophyll *a* concentration, but there remains uncertainty of the algorithm for a high chlorophyll *a* concentration. Mueller (2000) proposed 2 bands ratio of 490 to 555 nm to estimate a diffused attenuation coefficient, and also reported the uncertainty of the algorithm of diffused attenuation coefficient bigger than $0.25m^{-1}$. Chlorophyll *a* concentration and diffused attenuation coefficient are used to be independent parameters especially on the turbid water, where the difficulty of algorithm remains.

3-2. Variation of diffused attenuation coefficient

Figure 3 indicates a distribution of observation points as a function of chlorophyll *a* concentration and diffused attenuation coefficient for a monthly composite data of SeaWiFS in July 2001. Figure 3 shows a diffused attenuation coefficient exhibits a wide variation at a certain and higher chlorophyll *a* concentration. Figure 3 shows that optical properties of the water may not be given as a single function of diffused attenuation coefficient neither chlorophyll *a* concentration, especially on the case II water, which is a group of water with higher chlorophyll *a* and suspended matters.

We have tried to express the relationship between chlorophyll *a* concentration and diffused attenuation coefficient by a regression line. The equation (7) shows the regression line of the diffused attenuation coefficient as a function of chlorophyll *a* concentration.

$$Kd \;=\; -\exp(0.052\,C_0 - 0.06) + 1.1 \quad ..... (7),$$

where ***Chl*** is chlorophyll *a* concentration given from the ocean color measurements. The regression line is plotted on Figure 3 with a block line and hatched triangles. Then a deviation of the diffused attenuation coefficient from the regression line (⊿***Kd***) is computed by the next equation.

$$\varDelta Kd = Kd \;\; - \exp(0.052\,C_0 - 0.06) + 1.1 \quad ..... (8),$$

where, ***Kd*** is the diffused attenuation coefficient, given from the satellite observation. This deviation of the diffused attenuation coefficient (⊿***Kd***) will be estimated from chlorophyll *a* measurement.

3-3. Optimization of PAR

In this step, we modify the vertical distribution of PAR given by the equation (3) to satisfy the PAR vertical distributions estimated from chlorophyll *a* concentration to be between the vertical distributions of PAR estimated by ranges of diffused attenuation coefficients. The next empirical equation determines PAR distribution as a function of chlorophyll *a* concentration.

$$Log(PAR\%(z,C_0))=(-0.0018\ C_0^3 + 0.022\ C_0^2 - 0.11\ C_0 - 0.024)Z +2 \ldots\ldots (9).$$

Figure 4 shows the modified vertical distributions of PAR as a function of chlorophyll *a* concentration in the surface being located just between the vertical distributions of PAR estimated from diffused attenuation coefficient corresponding to each chlorophyll *a* concentration.

Vertical distributions of PAR estimated from chlorophyll *a* concentration in Figure 2 are drastically improved at high chlorophyll *a* concentration and high diffused attenuation coefficient. But Equation (9) is not sufficient to explain a variation of diffused attenuation coefficient at given chlorophyll *a* concentration.

Here, we combine two Equations (8) and (9) to explain a variation of vertical distribution of PAR as function of chlorophyll *a* concentration and diffused attenuation coefficient.

$$PAR(z) = PAR(0)\ exp\ \{ (- 0.0018\ C_0^3 + 0.022\ C_0^2 - 0.11\ C_0 - 0.024 + \Delta Kd)\ Z \} \ldots\ldots (10)$$

The PAR at the depth Z m, ***PAR(Z)***, is estimated from the PAR at the surface, ***PAR(0)*** with chlorophyll *a* concentration and diffused attenuation coefficient at the surface.

3-4. Model run with an optically optimized PAR

We conducted a model run with the optically optimized PAR dependent depth and time resolved primary productivity model. Equation (3) was replaced with Equation (10) to explain a various light fields as a function of chlorophyll *a* concentration and diffused attenuation coefficient. Following to this replacement, it is possible to have a significant change in the carbon fixation rate (Equation (2)) and a vertical distribution of chlorophyll a concentration (Equation (4)).

We grouped in-situ primary productivity data into an equatorial Pacific, a sub-tropic region including the East China Sea and the Kuroshio water off Kyushu Island to Choshi peninsula, and a sub-arctic region including a mixing region among the Kuroshio originated warm cores and the Oyashio water, as we could obtain more in-situ observations since the previous model run.

Figure 5 shows the result of comparison between the new model and in-situ data. The correlation coefficient for the revised model was 0.77, where the correlation coefficient of the previous model was 0.31. The revised model indicates a significant improvement in the correlation between model and in-situ primary productivity.

4. SUMMARY

We have proposed the time and depth resolved primary productivity model using chlorophyll *a* concentration and sea surface temperature. Through the validation process of our model based on the in-situ measurements on the equatorial Pacific, the northwestern Pacific, and the East China Sea, our model exhibited an over estimation in some waters. It was suggested that the optical properties in the water is the major reason for the over estimate.

We studied the optical property of the water around Japan as a function of chlorophyll *a* concentration and diffused attenuation coefficient based on SeaWiFS data. The water with a higher chlorophyll *a* concentration exhibited a wide range diffused attenuation coefficient for a certain chlorophyll *a* concentration. This variation suggested the error in estimating a vertical distribution of PAR and chlorophyll *a* concentration as a function of chlorophyll *a* concentration in the surface water. Figure 2 shows deviations of the vertical distribution of PAR from the optical field estimated from diffused attenuation coefficient. Our previous empirical equation for the vertical distribution of PAR is modified to fit the variation of diffused attenuation coefficient at given chlorophyll *a* concentration as indicated by Equation (9). Then, the variation of diffused attenuation coefficient at certain chlorophyll *a* concentration is estimated as the difference of satellite observed diffused attenuation coefficient and the empirical equation, which represents the diffused attenuation coefficient for given chlorophyll *a* concentration (Equation (10)). By combining the modified empirical equation for PAR with chlorophyll *a* concentration and the

variation of diffused attenuation coefficient, it is realized to express the vertical distribution of PAR.

As a result, the optically optimized PAR dependent depth and time resolved primary productivity indicated a good correlation between the model estimates and in-situ primary productivity measurements.

REFERENCES

Arrigo,K.R., D.Worthen, A.Schnell and M.P.Lizotte, 1998. Primary production in Southern Ocean waters. J. Geophys. Res., 103, C8, 15587-15600.

Asanuma, I., T. Tanaka, K. Matsumoto, T. Kawano, 2000: Primary productivity model based on photosynthetically available radiation. Hyperspectral Remote Sensing of the Ocean, Proc. of SPIE, V4154, 153-158.

Asanuma, I., K. Matsumoto, T. Kawano, H. Kawahata, 2001a: Satellite estimated primary productivity and carbon flux. Sixth International Carbon Dioxide Conference, 505-508.

Asanuma, I., K. Matsumoto, T. Kawano, 2001b: Validation of photosynthetically available radiation estimated from satellite data for primary productivity model. Proc. Of the CEReS Interna. Symp. on Remote Sensing of the Atmosphere and Validation of Satellite Data, 62-67.

Behrenfeld, M. and P. G. Falkowski, 1997. Photosynthetic rates derived from satellite-based chlorophyll concentration, Limnol. Oceanogr., 42(1), 1-20.

Bengtsson,L., E.Roeckner, and M.Stendel, 1999. Why is the global warming proceeding much slower than expected? J. Geophys. Res., 104, D4, 3865-3876.

Christian J.R., M.R.Lewis, and D.M.Karl, 1997. Vertical fluxes of carbon, nitrogen, and phosphorus in the North Pacific Subtropical Gyre near Hawaii. J. Geophys. Res., 102, C7, 15667-15677.

Falkowski,P.G, and M.J.Behrenfeld, W.Balch, J.W.Campbell, R.L.Iverson, D.A.Kiefer, A.Morel, and J.A.Yoder, 1998. Satellite Primary Productivity Data and Algorithm Development: A Science Plan for Mission to Planet Earth, SeaWiFS Technical Report Series, Vol.42, 37pp.

Frouin, R., 2000: http://orca.gsfc.nasa.gov/seawifs/ par/ doc/seawifs_par_wfigs.pdf.

Houghton,R.A., E.A. Davidson and G.M.Woodwell, 1997. Missing sinks, feedbacks and understanding the role of terrestrial ecosystems in the global carbon balance. Global. Biogeochem. Cycles, 12, 25-34.

Langenfelds,R.L., R.J.Francey and L.P.Steel, M.Battle, R.F.Keeling, and W.F.Budd, 1999. Partitioning of the global fossil CO2 sink using a 19-year trend in atmospheric O2. Geophys. Res. Lett., 26, 13, 1897-1900.

McClain, C., W. E. Esaias, W. Barnes, B. Guenther, D. Endres, S. B. Hooker, B. G. Mitchell and R. Barnes, 1992. SeaWiFS Calibration and Validation Plan, NASA Technical Memorandum 104566, 3, 43pp.

Morel,A., 1991: Light and marine photosynthesis: a spectral model with geochemical and climatological implications. Prog. Oceanog., 26, 263-306.

Muller, J. L., 2000: SeaWiFS Algorithm for the Diffuse Attenuation Coefficient, K(490), Using Water-Leaving Radiances at 490 and 555 nm. Vol.11 SeaWiFS Postlaunch Calibration and Validation Analyses, Part 3, 24-27.

Platt,T., S.Sathyendranath, C.M.Caverhill and M.R.Lewis, 1988: Ocean primary production and available light: further algorithms for remote sensing. Deep-Sea Res., 35, 855-879.

Simada, M., H. Oaku, Y. Mitomi, H.Murakami, and H.Kawamura, 1999. Calibration of the Ocean Color and Temperature Scanner. IEEE Trans. Geoscience and Remote Sensing, 37, 3, 1484-1495.

This study is supported by the special coordination fund of the Ministry of Education, Culture, Sports, Science and Technology, Global Carbon Mapping (GCMAP) from 1998 to 2002.

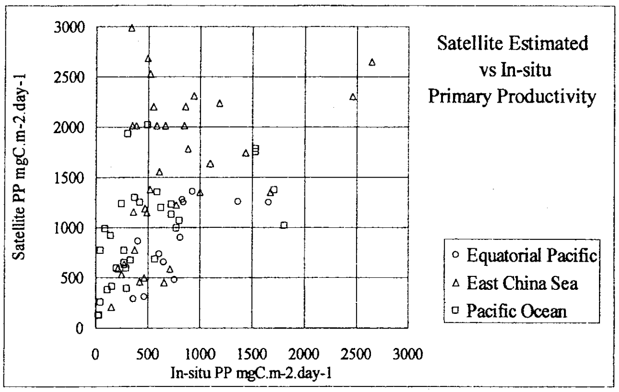

Figure 1. Primary productivity estimated by our model and in-situ primary productivity.

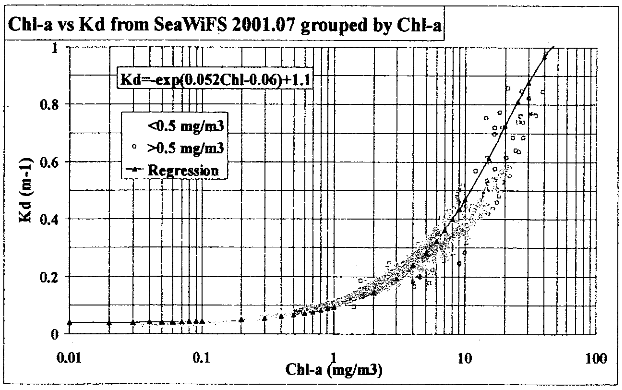

Figure 3. Distribution of water masses as a function of chlorophyll *a* concentration and diffused attenuation coefficient at 490 nm in July 2001, observed by SeaWiFS.

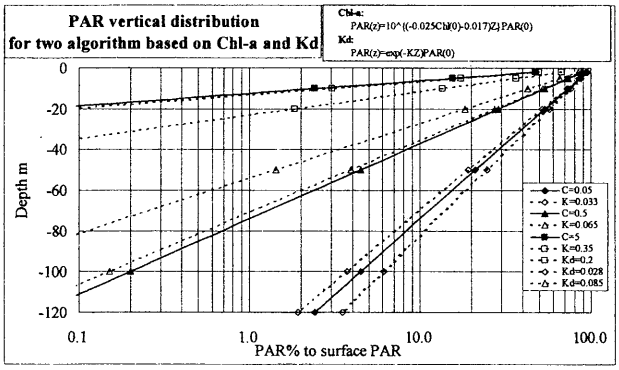

Figure 2. Vertical distributions of PAR for two algorithms based on chlorophyll *a* concentration (equation (3)) and diffused attenuation coefficient at 490 nm (eqution (6)).

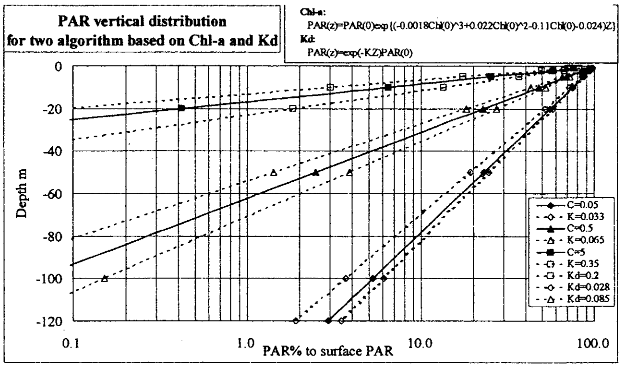

Figure 4. Vertical distributions of PAR for two algorithms based on chlorophyll *a* concentration (Equation (9)) and diffused attenuation coefficient at 490 nm (Equation (6))

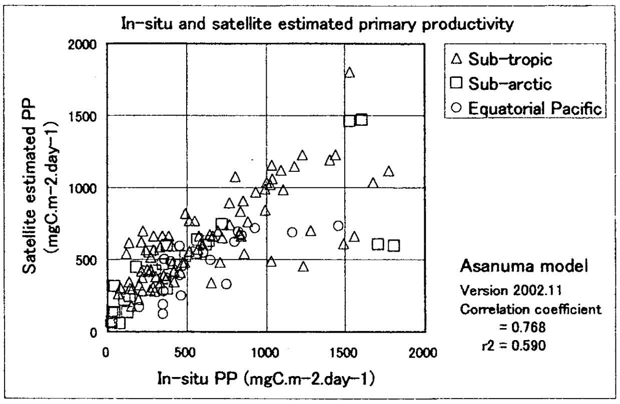

Figure 5. Primary productivity estimated by the optically optimized PAR dependent depth and time resolved primary productivity and in-situ primary productivity measurements.

Cross-validation of ocean color and sea surface spectral reflectance in the western equatorial Pacific Ocean

Katsutoshi Kozai
Kobe University, Faculty of Maritime Sciences
kouzai@maritime.kobe-u.ac.jp

Abstract

Cross-validation of ocean color represented as a chlorophyll-a concentration and sea surface spectral reflectance in the western equatorial Pacific Ocean is carried out not only to validate the model-derived chlorophyll-a concentration and surface reflectance estimates but also to propose an accuracy assessment method in terms of hyperspectral and operational context based on in situ sea surface spectral reflectance measurements onboard R/V Mirai and the optical water type classification model. The results of cross-validation indicate that model-derived estimates of chlorophyll-a and spectral reflectance are agreed well with in situ observed values. And the method proposed here can be utilized not only to validate the hyperspectal satellite-derived products but also to investigate the sensitivity of the satellite-derived products.

1. Introduction

Since Jerov proposed optical water types based on the spectral trasmittance of sea water in1976 (Jerlov, 1976), the classification of optical water type such as case 1(chloropyll-a dominated) and case 2 (suspended sediment dominated) water has been common among oceanographers and remote sensing scientists more than a decade. However the optically complex water type such as the water including colored dissolved organic matter (CDOM) has been found in coastal waters recently, the classification of optical water type needs to be further refined in terms of hyperspectral context. The purpose of the study is to propose an accuracy assessment method in terms of hyperspectral context based on the in situ sea surface spectral reflectance measurements onboard R/V Mirai and the optical water type classification model (Morel, 1988, Morel and Prieur, 1977) in the western equatorial Pacific Ocean.

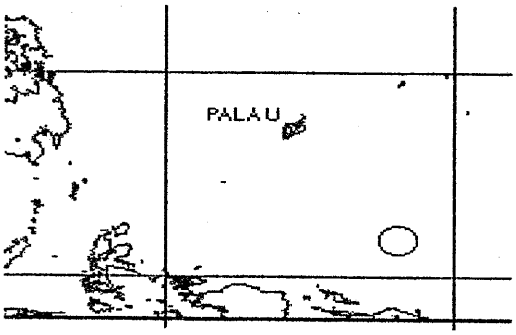

Fig.1 Study area with the stationary observation at 2N, 138E from Nov.22 to Dec.12,2002. (Circle represents the stationary observation area.)

2. In situ sea surface reflectance and chlorophyll-a concentration onboard R/V Mirai

Fig.1 shows the study area in the western equatorial Pacific Ocean. A circle indicates the stationary observation point of R/V Mirai at 2N, 138E during the MR02-K06Leg1 cruise from Nov.22 to Dec.12, 2002. During this period the ship was moving around the stationary point except the CTD (Conductivity-Temperature-Depth) profiler observations four times a day. Method of in situ observations include the measurement of sea surface spectral reflectance using the spectral radiometer GER1500, chlorophyll-a measurement and the other various meteorological and oceanographic parameters. Near-surface water at the depth of 4.5m is continuously pumped up at the rate of 200 litter per minute from the intake to the sea surface-monitoring laboratory (EPCS) for measuring fluorescence intensity.

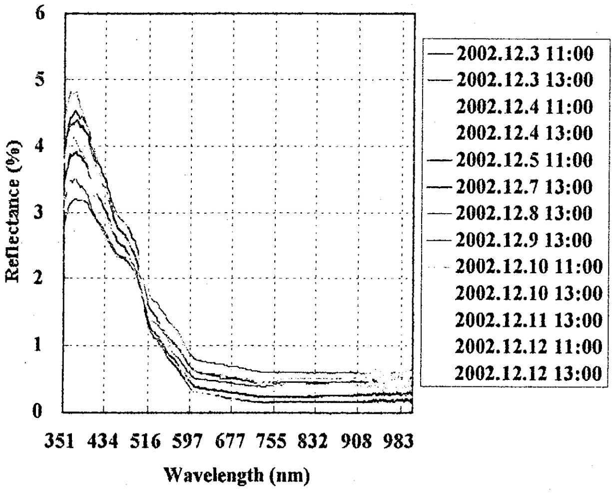

Fig.2 Spectral reflectance curves acquired from Dec. 3 to 12, 2002.

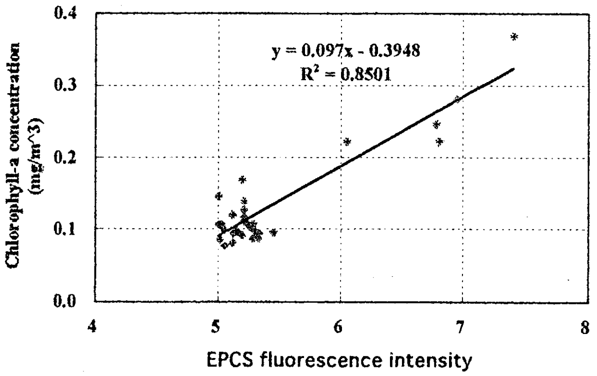

Fig.3 Relationship between EPCS fluorescence intensity and chlorophyll-a concentration.

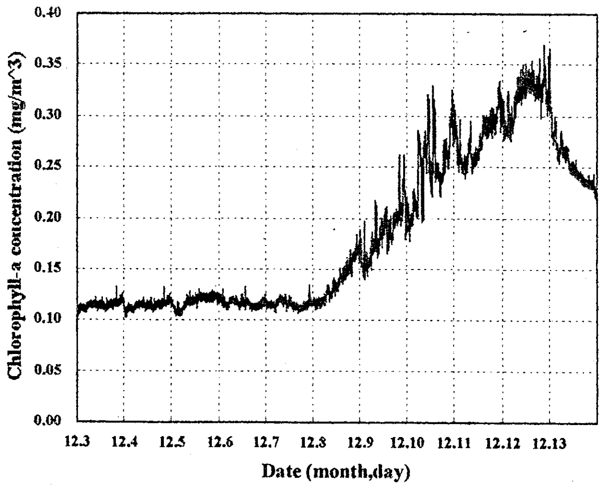

Fig.4 Variation of chlorophyll-a concentration based on EPCS fluorescence intensity.

Fig.2 shows the spectral reflectance curves of sea surface from Dec.3 to 12, 2002 observed by the spectral radiometer GER1500. The spectral reflectance reaches its maximum of 3.2 to 4.8 % at the wavelength of 370nm and its minimum at the one longer than 700nm. Since the electromagnetic energy in the near infrared wavelength region is absorbed at the sea surface, the high reflectance especially in the near infrared wavelength may be attributable to glittering or the reflectance from the breaking waves.

Fig.3 indicates the relationship between EPCS fluorescence intensity and chlorophyll-a concentration. Both parameters are positively correlated and show high squared-correlation coefficient. Based on this correlation continuous fluorescence intensity is converted to chlorophyll-a concentration described in Fig.4. During the first half of the cruise chlorophyll-a concentration is around 0.12 mg/m^3. After Dec.8 the concentration increases to the maximum of 0.36 mg/m^3 and decreases afterwards. Based on the SeaWiFS-derived chlorophyll-a products processed onboard R/V Mirai the increase of the concentration is caused by the high chlorophyll-a band associated with typhoon winds (Kozai and Miyake, 2003).

3. Method and Results

3.1 Estimation of sea surface reflectance based on the optical water type model and its validation

According to Morel (1988) the reflectance emerging from sea water is defined as the reflectance as observed just above the sea surface. This reflectance can be related to the reflectance Rw which is the ratio of the upwelling to downwelling radiance just below the sea surface as decribed below.

$$\rho_{sw}(\lambda) = \frac{Rw(\lambda) * t_d * t_u}{n^2 * (1 - 0.485 * Rw(\lambda))} \qquad (1)$$

where Rw(λ) is the ratio of the upwelling to downwelling radiance just below the sea surface, t_d, t_u is the transmittance for downwelling and upwelling radiance respectively, and n is the index of refraction. Since the ratio Rw(λ) is dependent on the inherent optical properties of the sea water, such as the total absorption coefficient and the total backscattering coefficient, More and Prieur (1977) proposed the following approximation.

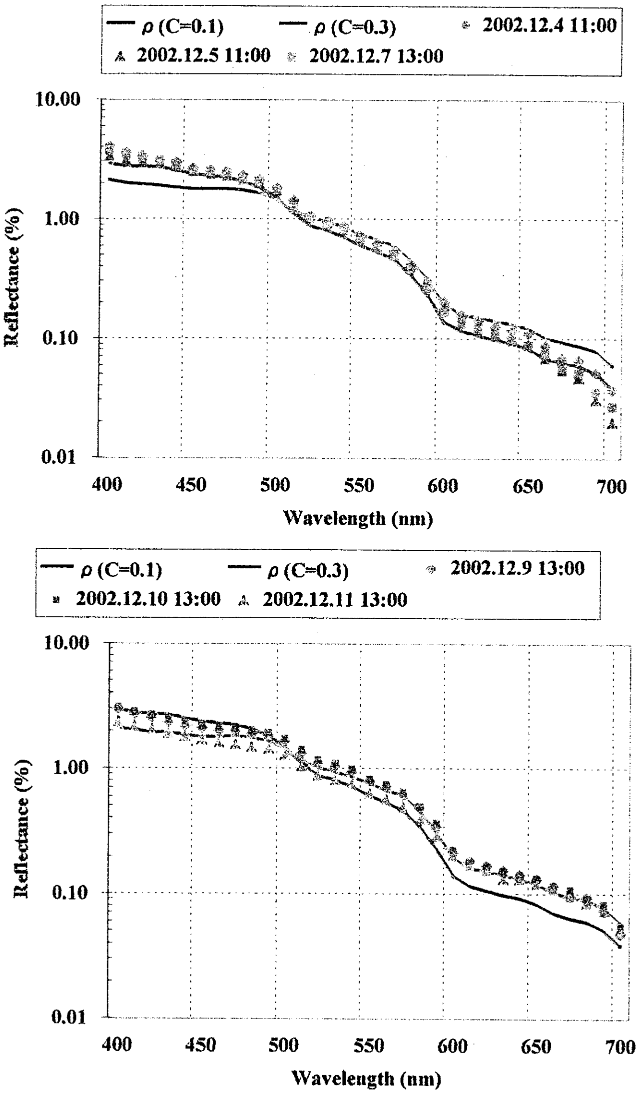

Fig.5 Comparison of sea surface spectral reflectances between the observed (dotted lines) and the estimated (solid lines) for three observations before (upper figure) and after (lower figure) Dec.8, 2002.

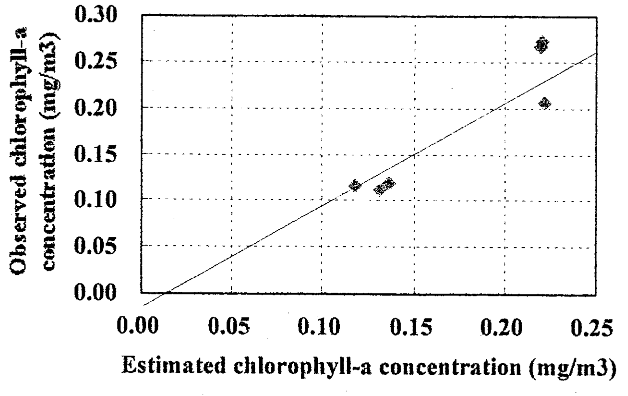

Fig.6 Comparison of chlorophyll-a concentration between the observed and the estimated.

$Rw(\lambda)=0.33*b_b(\lambda)/a(\lambda)$ (2)

where $b_b(\lambda)$ is the total backscattering coefficient and $a(\lambda)$ is the total absorption coefficient respectively. These parameters are also the functions of pigment concentration and diffuse attenuation coefficients. For the detailed relationship of the parameters please refer to Morel and Priur (1977) and Morel (1988). Based on the equations above sea surface spectral reflectances are estimated for validating the observed sea surface spectral reflectances acquired by the spectral radiometer GER1500. Fig.5 shows the comparison of sea surface spectral reflectances between the observed (dotted lines) and the estimated (solid lines) for three observations before (upper figure) and after (lower figure) Dec.8, 2002. Though the differences of chlorophyll-a concentration during both periods are very small, the estimated and the observed reflectances are corresponding well each other in terms of wavelength.

3.2 Estimation of chlorophyll-a concentration based on the SeaWiFS chlorophyll-a algorithm (OC4v4) and its validation

An algorithm of chlorophyll-a concentration estimation from SeaWiFS is used for validating the chlorophyll-a concentration acquired onboard R/V Mirai. The algorithm is called the Ocean chlorophyll 4-band algorithms version 4 (OC4v4) and it is defined as the fouth order polynomial equation as follows (O'Reilly et al., 1998, 2000)

$C=10.0\hat{}(0.366-3.067R_{4S}+1.930R^2{}_{4S}+0.649R^3{}_{4S}-1.532R^4{}_{4S})$ (3)

$R_{4S}=\log_{10}(R^{443}{}_{555}>R^{490}{}_{555}>{}^{510}{}_{555})$ (4)

where C is the estimated chlorophyll-a concentration (mg/m^3) using the OC4v4 algorithms. R_{4S} represents that the ratio of 4 bands of SeaWiFS is utilized and the argument of the logarithm is a shorthand representation for the maximum of the three ratios. Upper and lower subscripts of R stand for the wavelength bands of SeaWiFS. Based on the algorithm above estimated chlorophyll-a concentrations are validated for the observed chlorophyll-a concentrations. Fig.6 indicates the result of comparison between the estimated and the observed chlorophyll-a concentrations. These parameters are agreed well each other except some higher concentration values.

4. Summary

Based on the results and discussion above the study is summarized as follows.

(1) Cross-validation between ocean color represented as a chlorophyll-a concentration and sea surface spectral reflectance in the western equatorial Pacific Ocean is carried out not only to validate the model-derived chlorophyll-a concentration and surface reflectance estimates but also to propose an accuracy assessment method in terms of hyperspectral and operational context based on in situ sea surface spectral reflectance measurements onboard R/V Mirai and the optical water type classification model.

(2) The results of cross-validation indicate that the estimated and the observed reflectances are corresponding well each other in terms of wavelength. On the other hand the result of comparison between the estimated and the observed chlorophyll-a concentrations are agreed well each other except some higher concentration values.

(3) The method proposed here can be utilized not only to validate the hyperspectal satellite-derived products but also to investigate the sensitivity of the satellite-derived products.

Acknowledgements

The author acknowledges the captain and the crews of R/V Mirai for the support of the research during the MR02-K06Leg1 cruise in the western equatorial Pacific Ocean from Nov.13 to Dec.16, 2002. The author also acknowledges Dr.Asanuma of JAMSTEC and the personnels of GODI for assisting the reception of SeaWiFS data onboard R/V Mirai. The support of the study is partially provided through the cooperative research with the Center for Environmental Remote Sensing (CEReS), Chiba University.

References

Jerlov, N.G. (1976): MARINE OPTICS, Elsevier Scientific Publishing Company, 231p.

Kozai, K. and J. Miyake (2003): Verification of SeaWiFS product and in situ spectral reflectance observation of sea surface in the western equatorial Pacific Ocean –R/V MIRAI Research Cruise (MR02-K06Leg1)-, Proceedings of 34th Remote Sensing Society of Japan Annual meeting, pp.65-66.

Morel, A. (1988): Optical Modeling of the Upper Ocean in Relation to its Biogenous Matter Content (Case 1 waters), J. Geophys. Res., 93-C9, 10749-10768.

Morel, A. and L. Prieur. (1977): Analysis of variations in ocean color, Limnol. Oceanogr., 22, 709-722, 1977.

O'Reilly et al. (2000): Ocean Color Chlorophyll-a Algorithms for SeaWiFS, OC2 and OC4: Version 4, NASA Technical Memorandum 2000-206892, Vol.11, SeaWiFS Postlaunch Calibration and Validation Analysis, Part3, pp.9-23.

O'Reilly, J.E., S. Maritorena, B.G. Mitchell, D.A. Siegel, K.L. Carder, S.A. Garver, M.Kahru and C. McClain (1998): Ocean color chlorophyll algorithms for SeaWiFS, J. Geophys. Res., Vol.103, No.C11, pp.24937-24953.

Seasonal variation in primary production in the region off eastern Hokkaido, Japan

Hiromi KASAI
Hokkaido National Fisheries Research Institute, Fisheries Research Agency
E-mail: kasaih@fra.affrc.go.jp

1. Introduction

Hokkaido National Fisheries Research Institute, Fisheries Research Agency (HNFRI/FRA), has two oceanographic observation lines, the "A-line" in the Oyashio region, western subarctic Pacific, and the "N-line" in the southern Okhotsk Sea (Figure 1). The "A-line" observation was carried out since 1988. This line crosses the Oyashio current rectangularly, and also lays on the coastal Oyashio water and Mixed water. Through the observations along the A-line over 10 years, it is found that the large-scale phytoplankton bloom in the Oyashio region occurred in spring, April and May (Saito *et al.*, 1998; Kasai *et al.*, 2001). The spring blooming is consisted of chain-forming diatoms, and is supported by high nutrient supply from deep layer by vertical mixing of water column during winter (Kasai *et al.*, 1997). The southern Okhotsk Sea to which the "N-line" belongs is covered by sea ice during winter, generally the period between January and April. Phytoplankton blooming in spring is observed in the southern Okhotsk Sea accompanying disappearance of sea ice, suggesting ice-edge blooming. In 2000, HNFRI/FRA started oceanographic observation along the N-line in the non-ice season in order to examine seasonal variability in physical, chemical and biological oceanographic conditions. As part of biological observations, seasonality of primary production in the A-line and the N-line was examined.

2. Measurement of primary production

Primary productivity in unit volume in the sea (ranged in 0.1-10 mgC m^{-3} day^{-1}) is relatively lower than that in the terrestrials, due to low standing stock (ranged in 0.01-100mg m^{-3} as chlorophyll *a*). High sensitivity methods for carbon assimilation are needed to measure primary production in the sea, however, use of radioisotope for tracer is severely restricted in fieldwork in Japan. Instead of radioactive carbon, ^{14}C, many scientists in Japan use a stable isotope of carbon, ^{13}C, as a tracer for carbon assimilation by primary production.

In order to estimate primary production of entire water column, primary production is needed to measure vertically. Usually photosynthesis by phytoplankton in subarctic waters is done from the sea surface to the depth which reaches 1 % light at the sea surface. The layer which primary production is made is called euphotic layer. ^{13}C-labelled sodium bicarbonate ($NaH^{13}CO_3$) is used as tracer. After addition of tracer to seawater samples containing phytoplankton, samples is incubated under the conditions which are simulated to the depth collected samples. There are two methods to simulate environmental conditions such as light and temperature during incubation (Figure 2): 1) the *in situ* method; after addition of tracer, water samples are returned to the depth which the samples are collected. Using this method, conditions in temperature and light can be simulated qualitatively and quantitatively, however, this method is not adequate to the oceanographic surveys which the time for observations is limited because research vessel need to stand by near the mooring system set up for incubation. On the other hand, 2) the simulated *in situ* method is a simpler and easier method than the *in situ* method. When the simulated in situ method is used, incubation is conducted on the deck of the vessel, and temperature and light intensity during incubation is controlled artificially to those at the depth sampled. Shading filters are used for simulation of light intensity in the simulated in situ method. Neutral density filter is used as shading filter for the samples from shallow layers, shades in same proportion over the wavelength of visible light. In the deep layer of the euphotic zone, underwater light become bluish due to selective absorption of red light, use of blue acryl resin as a shading filter for the samples from deep layer is recommended. As termination of incubation, particulate (containing phytoplankton) in the water sample is collected onto glassfiber filter, and primary production is determined using the increase of ^{13}C:^{12}C ratio during incubation.

3. Seasonal variation of primary production

Temperature at the sea surface is minimum in March, and nutrient concentration at the sea surface is maximum in March (Figure 3), showing supply of nutrients from deep layer by winter mixing of water column. Nutrient concentration decreases since April, and chlorophyll *a* concentration (index of standing stock of phytoplankton) at the sea surface increased remarkably in April, showing spring phytoplankton blooming. Seasonal variation of daily primary production resembles to that of standing stock of chlorophyll *a* (Figure 4). Daily primary production increases since April, and decreases after May. During summer primary production is kept at low level. In autumn primary production shows small-scale increase accompanied with autumn blooming.

Through the observations in the N-line since 2000, seasonal variation of oceanographic conditions in the southern Okhotsk Sea is examined approximately during the non-ice season. Except one coastal station, a pycnocline at 20 m depth is always present, and gradient of the pycnocline increases from April to October (Figure 5). Constant presence of pycnocline within the euphotic zone controls vertical profile of chlorophyll *a*. After phytoplankton blooming in April, subsurface maximum of chlorophyll a is observed at the 20 m depth (Figure 6). Because of few observations about primary production in the N-line, seasonal variation of the primary production in the N-line can not showed clearly in this study. However, vertical profiles of primary production is controlled by vertical profiles of chlorophyll a and temperature, as well as previous study in the Oyashio region (Kasai *et al.*, 1998), it is suggested that seasonal variation of primary production in the southern Okhotsk Sea is estimated using ocean color remote sensing.

References

Kasai, H., H. Saito, A. Yoshimori and S. Taguchi (1997): Variability in timing and magnitude of spring bloom in the Oyashio region, the western subarctic Pacific off Hokkaido, Japan. *Fish. Oceanogr.*, **6**, 118-129.

Saito, H., H. Kasai, M. Kashiwai, Y. Kawasaki, T. Kono, S. Taguchi and A. Tsuda (1998): General description of seasonal varidations in nutrients, chlorophyll a, and netplankton biomass along the A-line transect, western subarctic Pacific, from 1990 to 1994. *Bull. Hokkaido Natl. Fish. Res. Inst.*, **62**, 1-62.

Kasai, H., H. Saito, M. Kashiwai, T. Taneda, A. Kusaka, Y. Kawasaki, T. Kono, S. Taguchi and A. Tsuda (2001): Seasonal and interannual variations in nutrients and plankton in the Oyashio region: A summary of a 10-years observation along the A-line. Bull. Hokkaido Natl. Fish. Res. Inst., **65**, 55-134.

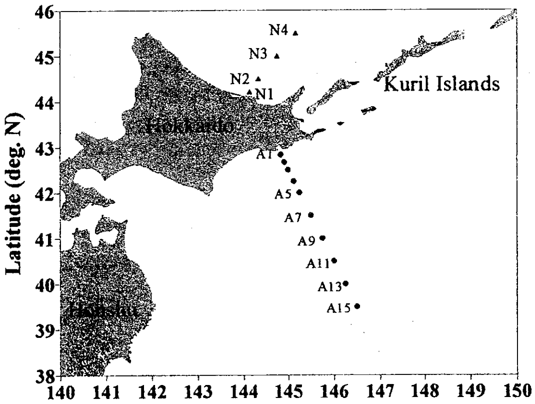

Figure 1. Location of the "A-line" and the "N-line".

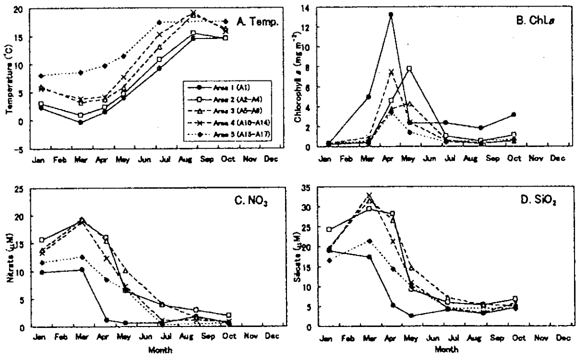

Figure 3. Seasonal change of temperature (A) and concentrations of chlorophyll a (B), nitrate (C) and silicate (D) at the surface water along the A-line (after Kasai et al. (2001)).

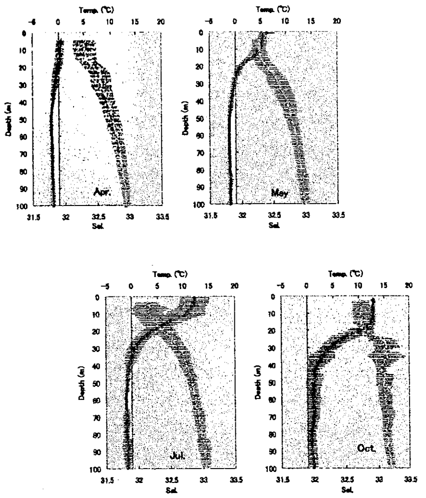

Figure 5. Vertical profiles of temperature and salinity in the oceanic N-line stations.

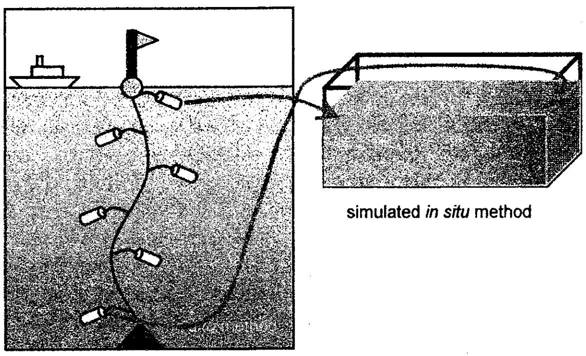

Figure 2. Schematic diagram of incubation methods for primary production.

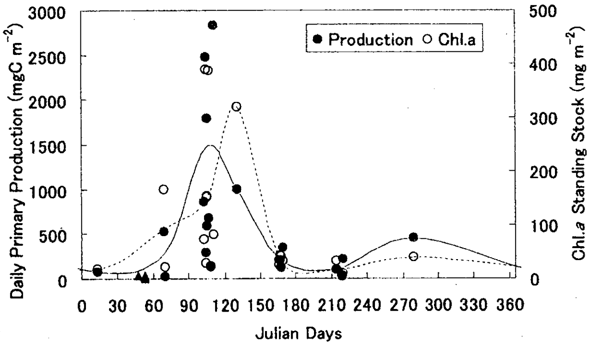

standing stock of chlorophyll a within the euphotic layer in the .Oyashio region.

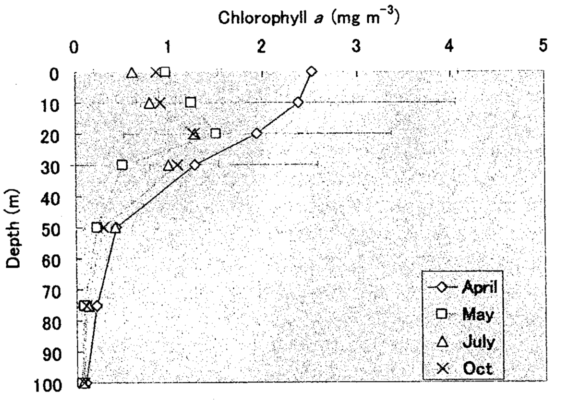

Figure 6. Seasonal change of vertical distribution of chlorophyll *a* in the oceanic N-line stations.

Sea Ice and Snow Cover

Retrieval of snow physical parameters with consideration of underlying vegetation

Teruo Aoki[1] and Masahiro Hori[2]
1 Meteorological Research Institute
E-mail: teaoki@mri-jma.go.jp
2 Japan Aerospace Exploration Agency
E-mail: hori@eorc.nasda.go.jp

Abstract

The Global Imager (GLI) aboard the ADEOS-II satellite launched in December 14, 2002 observed sunlight reflection and infrared emission from the Earth's surface globally, and detected various geophysical parameters (e.g. snow and sea-ice cover extent, snow grain size and impurity). Although the satellite stopped operation on October 25 due to a power supply decrease from the bus system, GLI data obtained during the 7-month scientific operation phase will contribute to investigation of global hydrological cycle and radiation budget that are primal factors of the global climate change. Preliminary analysis results of the GLI snow products with a few months data and their validation results are presented.

1. Introduction

Various snow physical parameters such as snow/ice cover extent, snow grain size, temperature and mass fraction of impurity etc. are to be retrieved as standard snow products from the ADEOS-II/GLI data acquired during its 7-month scientific operation phase (April 2nd ~ October 24th, 2003). Those snow parameters are of significant importance to understand how and where the snow melting process proceeds on the global scale being influenced by air pollution and the global warming. Calibration of sensor radiances and validation of those snow products are currently going on by using other satellite sensor's snow product (e.g. Near Real-Time SSM/I EASE-Grid Daily Global Ice Concentration and Snow Extent) and results of a field validation experiment conducted at Barrow, Alaska in April, 2003. This paper describes the preliminary results of GLI data analysis and its validation results.

2. Data Analysis

2.1 Cloud-free Composite of around the Northern Polar Region

To evaluate the performance of GLI snow algorithms daytime cloud-free composite images of around the Northern Polar region (Lat. > 40deg. N) were made using one month GLI Level-1B data (calibrated radiance) (**Fig. 1**). Pixel selection criteria is the minimum brightness temperature difference between GLI band 30 (3.7μm) and 35 (11μm) which is designed to ensure that clouds over snow surface are eliminated preferentially.

2.2 GLI Snow Algorithms

Two GLI snow algorithms are defined as standard; 1) cloud/clear and snow/ice discriminator and 2) the retrieval of snow grain size and mass fraction of impurity mixed in snow layer both developed by Japan Aerospace Exploration Agency (JAXA) with joint researches with K. Stamnes, Stevens Institue of Technology (Hori et al, 2001). The first algorithm identifies if IFOV is clear or not, and if the IFOV is clear then determines surface type such as snow, sea-ice, land or open ocean by using spectral information of sensor observed reflectances in the visible to near infrared wavelength regions and also of brightness temperatures in mid- to thermal-infrared regions. The second algorithm retrieves snow grain size (radius in μm) and

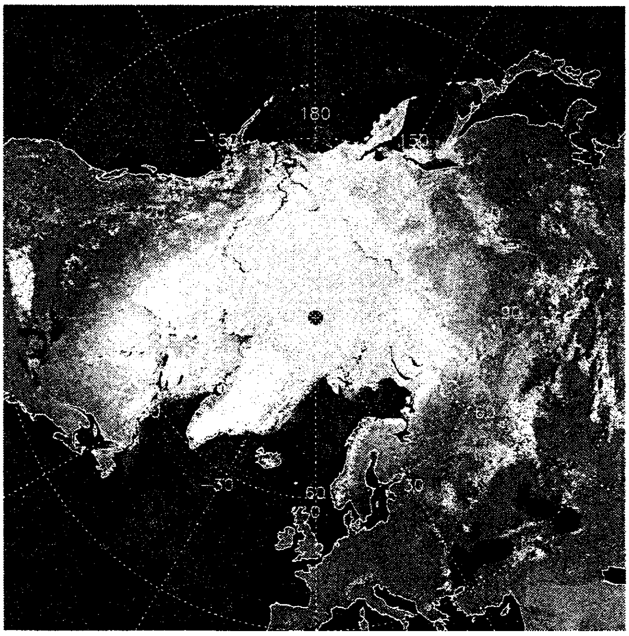

Fig. 1. Daytime cloud-free composite image of around the northern polar region (April, 2003).

mass fraction of impurity (soot in ppmw) from two channel reflectances at the GLI band 5 (460nm) and 19 (865nm) by making use of the dependence of snow reflectance upon both grain size and impurity concentration at those channels (Warren, 1982, Li et al., 2001).

3. Analysis Results and Validation

3.1 Analysis Results

Fig. 2 shows the spatial distribution of snow grain size and brightness temperature of snow surface at the window channel (11 μm) retrieved from the GLI cloud-free composite image of April, 2003. Spatial distribution of snow grain size indicates significant latitudinal dependence which is very much consistent with that of snow temperature. As the latitude decreases from the Pole to south, snow grain size and temperature increases coincidentally. There is a belt (around 40~65°N) where snow grain rapidly increases due to high snow temperature of around the melting point of ice. Snow impurity distribution is somewhat different from those mentioned above. Greenland and the northern Canadian Arctic region are identified as the cleanest area in the Arctic, while sea-ice area in the Arctic Ocean, particularly north of Siberia, is likely to be polluted by aerosols (or covered with shallower snow with low visible albedo).

Snow grain size exhibits significant dependence upon snow surface temperature (**Fig. 3**). Below the melting point (m.p.) of ice snow grain size moderately increases with increasing snow temperature due to the sintering process, while around m.p. grain size steeply increases in the melting process. Snow impurity also seems to correlate with snow temperature. These dependences indicate the close connection among those parameters.

3.2 Validation

To evaluate the accuracy of snow parameters retrieved, ground-based validation experiment were conducted at a snow field near Barrow, Alaska in April, 2003 and obtained ground truth data for snow grain size and impurity. Grain sizes measured at the ground were consistent with the satellite-derived grain size, while impurity data obtained at the ground tend to be apparently larger than those of satellite data. The latter is due to that the algorithm for satellite data analysis assumes pure soot as impurity, whereas ground observation measures the weight of actual impurity containing not only soot but also soil dust particles which is heavier than soot. Thus at the moment the satellite derived parameters are consistent with the truth data.

References

Hori, M., Te. Aoki, K. Stamnes, B. Chen and W. Li, Preliminary validation of the GLI algorithms with MODIS daytime data. *Polar Meteorol. Glaciol.*, 15, 1-20, 2001.

Li, W., K. Stamnes, B. Chen, and X. Xiong, Snow grain size retrieved from near-infrared radiances at multiple wavelengths. *Geophys. Res., Lett.*, 28, 1699-1702, 2001.

Warren, S.G., Oprical properties of snow. *Rev. Geophys. Space Phys.*, 20, 67-89, 1982.

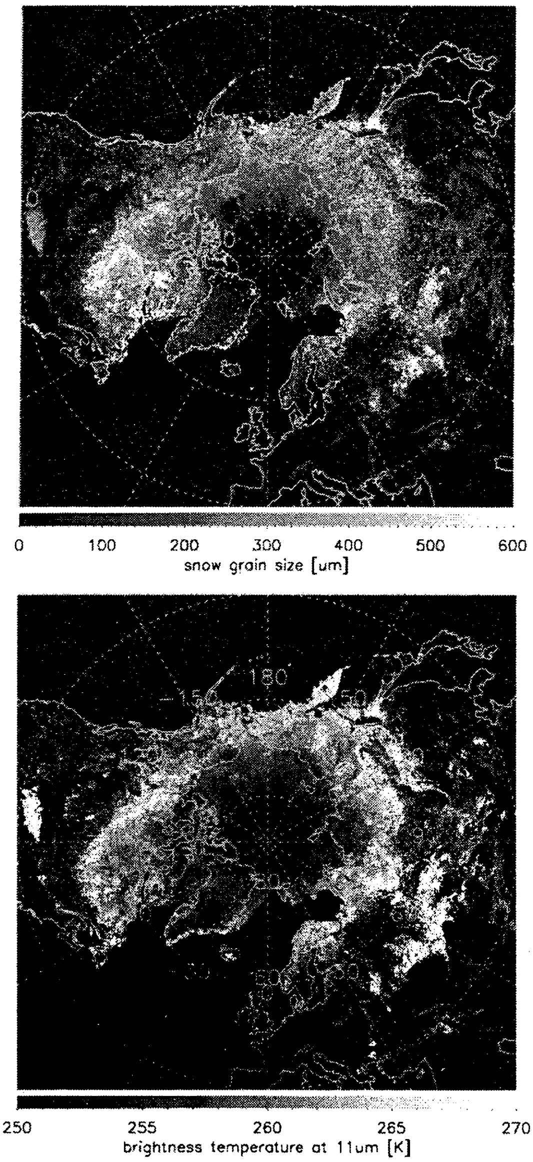

Fig. 2. Spatial distribution of snow grain size (upper) and brightness temperature at 11 μm (lower) of around the northern polar region retrieved from the composite data of April, 2003.

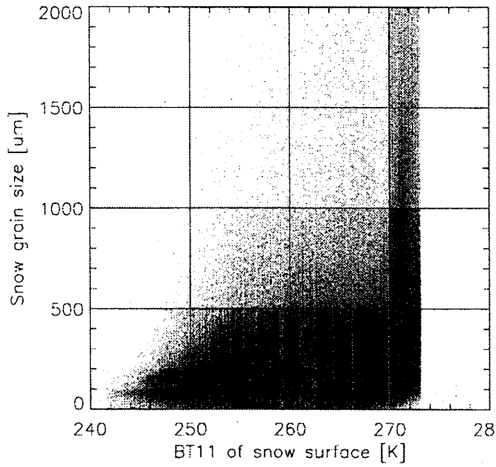

Fig. 3. Dependence of snow grain size upon $BT_{11\mu m}$ retrieved from the GLI composite data of April, 2003.

Antarctic Remote Ice Sensing Experiment (ARISE) with Australian National Antarctic Research Expedition in 2003

Atsuhiro Muto[1], Fumihiko Nishio[1], Hiroyuki Enomoto[2], Kazutaka Tateyama[3],
Takeshi Tamura[4], Shuki Ushio[5], Rob Massom[6]

1. Center for Environmental Remote Sensing, Chiba Univ., Japan
2. Kitami Institute of Technology, Japan
3. Sea Ice Research Laboratory, Institute of Low Temperature Science, Hokkaido Univ., Japan
4. Inst. of Low Temperature Science, Hokkaido Univ., Japan
5. National Institute of Polar Research, Japan
6. ACE CRC(Univ. of Tasmania), Australia

Abstract

An extensive sea ice experiment was conducted in East Antarctic seasonal sea ice area. The primary objective of the experiment was to validate sea ice products retrieved from new passive microwave satellite sensors, AMSR and AMSR-E and also to assess the performance of conventional algorithms. New instruments to measure ice thickness and snow depth over sea ice were also tested. The challenge was to collect enough data sufficient enough to validate AMSR and AMSR-E having wide pixel size. To overcome this, four different types of data having different areal coverage and altitude, in situ data from ice stations and helicopter floe hopping, aerial photography and video and along-track underway data were obtained. All these data complement each other and combined with visible range satellite data, the validation process is completed.

1.Introduction

Antarctic Remote Ice Sensing Experiment (ARISE), as part of Voyage 1 of *RSV Aurora Australis* for 2003/04 season was carried out in a region off the East Antarctic coast. The voyage was 49 days long, from 11 September to 30 October, of which 30 days were dedicated to the ARISE program. This program was a joint international effort (over 20 institutions from 6 different nations) to survey the sea ice and snow cover conditions in the area bounded by 64-65° S and 112-119° E (*Fig. 1*), with the main purpose being to acquire data for validation of both conventional and new satellite sea ice sensing systems using various instruments.

Japanese group focused on validating ADEOS II AMSR (Advanced Microwave Scanning Radiometer) sea ice products, through *in situ*, underway and aerial data acquisition.

Validation process is now underway. Data compiled during the voyage are being compared with AMSR data, also with visible range satellite data to extend the spatial coverage.

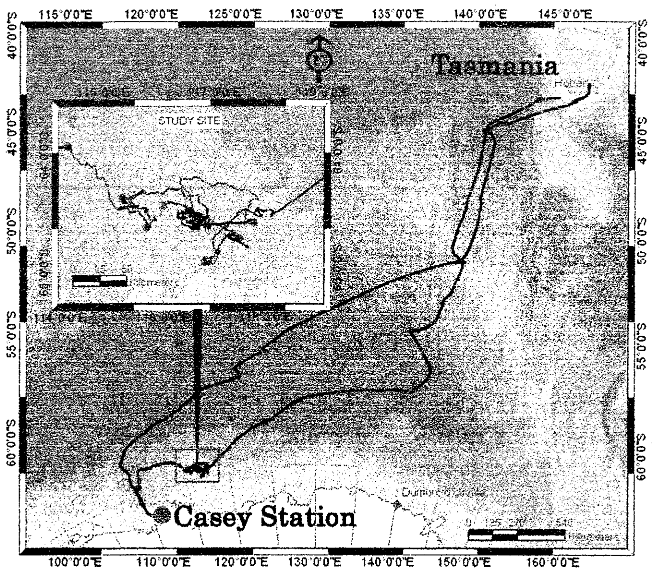

Fig.1 Ship's route between Hobart, Tasmania and Antarctica. Onset map shows the area in where the ARISE program was conducted. (©ACE CRC, 2003)

2. Program overview

Passive microwave remote sensing of sea ice in both north and south poles dates back to 1972, started with data collection by Electrically Scanning Microwave Radiometer (ESMR) in the Nimbus 5 (Cavalieri, 1992). Improvement of satellite microwave radiometers have been attempted by various nations and two new radiometers, AMSR (Advanced Microwave Scanning Radiometers) onboard Japanese satellite ADEOS II and AMSR-E onboard NASA's AQUA were launched in 2002. ARISE was aimed to validate sea ice concentration and extent, ice physical temperature and snow cover on sea ice retrieved by the new sensors. An attempt to validate and quantify error characteristics to improve the existing ice concentration algorithms such as the Bootstrap algorithm (Comiso, et al., 1997), was also a key component of this experiment.

Measurement strategy to collect sufficient data, to adequately validate AMSR and AMSR-E data products, consisted of ice stations, helicopter floe hopping, aerial photography and video filming and underway data collections from ship-borne sensors.

2.1 Ice stations

In order to obtain detailed *in situ* data on snow and ice properties, 13 ice stations were carried out. During the stations, which lasted for about 5 hours each, 50-100m transects were laid and snow and ice thickness, ice freeboard and snow/ice interface temperature were measured at 1m interval. Three snow pit works and ice core collections were conducted at 0m, 50m and 100m points of each transect. Ice cores were later processed and analysed in cold room for sea ice structural studies. Exceptions were station 4, which lasted for three days and transect stretched to three 500m lines, and station 6 where only snow depth was measured.

Other ice station works involved the measurements of ice thickness by EMIs (Electro Magnetic Induction devices) from Australian group and Japanese group, German ground penetrating radar and new radar system developed by Radar Systems & Remote Sensing Laboratory, University of Kansas, for measuring ice and snow thickness. Data from these instruments were calibrated against measurements of snow thickness and ice thickness along transects.

Although data acquired at each ice stations are only 'point' data compared to the resolution of AMSR and AMSR-E, they will help us develop more understanding of parameters affecting satellite observed data and enhance conventional algorithms and perhaps develop new ones.

2.2 Helicopter floe hopping

Ice physical temperature and snow cover thickness over sea ice are new standard products. One of the Australian group's focuses of this experiment was to validate those products. In order to achieve this at the AMSR pixel (10km) scale, snow/ice interface temperature and snow thickness were measured on numerous floes of different regimes. And the measurements were averaged Each floe was accessed by helicopter and snow thickness was measured at up to 40 different locations and snow/ice interface temperature at about 8 locations. Total number of floe accessed was 181.

2.3 Aerial photographing and video filming

Another strategy to overcome the large AMSR pixel size was aerial digital photographing conducted by Australian group and aerial video filming by Japanese group. Both aimed at collecting data for comparison with satellite derived sea ice concentration. Australian digital still camera (Nikon D1x) was fitted to the floor window on one of the helicopters onboard viewing the surface vertically, and photographing from 5000 feet in altitude. They successfully completed 7 flights on 5 clear days, each lasting over 2 hours. Digital photographs are in hi-colour TIFF format and will be made into mosaic images.

Japanese video camera (SONY TRV-900) was also mounted to the helicopter floor window looking vertically down, with the calculated image width being around 2100m from 8000 feet above sea level. Video was recorded in progressive scan which makes up footage with 15 separate frames per second, and enables smoother construction of continuous mosaic images.

Filming was carried out on 19 October when the weather condition was most favourable i.e. cloudless condition. The flight was nearly three hours long however the actual recorded video footage of use for validation purpose is about 60 minutes long. It follows the ship's track in the first 30 minutes, starting at around 65° 27′ S, 109 ° 30′ E going almost due north past the ship, and until cloud cover started to appear at around 64° 05′ S.

Footage covers transitional area from very thin new ice of about 5-10cm in thickness forming over coastal polynya, to unconsolidated or small broken up floes of a few tens of meters in diameters up to about 70cm thick, to consolidated large floes extending to a few hundred meters to kilometre scale and thickness around 1m.

This video filming proved to be an extremely useful validation tool. Not only it gave us wide areal coverage, it clearly shows thin new ice over coastal polynya which is hard to distinguish in MODIS images that will be used as a medium resolution validation data. Mosaic images developed from the video footage (*Fig. 2*) will be used as a reference to MODIS images in the actual validation process of AMSR derived sea ice concentration.

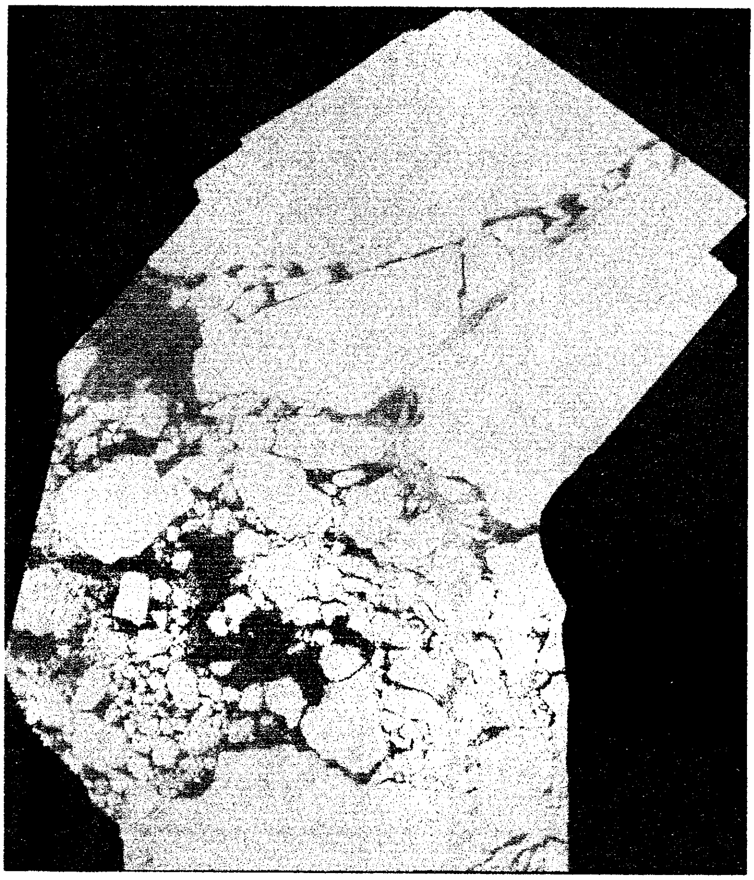

Fig.2. Example of a mosaic image constructed from aerial video footage.

2.4 Underway data

Supplementing the data from above three types of observations are underway data collected along the ship's track. Japanese group installed two 8mm analogue video cameras (SONY TR-11), one on the rail above the bridge (herein after referred to as roof deck camera) viewing the area straight ahead of the ship and another one on the port side rail. looking downwards (side camera).

Roof deck camera was used for continuously recording of ice conditions along the ship's track (*Fig. 3*). Aerial video data is also complemented by video footage from roof deck camera because roof deck camera gives a closer look at sea ice and can show smaller scale detail than aerial video i.e. differentiate open water and ice with thickness of less than 5 cm that is hard to achieve with aerial video alone. More details on the utilization of roof deck camera will be given in a later section. The total duration of roof deck video footage is nearly 140 hours.

Side camera was used to film ice floes turning on its side as the ship breaks ice (*Fig. 4*). Ice thickness can be measured visually by selecting floes that turn almost 90° on its side showing the broken facies. About

130 hours of video footage from side camera was collected.

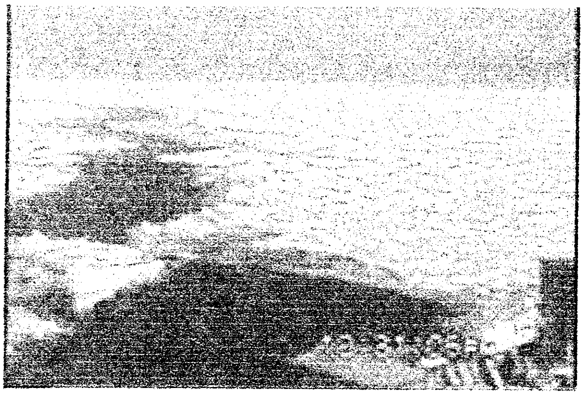

Fig.3 One scene from roof deck camera

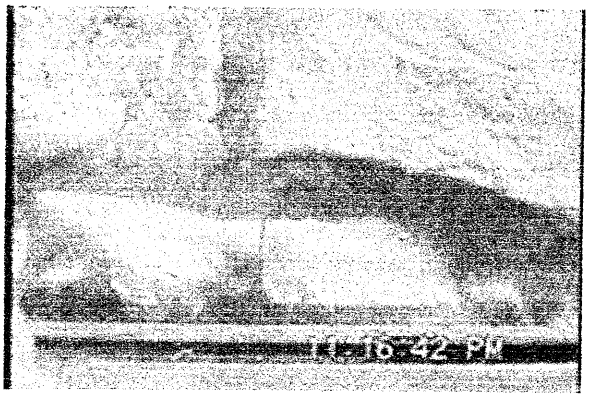

Fig.4 One scene from side camera

3. Validation of sea ice concentration derived from AMSR/AMSR-E data

Here we will briefly present the method for validation of sea ice concentration derived from AMSR/AMSR-E, using data acquired during ARISE and satellite data acquired later.

The primary tool in the validation process is the images from MODIS in the visible 250m channel, although data collected during ARISE is indispensable. MODIS achieves wide spatial coverage and relatively high resolution at the same time. Cloud free images will be selected and of desired area will be cut out.

First, within the cut-out image of MODIS, pixels with sea ice cover and open water will be distinguished. This is achieved by determining threshold DN (Digital Number) value in grey scale which differentiate sea ice and open water. Both images from roof deck camera and aerial video are effective in threshold determination because of difficulty in detecting thin new ice in MODIS images as discussed in the previous section. The image will then be made into binary image, giving white or 1 for pixel with sea ice coverage and black or 0 for open water.

Then to determine ice concentration, the number of pixels with value 1 will be counted within 10km grid corresponding to 1 pixel of AMSR/AMSR-E. For example, if the 10km grid has 1600 pixels with 1, then the concentration is 100% and if 800 pixels, then the concentration is 50%.

Sea ice concentration images derived from AMSR/AMSR-E and MOSDIS are compared and the error percentage of AMSR/AMSR-E will be calculated. The target error percentage for ice concentration product is below10%.

4. Concluding remarks

ARISE was one of the most extensive programs ever conducted in the Antarctic sea to collect various types of measurements on sea ice. The primary objective of the program was acquisition of data to validate new satellite sensors and existent sea ice products. To overcome large pixel size of satellite microwave radiometers, detailed in situ data, helicopter floe hopping, aerial photographing and video filming and continuous along-the-way data were strategically acquired. Also, several new type sensor measurements were carried out during the program.

As for the Japanese effort to validate AMSR/AMSR-E derived standard sea ice products, method is established and is now in the analysis process. The results are expected to come out shortly and it is much anticipated that error percentage to be carefully assessed and algorithms be improved.

Further validations are already planned for 2004 and 2005. In February 2004, similar but smaller scale program than ARISE will be conducted in the Sea of Okhotsk using Japan Coast Guard patrol boat SOYA. Validation using air-borne microwave radiometer onboard NASA P3 aircraft in the Wedell and Bellingshausen/Amundsen Sea areas of Antarctica will take place in September 2004, as AASI (Antarctic AMSR-E Sea Ice) campaign. AASI is also planned for September 2005 in the Ross Sea areas.

Acknowledgement

We are grateful to the Australian Antarctic Division and ACE CRC for the opportunity to participate in ARISE, National Maritime Research Institute of Japan (NMRI) for lease of their video cameras and equipment, National Polar Research Institute of Japan (NIPR) for their help in communicating with AAD before departure, JAXA Earth Observation Research and application Center (EORC) for AMSR and AMSR-E data, NASA Goddard Space Flight Center Distributed Active Archive Center for TERRA and AQUA MODIS data.

References

Cavalieri, D. J.(1992), The validation of geophysical products using multisensor data, Chapter 11, 233-242, *Microwave remote sensing of sea ice*, American Geophysical Union, Washington DC.

Comiso, J. C., Cavalieri, D. J., Parkinson, C. L. and Gloersen, P. (1997), Passive microwave algorithms for sea ice concentration: A comparison of two techniques. *Remote Sens. Environ.*, 60, 357-384.

Study on detecting thin sea ice area from satellite images

Kohei CHO, Yoshimi Yano, Miyuki Sasagawa, Norimi Takeda,
Yoshihide Obora, Haruhisa Shimoda
Tokai University
kcho@keyaki.cc.u-tokai.ac.jp

Abstract：

In order to verify the possibility of detecting thin sea ice area from satellite images, authors are collecting multi-stage remote sensing data of sea ice for the passed few years. This paper describes about the comparison of thin sea ice images acquired from different platforms.

1. Introduction

The thermal flux from the thin sea ice to the air is 10 to 100 times larger than that of the thick sea ice(Maykat, 1978). Thus, monitoring of thin sea ice is quite important for the study of global warming. Since the albedo of thin sea ice changes with it's thickness, visible & near infrared sensors onboard satellites may monitor the thickness differences of thin sea ice. However, since thin sea ice areas consist of various sea ice types, such as Nilas, Pancake ice, Young ice, the explanation of the areas are not easy. For example, algorithm difference of estimating sea ice concentration from satellite passive microwave sensor often appears in thin sea ice area (Cho et al., 1998). In order to verify the possibility of detecting thin sea ice area from satellite images, the authors are collecting multi-stage remote sensing data of sea ice for the passed few years (Cho et al, 2003).

2. Multi-stage remote sensing

Recently, various satellite sensors are becoming available for sea ice monitoring. However, the information of which we can acquire with each sensor changes according to the spacial resolution and spectral bands of each sensor. Various types of sea ice are randomly distributed in certain sea ice zone, and the sizes of which are different from one type to another. For example, the diameter of typical pancake ice may be 20 cm, while the diameter of typical medium floe could be 200m or more. These situations are making it difficult to monitor sea ice condition from space. In order to verify the possibility of extracting thin sea ice information from remotely sensed data, preparation of multi-stage remote sensing data set for comparing sea ice images of various sensors including in-situ data is very important. The multi-stage remote sensing which authors are performing consists of observations from ships, low altitude airplanes, and satellites (See Figure 1).

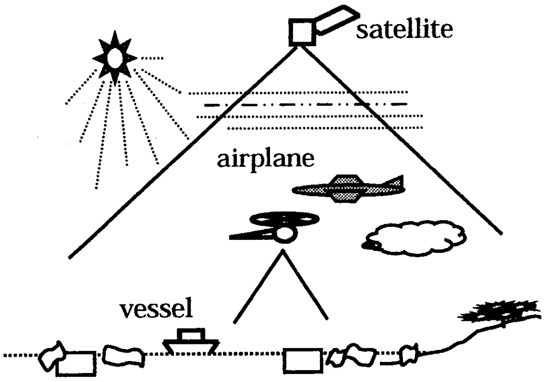

Figure 1. Muti-stage remote sensing of sea ice.

2.1 In-situ measurement

In-situ measurement is most important and most difficult. Since various types and scales of sea ice are often randomly distributed, the area for the measurement should carefully be selected. In this study, in-situ measurement consists of sea ice thickness measurement, spectral measurement, and photographing.

(1) Sea ice thickness measurement from an icebreaker

The authors have developed a system to measure sea ice thickness using stereo cameras equipped on a ice breaker(Cho et al. 2002). Figure 2 shows the concept diagram of the system. The sea ice thickness can be estimated with the error of 1.5cm when the stereo cameras are equipped 2.5m above the sea level.

(2)Spectral measurement

Spectral measurement of sea ice using radiometer is quite difficult. The condition of sea ice surface changes from one place to another. In order to compare the spectral data with satellite data, it is important to perform the spectral measurement at several points within certain area and calculate the averaged value.

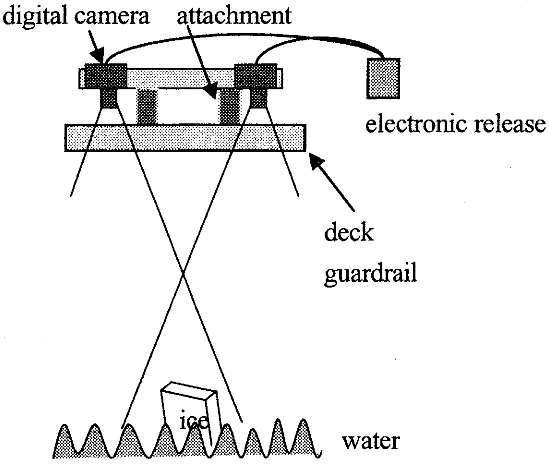

Figure 2. Stereo pair imaging system for sea ice thickness measurement.

(3) Photographing

In-situ images taken from ships and from land are important information for understanding the condition of the sea ice.

2.2 Aerial observation

Observations from low altitude helicopter/airplane provide very high resolution images of sea ice which are necessary for connecting in-situ measurement data with satellite observation. Multi-spectral imager observation from an airplane is quite useful. But even a digital camera imaging from a Cessna give us useful information for identifying in-situ measurement location on the satellite images.

2,3 Satellite observation

Satellite observation gives us wide view of sea ice. However there is always limitation for extracting detailed sea ice information from low/middle special resolution satellite images. High resolution satellite images such as of IKONOS may cover the gap between low/middle special resolution satellite images and aerial/in-situ images of sea ice.

3. Comparison of multi-stage remote sensing images of sea ice

3.1 Aerial images

(1) Images from a remote control helicopter

An experimental flight using a remote controlled(RC) helicopter was performed by Dr. Yoshiaki Honda's group of CERES of Chiba University in March 2000 along the coast of Hokkaido. Figure 3 show example images of sea ice area taken by the digital camera onboard the helicopter. The high resolution aerial images give us detailed information on sea ice condition and distribution. Even though the digital camera is only a color camera, the images give us good information on the condition of sea ice.

(2) Images from a Cessna

Figure 4 shows images of the icebreaker and it's surrounding sea ice area taken when the ice thickness measurement was performed on the icebreaker on March 6, 2003.

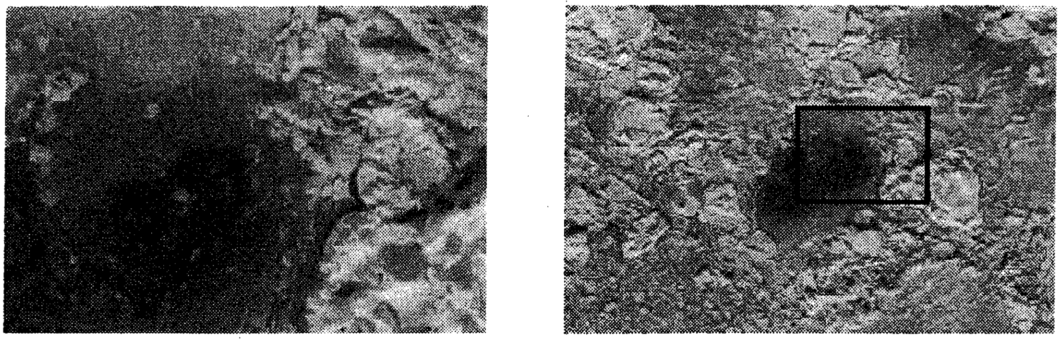

(a) Resolution : 4mm (altitude: 15m) (b) Rresolution : 16mm (Altitude: 60m)

Figure 3. Images from the hericopter.

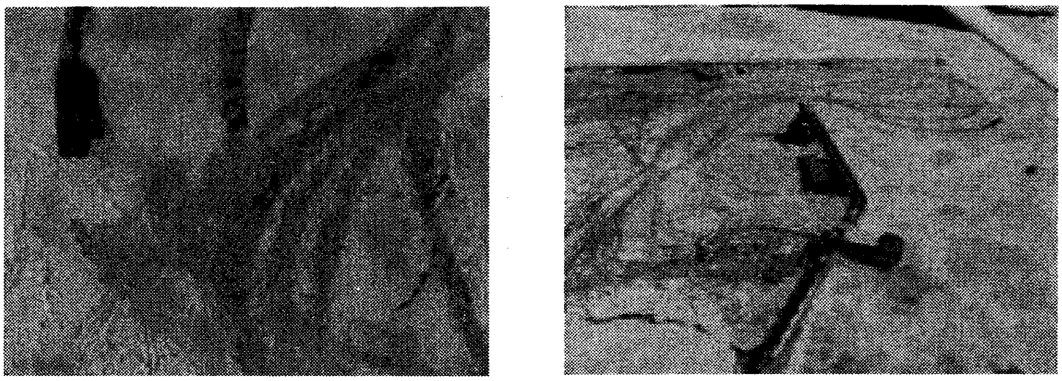

(a) Garinko-2 and it's trajectory (Resolution:35cm) (b) Monbetsu Bay and trajectories of Garinko-2

Figure 4. Aerial images of sea ice from a Cessna (Altitude: 150m)

3.2 Satellite Images

(1) IKONOS

Recently, 1m or higher resolution satellite images of IKONOS, OrbView-3, Quickbird etc. are becoming available. On March 10, 2000, IKONOS observation was performed over the Sea of Okhotsk. Figure 5 shows a part of the IKONOS image in different resolution. (a) is the original 1m resolution image and (b) is the averaged 10m resolution image. The images strongly suggest the advantage of using 1m resolution satellite images for thin sea ice identification.

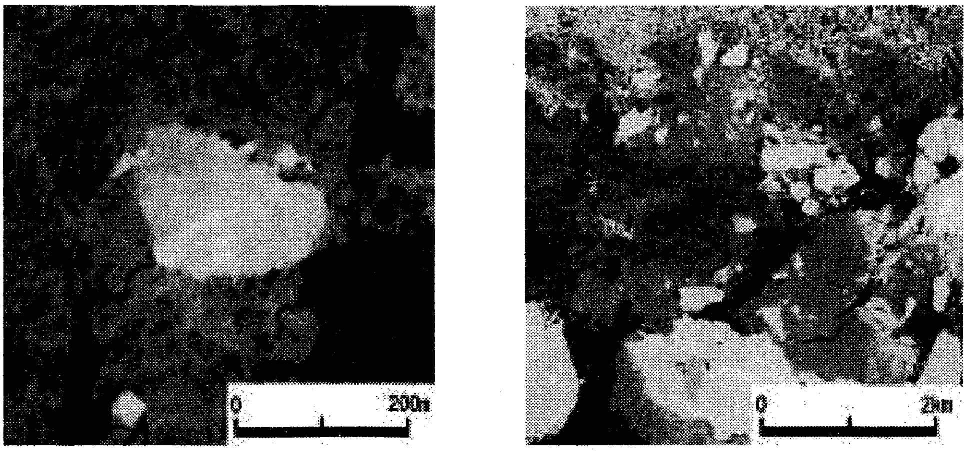

(a) Resolution : 1m (original) (b) Resolution : 10m (10x10 averaged)

Figure 5. IKONOS images of the Sea of Okhotsk(March 10, 2000) © Japan Space Imaging

(2) Landsat-7/ETM

The Landsat-7 observation over Hokkaido was performed on March 6, 2003. Figure 6 shows the ETM panchromatic image of Monbetsu Bay. The trajectories of the icebreaker Garinko-2 can clearly be seen on the image. By using the GPS data of the icebreaker, the in-situ sea-ice measurement data can easily be plotted on a map and overlay on the ETM imagery.

(3) Terra/MODIS

The Figure 8 shows the comparison of NOAA/AVHRR image with MODIS image. The advantage of 250m resolution of MODIS is clear.

Resolution:15m

Figure 6. Landsat/ETM image

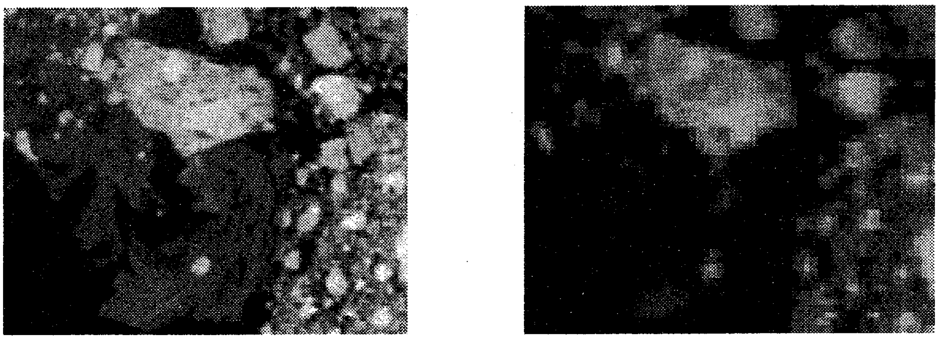

(a) Terra/MODIS image(Resolution:250m) (b)NOAA/AVHRR image(Resolution:1km)

Figure 8. Comparison of MODIS image and AVHRR image.(April 3, 2003)

5. Conclusion

The multi-stage remote sensing images of sea ice around Monbetsu Bay have been collected and compared. Even though the images are not all simultaneously collected, the images strongly suggest the importance of multi-stage remote sensing for sea ice. Our next step is to collect various multi-stage remote sensing data in same time to verify the possibility of detecting thin sea ice area from satellite images. This experiment was performed under the science project of the General Research Organization of Tokai University Educational System.

Acknowlegement

The authors would like to thank Mr. Souji Hamaoka, Mr. Ryuichi Nagata and other staffs of Okhotsk Garinko & Tower Co. Ltd. for their kind support on the experiment. The Landsat-7/ETM data was provided from JAXA under the framework of the ALOS Science Project. The IKONOS data was provided from Japan Space Imaging (JSI) under the science cooperation agreement. The authors would like to thank to JAXA, JSI and CEReS for their support on this study.

References

Maykut G. A., Energy exchange over young sea ice in the central Arctic, J. Geophys. Res., Vol. 83, pp. 3646-3658, 1978.

Cho K., T.Narabu, H.Shimoda, T.Sakata, Validation of SSM/I sea ice concentration algorithms for the Okhotsk Sea, Proceedings of the IGARSS'98, Vol.IV, No.D09, 1998.

Cho, K., Importance of Multi-stage Remote Sensing for Sea Ice Monitoring, Proceedings of the International Symposium on Remote Sensing of Cryosphere, Okhotsk Sea & Sea Ice, CERES, Chiba Univ., in print, 2003.

Cho, K., Y. Taniguchi, M. Nakayama, H. Shimoda, T. Sakata, Sea ice thickness measurement using stereo images, Proceedings of the 17th International Symposium on Okhotsk Sea & Sea Ice, pp.169-172, 2002.

A study on sea ice variation in Lützow-Holmbukta, Antarctica, with satellite data

Shuki Ushio[1], Teruo Furukawa[1] and Fumihiko Nishio[2]
1 National Institute of Polar Research
E-mail: ushio@pmg.nipr.ac.jp, furukawa@pmg.nipr.ac.jp
2 Center for Environmental Remote Sensing, Chiba University
E-mail: fnishio@ceres.cr.chiba-u.ac.jp

Abstract

Characteristics of sea-ice variation including breakup events in Lützow-Holmbukta, Antarctica, have been investigated for the period of 1980-2003. According to satellites images, it is found that spatial and temporal scales for breakups are different among each event and that breakups have occurred at least 19 times. The geographical sites of breakups are almost the same in the bay and commencement is usually in autumn. The 1997/1998 event covered a wide area and was of long duration. Since then, autumn to early winter breakup has continued until winter 2003. It is suggested that dominant southerly wind field, small snow depth and mild winter prior to the breakup are factors which favor breakup events. Long-term monitoring of such a coastal sea-ice condition is important and useful for better understanding of the Antarctic and global change.

1. Introduction

Land fast-ice covers almost throughout the year in Lützow-Holmbukta, Antarctica. Satellite images show that the ice field has frequently broken up there. Appearance of open water resulting from breakup performs active air-sea interaction, and will have an influence on regional climate and oceanic environment. The purpose of this study is to reveal a mechanism for the coastal sea-ice variation.

The Japanese Antarctic Research Expeditions (JAREs) have conducted satellite, meteorological, and snow depth observations at Syowa Station. Furthermore, wintering activities reports of JAREs are referred to estimate the ice condition. Then, some factors for sea-ice breakup are discussed based on these historical data.

2. Characteristics of sea-ice breakup in Lützow-Holmbukta

2.1 Where have the breakups occurred in the bay?

Figure 1 shows a typical appearance of the large-scale breakup from NOAA/AVHRR image. The image by thermal-infrared channel with resolution of ~1km is processed for features with relatively high surface temperatures to be presented in dark gray to black tones. As for the case of winter 1997, ice formation and discharge have been repeated through mid-winter 1998. Almost the breakup events occur north-central to eastern area of the bay. The boundary between unstable outflow and stable ice field is nearly consistent with the location of continental shelf break referred from the bathymetric chart (GEBCO). At the shallow region, stable ice field has a tendency to be left. Dynamic effect from ocean current or waves should be studied as a future work.

2.2 History of sea-ice breakup

Using satellite images and the JAREs wintering reports, breakup events have been compiled as shown in Figure 2. Here, "breakup" period is defined as occurrence of ice outflow to the south of 68.83S. In summer season, vigorous melting or water opening have been found at the eastern area of the bay as shown in Figure 2. Breakups frequently occur at autumn season and at least 19 times for the last 24 years. It is remarkable trend that breakups have been continued every year since 1997.

3. Discussion

Melting feature at summer season, as observed at the eastern area of the bay, is induced from strong insolation and high temperature. In this section, physical factors for breakup events occurred in autumn season are mainly discussed according to the historical data. The following three factors are possible to be considered; 1) dominant southerly wind, 2) snow depth, 3) air temperature anomaly (*Ushio, in press*).

3.1 Surface wind field

Table 1 shows frequencies percentage of surface wind direction for the case study of 1997 event. On April, before the remarkable breakup occurrence at early winter, strong northeasterly wind has blown at about twice as frequent as the normal value. Northeast wind at Syowa is usually very strong accompanied with blizzard. Such a strong onshore wind brings great swell inside the bay and causes fast-ice field to be broken down.

Southerly wind during the period from May to July has also blown with high frequencies as shown in Table 1. The frequent offshore wind is considered to transport broken ice floes northward. Thus the peculiar wind field contributes to occurrence of large breakup in July 1997.

3.2 Snow cover effect

Snow cover on ice plays an important role on heat exchange in the atmosphere-ice-ocean system. When snow depth is large, melting and refreezing cause formation of superimposed ice (like a mechanism for accumulation at temperate glaciers). Snow cover effect should be considered to estimate mass balance for sea ice. Such a snow metamorphosis affects mechanical properties of sea ice. Thick ice and much snow cover contribute to growth of hard ice floe, so ice field will be stable against heavy weather condition. In the Figure 2, years with much snow cover, above 60cm as maximum increase for each year, are indicated by asterisk. During the period of previous and middle of 1990s, much snow depth years have continued and coincide with relatively stable situation or no breakup era. For the other period, frequent breakup link up small snow cover. If snow depth is small, absorption of solar radiation is active from spring to summer and upward growth by superimposed ice is not expected.

3.3 Air temperature anomaly in the cold season

It is necessary for sea-ice breakup that ice floe should be broken down. Mechanical strength depends on brine volume ratio inside the ice. The brine volume increases with temperature, so mechanical strength lowers by warm environment, because ice temperature follows air temperature variations. Figure 3 shows monthly air temperature for cold season, August to October, in each year since 1980. For the past years, air temperature records the highest value in 1996. This warm winter is considered to be a trigger for the large breakup in 1997.

4. Conclusions

Variation of land fast-ice field has been investigated using satellite images and surface meteorological data. Breakup phenomena are often observed in autumn season. Sea ice condition in Lützow-Holmbukta is generally unstable. Remarkable anomalies for surface wind field, snow cover, and air temperature are presented to consider as possible factors for the breakup. Sea ice processes are important for the navigation of icebreaker SHIRASE as well as understanding of global change mechanism. Monitoring study should be continued with satellite remote sensing and in-situ observations by high technology device.

Table 1. Frequencies percentage of wind direction at Syowa Station in 1997.

wind direction	NE	S / SSE / SE		
year \ month	April (%)	May (%)	June (%)	July (%)
1997	42	13/8/9	12/8/6	12/11/6
NORMAL	22	7/6/4	6/7/6	6/6/4

Figure 1. Sea-ice breakup in Lützow-Holmbukta.

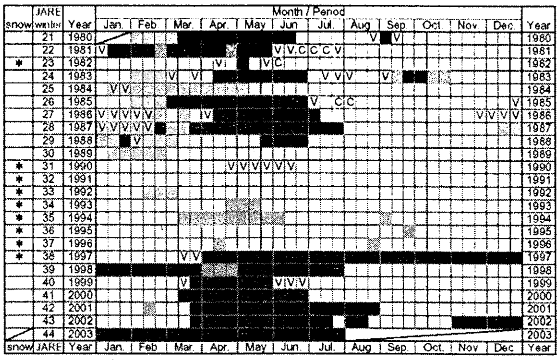

Figure 2. History of sea-ice breakup in Lützow-Holmbukta from 1980 to 2003. Black-colored period: breakup in the bay; hatched: breakup only eastern part; gray: inferred as period with high possibility of breakup; V: v-shaped crack; C: north-south crack; *:year with much snow at Syowa Station.

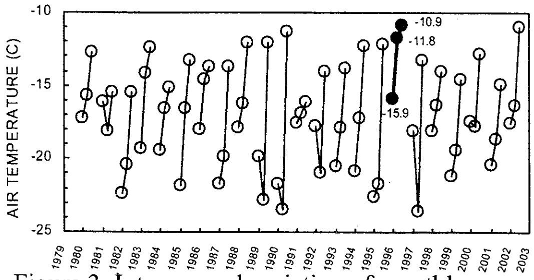

Figure 3. Inter-annual variation of monthly mean air temperature on August, September, and October. Closed circles indicate values of 1996 before breakup.

References

Ushio, S.(2003): Frequent sea-ice breakup in Lützow-Holmbukta, Antarctica, based on analysis of ice condition from 1980 to 2003. Antarctic Record, Vol.47, No.3, *in press.*

Observation of ice sheet and glacier movement in the Antarctica by JERS-1 SAR interferometry

Hiroshi Kimura[1], Takashi Kanamori[1], Hiroyuki Wakabayashi[2] and Fumihiko Nishio[3]
1 Dept.of Electrical & Electronic Engineering, Gifu University
E-mail: hkimura@cc.gifu-u.ac.jp and h3135006@guedu.cc.gifu-u.ac.jp
2 Japan Aerospace Exploration Agency
3 Center for Environmental Remote Sensing, Chiba University
E-mail: fnishio@cr.chiba-u.ac.jp

Abstract

From a series of three JERS-1 SAR interferograms over the Yamato mountains area in the Antarctica, ice surface movement and change of motion speed are detected. In spite of less accurate orbit information, baselines are estimated using 1 km global DEM and referring phases over bare rock areas. Results suggest that movement is not constant over the study are, and variations of ice motion speed and acceleration exit around bare rocks.

1. Introduction

In order to interpret changes in the Antarctic ice sheet as indication of global change on climate, it is necessary to observe the local changes in a regional context. This requires a comprehensive monitoring effort that addresses both the inland ice and changes in the ice margin. Objective of our study is regional observation of the Antarctic ice sheet using the interferometric SAR technique for detection of changes in the ice sheet margin. Spaceborne imaging SAR presents the opportunity for measuring surface displacement fields interferometrically by use of the radar beam. Application to the glacial flow and sea ice, interferometric phases contain the combined effects of the baseline separation, motion of ice sheet or glacier over the period of the repeated cycle of satellite between two images, and the surface topography. Goldstein et al. [1] and Kwok et al. [2] demonstrated measurements of ice sheet movements using ERS-1 InSAR. Accurate baselines of ERS-1 InSAR allow these measurements. JERS-1 satellite SAR has also a large potential for monitoring ice sheet and glacier movement [3]. The radar wavelength is 24 cm, so a fringe of phases appears every 12 cm displacement. However, the JERS-1 orbit information is not so good to extract only phase due to surface movement and topography. Ozawa et al. [4] assumed seacoast lines as 0-m height reference to generate a DEM of the Soya coast area, Antarctica from JERS-1 InSAR. This approach can be applicable for coastal regions. This situation prevents us from global monitoring of Antarctic ice movements by JERS-1 SAR. However, we can expect some conditions over the Antarctica, and they allow us to measure only ice movements inland of the Antarctica. In this study, we succeeded to extract surface movements in the Yamato mountains area, and detect change of motion speed from a series of three JERS-1 SAR interferograms.

2. Method

2.1 Study area and used interferograms

Our study area is the Yamato mountains area. One of JERS-1 SAR images (D187-422) and an optical image from JERS-1 are shown in Fig. 1. The area is located inland of the Antarctica, and bright features in the SAR image and dark features in the optical image are bare rocks. We use three interferograms from data takes of March, April, June and July 1996. Surface height changes from about 1700 m to 2400 m in the study area.

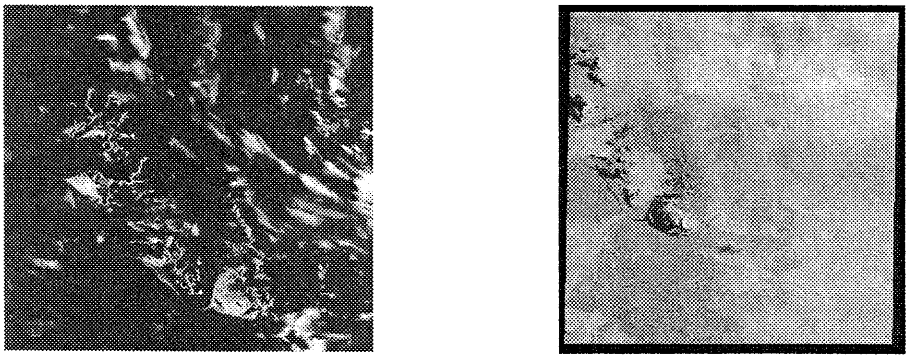

(a) JERS-1 SAR image (b) OPS image

Fig. 1. JERS-1 SAR and OPS images of the study area.

2.2 Anticipated conditions

SAR interferogram phase is given as a sum of three components as follows,

$$\phi = \phi_f + \phi_t + \phi_m \qquad (1)$$

where ϕ_f is flat Earth phase, ϕ_t is topographic phase and ϕ_m is movement phase. In this study, we anticipate three conditions over the Antarctica to apply interferometric technique to JERS-1 SAR data,

Condition 1: Short baseline,
Condition 2: Existence of stable bare rock areas,
Condition 3: Gentle undulating surface terrain.

Condition 1 comes from the fact that satellite orbits cross in the polar region, and means topographic phase has much less sensitivity to topographic height variations. Condition 2 means that these exists areas with only flat earth phase and topographic phase. Under condition 1 and 2, bare rock areas are expected to have only flat earth phase, and can be used to estimate an initial value of baseline (flat earth phase). Condition 3 comes from the fact that most of the Antarctica is covered with ice and snow, and height variations are dominated very low spatial frequency. This means that even low-resolution digital elevation model (DEM) is useful, and such 1 km Global DEM can be used to improved baseline estimation (flat earth phase and topographic phase).

2.3 Processing flow

Fig 2 shows the processing flow of our approach. Even from a unwrapped interferogram, only a relative phase is derived. In our approach, initial relative flat earth phase is expressed as,

$$\phi_{f\text{-}ref} = \phi_f - \phi_o = ax + by \qquad (2)$$

where ϕ_o is an offset phase from absolute phase at (0,0), (x,y) is the coordinate of (range, azimuth). Constants a and b are flat earth change rate in range and azimuth respectively, and derived from the phase over bare rock areas under the condition 1 and 2. Fig. 3 shows the interferometric phase ϕ_2 (April and June pair) over the largest bare rock, and indicates allowance of a linear function expressed in (2).

Processing steps are as follows,

Step 1: Using initial relative flat earth phase of (2) and orbit information of used JERS-1 data, baseline is estimated by the least square method.
Step 2: Using estimated baseline and 1 km global DEM, flat earth phase (ϕ_f) and topographic phase (ϕ_t) are generated.
Step 3: Movement phase is calculated ($\phi_m = \phi - \phi_f - \phi_t$).
Step 4: Standard deviation of movement phase over bare rock areas are calculated ($\sigma_{\phi m}$).
Step 5: If baseline is correct, should be 0, so if is more than 0.1 cycle, go to step 6, otherwise finish iteration.
Step 6: Update constants of flat earth phase function expressed in (2), using flat earth phase and movement phase over bare rock areas, and then go to step 2.

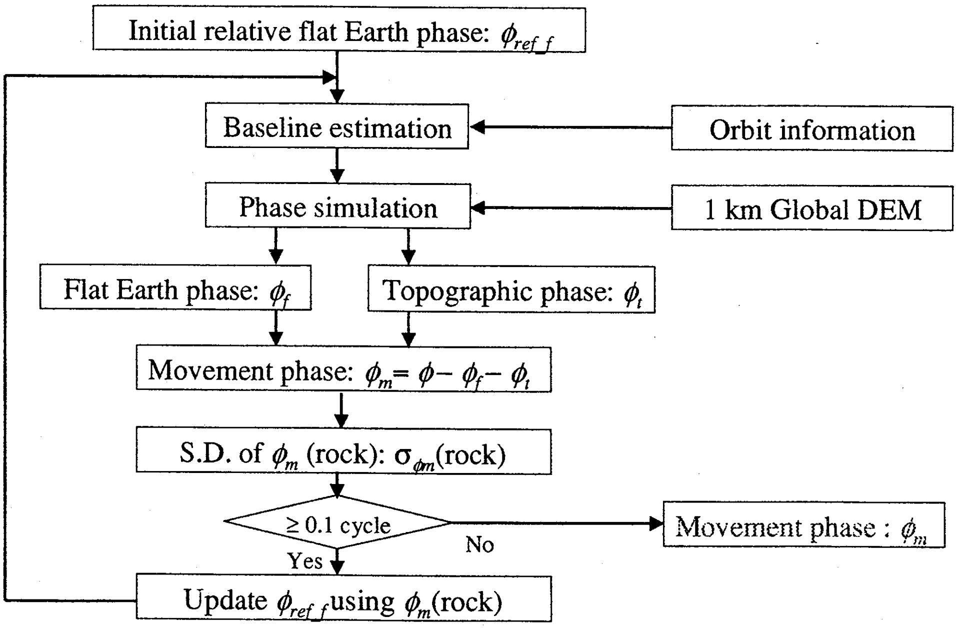

Fig. 2. Processing flow.

3. Results

3.1 Motion field

The interferogram from a pair of April and June is estimated to have the smallest baseline among three interferograms, because phase fringes are the sparsest. Therefore, it (ϕ_2) is firstly processed. The initial and three decomposed phases after processing described in 2.3 is shown in Fig. 3. Movement phase converged after only two times iteration. Calculated baseline, ranges of flat earth and topographic phases and Standard deviation of movement phase over bare rock areas are shown in Table 1. As anticipated, the estimated baseline is small (33 m), so topographic phase changes only 0.4 cycles. Fig. 4 shows histograms of movement phase over bare rock areas at first and second iterations. Table 1 and Fig. 4 shows a small improvement after iterations, but this is due to a small baseline. Criteria of convergence of movement phase over bare rock areas is 0.1 cycle, and this is based on the fact that 0.1 cycle corresponds to only 1 cm movement.

3.2 Decomposition of 3 elements

Based on an assumption of the movement parallel to slope, measured movement in line-of-sight direction is decomposed into three components. Fig. 5 shows the result. Each component is scaled to the range from each minimum to maximum. Fig 5 shows that the dominant movement is the range direction (x) and that high speed parts exist between bare rocks A and B, at the center from bottom-right to top-left direction, and at the top-right.

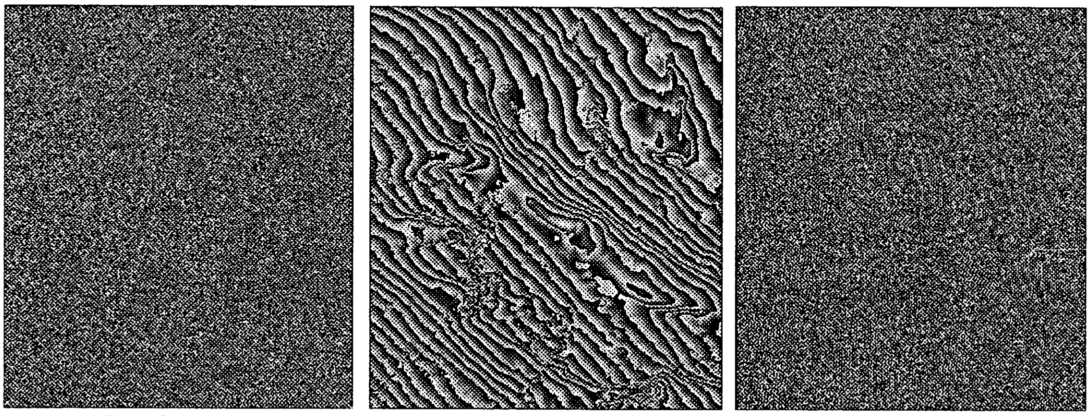

(a) Interferogram-1 (b) Interferogram-2 (c) Interferogram-3

Fig. 3. Initial interferograms.

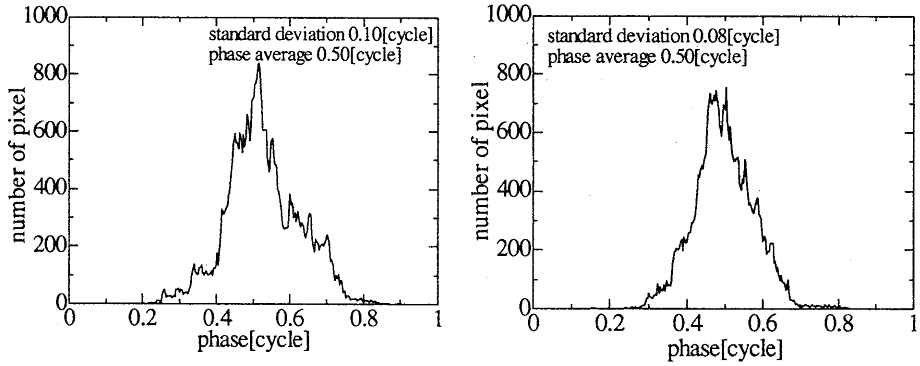

(a) Iteration 1 (b) Iteration 2

Fig. 4 Histograms of movement phase over bare rock areas from interferogram-2.

Table 1 Estimated baseline and phases from interferogram-2

iteration	$B_\perp$(m) [height change]	ϕ_f(cycle) min/max	ϕ_t(cycle) min/max	$\sigma_{\phi m}$(cycle) over rock
1	32.1 [2010m]	−18.7/23.3	1.0/1.4	0.10
2	33.0 [2070m]	−19.4/23.8	1.0/1.4	0.08

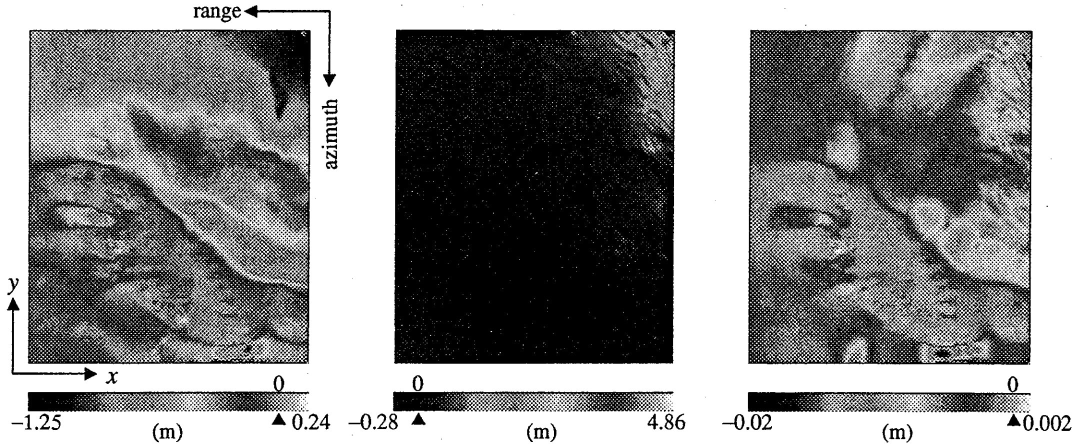

(a) x component (b) y component (c) z component

Fig. 5 Decomposition of derived movements from interferogram-2.

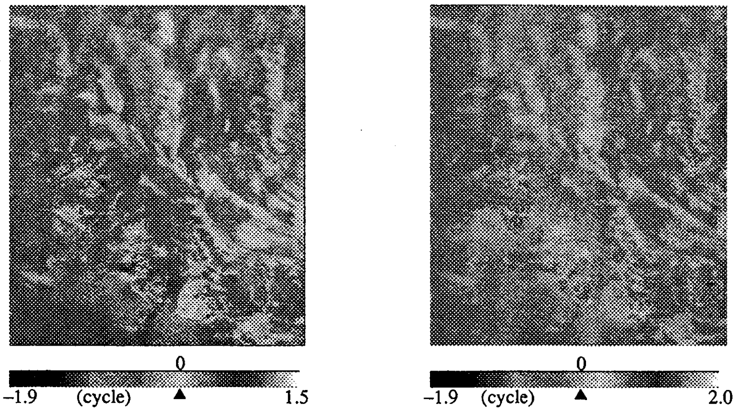

(a) Interferogram-1 (b) Interferogram-2

Fig. 6 Differentials of movement phase from the interfergram-2.

3.3 Change of motion speed

The same approach was applied to other two interferograms shown in Fig. 3, and then movement phases were derived. Fig. 6 shows differential phases of movement phase from the middle interferogram (ϕ_{2m}). These phases mean deviation from a constant velocity or acceleration of ice movement. We can find negative areas in $\phi_{1m}-\phi_{2m}$ around bare rocks, and those areas are positive in $\phi_{3m}-\phi_{2m}$. This shows that a constant movement is invalid over this area and some acceleration exits around bare rocks.

3. Conclusion

We succeeded to extract surface movements in the Yamato mountains area, and detect change of motion speed from a series of three JERS-1 SAR interferograms. Results suggest that movement is not constant over the study are, and variations of ice motion speed and acceleration exit around bare rocks. Further discussion based on hydrodynamics will clarify details of this phenomenon. This approach is expected to expand JERS-1 InSAR applications in the Antarctica.

References

[1] Goldstein R. M., H. Englehardt, B. Kamb and R. M. Frolich, "Satellite radar interferometry for monitoring ice sheet motion: Application to an Antarctic Ice Stream," Science, vol. 262, no. 1, pp. 525-1,530, 1993.

[2] R. Kwok and M. A. Fahnestock, "Ice sheet motion and topography from radar interferometry," IEEE TGRS, vol.34, no.1, 189-220, 1996.

[3] H. Kimura, F. Nishio, Y. Yamaguchi, T. Furukawa and K. Cho, Application of JERS-1 SAR interferometry, JERS-1 Science Program '99 PI Reports, pp.149-156, NASDA, 1999.

[4] T. Ozawa, K. Doi and K. Shibuya, "A case study of generating a digital elevation model for the Soya coast area, Antarctica, using JERS-1 SAR interferometry," Polar Geoscience, no.12, pp.227-239, 1999.

Earth Radiation Budget

TOA and Surface Radiation Budget from Satellites: Current developments and perspectives

Rainer Hollmann[1]
Institute for Coastal Research, GKSS Research Centre, Geesthacht, Germany

[1] now at Deutscher Wetterdienst, Satellitengestützes Klimamonitoring, Offenbach, Germany
E-mail: rainer.hollmann@dwd.de

Abstract

The radiation budget at the top of the atmosphere (TOA) and at the surface is of fundamental importance for monitoring and understanding the climate system and for many practical applications. Increasing concentrations of greenhouse gases are believed to be responsible for changing the radiation budget and for driving global warming. These changes may include stresses on water availability, which are of particular concern in different areas in the world. The components of the radiation budget at the TOA and at the surface must therefore be monitored over extended periods of time, both to evaluate and improve climate model predictions and to provide essential climatological information. The surface radiation budget plays a key role in determining the surface temperature and evaporation and hence the hydrological cycle. There are many practical applications (e.g. weather forecasting, hydrology and agriculture) over a wide range of timescales that require information on the surface radiation budget. For climate monitoring, evaluating climate models and for these practical applications, it is thus essential that high quality measurements of the radiation balance both at the top of the atmosphere and at the surface should be available.

1. The importance of TOA and surface radiation for climate modelling and studies

Defining the radiative energy exchange at the top of the Earth-atmosphere system and the Earth's surface has long been identified as key to the description of climate and identifying climate change processes (World Meteorological Organization, 1983; Suttles and Ohring, 1986). While the top-of-atmosphere (TOA) radiative energy exchange represents the response of the entire Earth-atmosphere system to the extraterrestrial irradiance by the Sun, the surface constitutes the energy exchange between the atmosphere and the Earth-surface itself. This exchange is accomplished by radiative, sensible and latent heating processes. Recent results from the Atmospheric Model Intercomparison Project (AMIP, Wild, personal communication) show that atmospheric GCM's show a range of globally averaged surface absorbed solar radiation from 148 Wm^{-2} to 180 Wm^{-2} and downwelling thermal infrared fluxes ranging from 325 Wm^{-2} to 359 Wm^{-2}. This indicates that the partitioning of radiative energy between the surface and atmosphere within these models is still uncertain to over 30 Wm^{-2}. Additionally, the incorporation of aerosols and their radiative effects in these models is still relatively crude and the uncertainties for the radiative effects of aerosols are still large (IPCC Assessment, 2001).

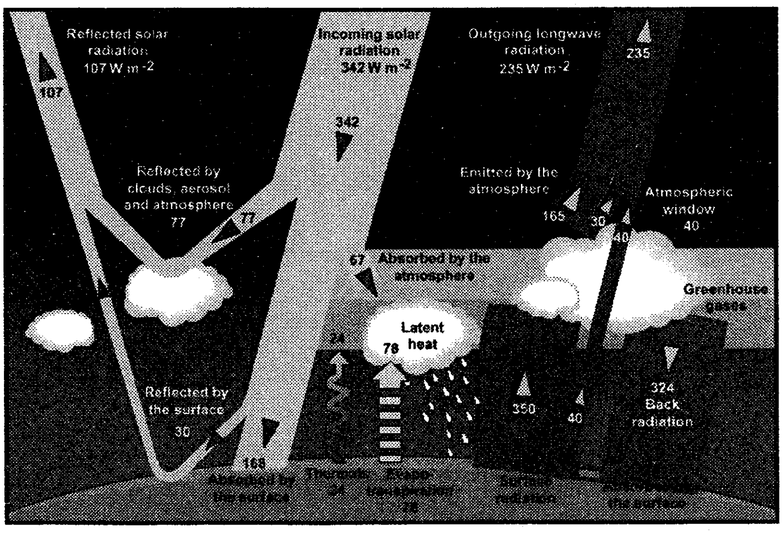

Fig. 1: The global energy cycle (Kiehl and Trenberth, 1997)

An accurate TOA radiative budget together with a SRB closes the atmospheric radiative budget determining the absorbed radiative energy by both the atmosphere and at the surface and improving calculations of implied heat transports within the Earth-atmosphere system. The understanding of global and regional climates and climate variability is crucially dependent upon these processes.

2. Current developments in TOA Radiation Budget from satellites

In this part two recent instruments to measure the TOA radiation will be shortly introduced. Beside them there is the most popular and well known Cloud's and the Earth Radiant Energy System (CERES) which is mounted to the TRMM, EOS TERRA and AQUA satellites and will be integrated to EOS AURA as well. A lot of detailed information can be obtained from the following CERES webpage at NASA Langley Research Center: http://asd-www.larc.nasa.gov/ceres/ASDceres.html. See also the papers by Wielicki et al. (1995 & 1998).

2.1 Scanner for Radiation Budget (ScaRaB)

Likewise CERES, the Scanner for Radiation Budget (ScaRaB) (Kandel *et al.* 1998) has been a recent successor of the scanning broadband instruments used by ERBE on a polar orbiting satellite. ScaRaB has four channels, a visible (0.5 to 0.7 µm), a shortwave (0.2 to 4.0 µm), an atmospheric window (10.5 to 12.5 µm) and a total channel (0.2 to 50. µm).

From March 1994 to March 1995 ScaRaB was flown in a non-sunsynchronous orbit. The height was about 1200 km, so that the field of view of the instrument for the nadir pixel is approximately 60 by 60 km_ (Viollier *et al.* 1995). One main emphasis during the development of ScaRaB was on calibration. The calibration error before launch was obtained to be less than 1.5% in the solar domain (Mueller *et al.* 1997). Bess *et al.* (1997) compared measurements of March 1994 ScaRaB observations with collocated ERBS nonscanner observations. Both data sets agree to 0.76 W/m_ for shortwave fluxes, to 0.55 W/m_ and 3.8 W/m_ for longwave fluxes at night and day, respectively.

2.2 Geostationary Earth Radiation Budget Instrument (GERB)

All the satellites carrying Earth Radiation Budget (ERB) instrumentation so far are on polar or other low Earth orbits. Four such satellites could provide coverage of the diurnal cycle with a temporal resolution of 3 hours (each of which provides 2 measurements per day), if the equator crossing times are arranged at this separation. It is most unlikely that four satellites will be available at one time. Furthermore, even a 3 hourly sampling still represents rudimentary temporal resolution. At least hourly measurements are needed to resolve the diurnal cycle of tropical convection properly, and no practicable system of polar orbiting or other LEO satellites can deliver this. It appears that the only viable solution to the problem of diurnal sampling of the Earth's radiation budget is the inclusion of suitable sensors on the operational geostationary satellites. For the first time ever a Geostationary Earth Radiation Budget instrument (GERB) has been launched on the Meteosat Second Generation (MSG) geostationary satellite in August 2002. It will become operationally after the commissioning period in late January 2004 together with main instrument onboard which is the SEVIRI imager.

The Instrument Optical Unit (IOU, Fig. 2) of GERB contains the main parts of the instrument: Telescope, detector, filter and calibration sources. GERB measures in two spectral broadband channels: total band 0.32µm -> 30µm, and a shortwave (SW) band 0.32µm - 4.0µm. By subtraction the IR band, 4.0µm ->30µm, is obtained. A removable quartz filter placed in and out of the beam at the front of the telescope provides the switching between bands. In order for the detectors to receive sufficient energy to meet the signal-to-noise requirement during each 15 minute MSG product, GERB removes the satellite spin by means of a rotating mirror which increases the length of available exposure per spin.

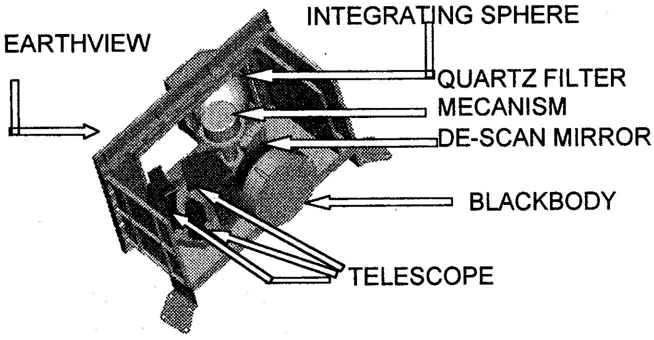

Fig. 2: The Instrument Optics Unit (IOU) of GERB. The systems are seen from inside MSG. The Earth is viewed through the window in the background. Three mirrors of the telescope are visible (a fourth folding mirror and the detector assembly are concealed).

The detector is a 256 element blackened thermoelectric array, mounted along the N-S direction, with broadband spectral coverage from 0.32 -> 30 µm. GERB is calibrated in orbit by an on-board blackbody and space view. Possible degradation of the SW spectral response can be corrected by means of occasional comparisons with a pre-flight characterised solar-illuminated integrating sphere on board. The basic measurement cycle comprises data from a channel covering the complete spectrum, and those from a SW channel, in which a quartz filter absorbs radiation of wavelength greater than 4µm.

As thermal detectors cannot register a complete East-West image within the time Earth is in the Field-of-View during one satellite rotation, the Line-of-Sight of the instrument is pointed continuously at a fixed location on Earth by the de-spin mirror. During this time, a complete North-South image column of 256 pixels is measured by the 256 detector array. At the next revolution of the satellite, another image column is measured. Thus, it takes approximately 2.5 minutes to obtain one image. During the next 2.5 minutes the procedure is repeated with the quartz filter in place. Three images with and without filter are averaged to meet the noise requirements. A full set of measurements is completed every 15 minutes.

The spatial sampling in the North - South direction is determined by the distance of the detector elements on the array which gives 1.25 mrad or 44.5 km at nadir.

Information about the instruments are given in http://www.ssd.rl.ac.uk/gerb/ and http://gerb.oma.be/ as well in Mueller et al. (1999).

3. Current developments in Surface Radiation Budget

The most direct effect of increased atmospheric concentration of greenhouse gases experienced at the surface is an enhanced longwave downward radiation (DLF). DLF is expected to undergo the largest change of all radiative and surface energy balance components, as the following Tab. 2 is demonstrating. These are ECHAM-4 model based estimates for changes in the energy balance in the atmosphere based on a change scenario 2 x CO_2 (Wild (2003), pers. Communication). Further more an increase in DLF will be detectable more quickly and thus emerging from the background noise in the data than the widely used surface temperature records will do.

Fluxes at TOA:	
Shortwave absorption	$+0.6\ Wm^{-2}$
Longwave emission	$-\ 0.3\ Wm^{-2}$
Fluxes at surface:	
Shortwave absorption	$-\ 1.5\ Wm^{-2}$
Sensible heat flux	$+\ 0.3\ Wm^{-2}$
Latent heat flux	$+\ 1.8\ Wm^{-2}$
Longwave upward radiation	$+\ 9.8\ Wm^{-2}$
Longwave downward radiation	**$+\ 13.4\ Wm^{-2}$**

Tab. 1: Estimate of changes due to a 2x CO_2 Szenario. (Wild 2003, pers. Communication)

From this it is evident to have a closer look into the variations of measured DLF on global and regional scale. Direct measurements of the surface radiation balance have been made from a few well instrumented stations for a few decades. The geographical distribution is extremely heterogeneous; there are virtually no measurements over the oceans, except during dedicated field experiments. Over land, the stations are biased towards the more populated areas such as Europe and North America, which is in part due to the established market for these data for meteorological, hydrological and climatological applications. Only limited amounts of data are available over large areas of the land surface, for example Africa and Asia. The data have been quality controlled and archived in the invaluable Global Energy Balance Archive (GEBA) by ETH Zurich. A few high quality observations have been made through the Baseline Surface Radiation Network (BSRN) (Fig. 5). Given the difficulties with obtaining sufficient direct measurements, many attempts have been made to infer the surface radiation budget from satellite data, culminating in the WCRP Surface Radiation Budget (SRB) project.

A first analysis of surface measurements from BSRN shows that the signal is at the moment not significant on the 95 % level at any station (Wild (2003) pers. Communication).

3.1 SRB-GEWEX project

Within the framework of the Global Energy and Water cycle experiment (GEWEX), in the beginning of the 1980's the SRB project has been established. The first data set (Whitlock et al., 1995) which was delivered a few years ago consists of 8 year of SRB data derived from satellites covering the period up to 1991. During the past years the NASA/GEWEX SRB Project has worked toward developing and assessing a climatology spanning from July 1983 – Oct 1995 at the spatial resolution of 1°x1°. The data set including surface and TOA shortwave (0.2 to 4.0 μm) fluxes and longwave surface fluxes (4.0 to 50 μm) was just recently completed and is available from the Langley archive DAAC (Gupta et al., 1999).

3.2 Satellite Application Facility on Climate Monitoring CM-SAF

In Europe in the phase of redefinition of the EUMETSAT ground segment, seven, so called Satellite Application Facilities (SAF), have been established, each of them serving dedicated user groups.

The SAF on Climate Monitoring (CM-SAF) will deliver a comprehensive set of climate variables, ranging from different cloud products, radiation budget at the top of the atmosphere (TOA), surface radiation budget (SRB), tropospheric humidity (Tab. 2). It derives a consistent dataset of cloud and radiation products in a high spatial resolution on a common grid. The CM-SAF is using satellite data from the new MSG (METEOSAT Second Generation) satellite and the available operational polar orbiting satellites (e.g. NOAA, in future METOP as well) to produce the SRB for Europe and part of the North Atlantic Ocean.

The CM-SAF is using existent well calibrated algorithms to obtain the SRB. Therefore the Gupta algorithm (Gupta et al., 1989, 1992) has been chosen for the longwave spectral domain. For the calculation of the surface incoming shortwave flux (SIS) an algorithm similar to the one developed by Pinker (e.g. Pinker and Laszlo, 1992) is used. The basic idea for the algorithm is that a relationship between the broadband (0.2-4.0 μm) atmospheric transmittance and the reflectance at the top of the atmosphere (TOA) does exist. Once the transmittance is determined from the TOA albedo, the surface irradiance can be computed from the incoming solar flux at the top of the atmosphere and the atmospheric transmittance. With a radiative transfer model, the broadband atmospheric transmittance is calculated once in relationship to the broadband TOA albedo for a variety of atmospheric and surface states. The actual computation of the surface irradiance involves two steps. First the broadband TOA albedo and the surface broadband albedo is determined from the satellite measurement. Then the atmospheric transmittance is determined from the TOA albedo together with information on the atmospheric and surface state from the pre-computed tables.

Product	**Resolution**				
	Spatial	**Temporal**			
		Daily	**Weekly**	**Monthly**	**MMDC**
Fractional cloud cover	15 x 15 km_	✓		✓	✓
Cloud type	15 x 15 km_	✓		✓	✓
Cloud top temperature and height	15 x 15 km_	✓		✓	✓
Cloud optical thickness	15 x 15 km_	✓		✓	✓
Cloud phase	15 x 15 km_	✓		✓	✓
Cloud water path	15 x 15 km_	✓		✓	✓
Surface incoming short-wave radiation	15 x 15 km_	✓		✓	✓
Surface albedo	15 x 15 km_		✓	✓	
Surface net short-wave radiation	15 x 15 km_	✓		✓	✓
Surface outgoing long-wave radiation	15 x 15 km_			✓	✓
Surface downward long-wave radiation	15 x 15 km_			✓	✓
Surface net long-wave radiation	15 x 15 km_			✓	✓
Surface radiation budget	15 x 15 km_			✓	✓
Incoming solar radiative flux at TOA	(50 km)^2	✓		✓	✓
Reflected solar radiative flux at TOA	50x100 km^2(150 km)^2	✓		✓	✓
Emitted thermal radiative flux at TOA	50x100 km^2(150 km)^2	✓		✓	✓
Humidity composite product	≤ 1 degree; ≥ 3 layers				

Tab. 2: Overview of CM-SAF products. For areas outside the field of view of MSG, the monthly mean diurnal cycle (MMDC) will not be calculated.

Input parameters into the algorithm are the broadband TOA albedo, solar zenith angle, surface albedo, cloud properties, aerosol and ozone data and the total water vapour content of the atmosphere. The broadband TOA albedo for the area covered by the MSG satellite, the surface albedo and the cloud properties are derived by other groups within the CM-SAF. All other input data are either from climatological data sets (aerosol, ozone) or NWP-data (water vapour). Depending on the availability of appropriate data sets, satellite derived values will be used. To calculate the TOA albedo for the CM-SAF region not covered by the MSG satellite, a narrow-to-broadband conversion of the satellite data is used. Further information can be obtained from http://www.cmsaf.dwd.de/ (Woick et al. (2002) and Hollmann and Gratzki, (2002))

3.3 Validation of SRB products

The surface radiation fluxes will be validated with all available surface measurements (e.g. BRSN sites, NMHSs networks) to ensure a good quality of the data.

An operational network is the Baseline Surface Radiation Network (BSRN, Ohmura, 1998), initiated by the World Climate Research Program (WCRP). BSRN measures, quality controls and archives surface radiation measurements from dedicated stations around the world. All stations use the same instruments, and common

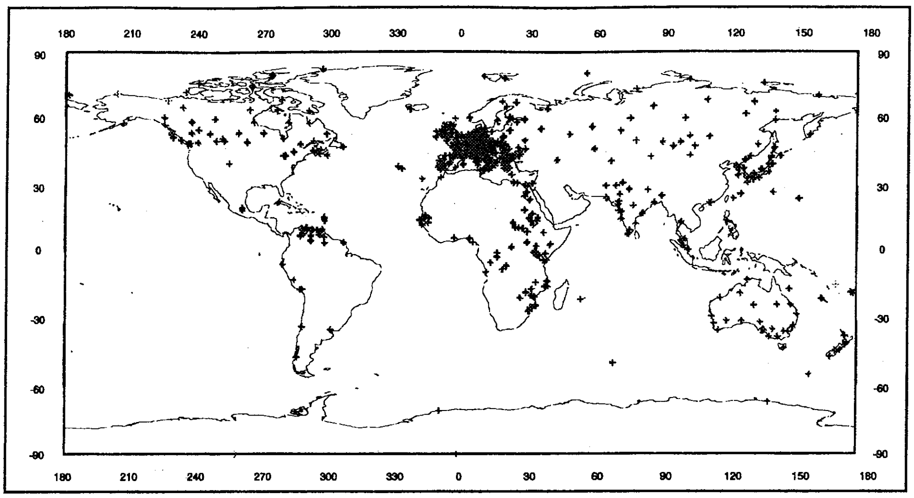

Fig. 3: SW Daily and monthly mean database from the World Radiation Data Center (WRDC) for 1986.

quality control procedures are performed on all measurements. One of the aims of the network is to provide high quality validation material for satellite remote sensing. In 2003, 35 stations were fully or partially operational. The basic measurement program comprises solar irradiance and downward longwave radiation. Measurements of other parameters are also done but not at every station. The data are archived at the World Radiation Monitoring Centre (WRMC) in Zurich, Switzerland. Fig. 4 and Fig. 5 give an overview of available data for validation. It can cleary been seen that the surface measurements of SIS are very often and widely common, whereas the SDL component is only measurement very sparsely around the globe. The database is available from the ETH Zurich (Switzerland, http://bsrn.ethz.ch)

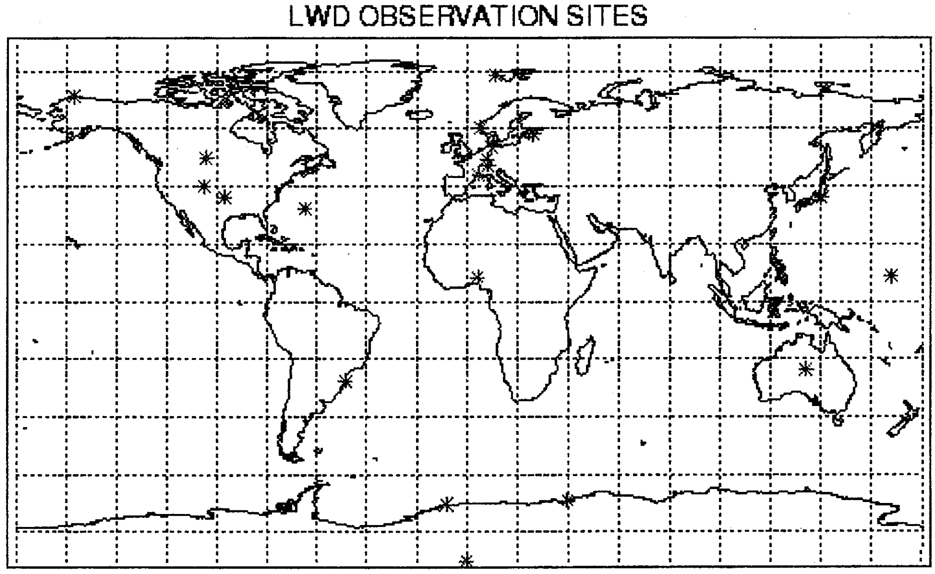

Fig. 4: worldwide distribution of DLF observation sites as currently available from BSRN. (http://bsrn.ethz.ch)

References

Bess, T. D., G. L. Smith, R. N. Green, D. A. Rutan, R. S. Kandel, P. Raberanto, and M. Viollier (1997): Intercomparison of scanning radiometer for radiation budget (ScaRaB) and earth radiation budget experiment (ERBE) results, *Preprints of 9th conference on atmospheric radiation, Long Beach (CAL), Amer. Meteorol. Soc.*, Boston, 203-207.

Gilgen, H. and A. Ohmura (1999): The Global Energy Balance Archive. *Bull. Amer. Meteorol. Soc.*, **80**, 831-850.

Gupta, S.K. (1989): A Parameterisation for Longwave Surface Radiation from Sun-Synchronous Satellite Data, *J. Climate, 2*, 302-315.

Gupta, S. K., W. L. Darnell, and A. C. Wilber (1992): A parameterization of longwave surface radiation from satellite data: Recent improvements. *J. Appl. Meteor.*, **31**, 1361-1367.

Gupta, S.K., N.A. Ritchey, A.C. Wilber, C.H. Whitlock, G.G. Gibson and Paul W. Stackhouse (1999): A climatology of surface radiation budgets derived from satellite data, *J. Climate*, **12,** 2691-2710.

Hollmann, R. and Gratzki, A., 2002: The satellite derived surface radiation budget for BALTEX. *Boreal Env. Res.*, 7, 247-251.

IPCC Assessment, *Climate Change 2001: The Scientific Basis*. Cambridge University Press

Kandel, R., M. Viollier, P. Raberanto, J. Ph. Duvel, L. A. Pakhomov, V. A. Golovko, A. P. Trishchenko, J. Mueller, R. Stuhlmann, and E. Raschke (1998): The ScaRaB Earth Radiation Budget Datasets. *Bull. Amer. Meteorol. Soc*, **79**, 765.

Kiehl J.T., and K. E Trenberth (1997): Earth's Annual Global Mean Energy Budget. *Bull. Amer. Meteorol. Soc.* **78**, 197-208.

Mueller, J., R. Stuhlmann, R. Becker, E. Raschke, H. Rinck, P. Burkert, J.-L. Monge, F. Sirou, R. Kandel, T. Tremas, and L. A. Pakhomov (1997): Ground characterisation of the Scanner for Radiation Budget (ScaRaB) flight model 1, *J. Atmos. Oceanic. Technol.*, **14**, 802.

Mueller, J., Stuhlmann, R., Dammann, K., Hollman, R., Harries, J.E., Kellock, S., Mossavati, R., Wrigley, R.T., Crommelynck, D., Dewitte, S., Allan, P., Caldwell, M. and Sawyer, E., 1999: GERB: An earth radiation budget instrument on second generation Meteosat, Adv. Space Res., **24**, 921-924.

Ohmura, A. (1998): Baseline Surface Radiation Network (BSRN/WCRP): new precision radiometry for climate research. *Bull Amer. Meteorol. Soc.*, **79,** 2115-2136.

Pinker, R. and I. Laszlo (1992): Modelling of surface solar irradiance for satellite applications on a global scale. *J. Appl. Meteor.*, **24,** 389-401.

Suttles, J.T. and G. Ohring, eds., (1986): Surface radiation budget for climate application, NASA RP-1169, NASA, Washington, D.C., 132 pp.

Viollier, M., R. Kandel, and P. Raberanto, (1995): Inversion and space-time-averaging algorithms for ScaRaB (Scanner for Radiation Budget). Comparison with ERBE, *Ann. Geophysicae*, **13**, 959.

Whitlock, C. H. et al. (1995): First global WCRP Shortwave Surface Tadiation Budget Dataset. *Bull. Amer. Meteorol. Soc.*, **76**, 905-922.

Wielicki et al. (1996): Clouds and the earth's radiant energy system (CERES): an Earth Observing System experiment. *Bull Amer. Meteorol. Soc.*, **77,** 853-868.

Wielicki, B. A. et al., (1998): Clouds and the Earth's Radiant Energy System (CERES): Algorithm Overview. IEEE Trans. Geosc. Rem. Sens., **36,** 1127-1141.

Woick, H., Dewitte, S., Feijt, A., Gratzki, A., Hechler, P., Hollmann, R., Karlsson, K.-G., Laine, V., Löwe, P., Nitsche, H., Werscheck, M. and Wollenweber, G., 2002: The Satellite Application Facility on climate monitoring, Adv. Space Res., **30**, 2405-2410.

World Meteorological Organization, 1983: Satellite systems to measure the Earth's radiation budget parameters and climate change signals, World Climate Programme, Geneva, Switzerland, *Rep. WCP-70*, 36 pp.

LATITUDINAL DISTRIBUTION OF SOLAR RADIATION UNDER CLEAR AND CLOUDY CONDITIONS ON THE TERRITORY OF MONGOLIA

Nas-Urt Tugjsuren

Mongolian University of Science and Technology, Ulaanbaatar-46/157
Center for Environmental Remote Sensing, Chiba University,
Chiba, 263-8522 Japan
Email: tugjurn@must.edu.mn
Email:<tugjsur@ceres.cr.chiba-u.ac.jp>

Abstract

The goal of this study is to determine the latitudinal distribution of solar radiation on the territory of Mongolia using solar radiation measurement data from the routine actinometrical stations and solar radiation measurement point of Mongolian State University. Last 20 years (1981-2001), we have studied the global, direct and diffuse solar radiation on the Earth horizontal surface under clear and cloudy skies in three ranges of latitude; $\varphi = 43.0^0-45.0^0$, $45.1^0-47.0^0$, $47.1^0-49.8^0$.

Amount of direct solar radiation increases in all considered latitudes from January to June and after that symmetrically decreases, while on the latitude range $45.1^0-47.0^0$ this amount is greater than on two other ranges. At noonday (12^h30^m), June average amounts of direct solar radiation are 865W/m^2 ($\varphi = 43.0^0-45.0^0$), 822 W/m^2 ($45.1^0-47.0^0$), 786 W/m^2 ($47.1^0-49.0^0$), but these values are less by 2.4 times for noonday in January.

Investigation of diurnal change of diffuse radiation incoming on horizontal surface in clear sky condition shows that the amount of this radiation on the latitude range of $43.1^0-45.0^0$ in any month slowly increases from morning to noonday with following decrease, while the same behavior of radiation is maintained in January-July and October-December period and the period of August-September diffuse radiation amount significantly decreases on latitudinal range of $45.1^0-49.0^0$ in noonday.

Amount of global solar radiation reaches maximum in noonday in June, namely 796-1040 W/m^2 ($\varphi = 43.0^0-45.0^0$), 838-936 W/m^2 ($45.1^0-47.0^0$), 842-922 W/m^2 ($47.1^0-49.0^0$) in the case of clear sky. But in the case of cloudy sky the amount of global solar radiation reaches maximum in noonday of May, which could be explained by peculiarity of recurrence of cloudiness, cloudy shape and optical properties of atmosphere on Mongolian territory.

1. Introduction

The amount of solar radiation reaching the Earth's surface varies greatly because of changing optical properties of atmosphere and the changing mutual position of the Sun and Earth, both during the day and throughout the year. As solar radiation passes trough the Earth's atmosphere, some of it is absorbed or scattered by air molecules, water vapor, aerosols, and clouds.

Investigation of solar radiation types (direct, diffuse and global radiation) and evolution, as well as nature of its regularities in the particular region are practical and scientific importance in development of agriculture, protection of public health, usage of solar energy, creating construction, compiling weather forecasts and etc. On the other hand, solar radiation drives atmospheric circulation. Since solar radiation represents almost all the energy available to the Earth, accounting for solar radiation and how it interacts with the atmosphere and the earth's surface is fundamental to understanding the earth's energy budget.

Mongolia is located in the northern part of Central Asia bordering with Russian Federation and the People's Republic of China. The total size of the territory is 1567 thousand square kilometers. The mean elevation of Mongolia is about 1500 meters above sea level which enhances the sharp continental climate, with warm, short summers, and cold, long winters. There is a short rainy season in June, July and August during which most of the yearly rain falls. Around 67-78 percent of all precipitation falls during these three summer months. The country averages 257 cloudless days a year, and it is usually at the center of a region of high atmospheric pressure.

2. Measurement and data

This study is based on the Climatic handbook of Mongolia and the results of Geophysical Center of Mongolian State University and Department of Physics of Mongolian University of Science and Technology research on the solar radiation. Last 20 years, we have studied the global, direct and diffuse solar radiation on the Earth horizontal surface under clear and cloudy skies in three ranges of latitude; φ = 43.0^0-45.0^0, 45.1^0-47.0^0, 47.1^0-49.8^0.

For the direct solar radiation were used thermo-electric Actinometer M-3 (AT50), which measures radiation at normal incidence. Global radiation is measured by Pyronometer M-80M with a black and white type sensor. These instruments produced in the former USSR. Diffuse radiation can either be derived from the direct radiation and the global radiation or measured by shading a pyronometer from the direct radiation so that the thermopile is only receiving the diffuse radiation.

Daily total global (Q_d) solar radiation is determined as:

$$\sum Q_d = \frac{Q_1}{2}\tau_1 + T\left(\frac{Q_1}{2} + Q_2 + Q_3 + \cdots + \frac{Q_N}{2}\right) + \frac{Q_N}{2}\tau_2 . \qquad (2.1)$$

where $Q_1, Q_2, ..Q_N$ is the measured global solar radiation at the observation time, τ_1 is the difference between of sunrise time on the given latitude and time of the first observation time of day. Standard meteorological observation time's difference is 3 hours in Mongolia, on this account T is the equal 180 minutes, τ_2 is the difference between of last observation time and sunset time.

3. Results and discussion

3.1. Direct Solar Radiation (S). The solar radiation that passes through directly to the Earth's surface is called direct solar radiation. Direct solar radiation incoming to the surface perpendicular to solar beam (S) is used for calculation of direct radiation on horizontal surface (S') by formula: $S' = S\sin h_0$, where h_0 is the Sun height.

Researches have studied dependence of direct solar radiation on particular surface from Sun height and optical properties of atmosphere. Investigation in this field was carried out in Research Center for Geophysics, Mongolian State University and Department of physics of Mongolian University of Science and Technology, for almost 20 years [2,3].

In clear sky conditions amount of direct radiation, incoming on the horizontal surface is at maximum in June, and at minimum in January on any latitude on the territory of Mongolia (Fig.1).

At noonday (12^h30^m), June average amounts of direct radiation are 865W/m^2 (φ = 43.0^0-45.0^0), 822 W/m^2 (45.1^0-47.0^0), 786 W/m^2 (47.1^0-49.0^0), but these values are less by 2.4 times for noonday in January. On the territory of Mongolia in the direct solar radiation decreases as the latitude increases. On the same latitude incident angle and intensity of solar radiation are the same. But in some cases depending on feature of landscape and atmospheric optical properties above mentioned regularities are not possible to observe.

Amount of direct solar radiation increases in all considered latitudes from January to June and after that symmetrically decreases, while on the latitude range 45.1^0-47.0^0 this amount is greater than on two other ranges. The amount of direct radiation incoming on horizontal surface under cloudy skies on all latitudinal ranges increases from January and reaches maximum in May ($\approx$501 W/m^2) and from June again decreases (Fig.2).

Furthermore the amount of direct radiation increases slowly on the range of 43.1^0-47.0^0 till August and decreases from September and August on 43.1^0-45.0^0 and to north of 45.1^0 respectively.

3.2.Diffuse Solar Radiation (D). A diffuse solar radiation is the total scattered radiation coming from celestial sphere. It is recognized that following Sun height decreases and increase in air pollution the amount of diffuse radiation increases. Diffuse solar radiation represents the short wave energy of solar origin scattered downwards by gas molecules, aerosols (or suspended particulate matter),water vapor and clouds in the atmosphere. Scattering of solar radiation on gas molecules with linear size, less than 0.1 fraction of its wavelength follows the Rayleigh law. The variability in the amount and type of cloud has a dominant role on the value of diffuse radiation. A cloud, which is not screening the Sun, considerably increases amount of diffuse radiation compared to clear sky, namely fleecy clouds lead to increase in diffuse radiation 4-5 times higher than that of clear sky. Also, snowy cover reflects back 70-80 % of incoming direct radiation (snow covers Mongolia between November and April of next year), which significantly increases amount of diffuse radiation [2.3]. On Fig.3 and 4 are shown annual changes of diffuse radiation amount for both cloudy and clear skies.

Investigation of diurnal change of diffuse radiation incoming on horizontal surface in clear sky condition shows that the amount of this radiation on the latitude range of 43.1^0-45.0^0 in any month slowly increases from morning to noonday with following decrease, while the same behavior of radiation is maintained in January-July and October-December period and the period of August-September diffuse radiation amount significantly decreases on latitudinal range of 45.1^0-49.0^0 in noonday. (Coment!) On any latitude amount of diffuse radiation incoming on horizontal surface in clear sky condition slowly increases in January-May, with slow decrease, while diffuse radiation decreases as latitude increases. After June on low latitudes diffuse radiation has a tendency to decrease. Amount of diffuse radiation is often greater in cloudy sky condition than in clear one and their ratio equals to 2, but common feature is maintained.

Diffuse radiation in cloudy sky increases from the morning to noonday with symmetrical decrease in the afternoon. In winter months amount of diffuse radiation increases, that is explained by small Sun height and snowy cover on the territory of Mongolia.

A smoke screen covers Ulaanbaatar, capital city of Mongolia, between the period of October and May next year. Diffuse radiation amount significantly increases in this period. The range of air pollution dispersion is mainly dependent on wind speed and under normal conditions.

3.3. Global Solar Radiation (Q). The direct component of sunlight and the diffuse component of skylight falling together on a horizontal surface make up global solar radiation. A long time series of global radiation measurements allow to reveal general regularities of its change and dependence on the weather condition and astronomical and geographical factors. It is known that global radiation depends on Sun height, cloudiness and atmospheric transparency. There are regularities that the global radiation is proportional to atmospheric transparency and increasing of solar height. Also has a tendency to increase the global radiation, when atmospheric transparency is increased and solar height is constant.

A cloudy sky affects to a great degree to the global solar radiation. It is necessary to study a regime of temporal distribution of radiation during the year on entire and particular territory. Researchers have thoroughly investigated the effect of share and size of clouds on incoming radiation. The amount of global radiation incoming on the Earth's surface often greater in case of existing of medium level cloud of 3-4 points or high level cumulus cloud of 6-7 points respectively when sky is clear. When there is snowy cover on the Earth surface the global radiation becomes greater, because the reflected radiation from snowy cover which in turn reflects back from the cloud. Thus, total amount of global radiation is increased and ratio of global radiation can reach to 1.3, when comparing of snowy cover to clear sky. Fig.5 and Fig.6 show annual variation of global solar radiation for clear and cloudy skies on the horizontal surface. From fig.5 and fig.6 one can see a common feature of global solar radiation in case of both clear and cloudy skies that is increases till noonday and after that decreases almost symmetrically during the year.

Amount of global solar radiation reaches maximum in noonday in June, namely 796-1040 W/m^2 (φ = 43.0^0-45.0^0), 838-936 W/m^2 (45.1^0-47.0^0), 842-922 W/m^2 (47.1^0-49.0^0) in the case of clear sky. But in the case of cloudy sky the amount of global solar radiation reaches maximum in noonday of May, which could be explained by peculiarity of recurrence of cloudiness, cloudy shape and optical properties of atmosphere on Mongolian territory. Amount of global solar radiation increase with decreasing of latitude either in clear or in cloudy skies.

CONCLUSIONS

1. On cloudy sky condition, in any range of latitude direct solar radiation increases from January till June and then decreases symmetrically. But in the range 45.1^0-47.0^0 the values of direct radiation in February and May are greater than the other two ranges of latitude. This peculiarity is connected with the locations of these places and conditions of the atmosphere. We discovered that direct radiation on the horizontal surface in any range of these latitudes on cloudy days increases from January and reaches the maximum 384.0-501 W/m^2 in May then in June in all ranges it decreases in the same way. Further study of this change shows that in the zone with a latitude of 43.0^0-47.0^0 it increases relatively slowly until August and in latitude $\varphi = 43^0$-45^0 it decreases from September.

2. Daily changes of diffuse radiation on the horizontal surface on cloudless days at the latitude φ = 43.0^0-45.0^0 slowly increased from January till May and then decreases slowly. But in the range of latitude between 45.0^0 and 49.0^0 this situation remains the same from January to July and from October to December, and diffuse radiation decreases noticeable in the midday from August to September.

   Diffuse radiation on the horizontal surface increases on cloudy days in all months from morning till midday and then decreases. This peculiarity is explained by the cloudiness and optical properties of atmosphere.
3. Regardless of clear or cloudy sky conditions the numerical values of global radiation increases until noonday and then decreases. This changes occurs during the entire year. On clear sky condition, global radiation reached a maximum in the noonday of June and these values are 796-1040W/m^2 ($\varphi = 43^0$-45^0), 838-936 W/m^2 (45.1^0-47^0) and 842-922 W/m^2 (47.1^0-49^0) respectively. The field of global solar radiation for all months shows a primarily zonal pattern, that is, one in which radiation decreases with latitude.

References

1. Climatic Data Handbook for Mongolia ;1985, Ulaanbaatar, Mongolia
2. Tugjsuren N, 1996: Investigation of solar radiation regime on dry and cool zone crop-growing region of Mongolia, Science and Technology report, Science and Technology Information Center, Ulaanbaatar, Mongolia, 75 pp. (In Mongolian).
3. Tugjsuren N., T.Takamura, 2001: Investigation for photosynthetically active radiation regime in the Mongolian grain farm region, J. Agric. Meteorol. 57(4), 201-207

Appendix 1.

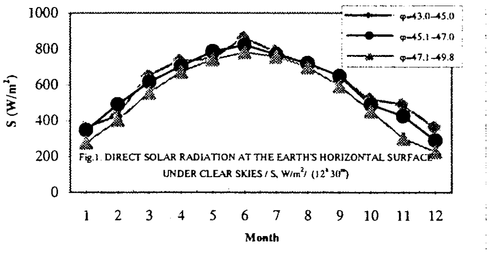

Fig.1. DIRECT SOLAR RADIATION AT THE EARTH'S HORIZONTAL SURFACE UNDER CLEAR SKIES / S, W/m^2/ (12^h30^m)

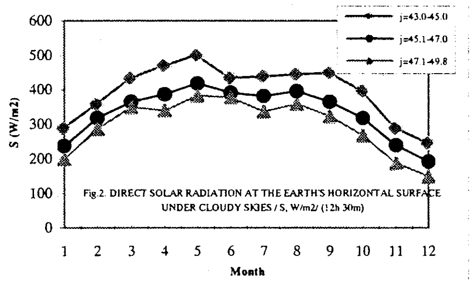

Fig.2. DIRECT SOLAR RADIATION AT THE EARTH'S HORIZONTAL SURFACE UNDER CLOUDY SKIES / S, W/m2/ (12h 30m)

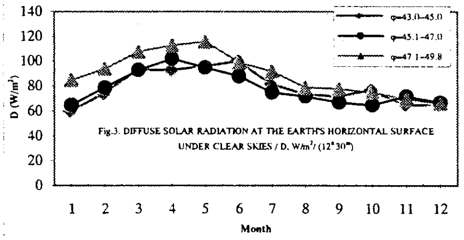

Fig.3. DIFFUSE SOLAR RADIATION AT THE EARTH'S HORIZONTAL SURFACE UNDER CLEAR SKIES / D, W/m^2/ (12^h30^m)

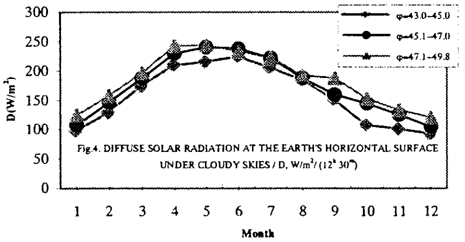

Fig.4. DIFFUSE SOLAR RADIATION AT THE EARTH'S HORIZONTAL SURFACE UNDER CLOUDY SKIES / D, W/m^2/ (12^h30^m)

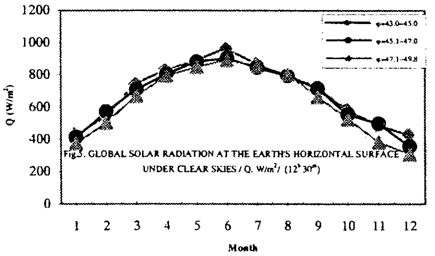

Fig.5. GLOBAL SOLAR RADIATION AT THE EARTH'S HORIZONTAL SURFACE UNDER CLEAR SKIES / Q, W/m^2/ (12^h30^m)

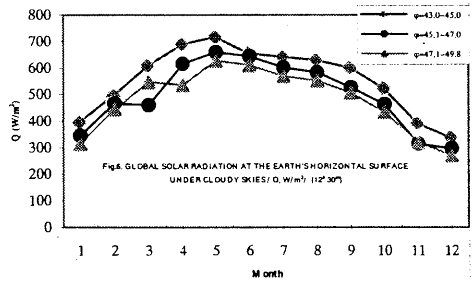

Fig.6. GLOBAL SOLAR RADIATION AT THE EARTH'S HORIZONTAL SURFACE UNDER CLOUDY SKIES / Q, W/m^2/ (12^h30^m)

Validation Experiment for Satellite Remote Sensing and Numerical Models of Low-Level Clouds: Shipboard Observation of YAMASE Clouds

Shoji ASANO[1)], Masaya KOJIMA[1)], Yukio YOSHIDA[1)], and Tamio TAKAMURA[2)]

1) Center for Atmospheric and Oceanic Studies, Tohoku University
(E-mail: asano@caos-a.geophys.tohoku.ac.jp, kojima@caos-a.geophys.tohoku.ac.jp,
yyoshida@caos-a.geophys.tohoku.ac.jp)
2) Center for Environmental Remote Sensing, Chiba University
(E-mail: takamura@ceres.cr.chiba-u.ac.jp)

Abstract
'*Yamase*' clouds are one of the typical marine boundary-layer clouds, and they appear over the North-Western Pacific Ocean east off the Sanriku area in early summer season under easterly cool winds, called *Yamase*, blown out from Okhotsk anti-cyclones. In order to validate numerical simulation and satellite remote sensing of *Yamase* clouds, we have carried out a few times of shipboard experiment in June of 2001, 2002, and 2003. Here we present an outline of the shipboard *Yamase* experiment and the preliminary results on atmospheric profiles and cloud structures for the *Yamase* event observed during 22June through 24 June 2003.

1. Introduction

Marine stratiform clouds appearing in the maritime atmospheric-boundary-layer (ABL) play a significant roll in the Earth's radiation balance due to their large horizontal extent, their long lifetime, and high reflectivity for solar radiation. The state-of-the-art performance of such numerical models as atmospheric general circulation models and weather prediction models is not good enough to simulate properly the low-level stratiform clouds mainly because of coarse spatial-resolution of these models. Generally, the marine stratiform clouds occur in a wide regional scale under some characteristic synoptic weather condition, but within the vertically thin ABL. Recently, many attempts have been done to simulate the boundary-layer clouds by using various cloud resolving models. However, even these high-resolution models still have difficulties to reproduce 'correct' features of cloud structure and physical properties; the simulated cloud structure and properties tend to differ for different models and/or resolutions used. Moreover, there are very few observational data available to validate the model performance. The cloud physical properties are generally different for different cloud types and different stages of the cloud lifetime, so they are highly variable with time and space. Satellite remote sensing is an efficient technique to observe wide distributions of cloud properties. However, it is critically important to validate the performance of satellite remote sensing through comparison with in-situ measurements.

'*Yamase*' clouds are one of the typical marine boundary-layer clouds, that appear over the ocean east off the Sanriku area (the east of the Northern District of the Main Island of Japan) in early summer season under easterly cool winds, i.e., the so-called *Yamase* [1], blown out from Okhotsk anti-cyclones. We are studying the formation processes of *Yamase* clouds through numerical simulations by using a non-hydrostatic cloud-resolving model [2]. The preliminary results suggest that the model-produced clouds strongly depend on the used spatial resolution as well as parameterizations of such physical processes as turbulence, cloud and radiation processes. Further, we are going to retrieve the cloud properties such as optical thickness and effective particle radius of *Yamase* clouds from the AVHRR data of NOAA satellites. To validate the results from the numerical simulation and satellite remote sensing of *Yamase* clouds, we have carried out a few times of shipboard observations in June of the latest years. Here we present the outline and preliminary results of the shipboard observations of *Yamase* clouds.

2. *Yamase* IOP aboard the R/V *Koufu-maru*

The shipboard observations of *Yamase* clouds have been carried out within the Yamase Intensive Experiment (YIE) conducted by the Sendai District Meteorological Observatory and the Hakodate Marine Observatory (HMO) of the Japan Meteorological Agency, in collaboration with the Center for Atmospheric and Oceanic Studies (CAOS), Tohoku University. The research vessel (R/V) *Koufu-maru* of HMO operated the shipboard observations in the areas east off the Sanriku. We had three times of shipboard observations of each about 10-days' cruise in Junes of 2001, 2002 and 2003. Unfortunately, the weather and cloud conditions were not *Yamase*-like during most of the YIE periods. We encountered only a very few cases of typical *Yamase* clouds (fogs) during the intervals from the evening of 30 June to the morning of 1 July in 2002 and from the evening of 22 June through the evening of 24 June 2003. **Figure 1** shows the area and periods of the *Koufu-maru* cruises in the recent YIE.

In addition to the routine marine weather observations and intensive GPS-sonde launchings, the CAOS-group conducted cloud observations using various radiometric instruments as well as an aerosol particle-counter aboard the R/V *Koufu-maru*. **Table 1** lists the used instruments and the measured physical parameters, which can be used in validation of the products from satellite remote sensing and numerical simulations. Among these parameters, cloud liquid-water-path (*LWP*) and cloud-base height are particularly useful parameters for the validation; they were measured by a dual-frequency microwave-radiometer (Radiometric Co., WVR-1100) and a laser ceilometer (ImpulsePhysik, LD-25), respectively. Further, the temperature, humidity and wind profiles measured by GPS-sondes can be used to compare with the model-simulated profiles.

3. Preliminary results: Atmospheric profiles and *Yamase* clouds

In the 2003 YIE, we encountered a typical *Yamase* event during a period from the evening of 22 June to the evening of 24 June, and we observed temporal variation of clouds on board the R/V *Koufu-maru* that stayed near the point 39.1°N and 143.0°E during the period. **Figure 2** shows the time variations of cloud-base height measured by the ceilometer and *LWP* measured by the microwave-radiometer for the 48 hours from 00:00 (JST) of 23 June to 24:00 (JST) of 24 June. At the point, the lower part of ABL became humid and cool with the inflow of Yamase wind in the evening of 22 June, and very low *Yamase* clouds (might be fogs) appeared with the cloud-base heights of a few tens meters in the night of 22 June through the early morning of 23 June. Then the cloud-base lifted up, at highest, to 300 m during the daytime of 23 June, although the cloud layer was rather thin and patchy; the cloud-base height gradually decreased during the night down to about 100 m in the morning of 24 June. On the other hand, the liquid-water-path *LWP* rapidly varied taking mostly values between about 20 gm^{-2} and 200 gm^{-2} during the period. The GMS (Geostationary Meteorological Satellite) images revealed that in the morning of 24 June the low-level stratiform clouds extended widely over the sea east off the Sanriku area and covered the eastern half of the Tohoku District, showing a typical feature of *Yamase* clouds. For the *Yamase* period, we launched GPS-sondes every 6 hours. **Figure 3** shows the vertical profiles of wind, temperature, and relative humidity measured by a GPS-sonde launched at 06 JST on 24 June as well as the equivalent-potentials estimated from the sonde-measured atmospheric profiles. At that time, the humid easterly *Yamase* wind prevailed in the ABL below about 500 m. The cloud-base height was detected at about 100 m above the sea surface, and the cloud-top height of 300 m was estimated from the equivalent-potential profile. The corresponding profiles are shown in **Fig. 4** for the six-hours later case around the noon time of 24 June, at which the lower part of ABL with easterly winds was rather sable and the cloud-base height of the low-level clouds was raised to about 700m. There might be another cloud layer between 2000 m and 2300 m, for which the atmosphere was humid and thermodynamically unstable under the westerly winds. The upper cloud layer might correspond to a frontal cloud-band passing over the *Koufu-maru* area at that time, as shown in the GMS images at 12 JST. These observational data of temporal variations of the atmospheric profiles and associated cloud fields will be useful for validation of simulations of the *Yamase* event.

4. Future studies

We are going to simulate the above-mentioned 2003 *Yamase* case by using the non-hydrostatic cloud-resolving model [2]. We are also going to retrieve the cloud physical properties from NOAA/AVHRR data for the clouds in a wide area where *Yamase* clouds prevail. The shipboard experiment should be continued to accumulate more observational data usable to validate the performance of numerical models and satellite remote sensing of *Yamase* clouds for different weather conditions and for different places.

Acknowledgements

The shipboard observations were carried out within the YIE under the cooperation with the Sendai District Meteorological Observatory and the Hakodate Marine Observatory. We are grateful to the *Koufu-maru* crews for their helpful collaboration during the shipboard observation. Thanks are extended to Drs. M. Murakami and K. Kusunoki of Meteorological Research Institute for their kind assistance to the microwave radiometer measurement. This study is partly supported by the joint program of CEReS, Chiba University.

References

[1] H. Kawamura (*Ed.*), 1995: YAMASE, *Meteorol. Res. Note* (Japan Met. Soc.), No. 183, 179pp (*in Japanese*).

[2] T. Iwasaki, S. Asano, H. Okamoto, and R. Nagasawa, 2002: A cloud study system using a nonhydrostatic multi-nested regional climate model. *Proc. EarthCARE Workshop* (Harumi, Tokyo, 17-18 July 2002), 171-174.

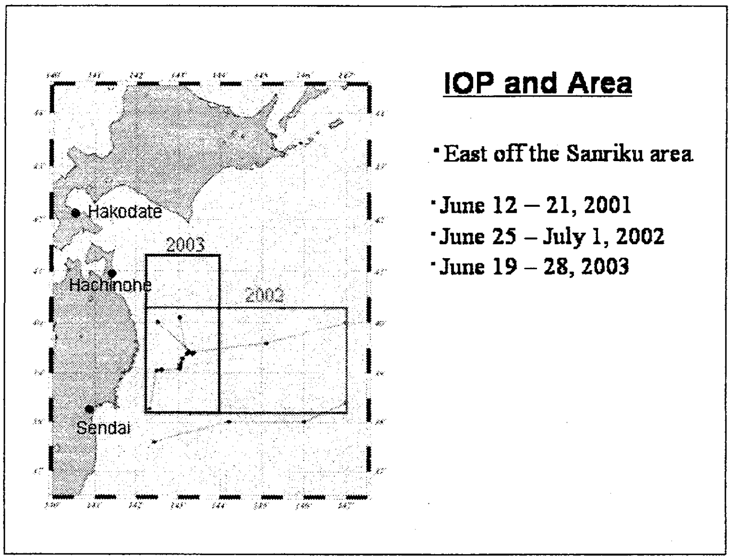

IOP and Area

- East off the Sanriku area

- June 12 – 21, 2001
- June 25 – July 1, 2002
- June 19 – 28, 2003

Fig. 1 Area and period of the *Yamase* IOPs on board the R/V *Koufu-maru.*

Table 1. Instrumentation abroad the R/V Koufu-maru and the strategy of cloud observation by the CAOS, Tohoku University group.

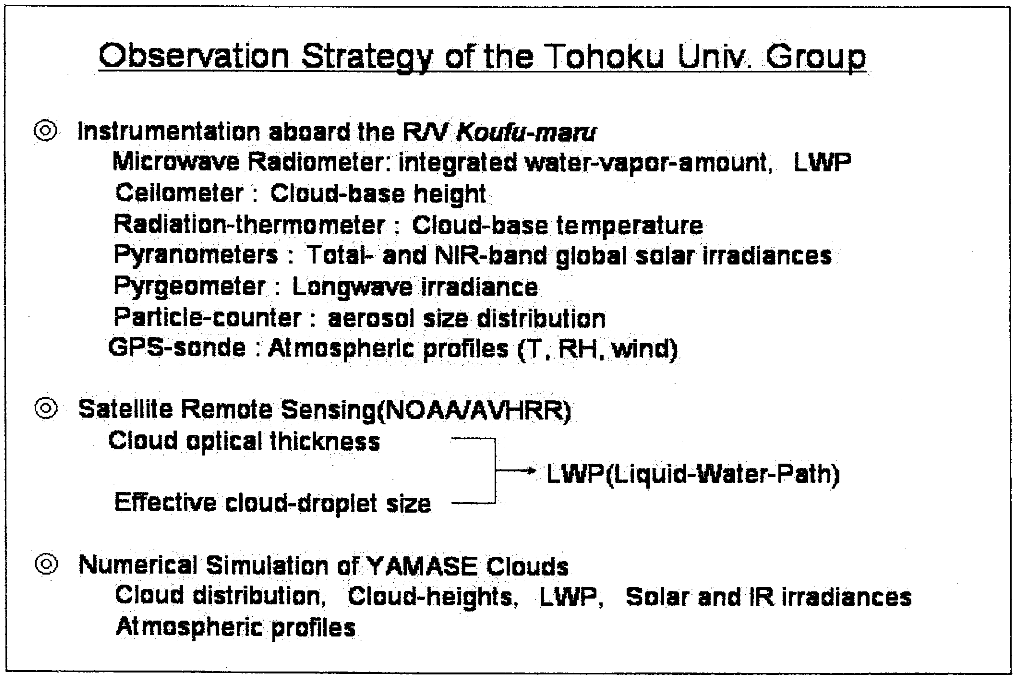

Observation Strategy of the Tohoku Univ. Group

◎ **Instrumentation aboard the R/V *Koufu-maru***
Microwave Radiometer: integrated water-vapor-amount, LWP
Ceilometer : Cloud-base height
Radiation-thermometer : Cloud-base temperature
Pyranometers : Total- and NIR-band global solar irradiances
Pyrgeometer : Longwave irradiance
Particle-counter : aerosol size distribution
GPS-sonde : Atmospheric profiles (T, RH, wind)

◎ **Satellite Remote Sensing(NOAA/AVHRR)**
Cloud optical thickness
Effective cloud-droplet size
→ LWP(Liquid-Water-Path)

◎ **Numerical Simulation of YAMASE Clouds**
Cloud distribution, Cloud-heights, LWP, Solar and IR irradiances
Atmospheric profiles

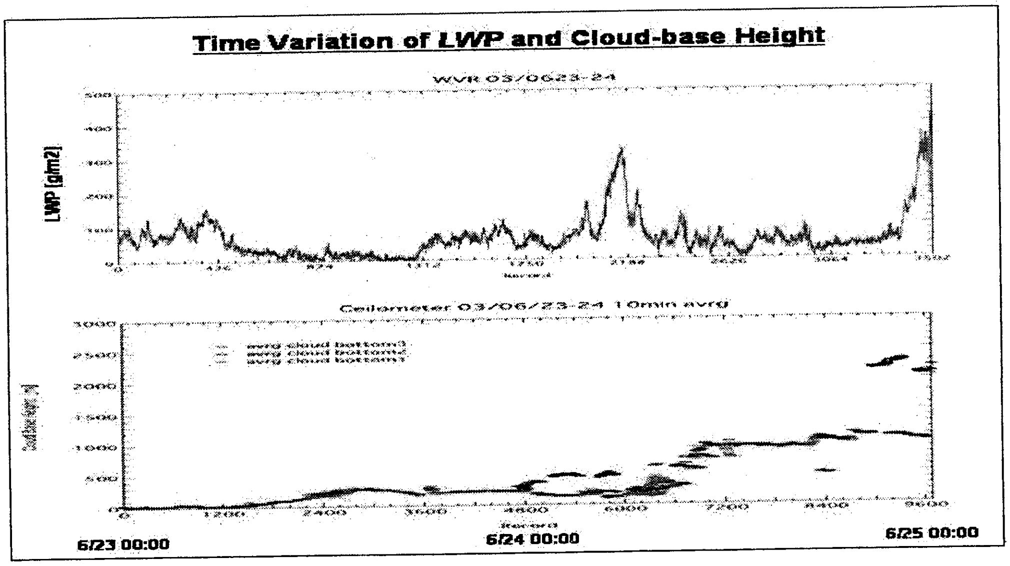

Fig. 2. Time variations of liquid-water-path (*LWP*) and cloud-base heights measured on board the R/V *Koufu-maru* for 48-hours from 00JST of 23 June to 00JST of 25 June 2003.

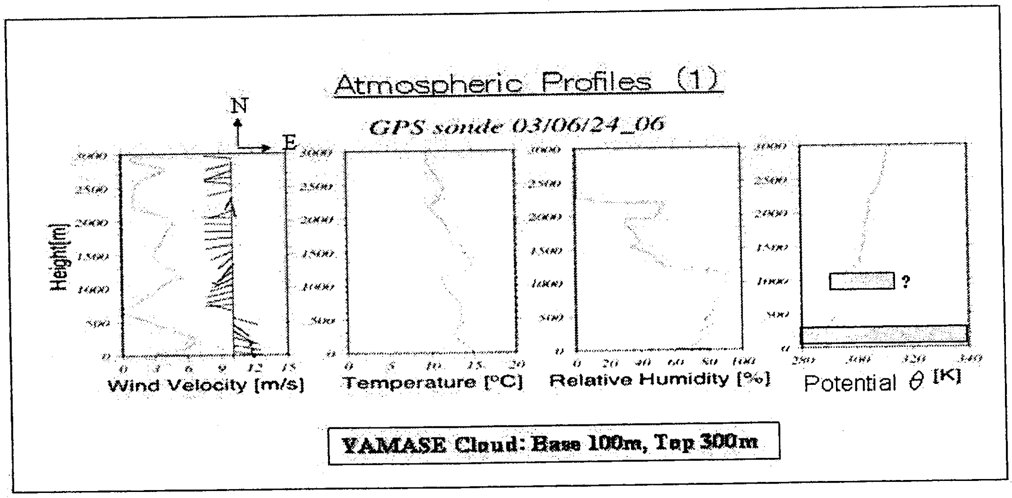

Fig. 3. Vertical profiles of wind, temperature, relative humidity, and equivalent potential temperature measured by a GPS-sonde launched at 06JST on 24 June 2003.

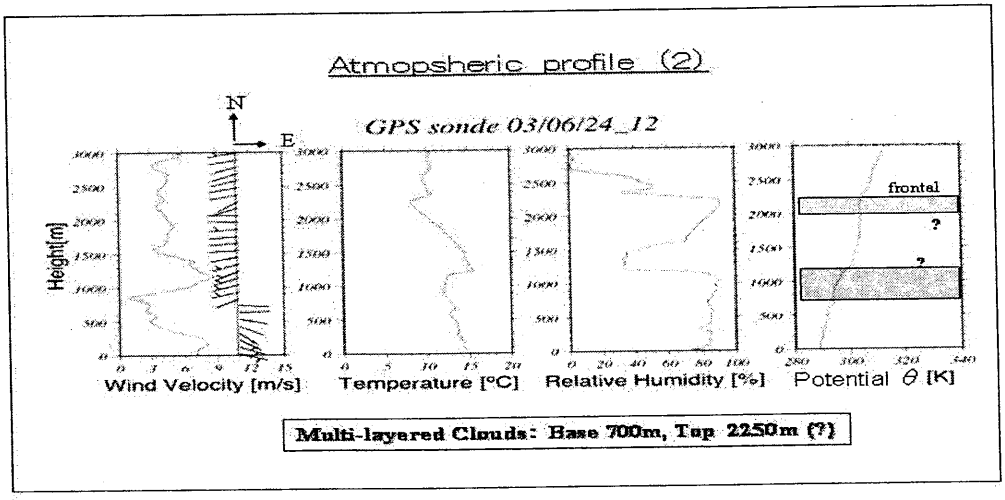

Fig. 4. Same as Fig. 3, but for the atmospheric profiles at 12JST on 24 June 2003.

Atmospheric correction of satellite data over Chiba area

Hiroaki Kuze, Mitsuo Minomura, Yusuke Furusawa, Yoshiyasu Todate
and Nobuo Takeuchi
Center for Environmental Remote Sensing (CEReS)
Chiba University, Chiba, 263-8522 Japan

Abstract:

This work is aiming at separating the ground and atmospheric contributions from the satellite remote sensing data. The result of atmospheric correction is validated by means of the ground albedo data. The 6S code is employed to accomplish the atmospheric correction of the band 1-4 data of Landsat 7 ETM+. The result is reasonably consistent with the ground albedo data measured with compact CCD spectrometers. The inhomogeneity of the aerosol optical thickness is studied by a reference albedo data based on the unsupervised land classification.

1. Introduction

Atmospheric correction (AC) is a process in which the effect of atmosphere, i.e. the extinction due to atmospheric molecules and aerosols, is removed from the satellite data to obtain intrinsic albedo values of various ground targets [1-6]. The application of AC has been proved to be successful especially to dark targets such as ocean surfaces and forest areas [2,3]. For such cases, it is even possible to derive the atmospheric information (two-dimensional distribution of aerosol optical thickness) from the satellite data [4,5]. Compared to these cases, the AC of satellite data over urban areas usually encounter difficulties, since the ground targets exhibit albedo values that vary in a wide range. This variability, in addition to the local inhomogeneity of the aerosol concentration, modifies the apparent albedo of the target.

Usually, the most important parameter in AC is the aerosol optical thickness τ_a at the time of the satellite overpass, and a sun photometer can be used to evaluate the values of τ_a for the relevant satellite bands in the visible and near-infrared regions. Once τ_a is given, and with the assumption that the atmosphere is horizontally homogeneous, it is rather straightforward to calculate various radiation components [6] using radiation codes such as the 6S [4] and Modtran [7] codes. The ground albedo values, then, are obtained from the condition that the calculated and the observed radiance agree with each other at the top of the atmosphere.

In this work, first, we validate the results of the atmospheric correction data (the band 1-4 data of Landsat 7 ETM+) for the urban Chiba area with the albedo data measured at some of the target pixels. Apart from the contributions from the adjacency effect and local aerosol inhomogeneity, this process yields reasonable agreement between the albedo values from the AC and the validation measurement. The resulting distribution of aerosol optical thickness, on the other hand, exhibits more or less uniform distribution, as naturally expected from the original assumption of the horizontal uniformity.

In order to check the uniformity of actual atmosphere, in the second part, we analyze the same satellite data on the basis of the unsupervised land classification. For every band, an appropriate albedo value is postulated for each class, and the atmospheric information is derived. If the albedo values are close to the real values, it is expected that the distribution of aerosol optical thickness τ_a can be determined.

2. Algorithm

Here we describe the method to obtain the albedo image after the AC (ρ_{ac}), the albedo image based on the ground measurement (ρ_{ref}), and the image of aerosol optical thickness.

2.1 Generation of ρ_{ac} image

The raw data of a satellite image consists of digital number (DN) values, and for each DN between 0 and 255, there exists a one-to-one correspondence between the aerosol optical thickness τ_a and the target albedo ρ. This relationship between τ_a and ρ can be calculated by the 6S code, provided an aerosol model is given. Figure 1 shows the relationship between ρ and τ_a for a DN value of 151 with the urban, continental and maritime aerosol models. The optical thickness τ_a is varied between 0 and 1.2. It is noted that when the aerosol optical thickness is relatively small ($\tau_a < 0.2$), the resulting ground albedo shows insignificant dependence on the aerosol model used in the retrieval.

The procedure of the AC is summarized in Fig. 2. The DN values are converted into radiance L_{obs} in the following manner [6]. In the 6S simulation a tentative value of ground albedo value ρ_0 is assumed (this assumption does not affect the results, as explained below) and the optical thickness τ_a at 550 nm is varied between 0 and 1.2. The total radiance L_{total} and the atmospheric radiance L_{atm},

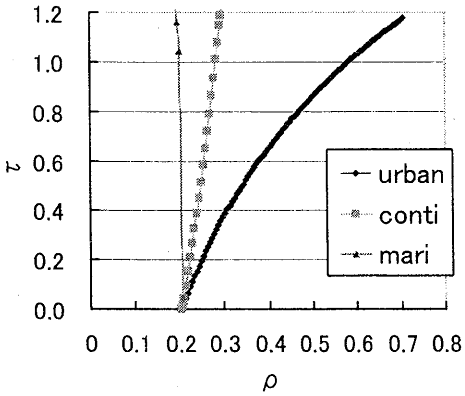

Fig.1 Relationship between the aerosol optical thickness τ_a and the ground albedo ρ for three aerosol models (urban, continental, and maritime): ETM+ band 3, *DN*=151.

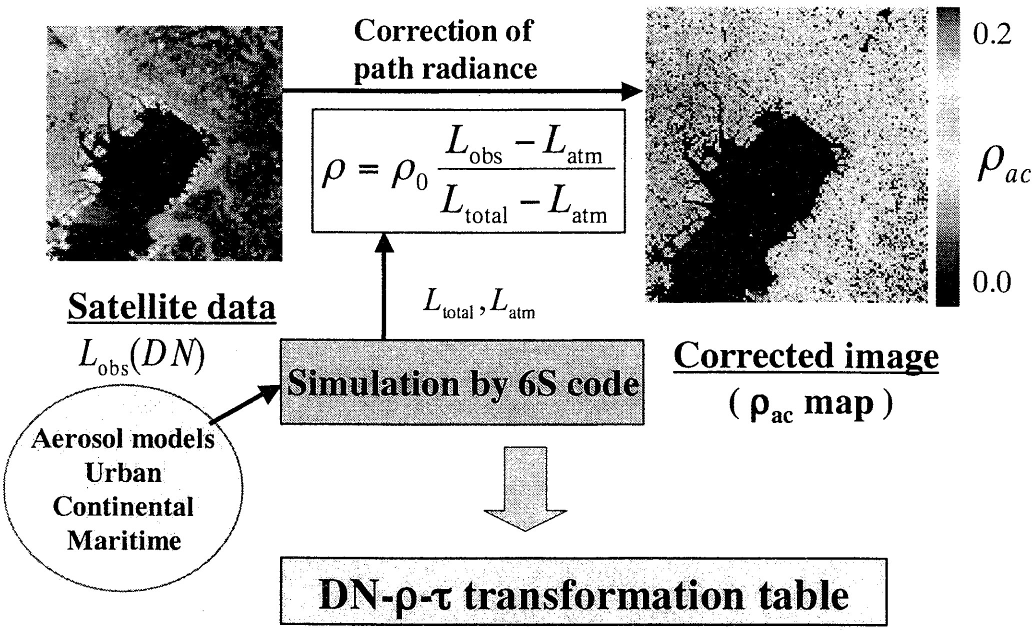

Fig.2 Procedure of the atmospheric correction.

both of which are derived by the simulation, are used in the equation of atmospheric correction:

$$\rho = \rho_0 \frac{L_{obs} - L_{atm}}{L_{total} - L_{atm}} \tag{1}$$

Here ρ is the albedo after the removal of the path radiance. The value of ρ is independent of ρ_0, since, to a good approximation, the denominator in eq.(1) is proportional to ρ_0. Equation (1) gives sets of ρ and τ_a, which are then registered in a form of a conversion table. The conversion table from DN to ρ_{ac} can then be determined by assuming that the aerosol optical thickness τ_a is equal to the value τ_{sp} observed with a sun photometer at Chiba University. Here we assume that this conversion is not affected by the geometric conditions of the satellite observation. In this manner, the raw data (DN map) is transformed into the albedo (ρ_{ac}) map.

2.2 Generation of ρ_{ref} image

The spectral reflectance of appropriately chosen soil- and vegetation-covered land surfaces are measured around Chiba University with compact CCD spectrometers (USB2000 for 350-850 nm, HR2000 for 650-1100 nm, both from Ocean Optics). The average albedo for each band of ETM+ sensor can be calculated by averaging the measured spectral reflectance with the ETM+ sensor response function. For the reference point over the sea area, a point with a representative DN value is chosen, and an albedo of 0.5 - 3% is assumed in accordance with the band wavelength [8]. Since we have three sets of (DN, ρ_{ref}), a linear fitting yields the relationship between the DN value and the albedo value. This process gives us the ρ_{ref} image on the basis of the ground validation.

2.3 Derivation of τ_a image

The ground albedo distribution must be assumed if one wishes to derive the aerosol

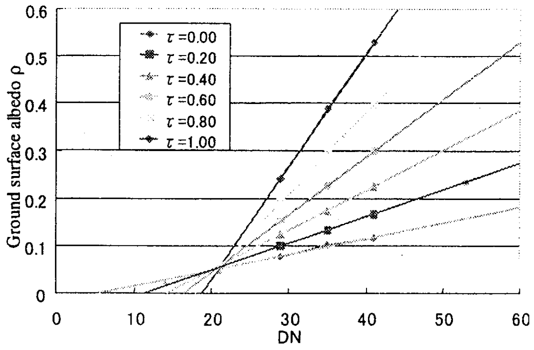

Fig.3 Relationship between DN and ρ for various values of τ_a (ETM+ band 3, urban aerosol model). The slope is larger for larger value of τ_a.

distribution (τ_a) map. In this work, we make use of two types of albedo maps. The first type is the ρ_{ac} map, and the second is the one generated through the classification of the ETM+ with a decision-tree classifier. In this latter case, first we derive 11 classes according to the NDVI values, and assign an average albedo (ρ_{cls}) to each class. It is desirable that this assignment be done on the basis of the true reflective properties of the targets included in the class (as determined from the ground observations, for example). In the present study, however, we adopted the albedo values (ρ_{cls}) from the ground classification scheme of the Aster Library data [9], with subsequent slight adjustment for each class so that the resulting τ_a map appeared more or less uniform. The process was applied to band 3. The DN-ρ relationship is calculated for various values of τ_a (Fig. 3), and consequently, a set of (DN, ρ) for a particular pixel specifies a value of τ_a.

3. Results and discussion

3.1 Comparison between ρ_{ac} and ρ_{ref}

The atmospheric correction gives the surface albedo ρ_{ac} as a function of DN, which is to be compared with the validation result of ρ_{ref} (Fig. 4). Here we assume a linear relationship between DN and ρ_{ref}. The histogram of the DN distribution (raw data) is also shown for band 3 (centered at

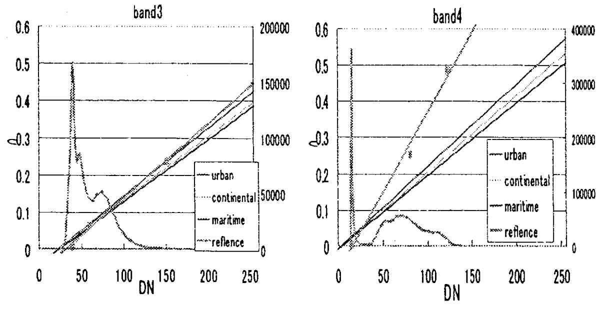

Fig.4 Conversion table (band 3) between DN and ρ calculated by the 6S code for urban, continental and maritime aerosol models. The fitted lines and a histogram of DN values are also shown.

661 nm, τ_{sp} = 0.142). Since the aerosol optical thickness is relatively small, the corrected albedo does not show significant dependence on the aerosol model, as mentioned above. The agreement between ρ_{ac} and ρ_{ref} is reasonable for bands 1 through 3: for band 1, there exists some discrepancy between the two in a DN range with a high population, leading to noticeable difference in the resulting images. For band 4, the difference of the ρ_{cls} and ρ_{ref} is still large, presumably because of inaccurate values of ρ_{ref} at the near-infrared region and/or the inappropriate selection of the reference points.

3.2 Distribution of aerosol optical thickness

The classification into 11 classes yields the τ_a distribution as shown in Fig. 5. This result indicates that suitable choice of albedo values indeed provides realistic information on the atmosphere over a metropolitan area. Nevertheless, it is apparent from Fig. 5 that this result is still affected by the ground structure, including the adjacency and topological effects. In particular, the appearance of geometric structures (e.g. seashore along the Tokyo bay) indicates that the original albedo distribution ρ_{cls} is not sufficiently accurate, and as a result, the atmospheric information is still contaminated by the land albedo distribution. It is expected that the accuracy of τ_a be improved by increasing the number of classes, and by assigning plausible (possibly measurement-based) albedo value for each class.

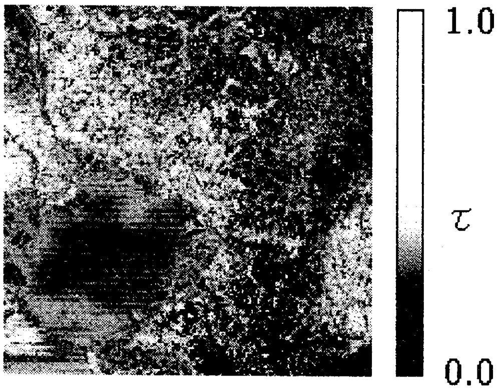

Fig.5 Distribution of the aerosol optical thickness τ_a obtained by the land classification with 11 classes.

4. Conclusions

We have described the atmospheric correction of Landsat ETM+ (bands 1-4) data over the Chiba area. The fact that the corrected albedo distribution ρ_{ac} agreed with the validation result ρ_{ref} suggests that the correction algorithm works well, even without considering the adjacency effect. For band 4, the two albedo data have shown discrepancies, inferring the problem associated with the accuracy of the ground data and/or the choice of the reference points. The two-dimensional inhomogeneity of the aerosol distribution has been considered by deriving the τ_a map from the albedo image based on the land classification. A network observation with sun photometers or the observation with a wide angle imaging lidar, for example, can serve to study the reliability of the resulting aerosol distribution.

References

1. D. Tanre, B.H. Holben, Y.J. Kaufman, Atmospheric Correction Algorithm for NOAA-AVHRR Products: Theory and Application, IEEE Trans. Geosci. Remote Sensing, 30(2), pp.231-248, 1992.

2. H. Ouaidrari and E. Vermote, Operational Atmospheric Correction of Landsat TM Data, Remote Sensing Environ, 70, pp.4-15, 1999.

3. H.R. Gordon, Atmospheric Correction of Ocean Color Imagery in the Earth Observing System era, J. Geophys. Res., 102(D14), pp.17081-17106, 1997.

4. E.F. Vermote, D. Tanre, J.L. Deuze, M. Herman, and J. Morcrette, Second Simulation of Satellite Signal in the Solar Spectrum, 6S: An Overview, IEEE Trans. Geosci. Remote Sensing, 35(3), pp.675-685, 1997.

5. K. Asakuma, M. Minomura, S. Otsutsumi, H. Kuze, N. Takeuchi, Estimation of aerosol optical thickness over land in Chiba area form AVHRR data, Adv. Space Res., 29(11) (2002) p.1747-1752.

6. M. Minomura H. Kuze, N. Takeuch, Atmospheric correction of visible and near-infrared satellite data using radiance components: an improved treatment of adjacency effect, J.Rem.Sen.Soc.Jpn., 21(3) pp. 260-271, 2001.

7. A. Berk, G.P. Anderson, P.K. Acharya, J.H. Chetwynd, M.L. Hoke, L.S. Berntein, E.P. Shettle, M.W. Matthew, and S.M. Adler-Gordon, MODTRAN4 Version2 USER'S MANUAL, Air Foece Reseatch Laboratory.

8. C.D. Mobley, Estimation of the remote-sensing reflectance from above-surface measurements, Appl.Opt. 38(36), pp.7442-7455, 1999.

9. http://speclib.jpl.nasa.gov/

Retrieval of Precipitable Water over Land using Near Infrared Satellite Remote Sensing Data

Makoto KUJI[1] and Akihiro Uchiyama[2]
[1] *Nara Women's University, Kita-uoya Nishimachi, Nara, 630-8506, Japan,*
E-mail: makato@ics.nara-wu.ac.jp
[2] *Meteorological Research Institute, Nagamine 1-1, Tsukuba, Ibaraki, 305-0052, Japan*

Abstract

Retrieval of precipitable water (vertically integrated water vapor amount) is proposed using near infrared channels of Global Imager onboard Advanced Earth Observing Satellite-II (GLI / ADEOS-II). The principle of retrieval algorithm is based upon that adopted with Moderate Resolution Imaging Spectroradiometer (MODIS) onboard Earth Observing System (EOS) satellite series. Simulations were carried out with GLI Signal Simulator (GSS) to calculate the radiance ratio between water vapor absorbing bands and non-absorbing bands. As a result, it is found that for the case of high spectral reflectance background (a bright target) such as the land surface, the calibration curves are sensitive to the precipitable water variation. For the case of low albedo background (a dark target) such as the ocean surface, on the contrary, the calibration curve is not very sensitive to its variation under conditions of the large water vapor amount. It turns out that aerosol loading has little influence on the retrieval over a bright target for the aerosol optical thickness less than about 1.0 at 500 nm wavelength. A preliminary analysis of GLI data was also carried out and the retrieved result is discussed. It is also anticipated that simultaneous retrieval of the water vapor amount using GLI data along with other channels will lead to improved accuracy of the determination of surface geophysical properties, such as vegetation, ocean color, and snow and ice, through the better atmospheric correction

1. Introduction

Water vapor is one of typical gas species governing the greenhouse effect. Investigation of water vapor distribution is a clue to understand the radiation budget of earth atmosphere system as well as the global energy and hydrological circulation. Although water vapor is mostly distributed in the lower atmosphere (planetary boundary layer from surface to a few kilometers), the water vapor amount often increases in the middle and upper troposphere accompanying horizontal advection of humid air mass. Thus, precipitable water, (i.e. the vertically integrated water vapor amount) is considered to be the most representative quantity of water vapor amount in the atmosphere.

GLI onboard ADEOS-II is designed to obtain data of both the surface properties (vegetation, ocean color, and snow and ice, etc.) and atmospheric properties (cloud, aerosol, and radiation budget, etc.). In general, atmospheric correction is indispensable when surface geophysical properties are retrieved from satellite remote sensing data. Correction of atmospheric ozone, aerosol, and in particular, water vapor is important for precise retrieval of vegetation conditions and ocean color. In the GLI mission, it is currently planned that the water vapor information is incorporated from the quasi-real-time objective analysis data. Nevertheless, it is desirable to use the water vapor information concurrently obtained with same spatial resolution as other channels. In this context, we study feasibility of using near infrared channels of GLI in the retrieval of precipitable water. The principle of the retrieval algorithm is described in Sec. 2 together with assumptions made in the present simulation. In Sec. 3, results of the simulation are analyzed and discussed. And also preliminary results with GLI data are discussed. Section 4 presents the summary and related future works.

2. Retrieval Algorithm and Simulation

The retrieval algorithm is based upon the radiance ratio method. The similar method was already adopted with MODIS / EOS series, and utilizes the radiance ratio between water vapor absorbing and non-absorbing bands to retrieve the precipitable water. In the MODIS case, 940 nm and 865 nm bands were adopted as the water vapor absorbing band and non-absorbing band 1), respectively, and the retrieved results on a global scale were already reported 2).

Principle of the retrieval algorithm is explained concisely here. Figure 1 illustrates transmittance curves of water vapor in the near infrared region calculated, using the LOWTRAN 7 code 3).

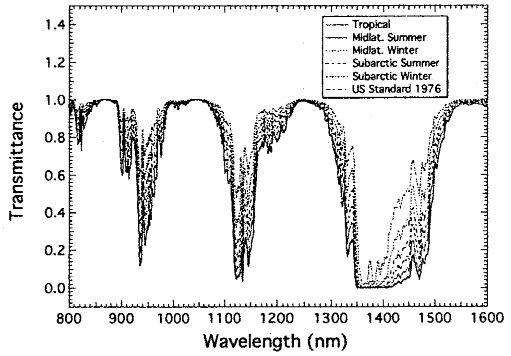

Fig. 1. Atmospheric transmittance related to water vapor in the near infrared spectral region. Curves are calculated with the LOWTRAN 7 code for vertical one way path, as products between water vapor absorption lines and continuum absorption. Each of the six transmittance lines correspond to the six model atmospheres.

As seen from Fig. 1, water vapor absorbing bands (spectral regions with smaller transmittance) are located at around 810 nm, 940 nm, 1135 nm, and 1380 nm, whereas non-absorbing bands (regions with larger transmittance; i.e., atmospheric window region) are found at 865 nm, 1050 nm and 1240 nm. The six atmospheric models are Tropical Atmosphere, Midlatitude Summer, Subarctic Summer, US Standard 1976, Midlatitude Winter and Subarctic Winter and their precipitable water are 40.0 mm, 28.5 mm, 20.4 mm, 13.9 mm, 8.38 mm and 4.10 mm, respectively. The retrieval algorithm utilizes these characteristics as follows: in the water vapor absorbing bands, transmittance (i.e., radiance to be observed) varies with the water vapor amount (precipitable water) assumed in each atmospheric model, while in the non-absorbing bands, changes are much smaller.

It is then proposed that for the GLI application, a retrieval method to make a calibration curve between the radiance ratio of water vapor absorbing band (e.g., Ch. 25; 1135 nm) to non-absorbing band (e.g., Ch. 24; 1050 nm) and water vapor amount (precipitable water) in a form of a nonlinear regressive curve. The GLI channel specifications are summarised in Nakajima et al. 4).

Based upon the principle of the retrieval algorithm, the channel which is most sensitive to variation of water vapor amount is feasible as a water vapor absorption channel and, on the other hand, the one which is least sensitive to it as a non-absorbing channel. As seen from Fig. 1, Ch. 25 (1135 nm; Band Width 70 nm) is selected as a water vapor absorbing channels. For non-absorbing bands, Ch. 24 (1050 nm; Band Width 20 nm) and Ch. 26 (1240 nm; Band Width 20 nm) are selected.

Simulations were carried out with GLI Signal Simulator (GSS) 5) so as to calculate radiances to be observed at the GLI / ADEOS-II. It enables us to calculate the radiance to be observed with GLI assuming several atmospheric models including aerosol loading as well as water vapor. In this feasibility study, two cases of a bright target (land) and a dark target (ocean) are considered as a ground surface condition with the GSS simulations.

The land model is assumed as a Lambertian surface whose spectral reflectance is 50 %, which is adopted as a representative of a bright target. This assumption is based upon the grass model adopted in the ASTER spectral library (http://speclib.jpl.nasa.gov/archive/jhu/becknic/vegetation/txt/grass.txt), which shows surface reflectance is 52.2 %, and 50.7 %, and 48.8 % for 1050 nm, 1135 nm, and 1240 nm spectral region, respectively. Further, the effect of bidirectional reflectance distribution function is not considered in this study for simplicity, too. The ocean model was assumed as a non-Lambertian surface with a flux albedo of around 2 to 6 %, a representative case of a dark target. This assumption corresponds to the situation with 5.0 m s^{-1} wind speed at the 10 m height 6).

Simulations were carried out under clear sky conditions. Moreover, effect of aerosol loading in the model atmosphere was examined. For the aerosol model, rural and oceanic ones incorporated in the GSS are utilized over land and ocean, respectively 5).

3. Results and Discussion

The simulated radiances to be observed were analyzed in two cases: over a bright target (i.e., land) and a dark target (i.e., ocean). Three bands, that is, one water vapor absorbing channel (1135 nm) and two non-absorbing channels (1240 nm and 1050 nm), were used to carry out the simulations. Two combinations were examined so as to make a calibration curve with a radiance ratio between two channels: (1) a combination of 1135 nm and 1240 nm and (2) a combination of 1135 nm and 1050 nm. In addition, two cases are assumed for scan geometry: (a) solar zenith angle 40°, satellite zenith angle 0° (nadir view), and (b) solar zenith angle 60°, satellite zenith angle 60°, and relative azimuthal angle 90°.

a. Analyses

At first, a radiance ratio (T_w) in this study is defined:

$$T_w(ch1, ch2) \equiv \frac{R_{ch1}}{R_{ch2}}, \tag{1}$$

where $ch1$ indicates a water vapor absorbing channel (e.g., 1135 nm spectral region), at which spectral region radiation undergoes a strong absorption due to water vapor, $ch2$ is a non-absorbing channel (e.g., 1240 nm or 1050 nm spectral region), and R is the radiance simulated with GSS at the top of the atmosphere for the specified channel. This definition becomes equivalent to that of Kaufman and Gao 1) in principle, except for a factor due to some ratio of the extraterritorial solar incident irradiance between specified channels.

Based upon the definition, a relationship (a calibration curve) between radiance ratio (T_w) and precipitable water (W) similar to Kaufman and Gao 1) is proposed:

$$T_w(ch1, ch2) = a + b\exp\left(-c\sqrt{W}\right), \tag{2}$$

where a, b and c are calibration coefficients. Without the coefficient a, this relationship is also equivalent to that of Kaufman and Gao 1) because it takes the factor of the ratio of the solar terrestrial incident irradiance into the calibration coefficient b. The coefficient a is added to take a bias due to little molecular scattering effect into the relationship explicitly.

In order to take the effect of scan geometry into the calibration curve, the precipitable water is converted to the water vapor path. The relationship between precipitable water (W) and water vapor path (W^*) is given as

$$W^* = W\left(\frac{1}{\cos\theta} + \frac{1}{\cos\theta_0}\right), \tag{3}$$

where θ is satellite zenith angle and θ_0 is solar zenith angle. Using W^* instead of W, Eq. (2) is modified as

$$T_w(ch1, ch2) = a^* + b^*\exp\left(-c^*\sqrt{W^*}\right). \tag{4}$$

In following analyses, once the radiance ratios (T_w) are estimated based upon Eq. (1) using the radiances simulated with GSS, then least-squares fit procedures are carried out with Eq. (2) or (4).

b. Results over a Bright Target (Land)

Figure 2 shows relationships between radiance ratio and precipitable water simulated with six atmospheric models in Fig. 1. This is the case with the solar zenith angle of 40° and satellite zenith angle of 0° (nadir view). From Fig. 2, it is found that both R_{1135}/R_{1240} and R_{1135}/R_{1050} are sensitive to the precipitable water, and they are well fitted with the calibration curve of Eq. (2). Root mean square errors (RMSE) for both cases are less than 0.002. These values are much smaller than the order of calibration curves of about 0.1 to 1.0. It is also found that R_{1135}/R_{1240} has greater dynamic range than R_{1135}/R_{1050} as a whole, since simulated R_{1050} is larger than R_{1240} by a few times.

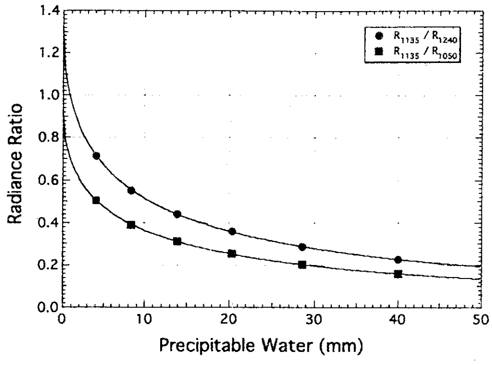

Fig. 2. Radiance ratio simulated as a function of precipitable water over a bright target (land). Closed circles denote the radiance ratio between the 1135 nm and 1240 nm channels, and closed rectangle between the 1135 nm and 1050 nm channels. Solar zenith angle is 40°, satellite zenith angle is 0° (nadir view). Curve fitting is applied to each result to obtain a calibration curve.

Figure 3 shows the radiance ratio calculated for the two cases of the scan geometry; in addition to the case in Fig. 2, results are shown also for solar zenith angle 60°, satellite zenith angle 60°, and relative azimuthal angle 90°. In order to minimize the effect of scan geometry, scaled water vapor path in Eq. (3) is used instead of the precipitable water in Fig. 2. It turns out that all the four cases are well fitted with calibration curves based on Eq. (4) with the RMSEs less than 0.002 for all the four cases. These results indicate that the use of water vapor path enables us to retrieve the precipitable water from the observed radiance ratio irrespective of the scan geometry over bright targets (land surfaces).

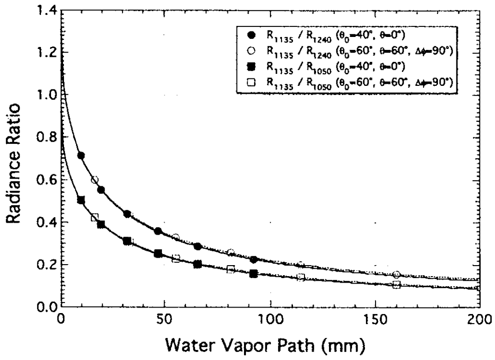

Fig. 3. Calibration curves between the radiance ratio and scaled water vapor path over a bright target (land). Closed and open circles denote the radiance ratio between the 1135 nm and 1240 nm channels, and closed and open rectangles between the 1135 nm and 1050 nm channels. Closed symbols are for the scan geometry of solar zenith angle 40° and satellite zenith angle 0° (nadir view), and open symbols are for solar zenith angle 60°, satellite zenith angle 60°, and relative azimuthal angle 90°. Solid lines are the fitting curves for closed symbols, and dotted lines are for open symbols.

c. Results over a Dark Target (Ocean)

Same as over a bright target (land), simulations were carried out to calculate radiance ratios over a dark target (ocean). Figure 4 shows the radiance ratio calculated for the two cases of the scan geometry; one is a case of solar zenith angle 40° and satellite zenith angle 0° (nadir view), and the other for solar zenith angle 60°, satellite zenith angle 60°, and relative azimuthal angle 90°. In order to minimize the effect of scan geometry, scaled water vapor path in Eq. (3) is also used. It turns that all the four cases are well fitted with calibration curves based upon Eq. (4) and the RMSEs are less than 0.003 for all the four cases. It is also found that the calibration curves are little sensitive to the water vapor amount under a condition of a long water vapor path, that is, larger water vapor amount.

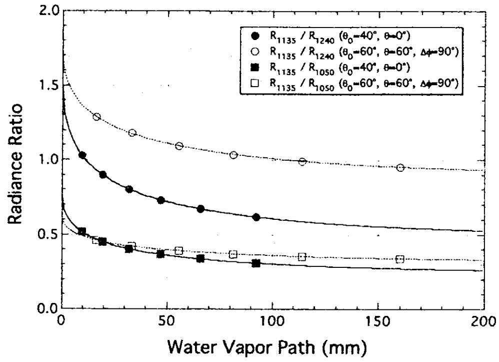

Fig. 4. Same as in Fig. 3, except for over a dark target (ocean).

Over ocean, calibration curves depend upon the scan geometry, which is different from the case over land. That is, ocean surface is not assumed as a Lambertian one in this simulation, although land surface is assumed as a Lambertian one for simplicity in spite of the bidirectional reflectivity in a actual environmental situation. As seen in Fig. 4 compared to Fig. 3, the dynamic ranges of each calibration curve over ocean are smaller than those over land.

d. Effect of Aerosol Loading

Effect of aerosol loading to the retrieval sensitivity in a clear atmosphere was investigated. Simulations with GSS were carried out with the six model atmospheres over both a bright target (land) and a dark target (ocean) changing with aerosol optical thickness at 500 nm (τ_a) of 0.0, 0.1, and 1.0 so as to calculate the radiance ratios.

Figure 5 shows the results of the case over a bright target (land) with rural aerosol loading. From Fig. 5, it is found that all the six cases are fitted well with calibration curve in Eq. (4) and calibration curves are almost identical to each other. The RMSEs are less than 0.002 for all the six cases.

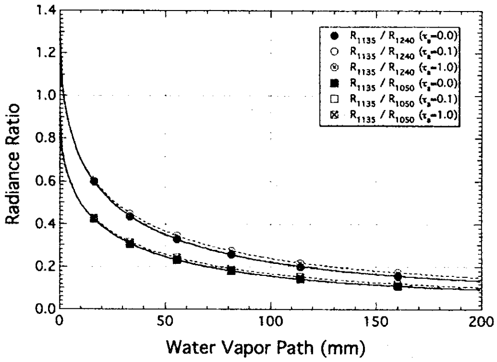

Fig. 5. Same as in Fig. 2, except for rural aerosol loading (τ_a=0.0, 0.1, and 1.0) over a bright target. Circles are used for the radiance ratio between the 1135 nm and 1240 nm channels, and rectangles between the 1135 nm and 1050 nm channels. All the cases are for a scan geometry of solar zenith angle 60°, satellite zenith angle 60°, and relative azimuthal angle 90°.

Figure 6 shows the results of the case over a dark target (ocean) with oceanic aerosol loading. It turns out that all the six cases are fitted well with calibration curves based on Eq. (4) even though the RMSEs are less than 0.01 for all the six cases. The dynamic range of R_{1135}/R_{1240} of calibration curves is larger than that of R_{1135}/R_{1050} because variation of R_{1240} is larger than R_{1050} compared to R_{1135} under this aerosol loading condition. Moreover, the dynamic range of calibration curves also become larger as the aerosol loading is heavier as a whole.

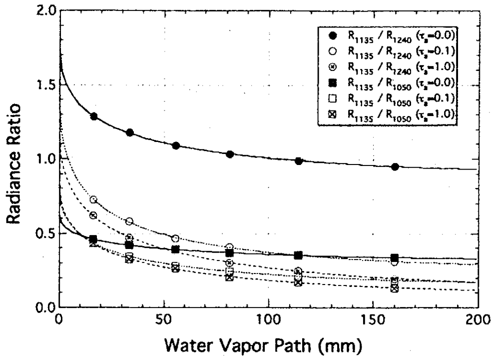

Fig. 6. Same as in Fig. 5, except for oceanic aerosol loading over a dark target.

e. Preliminary analysis of GLI data

The retrieval algorithm described in this study was applied to GLI Data. The data seem to be obtained in a good condition even during the initial checkout as seen in Fig. 7. Figure 7 shows the one of the RGB composite image of ADEOS-II / GLI, which is provided by Japan Aerospace Exploration Agency / Earth Observation Research and application Center (JAXA / EORC). The observation date of the image is March 20, 2003. There extended huge cloud system at the South of Japan. In this panel, there appears western part of Japan islands at the upper part while sunglint region does at the lower part of this panel.

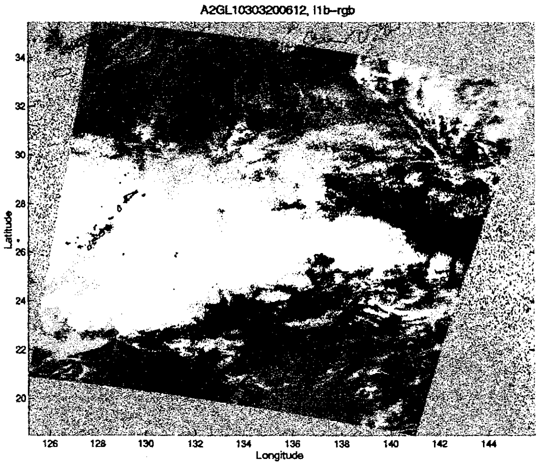

Fig. 7. RGB imagery of GLI data. This imagery is provided by JAXA / EORC.

Figure 8 shows the images of GLI data, same region in Fig. 7, except as a raster format. In Fig. 8, Japan islands locate at the right bottom portion in each panel.

In Fig. 8, panel (b) is strong water vapor absorbing channel, and on the other hand, panels (a) and (c) are non-absorbing (i.e., window) channels. You can see that the sunglint region at the left top corner in the panels (a) and (c) seems to be vague in the panel (b) due to the strong water vapor absorption in the atmosphere.

In this analysis, two channels were utilized such as Ch. 25 (1135nm) and Ch. 26 (1240nm) in the panels (b) and (c), respectively. The three calibration coefficients, a, b, and c for the algorithm in Eq. (2) are assumed as 0.690, 1.23, 0.209, respectively [7]. These coefficients are mainly suitable for land region. So, the retrieved result other than over land will be possibly erroneous. But, the analysis was carried out for the whole scene at this preliminary analysis stage.

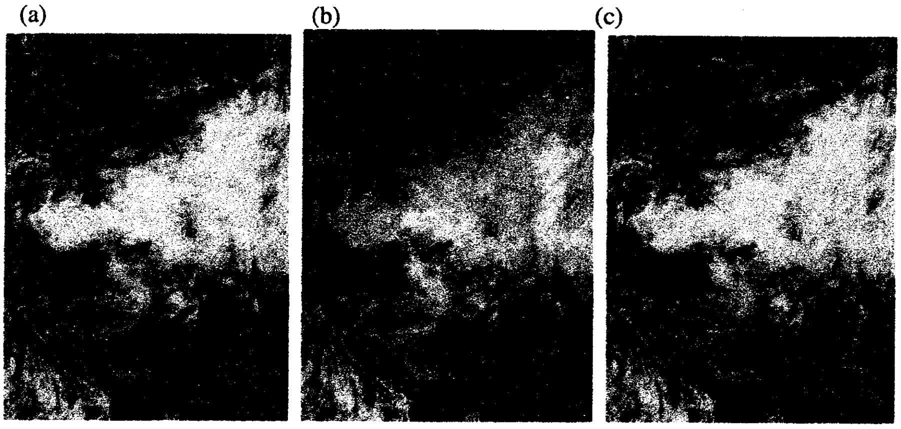

Fig. 8. Images of ADESO-II / GLI data for relevant channels: (a) Ch. 24 (1050nm), (b) Ch. 25 (1135nm), and (c) Ch. 26 (1240nm), respectively. A level slice is a linear gray scale from maximum (white) to minimum (black) radiances for each panel.

Retrieved precipitable water distribution is shown for the whole scene in Fig. 9.

Fig. 9. Retrieved precipitable water distribution. In this preliminary analysis, Ch. 25 (1135nm) and Ch. 26 (1240nm) were used to retrieve precipitable water. A level slice is a linear gray scale from maximum (white) to minimum (black) precipitable water.

As seen in Fig. 9, retrieved precipitable water distributes with great spatial contrast, which increases gradually from bottom (northern) to top (southern) portion. Larger precipitable water in the scene exists around the sunglint region, which is readily interpreted from larger spectral contrast between Fig. 8 (b) and (c). That is, around sunglint region, observed radiance at a non-absorbing channel (Fig. 8 (c)) is brighter, while observed radiance at an absorbing channel (Fig. 8 (b)) is darker in the scene.

Statistics of the retrieved precipitable water distributes averagely 58.4 mm with standard deviation 28.0 mm in the whole scene, which includes not only land region but also ocean and cloudy regions. The retrieved value seems to be much larger than usually observed values around the south of Japan islands region. The retrieved precipitable water should be validated with other observation methods such as radiosonde observation, which is one of the future works.

4. Summary and Concluding Remarks

We have proposed the retrieval of water vapor amount (precipitable water) using GLI near infrared channels. The results of simulations are summarized as follows:

- The combination of 1135 nm and 1240 nm channels is more sensitive to the precipitable water than that of 1135 nm and 1050 nm channels, as a whole.
- The sensitivity to the precipitable water is better over a bright target (higher reflectance at ground level) than over a dark target (lower reflectance at surface level).
- The precipitable water to which radiance ratios are most sensitive is about 5 to 12 mm as a whole, which is rather drier among the six atmospheric models assumed in this study.

- Over a bright target with Lambertian reflectivity, calibration curves using scaled water vapor path are almost independent of the scan geometry.
- Over a dark target with non-Lambertian reflectivity, calibration curves are largely dependent upon the scan geometry even with scaled water vapor path.
- Over a bright target with spectral reflectance of 50 %, aerosol loading with optical thickness not more than 1.0 at 500 nm is not influential in calibration curves.
- Over a dark target with flux albedo of several percent, aerosol loading should be taken into consideration to retrieve precipitable water.

There are further tasks to be worked on in the future:

- Other surface conditions not considered in this simulation should also be examined. It would be required to investigate dependency of calibration curves on scan geometry over land surface such as vegetation, in particular.
- Combined use of non-absorbing channel such as 1050 and 1240 nm channel is expected to improve the retrieval sensitivity, independent of surface reflectance (1).

Based upon the feasibility study, a preliminary analysis of ADEOS-II / GLI data was carried out. The retrieved water vapor amount is much larger than usually observed values with other observations such as radiosonde and so on. It is necessary to validate the retrieved values, comparing to other observations such as radiosonde, microwave radiometer, and so on, over land region in particular. Further, we hope that in situ observation on surface reflectance specification would be carried out by worldwide researchers in future. At that time, our method to correct water vapor absorption will be supportive for their estimation of surface geophysical parameters over bright targets, in particular. As surface reflectance specification of bright target region will be fulfilled, it is expected that the retrieval of precipitable water will be more accurate vice versa.

Acknowledgments

The authors thank GAIT / EORC / JAXA for simulations with GSS. This study was supported by National Space Development Agency of Japan (A2-RA-G-0030).

References

1) Y. J. Kaufman and B.-C. Gao: Remote Sensing of Water Vapor in the Near IR from EOS/MODIS. *IEEE Trans. Geoscience and Remote Sensing,* **30,** pp. 871-884, 1992.

2) G. -C. Gao and Y. J. Kaufman: Remote sensing of water vapor and thin cirrus clouds using MODIS near-IR channels. *Proc. of SPIE,* **4150,** pp. 217-224, 2000.

3) F. X. Kneizys, E. P. Shettle, L. W. Abreu, J. H. Chetwynd, G. P. Anderson, W. O. Gallery, J. E. A. Selby, and S. A. Clough: Users guide to LOWTRAN 7. **AFGL-TR-88-0177,** 146 pp, 1988.

4) T. Y. Nakajima, T. Nakajima, M. Nakajima, H. Fukushima, M. Kuji, A. Uchiyama, and M. Kishino: The optimization of the Advanced Earth Observing Satellite II Global Imager channels by use of radiative transfer calculations. *Appl. Opt.,* **37,** pp. 3149-3163, 1998.

5) T. Nakajima, T. Y. Nakajima, M. Nakajima, and GLI Algorithm Integration Team (GAIT): Development of ADEOS-II/GLI operational algorithm for earth observation. *Proc. of SPIE,* **3870,** pp. 314-322, 1999.

6) T. Nakajima and M. Tanaka: Effect of wind-generated waves on the transfer of solar radiation in the atmosphere-ocean system. *J. Quant. Spectrosc. Radiat. Transfer,* **29,** pp. 521-537, 1983.

7) M. Kuji and A. Uchiyama: Retrieval of precipitable water using near infrared channels of Global Imager / Advanced Earth Observing Satellite-II (GLI/ADEOS-II). *J. Remote Sens. Soc. Japan,* **22,** 149-162, 2002.

Atmospheric Gases

AEROSOL POLLUTION OF THE ATMOSPHERE AND ITS SOURCES FEATURES IN MONGOLIA

Nas-Urt Tugjsuren* and Tamio Takamura**

*Mongolian University of Science and Technology, Ulaanbaatar-46/157
**Center for Environmental Remote Sensing, Chiba University,
Chiba, 263-8522 Japan

Email:<tugjsur@ceres.cr.chiba-u.ac.jp>
Email:<takamura@ceres.cr.chiba-u.ac.jp>

Abstract

In the present work results of research of aerosol pollution of the atmosphere received according to measurement of solar radiation in the Mongolian grain farm region and capital city Ulaanbaatar are given. The major factor influencing to extinction of solar radiation in the atmosphere and source features of aerosol pollution above mentioned region of Mongolia are investigated.

The contribution of the aerosols to extinction of solar radiation to the real atmosphere of Ugtaal is 23.45% and Ulaanbaatar - 27.8% respectively. During the year the aerosol extinction on the average changes for Ugtaal 0.09 kW/m^2 - 0.18 kW/m^2 and Ulaanbaatar – 0.12 kW/m^2 - 0.21 kW/m^2.

Key words: Solar radiation, Atmospheric extinction, Atmospheric transparency, Aerosol pollution, Dust storm, Fine dust, Mongolian grain farm region.

1. Introduction

Among the different agents of climate change, anthropogenic greenhouse gases (GHG) and aerosols have the larger roles. As a consequence, the global increase in the CO_2 concentration of 1-2p.p.m.per year was measured almost 50 years ago using a single ground-based instrument (Yoram J et. al .2002, Keeling,C.D, 1960), while daily satellite observations (Husar,R.B et al. 1997) and continuous accuracy measurements (Clarke, A.D et al. 1985) are needed to observe the emission and transport of dense aerosol plumes downwind of populated and polluted regions, regions with vegetation fires, and deserts. The effect of GHGs on the energy budget occurs everywhere around the globe. Lately, researchers are focused one's attention on the various complex effects that different types of aerosols have on climate-from adding to the greenhouse effect to changing the reflective properties of clouds-and the great uncertainties in how large those effects are on climate warming. An air pollution is not only an industrial phenomenon. The part of the atmosphere that we thought to be the cleanest – the areas without a lot of industrialization- in fact can be very highly polluted, especially during the dry season. Asia is the largest source of aerosols in the world. That's largely because the region burns millions of tones of coal annually from its abundant coal deposits. It is visible, that the following facts. Between 1990 and 2000, annual releases of sulfur dioxide into the atmosphere in the United States dropped from about 20 million tons to 13 million tons, but in Asia they have climbed to about 45 million tons (Sylvia Wright, 2000). Aerosols are released from coal-burning power plants and coal-fired locomotives; heavy industry, such as metals production; automobile and truck exhaust; home heating; and the over tilling of dry-area farmland. In resent years, scientists have become increasingly concerned about the large-scale environmental effects of aerosols-particles suspended in air.

Every year in late winter and spring months, a number of Asian dust storms usually occurs in Gobi desert in China and Mongolia. Large amounts of yellow sand particles uplifted from those areas are transported to Japan, Korea and the North Pacific region by prevailing westerly wind (Jun Zhou al ets.2001).
Investigations of aerosol properties, distribution and variation, and its climate effect are now an urgent and important scientific problem, especially for developing countries.

2. Features of air pollutant sources on the territory of Mongolia

Although its total GHGs emissions is very low if compare to the world net total, Mongolia wishes to take a measures and actions to reduce GHGs concentrations in the atmosphere. The energy sector of Mongolia is the country's largest contributor to GHG emissions. The existing power sector of Mongolia consists of the Central Energy System with five coal-fired Combined Heat and Power Plant and 18 provincial interprises that operate isolated energy systems. Ulaanbaatar produced 75% of the total electricity in 1997 41.5%of the total domestic products of the state was done in Ulaanbaatar. Ulaanbaatar city is situated in an area that this sunk below its surroundings and is surrounded by 4 big mountains. Therefore, screen of smoke and dust is usually cover on the city. The cold continental climate, the reliance on wood and the low energy content of Mongolian coal contribute to high rate of carbon dioxide (CO_2) release per capita. The estimated national CO_2 emission in 1990 was 19.1 million ton or roughly 9.5ton per-capita. This estimate is larger than estimated per capita GHG emissions in the great majority of developing countries and exceeds the world average.

The present time in Mongolia has about 30 million cattle (five kinds of domestic animals; sheep, goats, horses, cows, camels) and they are increasing year by year. Mongolian livestock is a pastoral cattle breeding. Therefore from year to year wear processes of ground grow, in this connection loose soil of cattle legs is proportionally increased. Here, the main feature consists, in that a dust which have arisen from a legs of cattle is very thin a dust (fine particle). Certainly such dust is very easy to rise in the atmosphere when arises though weak winds. Aerosols, the tiny atmospheric particles well known as a human health hazard in air pollution, are increasingly being studied for their contribution to changes in the environment. The present time in Mongolia wear process of pastoral land reaches 7 million hectare. Wind and water are the main agents of natural soil erosion. In area of Ugtaal, number of day which reaches wind speed 24m/s, in April and May 5-6 times, 15-20m/s - 10-15 times. High winds can blow away loose soils from flat o hilly, terrain. In the Midwest much of the wind erosion occurs in winter when the ground is frozen. In Mongolia the wind erosion occurs mainly in spring when the ground is not frozen, but the upper most soil layer is dry and loose. Wind shear stress and soil surface characteristics are main factors controlling dust emission. Very fine particles can be suspended by the wind and then transported great distances. Fine and medium size particles can be lifted and deposited, while coarse particles can be blown along the surface. Dust emissions have consequently an impact on soil degradation but also on climate. Indeed, the very fine fraction of soil-derived dust has significant forcing effects on the radiative budget but also, climatic changes can modify the location and strength of dust sources. In Mongolian grain farm region already started intensive sand moving. Dust storm in those areas is characterized by high level of soil particles rising in the atmosphere in spring months.

Water erosion occurs during the spring with the thawing and melting action of the snow, also it occurs in summer when started rainy season in Mongolia. Water erosion generally occurs only on slops, and its severity increases with the severity of the slope.

Ground of agricultural region of Mongolian consists basically from light-clay ground. Lighter aggregate materials such as very fine sand, silt, clay and organic matter can be easily removed by the raindrop splash and runoff water; greater raindrop energy or runoff amounts might be required to move the larger sand and gravel particles. Without soil and plants the land becomes desert-like. Certainly, desert area will be one of the intensively source of dust storm.

A recent Mongolian report estimates that 30% of the country is moderately affected by degradation, and 4% severely to very severely (Batjargal Z., 2001). The significantly dry climate, low soil fertility and sparse vegetation cover of Mongolia, with over 40% of it's territory included in the geographic area of the Gobi Desert, make desertification a key issue of environmental concern. It has been estimated that over 78% of the total territory of Mongolia is under risk of desertification, of which nearly 60% is classed as highly vulnerable (View of Ministry of Nature and Environment, 1997).

Desertification is evident in Mongolia and the most important factors of it are the vulnerability of the ecosystem to human activities, especially crop cultivation and animal husbandry.

Land degradation induced by anthropogenic factors is common to all ecological zones of Mongolia. There are several specific human activities that have led to serious and widespread soil erosion and land degradation.

Crop cultivation is an important reason of soil erosion. Total land area of Mongolia is 156.5 million hectare of which 118.4 million hectare (75.8%) is capable of agricultural production, primarily extensive, pastoral livestock production. Cultivated land occupies 1.35 million hectare of the total land area. Over

57% of total arable land is located in the north-central aimags (provinces) of Tov (where located Ugtaal) and Selenge and the northeastern aimag of Dornod. It is estimated that over the past 30 years, an average of 35-50 tons of soils have been lost from each hectare of cultivated land due to erosion (Batjargal Z., 2001). Another factor is vehicle-induced degradation from overland travel in the absence of an established road system. It is estimated that nationwide there are four times as many vehicle tracks as are necessary, causing degradation and denudation of 0.7 million hectare of land.

Generally located on sloped or steep terrain, deforested areas as well as vehicle tracks are particularly subject to water erosion.

Mining and inadequate waste management can also make significant contribution to land degradation. An estimated 100.000 hectare of land have been degraded by coal and gold mining activities. Forest and steppe fire – it is one of the big source of the air pollution of Mongolia. Vegetation fires not only affect the composition bur also the circulation of the atmosphere. The effects of biomass burning extend from micro scale up to global processes. Forest-steppe pasture types comprise 27.1% of total pasture land area and occur primarily in the northwestern and north-central aimags. Forest covers 10% and grassland 70% of all territory. In Mongolia in average year occur the 50-60 forest fires and 80-100 steppe fires (IFFN No.26,2002). The average fire season usually has two peaks. One peak is during spring (from March to mid June) and accounts for 80 per cent of all fires. The other fire peak falls within a short period in autumn (September to October) and accounts for 5 to 8 percent of all fires. In summer, fires occur very rarely (only 2 to 5 percent of the total) because of heavy rains. From 1981 to 1995, forest and steppe fires burned an average of 1.74 million ha annually. In 1996 and 1997, the area affected by fire was 10.7 and 12.4 million ha respectively-an increase of more than six-fold. Within 1995-1999 was happened 857 cases of fires and burnt around 30 million hectares of forests and steppe areas (IFFN No26, 2002). Those fires were detected and monitored by NAOO satellite data. Above mentioned factors determined basic source features of aerosol pollution of the atmosphere on the territory of Mongolia.

3. Method for determination of aerosol pollution and Data processing

In the present work, we used investigative data at the Ugtaal Solar Station ($48^0 3'$N, $105^0 25'$ E, 1160m above sea level), which is located in the central grain farm region of Mongolia (Nas-Urt Tugjsuren and Tamio Takamura, 2001) and data at the Research Center for Geophysics of Mongolian State University ($47^0 55'$N, $106^0 52'$ E, 1306m above sea level). Data were collected at the Ugtaal 1986-1996 and at the Research Center for Geophysics 1979-2001 for every hour in the daytime. In order to measure the direct solar radiation received at the earth's surface, a thermo- electric actinometer (AT-50) was mounted. We simultaneously measured diffuse radiation using a thermo-electric pyronometer (M-80M) with a black and white type sensor. Also, we simultaneously measured meteorological elements, such as soil and atmospheric temperature, soil and atmospheric humidity, wind speed and direction, cloudy number and types etc.

As extinction of solar radiation in the atmosphere is caused basically, molecular (Rayleigh) scattering (ΔS_m), selective absorption of water vapor (ΔS_w), scattering and absorption by an aerosol (ΔS_a), for the general extinction of radiation in the atmosphere (ΔS) it is can be expressed by

$$\Delta S = \Delta S_m + \Delta S_w + \Delta S_a . \qquad (1.1)$$

Quantity ΔS is the important characteristics of the radiation regime of the atmosphere and the Earth, and can be received as a difference of intensity of a solar constant and the direct radiation measured on the Earth surface, at m=2. Extinction of radiation in the ideal atmosphere, ΔS_m at the accepted values of solar constant $S_0 = 1.38$ kW/m^2 and intensity of radiation in ideal atmosphere S_m=1.13 kW/m^2 (by S.I.Sivkov , 1965), is equaled 0.25 kW/m^2 (1.38 kW/ m^2 - 1.13 kW/m^2 = 0.25 kW/m^2).

At calculation of extinction of solar radiation by the water vapor is necessary for knowing general humidity content (ω) in all thickness of the atmosphere which is determined by an aerologic method or more simple way on ground measurements of absolute humidity of air (e_0) (Nikolskaya N.D., 1976). Many researchers have shown, that correlation connection (link) between ω and e_0 has local character. Therefore, for everyone physical - geographical area such connections should be investigated and specified. In this connection, we were established empirical dependence between humidity content in the atmosphere, the certain aerologic method and water vapor at the Earth surface for Ugtaal on seasons. A dependence between ω and e_0 for Ugtaal on seasons can be presented as follows:

$$\omega = 1.6e_0 + 1.3 \text{ (Winter)} \qquad \omega = 1.3e_0 + 5.6 \text{ (Summer)}$$

$$\omega = 2.0e_0 + 0.2 \text{ (Spring)} \qquad \omega = 2.1e_0 + 0.8 \text{ (Autumn)} \qquad (1.2)$$

Quantity ω, received by the regression equations can serve as characteristics of influence water vapor on the atmospheric transparency for Ugtaal. Also we used for definition of solar radiation absorbed by water vapor, ΔS_w. The solar radiation absorbed water vapor in the atmosphere is calculated under S.V.Zvereva formula (Zverova 1969):

$$\Delta S_w = 0.184(m\omega)^{0.27} \qquad (1.3)$$

where ω is the total water-vapor content in the atmosphere in the vertical direction, m is the atmospheric mass ($m=\cos z_{\odot}=1/\cos(90^0-h_{\odot})$), directed on the Sun. This dependence were checked up with use of the rich measuring data in Mongolia (D.Ganbaatar, 1985).

Aerosol extinction of solar radiation ΔS_a is received as a residual member from the equation (1.1) and can be expressed by

$$\Delta S_a = [\Delta S - (\Delta S_m + \Delta S_w)]. \qquad (1.4)$$

In the present work we were easily determined the aerosol extinction with use expression (1.4)

4. Results and discussion

Values of components of extinction of radiation ΔS_w and ΔS_a at m=2 are given in the table1.

Table1. General extinction of solar radiation and its components in the real atmosphere (in conditions cloudless sky, at m=2) of Ugtaal, (1986-1996)

Months	I	II	III	IV	V	VI	VII	VIII	IX	X	XI	XII	% of S_0
General extinction of direct solar radiation, kW/m^2													
$\Delta S \cdot 10^2$	44	44	46	53	57	55	56	56	54	51	48	46	36.83
Absorption of solar radiation by water vapor, kW/m^2													
$\Delta S_w \cdot 10^2$	10	10	11	12	14	17	19	20	16	14	13	11	10.09
Extinction of solar radiation by aerosol, kW/m^2													
$\Delta S_a \cdot 10^2$	9	9	10	16	18	13	12	11	13	12	10	10	8.64

From this table1. shows that, the general extinction of solar radiation for Ugtaal in the period 1986-1996 changes on the average from 0.44 kW/m^2 up to 0.57 kW/m^2 and for Ulaanbaatar in the period 1978-2001 changes on the average 0.50 kW/m^2 - 0.63 kW/m^2 . The contribution of an aerosol extinction of solar radiation in the real atmosphere of Ugtaal and Ulaanbaatar makes 23.45% and 28.5% respectively. During the year the aerosol extinction on the average changes Ugtaal from 0.09 kW/m^2 till 0.18 kW/m^2 . This change for Ulaanbaatar – 0.12 kW/m^2 - 0.21 kW/m^2 . If to compare the first 5 years (1986-1991) values of aerosol extinction of direct solar radiation with values of the last (1991-1996), aerosol extinction for spring months those values increased on 2-2.6%. It testifies to fast increase of aerosol pollution for this area. We can say that this view is connected not with human activities, and with natural origin. Last 10 years, aerosol extinction of direct solar radiation approximately increased on 7-9% for Ulaanbaatar, if compare with 1981-1991.

On fig.1 the annual course of components of extinction of solar radiation in the atmosphere is shown under conditions of the cloudless sky (at m=2) for Ugtaal.

In an annual course (fig.1) the maximum of aerosol extinction of radiation falls to April and May. It corresponds with the period of dust storm in region of Ugtaal. Observation data shows, that in area of Ugtaal the strong dust storm there will be 10-15 times in spring months of year.

Out appearance of this fig.1 shows that the general extinction of direct solar radiation similar with Ulaanbaatar. But aerosol pollution of Ulaanbaatar are observed much more than Ugtaal region in the winter months (For more details on Ulaanbaatar aerosol pollution, see Tugjsuren et al. 2003). It is clear, the region of Ugtaal covered with snow from November to April and there is no any industry which are polluting of atmosphere.

Depending on a combination of an annual course of extinction of the solar radiation the water vapor and an aerosol varies their percentage ratio. In conditions of Ugtaal, aerosol extinction prevails in April and May. Then aerosol pollution of Ulaanbaatar happens in winter months (November, December and January) much more than region of Ugtaal. In other words,we can say that for Ugtaal is too small a influence of anthropogenous factor on extinction of solar radiation in winter time. For an annual course of extinction of the direct solar radiation by aerosols, an autumn it is less, than in the spring. It we will be explain that dry of atmosphere and wind speed much less than spring in this region.

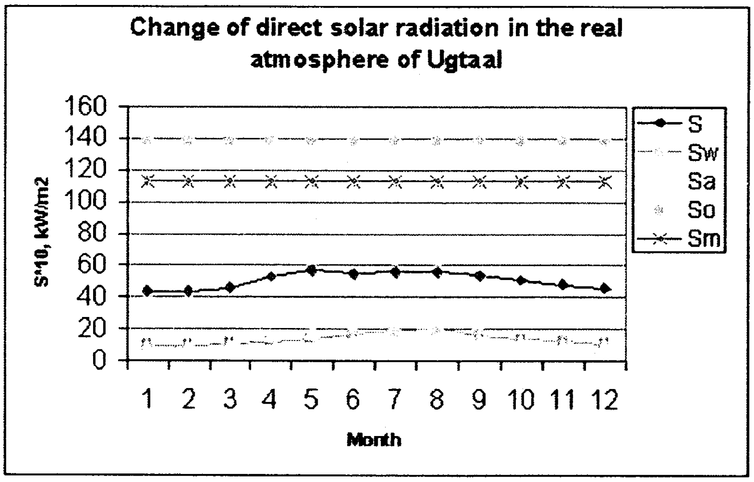

Fig.1.Change of direct solar radiation in the real atmosphere of Ugtaal (in conditions of the cloudless sky at m=2), 1986-1996. S_W - Absorption by water vapor; S_a - absorption by aerosol; S_m - Molecular scattering; x-value of a solar constant, S_0=1.38 kW/m^2 ; S – general extinction of direct solar radiation.

The least values of extinction of the solar radiation for Ugtaal is observed in the winter and an autumn. In the summer and in the spring the general extinction of direct solar radiation in the atmosphere grows and makes 39.01% of the solar constant (Table 2.)

Table 2. Seasonal changes of the general extinction of solar radiation and aerosol extinction

Season	Station	ΔS, kW/m^2	% of S_0	ΔS_a, kW/m^2	% of ΔS
Winter	Ugtaal	0.447	32.39	0.097	21.7
	Ulaanbaatar	0.536	38.8	0.163	30.4
Spring	Ugtaal	0.52	37.68	0.147	28.27
	Ulaanbaatar	0.597	43.3	0.196	32.8
Summer	Ugtaal	0.557	40.36	0.12	21.54
	Ulaanbaatar	0.593	43	0.14	23.6
Autumn	Ugtaal	0.51	36.96	0.117	22.94
	Ulaanbaatar	0.54	39.1	0.137	25.4

The received results show, that aerosol extinction of direct solar radiation of Ulaanbaatar high in the winter season. It is can be explain by air pollution of city Ulaanbaatar. Within the last 10 years air pollution levels in Ulaanbaatar have been continuously increasing and in winter time especially the issue one of the biggest ecological problems. The atmospheric levels of carbon dioxide and sulfur dioxide in Ulaanbaatar exceed the rate that should have a negative influence on human health by 1.5-2.6 and 1.3-2.8 times respectively. Mainly, among the atmospheric factors is a stable stationary atmospheric inversion that forms over the country annually, generally remaining in place from October to April. This inversion forms at approximately 600-700 meters above the ground surface and is accompanied by very low wind speed conditions. The wind speed and direction in Ulaanbaatar is usually traveling from northwest direction and the speeds decreasing to 1-2 m/s when they pass through Ulaanbaatar. It means that polluted air can not go far away from the city.

The aerosol extinction of Ugtaal in the winter on the average 19.17% less than long-term average value of ΔS_a and in the spring on 22.5% more, than average value ΔS_a. If calculate for Ugtaal, the per cent of the extinction of solar radiation by aerosols the winter and spring time of the general extinction of solar radiation as follows: 21.7% and 28.26%. Results of our researches of aerosol pollution of the atmosphere in Ugtaal testify, that the atmosphere of grain farm region of Mongolia contains an aerosol of a various origin in dependence from seasonally. By our calculations, an aerosol component in the period 1986-1996 increased approximately on 11.5% in comparison with aerosol component of 1976-1986, that be connected with dust storm in Mongolia.

The mean elevation of Mongolia is about 1500 meters above sea level which enhances the sharp continental climate, with warm, short summers, and cold, long winters. There is a short rainy season in June, July and August during which most of the yearly rain falls. Around 67-78 percent of all precipitation falls during these three summer months. Therefore, total water-vapor content in the atmosphere of above mentioned places is too high level and water-vapor absorption of solar radiation increasing in the summer season of Mongolia.

5. Concluding remarks

1. The contribution of the aerosols to extinction of solar radiation to the real atmosphere of Ugtaal is 23.45% and Ulaanbaatar - 27.8% respectively. During the year the aerosol extinction on the average changes for Ugtaal 0.09 kW/m^2 - 0.18 kW/m^2 and Ulaanbaatar – 0.12 kW/m^2 - 0.21 kW/m^2 . It shows, that the Ugtaal percentage value with Ulaanbaatar on 4.55% less, than its value. If to compare the first 5 years (1986-1991) values of aerosol extinction of direct solar radiation of Mongolian grain farm region with values of the last (1991-1996) the aerosol extinction for spring months those values increased on 2-2.6%. However, extinction of aerosol is increasing in spring and summer months, but winter time it is much less than Ulaanbaatar. It shows, that in grain farm region of Mongolia spring strong winds blow of a loose soil of cultivated area on the atmosphere. For Ulaanbaatar, by measurement data and calculation gives the last 10 years aerosol pollution increased on 7%-9% in winter season.

2. Results of our researches of aerosol pollution in the atmosphere in Mongolian grain farm region certifies, that the atmosphere of this area contains the aerosol basically of a natural origin seasonally. Dust pollution happens per spring months. For Ulaanbaatar, GHGs and smokes corresponds with the period of heating (between the period of October and May of next year) institutions, housing houses and so on. This period, the households living in ger district (ger-traditional Mongolian dwellings house) use 250.000 cubic meter of wood and 600.000tons of coal, hand operated small-scale power station - 400000 tons of coal and thermoelectric power stations 5 million tons of coal burning for every year. In addition, smoke by 60000 transport means makes contribution of the air pollution.

3. Air pollution in Mongolia can be attributed to coal and wood burning in houses, forest fires, industrial emission and vehicular emission in urban areas. Urban population is reported to be increasingly suffering from air pollution problems, especially during winter months.

4. It is necessary for us investigate aerosol physical and chemical characteristics ,including biomass burning aerosol particles. Many influences of biomass burning aerosol particles on atmospheric physics and chemistry are still poorly understood, which leads to contra dictionary statements in the resent literature such as that these aerosol particles do not affect precipitation formation or that they to a significant suppression of warm precipitation formation and increased optical thickness of clouds.

REFERENSES

1. Batjargal,Z., 2001: Desertification in Mongolia, RALA Report, **No200**.
2. Clarke, A.D. & Charlson, 1985: R.J. Radiative properties of the background aerosol: absorption component of extinction. Science 229, 263-265.
3. Fire situation in Mongolia, 2002: IFFN **No.26**-January, p.75-83)
4. Ganbaatar,D., 1985: Investigation of characteristics of atmospheric transparency in several points of Mongolia, PhD thesis, Mongolian State University, Mongolia, 163pp.
5. Greenhouse gases mitigation potentials in Mongolia, 2000: National Agency for Meteorology, Hydrology and Environment Monitoring, Mongolia,
6. Husar,R.B., Prospero, J.& Stowe, L.L., 1997: Characterization of tropospheric aerosols over the oceans with the NOAA AVHRR optical thickness operational product. J.Geophys. Res. **102,** 16889-16909.
7. Jun Zhou, Guming Yu, chuanjia, FudiQi,Dong Liu, Chenbo Xie, Huanling Hu., 2001: Lidar observations of Asian dust over Hefei, China in the spring of 2001. Proceedings of Nagasaki Workshop on Aerosol-Cloud Radiation Interaction and Asian Lidar Network, p18-22.
8. Keeling,C.D., 1960: The concentration and isotopic abundances of carbon dioxide in the atmosphere. Tellus 12, 200-203.
9. National plan of action to combat desertification in Mongolia., 1997: View of Ministry of Nature and Environment, Ulaanbaatar, pp71, (in English)
10. Nikolskaya N.D., 1976: To the questions on determination of the besieged water in the atmosphere, Journ.Meteor. and Hydrol.**№7**, 61-64 , Russia.
11. Sylvia Wright.,2003: Asian aerosol fingered in global pollution transport, Dateline.ucdavis.edu/080400/DL_aerosol.html.
12. Sivkov S.I., 1965: Extinction of solar radiation in the atmosphere. Scientific works of Central Geophysical Observatory, **169**, 66-75, Russia.
13. Tugjsuren N., Ganbaatar D., Dorjsuren B., Batsukh G., 2003: Determination of Aerosol pollution of the atmosphere over city Ulaanbaatar. Scientific Transaction of the Mongolian University of Science and Technology, **№49,** 222-228.
14. N.Tugjsuren, T.Takamura., 2001: Investigation for Photosynthetically Active Radiation Regime in the Mongolian Grain farm Region, J.Agric.Meteorol.,**57(4),** 201-207.
15. Yoram J.Kaufman, Didier Tanre, Olivier Boucher., 2002: A Satellite view of aerosols in the climate system. Nature, 12 September.
16. Zvereva S.V., 1969: About the extinction of solar radiation in areas of terrestrial pole. Scientific works of AANII, **287**, 171-187, Russia.

Lidar observations of Asian dust : Hefei, 1998 to 2003

Jun Zhou, Dong Liu, Guming Yu, Fudi Qi, Anyuan Fan
Anhui Institute of Optics & Fine Mechanics
Chinese Academy of Sciences, Hefei 230031, China
E-mail: jzhou@aiofm.ac.cn

Abstract

This paper presents main features of vertical distribution and temporal variation of Asian dust extinction coefficient at 532 nm wavelength over Hefei, China from 1998 to 2003.

1. Introduction

Every year in Spring months, a number of Asian dust storms usually occur in arid regions of Mongolia and northwestern China. Large amounts of yellow sand particles uplifted from those areas are transported to Korea, Japan and the North Pacific region by prevailing westerly wind. These dust particles sometimes are also southeasterly moved to Hefei area by cold front activities.

Hefei is located in the southeastern China (31.90° N, 117.16° E). SKYNET, AD-Net and ADEC projects have selected this site as one of the conventional stations. A Mie lidar there has been used to make intensive observations of Asian dust since Spring of 1998. These Asian dusts are also simultaneously observed by sky radiometer, sun-photometer, visible and infrared radiometers. This paper presents main features of vertical distribution and temporal variation of Asian dust extinction coefficient at 532 nm wavelength observed by the lidar from 1998 to 2003.

2. Asian dust events over Hefei from 1998 to 2003

Seventeen Asian dust events appeared over Hefei area during the six-year period. They were observed by lidar on January 4, April 16, 18-19 in 1998, February 27-28, March 4, April 5, 12 in 1999, March 27-28, April 5, 10 , May 12-13 in 2000, January 31, April 11,14 in 2001and February 8, March 17, 30 in 2002. We didn't find the dust event in 2003. Table 1 lists the wind data at 850 hPa, 700 hPa and 500 hPa at 2000 Beijing time (BT) (UTC plus 8) for the Asian dust event days in 2000 and 2001. They were measured by radiosonde in Fuyang, 300 km northwest of Hefei. It indicates that during these days strong northwestern winds existed over Hefei area. The meteorological data on surface also showed that the cold front was just past during these days.

Table 1. Wind at 850 hPa, 700 hPa and 500 hPa at 2000 BT for the Asian dust event days in 2000 and 2001.

Day	Wind speed (m/s) / Wind direction		
	850 hPa	700 hPa	500 hPA
March, 2000			
27	17/NW	28/W	50/WNW
28	10/NW	24/NNW	50/NNW
April			
5	4/NNE	12/NW	22/NW
10	8/NW	10/NW	42/NW
May			
12	10/NW	24/NW	22/NW
13	6/NW	8/WNW	24/NW
January, 2001			
31	14/NNW	17/WNW	26/WNW
April			
11	19/WNW	13/NNW	26/WNW
14	7/WNW	3/NNW	24/WNW

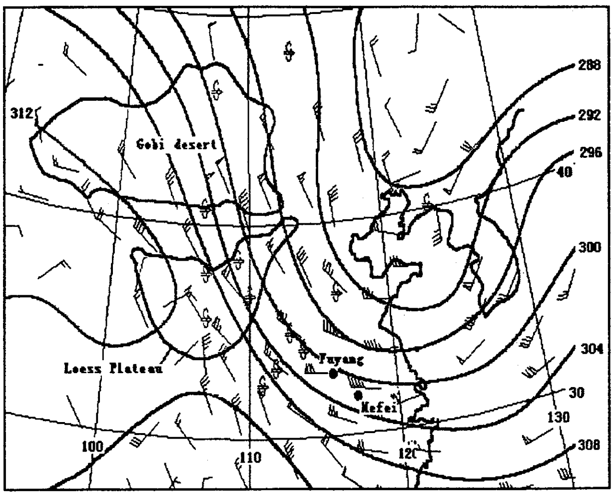

Figure 1. Wind speed and direction at 700 hPa geopotential height and Asian dust event observed on surfacc at 2000 BT on March 27, 2000.

As an example, figure 1 presents a map with wind speed and direction at geopotential height at 700 hPa over north and east of China at 2000 BT on March 27, 2000. The Asian dust event observed on the surface also is superimposed to the map. It clearly illustrates that northwestern current controlled over large part of northern and eastern China. It also shows that the Asian dust event was observed and reported by some weather stations between Asian dust source region and Hefei.

3. L300 Mie lidar and data processing

The L300 Mie lidar system is mainly composed of a double-frequency Nd:YAG laser transmitter, a receiving optics, a signal receiver and a data-acquisition. Table 2 lists main technical parameters for the lidar system.

The lidar is operated in cloudless night or early morning. The algorithm of Fernald is used to retrieve the aerosol extinction coefficient[1]. In this method, three assumptions have to be made: (1) the extinction to backscatter ratios for aerosol, S_1, is constant with altitude and equals 45 for 532nm wavelength, The corresponding one for air molecule $S_2 = 8\pi/3$; (2) the extinction coefficients of air molecule $\alpha_2(z)$ are known from U. S. Standard Atmospheric Model and Rayleigh scattering theory; (3) the boundary value $\alpha_1(Z_C)$ is determined through the matching method[2]. This method assumes a clear layer at a certain altitude around the tropopause, where the aerosol backscattering ratio $R(= 1 + \beta_1(Z_C)/\beta_2(Z_C))$ is assumed to be 1.01 .

Table2. Specifications of the L300 Mie lidar

Laser		**Signal receiver**	
Type	Nd:YAG	PMT	Hamamatsu R2257
Wavelength (nm)	532	Amplifier	LeCroy 612AM
Output energy/pulse (mJ)	70	Gain	40
Repetition rate (Hz)	10	Bandwidth (MHz)	140
Bean divergence (mrad)	1	**Data acquisition**	
Receiving optics		Transient recorder	DSP 2210
Type	Cassegrain telescope	Sample rate (ns)	200
Diameter (mm)	300	Accuracy	12-bit
Field of view (mrad)	4	**Data processing**	Pentium 586

4. Observational results and discussions

4.1 Typical Asian dust extinction profiles

There were two kinds of vertical distributions of Asian dust extinction coefficient over Hefei area. One are the profiles such as in the left of figure 2 and 3. They were observed by lidar on April 5, 1999 and March 28,2000.

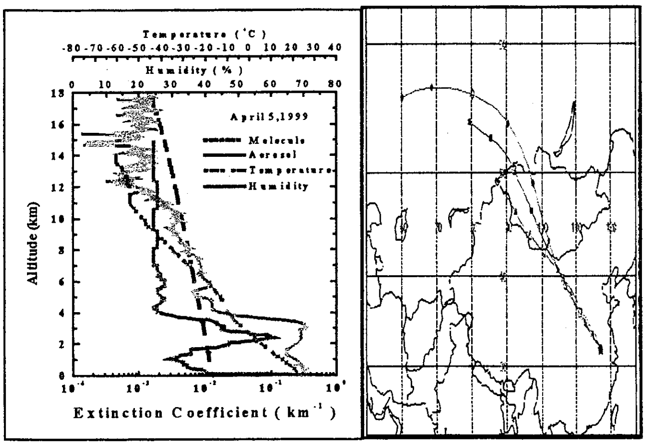

Figure 2. Profiles of air temperature, humidity and Asian dust extinction coefficient on April 5, 1999 and air backward trajectories at 1 km (red), 2 km (blue) and 4 km (green) heights (48 hours from 2000 BT on April 5, 1999).

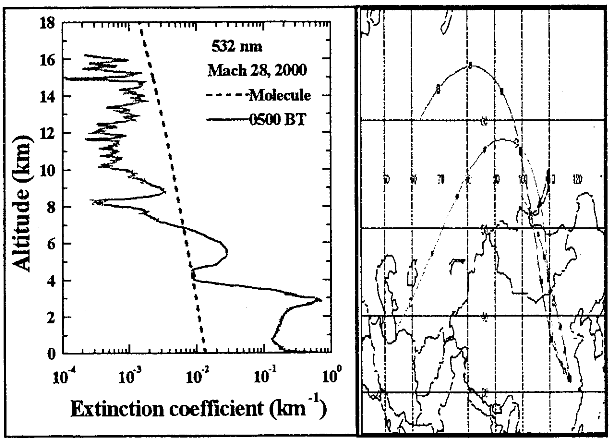

Figure 3. As the same as the figure 2, but no temperature and humidity on March 28, 2000.

The profiles of temperature and relative humidity are presented in the figure 2. They were measured by a radiosonde at the location of the lidar. The corresponding air backward trajectories at 1 km, 2 km and 4 km heights are shown in the right of these figures. They are obtained by using the HYSPLIT model developed by NOAA/ARL.

These extinction profiles were usually related to rather stronger Asian dust events over Hefei area. The noticeable feature in the extinction figures is the very thick boundary layer from surface to about 3~4 km. The aerosol extinction coefficients were nearly 1.0 km^{-1} on the ground, and were all larger than 0.1 km^{-1} throughout the boundary layer. For example, in the figure 3 the peak aerosol extinction coefficient at 3 km was as large as 0.7 km^{-1}. Such a big aerosol extinction value at this height was never observed before.

In the left of figure 2 , an inversion layer of temperature appeared at about 4 km and at this altitude the Asian dust extinction coefficient exhibited the steepest gradients. The humidity was also shown the sharpest decrease just at about 4 km. Moreover, the peak Asian dust extinction coefficient in 2-3 km range was associated with the highest moisture in the same range. Even the fine scale of Asian dust extinction coefficient also was well correlated with the fine relative humidity structure from ground to 4 km altitude.

It indicates that the initial dry Asian dust particles might be mixed with a humid air in the boundary layer while being transported to Hefei area. The aerosol particles and moisture are strictly related components. Both of them tend to be trapped within the boundary layer determined by temperature inversion. Aerosol particle extinction is very sensitive to relative humidity. The variations in air humidity affect the aerosol extinction mainly through modification of the aerosol size distribution and composition. Thus hygroscopic Asian dust particles contribute larger extinction. It indicated from the air trajectories that these Asian dust particles were coming to Hefei area from middle and western Mongolia.

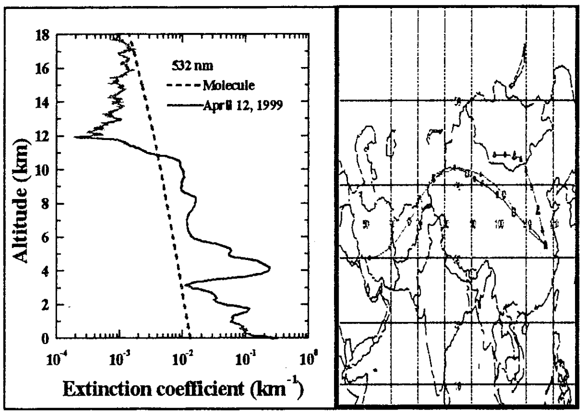

Figure 4. As the same as the Figure 3, but on April 12, 1999.

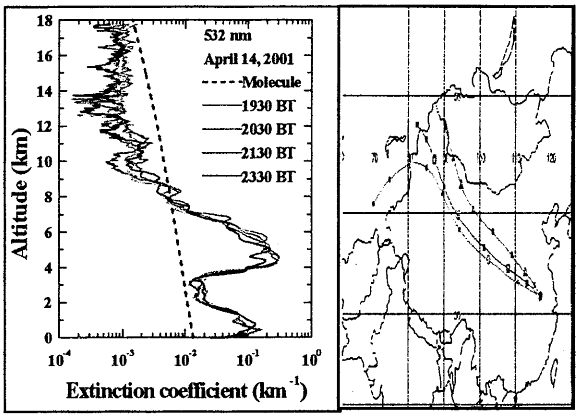

Figure 5. As the same as the Figure 3, but on April 14, 2001.

The other kind of Asian dust extinction profiles is shown in right of figure 4 and 5. They were observed by lidar on April 12, 1999 and April 14, 2001. The corresponding air backward trajectories at 2 km (red), 4 km (blue) and 6 km (green) heights are shown in the right of these figures.

It can be seen from the extinction profiles that the boundary layer was in a normal state with aerosol extinction coefficients of around 0.1 km^{-1} and depth of about 2 km. However, the aerosol extinction coefficients in the elevated aerosol layers within the middle troposphere from 3 to 6km were unusual large. For example, in the figure 5 the peak aerosol extinction coefficient as large as 0.3 km^{-1} was observed at 4.5 km. Such a big value at this height also was never observed before. This illustrates that the Asian dust particles might intrude into Hefei area mainly above the boundary layer. So, they had small effects on the local boundary layer. It indicated from the air trajectories figures that these Asian dust particles were coming to Hefei area from northwestern China.

4.2 Seasonal average aerosol extinction coefficient profiles

Seasonal average aerosol extinction coefficient profiles from 1998 to 2000 are shown in figure 6. The number of days of lidar observations was 112, 79, 90, 133 for Winter (December, January and February, and so forth for another seasons), Spring, Summer and Autumn, respectively. It should be noted that the extinction from very thin cirrus clouds are not removed from the statistics because of their small effect on the retrieved aerosol extinction profiles.

The figure clearly shows that larger aerosol extinction coefficients were observed from 1km to about 10 km altitude range in the springtime rather than any other season. The aerosol coefficient values from 1 km to about 4 km might be associated with the Asian dust events. The mechanism for bigger values in upper troposphere from 4 k to 10 km is not clear on the basis of lidar data alone. Further study to explain the observational result is needed.

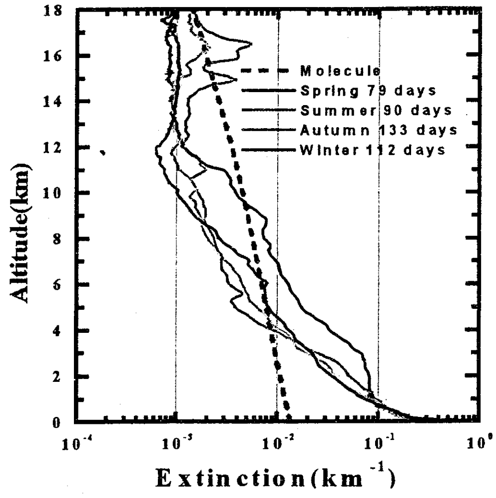

Figure 6. Seasonal average aerosol extinction coefficient profiles from 1998 to 2000.

4.3 Monthly average aerosol optical depth

The lidar derived monthly average aerosol optical depths (0.03-18 km) from June, 1997 to June, 2003 are shown in figure 7. It is clear that much large average value (>0.5) always was obtained in one of the spring months in 1998, 1999 and 2000. The results are mainly related to the intense Asian dust event occurred in that month. By comparison, after the year of 2000, the aerosol optical depth was not exhibited so large value in the springtime.

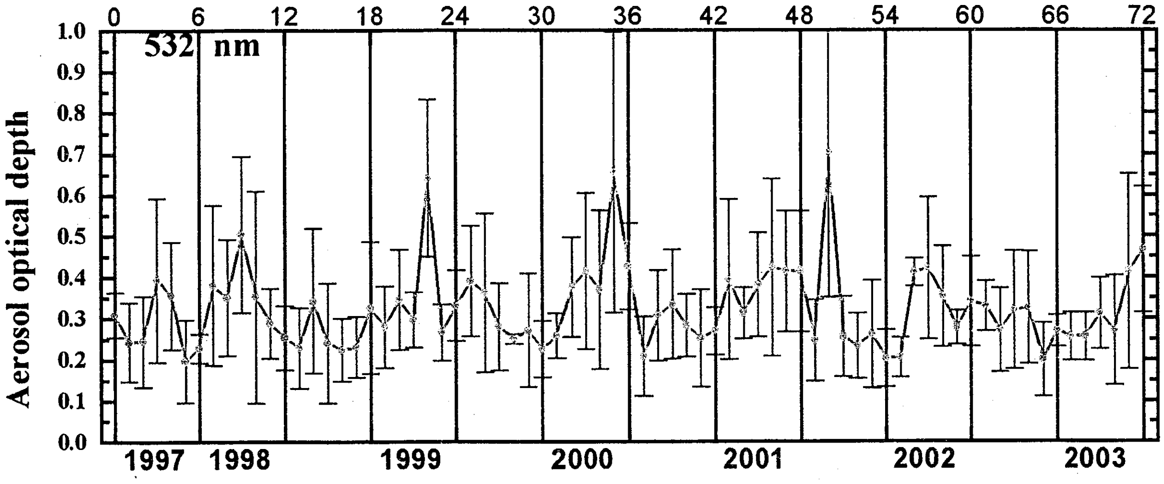

Figure 7. The lidar derived monthly average aerosol optical depths (0.03-18 km) from June, 1997 to June 2003.

References

1. F. G. Fernald , " Analysis of atmospheric lidar observations: some comments, " *Applied Optics, 23,*pp 652-653, 1984.
2. Y. Sasano, "Tropospheric aerosol extinction coefficient profiles derived from scanning lidar measurements over Tsukuba, Japan, from 1990 to 1993," *Applied Optics, 35,* pp4941-4952, 1996.

RETRIEVAL OF AEROSOL OPTICAL PARAMETERS FROM SATELLITE IMAGE DATA OVER LAND

Y. Kawata, H. Fukui and K. Takemata
Earth and Social Information Core, Dept. of Computer Science
Kanazawa Institute of Technology,
Ogigaoka 7-1, Nonoichi, Ishikawa 921-8501, Japan

ABSTRACT

We retrieved the aerosol optical thickness τ_a over Japan from several data sets of Terra/ASTER and Landsat-7/ETM+ using the correlation between the visible reflectance and middle IR reflectance. This band correlation method for aerosol retrieval was originally proposed for MODIS data analysis by Kaufman et al.(1977)[1]. The empirical surface reflectance ratios for certain land categories in Japan between the visible and infrared bands were computed using the observed sky radiometer data and 5 data sets of Terra/MODIS in 2002 and 2003. The results of retrieved aerosol optical thickness τ_A were compared with the simultaneous sky observation data at our study site. We found a good agreement between the retrieved and observed values. The aerosol optical thickness over sea was retrieved assuming no reflected contribution from sea in the near IR band[2].

1. INTRODUCTION

In the atmospheric correction of the remotely sensed earth image data we need the information on the aerosol optical parameters, such as the optical thickness τ_A, Ångström exponent α, and the size distribution type. Since simultaneous sky measurements are not always possible, a method for estimating them from the satellite-measured data itself is highly desirable. The band correlation method is a very useful tool to retrieve the aerosol optical parameters from satellite data itself. In the band correlation method the empirical surface reflectance ratios for certain land categories between the visible and infrared bands play an important role.

2. REFLECTANCE RATIOS

Kaufman et al.(1977)[1] found that there existed empirical band ratios for a few land categories between the visible reflectance and middle IR reflectance as follows:

$$r_{B1}/r_{B7} = C_{1v} \quad \text{(vegetation)} \qquad (1)$$
$$r_{B1}/r_{B7} = C_{1u} \quad \text{(urban, other)} \qquad (2)$$
$$r_{B3}/r_{B7} = C_{3v} \quad \text{(vegetation)} \qquad (3)$$
$$r_{B3}/r_{B7} = C_{3u} \quad \text{(urban, other)} \qquad (4)$$

where r_{B7}, r_{B1} and r_{B3} are the reflectance values in the band 7(2.16μm), band 1(0.645 μm) and band 3(0.469 μm) of Terra/MODIS. They obtained the reflectance ratios, C_{1v}=0.50, C_{3v}=0.25, C_{1u}=0.69, and C_{3u}=0.42 from ground and airborne measurement data in USA. In this study, we compute these reflectance ratios in Japan using the simultaneous sky measurement data and several image data sets of Terra/MODIS over Japan (May 06, 2002, April 07, April 16, May 09, and June 03 in 2003). First of all we classified the MODIS image data into 5 classes, namely, vegetation, urban, cloud & snow, sea, and other, by using the maximum likelihood method. The classification map is shown in Fig.1. The reflectance values for three classes of vegetation, urban and other were obtained from Terra/DODIS image data by removing the atmospheric effects using the observed aerosol optical thickness values in Bands 1 and 3. Since the aerosol scattering effects are negligible in the band 7(2.16μm), the surface reflectance in Band 7 was obtained by removing only molecular attenuation effect. We found the values of surface reflectance ratio for vegetation, urban and other classes in Bands 1 and 3, applicable in Japan, as follows:

C_{1v}=0.554, C_{3v}=0.547 for vegetation
C_{1u}=0.580, C_{3u}=0.489 for urban

C_{1o}=0.503, C_{3o}=0.417 for others

We should note a large discrepancy in the value of C_{3v} between USA and Japan. The scatter diagrams in reflectance ratio are given in Fig.2. For given reflectance ratios for those classes, we can retrieve distributions of aerosol optical thickness in Bands 1 and 3 by using LUT(Look Up Tables) in which the theoretical radiances at the top of the atmosphere(TOA) are tabulated as a function of the surface reflectance and the aerosol optical thickness for given bands and angles of the incident and reflection.

3. VALIDATION RESULTS

We retrieved the aerosol optical thickness values over land in Band 1 and 3 of MODIS data using pre-computed LUT of the theoretical radiance at TOP as a function of the reflectance for a given angular condition. The distribution maps of aerosol optical thickness in Band 3(0.469 μm) and 1(0.645 μm) are shown in Fig.3-(a) and -(b), respectively. The aerosol optical thickness values in both bands over the sea were estimated from those in Band 4, assuming measured Ångström exponent α at our study site. From seen in Fig.3 we can notice a smooth transition between the sea and land as shown. The validation results of the retrieved aerosol optical thickness τ_A are shown in Fig.4, based on the new surface reflectance ratios found in this study. In addition, we applied the band correlation method to Terra/ASTER and Landsat/ETM+ image data. Acquired dates of ASTER data sets are on April 02, 2002 and June 08, 2003

, and that of ETM+ on April 15, 2001

. The validation results of retrieve the aerosol optical thickness are shown in Fig.5. The retrieved aerosol optical thickness map of coastal area from ASTER data in Band 1(0.645 μm) is shown in Fig.6. As seen in Figs.5 and 6, we can find an excellent agreement in τ_A between the estimation and observation.

4. CONCLUSIONS

We can conclude by this study as follows:

(1) We presented new surface reflectance ratios between the visible and infrared bands using both MODIS data sets and simultaneously observed sky data.

(2) We confirmed that the band correlation method is a powerful method for retrieving the aerosol parameters over lands.

(3) We obtained much better results in the aerosol optical parameter retrieval over Japan with new reflectance ratios than with Kaufman's reflectance ratios. In addition, a very smooth continuation of aerosol at the boundary between the land and sea was obtained.

(4) Seasonal and regional variation in the reflectance ratio should be studied further.

(5) We should use the water vapor amount, deduced from MODIS data in computing the surface reflectance at 2.13 μ m, instead of adopting that from MODTRAN code.

ACKNOWLEDGEMENTS

This research was supported partially by CEReS, Chiba Uni., Joint Project Research 15-1. MODIS data sets were provided by Yasuoka Lab., ISS, Univ. of Tokyo and Frontier Research Center, Tokyo Univ. of Infor. Sciences. ASTER data set was provided by ERSDAC, Japan. We appreciate very much for their kindness.

REFERENCES

Kaufman et al., 1997. The MODIS 2.1mm Channel-Correction with Visible Reflectance for Use in Remote Sensing of Aerosol, IEEE Trans. GRS, vol.35, no.5, pp.1286-1298.

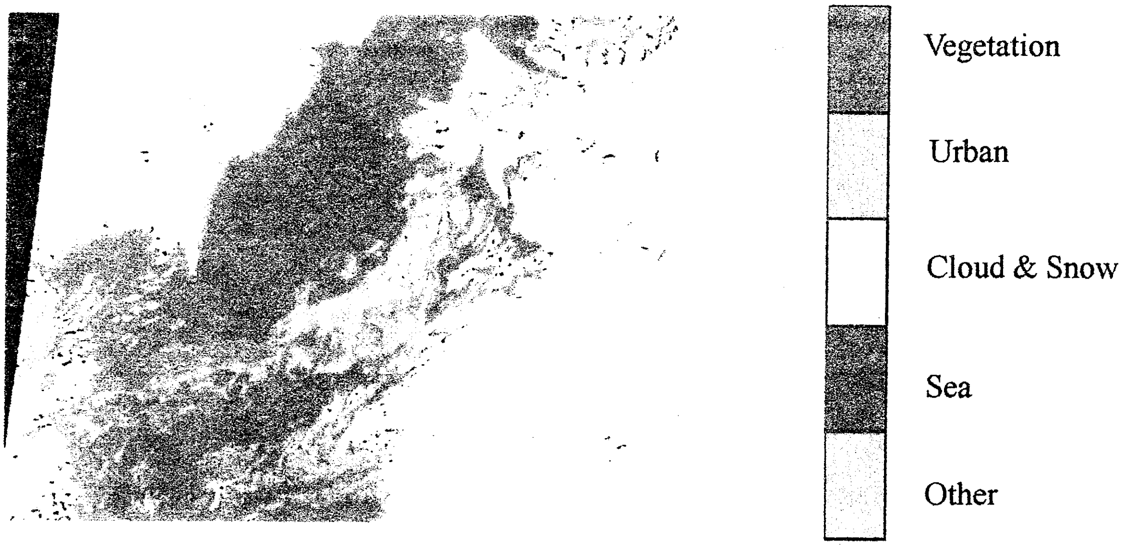

Fig. 1. Five class classification map from MODIS data.

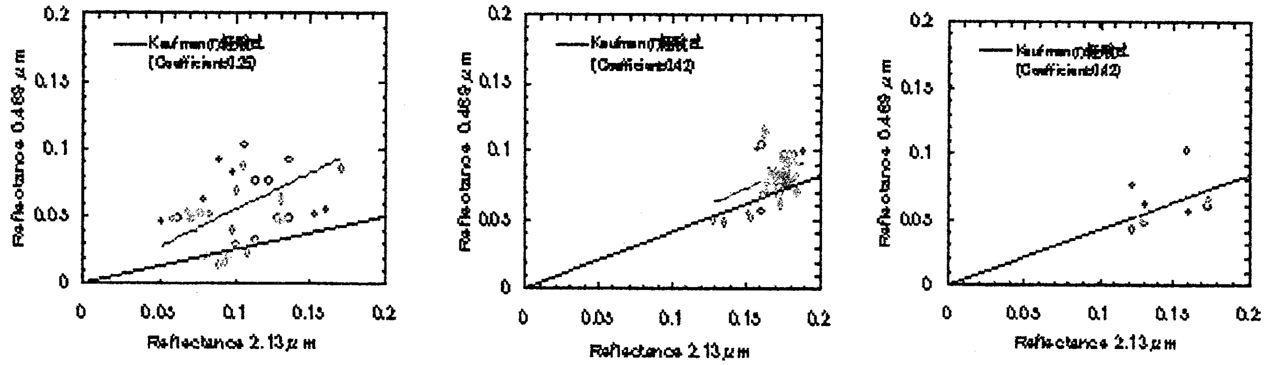

(a) Vegetation: C_{3v}=0.547 (b) Urban: C_{3u}=0.489 (c) Other: C_{3O}=0.417

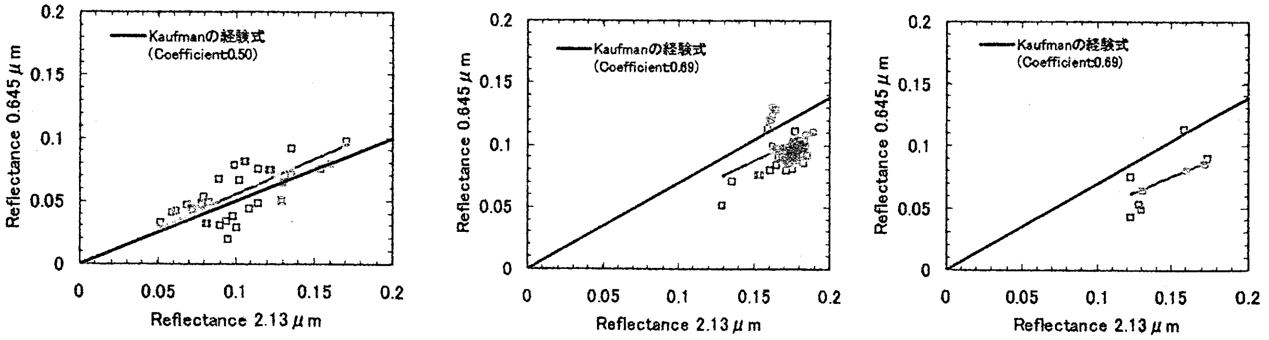

(d) Vegetation: C_{1v}=0.554 (e) Urban: C_{1u}=0.580 (f) Other: C_{1O}=0.503

Fig.2. Reflectance Ratios for three classes in Japan

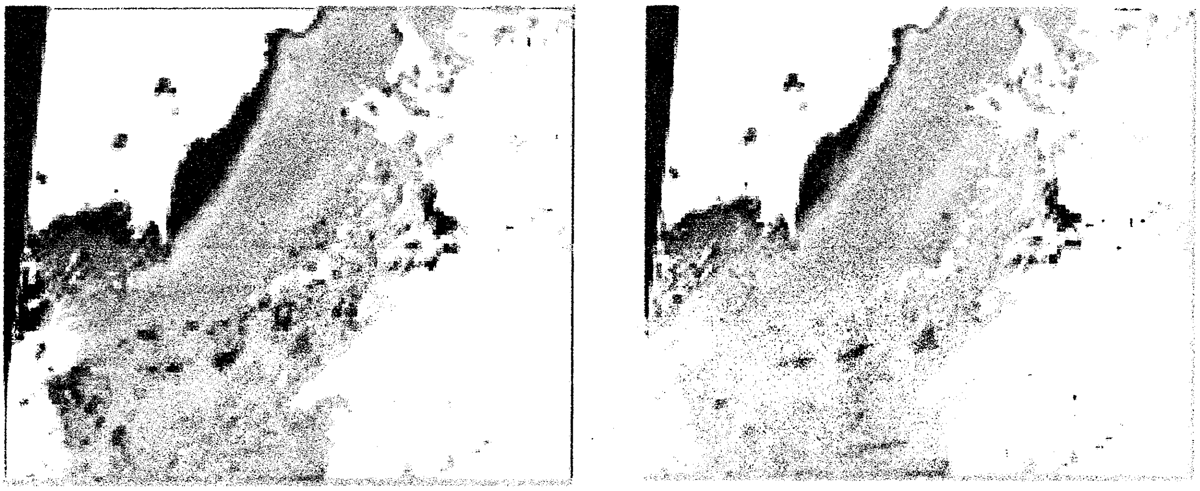

(a) Retrieved τ_A in Band 3(0.469μm) (b) Retrieved τ_A in Band 1(0.645μm)

Fig.3. Retrieved τ_A map near Japan, based on new reflectance ratios found in this study.

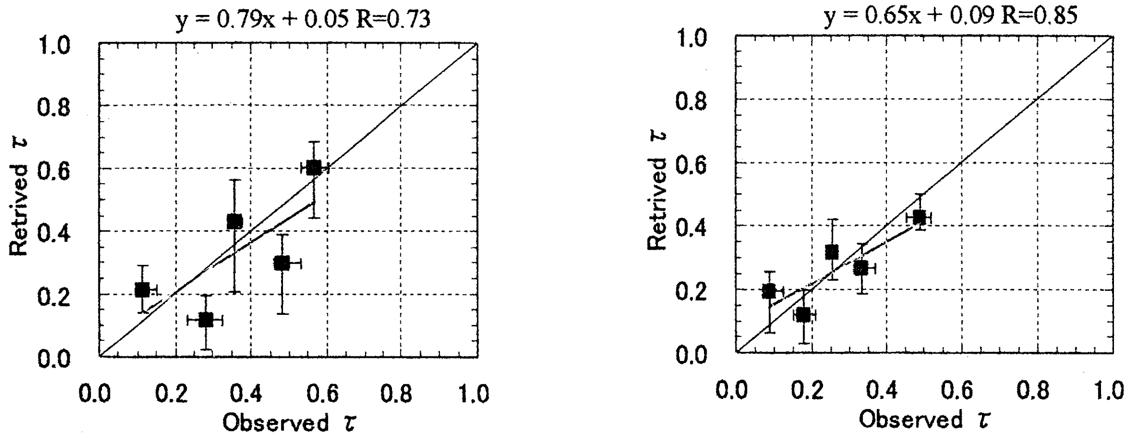

(a) at 0.469μm (b) at 0.645μm

Fig.4. Validation results of retrieved aerosol optical thickness from Terra/MODIS, using new reflectance ratios.

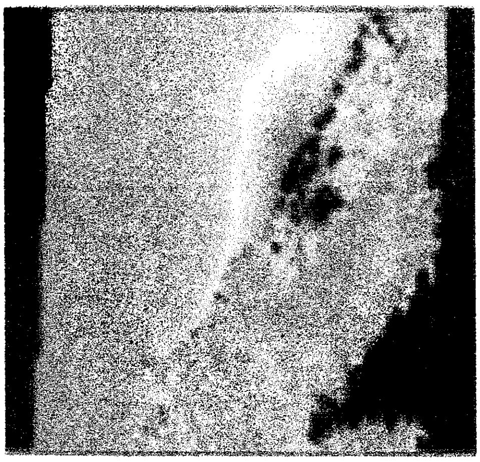

Fig.5. Retrieved τ_A map from ASTER data

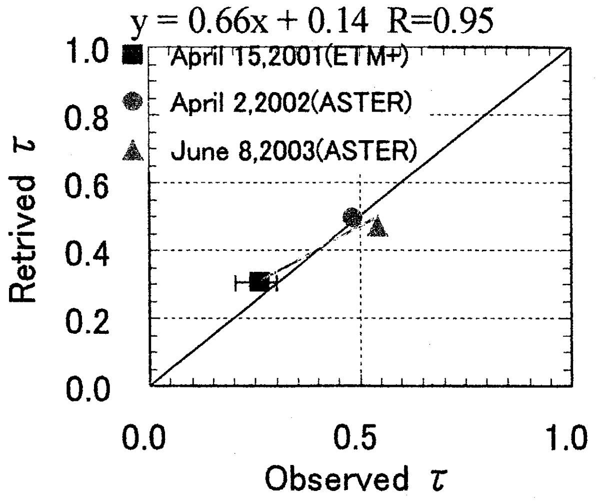

Fig.6. Validation of retrieved τ_A from ASTER and ETM+ data.

Observation of dust, smoke, and urban aerosols with multi-wavelength Raman lidar in Tokyo

Toshiyuki Murayama[1] and Katsuya Wada[2]
1 Faculty of Marine Engineering, Tokyo University of Marine Science and Technology
E-mail: murayama@e.kaiyodai.ac.jp
2 Graduate School of Marine Science and Technology, Tokyo University of Marine Science and Technology
E-mail: kwada@e.kaiyodai.ac.jp

Abstract

We have initiated multi-wavelength Raman lidar observation at Etchujima campus (35.66°N, 139.80°E) of Tokyo University of Marine Science and Technology (TUMST) since February 2002. It is an extension of our aerosol and cloud research using lidar based on Nd:YAG pulsed laser; now we can obtain vertical profiles of three backscatter coefficients at 355, 532, and 1064 nm, two extinction coefficients at 355 and 532 nm, one depolarization ratio at 532 nm of aerosol, and water-vapor mixing ratio. As of winter of 2003, we have acquired data sets of some particular tropospheric aerosol events such as Asian dust and forest fire smoke, and frequently observed urban haze. These data sets tend to show characteristic features of not only depolarization ratio but also wavelength dependence of backscatter, extinction coefficients and lidar ratio depending on aerosol type. In the smoke case, the backscatter-related Angström exponent was high while Angström exponent was low, which causes a lower lidar ratio at 355 nm than at 532 nm. Systematic analysis of UV-Raman shows the lidar ratio for aerosol at 355 nm distributed between 40 and 80 sr. The lidar ratio of water clouds favors lower values of ~20 sr. Water-vapor mixing ratio measured by the lidar well agrees with radiosonde observation. Further systematic analyses and monitoring are under going.

1. Introduction

We have extensively studied the optical properties of aerosols in the planetary boundary layer (PBL) and free troposphere with polarization and Raman lidar technique, Sun photometers and in-situ instruments at TUMST[1] in Tokyo [*Murayama et al.*, 1996; *Murayama et al.*, 1999; *Murayama et al.*, 2001; *Murayama et al.*, 2002]. Asian dust and pollution aerosols have been primary objects of our study. Recently, we have recognized that vertical variability of aerosol composition is significantly high in this region from ACE-Asia lidar-aircraft intercomparison [*Murayama et al.*, 2003]. Therefore, it is highly desirable to derive aerosol optical properties resolving with height, which is necessary to assess the radiative impact. However, intercomparison with airborne measurements is scare in this region. So far, we need to develop an advanced lidar that enables to characterize various kinds of aerosols and retrieve the comprehensive microphysical properties [*Müller et al.*, 2001]. Considering the feasibility, we have extended our lidar system to have additional capability of UV-Raman lidar based on third-harmonics emission from second Nd:YAG laser. Now our lidar system is capable of measuring backscattering coefficients at 355, 532, 1064 nm, extinction coefficients at 355 and 532nm, depolarization ratio at 532nm and water–vapor mixing ratio simultaneously. Here we present the outline of the lidar system, some results of the observations for urban haze, elevated Asian dust layer, and biomass-burning aerosol. We also show a systematic analysis of recent UV-Raman lidar observation and mention the perspective.

2. Instrumentation and Data Analysis

2.1 Multi-wavelength Raman Lidar System

We allocated a UV-Raman lidar system beside existed Mie-Polarization-Raman lidar using 532 (VIS) and 1064 nm (IR) lasers as shown in Fig. 1. The features of VIS/IR lidar system were described by *Murayama et al.* [1999, 2003]. Here we describe the UV Raman lidar system briefly. The system uses another Nd: YAG laser with third-harmonics generator and a Schmid-Cassegranian telescope in 35-cm diameter. The optical axis of the telescope was well co-aligned to visible/infrared laser beam too. The repletion frequency of the laser pulse is 10 Hz, which is triggered from another Nd:YAG laser's Q-switch signal with a 1-msec delay. These conditions allow us to observe nearly same aerosols and clouds in time and space for UV and VIS/IR lidar systems. Raman-shifted backscattered lights from nitrogen and water-vapor molecules, which wavelengths are 387 and 408 nm respectively, are detected with photomultiplier tubes (PMTs) after separated from strong elastic scattering by dichroic mirrors and narrow interference filters. Both analog and photon-counting methods of PMT are employed with Licel (Berlin, Germany) transient recorders. Raman lidar measurements have been done only during nighttime typically for two to hours after the sunset. Typical operation pulse powers are 100, 100, 200 mJ for 355, 532 and 1064 nm laser beams.

---

[1] Former institution is Tokyo University of Mercantile Marine

2.2 Analytical Method of Raman Lidar

Normally we average/integrate all acquired analog (AN) and photon-counting (PC) data during each nighttime observation. AN and PC data for each channel are glued carefully, consulting expected molecular-based scattering profiles. Extinction coefficient and scattering ratio of aerosols at 355 and 532 nm are derived by the methods developed by *Ansmann et al.*[1992] and *Whiteman et al.*[1992]. Water-vapor mixing ratio is obtained from the ratio of Raman backscatter signal from water-vapor molecules to that from nitrogen molecules in the UV-Raman lidar system. Atmospheric density profile is obtained from routine radiosonde observations at Tateno (36.05°N, 140.12°E) on 12UTC. Normalization of scattering ratio is made at an almost aerosol-free height typically over 10 km. Corrections due to difference of atmospheric transmittance at primary laser wavelengths and Raman-shifted wavelengths are made for both molecular and aerosol's extinctions. In these processes, we assumed the Angström exponent as 1.0 usually and often took into account of the error. Backscatter coefficients are derived from the scattering ratios. A treatise on the evaluation of Raman lidar technique is recently given by *Whiteman* [2003a, b]. Backscatter coefficient at 1064 nm is obtained from the Mie-Rayleigh signal by using *Fernald*'s method [1984] assuming that the extinction-to-backscatter ratio (lidar ratio) of aerosol is 40 sr.

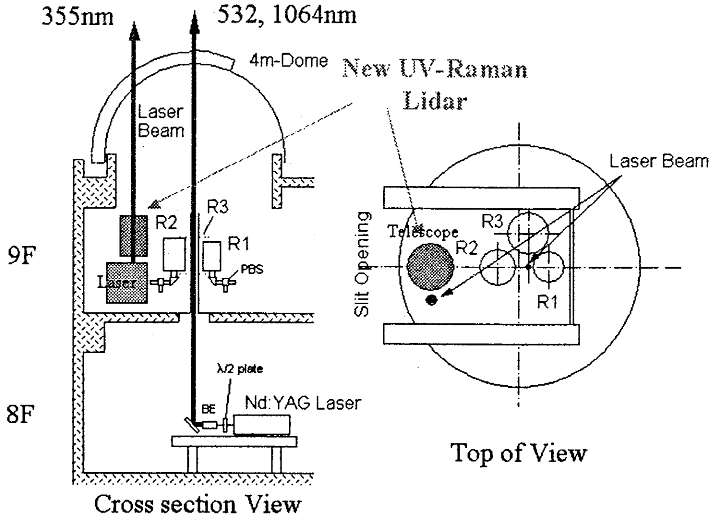

Fig. 1 Schematic view of TUMST Raman lidar system. Partly taken from *Murayama et al.* [1999].

3. Results of Observations

Here we describe features of aerosol optical properties derived from two-wavelength Raman lidar observations regarding to aerosol type. Outflow of tropospheric aerosols from Eurasian continent tend to be transported in middle and high troposphere, we often observed multi-layer structure decoupled with local urban haze in PBL. We can see how aerosol optical properties differ layer by layer.

3.1 Case of Urban Haze

Tokyo is one of the largest urban areas in the world. Thus we expected the urban aerosol plume has gave a large impact on western Pacific. Local urban haze is often observed under stable weather condition in all seasons. Fig. 2 shows such a case in winter. High backscatter coefficient β between 8.5 and 11 km indicate cirrus clouds. We can see that cirrus is a good object to check no wavelength-dependence of β and this fact is helpful to evaluate the calibration of β at 1064 nm. The data set shows relatively higher wavelength dependence in both β and extinction coefficient σ in the PBL, which seems to reveal features of urban-like aerosol composed from fine particles. The lidar ratio S at 355 nm (S_{355}) is apparently higher than that at 532 nm (S_{532}); the mean S_{355} and S_{532} between 0.9 and 2.1 km are 60.1±6.1 and 48.1±14.3 sr, respectively. We omitted the profile of depolarization ratio because it is quite small in urban haze case. We also note the S_{355} in cirrus is about 20 sr, which is much smaller than in PBL aerosols. We need more systematic analyses on urban aerosols as partly described in section 3.4.

3.2 Case of Mineral Dust

We have a smaller number of Asian dust events in the spring of 2003 at ground level than usual but still we observed some significant Asian dust layers in the free troposphere by lidar. We show the profiles obtained on March 12, 2003 in Fig. 3. We also indicated Angström exponent (AE) derived from extinction profiles at 355 and 532 nm and similarly backscatter-related Angström exponent (BAE) in the figure. As seen in Fig. 3, an elevated aerosol layer between 3 and 5 km can be decomposed to two components as indicated by horizontal lines A and

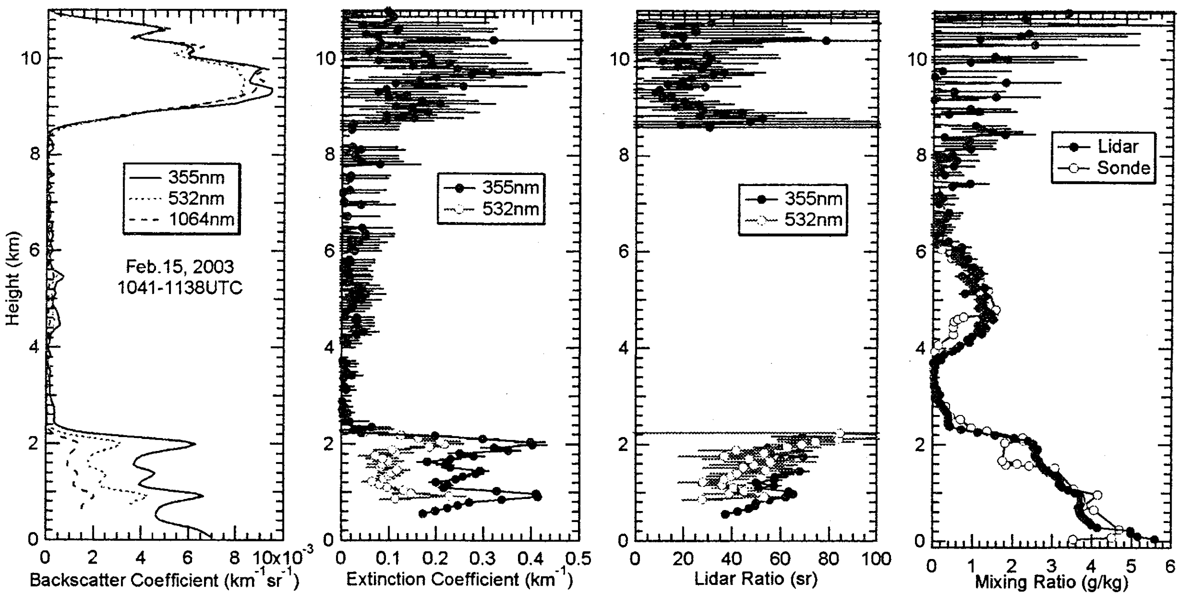

Fig. 2 Example of Raman lidar observation for urban aerosol and cirrus. The data were obtained during 1041-1138UTC on February 15, 2003. The radiosonde observation of water-vapor mixing ratio on 12UTC at Tateno is also shown.

B: the layer A is a sharp one peaked at 4.6 km and the layer B is a broader one peaked at 3.9 km. The lower layer B looks more dust-like as suggested from the aerosol depolarization ratio (ADR) profile. We obtained that the mean lidar ratio at 355 and 532 nm were 48.6±8.5 and 43.1±7.0 sr, respectively in the dust-like layer between 3.5 and 4.3 km. This value of S_{355} is comparable for the observation at 351 nm in southern Italy (~50sr) [*De Tomasi et al.*, 2003] but smaller than the observation in Leipzig, Germany (50-80 sr) [*Mattis et al.*, 2002]. Mie calculation based on mineral dust model [*Ackermann*, 1998] suggests that UV-absorbing effect increases the lidar ratio in UV-wavelength than in visible wavelength, which agrees with our observation. In addition, we can see interesting differences of aerosol optical properties in the layers A and B not only ADR but also AE and BAE; we can see high AE and BAE values in the layer A than in the layer B, which also suggest the layer A is composed from fine aerosols unlike mineral dust. Since the water vapor mixing ratios in the layers A and B are

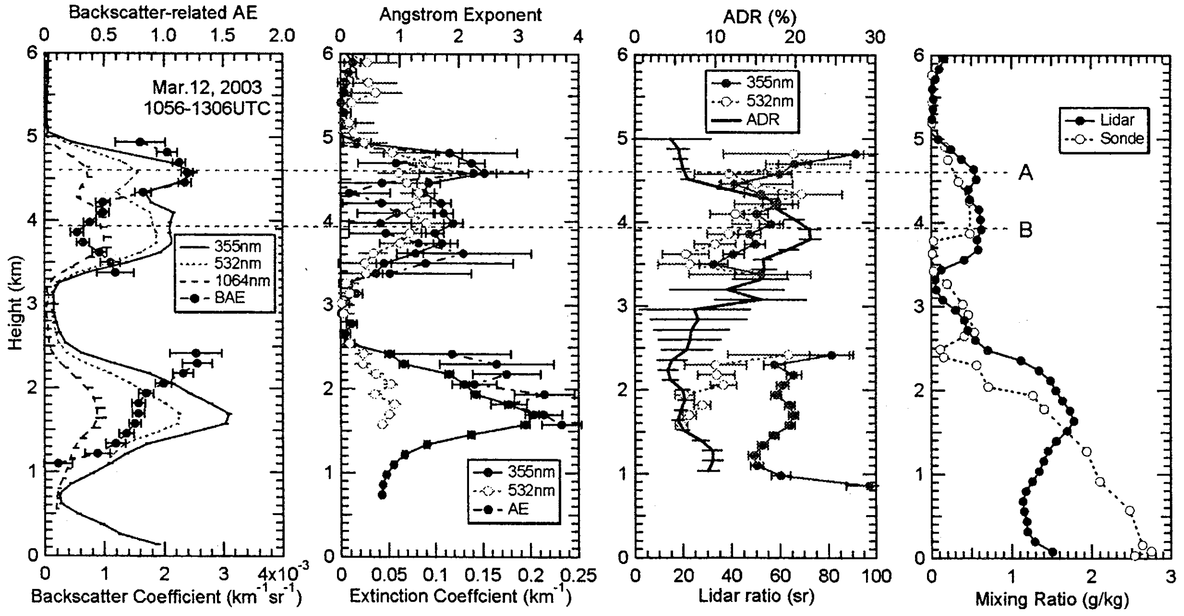

Fig. 3 Example of Raman lidar observation for elevated Asian dust. The data were obtained during 1056-1306UTC on March 12, 2003. The radiosonde observation of water-vapor mixing ratio on 12UTC at Tateno is also shown.

comparable as shown in Fig. 3, here we may reject "often-made assumption" that hygroscopic growth of mineral dust reduces the depolarization ratio. The fine aerosols in the layer A could be fine dust or pollution aerosol. We need more statistics to mention wavelength-dependence of the lidar ratio for dust case.

3.3 Case of Smoke

In May and June 2003, remarkable forest fire activity was occurred in eastern Russia region. Smoke plumes originated from these fires were transported over Japan, which is well shown by SeaWiFS RGB images [*J. Prospero*, private communication]. We show the profiles obtained in the night of May 21, 2003 in Fig. 4. A prominent aerosol layer between 2.5 and 4 km had a small but meaningful ADR (~6%). We can see further following distinct features in this smoke layer:

i) Extinction coefficient is very high (0.5-0.7 km^{-1} at the peak).

ii) The wavelength dependence of backscatter coefficient (BAE) is high (~1.7), while the Angström exponent (AE) is small (~0.5 at the peak).

iii) The lidar ratio at 532 nm (~60 sr) is apparently higher than the value at 355nm (~ 40 sr).

These results are consistent with our previous observation in the summer of 2002 [*Murayama*, 2003] and the observation in LACE98 for aged smoke [*Wandinger et al.*, 2002]. The small AE between at 355 and 532 nm in smoke layer is supported from observation by AERONET [*Eck et al.*, 1999], and in fact the AERONET level 1.5 data in Shirahama (33.69°N, 135.36°E) on May 21, 2003 shows such tendency near UV region (http://aeronet.gsfc.nasa.gov/). The relation iii): S_{355} is smaller than S_{532}, can be used to identify the smoke layer because opposite relation is usually seen as shown in previous sections.

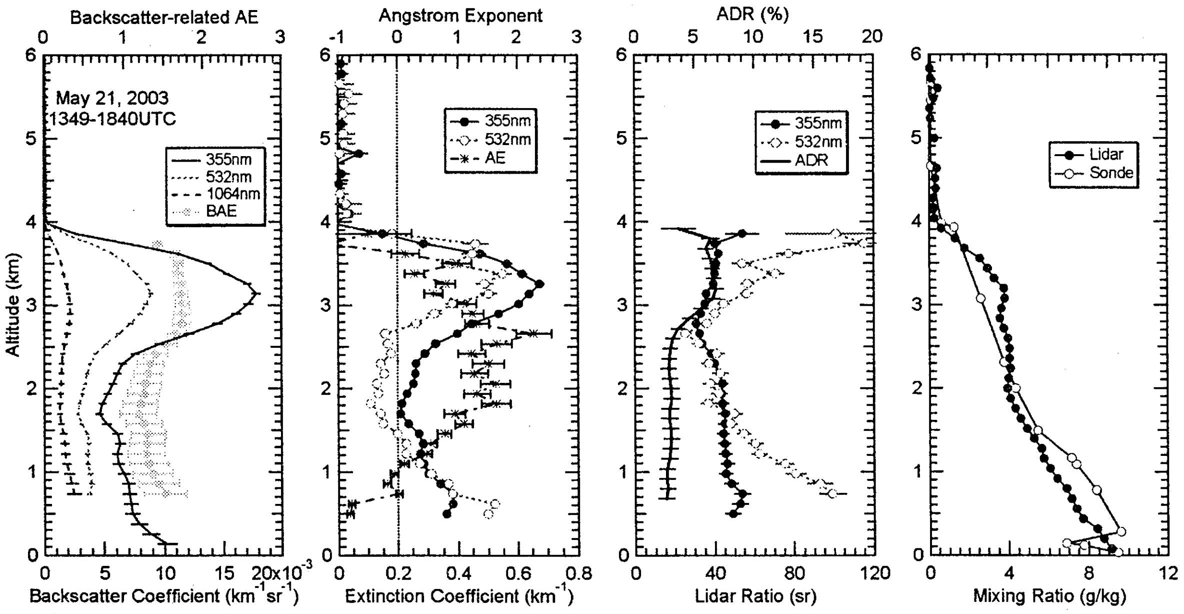

Fig. 4 Example of Raman lidar observation for biomass-burning aerosol. The data were obtained during 1349-1840UTC on May 21, 2003. The radiosonde observation of water-vapor mixing ratio on 12UTC at Tateno is also shown.

3.4 Systematic Analysis of UV-Raman Lidar Observation

Since the UV-Raman lidar observation is more efficient than visible in our current lidar system, we proceed the systematic analysis of aerosol optical properties and water vapor using the UV-Raman lidar data at first. Fig. 5 shows some examples of vertical profiles of derived aerosol optical properties and mixing ratio. The lidar derived mixing ratio using a constant normalization factor mostly agree well with the radiosonde observation at Tateno. Fig. 6 shows the histogram of averaged lidar ratio S_{355} in the lower troposphere including water clouds. The most probable value of aerosol lidar ratio is located between 50 and 60 sr. The S_{355} contaminated by water clouds shows certainly lower values and mostly located at 20-30 sr, which is consistent with calculated values (16-19 sr) for stratus and cumulus clouds by OPAC [*Hess et al.*, 1998].

4. Summary and Perspective

We have initiated two-wavelength Raman lidar observation of tropospheric aerosols and successfully derived height-resolved aerosol optical properties including Angström exponent. We demonstrated that the data set of three backscatter, two extinction coefficients, one depolarization ratio, and water-vapor mixing ratio is quite

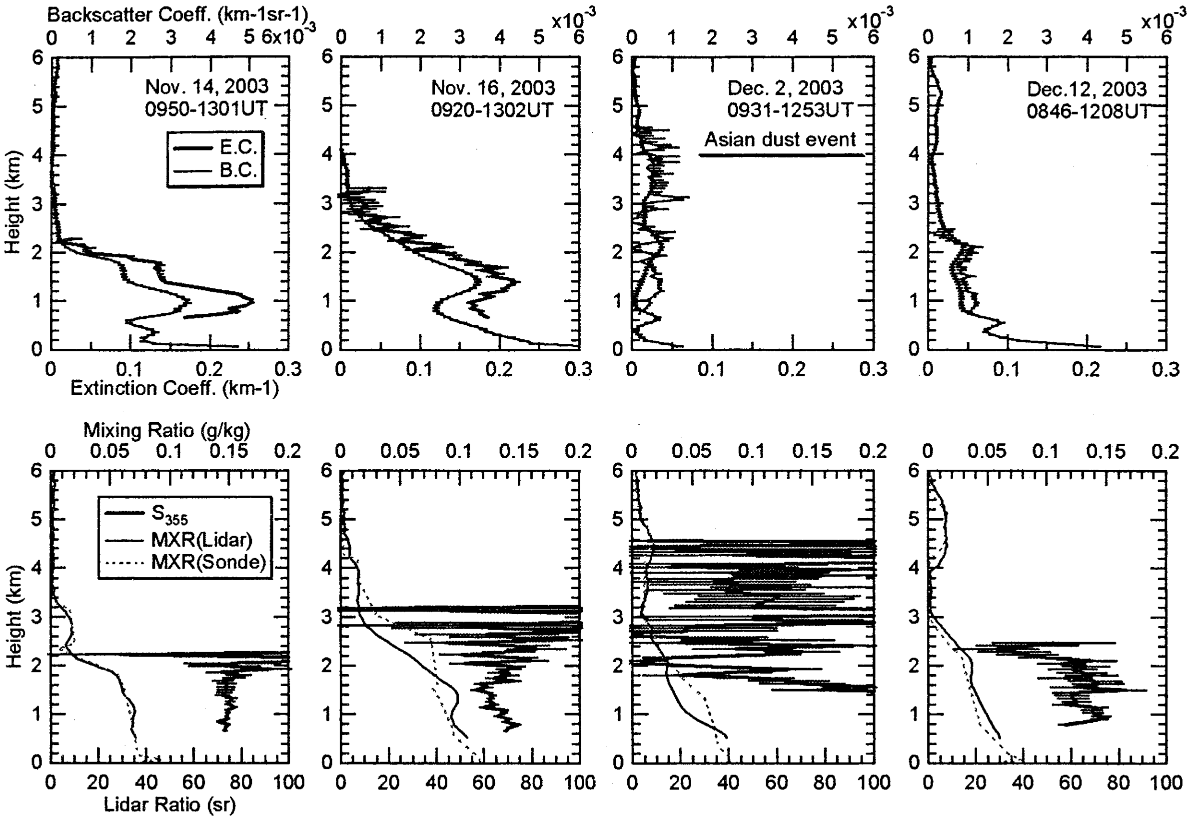

Fig. 5 Example of recent systematic analysis of UV-Raman observations. Mixing ratio observed by radiosonde is taken from Tateno on 12UTC of each day.

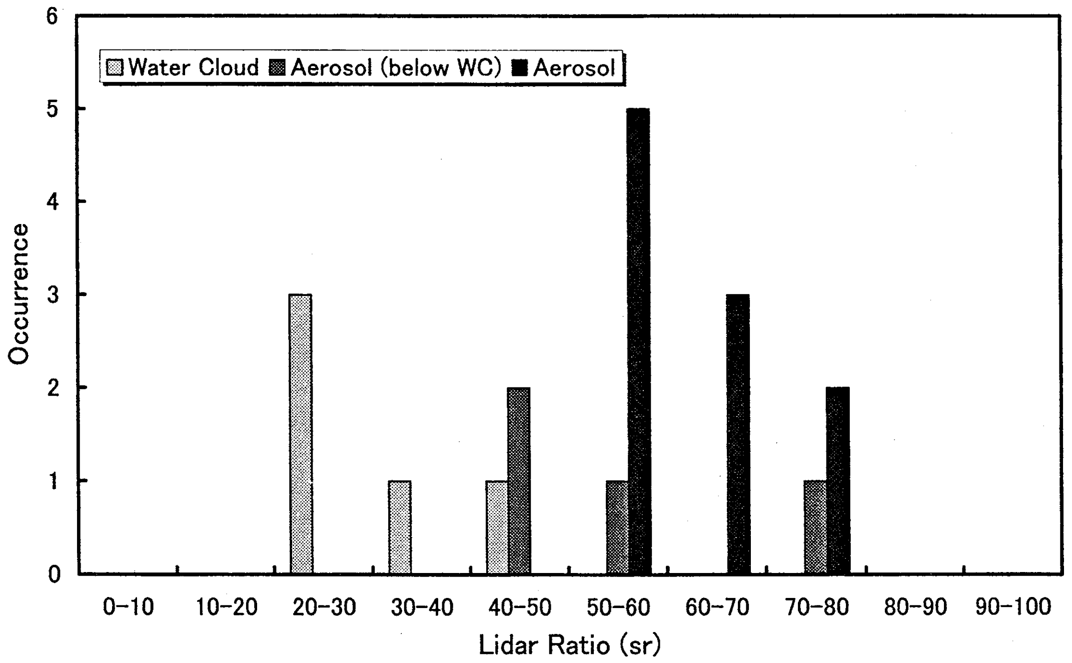

Fig. 6 Histogram of averaged lidar ratio for water cloud and aerosol at 355 nm during the period from Oct. 2nd and Dec. 8th in 2003. The values for aerosol are classified for "under water-clouds" (Aerosol below WC) and "cloud-free" (Aerosol) cases.

practical to characterize tropospheric aerosols, especially for mineral dust and biomass-burning smoke. We will perform a long-term observation of tropospheric aerosols and clouds with the multi-wavelength Raman lidar to derive climatological values of aerosol and cloud optical properties combined with Sun/sky photometers. We also intend to apply state-of-art inversion codes to derive microphysical aerosol properties [*Müller et al.*, 2001]. Thus we believe two-wavelength Raman lidar with a depolarization channel is the most feasible and powerful tool for aerosol and cloud research.

This work is financially supported by Grand-in-Aid for Scientific Research on Priority Areas under Grant No. 14048232 from the Ministry of Education, Culture, Sports, Science and Technology, and Global Environment Research Fund on Kosa (Asian dust) from the Ministry of the Environment. We also acknowledge partial supports to this study from the projects VMAP and APEX of CREST of Japan Science and Technology (JST). It is also supported by the joint research programs of CEReS, Chiba University (14-5) and (15-7).

References

Ackermann, J., The Extinction-to-Backscatter Ratio of Tropospheric Aerosol: A Numerical Study, *J. Atmos. Oceanic Technol., 15*, 1043-1050, 1998.

Ansmann, A., et al., Combined Raman elastic-bacbscatter LIDAR for vertical profiling of moisture, aerosol extinction, backscatter, and lidar ratio, *Appl. Phys., B55*, 18-28, 1992.

De Tomasi, F., A. Blanco, and M. R. Perrone, Raman lidar monitoring of extinction and backscattering of African dust layers and dust characterization, *App. Opt., 42*, 1699-1709, 2003.

Eck, T. F., B. N. Holben, J. S. Reid, O. Dubovik, A. Smirnov, N. T. O'Neill, I. Slutsker, and S. Kinne, Wavelength dependence of the optical depth of biomass burning, urban, and desert dust aerosols, *J. Geophys. Res., 104(D24)*, 31,333-31,349, 1999.

Fernald, F. G., Analysis of atmospheric lidar observations: some comments, *Appl. Opt., 23*, 652-653, 1984.

Hess, M., P. Koepke, and I. Schult, Optical Properties of Aerosols and Clouds: The Software Package OPAC, *Bull. Amer. Meteorol. Soc., 79*, 831-844, 1998.

Mattis, I., A. Ansmann, D. Muller, U. Wandinger, and D. Althausen, Dual-wavelength Raman lidar observations of the extinction-to-backscatter ratio of Saharan dust, *Geophys. Res. Lett., 29*, doi:10.1029/2002GL014721, 2002.

Müller, D., U. Wandinger, D. Althausen, and M. Fiebig, Comprehensive particle characterization from three-wavelength Raman-lidar observations: case study, *Appl. Opt., 40*, 4863-4869, 2001.

Murayama, T., M. Furushima, M A. Oda, N. Iwasaka, and K. Kai, Depolarization ratio measurements in the atmospheric boundary layer by lidar in Tokyo, *J. Meteorol. Soc. Japan, 74*, 571-578, 1996.

Murayama, T., H. Okamoto, N. Kaneyasu, H. Kamataki, and K. Miura , Application of lidar depolarization measurement in the atmospheric boundary layer: Effects of dust and sea-salts particles, *J. Geophys. Res., 104*(D24), 31,781-31,792, 1999.

Murayama, T., et al., Ground-based network observation of Asian dust events of April 1998 in east Asia, J. *Geophys. Res., 106*(D16), 18,345-18,359, 2001.

Murayama, T., Optical properties of Asian dust aerosol lofted over Tokyo observed by Raman lidar, in *Lidar Remote Sensing in Atmospheric and Earth Sciences (Proceedings of the 21th ILRC)*, edited by L. R. Bissonnette, G. Roy, and G. Vallée, pp. 331-334, Defense R&D Canada – Valcartier, Québec, 2002.

Murayama, T., Observation of optical properties of tropospheric aerosols by multi-wavelength Raman lidar, in Spring Assembly of the Meteorology Society of Japan, Tsukuba, 2003.

Murayama, T., et al., An intercomparison of lidar-derived aerosol optical properties with airborne measurements near Tokyo during ACE-Asia, *J. Geophys. Res., 108(D23)*, 8651, doi:10.1029/2002JD003259, 2003.

Wandinger, U., et al., Optical and microphysical characterization of biomass-burning and industrial-pollution aerosols from multiwavelength lidar and aircraft measurements, *J. Geophys. Res., 107(D21)*, 8125, doi:10.1029/2000JD000202, 2002.

Whiteman, D. N., S. H. Melfei, and R. A. Ferrare, Raman lidar system for the measurement of water vapor and aerosols in the Earth's atmosphere, *Appl. Opt., 31*, 3068-3082, 1992.

Whiteman, D. N., Examination of the traditional Raman lidar technique. I. Evaluating the temperature-dependent lidar equations, *Appl. Opt., 42*, 2571-2592, 2003a.

Whiteman, D. N., Examination of the traditional Raman lidar technique. II. Evaluating the ratios for water vapor and aerosols, *Appl. Opt., 42*, 2571-2592, 2003b.

Retrieval of aerosol optical thickness from the relation between satellite imagery and ground data over farmland in the Okhotsk area

Koji Asakuma and Hirotake Ito

Faculty of Bio-industry, Tokyo University of Agriculture
E-mail: k-asakum@cp.bioindustry.nodai.ac.jp

Abstract

We present a method for retrieving aerosol optical thickness over the Okhotsk area based on ground data of a vegetation index for farmland monitoring. In the first step, we developed a camera for observation of the vegetation index. A NDVI value from the camera around the wheat canopy showed a good relation with SPAD, the chlorophyll content meter, in the same farmland. The NDVI value from ground data in west Abashiri farmland was 0.355 (June 12, 2003). In the second step, we compare the ground data of NDVI and NDVI obtained from atmospherically corrected TERRA/MODIS imagery using 6S, the radiative transfer code (Channel 1 and channel 2, on June 12, 2003). Then the aerosol optical thickness value is 0.12 with the continental aerosol model and 0.07 with the maritime model. The methods appear to be useful to validate satellite remote sensing for non-regular atmospheric observation.

1. Introduction

The Okhotsk area is an exceedingly important place for both agricultural and environmental problems. Firstly, in it resides one of the foremost granaries in Japan for crops such as wheat, beets, and potatoes. In order to estimate the yield of crops accurately, it is important to determine the actual reflectance of the leaf canopy. However, in order to observe the exact ground reflectance using satellite remote sensing, we must remove the atmospheric impact. Satellite imagery is influenced by atmospheric effects, such as radiative decline and blur due to ray absorption or scattering by a molecule and atmospheric aerosol, because its vantage point of detection lies above the atmosphere (*Ouaidrari and Vermote, 1999*). Accordingly, atmospheric correction is greatly important when focusing on an agricultural field. Second, the Okhotsk area is an important environmental observation point because Asian dust passes through it. Asian dust originates from the eastern part of China, passes through Japan extensively and reaches the North American Continent where it covers a wide range of earth radiative forcing. Thus, the retrieval of aerosol optical properties at various observation points is important. An additional observation point, recommended to World Heritage is the Siretoko peninsula, which has a unique ecological system. In the future, the Okhotsk area is likely to become an important observation point for environmental remote sensing. Unfortunately, there is currently no regular observatory for atmospheric surveying such as a lidar system, sun-photometer or sky-radiometer, or exclusive spectrum radiometer for the ground surface in the Okhotsk area.

In this paper, we conducted a trial application of a vegetation index obtained via observation of wheat on farmland in Okhotsk to validate the retrieval of aerosol optical properties from satellite imagery as ground data. First, we developed a camera sensitive to the degree of chlorophyll activation in order to observe this activity in wheat. Second, NDVI values from the camera were validated by comparison with the SPAD values from ground data on the same farmland. Third, the value of optical thickness was determined based on agreement of the NDVI value obtained from atmospherically collected TERRA/MODIS image calculated using 6S as the radiative transfer code (*Vermote, et al., 1997*) with the value from the camera over the same farmland.

2. Methodology

2.1 Development of a camera for observation chlorophyll activation in wheat

In order to retrieve the normalized vegetation index (NVDI) of farmland in the Okhotsk area for comparison with NDVI from satellite imagery in same area, a camera capable of observing the degree of chlorophyll activation in wheat was developed. The camera was altered for separation of visible and near

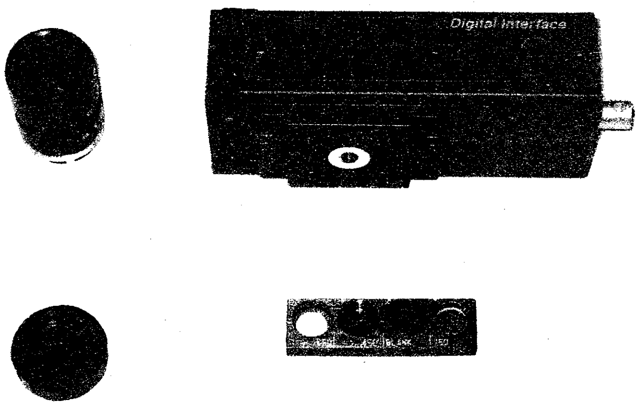

Figure 1. The exterior of XCD-X700

rays so that the NDVI could be calculated using a commercially available digital CCD camera, the XCD-X700 manufactured by SONY. The XCD-X700 has a wide band wavelength (400 nm to 1,000 nm) and high resolution (1,024 × 768 pixels). Two spectroscopic filters, representing the visible band (center wavelength 450 nm, HVHW 40nm) and near infrared band (center wavelength 970 nm, HVHW 40nm), were installed on the lens of the XCD-X700. These filters could be exchanged manually operated each other (see Fig. 1).

2.2 Calculate NDVI from the camera and validation data

Figure 2 shows a range of images from the camera used to calculate the average NDVI value. The range area was extracted from the images in the camera and averaged out per pixel. This operation was performed for each respective farmland image. In this camera system, NDVI is expressed as:

$$\mathrm{NDVI} = (r_{\mathrm{NIR}} - r_{\mathrm{VIS}})/(r_{\mathrm{NIR}} + r_{\mathrm{VIS}}),$$

where r_{NIR} and r_{VIS} are the ratio of each pixel value of observational farm land from the camera to the correction value from simultaneously photographed white board to which coats of barium sulfate had been applied. The average value of NDVI for each image of farmland was compared with the average SPAD value to obtain the difference between visible and NIR emission of a leaf, obtained using a MINORUTA SPAD-502 on the same farmland.

Figure 3 shows the variation in NDVI between the average of the camera-obtained images and average SPAD in the west Abashiri area of northern farmland on June 12, 2003. It appears that the NDVI values obtained from the images in the camera, which show the average vegetation index of the canopy of wheat, have only a slight correspondence with the average SPAD value for the flag leaf and second leaf from the top. The average

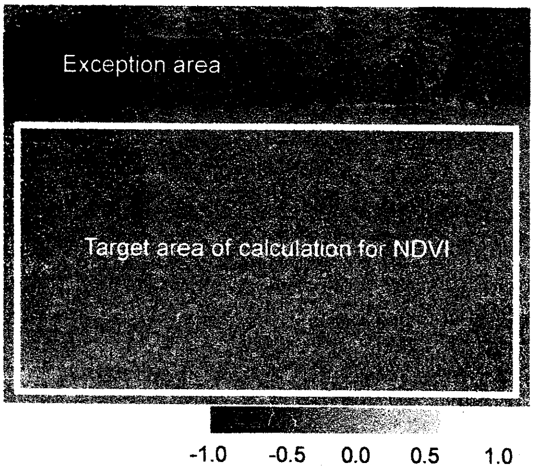

Figure 2. Range on the image from the camera for calculation of average NDVI

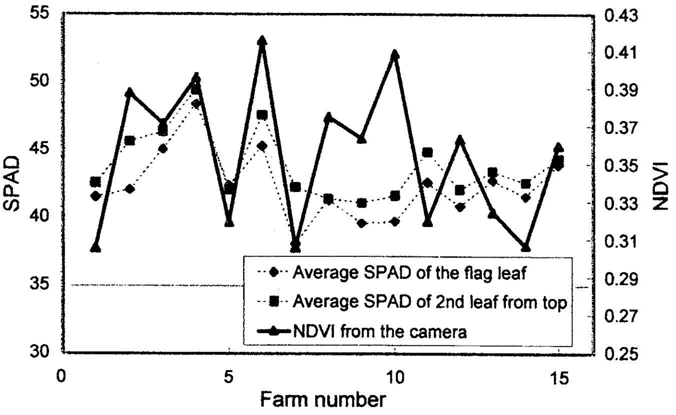

Figure 3. Variation of NDVI from the camera image and average SPAD on farmland of wheat (June 12, 2003)

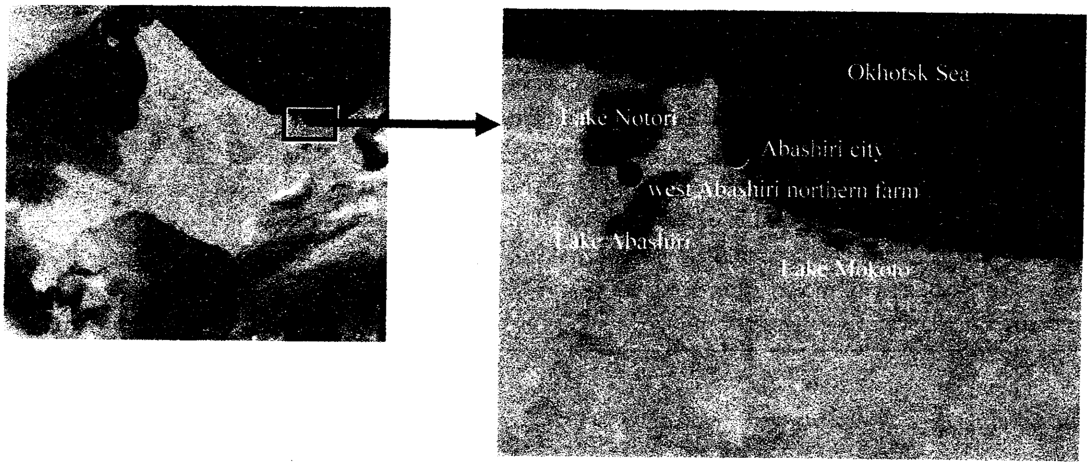

Plate 1. TERRA/MODIS imagery on June 12, 2003. The left image is the whole area of Hokkaido and the right is enlarged image of neighboring the Abashiri northern farm.

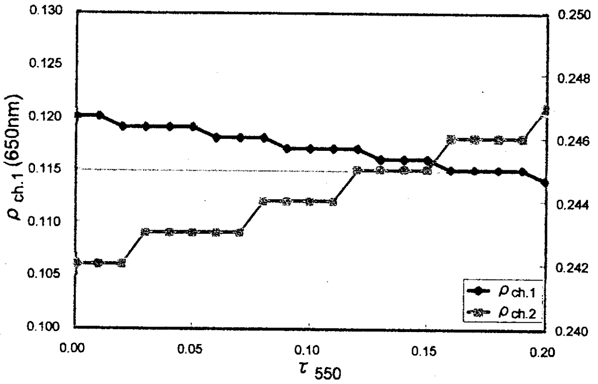

Figure 4. Relationship between atmospherically corrected reflectance and optical thickness with continental aerosol model (June12, 2003)

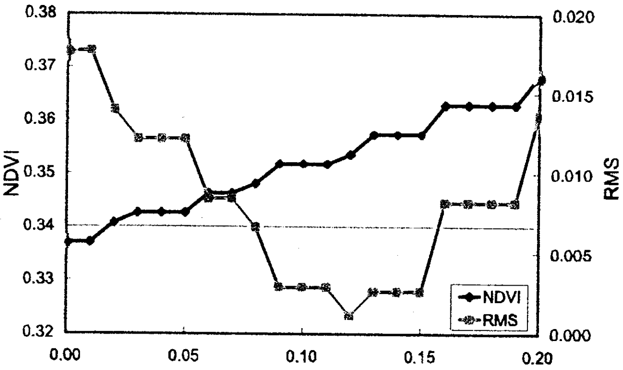

Figure 5. Relationship between atmospherically corrected NDVI and optical thickness with continental aerosol model (June 12, 2003)

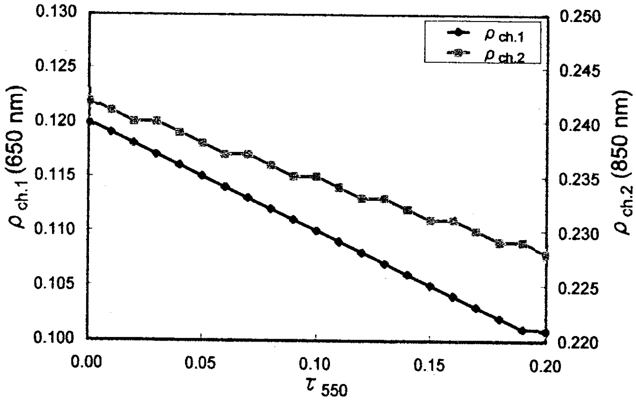

Figure 6. Relationship between atmospherically corrected reflectance and optical thickness with maritime aerosol model (June 12, 2003)

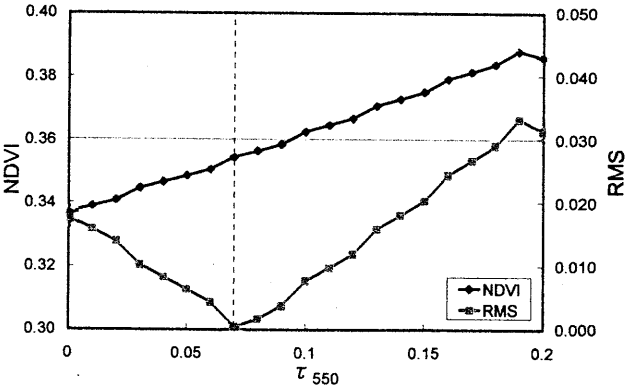

Figure 7. Relationship between atmospherically corrected NDVI and optical thickness with maritime aerosol model (June 12, 2003)

NDVI value was 0.355 on June 12, 2003. Further, the west Abashiri area is located on the south end of Lake Notori and each plot of farmland planted with wheat covers an area of approximately several hectares (see Plate 1). Accordingly, the average NDVI value observed in these areas is fit to be compared with satellite imagery, which represents each area with one pixe.

2.3 Application of TERRA/MODIS to retrieve aerosol optical thickness

In order to derive accurate surface reflectance, which we refer to as the atmospherically corrected image, it is necessary to determine τ_{550}, the atmospheric optical thickness at a 550 nm wavelength, using 6S code. A relationship between the surface reflectance $\rho_{ch.1}$, which is MODIS channel 1 (at the 650 nm center wavelength), $\rho_{ch.2}$ (850 nm) and τ_{550} were calculated by 6s code with τ_{550} variation from 0.0 to 0.2 using the continental and maritime aerosol models, respectively. The relation between NDVI and τ_{550} was obtained from this result of the visible reflectance $\rho_{ch.1}$ and the near infrared reflectance $\rho_{ch.2}$. Thus, we could determine the best fit τ_{550} value with each aerosol model from the condition of the NDVI value from the relation equal to 0.355 obtained from the camera.

3. Result and conclusion

On June12, 2003, the visible channel reflectance value from above the atmosphere observed from TERRA/MODIS over the west Abashiri farmland was 0.125 and the near infrared reflectance value was 0.243. Figure 4 shows the relationship between atmospherically corrected reflectance and optical thickness with the continental aerosol model. As seen in this figure, $\rho_{ch.1}$, the visible reflectance, appears to decrease with increasing τ_{550} value; that is, inversely, $\rho_{ch.2}$, the near infrared reflectance, is increased when the continental model is used. In Fig.5, the best fit τ_{550} value of 0.12 is found with the minimum value of the route mean square (RMS). Figure 6 shows the relationship between atmospherically corrected reflectance and optical thickness with the maritime aerosol model. In contrast to findings with the continental model, both $\rho_{ch.1}$ and $\rho_{ch.2}$ have a tendency to decrease with increasing τ_{550} value. The best fit τ_{550} value found with the maritime aerosol model was 0.07. In a comparison of the two aerosol models, the continental model appears to be more reliable, based on the fact that in same season of the year 2002, the τ_{550} value observed on Memanbetsu airport ranged from 0.14 to 0.17 (*Asakuma, 2002*).

In the future, we would like to compare the optical thickness value using MODTRAN, the radiative transfer code, and retrieve more detailed aerosol optical properties such as a radius, density, and refractive index.

References

Asakuma, K., S. Otsutsumi, T. Kubota, M. Yabuki, H. Kuze and N. Takeuchi: Retrieval of aerosol optical thickness from NOAA/AVHRR data and its application to the derivation over land area in Chiba, Proceedings of SPIE 4150, Optical Remote Sensing of the Atmosphere and Clouds II, 290 – 298, 1999

Asakuma, K.: Study for atmospheric correction from TERRA/MODIS imagery over Okhotsk area, Proceedings of the 3rd workshop of the sub-project studies on natural environment and culturein ASIA, 71 –80, 2002

Asakuma, K., M. Minomura, S. Otsutsumi, H. Kuze and N. Takeuchi: Estimation of aerosol optical thickness over land in Chiba area from AVHRR data, Advanced Space Research, Elsevier Science, Vol. 29, No. 11, 1747-1752, 2002

Ouaidrari, H. and E. F. Vermote: Operational atmospheric correction of Landsat TM Data, Remote Sens. Env., Vol. 70, 4-15, 1999

Vermote, E. F., D. Tanre, J. Deuze, M. Herman and J. Morcrette: Second simulation of the satellite signal in the solar spectrum, 6S ; An overview, IEEE Trans. on Geosc. and Remote Sens., Vol. 35, 675-686, 1997

A study on quantitative analyses of aerosol optical properties based on lidar measurements

Masanori Yabuki[1], Masataka Shiobara[2], Hiroaki Kuze[3], and Nobuo Takeuchi[4]

[1] National Institute of Polar Research, Tokyo, Japan
E-mail: yabuki@pmg.nipr.ac.jp
[2] National Institute of Polar Research, Tokyo, Japan
E-mail: shio@nipr.ac.jp
[3] Center for Environmental Remote Sensing, Chiba University, Chiba, Japan
E-mail: hkuze@faculty.chiba-u.jp
[4] Center for Environmental Remote Sensing, Chiba University, Chiba, Japan
E-mail: takeuchi@faculty.chiba-u.jp

Abstract

We propose a lookup table method to derive vertical distributions of aerosol optical parameters in the troposphere from two-wavelength observations using a Mie-scattering lidar. The method is characterized by the capability of treating generalized aerosol size distributions, as well as by rapid convergence of the iteration procedure. The methodology and numerical simulation are described.

1. Introduction

Mie-scattering lidars provide extinction profiles of atmospheric aerosols. Inversion of lidar signals is commonly accomplished by means of the Fernald method [1], in which a linear relationship is assumed between the aerosol extinction and backscattering coefficients (S_1 parameter). The uncertainty of this parameter often results in a significant error in the retrieval. Recently we have shown [2] that comparison of the four-wavelength lidar profiles with those predicted by a lookup table (LUT) makes it possible to determine the vertical profiles of not only the extinction coefficients, but S_1 parameters, complex refractive index, and size distribution. The practical application of this LUT method, however, has turned out to be difficult because of the considerable computation time and the incomprehensiveness of the LUT. In this paper, we propose a revised version of the LUT method to address these problems.

2. Theory

2.1 Construction of LUT

A LUT is constructed on the basis of the Mie-scattering theory, assuming that aerosol particles are spherical. In this revised algorithm, the aerosol size distribution is described as a sum of fine and coarse modes. The lognormal distribution function is defined as

$$n^{(\mathrm{f,c})}(r,u)=\frac{dN(r)}{d(\ln r)}=\frac{N_{(\mathrm{f,c})}}{\sqrt{2\pi}\,\ln\sigma_{(\mathrm{f,c})}}\exp\left[-\frac{(\ln r/R_{(\mathrm{f,c})})^2}{2\,(\ln\sigma_{(\mathrm{f,c})})^2}\right] \tag{1}$$

where r is the particle radius, R the mean radius, N the integral number concentration, and σ its width. Subscripts f and c refer to the fine and coarse mode parameters, respectively. In the present simulation, we put $R_{(f)} = 0.055$ μm and $\sigma_{(f)} = 2.1$, and $R_{(c)} = 0.49$ μm and $\sigma_{(c)} = 2.15$. The complex refractive index ($m - ki$) is varied between 1.35 and 1.65 for the real part (m), and between 0.0 and 0.03 for the imaginary part (k). For simplicity, we neglect the wavelength dependence of m and k.

The aerosol extinction coefficient $\alpha_1^{(f,\,c)}$ and the backscattering coefficient $\beta_1^{(f,\,c)}$ are calculated for each wavelength (532 and 1064 nm) using the assumed size distribution and complex refractive index. In this calculation $N_{(f)}$ and $N_{(c)}$ in eq.(1) are assumed unity, and by combining contributions from the two modes, we obtain

$$\alpha_1 = N_{(f)}\,\alpha_1^{(f)} + N_{(c)}\,\alpha_1^{(c)},$$
$$\beta_1 = N_{(f)}\,\beta_1^{(f)} + N_{(c)}\,\beta_1^{(c)}. \tag{2}$$

Figure 1 shows the wavelength dependence of α_1 for various values of the real part (m). In this case, the imaginary part is fixed at $k = 0.02$. It is seen from Fig. 1 that for fine particles, both α_1 and β_1 decrease with the wavelength λ, whereas for coarse particles, they increase with λ. This is a general tendency observed for any value of k between 0.0 and 0.03.

In the following, we denote the extinction and backscattering coefficients as $\alpha_1^{(f,c)}(l, m, k)$ and $\beta_1^{(f,c)}(l, m, k)$, respectively. ($l=1$ for $\lambda=532$ nm and $l=2$ for $\lambda=1064$ nm)

2.2 Inversion of lidar data

The altitude z is considered in a discrete way as z_j ($j = 1, 2, \ldots, J$), with z_J being the far-end boundary. The initial value $\beta_1(z_J, l)$ is taken to be 0 where the atmosphere is considered to be aerosol-free.

The two-wavelength lidar data are inverted for a small altitude range between z_j and z_{j+1}. Within this range, the form of the size distribution and the complex refractive index are assumed to be constant. In this analysis, the real part m takes a constant value in the column. We start our analysis by choosing an element k and calculate the theoretical ratio of signal intensities at z_j and z_{j+1}:

$$\frac{P(z_{j+1},l)}{P(z_j,l)}=\frac{z_1^{\,2}(\beta_1(z_{j+1},l)+\beta_2(z_{j+1},l))}{z_2^{\,2}(\beta_1(z_j,l)+\beta_2(z_j,l))}\exp\left[-2\Delta\tau(z_j,l)-2\alpha_2(l)(z_{j+1}-z_j)\right], \tag{3}$$

where subscript 2 refer to the molecular parameters and $\Delta\tau(z_j, l)$ is described as

$$\Delta\tau(z_j,l)=\left(\beta_1(z_{j+1},l)S_1(z_{j+1},l)+\beta_1(z_j,l)S_1(z_j,l)\right)(z_{j+1}-z_j)/2\,. \tag{4}$$

Here S_1 is the extinction-to-backscattering ratio ($S_1=\alpha_1/\beta_1$). In a first trial, we assume $S_1 = 50$ sr, since S_1 is unknown. The value $\beta_1(z_j, l)$ is to be determined by comparing this theoretical signal with the observed signal. For that purpose, we define an error vector Err as the difference between the calculated ratio and the observed ratio of the signal intensities at z_j and z_{j+1}:

$$Err=\frac{P(z_{j+1},l)}{P(z_j,l)}-\frac{P_{obs}(z_{j+1},l)}{P_{obs}(z_j,l)}\,. \tag{5}$$

The bisection method is applied to find the minimum value of $|Err|$ by varying $\beta_1(z_j, l)$: the resulting values for the two wavelengths are then denoted as $\beta_1(z_j, l)$ ($l=1, 2$).

The next step is to determine the ratio of $N_{(f)}$ and $N_{(c)}$ that is compatible with this set of $\beta_1(z_j, l)$. We define an error vector δ_1 as

$$\delta_1(m,k)=\ln\frac{\beta_1(z_j,1)}{\beta_1(z_j,2)}-\ln\frac{N'\beta_1^{(f)}(1,m,k)+(1-N')\beta_1^{(c)}(1,m,k)}{N'\beta_1^{(f)}(2,m,k)+(1-N')\beta_1^{(c)}(2,m,k)}\,. \tag{6}$$

Here N' is the ratio of $N_{(f)}$ and $N_{(f)} + N_{(c)}$ ($N'= N_{(f)}/(N_{(f)} + N_{(c)})$). Again, the best value of N' is determined by applying the bisection method in which the minimum value of $|\delta_1(m, k)|$ is sought. The difference in the wavelength dependence between the fine and coarse modes (Fig. 1) ensures the possibility of finding an appropriate value of N' in this process. Using the value of N' determined in this way, S_1 parameters are calculated as:

$$S_1(z_j,l)=\frac{N'\alpha_1^{(f)}(l,m,k)+(1-N')\alpha_1^{(c)}(l,m,k)}{N'\beta_1^{(f)}(l,m,k)+(1-N')\beta_1^{(c)}(l,m,k)}\quad(l=1,2). \tag{7}$$

The value of $S_1(z_j, l)$ is fed back to eqs. (3-4), and the process is iterated until changes in the resulting parameters become sufficiently small.

After that, the optical thickness between z_j and z_{j+1} is calculated from the derived parameters $\beta_1(z_j, l)$ and $S_1(z_j, l)$ using eq. (4). Then we define an error vector δ_2 as

$$\delta_2(m,k)=\left(\ln\frac{\Delta\tau(z_j,1)}{\Delta\tau(z_j,2)}-\ln\frac{N'\alpha_1^{(f)}(1,m,k)+(1-N')\alpha_1^{(c)}(1,m,k)}{N'\alpha_1^{(f)}(2,m,k)+(1-N')\alpha_1^{(c)}(2,m,k)}\right)^2. \tag{8}$$

The same procedure is repeated for each value of the imaginary part k. The relevant aerosol parameters are determined from the condition that δ_2 exhibits a minimum value.

3. Simulations

For the purpose of the testing the performance of the revised LUT method, two kinds of simulations are carried out. To test the performance, we prepare the vertical distributions of the number density for each mode as shown in Fig 2 (a) and Fig.2 (b), and calculate extinction coefficients (Fig2(c) for $\lambda=532$ nm and Fig2(d) for $\lambda=1064$ nm), backscattering coefficients, and S_1 parameters using the Mie theory, assuming that the real part is fixed at 1.50 and the imaginary part varies in a range of 0.005 (upper troposphere) to 0.015 (lower troposphere). After that, theoretical lidar signals are calculated.

The revised LUT method is applied to the prepared signals, and we obtains the results as illustrated in Fig. 3: (a) and (b) show the number densities of fine and coarse mode particles, and (c) and (d) the extinction coefficients at 532 nm and 1064 nm, respectively. Thick line shows the input data, and other five lines the retrieval results by varying the real part in a range of 1.40 to 1.60. The difference of the upper troposphere between the original and the retrieval parameters is the reason why the backscattering coefficient at z_J is assumed to be 0. Each retrieval parameter in the lower troposphere, however, agrees with the originally assumed parameters comparatively in spite of the changing of the real part. Therefore, this result proves that the revised LUT method is relatively immune to the assumed real part.

Figure 4 shows the simulation of the noise effect. Thick line shows the input data of the number concentrations. The other four lines show the retrieval results of the revised LUT method using the theoretical signals, which are subject to a random error with ±2%, ±5%, ±10%, and ±30%, respectively. The region with the small number density such as the upper troposphere is largely influenced by noise. On the other hand, the difference of the input and retrieval number densities is not so large in the mixed layer with the abundance of the aerosol particles. From the results in Fig. 4, one may say that quantitative analyses can be allowed for the data with the random error in signal within 10%.

4. Conclusions

We have described the principle and simulation of the LUT method used to determine the vertical profiles of the aerosol number size distribution and the extinction coefficient only from two-wavelength lidar observations. Compared with the previous version, advantages of the present approach are quicker convergence and the capability of treating more generalized size distributions. Further works are in progress in relation to the analysis of lidar signals involving cloud effects.

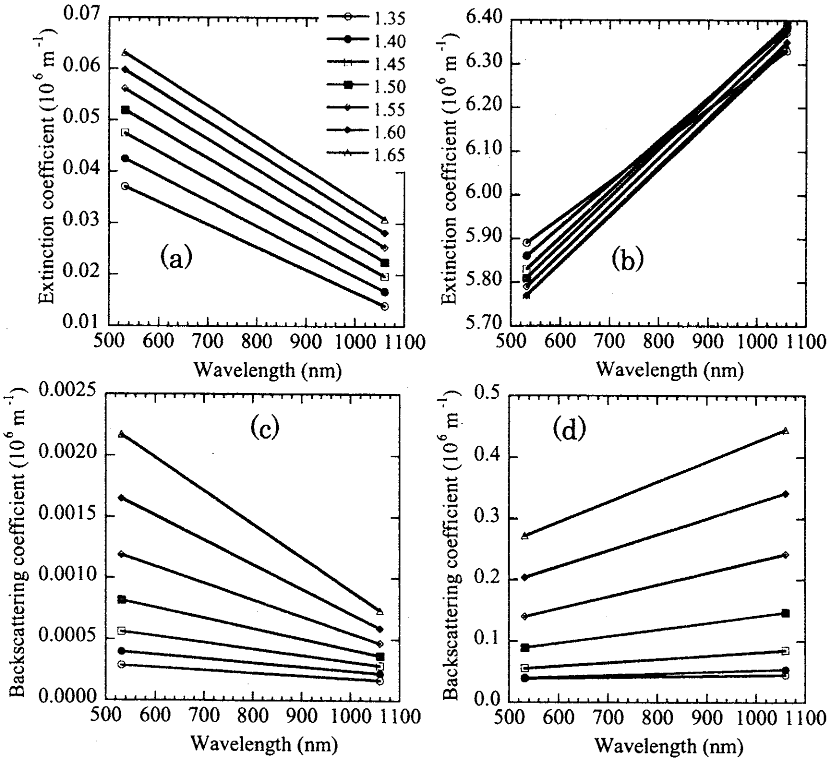

Fig. 1 Wavelength dependence of the extinction coefficient for (a) fine and (b) coarse mode particles, and the back scattering coefficient for (c) fine and (d) coarse mode particles. In this case, $N_{(f)}$ and $N_{(c)}$ described as eq. (1) are assumed to be unity and the imaginary part k is fixed at 0.02.

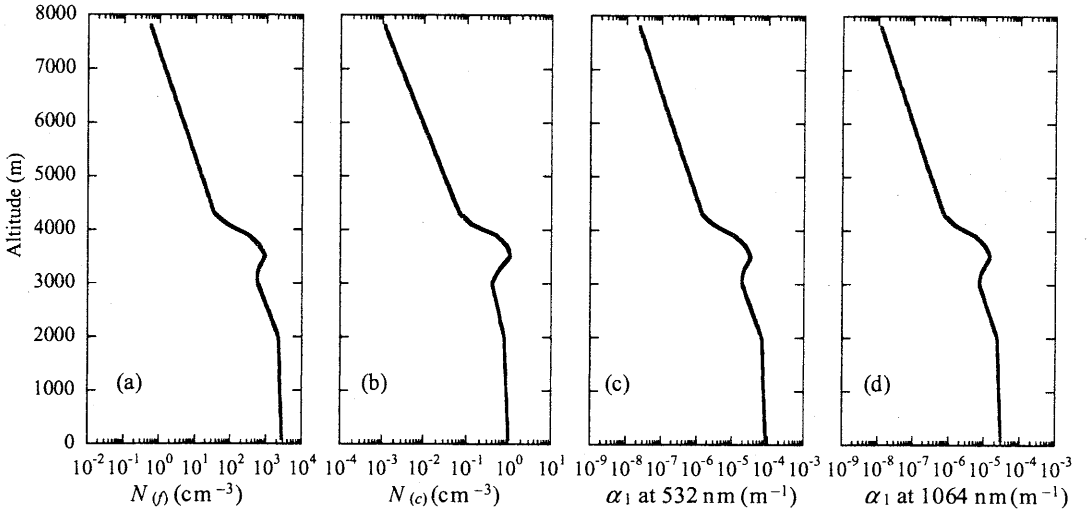

Fig.2 Input data for simulation. Profiles of the number density of the (a) fine and (c) coarse mode particles, and the extinction coefficient at (c) 532 nm and (d) 1064 nm, respectively.

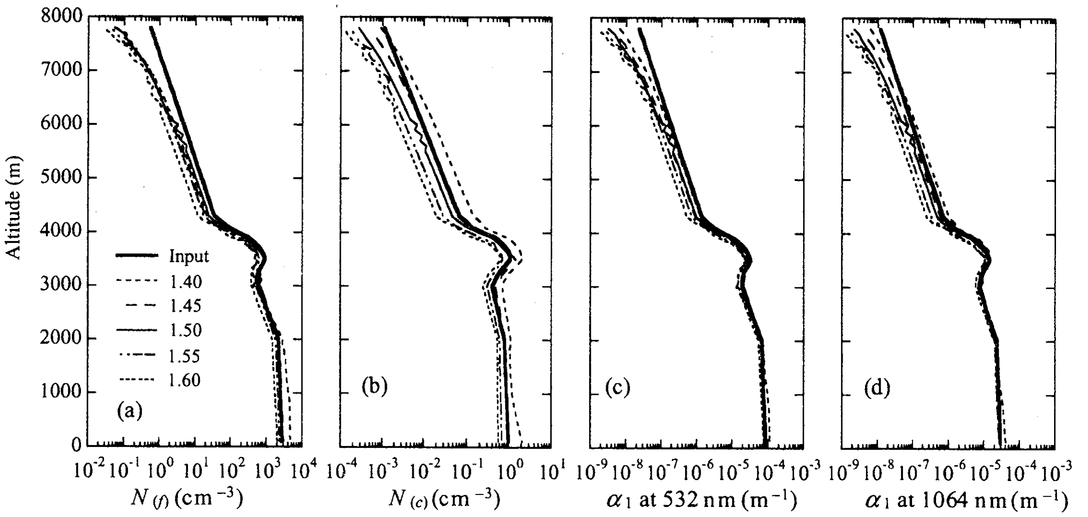

Fig.3 Retrieval results from the data in Fig. 2 by means of the revised LUT method, assuming several values of the real part *m*.

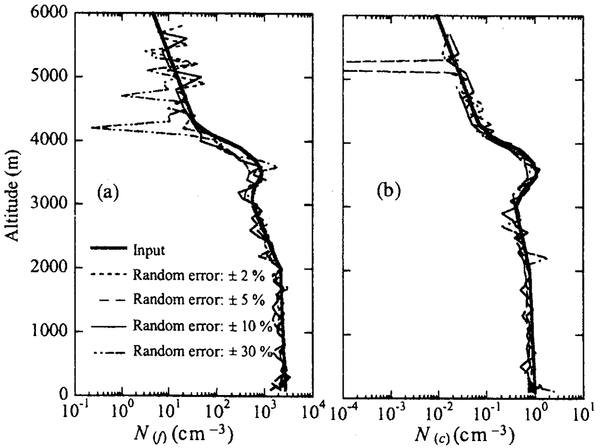

Fig. 4 Retrieval results of the revised LUT method using the theoretical signals, which are subject to a random error between 2% to 30%.

References

[1] F. G. Fernald, "Analysis of atmospheric lidar observations: some comments, *Appl., Opt.*, **23**, 652-653, 1984.
[2] M. Yabuki, H. Kuze, H. Kinjo, and N. Takeuchi, "Determination of vertical distributions of aerosol optical parameters by use of multi-wavelength lidar data", *Jpn. J. Appl. Phy.*, **42**, 2003.

Analysis of convective activity over the South Asia using geostational satellites

Nobuo Yamazaki[1] and Kiyotoshi Takahashi[2]
1 Meteorological Research Institute, Japan
E-mail: nyamazak@mri-jma.go.jp
2 Meteorological Research Institute, Japan
E-mail: ktakahas@mri-jma.go.jp

Abstract

Using METEOSAT-5 and GMS-5 data, and NCEP/NCAR 850 hPa wind, large-scale cloudiness variations over the Asian Pacific Ocean are examined.

In the Asian-Pacific region in Northern summer, the dominant variations are "dipole type pattern" in which convective activity are enhanced (suppressed) in the East Indian Ocean(from the Bay of Bengal to the Western Pacific). The associated wind fields well correspond to those convective activities.

Diurnal variation of convective activity is also investigated using the same METEOSAT-5 IR data. It shows the relationship with monsoon intraseasonal variation (onset, break).

1. Introduction

In Asian-Pacific regions, variability of convective activity is large in the intraseasonal to annual time scale as Indian monsoon is known well to show the prominent intraseasonal variability (cf. Monsoon onset and break). Its condition is very important in long-range weather prediction and social activity in the South Asia. Diurnal variability is also one of the prominent features of the convective activity in the tropics.

So, we study relationship between convective activity and lower level circulation in the intraseasonal to annual time scale and also examine the influence of the intraseasonal variations on the diurnal variations toward understanding the mechanisms of its variations.

Data used are cloud amount data derived from METEOSAT-5 and GMS infrared brightness temperature. Cloud amount c210 is calculated as percentage of the pixels whose temperature is less than 210°K. Similarly c240, c255, c270 are calculated. In order to see large-scale aspect consistent with low-level wind, 850 winds from NCEP/NCAR reanalysis are also used. Period of the analysis is Northern Hemisphere warm season from May to August during 1998 to 2002.

Empirical orthogonal function (EOF) is employed for combined cloudiness c240 and 850 wind data after both data are transformed into 2.5 by 2.5 degree grid resolution with pentad mean.

Regarding the diurnal variation, by using 3 hourly c255 with 1 x 1 degree resolution observed by Meteosat-5 and rainfall observed at Poona, India, we investigated the temporal relationship between the monsoonal intraseasonal variation and diurnal convective activity.

2. Results

2.1 Large-scale feature

Figure 1 shows mean wind cloud amount averaged over the period from 1998 to 2002. Mean convective activity is large over the Bay of Bengal, the Southeast Asia, the South China Sea through the Western Pacific.

Figure 2 shows the first 4 EOF modes for combined cloudiness c240 and 850 wind data, accounting for 13.08%, 7.36%, 4.98% and 4.76%. The 1st mode describes contrasting cloud activities between over the East equatorial Indian Ocean and the Bay of Bengal through the Western Pacific. Associated low troposphere wind at 850 hPa comes to the equatorial East Indian Ocean from the Southern Hemisphere mid-latitude, have easterly anomaly along the equatorial region and crosses the Equator around the mid Indian Ocean. In the northern hemisphere westerly anomaly prevails with cyclonic (anticyclonic) circulation in the Bay of Bengal , the South China Sea and the Western Pacific(Arabian Sea). These wind circulation pattern corresponds to that of cloud activities and are consistent with Matsuno-Gill Pattern.

The 2nd mode explains enhancement (suppression) of cloud activities and westerly (easterly) enhancement over India, the Arabian Sea, the Bay of Bengal and SPCZ. The westerly anomaly comes through off Somali and strengthens or weakens mean monsoon westerly. Clear cyclonic shear over the Bay of Bengal extends from NW to SE along the enhanced cloud activity. Anti-cyclonic circulation with suppressed convection over the subtropical western Pacific prevails.

Figure 3 shows time series of the first 4 modes corresponding to Figure 2. Period from May to August during 1998 to 2002 is plotted. Averaged over summer season, the year of 1998 is characterized by the negative 1st mode and positive 2nd mode. This is consistent with enhanced (suppressed) convection in the equatorial East

Indian Ocean (in the Bay of Bengal and Western Pacific) in the summer of 1998. In shorter time scale, 30-60 day variations can be seen. In particular in 2002 these variation are active over all summer time and definite phase relation as 5 to 10 day lag of the 1st mode relative to the 2nd mode is clearly seen. Actually time –latitude cross-section of cloudiness c240 averaged over 85°E to 95°E shows northward propagation with intraseasonal time scale.

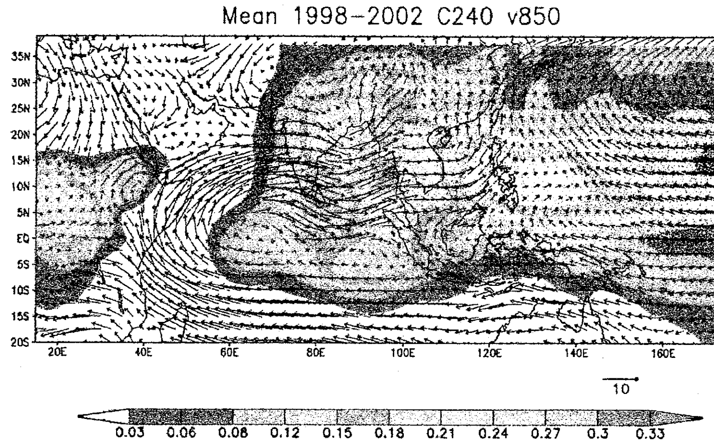

Figure 1: Mean 850 hPa wind and cloud amount c240 averaged over the period fron 1998 to 2002.

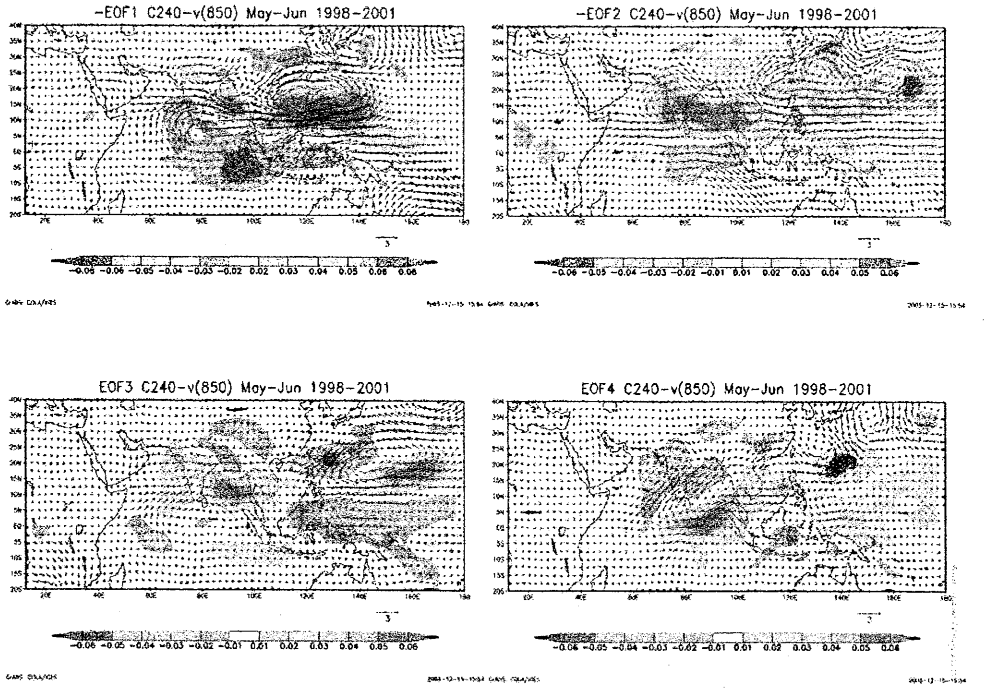

Figure 2: The first 4 EOF modes.

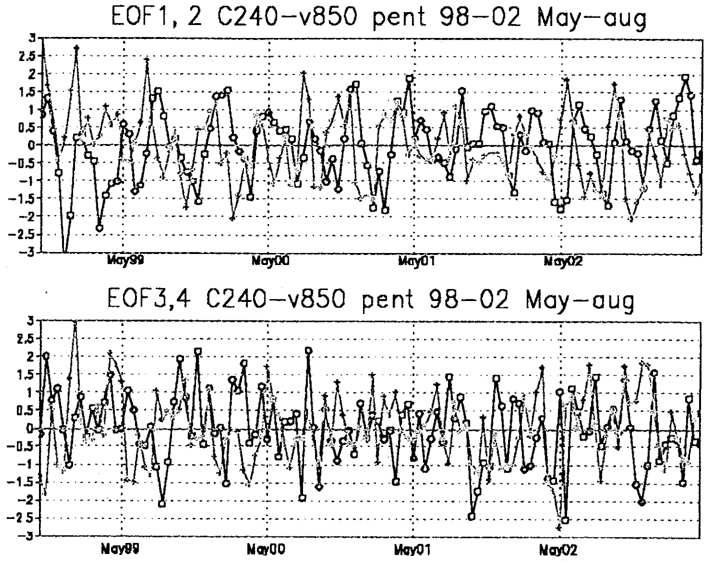

Figure 3: Time series of the first 4 EOF modes corresponding to Figure 2.

To see the difference of various cloudiness variations by the threshold, horizontal distribution of correlation of the 1st EOF and 2nd EOF time series with c210, c240, c255 and c270 are examined (figures omitted). The 1st mode has negative (no) correlation with the cloudiness c210 (c270) around the Western Ghats in west India. On the other hand the 2nd mode has no (positive) correlation with c210 (c270) in West India. The high cloud amount increases when the 1st mode becomes negative. Therefore, it is found from the wind field in Figure 2 that high cloud amount increases when large-scale cyclonic circulation develops in the Arabian Sea to the West or Southwest of India.

Usually EOF analysis is sensitive target regions. We checked regional dependence by employing EOF analysis with only Meteosat and 850 hPa wind. The obtained EOF 1st and 2nd modes are similar to modes as shown Figure 2. We also made EOF analysis for precipitation and 850 hPa wind fields as shown in Figure 4 during the period of 1979 to 2002. The 1st mode is again similar to the one in Figure 2, confirming that the 1st mode is robust.

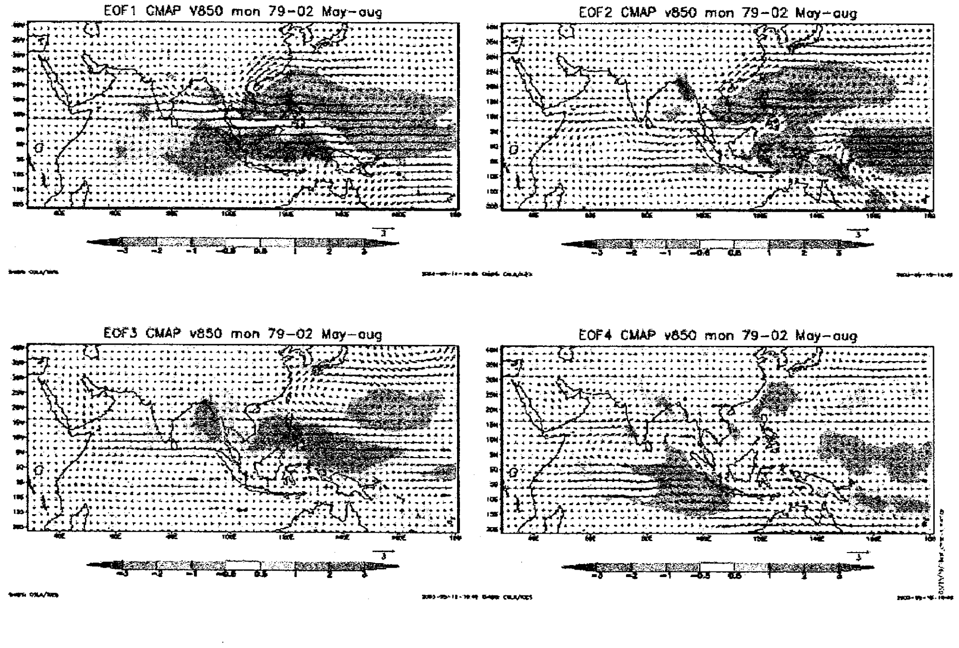

Figure 4: The first leading 4 EOF modes for precipitation and 850 hPa wind fields

2.2 Diurnal variations

Left panel of Figure 4 shows the case of 2000 year. Pentad time series of total and diurnal variance are shown with an orange and blue lines respectively. Black line shows the ratio of diurnal variance to the total one. The diurnal variance was computed from the band-passed time series with 21-27h period. Yellow bar shows accumulated rainfall during the corresponding pentad (value in mm is obtained by multiplying 300)..

You can see the high ratio state continuing from May to October. This period just corresponds to the Indian summer monsoon season. And also we should pay attention to the fact that c255 is considered to reflect clouds condition only.

From this figure we can notice the following points.

1) The ratio generally tends to be higher during the summer monsoon season.
2) The ratio tends to become higher in the inactive phase or just before and after the active phase.
3) Before the monsoon onset, the ratio has already become high a month before.

These features give us many suggestion regarding conditions associated to diurnal convection. 1) suggests that diurnal convective activity tends to become prominent in convectively active phase in the intraseasonal time scale. In other words, monsoon season is a suitable period for generation of convective clouds. This, however, looks to be contradicting with 2). But we should pay attention to the difference of time scale. Monsoon season continues several months. On the other hand, 2) describes within a month. Main factor which drives diurnal variation is diurnal variation of heating by sunshine. And atmospheric water vapor, ground and atmospheric stability conditions strongly affect convective activity. By taking these conditions into consideration, it is considered that humid condition with sunshine might be a suitable situation for enhancement of diurnal convective activity. In that sense, 2) can be understood without contradiction with 1). 3) also suggests that similar condition appears just before monsoon onset.

Right panel of Figure 4 is the 2002 case. Monsoon in this year is known as a bad monsoon. India was suffered from severe draught in July. However, at that time the ratio was kept with low level. This might be related to the situation of monsoon break, ex. stability condition, large scale anomalous circulation, wetness of ground, etc. It should be an important future task to investigate their roles and these interactions.

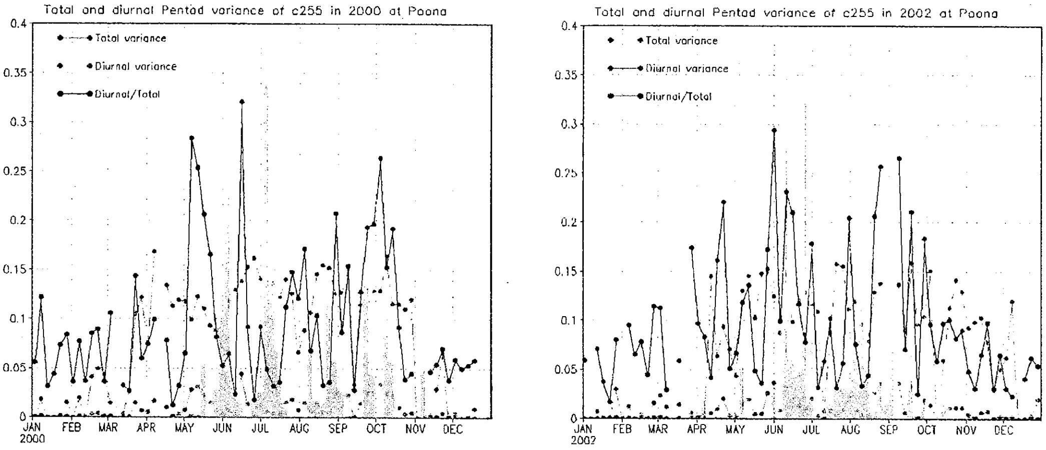

Figure 4. Pentad temporal variation of total, diurnal variance of c255, its ratio (Diurnal/Total) and pentad accumulated rainfall at Poona (18.53N,73.85E), India for 2000(left) and 2002 (right).

3. Summary

In the Asian-Pacific region in Northern summer, the dominant variations are “dipole type pattern” in which convective activity are enhanced (suppressed) in the East Indian Ocean(from the Bay of Bengal to the Western Pacific). The associated wind fields well correspond to those convective activities. These results are robust in the sense of independence of regions to be analyzed.

We have revealed some features regarding relationship between diurnal component and total variability of convective activity using METEOSAT IR data and station rainfall data.

These are summarized as follows.

1) Diurnal convective activity tends to be relatively enhanced in monsoon season.
2) Diurnal activity tends to be enhanced in inactive phases or just before and after rainy pentads.
3) At one month before the onset, enhancement of diurnal activity was already started.

However, we have to notice that these results were obtained through the analysis of just one station data. As we have suggested, there are many factors to be considered to understand diversity of convective activity regarding monsoon. We need to proceed further research including more other cases.

Ground and Satellite Monitoring of Volcanic Aerosols in Visible and Infrared Bands

K. Kinoshita[1], C.Kanagaki[1], A. Minaka[1], S. Tsuchida[1], T. Matsui[1], A. Tupper[2], H. Yakiwara[3] and N. Iino[4]
(Kagoshima University Volcanic Cloud Research Group)
1 Faculty of Education, Kagoshima University, Kagoshima 890-0065, Japan
E-mail: kisei@edu.kagoshima-u.ac.jp; chikara@edu.kagoshima-u.ac.jp; minaka@edu.kagoshima-u.ac.jp;
tsuchida@edu.kagoshima-u.ac.jp; matsui@edu.kagoshima-u.ac.jp
2 Darwin Volcanic Ash Advisory Centre, Commonwealth Bureau of Meteorology, , Australia
E-mail: a.tupper@bom.gov.au
3 Nansei-Toko Observatory for Earthquakes and Volcanoes, Kagoshima University, Kagoshima 890-0065, Japan
E-mail: yakiwara@sci.kagoshima-u.ac.jp
4 Department of Mechanical Engineering, Kagoshima University, Kagoshima, 890-0065, Japan
E-mail: iino@mech.kagoshima-u.ac.jp

Abstract

Methods of continuous monitoring of volcanic clouds from the ground are discussed, including NIR monitoring of volcanic aerosols, high temperature anomalies, and vegetation using an appropriate filter set and CCD camera. A combination of satellite and ground-based remote sensing techniques is effective for understanding various volcanic phenomena.

1. Introduction

Satellite-based remote sensing is used to analyze large eruption clouds, in order to detect otherwise unreported eruptions, identify ground and aviation hazards, evaluate eruption intensity and research the eruptions' climatic impacts. Satellite images showing the large-scale dispersion of volcanic clouds enable us to study long-range transport of atmospheric pollutants from fixed sources. On the other hand, ground-based monitoring of the clouds is also important for the observation of their occurrence, vertical structure and other dynamical characteristics in both large and small scales. Ground-based monitoring is often possible even when satellite observation is obscured by clouds, and can also be used to identify interactions between volcanic and meteorological water/ice clouds, such as orographic or convective clouds over the volcano.Visual recording of volcanic clouds has been done for quite a long time at Sakurajima in southern Kyushu, Japan, and gradually extended to other volcanoes as summarized in [1]. Recently, Near Infrared (NIR) observations of high temperature anomalies using the "night-shot" function of video cameras were reported [2, 3]. Here, the night-shot removes the NIR cut-off filter. The use of an IR filter further highlights the anomalies by the cut-off of visible light. In the daytime, the night-shot mode with the IR filter may give a NIR view from the ground similar to satellite imagery [4]. Such a view may be useful not only to study vegetation on the volcanoes, but also to distinguish clouds from the background sky on misty days. Furthermore, faint aerosols almost invisible in the ordinary view can be clearly recognized in the NIR view. In this report, we discuss the problems of continual observation of volcanic aerosols and other phenomena with visible and NIR bands, together with satellite remote sensing in visible and various infrared bands.

2. Ground monitoring of volcanic clouds

The Kagoshima University Volcanic Cloud Research Group is now conducting continual monitoring from the ground at three active volcanoes; Sakurajima, Satsuma-Iwojima and Suwanosejima in southwest Japan [1]. The latter two are located in the Nansei Islands south of Kyushu as shown in Fig. 1. A reason for observing the volcanic clouds is that the visible image of the cloud is a good approximation of the flow of invisible volcanic gases emitted from the crater. In order to analyze the gas concentration data at the foot of Miyakejima Volcano, the group members studied NOAA/AVHRR satellite images of volcanic plumes, and web-camera observations between September 2000 and May 2002 by the Earthquake Research Institute, University of Tokyo [1, 5]. Furthermore, the group, in collaboration with Philippine Institute of Volcanology and Seismology (PHIVOLCS), started continual observation of volcanic clouds at Mt. Mayon in the Philippines [6]. We summarize here the methods and problems in automatic continual recordings of volcanic clouds.

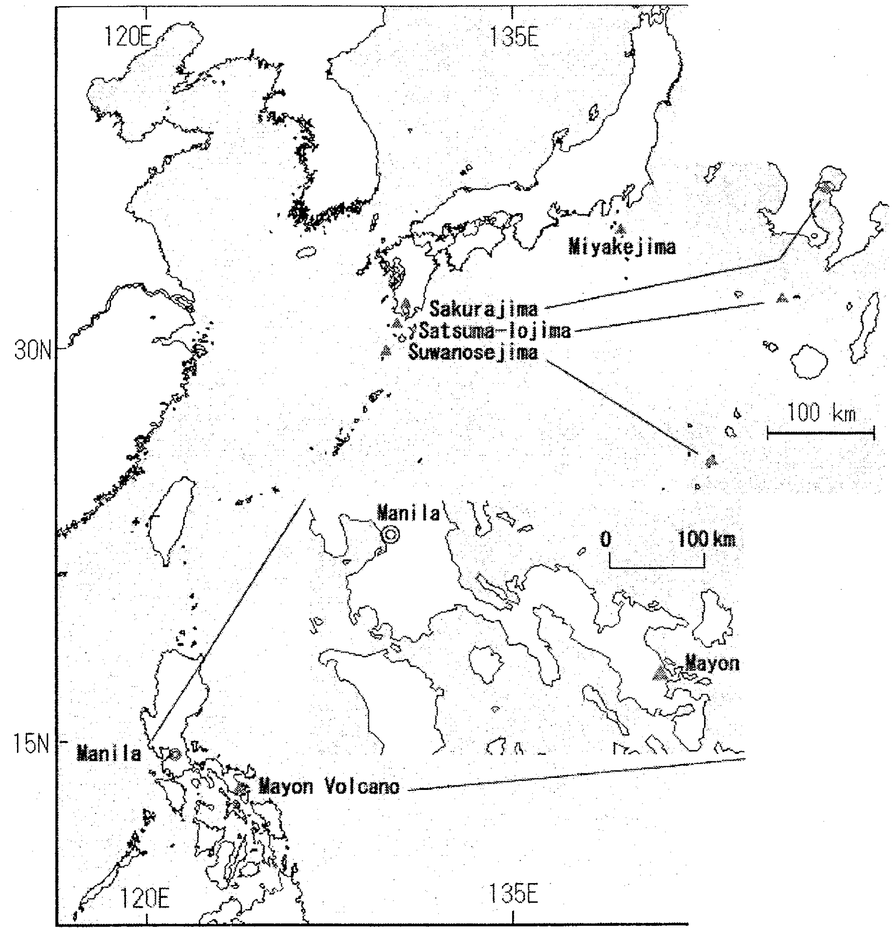

Fig. 1. Volcanoes Sakurajima, Satsuma-Iwojima, Suwanosejima and Miyakejima in Japan, and Mayon in the Philippines.

2.1 Methods of automatic recordings

There are basically three methods for automatic long-time recording of volcanic clouds using a digital camera head with a CCD sensor, as illustrated in Fig. 2.

(i) Digital still camera

Automatic recording with a fixed time interval is possible without changing the digital recording media for a few or several months, as long as the power supply is constant. Very few cameras have such specifications. A Sharp MD-PS1 was used successfully at Satsuma-Iwojima between July 1998 and February 2003, and at Tarumizu station to observe Sakurajima between December 1998 and February 2003[1], and is operating now at Mayon since June 2003[6]. This is a pioneering camera, allowing recording with hourly intervals, with 1950 pictures in a 160 MB mini disk (MD). A Casio QV-R4, using a 512 MB SD memory, is now operating in Changchun, China for the study of Asian dust since March 2003, also recording with an hourly interval [7]. Such records are useful to see diurnal changes, and are appropriate to make CD-R archives, or to display on the Internet

Though the production of these cameras has ceased, we found that a new camera Ricoh Caplio G4wide inherited the interval recording function, and we began operating one at Satsuma-Iwojima in December 2003.

(ii) Interval video recording

As the ejection of volcanic clouds is rather stationary most of the time, interval video recording is suited for covering a long duration in a cassette tape. The interval length is at most ten minutes with a half second recording in some recent video cameras such as the SONY DCR-TRV series, allowing the 100 days record in a 2 hour mini-DV cassette. Such recordings are now operating at Changchun and Mayon, as back-ups for the digital cameras. It should be noted that the continuity of rapid phenomena such as explosive eruption clouds is lost in ten-minute intervals. Smoother motion can be

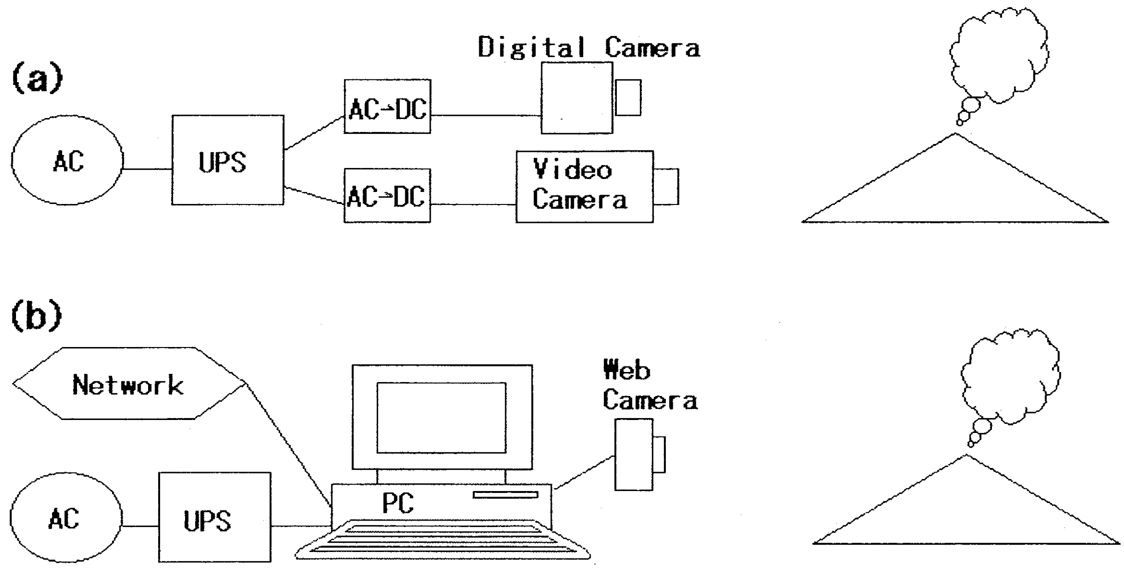

Fig. 2. Systems for automatic recording of volcanic clouds. (a) Digital and video cameras. (b) Web camera system.

obtained by frame recording with 8 sec. (or less) intervals by time-lapse video recorders such as the SONY SVT series, which has been used at Sakurajima since 1992. Random access to video records is now possible by converting them into mpeg files to be stored on CD-R or DVD.

(iii) Web camera system

For real time monitoring via Internet and archiving on a hard disk, a web camera system composed of a camera head and a computer is useful. Real time monitoring is especially important for aviation safety. This type of system has been operating at the Faculty of Education, Kagoshima University for Sakurajima monitoring since December 2000 [1], and at Satsuma-Iwojima since February 2003. A network camera server is a small all-in-one apparatus with the camera and server computer built-in. This type has been adopted at Nakanoshima to monitor Suwanosejima 25 km to the southwest, and also at Nansei-Toko Observatory, Kagoshima University and Tarumizu City Office to monitor Sakurajima from different directions [1]. As the network camera server is not suited for large archives, another computer with enough storage is necessary, which may be connected by a local or remote network.

For web-camera systems in general, the interval to get still images can be arbitrarily adjusted by programming. In the above systems, we use 5-20 minute intervals, which is not a problem for hard disks with enough capacity.

2.2 Environment for continual monitoring

We summarise the conditions for automatic long-term recording of volcanic clouds for up to a few months.

(i) An appropriate observation site inside a building with a window to see the volcano, hopefully with a wide view undisturbed by nearby obstacles and direct sunshine in the scene. Otherwise, outside a building or in the field, an apparatus housing is necessary.

(ii) Reliable electric power supply, equipped with UPS (uninterrupted power supply) against power shortages and surges.

(iii) A person to look after the performance of the apparatus, restart it after an unexpected stop, and exchange the media. There are many important points to adjust for the initial set-up at the restart, to be listed later.

(iv) Internet connection. If a continuous Internet connection is available, a network camera server alone is enough at the observation site for live monitoring with remote control, and the archived data can be stored on another server at remote laboratory. A permanent Internet connection is very useful for such a system, although not available in many regions. Otherwise, the data should be stored on a server in the local area network at the monitoring site, and downloaded daily to a remote server using a dial-up connection.

If the conditions (i)-(iii) are fulfilled, continual observation is possible by using interval recordings with digital still and/or video cameras, changing the media every few months. For real-time or near-real time monitoring, condition (iv) should be met.

Even if any of the above conditions is not satisfied, it may be possible to leave a digital camera for a month with an appropriate battery* in a sealed package with a transparent window. This risks theft or vandalism of the equipment, and protection against damage from sunshine, rain and wind should also be considered. For the same reason, it is often much more practical to use relatively cheap 'off-the-shelf' equipment for this purpose, rather than more expensive dedicated imagers (* An alternative to AC power supply is to use rechargeable battery pack for digital camera.)

2.3 Initial set up

Finally let us consider the essential points for the initial set up of interval recording mentioned in 2.2 (iii).

White balance: Outdoor, so as to record color information properly.

Focus: Infinity. (Manual focusing is necessary for the NIR observation, to be discussed in 3.2.)

Flash and Beep: Off.

Liquid Crystal Display: Off, to avoid its degradation and save power.

Framing: Relatively wide with a horizon or other horizontal line near the bottom.

There are many other points to be adjusted at the beginning of automatic recordings, depending on the type of apparatus.

3. Methods of visible and infrared observation of volcanic phenomena

3.1 Satellite imagery

A number of techniques have evolved over recent years to detect volcanic clouds or sense activity at volcanoes, which we briefly summarize here. In general, these techniques exploit differential reflective or absorptive properties of ash or sulfates in the volcanic cloud. The main gaseous eruption component is usually water, which can often interfere with detection techniques. However, clouds with a sufficiently high ash content, or with sufficient sulfate content, which induces a smaller particle size and inhibits cloud evaporation, are usually distinguishable from water/ice meteorological cloud, provided higher clouds do not obscure the satellites' view.

(i) Visible bands

Many eruptions are distinguishable in visible wavelengths because of the relatively low albedo of ash. The color of the cloud can be distinguished using satellites with the appropriate 'true-color' wavelengths (e.g. LANDSAT/(E)TM, SeaSTAR/SeaWiFS and EOS/MODIS), and may be white, light- or dark-gray or brown, depending on the ash content of the cloud.

(ii) Reflective infrared bands

Both NIR (e.g., 1.6 μm) and middle infrared (e.g., 3.7 μm) are highly sensitive to particle size and composition, a fact which has been exploited for volcanic ash detection [8] and detection of ash-poor, sulfate rich plumes such as from Miyakejima [9]. These images are also useful for the studies of the topography and vegetation coverage in order to investigate the effects of volcanic gas, and are also highly useful for 'hot-spot' (high temperature anomaly) detection as summarized in [10].

(iii) Thermal infrared bands

The difference of 12 and 11 μm bands is very effective in distinguishing lithic aerosols (in dry air) from water clouds, and is utilized for detection of ash cloud [11-14] and Asian dust [15]. The 8.6 μm band is utilized, combined with other thermal bands in Terra/ASTER [16] and MODIS, for the detection of SO_2 in the volcanic gas [17]. Ultra-violet reflection is also utilized to detect SO_2 in TOMS, but only with low resolution (39x39 km pixel size for Earth-Probe TOMS at nadir). MODIS data is highly useful for monitoring ash clouds because of its many useful channels [18-21]

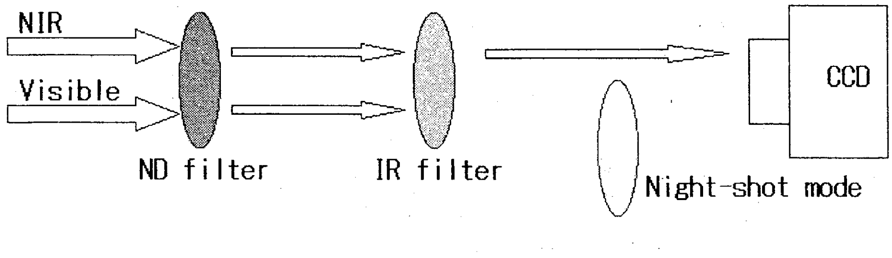

Fig. 3. Visible and NIR radiations versus filters for a CCD camera head.

3.2 Ground observation

Here we discuss a simple use of NIR images to supplement visible imagery, using filters as described in Fig. 3.

(i) Night-shot : Ordinary CCD sensors in video and digital cameras have some sensitivity to wavelengths up to about 1.1 μm such as gray line in Fig. 4. In the night-shot mode, the NIR cut-off filter is removed to increase the sensitivity under dark conditions, with the sacrifice of the color balance. The mode was utilized to detect the NIR radiation as a very hot anomaly at the vent of Mayon volcano in the Philippines, though it was invisible to the naked eye [2].

(ii) IR filter : Recently, IR filters to cut-off the visible band with the boundary around 840 nm are available, such as broken line in Fig. 4. In the night shot mode equipped with such a filter, one can get NIR images similar to MODIS band2, 841-876 nm. Very hot anomalies are enhanced by IR filters, as studied at the crater of Aso volcano [3]. It is preferred to avoid outdoor light even in twilight, as it contains NIR radiation originating from the sun.

(iii) ND filter : In the daytime, the night-shot mode with IR filter may give a NIR view from the ground similar to satellite imagery, when the solar reflection is adequately reduced by a neutral density (ND) filter. Such a view may be useful not only to study vegetation on the volcanic surface, but also to distinguish the clouds from the background sky on misty days. Furthermore, faint aerosols almost invisible in ordinary view can be clearly recognized in the NIR view, as shown in the next section.

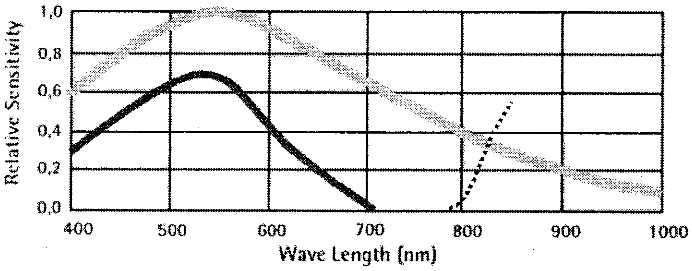

Fig. 4. Sensitivities of color (solid line) and IR (gray line) cameras of the network camera AXIS2420 series, and the IR filter of Fujifilm IR-84 (broken line).

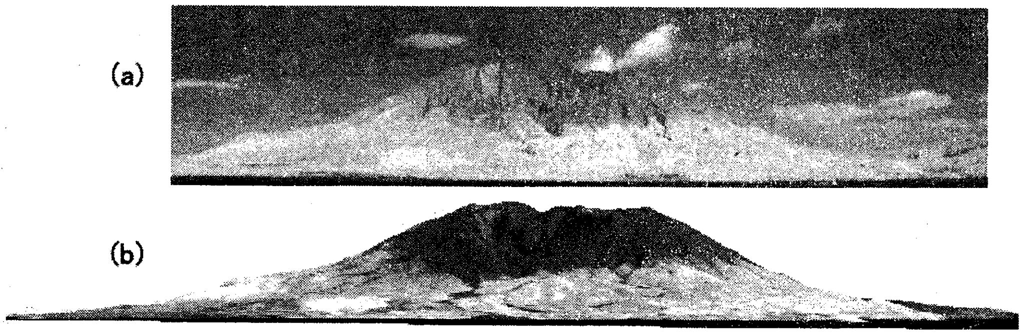

Fig.5. NIR images of Sakurajima.
(a) Ground observation at 9.8 km WSW from the crater on Oct. 2003 at 13:40, recorded on mini-DV tape in SONY DCR-TRV30with IR-84 filter in night-shot mode.
(b) A 3D view of the LANSAT-5/TM-4 data on 26 Aug. 1998 at 10:10 from WSW by using the SiPSE system.
(c) The top view of TM data as in (b).

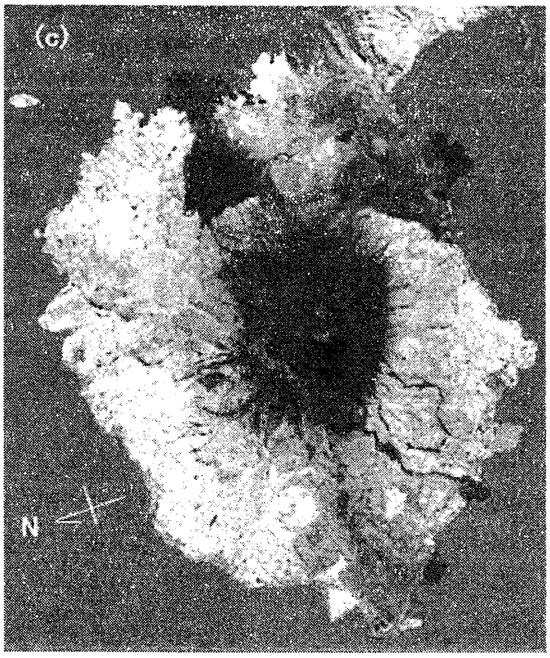

4. Results

4.1 Sakurajima

Previous works of ground observations and satellite imagery of Sakurajima volcano are summarized in a booklet [22]. The first tests of NIR observation of Sakurajima volcano from the main campus of Kagoshima University, about 10 km west of the crater, were summarized in [23]. Here we report a few additional results.

(i) Vegetation

Fig. 5 shows a comparison of NIR images from the ground (a) as described in 3.2 (iii), and the LANSAT-5/TM-4 (b and c), where 3D representation (b) of TM data combined with the DEM data of Geographical Survey Institute of Japan is obtained by using Satellite Image Presentation System for Education (SiPSE) [24]. We see that the vegetation is absent near the summit, because of the adverse conditions. It should be noted that the range of the ground observation, 0.84-1.1 μm, is not quite the same as that of TM-4, 0.76-0.90 μm, aside from the difference of the solar elevation and direction. As a result, the reflections from rocks and barren lands are somewhat stronger in the ground observation than TM-4. This problem will be discussed in more detail in near future.

(ii) Aerosol

Ground observation of a faint plume at Sakurajima in fine weather is shown in Fig. 6, where (a), (b) and (c) are NIR, red and green components of visible picture. We see that the contrast of the plume against the background sky is stronger in longer wave lengths, i.e., the plume is clear in (a), not so clear in (b) and almost invisible in (c). In the blue color not shown here, there is no contrast. This situation is quite opposite to the satellite image of a faint plume over the sea [25]. In the case of Fig. 6, the morning sun is right of the scene, and the background sky is most dark in NIR, while the scattering by plume aerosol is seen. Similar results are obtained in other configurations of the sun.

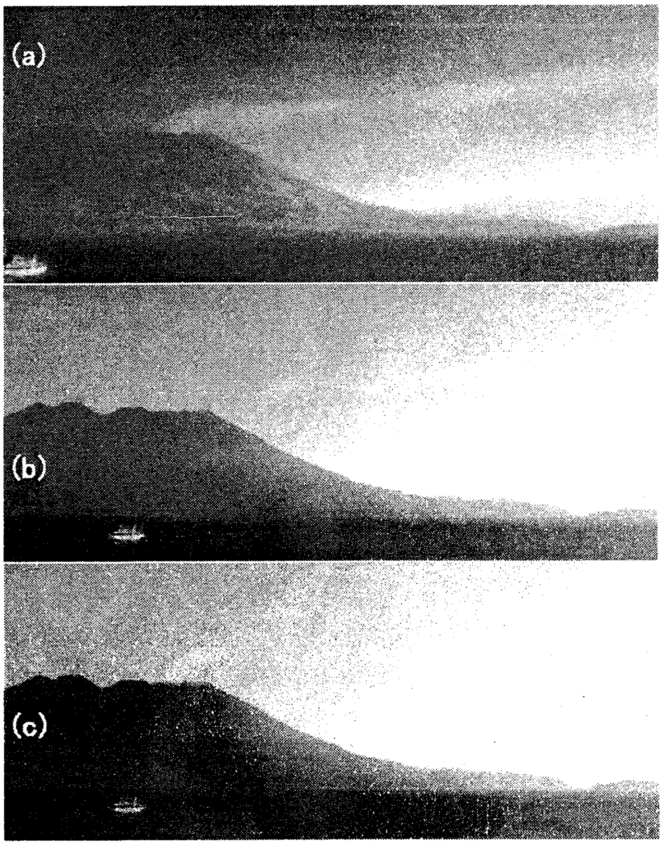

Fig. 6. A faint plume at Sakurajima on 2 Dec. 2003 at 8:00, with the camera as in Fig. 5(a).
(a) NIR, (b) and (c): Red and green components of a visible image.

4.2 Satsuma-Iwojima

Since July 1998, hourly volcanic cloud observations such as those in Fig. 7 have been displayed on a homepage. Recently, we started the observation in the NIR band.

(i) Hot anomalies

In the nighttime, hot anomalies inside the crater and on the outside wall have been observed in LANDSAT-5/TM images [26]. From the ground, it is expected to observe the anomalies on the outside wall. We started NIR observation of 0.85-1.1 μm by using a Kenko IR-85 filter on a SONY DCR-TRV30 in the night-shot mode since the end of July 2003. The first trials, lasting until November 2003 were unsuccessful.

(ii) Volcanic clouds and aerosols

In the night-shot mode with IR-85 filter mentioned above, the daytime images were over-exposed except for in the morning before sunrise, and during the evening. Therefore, we have added a ND filter (1/100) to reduce over-exposure since 2 Dec. 2003. On the other hand, the Creative Webcamplyus web-camera, having a CMOS sensor, has been used equipped with a Fujifilm IR-84 filter for recording with 30 min. interval between 7:00 and 17:30 on a server computer. Though this head has neither the night-shot mode nor the NIR-cut filter, a color image may be obtained by a software cancellation of IR components. We see that NIR image is obtained by using the IR filter. In the interval recording, faint plumes are obtained successfully, as shown on the homepage, http://arist.edu.kagoshima-u.ac.jp/volc/iwo/ .

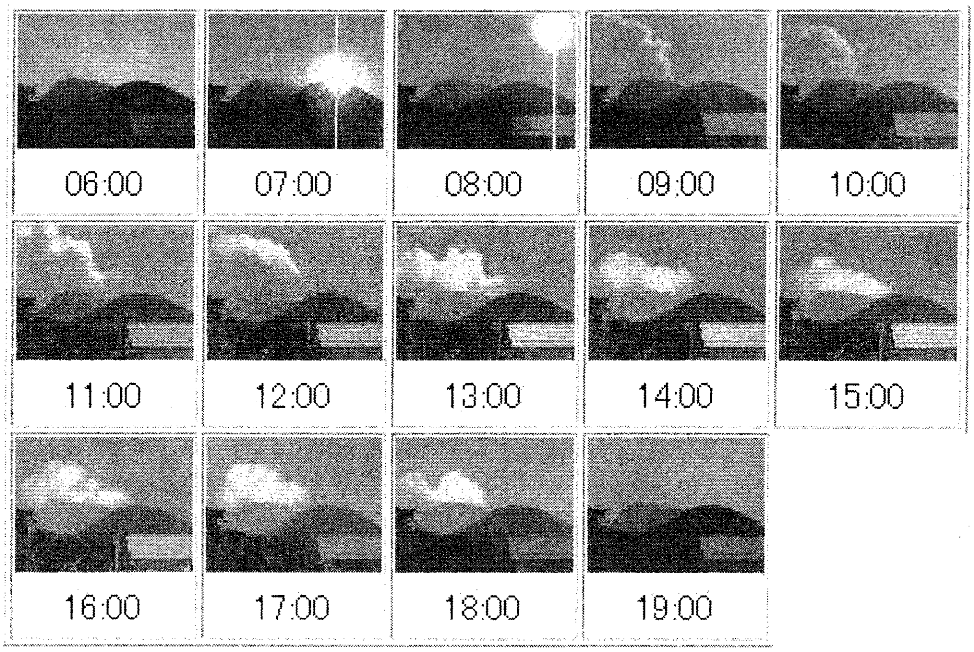

Fig. 7. Volcanic clouds of Satsuma-Iwojima observed from 3 km west of the crater, with one-hour interval on 22 Aug. 2002.

Fig. 8 shows a comparison of southern flank of Iwo-dake from a ferryboat without and with the IR filter on the digital camera Sharp VN-EZ5. We see that IR filter is enough to obtain NIR image, though the exposure time should be somewhat long.

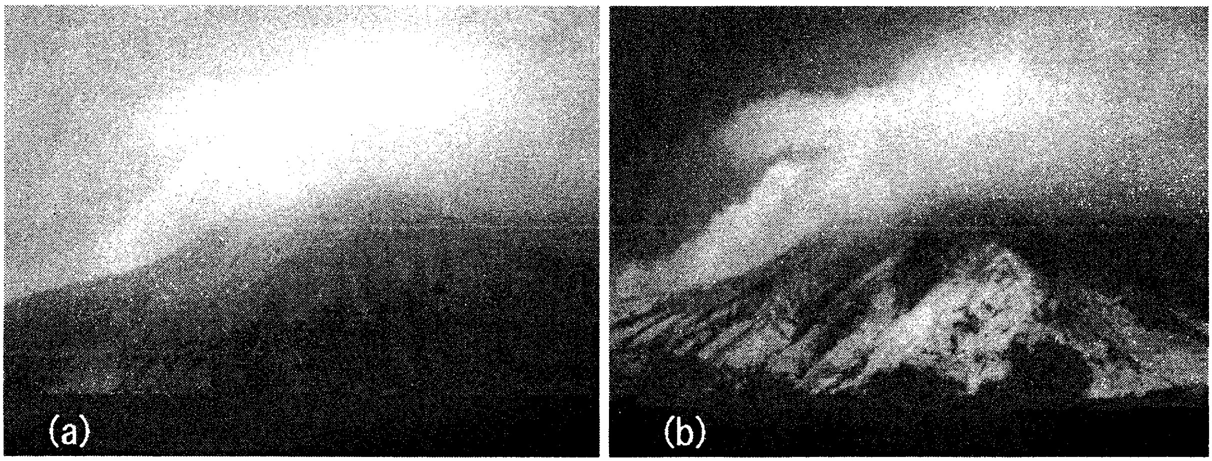

Fig. 8. Southern flank of Iwo-dake from a ferry-boat, by using the Sharp VN-EZ5 (a) without and (b) with the IR-84 filter, respectively.

4.3 Suwanosejima

In recent years, Suwanosejima volcano has been the most eruptive in Japan, with the eruption columns a few km above the crater occasionally. We have done satellite detection with NOAA/AVHRR and EOS/MODIS, and web camera observation [27, 28]. Together with manual photos from the inhabitants, we have listed them in the homepages,

Topics of SiNG-Kagoshima (in Japanese): http://arist.edu.kagoshima-u.ac.jp/sing/topics/

MODIS Database of Volcanic Eruptions in the Western Pacific: http://arist.edu.kagoshima-u.ac.jp/volc/ocean/

Suwanosejima is a target of the near real time NOAA image browsing system for volcano monitoring of Tokai University Research and Information Center, together with Sakurajima and Miyakejima [29].

(i) Web camera observation

The site of the web camera at Nakanoshima, started on 6 Aug. 2002, is 25 km northeast of the crater, separated by the sea. Though the eruption clouds are often well observed such as shown in Fig. 9, the images are almost always partially obscured by haze or mist. We may expect to obtain better images in NIR.

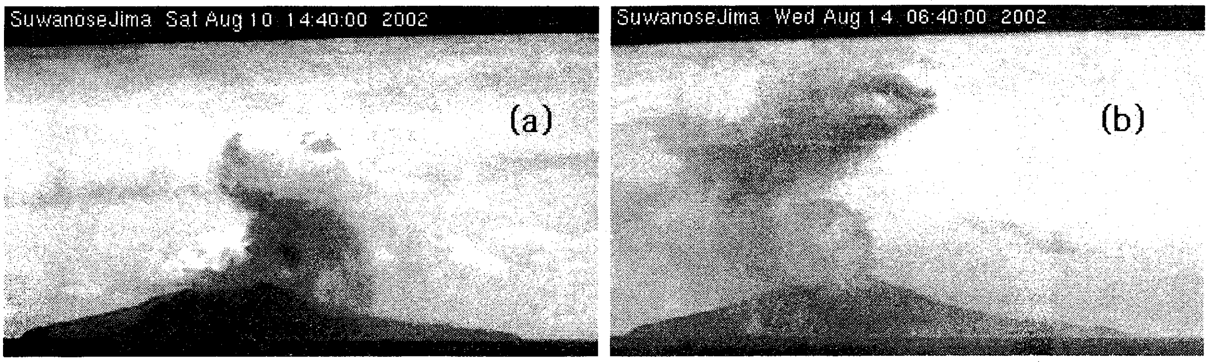

Fig. 9. Eruption clouds at Suwanosejima, imaged by the web camera at Nakanoshima, after stretching the contrast. (a) Aug. 10, 2002 at 14:40 JST. (b) Aug. 14, 2002, 6:40 JST.

(ii) Highlights of ground and satellite observations

In 2002, Suwanosejima volcano was especially eruptive. Here we make a brief list of remarkable events [27, 28].

April 12: In the nighttime, a hot spot was observed on AVHRR band3, and in MODIS (22:20 JST). Next day, plumes about 400 km long were seen in AVHRR and MODIS.

June 18: Eruption column of height 3 km was recorded in photos and AVHRR imagery.

July 23-24: Inhabitants observed several eruptions, and their photos and AVHRR were obtained.

Aug. 19-22: Several strong eruptions were observed accompanied with roaring sounds and vibrations, and also with volcanic lightning and red sky in the nighttime. Web camera images, photos were obtained as well as AVHRR and MODIS images.

Dec. 5: The volcanic plume rose high over the island during 10:00 to 11:00, 15:00 to 16:00JST, with 11-15 explosive eruptions, in spite of strong winds for the whole day, as recorded by the web camera, photos, MODIS and GMS-5 visible images.

4.4 Vegetation of volcanic island Miyakejima

Volcanic clouds at Miyakejima are discussed in [9, 18] in terms of ground observation and satellite images. Here we show the Terra/ASTER images of Miyakejima Island in Fig. 10, in which the damage of the vegetation due to the gas is evident at specific directions, consistent with the appearance of high concentration events of SO_2 around the island [1, 9, 18].

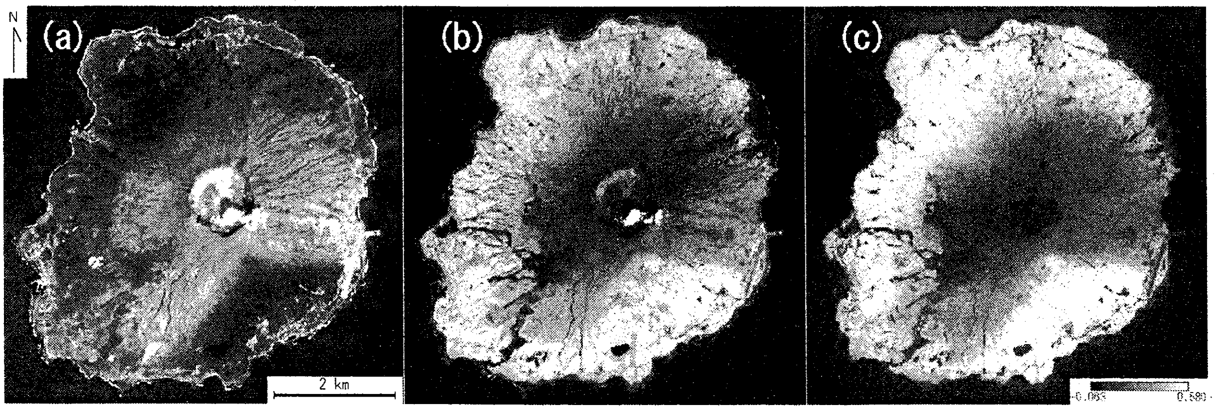

Fig. 10. ASTER images of Miyakejima on 7 April 2003.
(a) VNIR-2 (0.63-0.69 μm). (b) VNIR-3 (0.78-0.86 μm). (c) NDVI.

We note that the NIR image gives a similar result for the vegetation as the normalized vegetation index (NDVI) defined as NDVI = (NIR-Vis) / (NIR+Vis), where we have used the red band of VNIR for Vis.

5. Concluding remarks

Long-interval, automatic, ground-based camera observation is useful for studies of volcanic clouds, Asian dust, and meteorological clouds. Real-time cameras are important for disaster prevention, and the archived records serve to understand the phenomena scientifically. The use of 'off-the-shelf' equipment has great practical advantages over more expensive infrared equipment. Combining these data with satellite information is very effective.

The use of the NIR band has opened a new era of the ground observation. It is very desirable that the makers disclose the detailed properties of the CCD sensors and filters. Then, the cameras may be used as a measuring apparatus similar to the satellite sensors, and the manipulations by using different bands such as tried in [23] may find firm basis. The calibration studies of them are important problems to be done.

Acknowledgements

This work was done as a part of the Kagoshima University 2003 project "Monitoring Volcanic Clouds of Western Pacific". We are grateful to the University for the support of the project, and Mr. K. Kawano, Mr. S. Hamada and Mr. M. Yamamoto for related collaborative works. We thank CEReS, Chiba University, for the support as the joint project " Analysis of lithic aerosol by using multi-spectral satellite data ". LANDSAT/TM data of NASA was received and provided by NASDA (converted into JAXA now), while the ASTER data by ERSDAC, Japan, as a part of ASTER-AO activity. We also thank the courtesy of these organizations.

References

[1] K. Kinoshita, C. Kanagaki, A. Tupper and N. Iino, Observation and Analysis of Plumes and Gas from Volcanic Islands in Japan, *Proc. International Workshop on Physical Modeling of Flow and Dispersion Phenomena*, Prato, Italy, 2003, pp.78-83.

[2] E. G. Corpuz, Active Volcano in the Philippines - Mayon, Pinatubo and Taal, *Talk at the Seminar in IUGG Pre-Conference Fieldtrip*, June, 2003.

[3] Kyoto Univ. Earth Science Craftspeople, Use the Night Shot in the right way. - Measurement of temperature in volcano crater -, *Japanese Earth Sci. Conf.*, 2002, J067-006;
http://www-jm.eps.s.u-tokyo.ac.jp/2002cd-rom/pdf/j067/j067-006_e.pdf;
T. Saito et al., Crater glow at Aso Volcano in the movie, *Japanese Earth Sci. Conf.*, 2003, J077-010,
http://www-jm.eps.s.u-tokyo.ac.jp/2003cd-rom/pdf/j077/j077-010_e.pdf

[4] N. Yuba, NIR Photo by Digital Camera, *Shinrin Kosoku*, **193**, 12, 2001 (in Japanese).
H. Hayashi, http://homepage2.nifty.com/harry3/kenkyu/ir-photo/ (in Japanese).
T. Soma, http://akikoma.remos.iwate-u.ac.jp/still_shott/ircam/ircam1.html (in Japanese).

[5] A. Terada and Y. Ida, Characters of Dynamics of Injected Volcanic Gasses from Miyakejima Volcano, *Kagoshima Univ. Res. Center Occasional Papers*, **37**, 40-49, 2003 (in Japanese with English abstract).

[6] Continual Observation of Eruption Clouds at Mayon Volcano, http://arist.edu.kagoshima-u.ac.jp/volc/mayon/

[7] K. Kinoshita, Wang Ning, Zhang Gang, A. Tupper, N. Iino, S. Hamada and S. Tsuchida, Continual observation of Asian dust in Changchun and Kagoshima, *2nd International Workshop on Sandstorms and Associated Dustfall*, Nagoya, Nov. 2003; http://arist.edu.kagoshima-u.ac.jp/adust/chang/

[8] G. P. Ellrod, B. Connell, and D. Hillger, Improved Detection of Airborne Volcanic Ash Using Multispectral Infrared Satellite Data. *J. Geophys. Res.*, **108**(D12), 4356, 2003.

[9] M. Koyamada, K. Kinoshita, N. Iino and C. Kanagaki, Satellite detection of volcanic aerosol at Miyakejima and Sakurajima, *Proc. Nagasaki Workshop on Aerosol-Cloud Radiation Interaction and Asian Lidar Network*, 2001, pp.96-101.

[10] C. Oppenheimer, Volcanological applications of meteorological satellites, *Int. J. Rem. Sens.*, **19**, 2829 - 2864, 1998.
M. Urai, Volcano monitoring with Landsat TM short wave infrared bands: the 1990-1994 eruption of Unzen Volcano, Japan, *Int. J. Rem. Sens.*, **21**, 861-872, 2000.

[11] A. J. Prata, Observations of volcanic ash clouds in the10-12 μm window using AVHRR/2 data. *Int. J. Rem. Sens.*, **10**, 751-761, 1989.

[12] K.Kinoshita, S.Hosoyamada, A.Goto and S.Saitoh, NOAA-AVHRR Imagery of Volcanic Clouds in Kyushu, Japan, *Proc. 1993 Int. Geoscience and Remote Sensing Symposium*, Tokyo, 1993, pp.1824-1826.

[13] W.I. Rose, G.J.S. Bluth, and G.G.J. Ernst, Integrating retrievals of volcanic cloud characteristics from satellite remote sensors: a summary, *Phil. Trans. R. Soc. Lond.*, **A358**, 1585-1606, 2000.

[14] A. Tupper, S. Carn, J. Davey, Y. Kamada, R. Potts, F. Prata, and M. Tokuno, An evaluation of volcanic cloud detection techniques during recent significant eruptions in the western 'Ring of Fire'. *Rem. Sens. Env.*, 2003, in review.

[15] Kagoshima Kosa Analysis Group, Satellite Imagery of Asian Dust Events, *Kagoshima Univ.*, 2001; T. Masumizu, R. Iwasaki, M. Koyamada, K. Kinoshita, I. Uno, S. Satake, T. Yano and N. Iino, Asian dust events in 2001 observed by GMS-5/VISSR and NOAA/AVHRR, *Proc. Nagasaki Workshop on Aerosol-Cloud Radiation Interaction and Asian Lidar Network*, 2001, pp.102-107.

[16] M. Urai, Sulfur dioxide observation with ASTER and MODIS at Miyakejima volcano, Japan, *Kagoshima Univ. Res. Center Occasional Papers*, **37**, 50-57, 2003 (in Japanese with English abstract).

[17] V. J. Realmuto, A. J. Sutton, and T. Elias, Multispectral imaging of sulfur dioxide plumes from the East Rift Zone of Kilauea volcano, Hawaii, *J. Geophys. Res.*, **102**, 15057-15072, 1997.

[18] K. Kinoshita, C. Kanagaki, N. Iino, M. Koyamada, A. Terada and A.C. Tupper, Volcanic plumes at Miyakejima observed from satellites and from the ground, *Proc. SPIE **4891**, Optical Remote Sensing of the Atmosphere and Clouds III*, 227-236, 2003.

[19] G.P. Ellrod and J-S. Im, Development of Volcanic Ash Image Products using MODIS Multi-spectral data, *AMS conference paper*, 2003. http://orbit-net.nesdis.noaa.gov/arad/fpdt/fpdt_pubs/amssat03_modis_volc.pdf.

[20] Meteo-France/CMS, Use of MODIS to enhance the PGE01-02 of SAFNWC/MSG *AF/NWC/MFL/SCI/PSD/2*, Issue 1, Rev. 0, 2001. http://www.meteorologie.eu.org/safnwc/publis/modsci10.pdf

[21] I. Sokolik, Remote sensing of mineral dust aerosols in the UV/visible and IR regions, *Proc SPIE **4891**, Optical Remote Sensing of the Atmosphere and Clouds III*, 265-271, 2003.

[22] K. Kinoshita (ed.), Analysis of Satellite Images on the Dispersion of Volcanic Ash Clouds from Mt. Sakurajima, *Kagoshima Univ.*, 2001.

[23] C. Kanagaki,K. Kawano and K. Kinoshita, Study of Near-Infrared Images using Video-camera, *Bull. Fac. Edu., Kagoshima Univ., Natural Sci.*, **55**, in press, 2004 (in Japanese with English abstract).

[24] H. Togoshi, K. Kinoshita and N. Tomioka, Development of 3D image presentation system for education using digital evaluation model and remote sensing data, *27th Japanese Conf. Rem. Sens.*, 1999, pp273-274 (in Japanese with English abstract).

[25] K. Kinoshita, N. Iino, I. Uno, A. Mori, J. Kohno, Day and Night detection of Volcanic Clouds and Aerosol by NOAA/AVHRR Data, *CEReS Int. Symp. on the Atmospheric Correction of Satellite Data and its Application to Global Environment*, 1998, pp.37-44.

[26] H. Takahara and M. Urai, Surface temperature observation of Satsuma Iojima volcano with satellite image, *24th Japanese Conf. Rem. Sens.*, 1998, pp.23-24 (in Japanese with English abstract).
S. Machida, H. Takahara, H. Yoshizawa, K. Kinoshita, M. Urai and M. Kato, Study for Vocano Observation with Terra/ASTER Data, *J. Rem. Sens. Soc. Japan*, **20**, 87-91, 2000 (in Japanese with English abstract).

[27] C. Kanagaki, K. Kinoshita, A. Minaka, S. Tutida, H. Yagihara and T. Hukuzumi, Ground observation and satellite images of Suwanosejima plumes, *Kagoshima Univ. Res. Center Occasional Papers*, **37**, 136-143, 2003 (in Japanese with English abstract).

[28] C. Kanagaki, K. Kinoshita, A. Tupper, H. Yakiwara and T. Fukuzumi, Ground and Satellite Observation of Eruptions and Plumes at Suwanosejima, *IUGG 2003 Scientific Program*.

[29] S. Mitsumoto, K. Cho, H. Shimoda, T. Sakata and K. Kinoshita, A study on the development of a near real time NOAA image browsing system for volcano monitoring, *33th Japanese Conf. Rem. Sens.*, 2002, pp.11-12 (in Japanese with English abstract); K. Cho, S. Mitsumoto, H. Shimoda and Y. Matsumae, A study on satellite image dissemination system for volcano monitoring, *Kagoshima Univ. Res. Center Occasional Papers*, **37**, 164-171, 2003 (in Japanese with English abstract). http://www.tric.u-tokai.ac.jp/rsite/r1/vol/vol.htm

Comparison between Monthly Mean Precipitation as estimated from TRMM Precipitation Rader observations and from Rain Gauge Data

Naoto Iwasaka[1] and Makoto Sato[2]
Tokyo University of Mercantile Marine
1)Present affiliation: Tokyo University of Marine Science and Technology, Faculty of Marine Technology,
2-1-6 Etchujima, Koto-ku, Tokyo 135-8533
e-mail: iwasaka@e-kaiyodai.ac.jp
2)Present affiliation: R/V Hakuhomaru of Ocean Research Institute, University of Tokyo,
1-15-1 Minamidai, Nakano-ku, Tokyo 164-8639

Abstract

The monthly mean precipitations observed by the Tropical Rainfall Measuring Mission (TRMM) Precipitation Rader (PR), which were compiled and released by Japan Aerospace Exploration Agency, were compared with those observed at 180 rain gauge stations, including island stations in the Pacific Ocean, TAO/TRITON and PIRATA buoys, JMA Meteorological Observatories and AMeDAS stations. The correlation coefficient between the PR observations and those of the gauges was 0.53; the PR precipitation data were about 66% as large as the corresponding gauge data. The PR precipitation data are thus shown to be useful for qualitative analysis of distribution and variations in oceanic rainfall, although the PR data need quantitative improvement.

1. Introduction

Precipitation is one of the important factors controlling sea surface density through changing sea surface salinity. Thus, the precipitation over the ocean is very important for determining dynamic structure of the ocean and formation of water masses. Despite its importance, distributions and time change of the precipitation over the ocean have not been understood very well quantitatively. Because in situ observation of the rainfall aboard a ship is not required (Japan Meteorological Agency, 2001), and is technically very difficult (e.g. Iwasaka et al., 1999), the observations have been made on only some of research vessels and surface meteorological buoys (e.g., Serra and McPhaden, 2003). Thus, precipitation over the ocean has been estimated from satellite observations by using infrared and/or microwave sensors (e.g., Adler et al., 2001; Huffman et al., 1997; Arkin and Xie, 1994), or re-analyses of atmospheric conditions by using numerical weather prediction models (Climate Prediction Center, http://www.cdc.noaa.gov/cdc/reanalysis/; European Centre for Medium-Range Weather Forcasts;http://www.ecmwf.int/products/), with few sea truth data.

In November 1997, TRMM (Tropical Rainfall Measuring Mission) satellite was launched, and has continued observation successfully. The major mission of the satellite is to observe three dimensional structure of precipitation in the tropics and subtropics by using a newly developed Precipitation Radar (PR), the first sensor of this kind for satellite observation. Japan Aerospace Exploration Agency (JAXA: former National Space Development Agency of Japan) has released several kinds of the product from TRMM observations, including monthly mean, gridded precipitation data sets. These products are provided through internet home page of JAXA, enable researchers to use TRMM data without knowing technical details of TRMM observations and data processing procedures.

In the present study, we compared monthly mean, gridded precipitation observed by TRMM PR to rain gauge data at islands, buoys and coastal observatories and discuss usefulness of the PR data in physical oceanographic studies.

2. Data

2.1 TRMM PR data

TRMM has two precipitation sensors aboard; one is the Precipitation Radar (PR) and the other is the TRMM Microwave Imager. PR is the first radar developed to observe three dimensional structure of precipitation from space. In the present study, we will compare the observation made by this newly developed sensor to the rain gauge measurements. Major specifications of the PR sensor are as follows; the radar is an active phase array system with frequencies of 13.796 and 13.802 GHz, which is capable of scanning over a 215 km swath. Measured range of altitude is from ground level to 20km or higher. Range and horizontal resolutions are 250m and 4 to 5 km, respectively. Measurable rainfall intensity is 0.5mm h^{-1}.

The satellite flies in a non-sunsynchronous orbit. The inclination angle of the orbit is 35 degree, and the satellite goes round the Earth every 90 minutes, 16 times per day and observes rainfall between 35°N and 35°S. The frequency of observation is about twice a day in the highest latitudes of the observation region while once per two to three days in equatorial region.

Monthly mean gridded data of precipitation at the level of near surface, 2km, 4km and 6km are provided as a level 3 product of PR observations because PR has a capability to measure vertical profile of rainfall. In the present study we treated the near surface rainfall as a precipitation at sea surface and used them for comparison. The algorithm to calculate precipitation from PR backscattering data is called 3A25G2 (version 5), of which primary product is monthly mean precipitation averaged over 5°×5° longitude-latitude grid, but we used 0.5°×0.5° degree average, monthly mean precipitation, which is a sub-product of the algorithm. The data source is shown in Table 1. The period of the data used in the present study is from 1998 through 2000.

2.2 Rain gauge data

Data sources of the rain gauge observations used in the present study are summarized in Table 1. Locations of the gauges are indicated in Figs. 1a and 1b. The period of the data is from 1998 through 2000.

(1) PACRAIN Data

Rain gauge data obtained on many islands in the subtropical and the South Pacific Ocean have been collected and provided by The Pacific Rainfall Database (PACRAIN), which was founded by NOAA (National Oceanic and Atmospheric Administration) and currently run as a NOAA/NASA (National Aeronautics and Space Administration) joint activity. We obtained monthly rainfall data obtained at 56 stations.

(2) Buoy rain gauge data

Oceanic rainfall is observed at some of the surface mooring buoys of TOGA/TAO array in the tropical Pacific (McPhaden et al., 1998), operated by NOAA and JAMSTEC (Japan Marine Science and Technology Center), and PIRATA (Pilot Research Moored Array in the Tropical Atlantic; Servain et al., 1998) array in the tropical Atlantic operated by multi institutes in U.S.A, France and Brazil. Specifications of the rain gauge installed on the buoys are shown in Serra et al. (2001).

We downloaded the daily mean rain rate data through TOGA/TAO home page run by NOAA PMEL (Pacific Marine Environmental Laboratory), and calculated monthly rainfall. When rainfall data are not available for more than 3 days in a month, the monthly mean is not calculated for the month at the station. The precipitation data of 40 buoys are used.

(3) JMA data

Rainfall data obtained at rain gauges of 16 Japan Meteorological Agency's observatories and 66 AMeDAS (Automated Meteorological Data Acquisition System) gauges located in islands and coastal regions are used for the comparison.

3. Comparisons of monthly mean TRMM PR precipitation at near surface to gauge observations

We compared the TRMM PR precipitations and the gauge observations based on monthly rainfall (mm mo^{-1}). Some of the gauge rainfall data that are not monthly value are converted to monthly rainfall for the comparison as mentioned in Section 2. We computed a correlation coefficient and an inclination of the regression line with zero intercept for each comparison. Here after we call the inclination of the regression line with zero intercept as "Regression Coefficient". The Regression Coefficient is employed as a measure of over- or underestimate of the PR observation, and the correlation coefficient as a measure of correspondence of the PR precipitation to the gauge data.

3.1 Comparisons for individual monthly means

(1) Overall comparisons

A scatter plot of TRMM PR monthly means against all gauge observations for the entire analysis period is shown in Fig. 2. The correlation coefficient is 0.53, which is statistically significant with 10 % significance level. The Regression Coefficient is 0.66, much smaller than unity, suggesting the underestimation of the PR observation.

We compared the PR observations to 0.5°×0.5° grid average gauge rainfall values but almost similar results are obtained.

(2) Comparison for each latitude belt

Observation frequency is higher in higher latitudes of the observation region of the TRMM satellite as mentioned in Section 2. Thus, one may expect the difference in observation frequency between latitudes causes difference of relationship between monthly mean precipitation observed by PR and those of gauge measurements. In order to examine the difference, we compared the PR and gauge monthly rainfalls for each latitude belt of which width is 10°. In each latitude belt, rain gauges located on the southern boundary of the belt belong to the latitude belt.

The results shown in Table 2 suggest that the relationship between the PR and gauge observations does not seem to depend on latitude. The correlation coefficient for the latitude belt of 30°-40°N is statistically different from those for 20°-30°N and 20°-30°S belts, and that for 0°-10°N is different from that for 20°-30°N belt with significance level of 5% but there is no clear latitudinal dependence of the correlation coefficient. The Regression Coefficients differ from 0.78 in 30°-40°N to 0.4 in 10°-20°N belts and minimum value of 0.4 is obtained in 10°-20°N but no clear latitudinal dependence is found.

(3) Comparison for each observation platform

We examined whether or not the PR-gauge relationship depends on observation platform. In Fig. 3 and Table 3, scatter plot, correlation coefficient and Regression Coefficient for each platform are shown. The correlation coefficients take their values of 0.51 to 0.54 and the plots are very scattered for each platform. There is no significant difference between platforms although the Regression Coefficients for the JMA observatories and AMeDAS are slightly larger than others.

3.2 Comparison based on 10mm mo^{-1} average precipitation

The correlation coefficients and the Regression Coefficients computed in Section 3.1 may be strongly influenced by the relationship between the PR and gauge observations in low precipitation range because observation frequency of low precipitation was much larger than that of high values. Thus, in this subsection we examined the relationship between the PR and gauge data based on mean values of the gauge rainfall averaged every 10mm mo^{-1} bin. In the comparison, gauge precipitation data larger than 800mm mo^{-1} are excluded because of smallness of the observation frequency. The scatter plot and histograms of the rainfall are shown in Figs.4 and 5, respectively. The histograms are normalized; that is, we divided average frequency of precipitation in each 10mm mo^{-1} bin by the total number of the observation.

The PR rainfall is smaller than gauge observations even after taking 10mm mo^{-1} average as shown in Fig. 4. The correlation coefficient is 0.80 and the Regression Coefficient is 0.64. The PR rainfall tends to be larger than the regression line with zero intercept in the precipitation range smaller than 300-400mm mo^{-1} of the gauge observation but it tends to be smaller beyond the range. The standard deviation for each 10mm mo^{-1} becomes larger as average precipitation increases from 0 to 200mm mo^{-1}, but the standard deviation does not seem to depend on average rainfall for the range of 200-800mm mo^{-1}. Mean value of the standard deviation for each 10mm mo^{-1} bin is 213mm mo^{-1}. The histograms show that normalized observation frequency of the PR observation are larger than gauge observation for the range of 0-100mm mo^{-1} but are smaller for the range larger than 150mm mo^{-1}. This tendency is consistent to the fact that the Regression Coefficients are smaller than unity.

4. Discussion

Validation studies of TRMM rainfall observations by comparing them to the ground data have been done several researchers such as Oki (1999, 2000), Kummerow et al., (2000), Serra and McPhaden (2003). Oki (1999, 2000) made comparisons of the TRMM PR to AMeDAS observations. She showed that the relationship between the PR and AMeDAS data differed from month to month but the PR precipitation tended to be smaller than that of AMeDAS. Kummerow et al. (2000) compared the TRMM rainfall observations to precipitation measured in 1998 at atolls and indicated that the PR observation tended to overestimate. Rainfall data obtained at surface meteorological buoys of TOGA/TAO array are used to evaluate the TRMM observation by Serra and McPhaden (2003). Their results are almost similar to that in the present study, but they discussed the possibility that the PR rainfall might be only 40% as large as real precipitation because the rain gauges installed on the buoys might underestimate precipitation due to wind effect. In general, however, we can say that the results shown in the previous studies and those of the present study are consistent.

One may conclude that the PR observation of precipitation at near surface is underestimated because it shows only 65% as large as that observed at surface rain gauge stations. Degree of the underestimation of the precipitation by the PR seems large in low latitudes (e.g., Kummerow et al., 2000; Kodama and Tamaoki, 2002). One possible cause of the underestimation is low sampling rate of the PR observation in low latitudes.

When the clouds, of which base height is low and rain rate increases as the altitude decreases, occupy large portion of the cloud area, the PR near surface rain rate should be underestimated because the "near surface" rainfall of the PR observation is actually the average rain rate at different altitudes from surface to 1.5km depending on the scan angle of the PR. In addition, the fact that minimum rain rate that the PR can detect is 0.48mm h^{-1} (Kozu and Kuroiwa, 1998) may also cause underestimation of the monthly precipitation if weak precipitation frequently occurred in the analysis domain.

On the other hand, the rain gauge observations at islands and ground stations might overestimate the surface precipitations due to topographic effects on the rainfall at the stations. For example, one can expect convective rainfall due to surface solar heating or orographic rain around high mountains on an island, even if there is no rainfall in surrounding ocean area. However, the results of the comparisons between the PR and the buoy observations do not differ significantly from those of the comparisons for other gauge stations. Thus, we can conclude that the monthly mean rainfall estimated by the PR observation is really underestimated.

Degree of underestimation of the PR rainfall in the 10-20°N latitudes is larger than that in the other latitudes, i.e., the Regression Coefficient for the 10-20°N latitude belt is about 0.4. Most of the gauge data in this latitude belt are come from the PACRAIN data base. Thus, the smallness of the Regression Coefficient might be due to problems inherent in the PACRAIN data. Kodama and Tamaoki (2002) show, however, the zonal mean PR rainfall between 5-15°N latitudes is much smaller than the climatological mean, zonally averaged rainfall estimated by The Global Precipitation Climatology Project (GPCP; Arkin and Xie, 1994). Although the latitudes are slightly different from that of Kodama and Tamaoki (2002), the PR might underestimate rainfall significantly in the subtropics in the Northern Hemisphere. We can not identify the causes of the underestimation in the latitudes in the present study but one possible cause of the underestimation is the model size distribution of the rain droplet used in the algorithm to compute rain rate from the PR reflectivity may differ from latitude to latitude because rainfall types are different between latitudes.

The standard deviation of the PR rainfall for each 10mm mo^{-1} bin of the gauge observation is about 210mm mo^{-1}. If this is the most probable value of the sampling error of the 0.5°×0.5° grid averaged monthly precipitation estimated by the PR, the sampling error of the 5°×5° grid average monthly mean is about 21mm mo^{-1} and 5°×5° grid average seasonal mean is about 12mm mo^{-1}, respectively.

Based upon the results of the present study, we can conclude that the grided, monthly mean data set of the PR precipitation at near surface (Level 3 data, version 5) is possibly underestimated by about 35%, i.e. the PR observation shows about 65% as large as the real rainfall. One should reduce the sampling error by averaging the gridded PR data in space and time when using the data set. Even though the underestimation, the PR data set of the current version is very useful for studying distribution and time change of the precipitation over the ocean if one treat the data set properly.

Acknowledgement

The present study was carried out by the joint research program of CEReS (Center for Environmental Remote Sensing), Chiba University (15-35). The present study will be published in the coming issue of the Japanese journal of the Oceanography Society of Japan, "Umi no Kenkyu (Oceanography in Japan)" (Iwasaka and Sato, 2004).

References

Adler, R. F., C. Kidd, G. Petty, M. Morissey, and H. M. Goodman （2001） : Intercomparison of global precipitation products: the third Precipitation Intercomparison Project （PIP-3） . *Bull. Amer. Meteor. Soc.*, **82**, 1377-1396.

Arkin, P. A. and P. Xie （1994） : The Global Precipitation Climatology Project: First Algorithm Intercomparison Project. *Bull. Amer. Meteor. Soc.*, **75**, 401-419.

Huffman, G. J., R. F. Adler, P. Arkin, A. Chang, R. Ferraro, A. Gruber, J. Janowiak, A. McNab, B. Rudolf, and U. Schneider （1997） : The Global Precipitation Climatology Project （GPCP） Combined Precipitation Dataset. *Bull. Amer. Meteor. Soc.*, **78**, 5-20.

Iwasaka, N., H. Otobe, and M. Aoshima, (1999): Field experiments of a compact, self-contained surface meteorological observation system for merchant ships. *J. Tokyo Univ., Mercantile Marine*, **50**, 13-24

Iwasaka, N., M. Sato, (2004): Comparison between monthly mean precipitation as estimated from TRMM precipitation rader observations and from rain gauge data, *Umi no Kenkyu (Oceanography in Japan)*, in press.

Japan Meteorological Agency, (2001): *Guide to ships' weather reports*. Japan Meteorological Agency, pp80.

Kozu, T., and H. Kuroiwa (1998): TRMM Precipitation Radar. *J. Remote Sensing Soc. Japan*. **18**, 436-447.

Kodama, Y. and A. Tamaoki （2002） : A re-examination of precipitation activity in the subtropics and the mid-latitudes based on satellite-derived data. *J. Meteor. Soc. Japan*, **80**, 1261-1278.

Kummerow, C., J. Simpson, O. Thele, W. Barnes, A. T. C. Chang, E. Stocker, R. F. Adler, A. Hou, R. Kakar, F. Wentz, P. Ashcroft, T. Kozu, Y. Hong, K. Okamoto, T. Iguchi, H. Kuroiwa, E. Im, Z. Haddad, G. Huffman, B. Ferrier, W. S. Olson, E. Zipser, E. A. Smith, T. T. Wilheit, G. North, T. Krishnamurti, and K. Nakamura （2000） : The status of the Tropical Rainfall Measuring Mission （TRMM） after two years in orbit. *J. Appl. Meteor.*, **39**, 1965-1982.

McPhaden, M.J., A.J. Busalacchi, R. Cheney, J.R. Donguy, K.S. Gage, D. Halpern, M. Ji, P. Julian, G. Meyers, G. T. Mitchum, P.P. Niiler, J. Picaut, R.W. Reynolds, N. Smith, and K. Takeuchi （1998） : The Tropical Ocean-Global Atmosphere （TOGA） observing system: A decade of progress. *J. Geophys. Res.*, **103**, 14,169-14,240.

Oki, R., K. Furukawa, S. Shimizu, Y. Suzuki, S. Saton, H. Hanado, K. Okamoto, K. Nakamura (1999): Preliminary Results of TRMM: Part 1, A Comparison of PR with Ground Observations. *Marine Technology Society Journal*, **32**, 13-23.

---, and T. Kozu, (2000): Comparison of TRMM/PR rain rate with ground based observation. *Proc. Microwave Remote Sensing of the Atmosphere and Environment, II*, 159-166. Society of Photo-Optical Instrumentation Engineerings.

Serra, Y. L., P. A'Hearn, H. P. Freitag, and M. J. McPhaden (2001) : ATLAS self-siphoning rain gauge error estimates. *J. Atmos. Ocean. Tech.*, **18**, 1989-2002.

Serra, Y. L. and M. J. McPhaden (2003) : Multiple time- and space-scale comparison of ATLAS buoys gauge measurements with TRMM satellite precipitation measurements. *J. Appl. Meteor.*, **42**, 1045-1059.

Servain, J., A.J. Busalacchi, M.J. McPhaden, A.D. Moura, G. Reverdin, M. Vianna, and S.E. Zebiak (1998) : A Pilot Research Moored Array in the Tropical Atlantic (PIRATA) . *Bull. Am. Meteor. Soc.*, **79**, 2019-2031.

TRMM Precipitation Radar Team (2000) : *Tropical Rainfall Measuring Mission (TRMM) Precipitation Radar Algorithm Instruction Manual version 2*, National Space Development Agency of Japan and National Aeronautics and Space Administration, 115pp. (Available from http://www.eorc.nasda.go.jp/TRMM/document/index_j.htm)

Table and figure captions
Table 1: Data sets used in the present study

Table 2: Comparison between monthly mean TRMM PR precipitation and rain gauge observation for each 10-degree latitude belt.

Table 3: Comparison between TRMM PR rainfall and ground observation obtained from each data source.

Figure 1: Distribution of rain gauge stations used in the present study. (a) PACRAIN stations (open circles) and TAO/TRITON/PIRATA buoys (asterisks), and (b) JMA observatories (open circles) and AMEDAS stations (solid squares).

Figure 2: Comparison between monthly mean precipitations observed by TRMM PR and those by rain gauge at ground stations. Abscissa indicates the precipitations observed by ground stations and ordinate shows those observed by TRMM PR. A regression line with zero intercept is shown in each panel.

Figure 3: The same as Fig. 2, except for each ground station category. Upper left panel for JMA observatory, upper right for AMeDAS, lower left for PACRAIN and lower right for TAO/TRITON/PIRATA buoys, respectively.

Figure 4: Scatter plot of precipitation averaged for each 10-mm mo^{-1} bin of the rain gauge data. Asterisk shows mean value of TRMM PR rainfall for each bin and bars indicate the standard deviation.

Figure 5: Histograms of precipitation observed by ground stations and TRMM. The histograms were constructed from all observations used in the present study but showed for the precipitation range of 0-800 mm mo^{-1}. Frequency is counted for each 10-mm/month bin and normalized by total number of observations for each observation method. Asterisks indicate the histogram for rain gauge data, and open circles for TRMM PR, respectively.

Table 1: Data sets used in the present study

Data Set	Provider
TRMM PR monthly Rain Data Set	NASDA EORC/TRMM Homepage http://www.eorc.nasda.go.jp/TRMM/index_i.htm
PACRAIN	The Pacific Rainfall Database http://www.evac.ou.edu/pacrain/
TAO/TRITON/PIRATA	NOAA's Pacific Marine Environmental Laboratory (PMEL) Home page http://www.pmel.noaa.gov/tao/data_deliv/deliv.html
AMeDAS DATA OF JAPAN 1998, 1999, 2000	The Japan Meteorological Agency (Available from Japan Meteorological Business Support Center, 3-17, Kanda Nisikicho, Chiyoda-ku Tokyo, 101-0054)
ANNUAL REPORT OF THE JAPAN METEOROLOGICAL AGENCY 1998, 1999, 2000	

Table 2: Comparison between monthly mean TRMM PR precipitation and rain gauge observation for each 10-degree latitude belt.

Latitude	Correlation coefficient	Inclination (*)	Number of stations	JMA observatory	AMeDAS	PACRAIN	TAO/ TRITON/ PIRATA
20S-30S	0.45	0.56	7	0	0	7	0
10S-20S	0.50	0.52	7	0	0	7	0
EQ-10S	0.50	0.63	16	0	0	4	12
10N-EQ	0.53	0.51	53	0	0	27	26
20N-10N	0.51	0.40	13	0	0	11	2
30N-20N	0.42	0.59	42	11	31	0	0
40N-30N	0.57	0.78	42	7	35	0	0

(*) Inclination of the linear regression line with zero intercept

Table 3: Comparison between TRMM PR rainfall and ground observation obtained from each data source.

	Correlation coefficient	Inclination (*)	Number of stations
JMA observatory	0.54	0.73	18
AMeDAS	0.51	0.70	66
PACRAIN	0.52	0.58	56
TAO/TRITON/PIRATA	0.51	0.61	40

(*) Inclination of the linear regression line with zero intercept

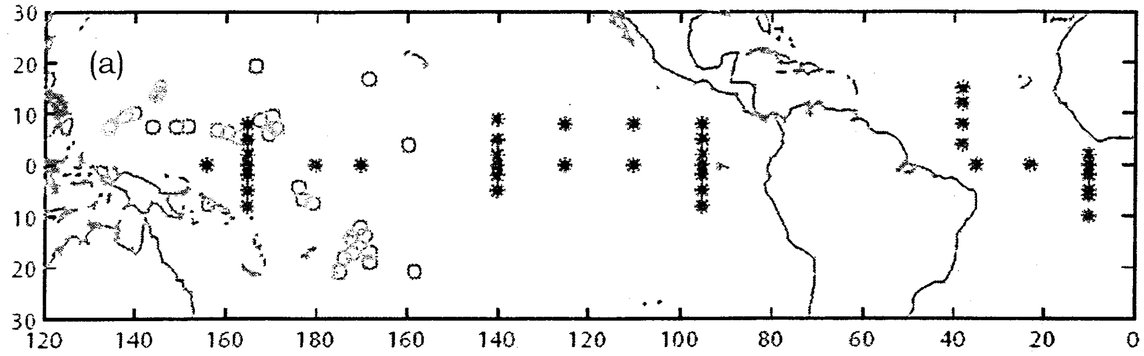

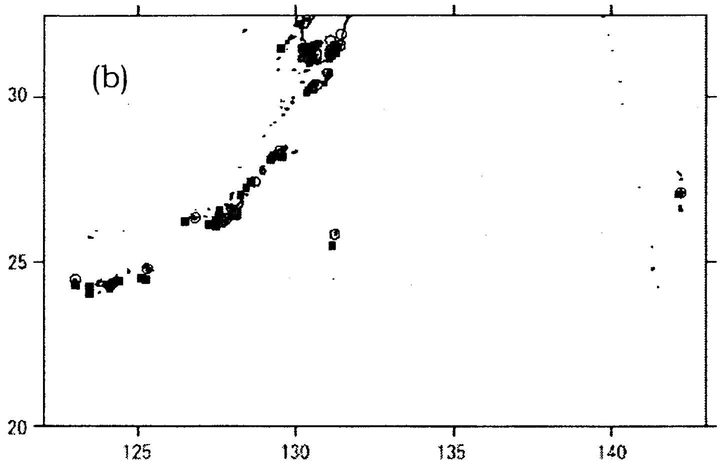

Figure 1. Distribution of rain gauge stations used in the present study. (a) PACRAIN stations (open circles) and TAO/TRITON/PIRATA buoys (asterisks), and (b) JMA observatories (open circles) and AMEDAS stations (solid squares)

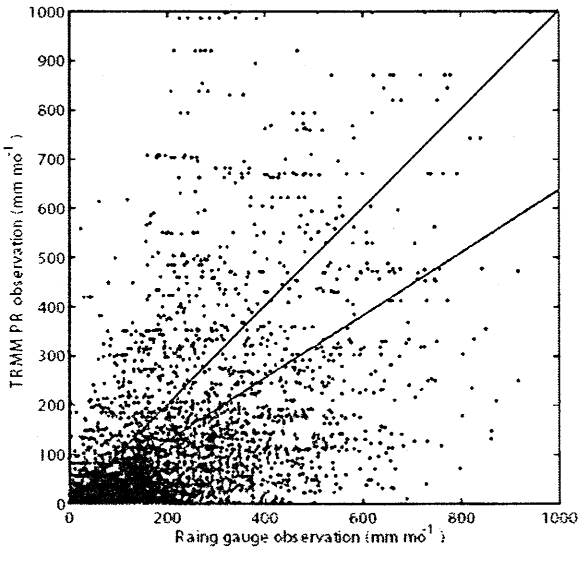

Figure 2: Comparison between monthly mean precipitations observed by TRMM PR and those by rain gauge at ground stations. Abscissa indicates the precipitations observed by ground stations and ordinate shows those observed by TRMM PR. A regression line with zero intercept is shown in each panel.

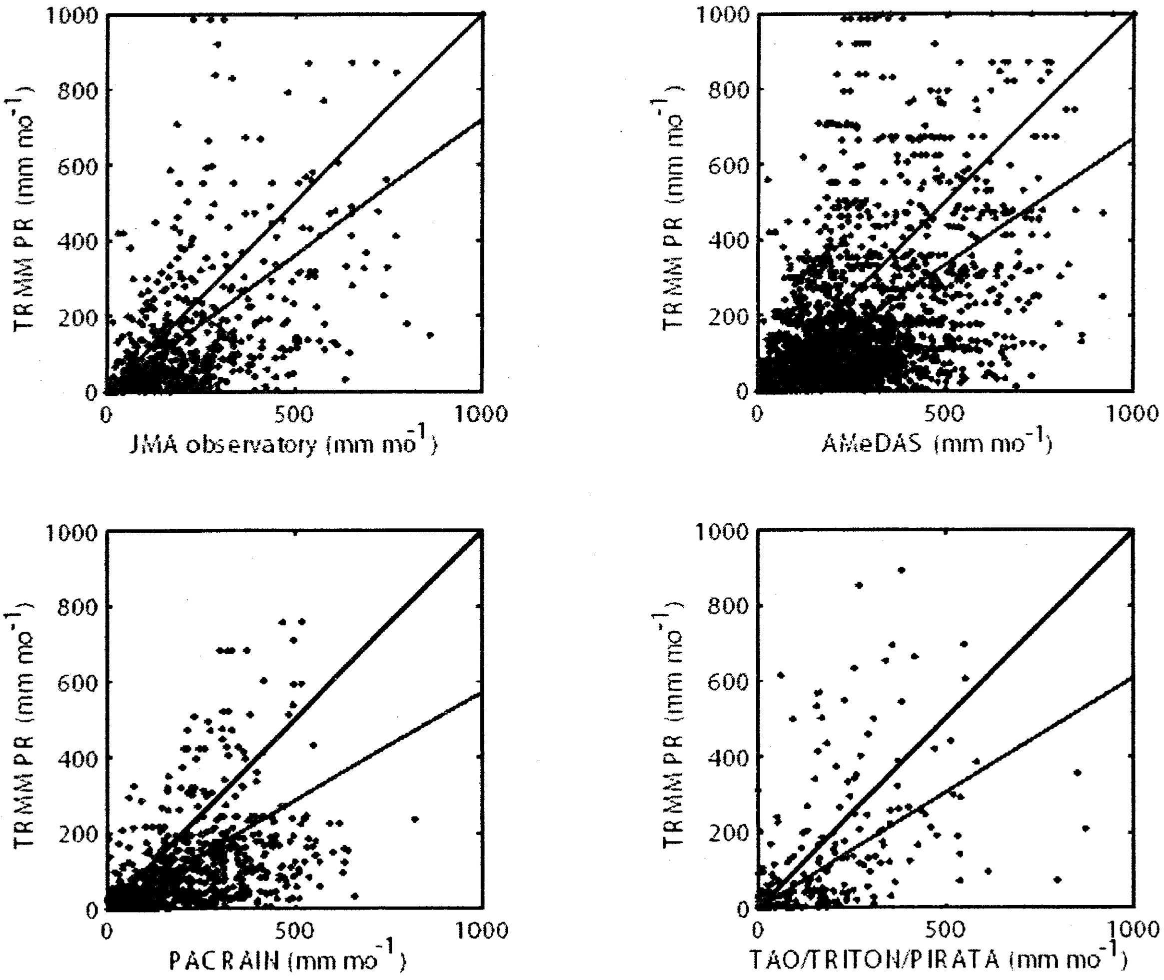

Figure 3: The same as Fig. 2, except for each ground station category. Upper left panel for JMA observatory, upper right for AMeDAS, lower left for PACRAIN and lower right for TAO/TRITON/PIRATA buoys, respectively.

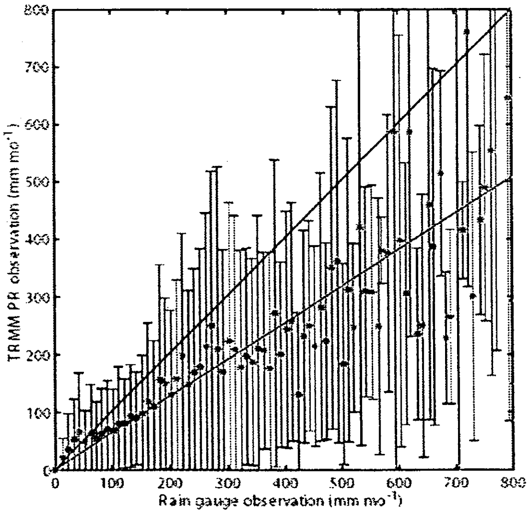

Figure 4: Scatter plot of precipitation averaged for each 10-mm mo^{-1} bin of the rain gauge data. Asterisk shows mean value of TRMM PR rainfall for each bin and bars indicate the standard deviation.

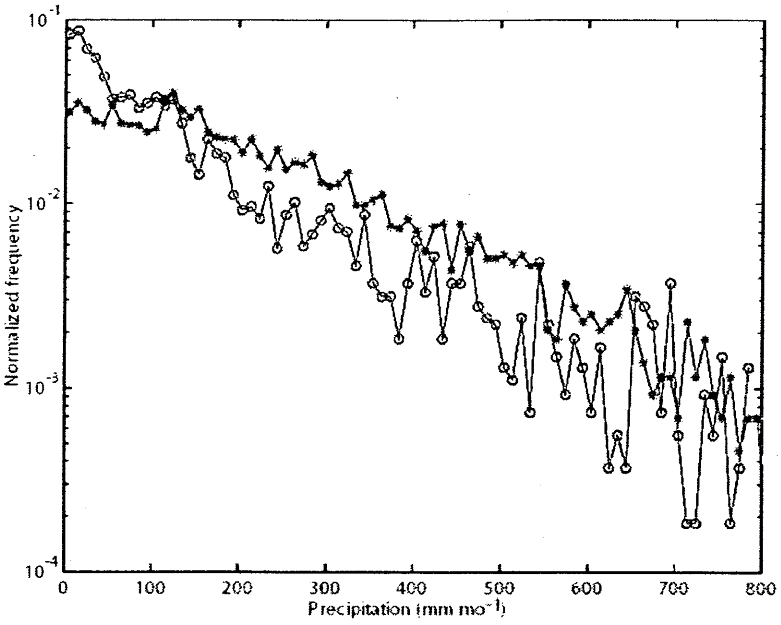

Figure 5: Histograms of precipitation observed by ground stations and TRMM. The histograms were constructed from all observations used in the present study but showed for the precipitation range of 0-800 mm mo^{-1}. Frequency is counted for each 10-mm/month bin and normalized by total number of observations for each observation method. Asterisks indicate the histogram for rain gauge data, and open circles for TRMM PR, respectively.

Relation between the automatic alignment PAL lidar data and air pollution monitoring

S. Naito, J. Okazaki and A. Someya
Chiba Prefectural Environmental Reseach Center(CERC)
Ichihara, 290-0046 Japan
N. Lagrosas, Y. Yoshii, H. Kuze and N.Takeuchi
Center for Environmental Remote Sensing (CEReS)
Chiba University, Chiba, 263-8522 Japan

Abstract:

PAL is a portable automated lidar. Lidar data contains the laser beam backscattered signal, from which we can obtain much information, such as boundary layer height, aerosol concentration, raindrop size and so on. In this paper, the development of PAL with automated alignment system is described and some useful data of PAL are presented.

1. Introduction

Lidar (Light Detection and Ranging. Lidar) sends laser pulses to the atmosphere and detects the backscattered signal from molecules and particulates present in the atmosphere. As the beam passes through the atmosphere, the gas molecules and particles cause the light to be attenuated or scattered. The backscattered light is then gathered by a receiving optics and detected by photon-detectors which convert the light signal to electrical. Lidar is a powerful tool for monitoring the atmosphere, especially in the upper atmosphere. An automatic (no person attended) lidar system which equips the automatic alignment mechanism, has been developed and operated for more than a year. The feature of the system and some example of observation are presented.

2. Objectives

2.1 Analysis of the Boundary Layer Height (BLH)

The boundary layer is characterized by the abundant presence of aerosols, so the boundary layer height can be observed in the altitude where there is a sudden drop in aerosol concentration.

2.2 Comparison of SPM Concentration Measurements with Lidar

The signal derived from the Lidar system is compared to the SPM concentration measurement by a β-ray absorption dust counter.

Extinction coefficient is important factor to calculate aerosol concentration. There Fernald's inversion method was used in the software to compute in the Lidar signal.

2.3 Measurement of Cloud Base Height (CBH)

In computing the cloud base height, the slope of two consecutive data points is checked and when it satisfies a certain condition, it will be considered as a cloud base height. The value of slope is varied from 3 to 8 range squared signal / range step (RSS/RS) (corresponding to Normalized Concentraton Graduent of 7%/m) depending on the level of noise in the signal.

2.4 Raindrop Size vs. Downward Speed

A falling drop feels a frictional force from the air's viscosity that opposes gravity (the drop has to push its way through the air), the drop reaches a constant terminal velocity, and this terminal velocity is smaller for the smaller radius of a fluid particle or ice crystal. It turns out that this terminal velocity is quite small for drops with the size of a few millimeters and so, although the drops in a cloud fall, they fall so slowly that only careful measurements would reveal this fact.

More quantitatively we can say the following: The weight of a drop of air of radius R is $(4\pi/3)R^3\rho_w g$ where ρ_w is the density of the water (=10^3 kg/m^3, and g (=9.8 m/sec^2) free-fall acceleration. If the drop is falling through air with velocity v, the viscosity of the air n (=$1.75*10^{-5}$ N*sec/m^2) will cause friction (Stokes law) $6\pi nRv$. [Here we neglect the density of the air and assume that the viscosity of the drop is much larger than viscosity of the air; we also assume that the drop is approximately spherical.] The terminal velocity of the falling drop is obtained by equating the weight and the friction force, and is given by

$$v = \frac{2\rho_w g R^2}{9n}.$$

Thus 1 μm drop will have velocity of 0.13 mm/sec, or 11 m/day. Larger, 10 μm drops will still fall slowly, ~ 1.1km/day. Such fall rates can be neglected, especially since the motion of the air itself can be faster than that.

Drops significantly smaller than 1 μm are not visible and will not be perceived as clouds, while 0.1 mm drops will fall with velocity of about 1 m/sec, i.e. it will rain. Larger drops will fall with even larger velocities; however, the air-friction starts increasing faster than v, i.e. the velocity will not increase as fast with increasing drop size. At such large speeds the weight of the drop is balanced by the drag force $(1/2)\rho_a C\pi R^2 v^2$, where ρ_a is the density of the air (=1.2kg/m^3) and C=1.2 is the drag coefficient for sphere. According to this equation 1 mm drop will fall with velocity of 4.3 m/sec and 10 mm drop will fall with velocity of 13.6 m/sec. However, drops larger than 5 mm are usually broken into smaller drops that fall more slowly(Melinger,1998).

3. Method

3.1 Specification

Table 1 Specification of PAL

Laser	LD Diode(LD)-pumped Q-switched Nd:YAG
Wavelength	532nm
Laser Pulse Width	50ns
Laser Pulse Energy	15 μ J/pulse
Pulse Repetition Rate	1.4 kHz
Telescope type	Schmidt-Cassegrainian
Telescope diameter	20cm
Field of view	0.2 mrad
PMT Detector	Hamamatsu:HPK-R1924P
Resolution	160ns (ΔR=24 m)
Integration	20sec
Photon counting	SR430 (Stanford Research)
Remote control	Via Internet (ADSL modem)
Alignment interval	15 min

PAL system specification is summarized in Table 1. A Nd-YAG laser emitting is operated in pulse mode generated by an acoustic-optical modulator at 1.4 kHz. A KTP crystal doubles the laser frequency to 532 nm with a typical output of 15 μJ/pulse. The output beam is expanded by a beam expander and is reflected by two prisms so that the emitted beam spatially coincides with the optical axis of the telescope. In order to reduce the background due to the skylight during daytime, a narrow field-of-view angle of 0.2 mrad is employed. The backscattered signal is collected by a 20 cm diameter Cassegrainian telescope, detected by a photomultiplier tube in a photon counting scaler (Stanford Research SR430), accumulated for 20 seconds, and stored in a personal computer (PC). To stabilize the alignment of the laser and telescope's axes, automated alignment system is developed, described in the next section .

PAL system is located at CERC in Ichihara City, Chiba Prefecture, as shown in Fig.1.

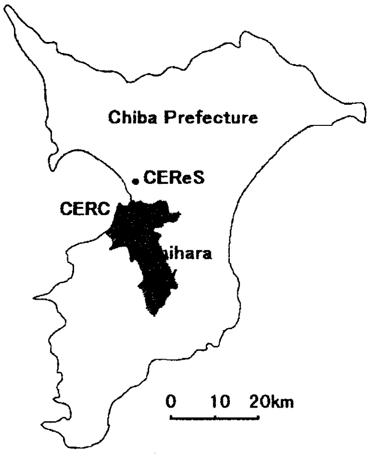

Fig.1 Location of PAL

Since the CERC is located in an industrial area, it is plausible that aerosol particles observed by the PAL system is significantly contributed by anthropogenic origins. The system is installed indoor at about 4 m from the ground level, looking toward the north sky with an elevation angle of 38°.

3.2 Automatic Alignment System

A computer software was made to control the acquisition of the data and the alignment of the laser beam. The alignment is checked every 15 min. During the alignment procedure, the PC commands the controller to move the actuator for vertical direction about −10 units, then moves + direction by 1 unit step and integrate the signal for 1 second. Here 1 unit motion of the actuator (equivalent to the actuator resolution) corresponds to a change of 50 μrad in the tilt angle of the laser beam. The vertical actuator then is moved back to the peak signal position and the same procedure is applied to the actuator for the horizontal direction. It takes around 100 seconds to complete the whole process. After the alignment is finished, the PC continues to measure.

4. Results

4.1 The Boundary Layer Height (BLH)

Figure 4.1 below shows a THI map taken on 18 April 2003. The boundary layer height calculated is represented by the white line, in this particular data, the boundary layer height was found to be in an altitude of around 1.0 km to 1.1 km. The highest computed height, which is highlighted by the enclosure, corresponds to the highest recorded temperature during that day.

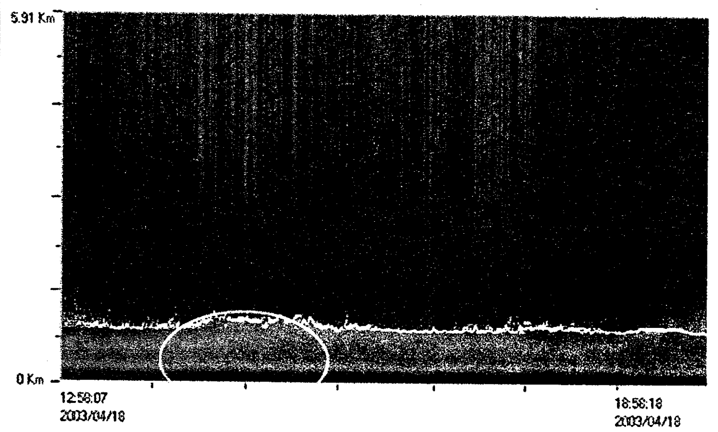

Fig. 1

Fig. 4.1 Computed boundary layer height (18 April 2003)

4.2 Comparison of SPM Concentration and PAL Data

Figure 4.2 shows comparison between the dust counter measurement (blue line) and the range squared corrected signal of the lidar (red line). Since the dust counter measurements are done on a per hour basis, the range squared corrected signal of the lidar was also averaged per hour. The data of Fig. 4.2 was taken on 3 and 4 August 2003, the two lines show a very similar pattern.

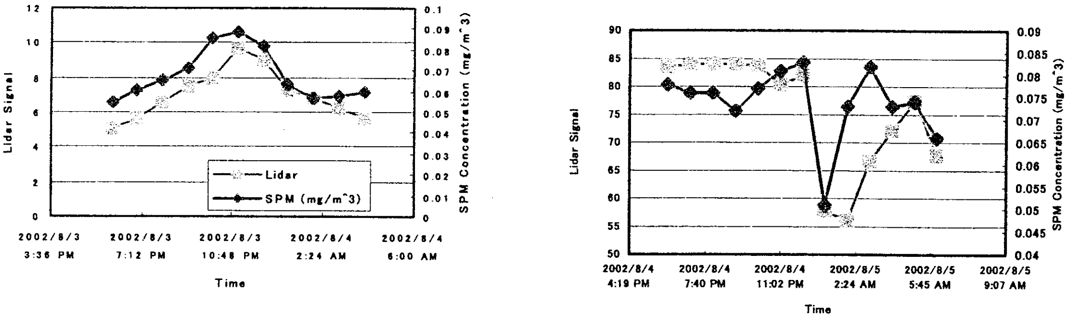

Fig. 4.2 SPM data and PAL data

4.3 The Cloud Base Height (CBH)

Figure 4.3 is computed CBH by the lidar data taken on the 2nd of June 2003 with the slope criterion set to 5, the figure shows the presence of clouds throughout the day at an altitude of around 1.8 km up to as high as 3 km above the ground.

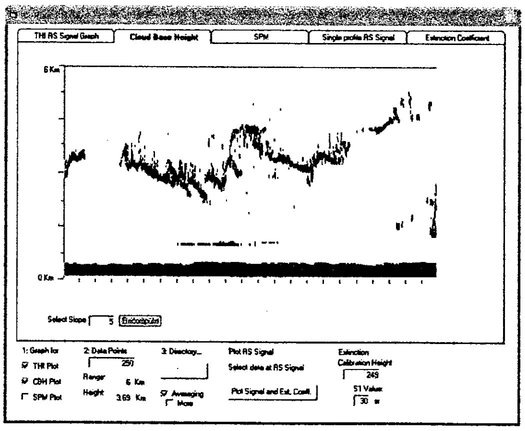

Select Slope 5

1: Graph for
☑ THI Plot
☑ CBH Plot
☐ SPM Plot

2: Data Points 250
Range 6 Km
Height 3.69 Km

☑ Averaging
☐ More

Select data at RS Signal

Extinction Calibration Height 249
S1 Value 30 sr

Fig.4.3 CBH graph

4.4 The Raindrop Size

Figure 4.4 shows a THI map of the range squared corrected lidar signal taken on 28 June 2003. The slant profile seen in the image is actually rain fall. Considering the portion surrounded by the orange enclosure, as a rain drop is detected at the top portion of the enclosed portion, it is seen in the upper center of the enclosure. In the lower part of the enclosure, the drop is seen to lean towards the right, projecting a slant image. This is due to the fact that as the time changes, the rain drop's altitude also changes, this is shown in the graph as the change in x-axis and the change in y-axis, respectively.

Therefore by getting the ratio of the change in y-axis (change in altitude) and the change in x-axis (change in time), the velocity of the rain drop is computed. In the program, this is done by drawing a line parallel to the observable rain image in the THI graph. For Fig. 4.4, the white line highlighted by the orange enclosure was drawn, and a terminal velocity of 3.90m/s was computed, its corresponding drop size is 0.97mm in diameter. The computed values agree with the ground base precipitation rate measurement of 0.5mm/hr, which is consistent with light rain conditions.(Geerts, 2000)

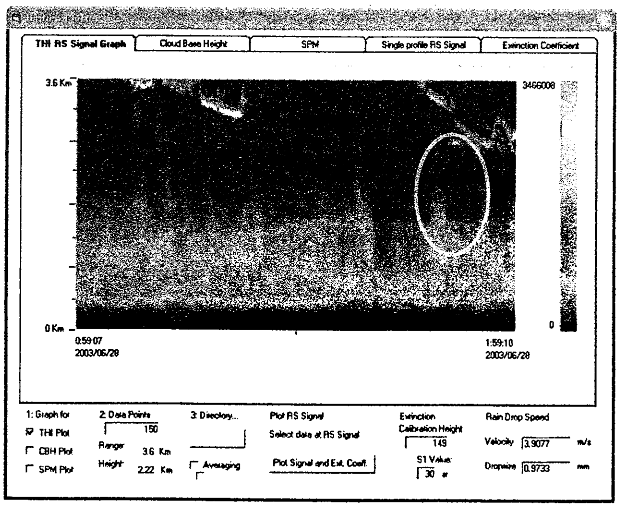

☑ THI Plot
☐ CBH Plot
☐ SPM Plot

Data Points 150

Ranger 3.6 Km

Height 2.22 Km

Calibration Height 149

S1 Value 30

Velocity 3.9077 m/s

Dropsize 0.9733 mm

Fig.4.4 Raindrop size analysis

5. Conclusions

The PAL system was able to accurately display the boundary layer height with the use of the Normalized Concentration Gradient algorithm. A very good correlation was obtained in the comparison of the SPM concentration measurement by the β-ray dust counter and the lidar derived extinction coefficient. The simple method in getting the cloud base height proved to be very efficient in the calculation of cloud base height. The derivation of rain drop size from lidar return signal is reliable and is consistent with ground base precipitation rate measurements.

References

Geerts, B., Fall Speed of Hydrometeors, April 2000, http://www-das.uwyo.edu/~geerts/cwx/notes/chap09/hydrometeor.html

Melinger, O., et al, 1998, http://quiz.thphy.uni-duesseldorf.de/98/A10.98.html

Performance of the developed 95 GHz FM-CW cloud profiling radar

Toshiaki TAKANO (1,2,3,4), Yumiro SUGA(1), Kenichi AKITA(1),
Youhei KAWAMURA(2), Hiroshi KUBO(1), Hiroshi KUMAGAI (4,5),
Tamio TAKAMURA (4,6), Yuji NAKANISHI(7), and Teruyuki NAKAJIMA(4,8)

(1)Graduate School of Science and Technology, Chiba University,
Inage, Chiba 263-8522, Japan, takano@cute.te.chiba-u.ac.jp,
(2)Faculty of Engineering, Chiba University,
(3)Center for Frontier Electronics and Photonics, Chiba University,
(4)APEX Project, CREST of Japan Science and Technology Corporation,
(5)Communications Research Laboratory,
(6)Center for Environmental Remote Sensing, Chiba University,
(7) SciTech,
(8)Center for Climate System Research, The University of Tokyo

ABSTRACT

We developed a cloud profiling radar transmitting frequency-modulated continuous wave (FM-CW) at 95 GHz for ground-based observations. Millimeter wave at 95 GHz is used to realize high sensitivity to small cloud particles. An FM-CW type radar would realize similar sensitivity with much smaller output power to a pulse type radar. Two 1m-diameter parabolic antennas separated by 1.4m each other are used for transmitting and receiving the wave. The direction of the antennas is fixed at the zenith. The radar is designed to observe clouds between 0.3 and 15 km in height with a resolution of 15 m. Using the facility, test observations and long term campaign observations have been done. Results of observations show that the system is sensitive and stable enough to observe various clouds.

Keywords: Cloud Profiling Radar, Millimeter Wave Radar, FM-CW Radar, Cloud Properties, Active Measurements of Clouds

1. INTRODUCTION

It is getting more important to know the global environment and the global change of climate for the human beings. It is necessary to know balance of solar energy coming to the Earth and cycle of water for the comprehension and to solve severe problems such as the greenhouse warming, the drying, the ozone holes and so on. One of the most significant features to know them is cloud, which reflects and absorbs incoming solar radiation, traps the radiation from the ground, transfers the energy in it, and radiates it outside. Information on 3-dimensional structures of clouds, sizes and distribution of cloud particles, dependence on size of optical characteristics of cloud particles, motions of particles in clouds, and so on are all desirable to solve role of clouds.

Characteristics of clouds described above, however, have not been well known yet because of lack of enough observational data to present confidential results. Observations of clouds with radars would be most powerful method to derive the information because of following advantages: a) radio waves do not suffer from heavy extinction such as visible light, and consequently can investigate interior of clouds, b) the radar technique, which is an active sensing method, has great advantage of investigating interior structures of clouds to passive methods such as total power observations of irradiance of clouds, c) Doppler measurements of clouds which have low velocities around 10 m/sec is applicable only to radio frequency waves.

Conventional radars operated at 5GHz can detect precipitation particles but are not able to detect particles in clouds because their sizes, less than a few tens microns, are much smaller that the wavelengths and, therefore, their cross sections are quite small. The cross sections of particles increase rapidly with frequency in Rayleigh scattering region. Rader observations of cloud particles at millimeter waves, which have been realized recently, have much more sensitive [1]. Several groups have reported the development and preliminary observational results that demonstrate powerful performances to investigate cloud particles [2],[3],[4].

We have designed and developed a cloud profiling radar at 94GHz. The purposes of the development of the FM-CW radar are a) evaluation and verification of an FM-CW radar at 95 GHz in Japan comparing to a pulse radar, b) obtaining millimeter wave FM-CW radar techniques and algorism of data reduction, and c) contribution to scientific research on cloud physics. In this paper, we present first observational results with the newly developed cloud profiling FM-CW radar as well as design concepts and specifications of the radar.

2. DESIGN CONCEPTS AND CONSTRUCTION

Whole view of the developed radar is shown in Fig.1 [5]. Diameter of each antenna is 1m.

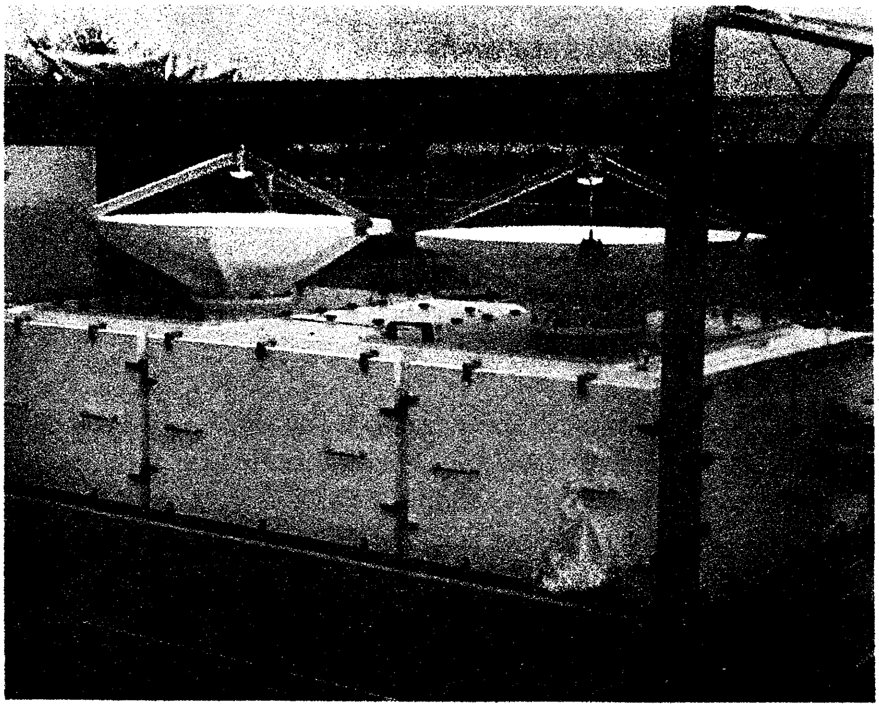

Fig.1. The developed cloud profiling FM-CW radar at 94GHz.

2.1 FM-CW radar

We adopt a frequency-modulated continuous wave (FM-CW) radar rather than a pulse radar because the former can achieve more sensitive system than the latter if comparing with same instantaneous output power of transmitted millimeter wave. The principle of an FM-CW radar is shown in Fig.2. The signal frequency is modulated in the range of f_0 +/- F. Transmitted signal from one of the antennas is reflected by cloud particles, returns, and is received by the other antenna with a delay time of t relative to the original transmitted signal. Mixing the transmitted and received frequencies, beat frequencies f_b are observed in the spectra, which are caused by ensemble of clouds particles:

$$f_b = 4Fr/(cT_m) \qquad (1),$$

where r is the height of the clouds, T_m is the modulation interval, and c is the light velocity. When the objects move in the line of sight, the frequencies of reflected signals change by f_d :

$$f_d = -2(f_0/c)(dr/dt) \qquad (2).$$

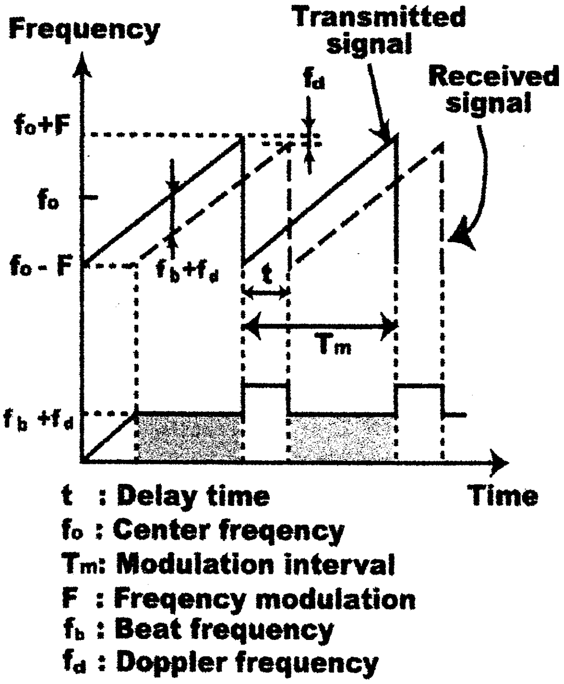

Parameters

f0 = 94.78 GHz
F = ±10 MHz
Tm = 1 m sec
Pt = +27 dBm
Noise Figure of Receiver 5 dB

Fig.2. Principle of an FM-CW radar.

2.2 Design concept and requirement

Because one of the purposes of the facility is evaluation and verification of an FM-CW radar at 94 GHz, we design it to be a simple system so as to develop with commercially available components and to make maintenance and upgrade by ourselves.

We designed the facility to observe clouds between 0.3 and 15 km in height with a resolution of 15 m. The velocities measured as Doppler shift should be less than 1 m/sec. The facility should be mobile for measurement at variety of places.

Table 1. Designed parameters of antennas.

Antenna Diameter	1 m
f/D ration of Antenna	0.35
Antenna Optics	Cassegrain
Gain of Antennas	57 dBi
Beam Width	0.18 degree
Antenna Separation	1.4 m
Direction of Antennas	Zenith
Polarization	1 Linear

2.3 Antennas and mounting

According with the requirements described above, we decided parameters of antenna listed in Table 1 [6].

2.4 Transmitter and receiver section

The block diagram of the transmitter and receiver section is shown in Fig.3 and parameters are summarized in

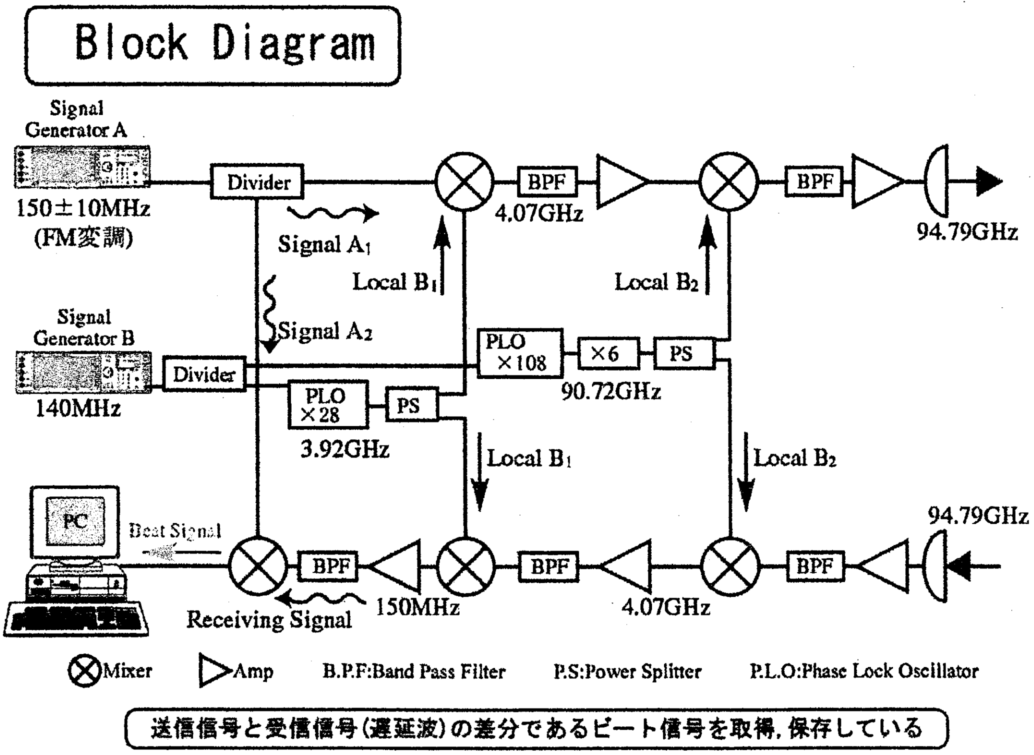

Fig.3. Block diagram of the transmitter and receiver section.

Fig. 2. All signals including the transmitted FM-CW signal at 95GHz and local frequencies are generated from and/or referred to two signal generators in 140 MHz range, which are synchronized each other.

The integrated transmitter section is shown in Fig. 4. The integrated system has been measured on its stabilities and sensitivities in laboratories [7]. Facilities for radar measurements, high stabilities of transmitted signals are necessary to obtain useful data. We measured stability of the system. In order to stabilize the output of the power of the transmitting wave, the final power amplifier for transmitting signal at 95GHz is cooled with a Peltier cooler to be around 50 ^{o}C otherwise it goes as hot as 90 ^{o}C.

The noise figure of the pre-amplifier at 95GHz was measured to be around 5.5 dB. Long term stabilities and sensitivities were measured and are good enough for our purpose.

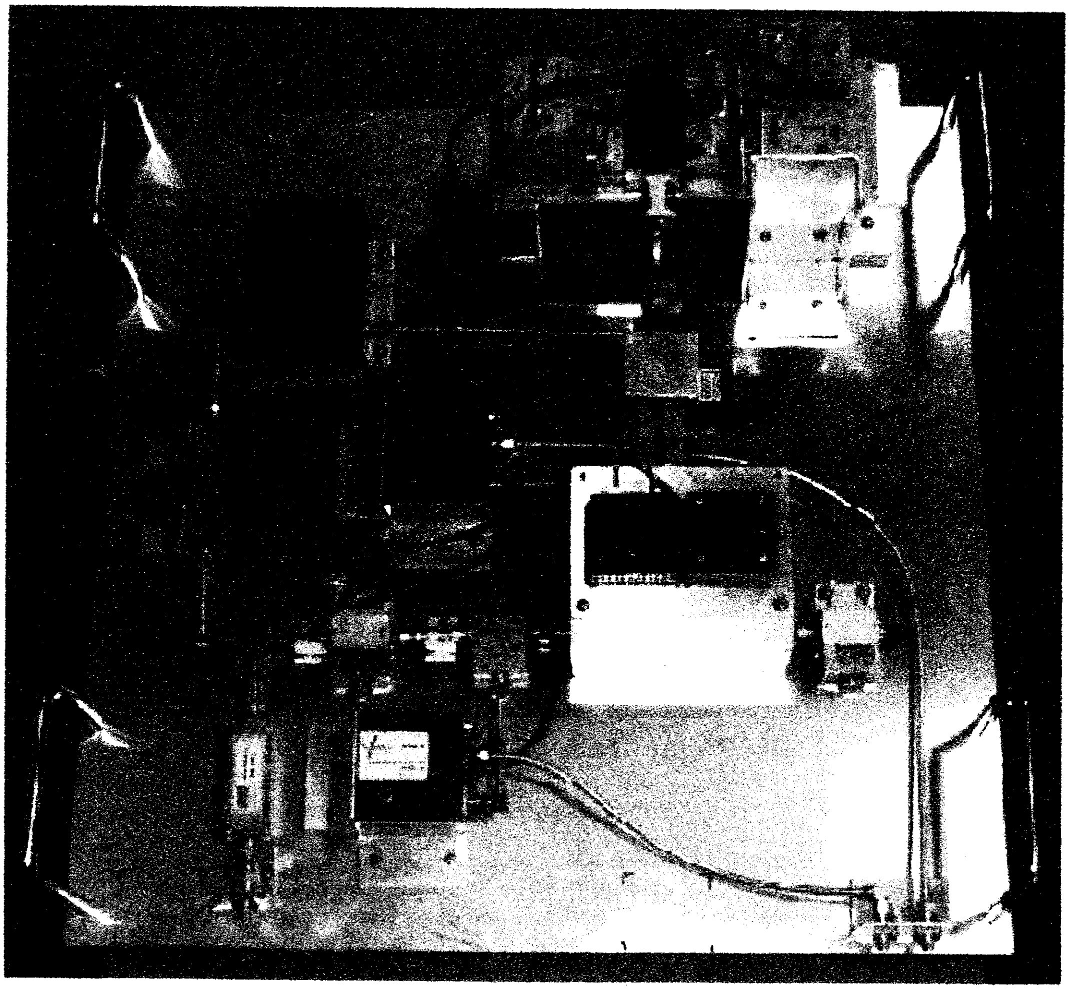

Fig.4. The transmitter section of the developed FM-CW radar.

3. FIRST OBSERVATIONAL RESULTS

Simultaneous Observations with a pulse radar SPIDER

After measurements of long-term stabilities, we made simultaneous observations with a pulse radar named SPIDER shown in Fig.5 of the Communications Research Laboratory, Japan. Comparison between the developed FM-CW radar and SPIDER is summarized in Table 2. We have to stress that the output power at 95 GHz of SPIDER is 3000ntimes higher than that of our FM-CW radar. An example of results is shown in Fig.6. We can recognize that same clouds were detected in both data. There results show that the radar has good performance to detect thin clouds.

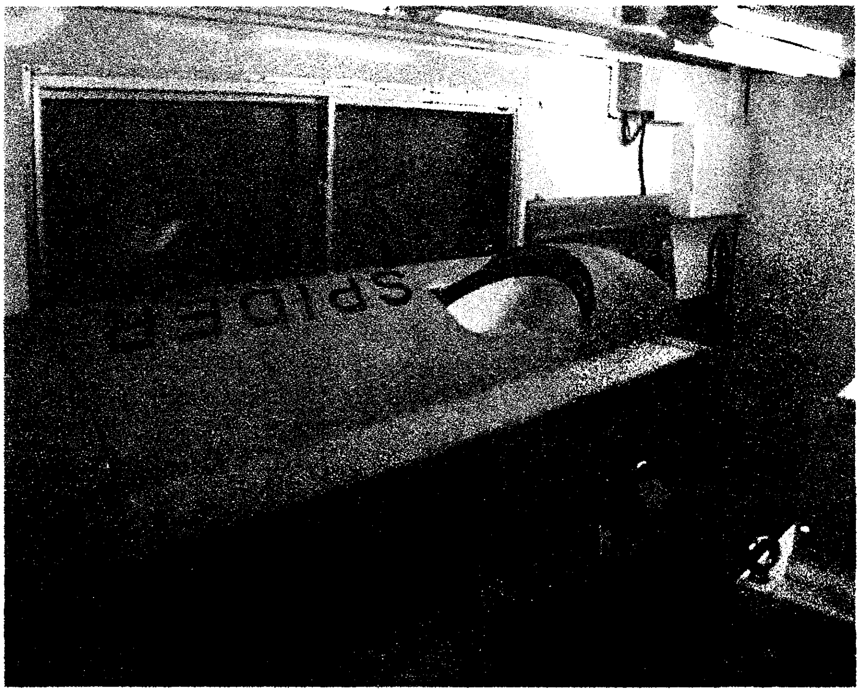

Fig.5. SPIDER: a pulse radar of the Communications Research Laboratory, Japan.

Table 2. Comparison between the developed FM-CW radar and SPIDER.

FM-CW Radar and SPIDER

	FM-CW Radar	SPIDER (CRL)
Purpose	Ground based obs.	Airborn obs.
Obs. direction	at Zenith	Downword to horizon
Type of radar	FM-CW	Puls
Antenna	1 m × 2 antennas	0.4 m × 1 antenna
Frequency	94.78 GHz	95.04 GHz
Output Power	0.5 W	1600 W
Duty Rate	Continuous	100-1000
Sensitivity (at 5km)	-32 dBZ	-35 dBZ

雲粒子観測結果

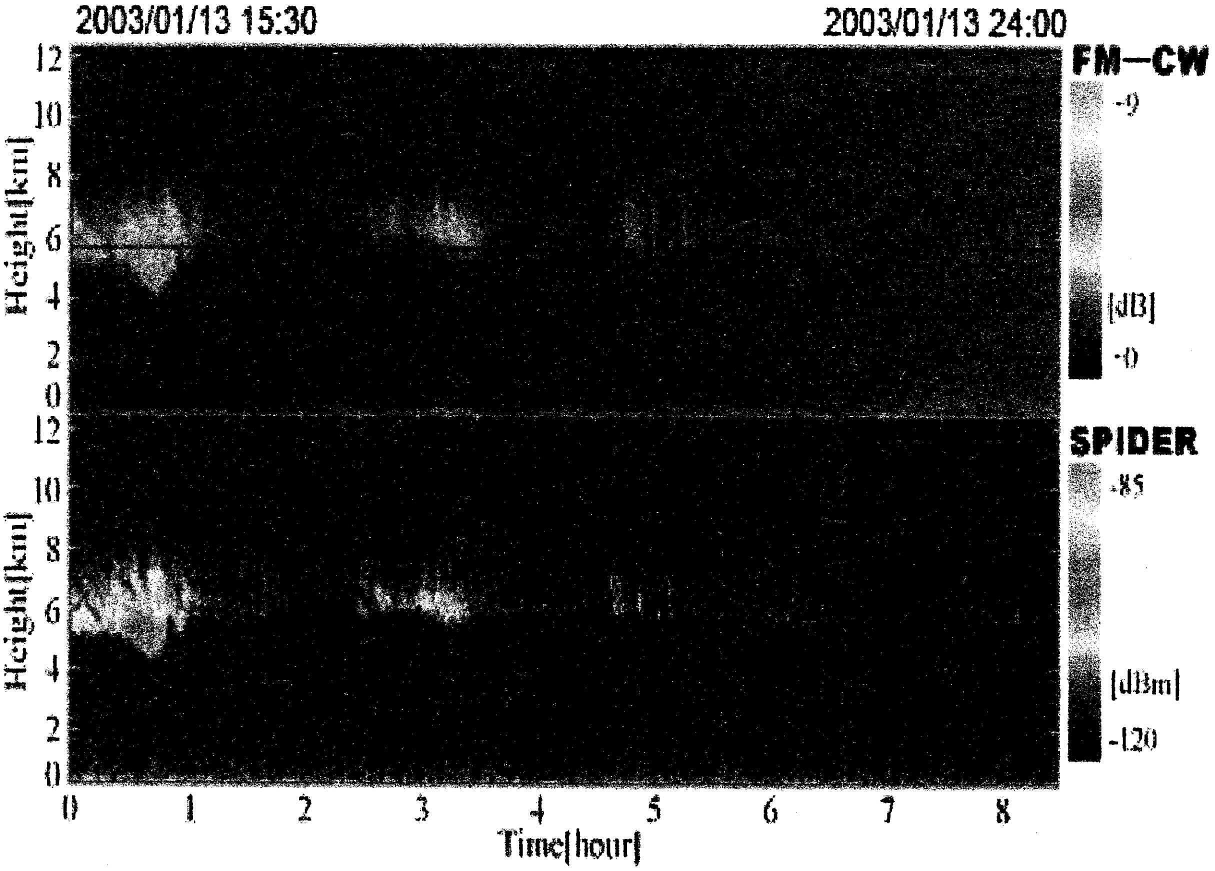

Fig.6 First results of test measurements of clouds. Measurement started 11:30 JST on 2002 June 26th and continued for 7 hours. The gap between 5 and 6 hours is caused by putting an absorber of millimeter wave in front of the feed horn of the transmitting antenna. We can recognize the bottom of the clouds in several hundred meters high and clouds spread up to around 3 km high.

Acknowledgements

This work is supported with the project APEX (Asian Atmospheric Particle Environment Change Studies) in CREST (Core Research for Evolutional Science and Technology) of Japan Science and Technology Corporation and is in part supported with the Grant-in-Aid for Scientific Research by the Japanese Ministry of Education, Culture, Sports Science and Technology (14380241) and with an open use program in the Center for Environmental Remote Sensing, Chiba University (#14-12 and #15-12).

References

[1] Clothiaux, E.E., M.A.Miller, B.A.Albrecht, T.P. Ackerman, J.Verlinde, D.M.Babb, R.M.Peters, and W.J.Syrett, "An evaluation of a 94-GHz radar for remote sensing of cloud properties", Journal of Atmospheric and Oceanic Technology, Vol.12, No.2, p.201, 1995.

[2] Horie, H., T.Iguchi, H.Hanado, H.Kuroiwa, H.Okamoto, and H.Kumagai, "Development of a 95-GHz cloud profiling radar (SPIDER) – Technical aspects", The Transactions of the Institute of Electronics, Information and Communication Engineers, Vol.E83-B, No.9, p.2010, 2000.

[3] Kumagai, H., H.Okamoto, H.Horie, H.Kuroiwa, and S.Iwasaki, "Vertical profiling of liquid cloud properties retrieved from 95-GHz cloud radar and microwave radiometer", 2001 Asia-Pacific Radio Science Conference (Tokyo), PF-27 (p.333), 2001.

[4] Matkin, N., J.Nash, T.Oakley, B.Ellison, M.Oldfield, and J.Bradford, "A trial of the Rutherford Appelleton Laboratory (RAL) 78.2GHz cloud radar", Fifth International Symposium on Tropospheric Profiling, Adelaide, Australia, Dec.4-8, p.113, 2000.

[5] Suga, Y., S.Hoshi T.Takano, S.Shimakura, H.Kumagai, T.Takamura, and T.Nakajima, "Design and development of an FM-CW radar at 94GHz for observations of cloud particles", 2001 Asia-Pacific Radio Science Conference (Tokyo), PF-28 (p.333), 2001.

[6] Hoshi, S., Y.Suga, Y.Kawamura, T.Takano, and S.Shimakura, "Development of an FM-CW radar at 94GHz for observations of cloud particles – Antenna section", Proceedings of the Society of Atmospheric Electricity of Japan, No.58, p.116, 2001 (in japanese).

[7] Takano, T., Y.Suga, K.Takei, Y.Kawamura, T.Takamura, H.Kumagai, and T.Nakajima, "Development of a Cloud Profiling FM-CW Radar at 94GHz", Proceedings of the 27nd General Assembly of the International Union of Radio Science (URSI) (Maastricht, The Netherlands), FP-11, p1789, 2002.

Observation and Data Archive System for RS

An attempt to detect earthquake-related Ionospheric disturbances with the use of GPS data

Katsumi Hattori[1], Takeshi Akasaka[2], Masashi Kamogawa[3], and Nobuhiro Isezaki[4]
1 Marine Biosystems Research Center, Chiba University
E-mail: hattori@earth.s.chiba-u.ac.jp
2 Graduate School of Science and Technology, Chiba University
3 Tokyo Gakugei Univerersity
E-mail: kamogawa@u-gakugei.ac.jp
4 Department of Earth Sciences, Faculty of Science, Chiba University
E-mail: nisezaki@earth.s.chiba-u.ac.jp

Abstract

Ionospheric disturbances preceding large earthquakes have been reported, recently. Those are devided into two types; one is transmission anomaly of radio station signals such as VLF navigation system (Omega system) and VHF broadcasting signals and the other is anomalous density distribution of ionosphere. As for latter one, convincing results were reported by Liu et al(2000, 2001). It was pre-seismic ionospheric phenomena associated with Chi-Chi earthquake, Taiwan (21/09/1999, Mw 7.8) by using Ionosonde. The aim of this study is to verify the ionospheric disturbances of electron density associated with large earthquakes. In this paper, we analyzed total electron content (TEC) variation with the use of GPS (Global positioning System) data around the day of Tottori earthquake (06/10/2000 M7.3) and Geiyo earthquake(24/03/2001 M6.4).

1. Introduction

Electromagnetic phenomena are recently considered as a promising candidate for the short-term prediction of large earthquakes. There have been accumulated observational reports in a very wide frequency range (e.g. Hayakawa and Fujinawa (eds.),1994; Hayakawa (eds.),1999; Hayakawa and Molchanov (eds.), 2002). Measurements of electromagnetic phenomena can be classified into three types, which are the passive ground-based observation, the ground-based observation with use of transmitter signals, and the satellite observation. Ionospheric disturbances preceding large earthquakes are discovered by active transmission signals such as VLF and VHF broadcasting signals. They are one of the most promising approach to establish the short-term earthquake prediction. This approach is divided into two types; one is transmission anomaly of radio station signals such as VLF navigation system (Omega system) and VHF broadcasting signals and the other is anomalous density distribution of ionosphere. As for latter one, convincing results were reported by Liu's group (Liu et al., 2000, 2001, Chuo et al., 2002). They were pre-seismic ionospheric phenomena associated with Chi-Chi earthquake, Taiwan (21/09/1999, Mw 7.8) by using Ionosonde. The aim of this study is to verify the pre-seismic ionospheric disturbances of electron density for large earthquakes (Tottori earthquake 2000 and Geiyo earthquake 2001) in Japan.

2.Total Electron Content (TEC) and differential TEC

A GPS satellite broadcasts radio signals at 1.57542GHz and a1.2276GHz. The dispersive property of ionospheric medium causes the delay with respect to f^2. Using this delay, TEC (total electron content) can be estimated. Total Electon Content TEC is defined as follows,

$$\mathrm{E} = \int_R^S n_e(s)ds \tag{1}$$

where n_e is dencity ($/\mathrm{m}^3$). Unit of TEC is TECU (1 TECU = $10^{16}/\mathrm{m}^3$). Refractive index depends on the frequency of radio wave due to dispersion.

$$n_I = 1 - \frac{\alpha\, n_e}{f^2} \tag{2}$$

where α is constant ($=4.03\times10^{17}\mathrm{ms}^{-2}\mathrm{TECU}^{-1}$)、 f corresponds to the career frequency of GPS system. Using (1) and (2), delay of ionosphere $\Delta\rho_I$ is calculated

$$\Delta\rho_I = \int_s (n_I - 1)ds = -\frac{\alpha \mathrm{E}}{f^2} \qquad (3)$$

Then, we assume the length of free space is ρ, delays of ρ_1 for L1 and ρ_2 for L2 observed at a receiver are described as follows.

$$\rho_1 = \rho - \frac{\alpha \mathrm{E}}{f_1^2} + \lambda_1 N_1 \qquad (4)$$

$$\rho_2 = \rho - \frac{\alpha \mathrm{E}}{f_2^2} + \lambda_2 N_2 \qquad (5)$$

In the right hand, the third term is bias. The corresponding wavelength is multiplied. Then, ionospheric delay effect is obtained as follows,

$$LG = \rho_1 - \rho_2 = -\alpha\left(\frac{1}{f_1^2} - \frac{1}{f_2^2}\right)\mathrm{E} + \mathrm{B} \qquad (6)$$

where $\mathrm{B} = \lambda_1 N_1 - \lambda_2 N_2$. From this,

$$\mathrm{E} = \frac{1}{\alpha} \times \frac{f_1^2 f_2^2}{f_1^2 - f_2^2}(LG - B) \qquad (7)$$

This E gives TEC along the path between satellite and receiver. Therefore, a mapping function F (z') is adopted to estimate the vertical TEC E_V at the sub-ionospheric point under the assumption of single layer model which means that ionosphere is considered as single and thin layer at a certain height and all electrons exist in the layer.

$$\mathrm{E}_v = \mathrm{E} \times F(z') \qquad (8)$$

R is earth's radius and H is altitude of ionosphere from the surface. Corresponding zenithal angles are z and z', then

$$F(z') = \cos z'$$

$$\sin z' = \frac{R}{R+H}\sin z$$

Note the obtained E_V is the value at the sub-ionospheric point and not at the site. Therefore, we have to get the coordinate of the sub-ionospheric point from the site and satellite location. Then, TEC is estimated with the use of Taylor expansion in Bernese.method

$$\mathrm{E}(\beta, s) = \sum_{n=0}^{n\,\max} \sum_{m=0}^{m\,\max} \mathrm{E}_{n,m} (\beta - \beta_0)^n (s - s_0)^m \qquad (9)$$

Here, n max and m max is maximum order of latitude β and longitude s, respectively. $\mathrm{E}_{n,m}$ is TEC coefficient, (β_0, s_0) is the coordinate of the site, (β, s) is the coordinate of the sub-ionospheric point, where s is the sun-fixed longitude. The estimated TEC coefficient E_{00} indicate the TEC at the site.

However, eq. (6) includes bias B, so absolute TEC cannot be estimated. Therefore, P code is used for calculation of absolute TEC as follows.

$$PG = -(P_1 - P_2) = \alpha\left(\frac{1}{f_1^2} - \frac{1}{f_2^2}\right)\mathrm{E} \qquad (10)$$

P_1 and P_2 correspond to the P code of L1 and L2 bands, respectively. Then, TEC is

$$\mathrm{E} = \frac{1}{\alpha} \times \frac{f_1^2 f_2^2}{f_1^2 - f_2^2}(PG) \qquad (11)$$

Using the mapping function, the vertical TEC is obtained.

$$\mathrm{E}_v = \mathrm{E} \times F(z') \qquad (12)$$

$$F(z') = \cos z'$$

$$\sin z' = \frac{R}{R+H} \sin z$$

In this study, we take earth's radius $R = 6371$ km, height of ionosphere $H=350$ km. In the Bernese method, Taylor expansion of Ev is used but we use Ev without expansion. When the zenith angle is law, the effects of cycle slip and multiple paths from contamination of reflected waves. To avoid this, satellites with zenith angle > 60 degree have been used for this analysis.

In this analysis P code have been used to avoid the influences of the bias. The sampling rate was 30 seconds. We also took account of background variation of TEC. 15 days backward median values at each sampling time were considered as the standard background values of TEC. It is mainly diurnal variation of TEC. The variation of the differential between the estimated and the standard TEC have been investigated in this paper. This is called dTEC.

3. Application to Tottori earthquake (M7.3) and Geiyo earthquake (M6.4)

For Tottori EQ, the data using this paper were observed in Chugoku-Shikoku area by GEONET operated by Geophysical Survey Institute, Japan. The number of ground-based station was 76. TEC have been calculated with the use of GAMIT GPS software over one year data from August 2000 to July 2001.

The temporal and spatial distribution of dTEC has been investigated. The result shows the dTEC variation around the origin time of the earthquake there is no apparent anomalous behavior on the day. 4 days before the EQ, dTEC apparently increased by 30TECU and the disturbance of dTEC lasted 3 days. And one day before the EQ, dTEC recovered the standard level and the day of the earthquake, dTEC showed the lower values against the standard level. This is the opposite result to the Liu's ionosonde result.

The relationship between dTEC and geomagnetic variations (ΣKp and Dst indexes) has been also examined. Periods of larger values of ΣKp index and disturbed Dst index correspond to the geomagnetic storm day. The beginning of Dst disturbance shows the onset of the storm. Generally, the probability for the appearance of dTEC disturbance after the magnetic storm is higher over the analyzed period. On the day of the earthquake, however, there is a fluctuation of dTEC and then a magnetic storm occurred.

As for Geiyo EQ, TEC over the site has been investigated but dTEC have been not investigated so far. But this preliminary result shows a good agreement with Liu's result. It means that there was a decrease of density 3 days before the earthquake. However, the very limited data have been used and no spatial and temporal variations have been investigated deeply yet. So further analysis is highly required.

4. Conclusion and future problems

The results showthat 4 days before the EQ, dTEC increased by 30TECU and it lasted 3 days. And one day before the EQ, dTEC deceased. The probability for the appearance of dTEC disturbance after the magnetic storm is higher. This is the opposite result against the Liu's ionosonde result.

As for Geiyo EQ, similar analysis had been done. The result seems consistent with Liu's result. It means that there was a decrease of density 3 days before the eqrthquake. However, the very limited data have been used and no spatial and temporal variations have been investigated yet. So further analysis is highly required.

Investigation on ionospheric disturbances associated with 2000 Tottori EQ with the use of dTEC analysis based on GPS satellite data provides us the following results

(1) 4 days before the EQ, dTEC increased by 30TECU and it lasted 3 days.
(2) One day before the EQ, dTEC deceased.
(3) The probability for the appearance of dTEC disturbance after the magnetic storm is higher.
(4) I is important to find out the clear criteria between normal TID (travel ionospheric disturbances) and earthquake related ionospheric disturbances.
(5) Further investigation will be required for verification of existence of pre-seismic ionospheric disturbances at mid-latitude; accumulation of events, statistical analysis, and so on.

References

Chuo, Y. Liu, J.Y., Kamogawa, M., and Chen, Y. I., The anomalies in the foEs prior to M≥6.0 Taiwan earthquakes, Seismo Electromagnetics: Lithosphere-Atmosphere-Ionosphere Coupling, Eds. M. Hayakawa and O. A. Molchanov, TERRAPUB, Tokyo, 309-312, 2002.

Hayakawa, M. and Fujinawa, Y., Editors, "Electromagnetic Phenomena Related to Earthquake Prediction", Terra Scientific Pub. Comp., Tokyo, pp.677, 1994.

Hayakawa, M., Editor, "Atmospheric and Ionospheric Electromagnetic Phenomena Associated with Earthquakes", TERRAPUB, Tokyo, pp. 996, 1999.

Hayakawa, M., and Molchanov, O. A., Editors, "Seismo Electromagnetics Lithosphere-Atmosphere-Ionosphere Coupling", TERRAPUB, Tokyo, pp. 477, 2002.

Liu, J. Y. Chen, Y. I Pulinets, S. A. Tsai, Y. B. Chuo, Y. J. : Seismo-ionospheric signatures prior to M>6.0 Taiwan earthquakes, Geophys. Res. Lett., 27, 19, 3113-3116, 2000

Liu, J.Y. Chen, Y.I. Chuo, Y.J. Tsai, H. F. : Variation of ionospheric total electron content during the Chi-Chi earthquake, Geophys. Res. Lett., 28, 7, 1383-1386, 2001

Remote sensing, GIS and Public Health.

HIROKI SUGIMORI, MD PhD,
Department of Preventive Medicine,
St. Marianna Univ., School of Medicine,
Sugao 2-16-1, Miyamae-ku,
Kawasaki, 2168511, Japan,
Tel +81-44-977-8111(Ext3416),
FAX +81-45-961-5079
hsugimor@marianna-u.ac.jp

ABSTRACT

The role of remote sensing (RS) and Geographic Information Systems (GIS) in public health is potentially great. As computer technology continues to transform our ability to gather, analyze, and map health data, new roles for RS and GIS in public health may emerge.

Keywords: Public Health, Disease Mapping,

INTRODUCTION

Remote sensing (RS) and Geographic Information Systems (GIS) have capabilities that suite for use in public health and epidemiology fields such as infectious disease surveillance and control. They are also highly relevant to meet the demands of outbreak investigation and response, where prompt location of cases, rapid communication of information, and quick mapping of the epidemic's dynamics are vital.

Geographic information (i.e. disease mapping) in public health and epidemiology has a long history and maps showing the geographical distribution of yellow fever were produced in 1798 [1], and in the 1850s an English anesthesiologist, John Snow (**Figure 1**), mapped the locations of cholera cases in Soho, London (**Figure 2**), leading him to the conclusion that water from the Broad Street pump was responsible for the cholera outbreak [2, 3].

Figure 1. John Snow

However, until recently, the use of both RS and GIS tools in public health were limited due to problems: high cost of hardware and great complexity of GIS software that made it extremely time-consuming as well as costly to extract information relevant to the practical demands of disease prevention and control. The situation has changed dramatically over the past few years. Hardware prices have dramatically dropped, simple new devices are now available, and a new generation of civilian satellites is in orbit, circling the world.

Practical uses of RS and GIS in public health area can be as follows,

- Determining geographic distribution of diseases
- Analyzing spatial and temporal trends
- Mapping populations at risk
- Stratifying risk factors
- Assessing resource allocation

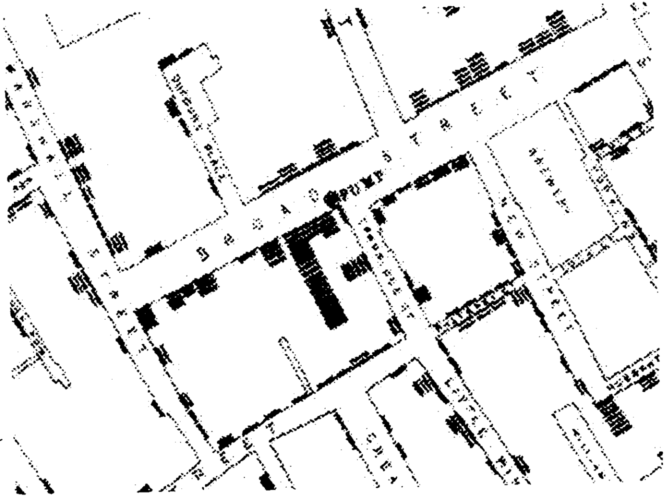

Figure 2. Broad Street Pump Outbreak

- Planning and targeting interventions
- Monitoring diseases and interventions over time

WHO'S PUBLIC HEALTH MAPPING PROGRAMME

WHO's public health mapping programme has been started since 1993, to promote and implement GIS into decision-making for a wide range of infectious disease and public health programmes. The Public Health Mapping Program based WHO Communicable Diseases [4] has been developed with the goal of providing greater access to simple, low-cost geographic information and related data management and mapping systems to public health administrators at all levels of the health system.

In support of remote field data collection activities, WHO has been routinely using GPS to map and track infectious diseases at community levels. GPS are now routinely used by village outreach teams for infectious diseases such as onchocerciasis, guinea worm, African Trypanosomiasis (sleeping sickness), lymphatic filariasis. The systems are used during the investigations of disease outbreaks for rapid mapping of cases and deaths and within the context of complex emergency situations they are being used for mapping internally displaced persons, refugee camps and rapid epidemiological assessments. This is one of the most successful programs that utilize RS/GIS techniques in public health area.

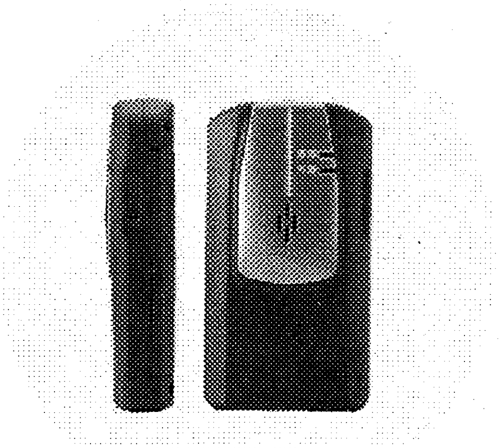

Figure 3. GPS/CDMA device (SECOM)
height 7.9 cm × length 4.3 cm × thickness 1.82 cm
weight: approximately 48 g (including battery)

ANALYSIS OF JAPANESE ELDER'S BEHAVIOR USING HUMAN RS (OUR ATTEMPS)

In Japan, we are now facing aging society rapidly. Therefore, to support elderly person and sustain their comfortable life (golden years), it is necessary to detect trivial behavioral change of elderly in daily life as

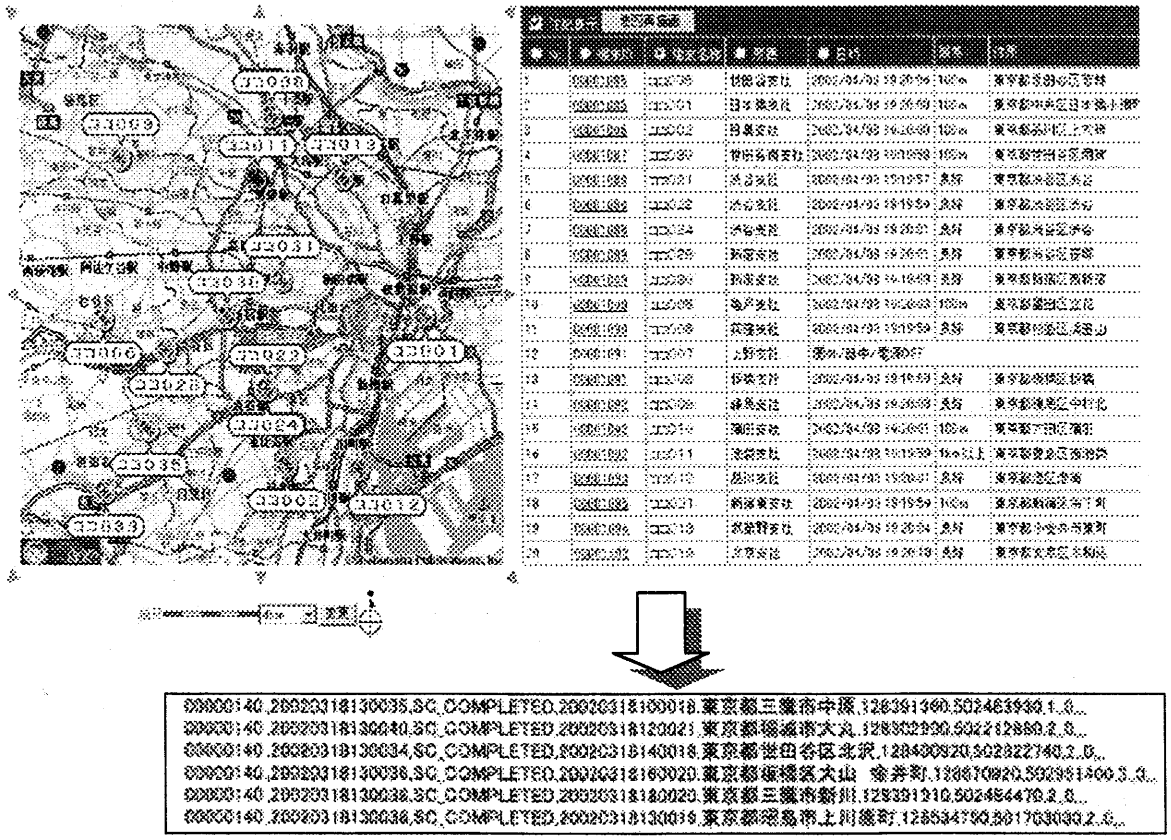

Figure 4. G-manager
Remote sensing subjects' position (longitude, latitude, address) and concurrent time

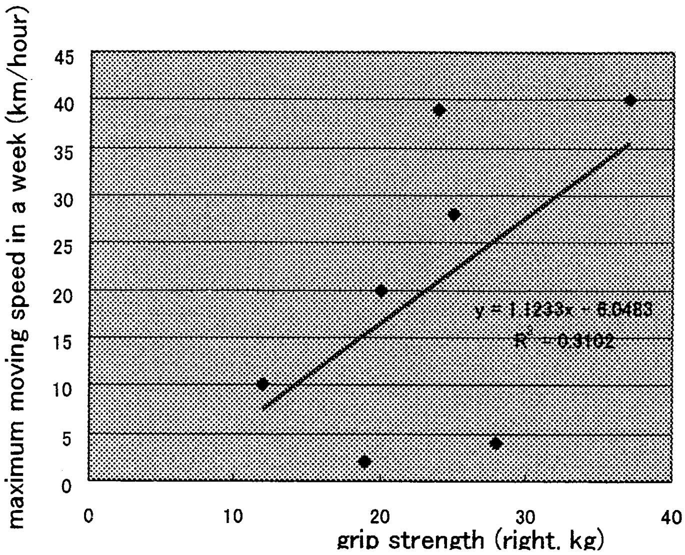

Figure 5. grip strength (right, kg) and maximum moving speed in a week (km/hr) assessed by GPS/CDMA portable device in 7 Japanese elderly. They showed significant correlation (r^2=0.31).

early as possible, and prevent behavioral abnormality such as "*TOJIKOMORI* (in Japanese word, means behavioral abnormality that elderly lock or shut themselves in a room or house, or generally withdrawing), leading to bed-ridden.

Until recently assessment of elderly behavior, we usually collect subjective information by using questionnaires responded by elders themselves or their cohabitant families. However, since cognition impairments (recalling bias) or family cohabitant status would influence behavioral assessment using questionnaire, their reproducibility and validity is quite doubtful.

We aimed to investigate the behavioral change and the factor that is tied up to the abnormal behavior of elderly, using commercially available device, which had dual remote sensing system composed of both GPS and CDMA technique (Figure 3, GPS/CDMA device, SECOM, Tokyo Japan, height 7.9 cm×length 4.3 cm ×thickness 1.8 cm, weight including battery: approximately 48 g).

CDMA technique could improve position sensing by intercommunicating with cellular phone stations frequently, and the device could collect demographic data more accurately (highest precision level: 5~10 m). Although GPS position sensing by itself works only 20% approximately in daily life of elderly at urban area in Japan (our preliminary data), due to obstacles such as high buildings, high trees, and indoor stay, CDMA technique covers the shortcomings of GPS.

We recorded GPS/CDMA log (**Figure 4**) of 7 non-institutionalized community-dwelling elders (mean age 78) in Kawasaki city urban area, Japan who do not need nursing care. There was neither hospital patient nor bedbound individual. We evaluated the maximum moving velocity (MMV) during 7 days by GPS/CDMA logs, and we found that the MMV seems to correlate with right grip strength. (**Figure 5**)

Low grip strength is known for one of the risk factors of low bone density[5], falls, and fractures[6] in elders. Therefore, evaluating behavioral changes or predicting grip strength by MMV using RS indirectly might have possibilities to prevent senior publich health problems, such as "bed-ridden".

Our findings suggest that RS application to human could provide useful biomechanical parameters for analysis of human behavior, and hence RS could contribute to improvement of public health.

ACKNOWLEDGEMENT

This study was supported by the joint research program of CEReS, Chiba University.

REFERENCES

---

[1] Robinson AH. Early thematic mapping in the history of cartography. Chicago. University of Chicago Press 1982.

[2] Snow J. On the mode of communication of cholera. London, Churchill, 1849.

[3] Laura Lang. GIS for Health Organizations. Independent Pub Group (C). 2000.

[4] WHO. Communicable Disease Surveillance and Response. http://www.who.int/csr/mapping/

---

[5] Osei-Hyiaman D, Ueji M, Toyokawa S, Takahashi H, Kano K alcif Tissue Int. Influence of grip strength on metacarpal bone mineral density in postmenopausal Japanese women: a cross-sectional study.1999;64:263-6.

[6] Eriksson SA, Lindgren JU. Outcome of falls in women: endogenous factors associated with fracture. Age Ageing. 1989;18:303-308.

A simplifying method for the transmittance calculation based on a Fourier-transformed Voigt function considering the instrument function

Hirokazu Kobayashi[1] and , Akiro Shimota[2]
1 Central Research Institute of Electric Power Industry
E-mail: koba@criepi.denken.or.jp
2 Central Research Institute of Electric Power Industry
E-mail: akiro@criepi.denken.or.jp

Abstract

A line-by-line transmission calculation for a homogeneous atmospheric layer based on a pure Voigt function with no approximation can be performed using the Fourier-transformed Voigt profile. This method also includes an interference term that takes into account the line mixing effect. The method can be used to calculate transmittance/radiance considering each line shape under the effects of temperature and pressure using the line database with an arbitrary wave number range and resolution. This method adopts line-by-line calculation in the Fourier space, then considering the instrument function, we can reduce total calculation cost to use this method for practical applications. Evaluation was performed comparing this method with a conventional atmospheric transmittance calculation model.

1. Introduction

Recently, Kobayashi [1] showed an algorithm to calculate the Fourier transformed Voigt function directory, and indicated a way of the simple line-by-line calculation method. When the Voigt function is represented with Fourier form, it is easily expected the line-by-line calculation becomes simple because all the lines are simply summed in the Fourier space. An arbitrary wave number resolution can be obtained by this method and neither the line-wing part cutoff nor the mapping procedure of each different centered line shape to the wavenumber space are required. Also, Kobayashi [2] made the comparison between the widely using model (FASCOD) and his model and showed that results of two models are identical.

In general, practical atmospheric transmission calculations involves the instrument function because the atmospheric transmission observations are carried out by the instrument which restricted by the instrument function, in this case, the response of the instrument in wavenumber space, such as amplitude response and wavenumber resolution. This paper shows the path to reduce the calculation cost of the line-by-line model using Fourier transformed Voigt function considering the practical transmittance calculation always associates the convolution of instrument function.

2. Numerical Expression of the Voigt Profile Using the Discrete Fourier Transform

Armstrong[3] showed the expression of the Voigt function K(x,y) with the Fourier-transform style as

$$K(x,y)=\frac{1}{\sqrt{\pi}}\int_0^\infty \{\exp(-yt-t^2/4)\}\cos(xt)dt \quad , \tag{1}$$

where y is the ratio of Lorentz to Doppler widths. As Karp[4] showed, the integrand of Eq. (1) for the multiple absorption lines is represented as

$$f(t)=\sum \exp\{-y(t\nu)-(t\nu)^2/4\}\exp(-it\nu\alpha_h)\nu \quad , \tag{2}$$

where for each line j, ν_j is the line center. Eq. (2) is basically equal to the Karp's conclusion, but Kobayashi[1] introduced νmax to normalize the line center as $\nu_j = \nu 0_j/\nu_{max}$. Introducing the wavenumber calculation maximum, we can reduce the total calculation number, and perform the line-by-line calculation on the arbitrary band range from $\nu_{min}=\nu_{max}-\nu_{max}/l$ to ν_{max} where l is the Fourier transform computation scale (l =1,2, ... m) . We call this method L2FTV (line-by-line calculation using Fourier transformed Voigt function).

Figure 1 shows an example of the results of the FASCOD and the L2FTV. The corresponding line peak values are identical when neglecting very small computational error (discrepancy is less than 10^{-4}.

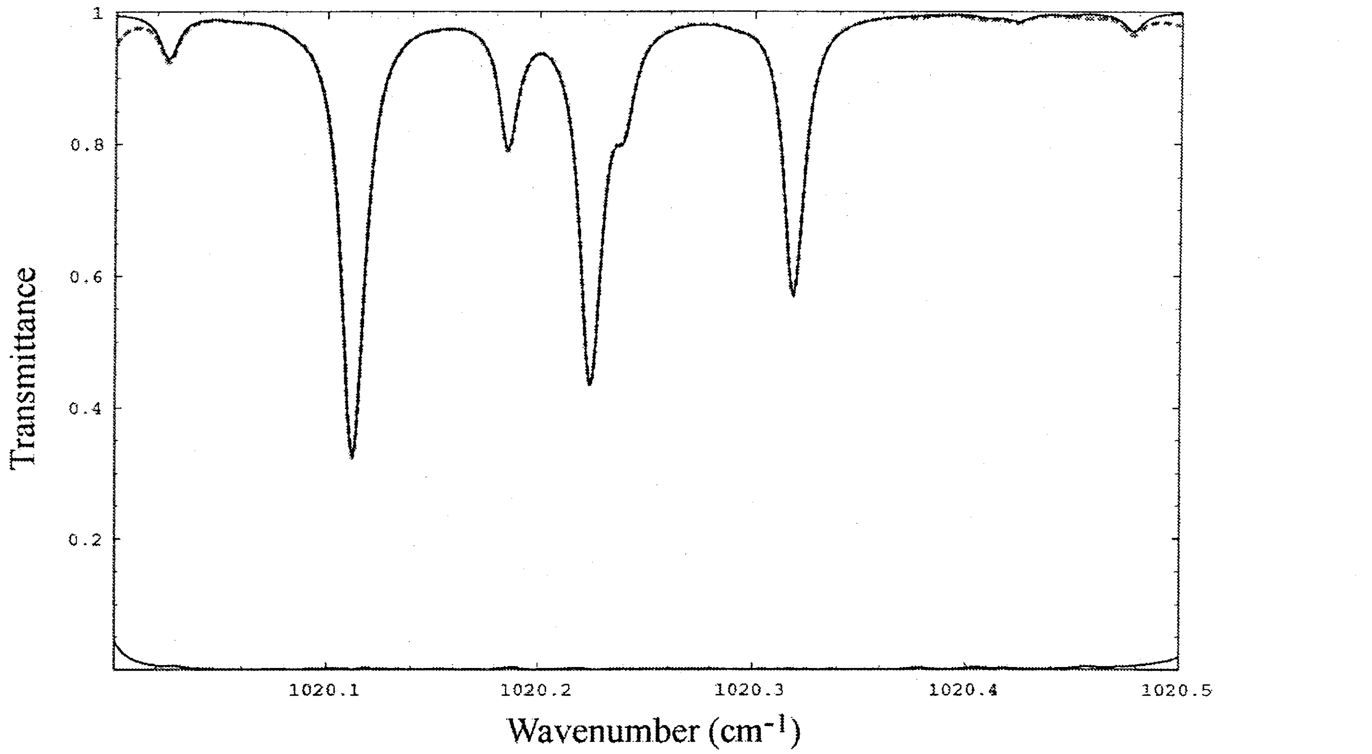

Fig. 1. Sample transmittance calculation using FASCOD version 3P (dashed line) and the L2FTV (solid line) for the wavenumber region 1020.0 to 1020.5 cm^{-1}.

The thin solid line at the bottom is the difference between the two models, defined as the root of the squared difference. The FASCOD calculation conditions are P: 55.29 hPa, T: 216.7 K (Z= 20 km of U.S. standard atmosphere 1976), and horizontal path of 1 km for O_3 only. In this case, the FASCOD parameter DV, the wavenumber spacing for the interpolated result, is set to 0 which induces 0.001314 cm^{-1} internally. The molecular density is 4.769 $x10^{12}$ molecules/cm^3. The scanning function is the rectangular convolution for the transmission, and the parameter SCAN is set to 0.0005 cm^{-1}. The minimum optical depth parameter DPTMIN is set to the default value, 2 x 10^{-4}. The L2FTV model parameters are scale l=400, ν_{max}=1021.5 cm^{-1}, ν_{min}=1018.95, res=0.1247 cm^{-1}, and Fourier-transform size F=2048. For the L2FTV calculation, 74-line data included in the target wavenumber range are used taking into account of the line intensity. The temperature dependency of the line intensity was calculated following Rothman and Gamache.

3. L2FTV calculation cost saving considering instrument function

The L2FTV calculation cost saving is performed by apodizing the optical depth in the Fourier space. In the Fourier space this apodization is accomplished by zero filling which introduces the calculation cost reduction. The focusing point is that the convolution of the instrument function is applied to the transmittance and the L2FTV calculation cost saving is performed by apodizing the optical depth in the Fourier space. Because the transmittance is obtained applying the exponential function to the optical depth, even if using a same instrument-apodizing function, there is a difference between the instrument function applied transmittance and the same instrument applied transmittance but using a optical depth derived by the calculation cost saving. The evaluation steps are followings; (1) define the reference transmittance spectrum obtained from the L2FTV applying appropriate instrument function, (2) confirm the first step comparing FASCOD produced transmittance applied same instrument function, (3) apply weak (which means small effect for the resolution response) apodizing function (rectangular function) onto the optical depth derived by the L2FTV in the Fourier space, (4) apply stronger apodizing function, (5) evaluate critical strength of the apodizing function. Figure 2 shows this evaluation process.

We can estimate the relationship between the masking function and the instrument function as follows. When we observe the actual atmosphere radiance using a spectrometer such as FTS, observed spectrum S_{fts} is represented using blackbody radiation Br, atmospheric transmittance Tr and the instrument function f*as,

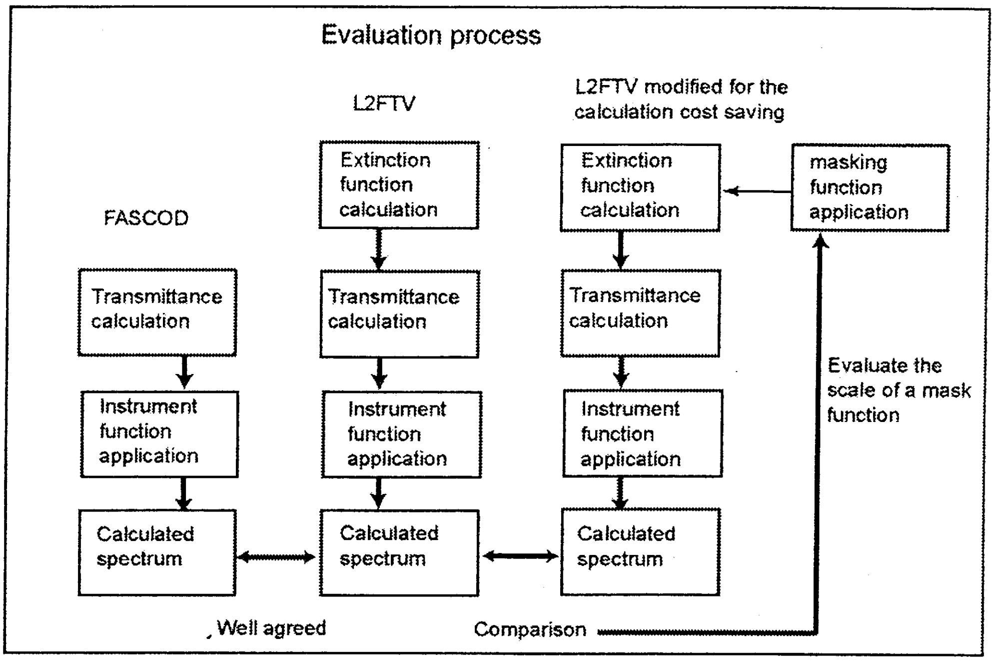

Fig. 2. The evaluation process of calculation cost saving method considering the instrument function.

A conventional line by line calculation code, such as FASCOD, can calculate the transmittance spectrum applying an instrument function to simulate a spectrometer such as the FTS. On the L2FTV model, calculation cost saving is performed applying a masking function onto the extinction calculation process. An evaluation for the tradeoff between the strength of the masking function and the error of the resulted spectrum was performed.

$$S_{fts}=f^{*}\otimes(Br \cdot Tr) \qquad (3)$$

where Br variation in wavenumber is relatively small considering the resolution of actual FTS application, and Tr=exp(-r k*) then we obtain ignoring constant r,

$$S_{fts}=f^{*}\otimes exp(-k^{*}) \qquad (4).$$

In L2FTV calculation cost saving process, calculated spectrum S_m is represented as,

$$S_m=exp(-f'^{*}\otimes k^{*}) \qquad (5)$$

where f'* is the masking function for the extinction function calculation. We can represent these relations using Fourier transformation F when each of k, f, f' is Fourier transformed form of k*, f*, f'*,

$$S_{fts}=F\{f \cdot F^{*}(exp(-k^{*})) \qquad (6)$$

$$S_m=exp(-F\{f' \cdot k\})$$

Then applying the series expansion around 0, these equations become

$$S_m=1-F\{f' \cdot k\}+F\{f' \cdot k\}2/2-F\{f' \cdot k\}3/6+O \qquad (7)$$

$$S_{fts}=F\{f \cdot F^{*}(1-k^{*}+k^{*}2/2-k^{*}3/6+O)\} \qquad (8)$$

Executing Fourier transform of inner part of Eq.8, we obtain

$$S_{fts}=F\{f \cdot d\}-F\{f \cdot k\}+\{f \cdot F^{*}(k^{*}2/2)\}-\{f \cdot F^{*}(k^{*}3/6)\}+O \qquad (9).$$

Comparing Eq.7 and 9 from the standing point of the effect strength of the masking function f' and the instrument function f, we found the second term is same, and in the third term of Eq.7, the masking function f' has quadratic form, however the instrument function f has linear form in Eq.9. So, we can estimate that the masking function affect strongly to the spectrum comparing the effect of the instrument function.

in this evaluation, we use the Norton-Beer[4] instrument function, and the rectangular mask function. First, we apply the Norton-Beer instrument function to the L2FTV spectrum to confirm that is equal to the FASCOD provided spectrum as shown in Fig.1. Hence, we use the effective instrument/mask function width that is defined as the relative size where function becomes 0 considering calculation scale, which is, in the L2FTV, the Fourier transform size.

Figure 3 shows the original L2FTV calculation and the instrument function applied low resolution transmittance spectrum. Figure 4 shows the R.M.S error between the original spectrum and rectangular mask function applied transmittance when a reference instrument function effective width is 0.121. The figure shows that the mask function worked well for the reduction of the calculation cost when its effective size is relatively equal or larger than that of the instrument function.

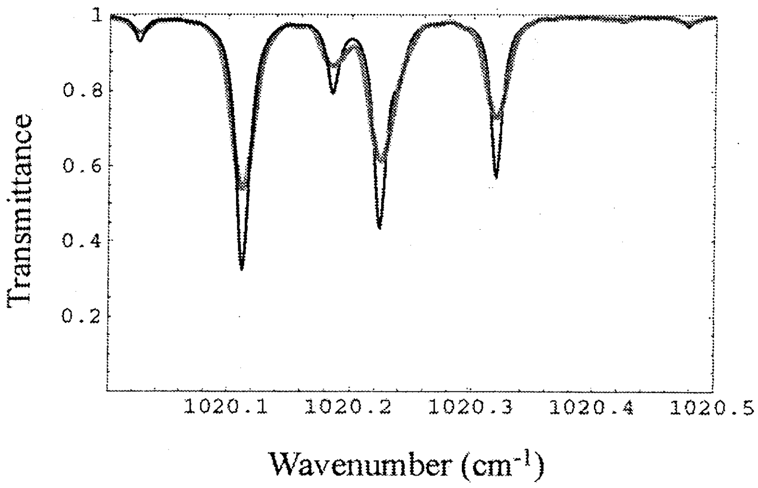

Fig. 3. An effect of the instrument function.
Thin solid line is the original L2FTV provided spectrum, and bold one is a spectrum applied the Norton-Beer instrument function.

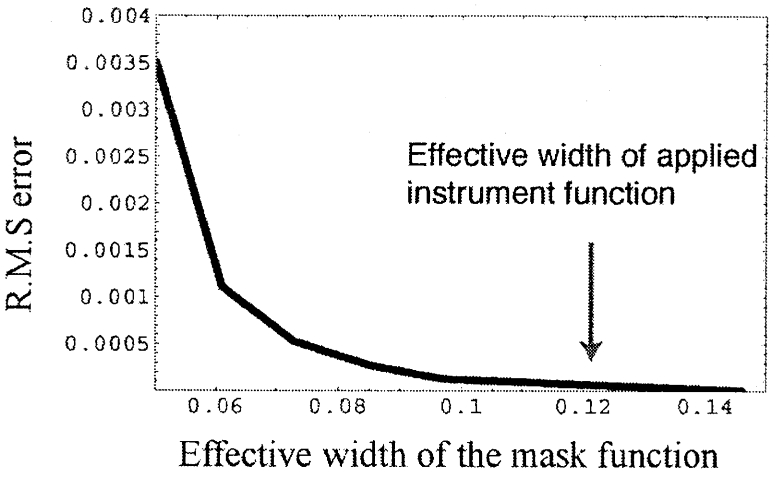

Fig. 4. The effect of the mask function
Wider mask function reduces rms error of re-produced spectrum, however, comparatively equal width to the instrument function gives small and acceptable error.

4. Conclusion

The developed calculation cost saving method was evaluated and it is confirmed that the rectangular calculation mask can reduce the total calculation cost. Applying this method, the L2FTV line by line calculation cost can be reduced to the comparable level of the conventional line by line model, keeping its simplicity and exactness produced by the analytical representation of Voigt profile.

References

1. H. Kobayashi, JQSRT 62, 477 (1999).
2. H. Kobayashi, Appl. Optics, 41, 33, (2002).
3. B.H. Armstrong, JQSRT 7, 61 (1967).
4. A. H. Karp, JQSRT 20, 379 (1978).
5. R.H. Norton and R. Beer, J. Opt. Soc. Am.66, 259 (1976).

Development of the Satellite Image Database (SIDaB) for Agriculture, Forestry and Fisheries, and Its Applications

Genya Saito[1], Shigeo Ogawa[1], Izumi Nagatani[2], Nobuhiro Nishida[2], Naoki Ishitsuka[3],
Haruo Sawada[4], Kyohei Segawa[5] and Xianfang Song[6]

[1]National Institute for Rural Engineering
[2]The Computer Center for Agriculture, Forestry and Fisheries Research
[3]National Institute for Agro-environmental Sciences
[4]Forestry and Forest Products Research Institute
[5]National Research Institute of Far Seas Fisheries, Fisheries Research Agency
[6]Institute of Geographical Sciences & Natural Resources Research, CAS

Abstract

First, in order to establish SIDaB as near real time monitoring system, we investigated satellite data receiving system, network system for data distribution, hardware system for data archive, monitoring method for the phenomena, necessary framework of international, and domestic collaboration system. Next, we mentioned to some examples of the monitoring as applications for SIDaB and they were monitoring of fishing boats at Japanese Sea, monitoring of forest fires, and Monitoring of agriculture.

1. Introduction

Satellite remote sensing technique can observe at large area for a monument and at regularly interval, and it is only method of monitoring for agricultural area[1)], forest and ocean. We will be able to use of satellite data for safety and steady life of peoples and prosperity of agriculture, forestry and fishery, but in our situation, the data that satellite observed take long time to use and we cannot use the data that are valuable for applications. First, in order to establish SIDaB as near real time monitoring system, we investigated satellite data receiving system, network system for data distribution, hardware system for data archive, monitoring method for the phenomena, necessary framework of international, and domestic collaboration system. Next, we mentioned to some examples of the monitoring as applications for SIDaB.

2. Development of SIDaB

To estimate agricultural and fishery productions and forest fire determination, the monitoring must be performed at near real-time. We need the framework for network of data movements, and data archives that huge old data are necessary as standard. For this reason we are developing a Satellite Image Database System (SIDaB) in the Computer Center for Agriculture, Forestry and Fisheries Research. Satellite data flow and collaboration scheme are listed Fig. 1.

3. Monitoring of fishing boats at Japanese Sea

DMSP/OLS is almost same the senor of NOAA/AVHRR, and it operated America, and it is measuring to lights of nighttime all over the world. The night-lights data are stored in the recorder on board, and downlink at the sky of America. The data are processed and transmitted to SIDaB using TransPAC etc. under the Asia-Pacific Advanced Network Consortium, and we can get the data within 24 hours. Fig. 2 is the time-series images of lights of nighttime using DMSP/OLS at Japan Sea and the surroundings from August 1999 to January 2000. We can easily distinguish fishing boats as white spots in Japan Sea, and larger white points in January at Hokkaido (north island in Japan) are the illuminations of ski-fields. We can get sea surface temperature automatically, and Fig. 3 is the sea surface temperature image of same area and almost same date using NOAA/AVHRR data. To compare with Fig. 2 and Fig. 3, we can realize the locations of fishing boats are depend on sea surface temperature.

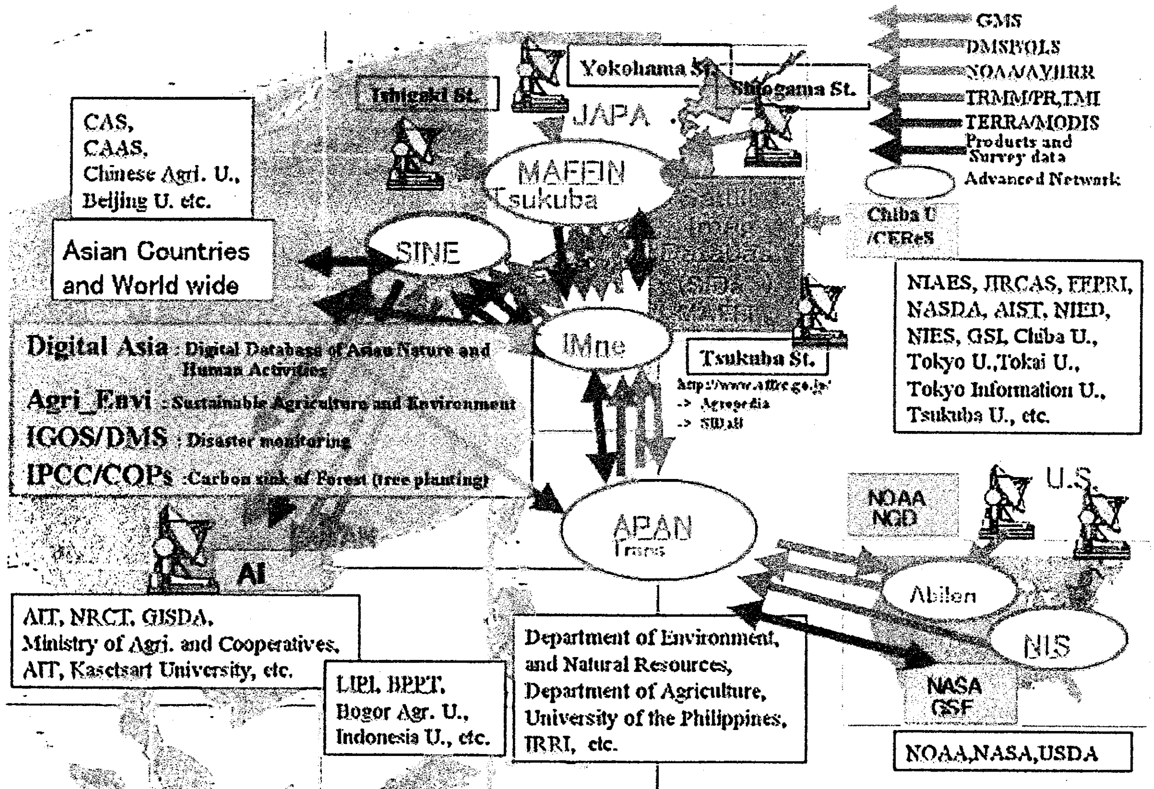

Fig. 1 Satellite data flow and collaboration scheme

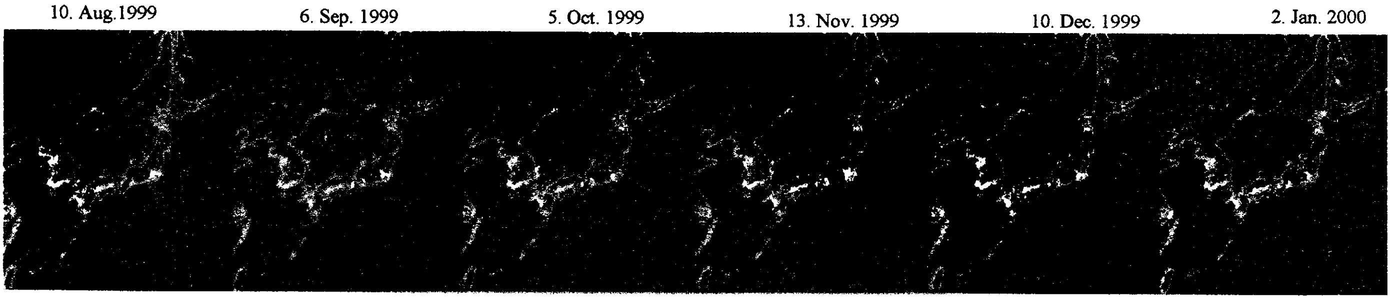

Fig. 2 Nigh light Images using DMSP/OLS

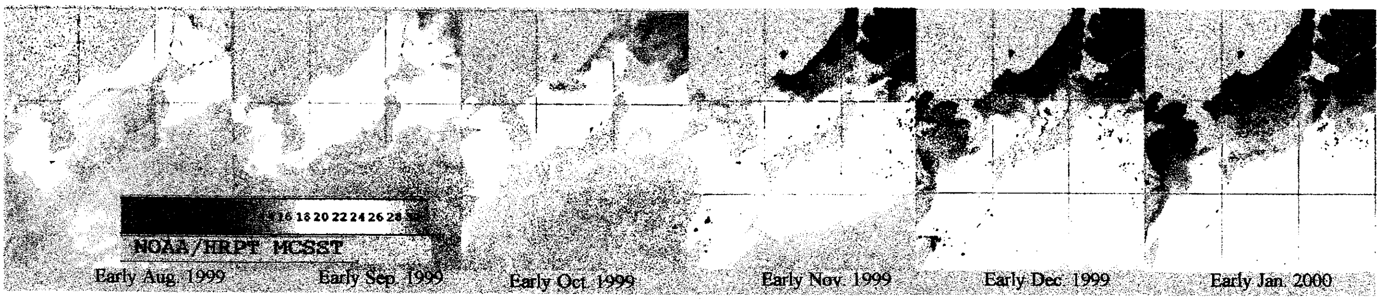

Fig. 3 Sea surface temperature images using NOAA/AVHRR

4. Monitoring of forest fires

Forest fires can be detected as high temperature using NOAA/AVHRR, and unusual nighttime lights spots using DMSP/OLS. Forestry and Forest Products Research Institute (FFPR) and the Computer Center for Agriculture, Forestry and Fisheries Research (CCAFFR) made automatically detection system of fire possibility area using NOAA/AVHRR and DMSP/OLS, and open to the public using web (http://www.affrc.go.jp/ANDES/). The temperature of fire possibility area or normal area is determined FFPR researcher, and the steady nightlights data were provided by NOAA/NDGC. The examples of forest fire possibility spots were indicated to the Fig. 4, and it is from the date is 10 March 2002 to 12 March 2002 at Sumatra Island.

5. Monitoring of agriculture

We are developing an agriculture monitoring system in East Asia using NOAA/AVHRR data. Every ten days the maximum Normalized Difference Vegetation Index (NDVI) is compared with the past three-year average (Fig. 5) of ten-day composites for the maximum NDVI value. The composite ten-day NDVI images are derived from AVHRR archives of 1997-1999. To reduce the cloud noise, the maximum value NDVI is used for ten-days composites. When the average value is calculated, the negative NDVI pixels are eliminated, because there still remains cloud pixels even in ten-day composites. The NDVI images of the difference between the reference ten-day NDVI images and the current ten-day NDVI images are calculated (Fig. 6). Using these difference NDVI images, it is possible to detect the area of drought damage of crops. The minus difference (<-0.1) pixels are classed as the drought risk area in spring and summer. Using this system, the drought effects on agriculture for China in 2000 were detected and monitored successfully (Fig. 7).

Reference

1) Genya Saito, Naoki Ishitsuka, Ayumi Fukuo, Michio Anazawa, and Xianfang Song (2002): Application of Satellite Data for Agriculture in East Asia, Advances in the Astronautical Sciences, 110, 233-243

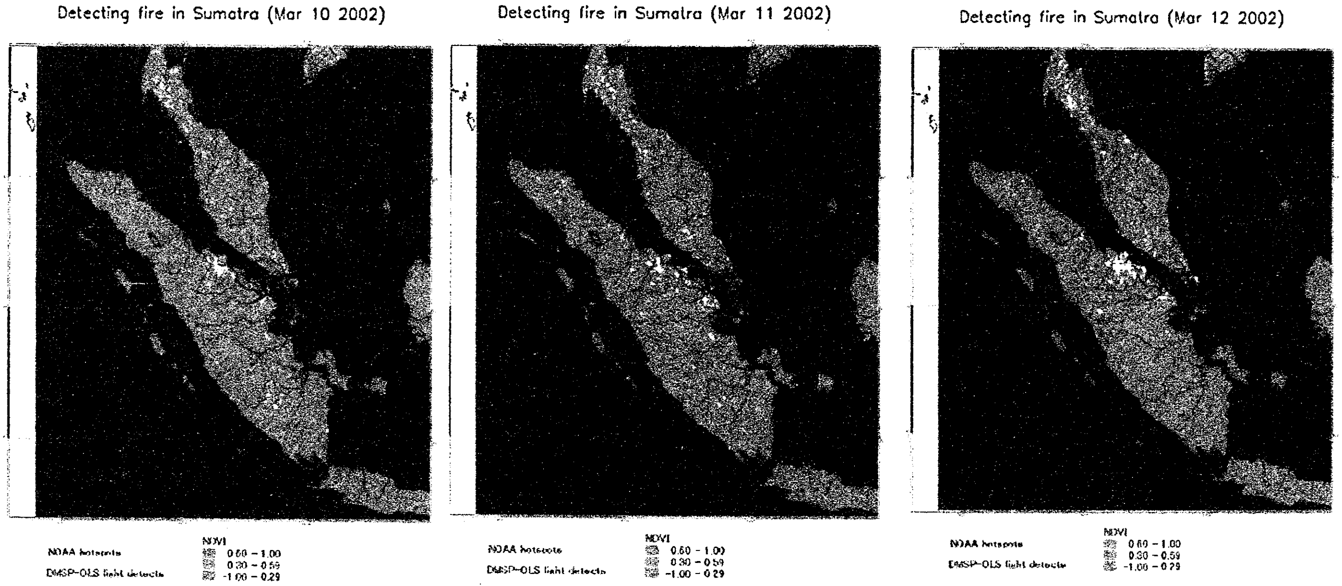
Detecting fire in Sumatra (Mar 10 2002)

Detecting fire in Sumatra (Mar 11 2002)

Detecting fire in Sumatra (Mar 12 2002)

Fig. 4 Possibility images of forest fire in Sumatra at 10 – 12 May 2002

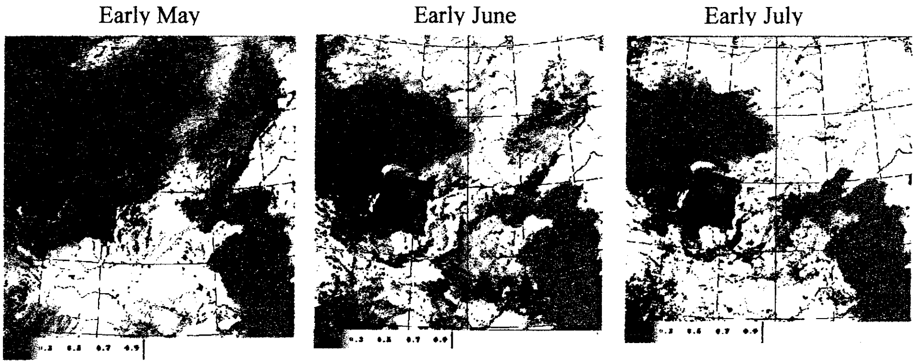

Fig. 6 Average NDVI images from 1997 to 1999

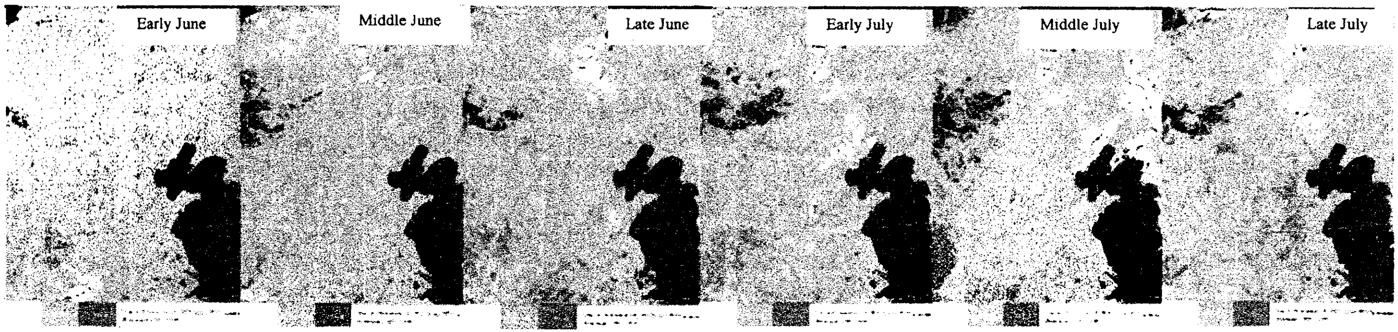

Fig. 6 Difference image of NDVI between 2000 and average year White: NDVI of 2000 year < average

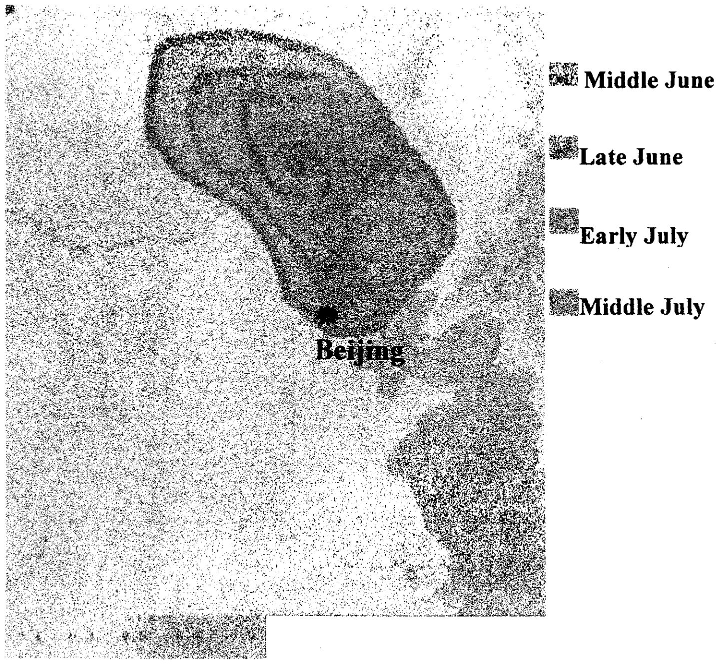

Fig. 7 Enlargement of the drought area at north China in 2000 year by the agricultural monitoring system using NOAA/AVHRR

Development and operation of interoperable system for earth observation satellite image and spatial data in Asia

Shinobu Kawahito[1], Akihiko Kondoh[2], Osamu Ochiai[3], Ryutaroh Tateishi[2], and Tomotaka Sekiya[1]

1 Remote Sensing Technology Center of Japan (RESTEC)
E-mail: kawahito@restec.or.jp, sekiya@restec.or.jp
2 Center for Environmental Remote Sensing, Chiba University (CEReS)
E-mail: kondoh@faculty.chiba-u.jp
3 Japan Aerospace Exploration Agency (JAXA)
E-mail: ochiai.osamu@jaxa.jp

Abstract

CEReS and RESTEC developed a prototype of interoperable system to exchange Earth observation satellite data and geo-spatial data of Asian region via the Internet in cooperation with JAXA. A standard interface of Web based GIS technology, that is, OpenGIS Consortium (OGC) technology is adopted to develop this interoperable system. The purpose of this prototype system is to verify the interoperability of multiple data sources dispersed in CEReS and in JAXA. Interoperable system is considered effective method to establish regional environmental database in distributed data servers in the Internet, and is expected to promote further development of practical application using regional environmental data.

1. Introduction

Earth observation data has not yet being used effectively in operational systems, though it is highly effective in practical applications like environmental monitoring. Through the rapid development of the Internet, GIS has grown from local applications to network applications to diffuse images, maps, and spatial data for multiple users in the Internet. Using Web based GIS technology, regional data such as Earth observation satellite data and map data created by different organizations can be accessed and combined together in accordance with user requirements. Thus, Web GIS technology is considered an effective method to establish various regional databases that allow public users to utilize them. And by adopting a standard interface of Web GIS technology, vendor free interoperable system can be developed which can exchange spatial data independently from the configuration of each system.

As a prototype of interoperable system, CEReS and RESTEC developed a Web Map Server (WMS), which provides Asia Land Cover Image, in the Internet. This WMS has a link with another Web GIS system of JAXA. JAXA system was developed as a part of joint research project between JAXA and the Ministry of Agriculture, Forestry and Fisheries of Japan (MAFF) for forest fire monitoring in Thailand.

2. Overview of interoperable system

2.1 OpenGIS Standards for Web Mapping

OpenGIS Consortium (OGC) is a non-profit international association, which specifies various standards for interoperable geo-location services. Among them, standard interface of Web GIS is included. Through the standard interface, spatial data can be exchanged flexibly in the Internet independently from hardware/software environment of each system.

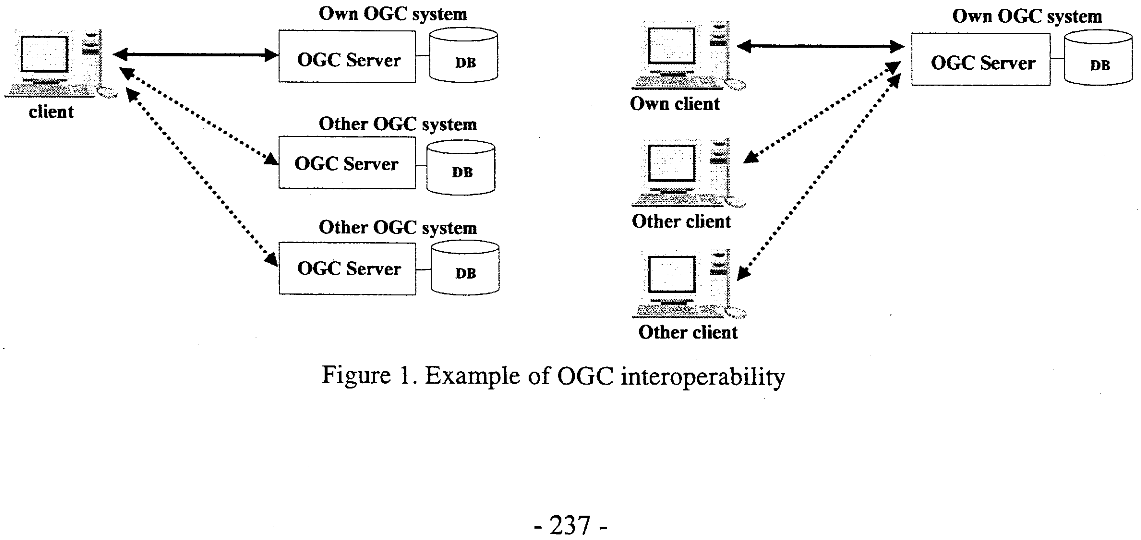

Figure 1. Example of OGC interoperability

2.2 System Configuration

OGC standards define various OGC Web Servers: Web Map Server (WMS) provides map images (JPEG, GIF, etc.) and Web Feature Server (WFS) provides spatial data (road, rivers, etc.).

CEReS and RESTEC developed a prototype of WMS that provides 1 km mesh Asia Land Cover Data generated by CEReS. Another system of JAXA consists of two WMSs, a WFS, and a web-based Viewer Client system. Web Map Servers provide Fire Risk map generated by MAFF, JERS-1/SAR mosaic image generated by JAXA, and other images. The Web Feature Server provides hotspot location data generated by MAFF derived from NOAA/AVHRR and DMSP/OLS. This JAXA system is designed to provide hotspot information and related images timely to the assumed target users, that is, forest fire monitoring operators in Thailand, with easy and simple operation to promote practical satellite data application.

Figure 2 shows the configuration of the whole system.

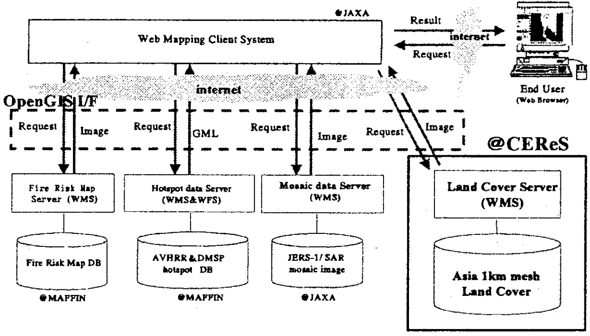

Figure 2. Overview of the system configuration

2.3 Output

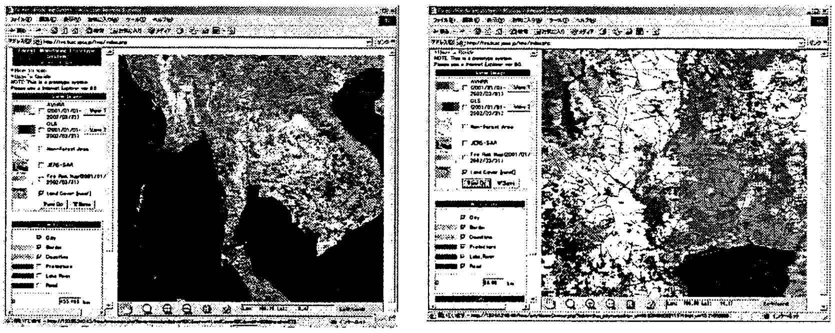

Figure 3. Snapshot of the system

Figure 3 shows a snapshot of the prototype system. In these images, the base is land cover image, and map data such as prefecture border and river data are overlaid onto the base image. User can select the data layer and observation date using check boxes in the left frame.

2.4 Conclusions

This prototype WMS set at CEReS is successfully confirmed its interoperability with JAXA Web GIS system, which is also compliant with OGC standard interface. User can select and overlay hotspot and other information to overview the location of latest hotspot and its surrounding through the Viwer Client system in which multiple data are combined. As of now, this prototype system can be accessed freely with web browser via WWW (http://fire.tksc.jaxa.jp/fms/index.php)

3. Future Prospects

Further study of data providing services using this prototype WMS is in planning phase to promote regional application of Earth observation satellite data and geo-spatial data for effective use of archived data in CEReS and in JAXA. Interoperable Web GIS system has a possibility of expanding database infrastructure in the Internet in a distributed way, and furthermore, has a potential of expanding data providing services using geo location information.

References

[1] OpenGIS Consortium Inc. Oct. 17, 2001, web Feature Server Implementation Specification version 0.0.14

[2] OpenGIS Consortium Inc. Apr. 4, 2002, web Map Server Implementation Specification version 1.1.0

Authors Index

CEReS

(February 2004)